Characterization and Activation of Bioinspired Peroxomanganese(III) Complexes

By

Hannah E. Colmer

Submitted to the graduate degree program in Chemistry and the Graduate Faculty of the University of Kansas in partial fulfillment of the requirements for the degree of Doctor of Philosophy.

_____

Chairperson: Dr. Timothy A. Jackson

_____

Dr. Mikhail V. Barybin

_____

Dr. Ward H. Thompson

_____

Dr. James D. Blakemore

_____

Dr. Juan J. Bravo-Suarez

Date Defended: April 19, 2016

The Dissertation Committee for Hannah E. Colmer

certifies that this is the approved version of the following dissertation:

Characterization and Activation of

Bioinspired Peroxomanganese(III) Complexes

_____

Chairperson: Dr. Timothy A. Jackson

Date approved: April 27, 2016

Abstract

Many biochemical reactions critical for life require catalysis by manganese-containing enzymes that react with dioxygen or its reduced forms to generate manganese-oxo, peroxo, or hydroxo intermediates. These reactions are prevalent throughout nature and include the synthesis of DNA by ribonucleotide reductases, free radical detoxification by superoxide dismutases, and metabolic pathways catalyzed by cytochrome P450 enzymes. Peroxomanganese(III) intermediates are proposed in many of the catalytic cycles that are governed by manganese-containing enzymes, and are often precursors to high-valent active oxidant species that are capable of substrate oxidation. While there have been successful synthetic models of the active sites of many enzymes, the factors that direct the reactivity of these peroxomanganese(III) intermediates are not well defined. In particular, the electronic and geometric effects of the supporting ligand system on the reactivity of peroxomanganese(III) species are poorly understood. To characterize the geometric structures and inherent reactivity of these intermediates, low-temperature spectroscopic techniques have been utilized, including electronic absorption, electron paramagnetic resonance (EPR), magnetic circular dichroism (MCD), and X-ray absorption spectroscopy (XAS). In addition, these complexes and their reactivity have been computationally explored through density functional theory (DFT), time-dependent DFT (TD-DFT), and multi-reference *ab initio* computations.

A Mn^{III}-peroxo species supported by the neutral, cross-clamped Me_2EBC ligand was prepared and spectroscopically and computationally characterized. The reactivity of the $[Mn^{III}(O_2)(Me_2EBC)]^+$ species with redox-active Mn^{II} was explored and found to display unique reactivity compared to other Mn^{III}-peroxo species by generating mononuclear high-valent products and avoiding dinuclear product formation. This reactivity is reminiscent of the catalytic cycle observed in enzymatic systems and is the one of the few examples of activation of a Mn^{III}-

peroxo species to mononuclear, high-valent intermediates. Additional reactivity studies of $[Mn^{III}(O_2)(Me_2EBC)]^+$ were explored, including activation by the addition of protons from Brønsted acids, hydrogen atom addition from electrophilic substrates, and modulation of the electron density of the Mn^{III}-peroxo moiety through Lewis acid addition.

A trispyrazolylborate scorpionate-type ligand (Tp^{Ph2}) was used to support a stable Mn^{III}-peroxo species that was characterized by spectroscopic and computational methods. The $[Mn^{III}(O_2)(Tp^{Ph2})(THF)]^+$ complex displays a blue-shift in the lowest energy transition compared to other Mn^{III}-peroxo species, and this shift was determined to be a result of an axial bond elongation that stabilized the donor MO in this transition. Perturbations in the electronic structure of this Mn^{III}-peroxo species and two isomers of the related $[Mn^{III}(O_2)(Tp^{iPr2})(pz^{iPr2}H)]$ species were explored through TD-DFT and multireference *ab initio* computations.

Controlling O—O bond reactivity is a critical step in the modulation of the activation of Mn^{III}-peroxo species, but there are few successful studies in this area. A Mn^{III}-peroxo species supported by a pentadentate, N_4O^- ligand was electrochemically formed and displayed reductive activation that was controlled by the strength acid added to the reaction. In the presence of a strong acid, Mn—O bond cleavage with generation of H_2O_2 occurred; but in the presence of a weak acid, O—O bond cleavage was observed. The mechanism of O—O bond activation in Mn^{III}-peroxo species supported by the N_4O^-, Me_2EBC, and TMC ligands was explored by DFT calculations, and the role of the ligand in in the reductive activation process was evaluated. These calculations indicate that a stable supporting framework with a moderate amount of steric bulk is optimal for the reductive activation of Mn^{III}-peroxo species.

In addition to characterization and reactivity of Mn^{III}-peroxo species, this work also contributes to the investigation of Mn^{III} complexes with unusual spin states. While most Mn^{III} complex are high-spin (S=2), several low-spin (S=1) Mn^{III} species supported by

trispyrazolylborate scorpionate-type ligands (Tp, Tp*) and a related N-heterocyclic carbene ligand were evaluated spectroscopically and computationally. The effect of the ligand in stabilizing these unusual spin states was examined through variable-temperature variable-field MCD spectroscopy and multireference *ab initio* calculations. While there are few methods available to treat the potentially orbitally-degenerate ground state of these low-spin Mn^{III} complexes, NEVPT2/CASSCF computations were used to successfully reproduce the experimental zero field splitting parameters of these complexes. The results from these studies determined that a shift in the lowest lying triplet state is a result of strong σ-donation from the ligand.

In many enzymatic catalytic cycles, metal-peroxo intermediates are precursors to the active metal-oxo species, and these metal-oxo species display high specificity for product distribution in substrate oxidation. While there are synthetic Mn^{IV}-oxo model species that display substrate reactivity, it is an ongoing investigation to replicate the controlled specificity present in enzyme systems. Two model complexes, $[Mn^{IV}(OH)_2(Me_2EBC)]^{2+}$ and $[Mn^{IV}(O)(OH)(Me_2EBC)]^{+}$ differ only by one proton and are able to the direct the reaction with DHA to desaturated and hydroxylated products, respectively. To determine the fundamental parameters directing this reactivity, DFT calculations of hydrogen atom transfer, as well as the product formation steps, were performed for both Mn^{IV} species with DHA.

Acknowledgements

Most importantly, I want to thank my research advisor, Professor Tim Jackson. Thank you for teaching me, not just about chemistry, but how to think critically, tackle problems, and how to be confident as a scientist. Thank you for being supportive and believing in me throughout this process. I have learned so much from you about what it means to be a good teacher and mentor, both in the lab and the classroom, and I will take these lessons with me for the rest of my career. Thank you for being patient and understanding while still pushing me to do my best and strive for excellence. I could not imagine a better Ph.D. advisor, and I am thankful to have been a part of the Jackson group.

To Professor Misha Barybin, thank you for all of your assistance and helpful conversations over the years. I have enjoyed being a TA for your general chemistry class, and I have learned so much from watching you teach. You make the chemistry department at KU a fun place, and I'm so glad to have worked with you. Professor Ward Thompson, thank you for helping me get started as a graduate student at KU. I enjoyed being in classes you taught, whether as a student or as a TA for your class. I learned a lot of great teaching ideas (and jokes!) from your classes, and I am thankful to the opportunity to work with you. To the rest of my committee, Professor James Blakemore and Professor Juan Bravo-Suarez, thank you for being on my committee and taking the time for my dissertation and defense. Thank you to my undergraduate research advisor, Professor Christine Aikens at Kansas State University, for encouraging me to go to graduate school and for being an incredible mentor. I want to thank everyone with the Chemical Biology Training Grant, especially Professors Audrey Lamb, Paul Hanson, and Tom Prisinzano. I had so many opportunities to broaden my horizons through this grant, and I am thankful for the chance to participate. Thanks to Dr. Roderick Black, for many helpful conversations about teaching, and for always remembering that I like to teach. Many

thanks to Dr. Justin Douglas for countless hours of assistance with EPR experiments, and to Dr. Erik Farquhar at Case Western Reserve University for exceptional assistance with XAS experiments as NSLS and SSRL.

To all of the past and present members of the Jackson group, thank you for teaching me and walking with me through this journey. Gayan, we both grew so much as graduate students in our four years of working together, and I learned so much from you about research and how to be a good leader. I will always appreciate your kindness and all of the fun times in the lab. Domenick, thank you for teaching me techniques in the lab and for the many helpful conversations. Amanda, I will always remember how you encouraged me to join the group and were so supportive during my first year. Thank you for your encouragement and friendship. Melissa, I can't imagine life this last year if you hadn't joined the group. You have been such a good buddy, and I'm so thankful for your friendship. Keep at it, and don't let anyone tell you you're too sassy. Allyssa, thanks for all of the wonderful chats and afternoon caffeine runs. You have made the last few years more fun. Derek, thanks for all of the helpful conversations- I was so excited when you joined the group to have another graduate student who loved computational chemistry too. Josh(y), you are just a gem, and you are always able to brighten my day. Thanks for all of the fun. To Aruna and Ashlie, it's fun to see you grow, and I wish you all the best! Andrew, it's been fun to work together these last few years- it seems like just yesterday you were a freshman starting research in the lab. To all of the wonderful undergraduates that I have worked with, Shannon, Anthony, and Nicci, thanks for working with me, putting up with me, and for teaching me so much.

To the amazing support group of graduate students, Mary, Theresa, Jess, and everyone in the Barybin group, thanks for making KU a great place to work. I would not have made it through the last five years without all of the lunch dates, coffee breaks, and encouragement from

all of you. Drew, you were one of the first people I met at KU, and I will never forget your kindness.

To my loving parents, Chuck and Linda, thank you for always believing in me and supporting me through this long process, even when it seemed kind of crazy. To my siblings, Katie and Daniel, thanks for listening to me complain, for encouraging me, and for being so supportive. To all of my grandparents, Kimi, Charles, and Edith, your hard work has always inspired me to be the best I can be, and I'm grateful for your example. To my wonderful in-law family, George, Cheri, Leah, Jordan, Laura, Ryan, Emma, and Matt, I never imagined what an amazing family I'd marry into. You have always been so supportive of me. Thanks to all my little nieces and nephews, Nathan, Lucy, Selah, Sonny, and baby girl arriving soon, for showing me how happy life can be. Thanks to wonderful friends, Tim and Becca, for being loyal friends, and for always checking up on me. To all of my wine night girls, Kathryn, Joanne, Michelle, Bridget, and Megan, thanks for listening to me, for understanding when I would disappear for weeks at a time to work, and for being the best friends I could ask for. Thanks to all of my fur babies, Willie, Sunny, Jake, and Einstein, for providing the unconditional love of a pet.

Finally, thank you to my husband and best friend, David. Graduate school has seen us through our engagement, wedding, and first three years of marriage. You have walked with me through the good and the bad times, through all of the crazy and the mundane. You have kept me grounded, you have been my peace when things got stressful, and you have encouraged me and cheered me on when I've struggled. I couldn't have done any of this without you. Thanks for going on this journey with me, and I'm excited to see where life takes us next.

Table of Contents

Abstract iii
Acknowledgements vi
Table of Contents ix
Abbreviations and Acronyms xi

Chapter 1. Biological Significance of the Activation of Mn^{III}-peroxo Intermediates

1.1 Introduction 2
1.2 Reactivity of Nonporphyrinoid Mn^{III}-peroxo Intermediates 9
1.3 O—O Bond Activation by Redox Active Mn Centers 11
1.4 Acid-assisted Mn^{III}-peroxo Reactivity 14
1.5 Reactivity of $[Mn^{III}(O_2)(H_3bupa)]^-$ with Electrophilic Substrates 15
1.6 Reactivity with Lewis Acids. 17
1.7 References 19

Chapter 2. Formation, Characterization, and O—O Bond Activation of a Peroxomanganese(III) Complex Supported by a Cross-Clamped Cyclam Ligand

2.1 Introduction 25
2.2 Experimental Section 28
2.3 Results and Analysis 34
2.4 Discussion 55
2.5 Conclusions 62
2.6 References 62

Chapter 3. Activation of a Mn^{III}-peroxo Intermediate by Brønsted Acid, Electrophilic Substrates, and Lewis Acids

3.1 Introduction 69
3.2 Experimental Section 71
3.3 Results and Analysis 74
3.4 Discussion and Outlook 87
3.5 References 88

Chapter 4. Geometric and Electronic Structure of a Peroxomanganese(III) Complex Supported by a Scorpionate Ligand

4.1 Introduction 90
4.2 Experimental Section 93
4.3 Results and Analysis 99
4.4 Discussion 119
4.5 Conclusions 122
4.6 References 123

Chapter 5. **Mechanisms of O—O Bond Cleavage in Mn^{III}-peroxo Intermediates by Electrochemical Methods**

5.1 Introduction 127
5.2 Experimental Section 132
5.3 Results and Analysis 134
5.4 Discussion 144
5.5 Conclusions 148
5.6 References 148

Chapter 6. **Spectroscopic and Computational Investigation of Low-Spin Mn(III) Bis(scorpionate) Complexes**

6.1 Introduction 151
6.2 Experimental Section 155
6.3 Results and Discussion 156
6.4 Conclusions 175
6.5 References 176

Chapter 7. **Oxidation Pathways of High-Valent Mn^{IV} Intermediates**

7.1 Introduction 180
7.2 Experimental Section 182
7.3 Results and Discussion 183
7.4 Conclusions and Outlook 202
7.5 References 205

Chapter 8. **Summary**

8.1 Summary 208
8.2 References 214

Appendix **A2.** 217
A3. 236
A4. 239
A5. 271
A6. 301
A7. 324

Abbreviations and Acronyms

Abs	absorption
DFT	density functional theory
DHA	9,10-dihydroanthracene
DCM	dichloromethane
DMF	dimethylformamide
DPH	diphenylhydrazine
CASSCF	complete active space self-consistent field
CV	cyclic voltammetry
EPR	electron paramagnetic resonance
ESI-MS	electrospray ionization mass spectrometry
EXAFS	extended X-ray absorption fine structure
HAT	hydrogen atom transfer
GOF	goodness-of-fit
*m*CPBA	*m*-chloroperoxybenzoic acid
MCD	magnetic circular dichroism
MHA	monohydroanthracene
MLCT	metal to ligand charge transfer
Mn RNR	manganese ribonucleotide reductase
Mn SOD	manganese superoxide dismutase
MO	molecular orbital
NEVPT2	second-order-*N*-electron valence state perturbation theory
NMR	nuclear magnetic resonance
NSLS	National Synchrotron Light Source
OEC	oxygen evolving center
PhIO	iodosobenzene

RNR	ribonucleotide reductase
SOD	superoxide dismutase
SSRL	Stanford Synchrotron Radiation Lightsource
TD-DFT	time dependent density functional theory
THF	tetrahydrofuran
TTBP	2,4,6-tri-*tert*-butylphenol
UV	ultraviolet
VTVH	variable temperature variable field
XANES	X-ray absorption near-edge structure
XAS	X-ray absorption spectroscopy
XRD	X-ray diffraction
ZFS	zero field splitting

CHAPTER 1

Biological Significance of the Activation of Mn^{III}-peroxo Intermediates

1.1 Introduction

The activation of dioxygen and its derivatives is a fundamentally critical reaction necessary for processes essential for life, including metabolism through the cytochrome P450 enzymes,[1,2] detoxification from free radicals by the superoxide dismutases (SOD),[3-7] and the synthesis of DNA from ribonucleotide reductases (RNR).[8,9] These vital biochemical reactions are catalyzed by metalloenzymes that react with dioxygen to form metal-peroxo and metal-oxo species in their catalytic cycles. Specifically, Mn-peroxo adducts are proposed to form in Mn SOD,[3-7] Mn RNR,[8,9] Mn oxalate oxidase[10,11] and oxalate decarboxylase.[12-14] While there has been spectroscopic detection and characterization of only a limited number these intermediates, it is not fully understood how these Mn-peroxo adducts can be activated to form reactive, high-valent, Mn—oxo species that are capable of powerful oxidation reactions, such as oxidation of a stable tyrosine radical essential for DNA synthesis by Mn RNR.[9] Other metal-peroxo species, such as an Fe—hydroperoxo species in cytochrome P450 enzymes, are precursors to reactive, high-valent Fe—oxo species that are able to perform oxidation of strong C—H bonds.[1,2,15] In recent years, there have been examples of successful generation and characterization of Mn^{III}-peroxo intermediates supported by model ligand systems,[16] however, both in model and enzymatic systems, the factors that direct the reactivity of these metal-peroxo intermediates are not well established. Specifically, it remains to be determined how to control the addition of electrons and protons to these systems to selectively promote the formation of high-valent, reactive oxidants from metal-peroxo intermediates.

1.1.1. Cytochrome P450 Paradigm. The cytochrome P450 enzymes provide a critical framework for understanding O—O bond activation by a controlled delivery system of electron and protons. P450 enzymes are prevalent across many biological kingdoms including mammals, bacteria, plants, yeast, and insects,[1,15,17] and are able to catalyze a diverse range of reactions such

as C—H hydroxylation, olefin expoxidation, amine dealkylation, thiol sulfoxidation, and halogenated alkane dehalogenation.[1,15,17] In the catalytic cycle of these enzymes, an iron-peroxo intermediate is activated to form a powerful, high-valent iron-oxo that is responsible for substrate oxidation. Mechanistic studies of this reactivity paradigm has proven useful in understanding the field of O—O activation for both enzymes and model complexes. While this superfamily of enzymes contains a diverse range of secondary structure and functions,[15] the typical active site of these enzymes contain an iron protoporphyrin IX in the active site pocket of the enzyme with an axial cysteine ligand and an open axial coordination site (Figure 1.1).[1]

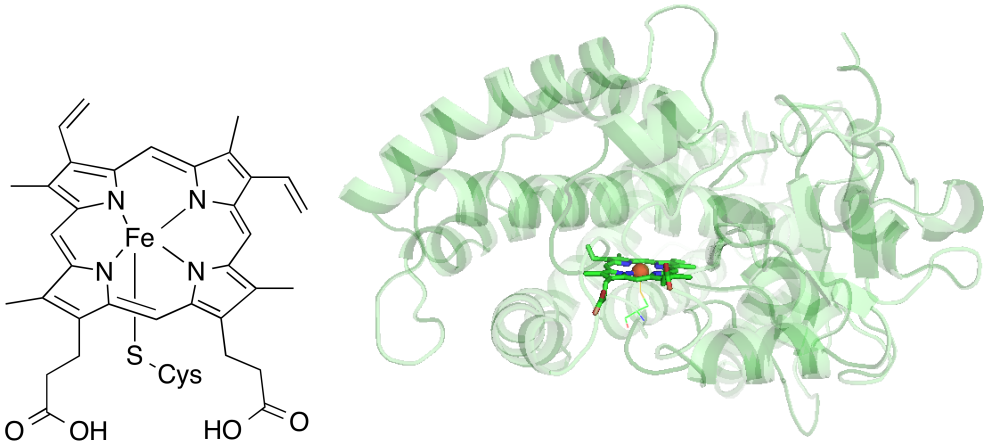

Figure 1.1. Typical cytochrome P450 active site[1] with a protoporphyrin IX and axial cysteine ligand (left) and $P450_{cam}$ crystal structure[18] with heme active site (sticks) in hydrophobic pocket.

These and other metalloenzymes are responsible for the activation of dioxygen to perform synthetically difficult reactions to generate biochemically important substrates, such as the hydroxylation of fatty acids and biosynthesis of steroid molecules.[15,19] In the absence of a metal active site, the reaction of triplet dioxygen with a singlet substrate is spin-forbidden, and therefore, kinetically slow due to a high activation energy.[20] Reaction of the substrate with dioxygen requires a metalloenzyme to reduce this kinetic barrier through spin-orbit coupling by the metal center, facilitating a more rapid reaction for oxidation by molecular oxygen. The

reactivity of the P450 enzymes provides insight into the elementary steps of this process, highlighting the sophisticated controlled delivery of electrons and protons.

The catalytic cycle for C—H bond hydroxylation (Scheme 1.1) is initiated by substrate binding in the active site pocket, which contains a ferric iron resting state. Substrate binding prompts a spin state change from low-spin (S=1/2) to high spin (S=5/2) Fe^{III} to more easily facilitate electron transfer.[2] An electron transfer from NADP(H) takes place, reducing the Fe^{III} center to Fe^{II}, and dioxygen binds axially to the Fe^{II} center to form an Fe^{III}-superoxo species. Then, a second electron and proton transfer takes place to generate a nucleophilic Fe^{III}-hydroperoxo species. A second protron transfer to this hydroperoxo adduct results in heterolytic cleavage of the O—O bond with generation a molecule of water and the high-valent, Fe^{IV}-oxo species (Compound I) with a cation radical delocalized onto the porphyrin ring. This powerful Fe^{IV}-oxo species can then oxidize the adjacent substrate molecule. Release of the product returns the enzyme to its Fe^{III} resting state. An alternative "peroxide shunt" pathway involves reaction of the Fe^{III} species with a peroxide to bypass the intermediate steps and directly form the Fe^{IV}-oxo cation radical. Although there has been much debate about the identity of Compound I,[21,22] Green and coworkers were able to trap and spectroscopically and kinetically characterize Compound I by reacting the ferric enzyme from the thermophilic organism *Sulfolobus acidocaldarius* (CYP119) with the oxygen-atom donor *m*CPBA (*m*CPBA = *m*-chloroperoxybenzoic acid).[23]

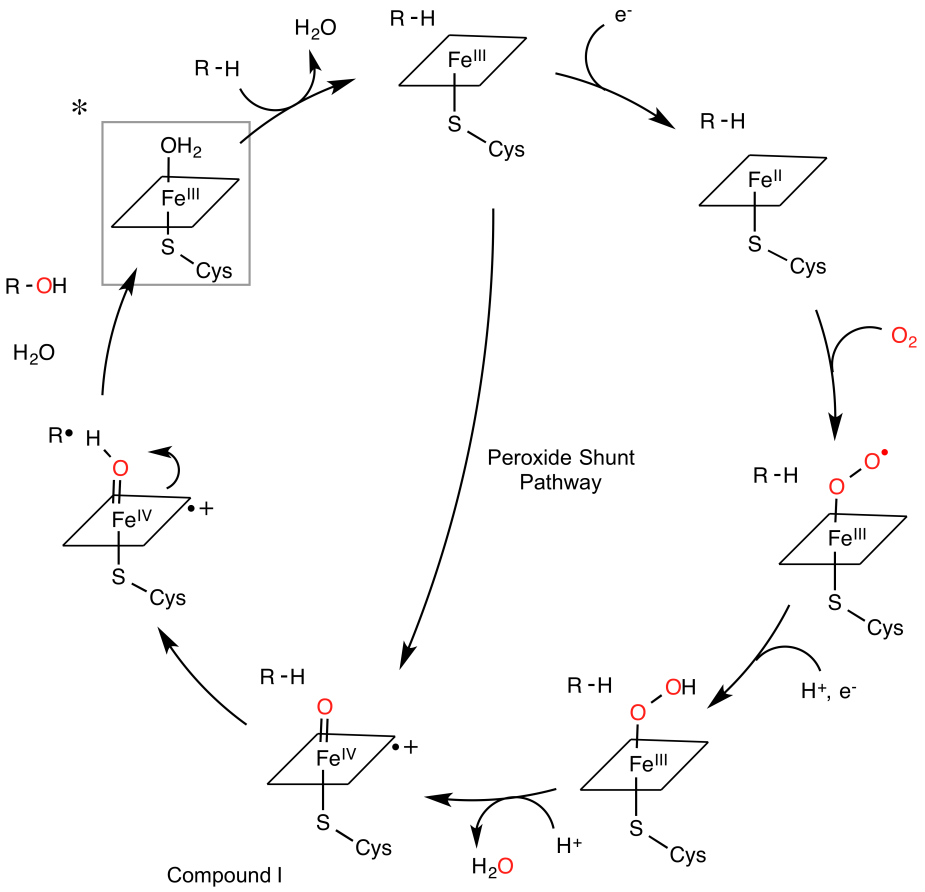

Scheme 1.1. Catalytic cycle for cytochrome P450 enzymes. The Fe resting state of the enzyme is the species in the grey box indicated by the asterisk.

Initial support for the assignment of Compound I as an Fe^{IV}-oxo cation radical species came from work with synthetic porphyrin model systems. The first Fe-oxo species was generated by Groves and coworkers with the porphyrin-type TMP ligand (TMP = meso-tetramesityl porphinate anion; see Figure 1.3). This species was prepared from the [Fe^{III}(Cl)(TMP)] species with oxidation by *m*CPBA at -78 °C. This species was found to contain an Fe^{IV}-oxo cation radical that was extensively characterized with electronic absorption, EPR, NMR, Mössbauer, and Fe K-edge extended x-ray absorption fine structure (EXAFS) spectroscopy.[24-28] In addition to possessing similar characterization features, this and other complexes also showed reactivity of alkane hydroxylation[29] and olefin epoxidation.[24,30] Since Grove's initial Fe-oxo complex,

numerous other Fe-oxo species have been generated supported by porphyrin based ligands,[31,32] macrocyclic ligands,[33-38] and tripodal and tetrapodal chelate ligands.[39-45] These model species contain a large variety of structural diversity, but it remains an ongoing challenge to mimic P450 enzymes and generate efficient catalysts capable of sterospecific and selective oxidations. However, these model complexes, as well as the P450 enzymes themselves, have provided a basis of understanding of O—O bond reactivity and the activation of dioxygen and it's reduced derivatives.

1.1.2. Manganese Analogs of P450 Reactivity. In addition to Fe-containing synthetic model complexes, the reactivity of dioxygen with Mn complexes supported by porphyrin-based ligands has also been explored. Groves and coworkers expanded the use of the porphyrin-based TPP (TPP = tetraphenylporphyrin) and TMP ligands that contain a porphyrin base with substitutions at the four *meso* carbon positions (Figure 1.2). Groves expanded work with this ligand from Fe to Mn chemistry, forming Mn-peroxo and –oxo intermediates.[46,47] These complexes are also able to perform selective C—H bond halogenations.[48] Further modification of the porphyrin moiety at the *meso* carbons resulted in the TDMImP and other derivatives (Figure 1.2).[49] A Mn^{IV}-oxo species supported by the TDMImP ligand was observed by stopped-flow spectroscopy. However, intermediates supported by these porphyrin ligands have proven to be difficult to characterize due to their reactive nature.

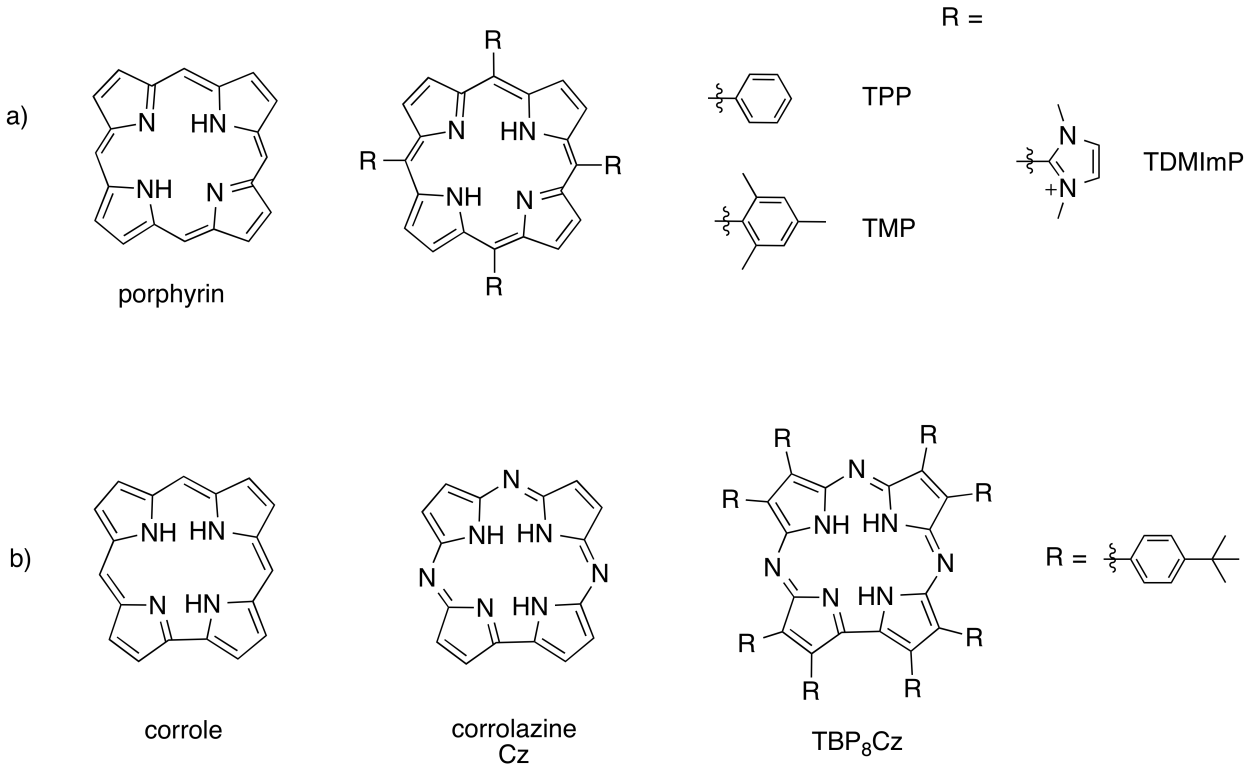

Figure 1.2. Ligand used in Mn model complexes, a) porphyrinoid ligands and b) corrole and corrolazine ligands.

In an effort to stabilize these highly reactive intermediates for characterization and more fully investigate their structure and reactivity, the porphyrin-based core of the ligand has also been modified. Goldberg and coworkers have had success in this area with the porphyrinoid corrole and corrolazine ligands (Figure 1.2).[50] Initial work was performed with the corrole ligand with a ring contraction at a *meso* carbon atom in the porphyrin framework; however, difficult syntheses limited the success and scope of this ligand. Further ligand modifications afforded the more synthetically accessible corrolazine ligand, with a ring-contraction at the *meso* carbon atom in addition to the incorporation of three *meso* nitrogen atoms.[51] A Mn^{III} species supported by the four-coordinate $(TBP_8)Cz$ corrolazine ligand (Figure 1.2) was generated with axial coordination of a methanol molecule or a neutral or anionic ligand.[52,53] Upon reaction of the $[Mn^{III}(TBP_8)Cz]$ complex with PhIO at room temperature, a stable terminal Mn^{V}-oxo species was formed.[52,54]

This species displayed unique stability and ease of purification, and was thoroughly characterized by NMR, resonance Raman, XANES and EXAFS techniques.[52,54]

More recently, an alternative preparation of this high-valent Mn^{V}-oxo species was achieved by reaction with dioxygen and visible light in the presence of a C—H substrate. Not only does this reaction represent one of the few examples of the formation of a high-valent Mn-oxo without using powerful chemical oxidants, but this reaction was also found to be catalytic in the presence of strong proton donors.[55] The $[Mn^{III}(TBP_8Cz(H)]^+$ complex requires protonation of two of the *meso* nitrogen atoms for catalytic activity; in the absence of the proton donors, the complex reacts stoichiometrically.[55] Additionally, transient absorption studies showed that the O_2-reactive form of the complex was an excited state of $[Mn^{III}(TBP_8Cz(H)]^+$.[56] The proposed catalytic cycle (Scheme 1.2) for the reaction of the excited state of $[Mn^{III}(TBP_8Cz(H)]^+$ with dioxygen and 2 equiv. H^+ first generates a Mn^{IV}-superoxo intermediate. This species abstracts a hydrogen atom from the hexamethylbenzene (HMB) substrate with a BDFE (C—H) = 83.2 kcal/mol,[57] leaving a Mn^{IV}-hydroperoxo species and a HMB radical. The Mn^{IV}-hydroperoxo species undergoes homolytic O—O bond cleavage to form the Mn^{V}-oxo and a hydroxylated substrate molecule. In the presence of excess H^+, the Mn^{V}-oxo oxidizes the substrate molecule and forms the resting state Mn^{III} species.[55,58] This reactivity is reminiscent of that observed in the cytochrome P450 catalytic cycle, and illustrates that similar O—O bond reactivity can be achieved with a Mn center with a modified porphyrin-based ligand.

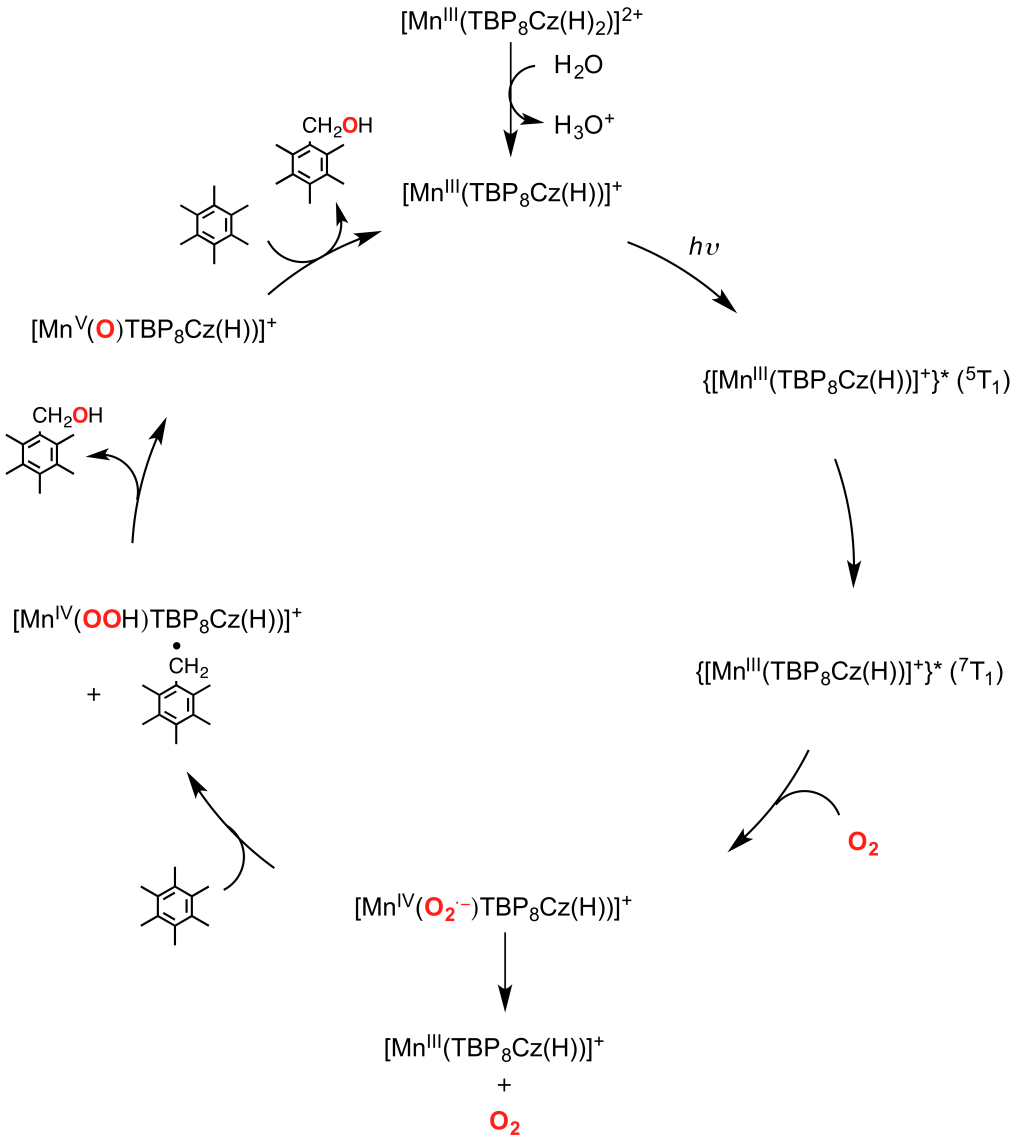

Scheme 1.2. Catalytic reactivity of $[Mn^{III}(TBP_8Cz(H)]^+$ with dioxygen and HMB in the presence of acid.

1.2 Reactivity of Nonporphyrinoid Mn^{III}-peroxo Intermediates

An ideal ligand scaffold for defining the electronic structure and reactivity of these Mn-oxygen intermediates is one that maintains an appropriate balance of stability and reactivity. It is necessary to utilize a ligand system that stabilizes reactive Mn-peroxo and Mn-oxo intermediates long enough to be trapped and characterized, while simultaneously allowing the reactivity of the complex to be explored. In an effort to achieve this balance of stability and reactivity, model

systems that support Mn^{III}-peroxo species have expanded beyond the framework of the porphyrin core.[16] There have been many successful efforts to generate model Mn^{III}-peroxo intermediates with a variety of non-porphyrinoid ligands,[16,59] but it remains an ongoing challenge to sustain the fundamental reactive nature of the Mn^{III}-peroxo moiety while stabilizing intermediates for characterization. In particular, few cases have been observed of activation of the Mn^{III}-peroxo to high-valent oxidants. These model complexes aim to illuminate the factors that drive Mn^{III}-peroxo reactivity and formulate a structure-function relationship. A mechanistic understanding of the activation of these Mn^{III}-peroxo species to reactive, mononuclear, high-valent Mn species is of particular interest in the fields of industrial catalysis as well as enzyme mechanisms.

Mn^{III}-peroxo species are characteristically nucleophilic and participate in aldehyde deformylation reations with attack of the Mn^{III}-peroxo on an aldehyde molecule and formation of an oxidized substrate (Scheme 1.3).[60] This process is driven by the large amount of negative charge residing on the Mn^{III}-peroxo moiety. Mn^{III}-peroxo species supported by ligands with a wide variation of structural features have shown this characteristic reactivity. These ligands include neutral macrocyclic ligands (TMC and 13-TMC),[61-63] neutral aminopyridyl ligands ($L^7py_2^R$ and $L^8py_2^R$),[64] and anionic tripodal ligands with a hydrogen bonding scaffold (H_3bupa^{2-} and H_2bpaa^-).[65-67] Axial ligand effects have been shown to affect the rate of the aldehyde deformylation reaction. For Mn^{III}-peroxo species supported by the macrocyclic TMC-based ligand, a series of axial ligands (N_3^-, $CF_3CO_2^-$, $OOCCF_3$, NCS^-, and CN^-) with the $[Mn^{III}(O_2)(13\text{-TMC})]^+$ complex were studied. These *trans* axial ligands increased the rate of aldehyde deformylation by promoting increased nucleophilicity of the peroxo moiety.[61-63] Another consequence of axial ligand binding bears resemblance to heme systems[68,69] by pulling the Mn ion down into the plane of the ligand, introducing stronger steric effects and promoting end-on coordination of the peroxo moiety. Another structural correlation study was performed with

Mn^{III}-peroxo species supported by a series of derivatives of the neutral, aminopyridyl $L^7py_2^R$ ligands.[64] Here, the bulk around the peroxo moiety was varied with R = H, 6-Me, 4-Me and the L^8py^H ligands. Although it was not as dramatic an effect as for the axial ligand substitutions, as the steric hindrance around the peroxo unit increased, the rate of deformylation decreased. However, in other cases, large steric bulk did not hinder aldehyde deformylation. A Mn^{III}-peroxo species supported by the bulky, tripodal H_3bupa^{2-} ligand designed by Borovik and coworkers also displays deformylation activity, although in that case, the bulky ligand also supplies a hydrogen bonding network about the peroxo moiety that is known to interact with the Mn^{III}-peroxo unit.[65-67]

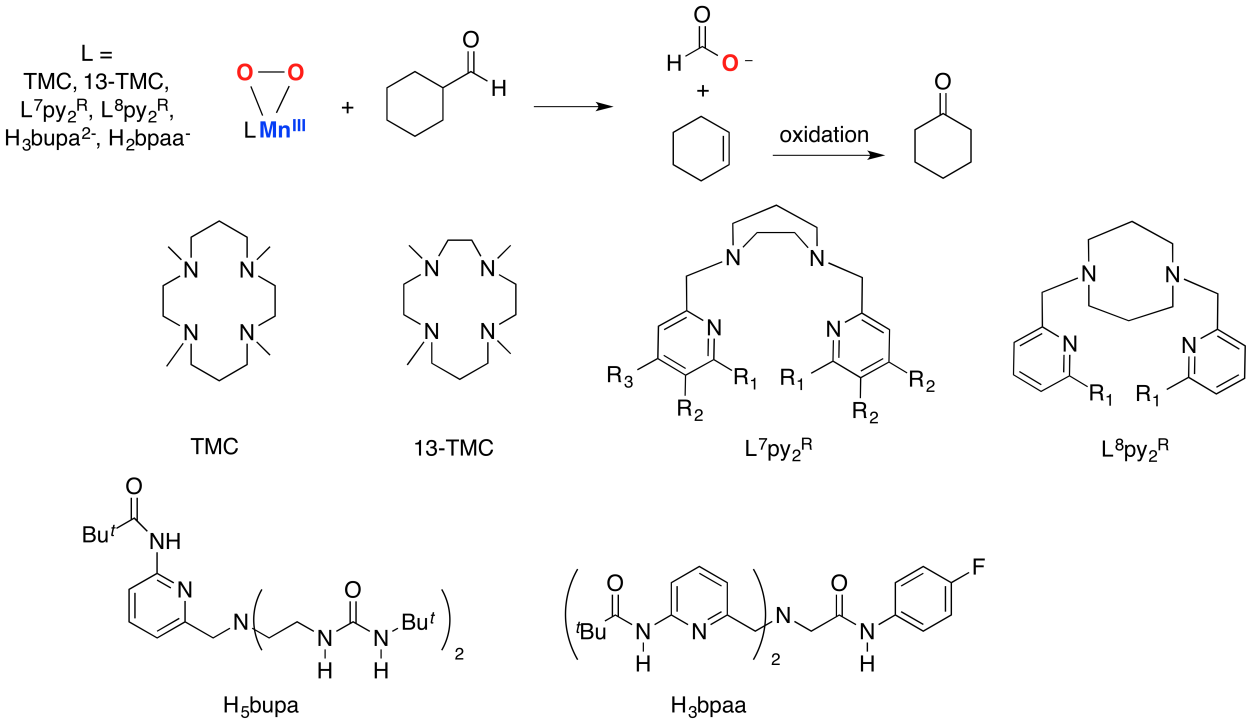

Figure 1.3. Aldehyde deformylation by Mn^{III}-peroxo species.

1.3 O—O Bond Activation by Redox Active Mn Centers

More recently, other types of reactivity more reminiscent of the activation observed in the P450 cycle have been explored. However, activation of Mn^{III}-peroxo species to mononuclear,

high-valent intermediates has proven to be challenging. There are limited reports of activation to high-valent species, with only a handful of examples of activation to form dinuclear oxo-bridged $Mn^{III}Mn^{IV}$ species.[70,71] Even fewer studies exist of activation of Mn^{III}-peroxo species to mononuclear, high-valent oxidants, and isolation and characterization of these species has been difficult. To activate the Mn^{III}-peroxo bond, a two electron reduction process must occur to break the O—O bond. Additionally, the Mn—O bond can also be broken. It is of great interest, both for catalytic as well as biological applications, to define reaction conditions and ligand systems that promote the formation of powerful, mononuclear species that are able to perform oxidation chemistry, but this challenge is ongoing. In general, a controlled delivery of electrons and protons to the Mn^{III}-peroxo moiety is critical for clean conversion. To achieve this, parameters such as ligand support, reduction potential, and potential outer sphere electron transfer must be considered. In several cases,[70,71] reduction and activation of the Mn^{III}-peroxo species has been facilitated by reaction with Mn^{II} or Mn^{III} complexes.

1.3.1. Reactivity of $[Mn^{III}(O_2)(N4py)]^+$ with $[Mn^{II}(OTf)(N4py)]^+$. The pentadentate N4py ligand (Figure 1.4) has been used to support a Mn^{III}-peroxo species formed from Mn^{II} and KO_2.[71] The N4py ligand is more flexible with multiple binding modes possible with potential dissociation of a pyridine constituent. The Mn^{II} starting complex exists as a five coordinate complex $[Mn^{II}(OTf)(N4py)]^+$ with a triflate ion completing the sixth coordination site in octahedral geometry.[72,73] Leto *et al.* demonstrated that upon binding of the side-on η^2-O_2 ligand to form the Mn^{III}-peroxo species, there is dissociation of one pyridine arm to give tetradentate κ^4-N4py ligand binding. The $[Mn^{III}(O_2)(N4py)]^+$ species reacts with an equiv. of $[Mn^{II}(OTf)(N4py)]^+$ to generate a dinuclear oxo-bridged $Mn^{III}Mn^{IV}$ product (Figure 1.4). This proposed pathway for this reaction is through a μ-peroxodimanganese(II,III) intermediate that

undergoes O—O bond cleavage and generates the bis(μ-oxo)dimanganese(III,IV) oxidized species. This dinculear product retains the tetradentate N4py ligand binding and was extensively characterized by EPR, MCD, variable-temperature variable field MCD (VTVH-MCD), and Mn K-edge XAS, and XRD.[71] While this work did not form a mononuclear, high-valent oxidant, it offered insight into activation pathways resulting in dinuclear species, which mimics the chemistry of Mn ribonucleotide reductases.[9]

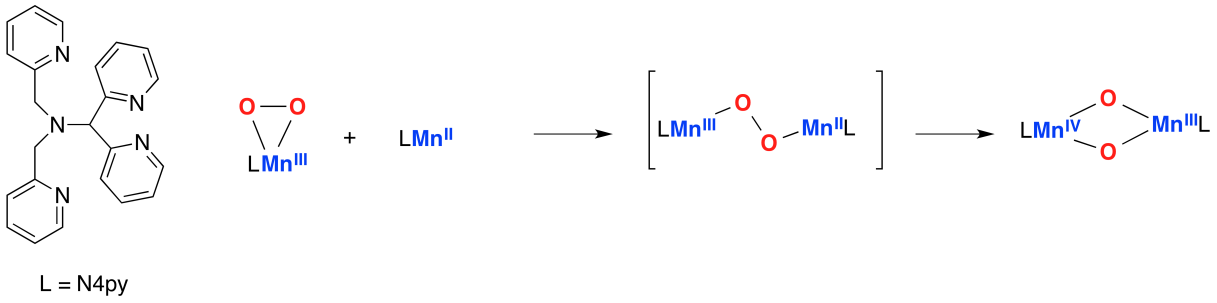

Figure 1.4. Reactivity of the $[Mn^{III}(O_2)(N4py)]^+$ intermediate with $[Mn^{II}(OTf)(N4py)]^+$.

1.3.2. Reactivity of $[Mn^{III}(O_2)(mL_5^2)]^+$ with $[Mn^{III}(OH_2)(mL_5^2)]^{3+}$. Another Mn^{III}-peroxo complex that exhibits reactivity with other redox active metals centers is the $[Mn^{III}(O_2)(mL_5^2)]^+$ species that is supported by the aminopyridyl, pentadentate mL_5^2 ligand (Figure 1.5).[70] Unlike the Mn^{III}-peroxo species supported by N4py ligand that is generated with KO_2, this Mn^{III}-peroxo adduct is formed from the addition of H_2O_2 to $[Mn^{II}(mL_5^2)]^{2+}$. This ligand system bears strong resemblance to the N4py ligand with tetradentate binding of the ligand with the dissociation of one pyridylmethyl arm in the side-on Mn^{III}-peroxo complex. While there are structural similarities between the N4py and mL_5^2 ligands, there are marked differences in their reactivities as well. In basic, aqueous solution, the $[Mn^{III}(O_2)(mL_5^2)]^+$ complex reacts with $[Mn^{III}(OH_2)(mL_5^2)]^{3+}$ to presumably form a μ-peroxodimanganese(III,III) intermediate. This species then undergoes O—O bond cleavage and a one-electron reduction to form a dinuclear

oxo-bridged $Mn^{III}Mn^{IV}$ product (Figure 1.5). In acidic conditions, this dinuclear pathway does not occur as formation of the oxo bridges is unfavorable, and oxidation of the ligand is observed instead.

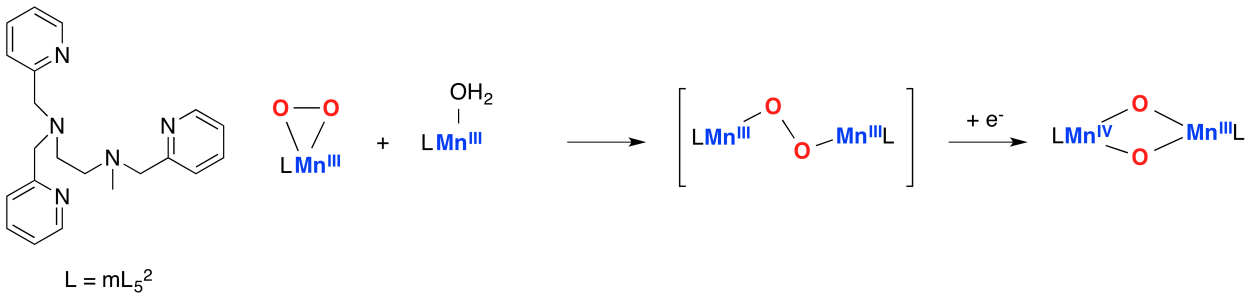

Figure 1.5. Reactivity of the $[Mn^{III}(O_2)(mL_5^2)]^+$ intermediate with $[Mn^{II}(mL_5^2)]^{2+}$.

1.4 Acid-assisted Mn^{III}-peroxo Reactivity

In addition to reactivity by redox active metal centers, acid-assisted activation of Mn^{III}-peroxo units has also been observed. Acidic conditions could potentially cause the protonation of the Mn^{III}-peroxo moiety to generate a Mn^{III}-hydroperoxo species similar to the precursor species to Compound I in the P450 catalytic cycle (Scheme 1.1). Attempts to control the reactivity of the Mn^{III}-peroxo species have been successful with the neutral, macrocyclic TMC ligand.[74] Activation by acidic conditions has been attempted with other Mn^{III}-peroxo species, although achieving the appropriate balance of stability and reactivity to examine discernable reactivity has proven to be challenging.[16] The TMC ligand supports a Mn^{III}-peroxo species that undergoes protonation of the peroxo moiety in the presence of acid to form a Mn^{III}- hydroperoxo species. This is of great interest as a Fe^{III}-hydroperoxo complex is formed en route to the ubiquitous Fe^{IV}-oxo species in the catalytic cycle of cytochrome P450 enzymes. Developing methods to control the reactivity of Mn^{III}-peroxo species toward a Mn^{III}-hydroperoxo intermediate has proven to be challenging and, to date, there is only one example. Nam and coworkers used the macrocyclic

TMC ligand to support a Mn^{III}-peroxo species that has been extensively studied, both spectroscopically and structurally by X-ray crystallography.[61,62] A Mn^{III}-hydroperoxo species supported by the TMC ligand was generated by adding 3 equiv. of $HClO_4$ to $[Mn^{III}(O_2)(TMC)]^+$ at -40 °C in CH_3CN.[74] The Mn^{III}-hydroperoxo intermediate formed from this reaction was characterized by resonance Raman and Mn K-edge XAS spectroscopy. Additionally, the formation of the Mn^{III}-hydroperoxo is reversible upon the addition of 3 equiv. NEt_3 to the Mn^{III}-hydroperoxo to reform the Mn^{III}-peroxo species. The Mn^{III}-hydroperoxo intermediate displayed different reactivity from the nucleophilic Mn^{III}-peroxo species. While the Mn^{III}-hydroperoxo species did not display hydrogen atom transfer (HAT) reactivity, it was able to perform sulfoxidation reactions with a set of *para*-substituted thioanisoles. This oxygen atom transfer (OAT) reactivity is in agreement with the expected electrophilic character of a Mn^{III}-hydroperoxo species.

1.5 Reactivity of $[Mn^{III}(O_2)(H_3bupa)]^-$ with Electrophilic Substrates

Borovik and coworkers have developed an anionic, tripodal ligand system (H_3bupa^{2-}) that is able to sustain a cavity with an intramolecular hydrogen bonding network and can support a Mn^{III}-peroxo in in this cavity.[65-67] This Mn^{III}-peroxo species provides insight into two new areas for Mn^{III}-peroxo reactivity. First, this Mn^{III}-peroxo species can be generated utilizing dioxygen as an oxidant, instead of harsh chemical oxidants such as H_2O_2 or KO_2. This complex is able to convert dioxygen to water at room temperature. Second, the activation of this Mn^{III}-peroxo intermediate is achieved by the addition of an electrophilic substrate, diphenylhydrazine (DPH). This substrate provides an excellent means to provide a controlled delivery of electrons and protons necessary for the activation of the Mn^{III}-peroxo species. The $[Mn^{III}(O_2)(H_3bupa)]^-$ intermediate is formed from the reaction of $[Mn^{II}(H_2bupa)]^-$ with dioxygen and 0.5 equiv. of

DPH at room temperature.[66,67] Presumably, the Mn^{III}-peroxo forms via formation of a Mn^{III}-superoxo intermediate, although this species is not experimentally observed. With an η^2-O_2 ligand, the carboxyamido group in the hydrogen bonding cavity of the ligand extends a hydrogen bond to the peroxo unit. The Mn^{III}-peroxo is activated by the delivery of two hydrogen atoms from another equiv. of DPH that promotes O—O bond cleavage of the peroxo (Figure 1.6). This formally generates a $[Mn^{III}(OH)_2(H_3bupa)]^-$ species that releases a molecule of H_2O and forms a Mn^{III} species. Borovik and coworkers described the Mn^{III} product as a hybrid Mn^{III}-O/OH complex. A crystal structure of this hybrid Mn^{III}-O/OH species reveals a short distance between the manganese-bound oxygen ligand and the nitrogen of the carboxyamido group of the ligand, indicating a strong hydrogen bonding interaction, although the positions of the hydrogen atom (*i.e.*, oxygen-bound or nitrogen-bound) is not well-defined in this structure. Additionally, the Mn—O bond length (1.822(4) Å) in the hybrid Mn^{III}-O(H) complex is intermediate between the Mn—O bond lengths previously observed for Mn^{III}-oxo and Mn^{III}-hydroxo species supported by the structurally related H_3buea ligand (1.780(5) and 1.872(2) Å, respectively, H_3buea = tris[(*N'*-*tert*-butylureaylato)-*N*-ethyl]aminato).[75] This system represents one of the only Mn^{III}-peroxo species to attain the controlled delivery of electrons and protons throughout the catalytic cycle as the P450 enzymes are able to do.

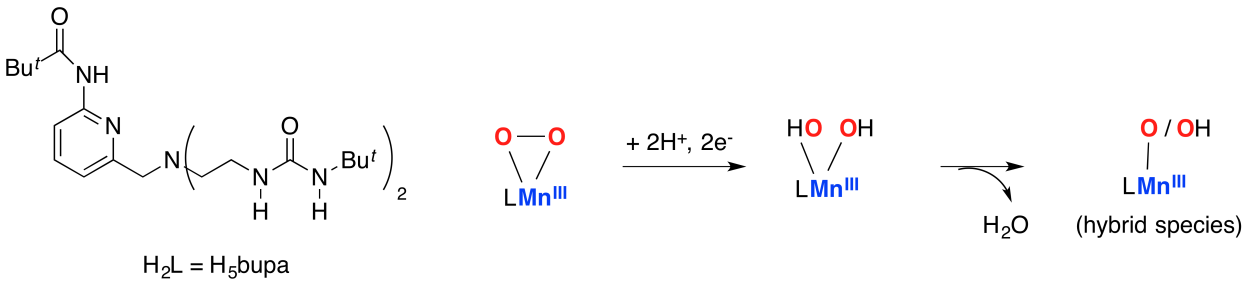

Figure 1.6. Reactivity of $[Mn^{III}(O_2)(H_3bupa)]^-$ with DPH.

1.6 Reactivity with Lewis Acids.

Transition metal complex reactivity with Lewis acid has long been an intriguing area for biological and catalytic communities due to the presence of a calcium ion in the catalytic active site, the oxygen evolving center (OEC) of the photosystem II enzyme.[76-78] Photosystem II has been explored and modeled due to its ability to efficiently split water into protons and dioxygen.[79] The role of this calcium atom in the OEC has been debated, and its complete role and function is not well understood. Recently, a 1.9 Å crystal structure of photosystem II showed the OEC as a Mn_4CaO_5 unit with a cubane structure consisting of three Mn atoms, four O atoms, and one Ca atom as the vertices of the cube. A dangling Mn—O from one of the Mn cube vertices completes the OEC structure (Figure 1.7).[76]

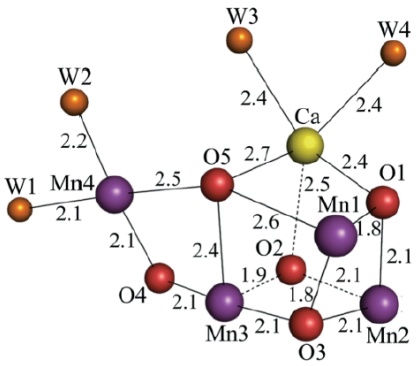

Figure 1.7. Crystal structure of the oxygen evolving center of Photosystem II.[76]

1.6.1. Mn Cluster Models of the OEC. Attempts to reproduce the structure and reactivity of the OEC have been explored through activation of transition metal complexes with Lewis acids.[33,80,81] Although activation of Mn^{III}-peroxo species by Lewis acids is an ongoing area of research, there have been important developments in the synthesis of model Mn clusters with Lewis acids designed to mimic the cubane structure of the OEC. Agapie and coworkers have generated a Mn_3CaO_4 cluster, characterized by XRD, that is supported by a rigid, triarylbenzene

ligand containing six pyridine and three alcohol groups.[82] The Mn_3CaO_4 structure displays similarity to the structure of the OEC, although it lacks the dangling Mn—O moiety. In the model complex, each Mn atom is in psuedo-octahedral geometry, with bridging oxido groups, and binds to an alkoxide and a pyridyl group from the ligand. Three oxides, three acetates, and a solvent molecule are coordinated to the Ca^{2+} atom. Although this and other, similar structures[83,84] provide insight into rational design of these clusters, it has been difficult to reproduce the reactivity of the OEC as well as define the complete role of the Lewis acid in the structure. Experiments investigating the reduction potential of the synthetic clusters suggest that the Lewis acid modulates the charge and reduction potential. If similar effects are employed by the OEC, this could stabilize the formation of high oxidation states and promote the production of dioxygen.[82,85] Although direct production of dioxygen from these synthetic Mn clusters has been evasive, oxygen atom transfer activity has been observed with a $Mn^{III}_2Mn^{IV}_2O_4Ca$ cluster.[83]

1.6.2. Fe^{III}-peroxo Activation by Lewis Acids. Activation of the peroxo moiety by Lewis acids has recently been demonstrated with an Fe^{III}-peroxo complex supported by the TMC ligand. The stability and multiple modes of reactivity of the TMC ligand have been routinely demonstrated by the formation of important metal-oxygen intermediates in both iron and manganese systems.[61-63] In the field of Lewis acid activation, this ligand also provides an ideal framework to probe mechanistic reactivity. Recently, Que and coworkers were able to form and characterize an η^2-O_2 Fe^{III}-peroxo adduct activated by a Sc^{3+} ion.[86] Fe K-edge XAS studies indicate that the η^2-O_2 binding is retained upon reaction with Sc^{3+}, and generates an Fe^{III}-(μ-η^2:η^2-O_2)-Sc^{3+} adduct (Figure 1.8). The addition of this Lewis acid to the Fe^{III}-peroxo adduct triggered formation of the Fe^{IV}-oxo intermediate that has previously been generated from the $[Fe^{II}(TMC)(NCCH_3)]^{2+}$ complex by reaction with PhIO, or with dioxygen in the presence of H^+ and BPh_4^-.[87]

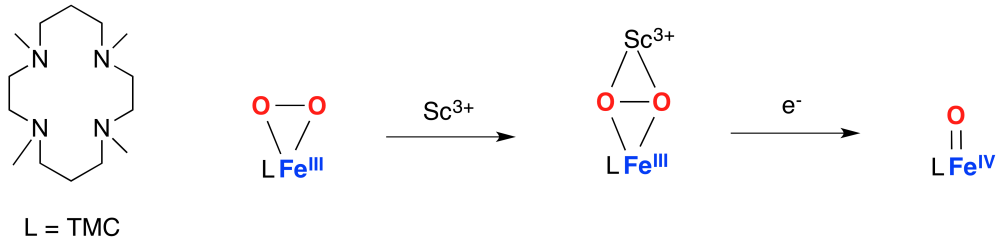

Figure 1.8. Adduct formed from $[Fe^{III}(O_2)(TMC)]^+$ with Sc^{3+}.

Nam and coworkers have also generated and characterized an Fe^{III}-peroxo supported by the TMC ligand that formed an adduct with Sc^{3+} as well as with Y^+.[88] Here, addition of the Lewis acid allowed for reaction with ferrocene as an electron donor and cleavage of the O—O bond, forming an Fe^{IV}-oxo. Although the exact mechanism of the activation is yet unknown, there is some neutralization of the large negative charge that the peroxo unit sustains. These alternative methods of formation of high-valent oxo species are exciting developments as they provide a pathway through peroxo intermediates that is reminiscent of the cytochrome P450 enzymes. Additionally, the activation of these peroxo species is uniquely facilitated by the presence of Lewis acid adducts, which is a promising area of reactivity for both Fe and Mn-peroxo chemistry.

1.7 References

(1) McLain, J. L.; Lee, J.; Groves, J. T. In *Biomimetic Oxidations Catalyzed by Transition Metal Complexes*; Meunier, B., Ed.; Imperial College Press: London, 2000, p 91-169.
(2) Meunier, B.; de Visser, S. P.; Shaik, S. *Chem. Rev.* **2004**, *104*, 3947-3980.
(3) Bull, C.; Niederhoffer, E. C.; Yoshida, T.; Fee, J. A. *J. Am. Chem. Soc.* **1991**, *113*, 4069-4076.
(4) Grove, L. E.; Brunold, T. C. *Comments Inorg. Chem* **2008**, *29*, 134-168.
(5) Hearn, A. S.; Stroupe, M. E.; Cabelli, D. E.; Lepock, J. R.; Tainer, J. A.; Nick, H. S.; Silverman, D. N. *Biochemistry* **2001**, *40*, 12051-12058.
(6) Jackson, T. A.; Karapetian, A.; Miller, A.-F.; Brunold, T. C. *Biochemistry* **2005**, *44*, 1504-1520.
(7) Miller, A.-F. *Curr. Opin. Chem. Biol.* **2004**, *8*, 162-168.
(8) Boal, A. K.; Cotruvo, J. A.; Stubbe, J.; Rosenzweig, A. C. *Science* **2010**, *329*, 1526-1530.

(9) Cotruvo, J. A. J.; Stich, T. A.; Britt, R. D.; Stubbe, J. *J. Am. Chem. Soc.* **2013**, *135*, 4027-4039.
(10) Borowski, T.; Bassan, A.; Richards, N. G. J.; Siegbahn, P. E. M. *J. Chem. Theory Comput.* **2005**, *1*, 686-693.
(11) Opaleye, O.; Rose, R.-S.; Whittaker, M. M.; Woo, E.-J.; Whittaker, J. W.; Pickersgill, R. W. *J. Biol. Chem.* **2006**, *281*, 6428-6433.
(12) Reinhardt, L. A.; Svedruzic, D.; Chang, C. H.; Cleland, W. W.; Richards, N. G. J. *J. Am. Chem. Soc.* **2003**, *125*, 1244-1252.
(13) Svedružic, D.; Jónsoon, S.; Toyota, C. G.; Reinhardt, L. A.; Ricagno, S.; Lindqvist, Y.; Richards, N. G. J. *Arch. Biochem. Biophys.* **2005**, *433*, 176-192.
(14) Tanner, A.; Bowater, L.; Fairhurst, S. A.; Bornemann, S. *J. Biol. Chem.* **2001**, *276*, 43627-43634.
(15) *Cytochrome P450: Structure, Mechanism, and Biochemistry*; Plenum: New York, 1995.
(16) Leto, D. F.; Jackson, T. A. *J. Biol. Inorg. Chem.* **2014**, *19*, 1-15.
(17) Sono, M.; Roach, M. P.; Coulter, E. D.; Dawson, J. H. *Chem. Rev.* **1996**, *96*, 2841-2887.
(18) Raag, R.; Li, H.; Jones, B. C.; Poulos, T. L. *Biochemistry* **1993**, *32*, 4571-4578.
(19) Kille, S.; Zilly, F. E.; Acevedo, J. P.; Reetz, M. T. *Nat. Chem.* **2011**, *3*, 738-743.
(20) Filatov, M.; Reckien, W.; Peyerimhoff, S. D.; Shaik, S. *J. Phys. Chem. A.* **2000**, *104*, 12014-12020.
(21) Ener, M. E.; Lee, Y.-T.; Winkler, J. R.; Gray, H. B. *Proc. Natl. Acad. Sci.* **2010**, *44*, 18783-18786.
(22) Rittle, J.; Younker, J. M.; Green, M. T. *Inorg. Chem.* **2010**, *49*, 3610-3617.
(23) Rittle, J.; Green, M. T. *Science* **2010**, *330*, 933-937.
(24) Groves, J. T.; Haushalter, R. C.; Nakamura, M.; Nemo, T. E.; Evans, B. J. *J. Am. Chem. Soc.* **1981**, *103*, 2884-2886.
(25) Penner-Hahn, J. E.; McMurry, T. J.; Renner, M.; Latos-Grazynsky, L.; Eble, K. M.; Davis, I. M.; Balch, A. L.; Groves, J. T.; Dawson, J. H.; Hodgson, K. O. *J. Biol. Chem.* **1983**, *258*, 12761-12764.
(26) Penner-Hahn, J. E.; Eble, K. M.; McMurry, T. J.; Renner, M.; Balch, A. L.; Groves, J. T.; Dawson, J. H.; Hodgson, K. O. *J. Am. Chem. Soc.* **1986**, *108*, 7819-7825.
(27) Groves, J. T.; Quinn, R.; McMurry, T. J.; Lang, G.; Boso, B. J. *J. Chem. Soc., Chem. Commun.* **1984**, 1455-1456.
(28) Boso, B. J.; Lang, G.; McMurry, T. J.; Groves, J. T. *J. Chem. Phys.* **1983**, *79*, 1122-1126.
(29) Groves, J. T.; Nemo, T. E.; Myers, R. S. *J. Am. Chem. Soc.* **1979**, *101*, 1032-1033.
(30) Groves, J. T.; Watanabe, Y. *J. Am. Chem. Soc.* **1988**, *110*, 8443-8452.
(31) Groves, J. T. *J. Inorg. Biochem.* **2006**, *100*, 434-447.
(32) Hohenberger, J.; Ray, K.; Meyer, K. *Nat. Comm.* **2012**, *3*, 1718.
(33) Fukuzumi, S.; Morimoto, Y.; Kotani, H.; Naumov, P.; Lee, Y.-M.; Nam, W. *Nature Chem.* **2010**, *2*, 756-759.
(34) Grapperhaus, C. A.; Mienert, B.; Bill, E.; Weyhermueller, T.; Wieghardt, K. *Inorg. Chem.* **2000**, *39*, 5306-5317.
(35) Lee, Y.-M.; Hong, S.; Morimoto, Y.; Shin, W.; Fukuzumi, S.; Nam, W. *J. Am. Chem. Soc.* **2010**, *132*, 10668-10670.

(36) Li, F.; Meier, K. K.; Cranswick, M. A.; Chakrabarti, M.; Van Heuvelen, K. M.; Münck, E.; Que, L., Jr. *J. Am. Chem. Soc.* **2011**, *133*, 7256-7259.
(37) Rohde, J.-U.; In., J., -H.,; Lim, M. H.; Brennessel, W. W.; Bukowski, M. R.; Stubna, A.; Münck, E.; Nam, W.; Que, L., Jr. *Science* **2003**, *299*, 1037-1039.
(38) Tiago de Oliveira, F.; Chanda, A.; Banerjee, D.; Shan, X.; Mondal, S.; Que, L., Jr.,; Bominaar, E. L.; Münck, E.; Collins, T. J. *Science* **2007**, *315*, 835-838.
(39) Betley, T. A.; Peters, J. C. *J. Am. Chem. Soc.* **2004**, *126*, 6252-6254.
(40) England, J.; Guo, Y.; Farquhar, E. R.; Young, V. G., Jr.,; Münck, E.; Que, L., Jr. *J. Am. Chem. Soc.* **2010**, *132*, 8635-8644.
(41) England, J.; Martinho, M.; Farquhar, E. R.; Frisch, J. R.; Bominaar, E. L.; Münck, E.; Que, L., Jr. *Angew. Chem. Int. Ed.* **2009**, *48*, 3622-3626.
(42) Hong, S.; Lee, Y.-M.; Shin, W.; Fukuzumi, S.; Nam, W. *J. Am. Chem. Soc.* **2009**, *131*, 13910-13911.
(43) MacBeth, C. E.; Golombek, A. P.; Young, V. G., Jr.,,; Yang, C.; Kuczera, K.; Hendrich, M. P.; Borovik, A. S. *Science*, *289*, 938-941.
(44) Rohde, J.-U.; Betley, T. A.; Jackson, T. A.; Saouma, C. T.; Peters, J. C.; Que, L., Jr. *Inorg. Chem.* **2007**, *46*, 5720-5726.
(45) Vogel, C.; Heinemann, F. W.; Sutter, J.; Anthon, C.; Meyer, K. *Angew. Chem. Int. Ed.* **2008**, *47*, 2681-2684.
(46) Groves, J. T.; Stern, M. K. *J. Am. Chem. Soc.* **1987**, *109*, 3812-3814.
(47) Groves, J. T.; Watanabe, Y.; McMurry, T. J. *J. Am. Chem. Soc.* **1983**, *105*, 4489-4490.
(48) Liu, W.; Groves, J. T. *J. Am. Chem. Soc.* **2010**, *132*, 12847–12849.
(49) Umile, T. P.; Wang, D.; Groves, J. T. *Inorg. Chem.* **2011**, *50*, 10353-10362.
(50) Goldberg, D. P. *Acc. Chem. Res.* **2007**, *40*, 626-634.
(51) Ramdhanie, B.; Stern, C. L.; Goldberg, D. P. *J. Am. Chem. Soc.* **2001**, *123*, 9447-9448.
(52) Lansky, D. E.; Mandimutsira, B.; Ramdhanie, B.; Clausén, M.; Penner-Hahn, J.; Zvyagin, S. A.; Telser, J.; Zhan, R.; Ou, Z.; Kadish, K. M.; Zakharov, L.; Rheingold, A. L.; Goldberg, D. P. *Inorganic Chemistry* **2005**, *44*, 4485-4498.
(53) Licoccia, S.; Morgante, E.; Paolesse, R.; Polizio, F.; Senge, M. O.; Tondello, E.; Boschi, T. *Inorg. Chem.* **1997**, *36*, 1564-1570.
(54) Mandimutsira, B. S.; Ramdhanie, B.; Todd, R. C.; Wang, H.; Zareba, A. A.; Czernuszewicz, R. S.; Goldberg, D. P. *J. Am. Chem. Soc.* **2002**, *124*, 15170-15171.
(55) Neu, H. M.; Jung, J.; Baglia, R. A.; Siegler, M. A.; Ohkubo, K.; Fukuzumi, S.; Goldberg, D. P. *J. Am. Chem. Soc.* **2015**, *137*, 4614-4617.
(56) Jung, J.; Ohkubo, K.; Prokop-Prigge, K. A.; Neu, H. M.; Goldberg, D. P.; Fukuzumi, S. *Inorg. Chem.* **2013**, *52*, 13594-13604.
(57) Warren, J. J.; Tronic, T. A.; Mayer, J. M. *Chem. Rev.* **2010**, *110*, 6961-7001.
(58) Neu, H. M.; Baglia, R. A.; Goldberg, D. P. *Chem. Rev.* **2015**, *48*, 2754-2764.
(59) Colmer, H. E.; Geiger, R. A.; Leto, D. F.; Wijeratne, G.; Day, V. W.; Jackson, T. A. *Dalton Trans.* **2014**, *43*, 17949-17963.
(60) Sismore, M. F.; Selke, M.; Burstyn, J. N.; Valentine, J. S. *Inorg. Chem.* **1997**, *36*, 979-984.
(61) Annaraj, J.; Cho, J.; Lee, Y.-M.; Kim, S. Y.; Latifi, R.; de Visser, S. P.; Nam, W. *Angew. Chem. Int. Ed.* **2009**, *48*, 4150-4153.

(62) Kang, H.; Cho, J.; Cho, K.-B.; Nomura, T.; Ogura, T.; Nam, W. *Chem. Eur* **2013**, *19*, 14119-14125.
(63) Seo, M. S.; Kim, J. Y.; Annaraj, J.; Kim, Y.; Lee, Y.-M.; Kim, S.-J.; Kim, J.; Nam, W. *Angew. Chem. Int. Ed.* **2007**, *46*, 377-380.
(64) Geiger, R. A.; Chattopadhyay, S.; Day, V. W.; Jackson, T. A. *Dalton Trans.* **2011**, *40*, 1707-1715.
(65) Shook, R. L.; Borovik, A. S. *Inorg. Chem.* **2010**, *49*, 3646-3660.
(66) Shook, R. L.; Gunderson, W. A.; Greaves, J.; Ziller, J. W.; Hendrich, M. P.; Borovik, A. S. *J. Am. Chem. Soc.* **2008**, *130*, 8888-8889.
(67) Shook, R. L.; Peterson, S. M.; Greaves, J.; Moore, C.; Rheingold, A. L.; Borovik, A. S. *J. Am. Chem. Soc.* **2011**, *133*, 5810-5817.
(68) de Visser, S. P.; Ogliaro, F.; Gross, Z.; Shaik, S. *Chem. Eur. J.* **2001**, *22*, 4954-4960.
(69) Shaik, S.; Cohen, S.; Wang, Y.; Chen, H.; Kumar, D.; Thiel, W. *Chem. Rev.* **2010**, *110*, 949-1017.
(70) Groni, S.; Dorlet, P.; Blain, G.; Bourcier, S.; Guillot, R.; Anxolabéhère-Mallart, E. *Inorg. Chem.* **2008**, *47*, 3166-3172.
(71) Leto, D. F.; Chattopadhyay, S.; Day, V. W.; Jackson, T. A. *Dalton Trans.* **2013**, *42*, 13014-13025.
(72) Chen, J.; Lee, Y.-M.; Davis, K. M.; Wu, X.; Seo, M. S.; Cho, K.-B.; Yoon, H.; Park, Y. J.; Fukuzumi, S.; Pushkar, Y. N.; Nam, W. *Journal of the American Chemical Society* **2013**, *135*, 6388-6391.
(73) Leto, D. F.; Ingram, R.; Day, V. W.; Jackson, T. A. *Chemical Commun.* **2013**, *49*, 5378-5380.
(74) So, H.; Park, J.-H.; Cho, K.-B.; Lee, Y.-M.; Seo, M. S.; Cho, J.; Sarangi, R.; Nam, W. *J. Am. Chem. Soc.* **2014**, *136*, 12229−12232.
(75) MacBeth, C. E.; Gupta, R.; Mitchell-Koch, K. R.; Young, V. G., Jr.,; Lushington, G. H.; Thompson, W. H.; Hendrich, M. P.; Borovik, A. S. *J. Am. Chem. Soc.* **2004**, *126*, 2556-2567.
(76) Umena, Y.; Kawakami, K.; Shen, J.-R.; Kamiya, N. *Nature* **2011**, *473*, 55-61.
(77) Yocum, C. F. *Coord. Chem. Rev.* **2008**, *252*, 296-305.
(78) Tsui, E. Y.; Tran, R.; Yano, J.; Agapie, T. *Nat. Chem.* **2013**, *5*, 293-299.
(79) McEvoy, J. P.; Brudvig, G. W. *Chem. Rev.* **2006**, *106*, 4455-4483.
(80) Park, Y. J.; Cook, S. A.; Sickerman, N. S.; Sano, Y.; Ziller, J. W.; Borovik, A. S. *Chem. Sci.* **2013**, *4*, 717-726.
(81) Park, Y. J.; Ziller, J. W.; Borovik, A. S. *J. Am. Chem. Soc.* **2011**, *133*, 9258-9261.
(82) Kanady, J. S.; Tsui, E. Y.; Day, M. W.; Agapie, T. *Science* **2011**, *333*, 733-736.
(83) Kanady, J. S.; Mendoza-Cortes, J. L.; Tsui, E. Y.; Nielsen, R. J.; Goddard, W. A.; Agapie, T. *J. Am. Chem. Soc.* **2013**, *135*, 1073-1082.
(84) Kanady, J. S.; Lin, P.-H.; Carsch, K. M.; Nielsen, R. J.; Takase, M. K.; Goddard, W. A.; Agapie, T. *J. Am. Chem. Soc.* **2014**, *136*, 14373-14376.
(85) Tsui, E. Y.; Agapie, T. *Proc. Natl. Acad. Sci.* **2013**, *110*, 10084-10088.
(86) Li, F.; Van Heuvelen, K. M.; Meier, K. K.; Münck, E.; Que, L., Jr. *J. Am. Chem. Soc.* **2013**, *135*, 10198-10201.
(87) Thibon, A.; England, J.; Martinho, M.; Young, V. G., Jr.,; Frisch, J. R.; Guillot, R.; Girerd, J.-J.; Münck, E.; Que, L., Jr.,; Banse, F. *Angew. Chem. Int. Ed.* **2008**, *47*, 7064-7067.

(88) Lee, Y.-M.; Bang, S.; Kim, Y. M.; Cho, J.; Hong, S.; Nomura, T.; Ogura, T.; Troeppner, O.; Ivanović-Burmazović, I.; Sarangi, R.; Fukuzumi, S.; Nam, W. *Chem. Sci.* **2013**, *4*, 3917-3923.

CHAPTER 2

Formation, Characterization, and O—O Bond Activation of a Peroxomanganese(III) Complex Supported by a Cross-Clamped Cyclam Ligand

2.1 Introduction

Manganese containing enzymes are capable of a wide variety of biological functions, often involving reaction with dioxygen and its derivatives.[1-4] Peroxomanganese(III) adducts[5] are proposed as intermediates in many of these reactions, including the detoxification of reactive oxygen species by Mn superoxide dismutase,[3,6-10] the conversion of nucleotides to deoxynucleotides by Mn ribonucleotide reductase,[11,12] and oxalate degradation by oxalate oxidase[13,14] and oxalate decarboxylase.[15-17] While there are many examples of synthetic modeling of these active sites and their corresponding reactivity,[5,18-32] a description of factors directing the reactivity of specific Mn-oxygen intermediates, especially peroxomanganese(III) adducts, is lacking.

One of the most well-known types of reactivity of Mn^{III}-peroxo species is the deformylation of aldehydes, which is driven by the nucleophilicity of the peroxo moiety (Scheme 2.1a).[33] This reactivity has been observed for a wide range of supporting ligand structures, such as anionic tripodal ligands with an intramolecular hydrogen bonding network around the peroxo ligand (H_3bupa^{2-}, H_2bpaa^{-}; for a full list of ligand abbreviations, see footnote 34),[26,27,34,35] a series of neutral tetradentate aminopyridyl ligands, ($L^7py_2^R$),[34,36] as well as a series of neutral macrocyclic ligands (TMC).[18,23,25,34] With the TMC-type ligands, the rate of deformylation was shown to increase as the electron donating ability of the ligand *trans* to the peroxo moiety increased within a series of axial ligand substituents.[18,23,25] In contrast, a series of $L^7py_2^R$ ligands displayed decreasing rates as a function of increased steric hindrance around the peroxo unit, although the correlation between reactivity and ligand structure was not very strong.[34,36]

Peroxomanganese(III) species have also been proposed to undergo O—O activation by reaction with acids and other metals to form high-valent species. Groni *et al*. reported a peroxomanganese(III) species supported by an aminopyridyl, pentadentate ligand (mL_5^2),

$[Mn^{III}(O_2)(mL_5^2)]^+$, that reacted with an equivalent of $[Mn^{III}(OH_2)(mL_5^2)]^{3+}$ in basic, aqueous solution to form a bis(μ-oxo)dimanganese(III,IV) species, presumably via O—O bond cleavage of an unobserved μ-peroxodimanganese(III,III) intermediate (Scheme 2.1b).[34,37] Similarly, the pentadentate N4py ligand supported a peroxomanganese(III) species that likely undergoes O—O bond cleavage upon reaction with an equivalent of $[Mn^{II}(N4py)(OTf)]^+$, forming a bis(μ-oxo)dimanganese(III,IV) complex (Scheme 2.1c).[34,38] Electrochemical Mn^{III}-peroxo activation was reported for a complex supported by a pentadentate, N_4O^- (phenolato-containing) ligand.[34,39] In that study, the strength of the added acid directed the electrochemical reaction. With a weak acid, concerted two-electron reduction and O—O bond cleavage occurred; however, characterization of the products of this reaction was hindered by their instability. With added strong acid, the Mn—O bond was broken and H_2O_2 was released upon electrochemical reduction (Scheme 2.1d). Finally, Shook *et al*. reported O—O bond activation of a peroxomanganese(III) species supported by the H_3bupa^{2-} ligand by reaction with electrophilic substrates that serve as H-atom donors; i.e., diphenylhydrazine and hydrazine (Scheme 2.1e).[27,34] Thus, in all cases, activation of the Mn^{III}-peroxo unit is coupled with chemical or electrochemical reduction, with the electrons supplied by a second Mn center, a sacrificial reductant, or an electrode.

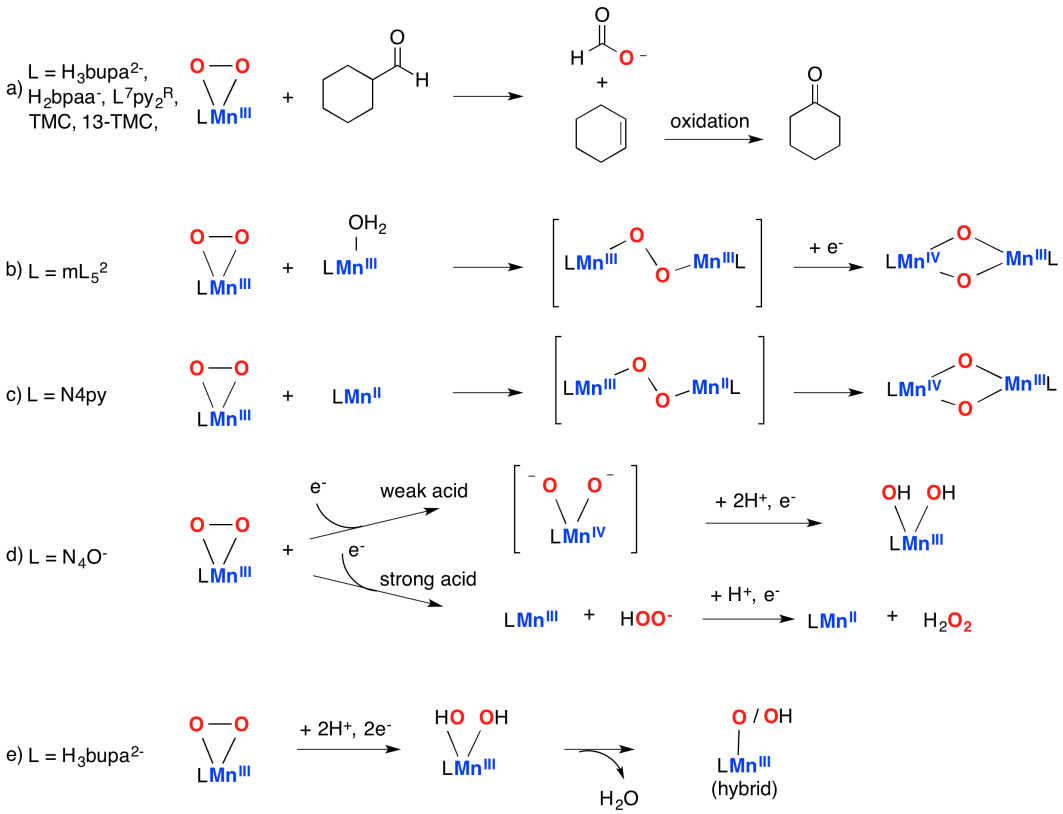

Scheme 2.1. Reactivity of peroxomanganese(III) complexes, highlighting the nucleophilic reactivity (a, b, and c) and O-O bond activation upon electrochemical (d) or chemical (e) reduction. Ligand abbreviations are defined in footnote 34.

These synthetic complexes, as well as the enzymatic active sites, are structurally and electronically diverse, and the factors that direct specific reactivity are not well understood. Moreover, in most cases, Mn^{III}-peroxo activation has led to either the formation of multinuclear, high-valent species, or the fleeting formation of mononuclear, high-valent intermediates that have not been amenable to characterization. In fact, although peroxo-bridged dimanganese intermediates are invoked in several decay pathways, there is only one example of a peroxo-bridged dimanganese species, the $[Mn^{III}_2(\textit{trans}\text{-}\mu\text{-}O_2)(S^{Me2}N_4(6\text{-Me-DPEN}))_2]^{2+}$ complex reported by Kovacs and co-workers.[34,40]

In this work, we investigate the reactivity of the peroxomanganese(III) species, $[Mn^{III}(O_2)(Me_2EBC)]^+$, supported by a neutral, cross-clamped macrocyclic ligand (Me_2EBC, Scheme 2.2). This Me_2EBC ligand provides a rigid, stable framework that is able to support a

range of Mn oxidation states. In particular, this ligand is known to support the high-valent oxidants $[Mn^{IV}(O)(OH)(Me_2EBC)]^+$ and $[Mn^{IV}(OH)_2(Me_2EBC)]^{2+}$ that are well-characterized structurally and spectroscopically.[41-43] Thus, these Mn^{IV} species have established spectroscopic fingerprints with which to compare to intermediates formed upon activation of the $[Mn^{III}(O_2)(Me_2EBC)]^+$ species. Here we describe the characterization of $[Mn^{III}(O_2)(Me_2EBC)]^+$ by a variety of spectroscopic methods, such as electronic absorption, electron paramagnetic resonance (EPR), and Mn K-edge X-ray absorption (XAS) spectroscopies. We also investigated the decay products of $[Mn^{III}(O_2)(Me_2EBC)]^+$. When formed in high yields, $[Mn^{III}(O_2)(Me_2EBC)]^+$ decays slowly to give a mononuclear Mn^{III} product. In contrast, when formed in lower yields (~60%), or when treated with $[Mn^{II}(Cl)_2(Me_2EBC)]$, the Mn^{III}-peroxo species decays to give a mononuclear Mn^{IV} species, among other products. The Mn^{IV} adduct is unstable in CH_2Cl_2 and decays to a mononuclear Mn^{III} complex. Potential pathways for this observed chemistry are proposed.

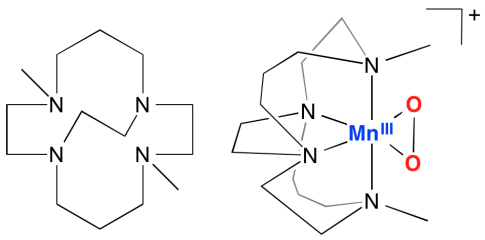

Scheme 2.2. Me_2EBC ligand (left) and $[Mn^{III}(O_2)(Me_2EBC)]^+$ (right).

2.2 Experimental Section

Chemicals and reagents used were ACS reagent grade or better and were obtained through commercial vendors. Electronic absorption experiments were performed on a Cary 50 Bio spectrophotometer (Varian) interfaced with a Unisoku cryostat (USP-203-A). Electrospray ionization-mass spectrometry (ESI-MS) data were collected on an LCT Primers MicroMass

electrospray-ionization time-of-flight instrument. EPR spectra were collected on a Bruker EMXPlus instrument with a dual-mode cavity.

2.2.1. Preparation of $[Mn^{III}(O_2)(Me_2EBC)]^+$. Optimized formation of the blue species $[Mn^{III}(O_2)(Me_2EBC)]^+$ was achieved by reacting a 2 mM solution of $[Mn^{II}(Cl)_2(Me_2EBC)]$ in CH_2Cl_2 at -60 °C with a KO_2 slurry. The KO_2 slurry was prepared under ambient conditions by stirring a solution of 100 equivalents (equiv.) of KO_2 and 100 equiv. of 18-crown-6 in 1 mL of butyronitrile for 10 minutes. 100 μL (10 equiv. KO_2 and 18-crown-6) of the slurry was added via syringe to a cuvette containing a 2 mM solution of $[Mn^{II}(Cl)_2(Me_2EBC)]$ in CH_2Cl_2 in a cryostat at -60 °C. The addition of the slurry generates a deep blue intermediate with intense features in the visible region that can be monitored by electronic absorption spectroscopy. The use of fewer equiv. of KO_2 resulted in a lower yield of the blue intermediate, as assessed by electronic absorption spectroscopy, and a thermal decay reaction to additional intermediates. The thermal decay reaction was optimized to maximize formation of the ensuing intermediates by preparing a slurry with 40 equiv. of KO_2 and 200 equiv. of 18-crown-6. When 100 μL (4 equiv. KO_2 and 20 equiv. of 18-crown-6) of this less concentrated slurry was added to a 5 mM solution of $[Mn^{II}(Cl)_2(Me_2EBC)]$ in CH_2Cl_2 at -60 °C, $[Mn^{III}(O_2)(Me_2EBC)]^+$ was generated in a yield 60% of that observed when using 10 equiv. of KO_2.

2.2.2. Preparation of Room-temperature Decay Products of $[Mn^{III}(O_2)(Me_2EBC)]^+$. When $[Mn^{III}(O_2)(Me_2EBC)]^+$ was prepared using 10 equiv. KO_2 in CH_2Cl_2 at -60 °C, an orange solution was formed as the thermal decay product upon warming the solution of $[Mn^{III}(O_2)(Me_2EBC)]^+$ to 25 °C. Excess 18-crown-6 was removed from this solution by filtering the solution with a syringe filter. Crystallization at room temperature by ether diffusion into CH_2Cl_2 yielded orange crystals which were used for subsequent ESI-MS and XAS experiments.

This orange solution was also observed as the final thermal decay product of $[Mn^{III}(O_2)(Me_2EBC)]^+$ prepared with 4 equiv. KO_2 in CH_2Cl_2 at -60 °C.

2.2.3. Preparation of Low-temperature Decay Product of $[Mn^{III}(O_2)(Me_2EBC)]^+$. When $[Mn^{III}(O_2)(Me_2EBC)]^+$ was prepared with 4 equiv. KO_2 in CH_2Cl_2 at -60 °C, a pink solution formed as the initial thermal decay product. Under these conditions, the products showed low solubility in CH_2Cl_2 at -60 °C and rapidly formed a purple precipitate that could not be isolated. When $[Mn^{III}(O_2)(Me_2EBC)]^+$ was instead prepared using 2 equiv. KO_2 in CH_2Cl_2 at -60 °C, the pink chromophore formed in lower yield and no precipitate was observed. Under these conditions, the pink solution converts to an orange solution over 15 minutes. The pink solution could also be generated when $[Mn^{III}(O_2)(Me_2EBC)]^+$, prepared in high yield using 10 equiv. KO_2, was treated with 1 equiv. of $[Mn^{II}(Cl)_2(Me_2EBC)]$ in CH_2Cl_2 at -60 °C.

2.2.4. Preparation of $[Mn^{IV}(O)(OH)(Me_2EBC)]^+$. $Mn^{IV}(OH)_2(Me_2EBC)]^{2+}$ was prepared from $[Mn^{II}(Cl)_2(Me_2EBC)]$, H_2O_2 and NH_4PF_6 in H_2O as reported previously.[44] A 2 mM solution of $[Mn^{IV}(OH)_2(Me_2EBC)]^{2+}$ was prepared in a 3:1 CH_2Cl_2/acetone mixture and reacted with 1 equiv. NEt_3 in CH_2Cl_2 at -30 °C to form $[Mn^{IV}(O)(OH)(Me_2EBC)]^+$. Formation of $[Mn^{IV}(O)(OH)(Me_2EBC)]^+$ was monitored by electronic absorption and EPR spectroscopies.

2.2.5. EPR Experiments. A 2 mM sample of $[Mn^{III}(O_2)(Me_2EBC)]^+$ was prepared by using a pre-cooled pipette to transfer 250 μL of the blue solution in CH_2Cl_2 at -60 °C to a pre-cooled quartz EPR tube that was quickly flash-frozen in liquid N_2. A frozen sample of the orange solution (250 μL) was prepared from the decay of a 2 mM solution of $[Mn^{III}(O_2)(Me_2EBC)]^+$ at 25 °C and transferred to a quartz EPR tube and flash-frozen in liquid N_2. An EPR sample of the independently prepared 2 mM $[Mn^{IV}(O)(OH)(Me_2EBC)]^+$ complex (250 μL) in 3:1 CH_2Cl_2/acetone was prepared at -30 °C and transferred to a pre-cooled quartz EPR tube and flash frozen in liquid N_2. An EPR sample of the pink solution was prepared from the decay of a 5 mM

solution of $[Mn^{III}(O_2)(Me_2EBC)]^+$ that was formed with 4 equiv. KO_2 and 20 equiv. 18-crown-6 at -60 °C in CH_2Cl_2. 250 μL of this pink solution was quickly transferred to a pre-cooled quartz EPR tube and flash-frozen in liquid N_2. An additional sample of the pink solution (250 μL) was prepared from the decay of a 2 mM solution of $[Mn^{III}(O_2)(Me_2EBC)]^+$ that was prepared with 2 equiv. KO_2 and 4 equiv. 18-crown-6 at -60 °C in CH_2Cl_2 and flash frozen in a pre-cooled quartz EPR tube. EPR samples of $[Mn^{II}(Cl)_2(Me_2EBC)]$ were prepared by transferring 250 μL of 2 mM solutions of $[Mn^{II}(Cl)_2(Me_2EBC)]$ in CH_2Cl_2 or in 1:10 butyronitrile/CH_2Cl_2 mixture and flash frozen in liquid N_2. EPR spectra were acquired on an X-band (9 GHz) Bruker EMXPlus spectrophotometer with an Oxford ESR900 continuous-flow liquid helium cryostat and an Oxford ITC503 temperature system. Parallel and perpendicular-mode spectra were collected using a Bruker ER4116DM dual-mode cavity. All spectra were collected under non-saturating conditions at 20 dB (for $[Mn^{III}(O_2)(Me_2EBC)]^+$ and the orange and pink solutions) and 38 dB for $[Mn^{II}(Cl)_2(Me_2EBC)]$, with frequencies near 9.3918 GHz (parallel-mode) or 9.6375 GHz (perpendicular mode) microwave frequency, 0.6 mT modulation amplitude, 100 kHz modulation frequency and 163 ms time constant. The Matlab-based EPR simulation software, *EasySpin*, developed by Stoll,[45] was used to simulate EPR spectra and define zero-field splitting parameters.

2.2.6. Mn K-edge X-ray Absorption Spectroscopy (XAS). An XAS sample of $[Mn^{III}(O_2)(Me_2EBC)]^+$ was prepared from 400 μL of a 15 mM solution in CH_2Cl_2 that was frozen in a pre-cooled sample cup. XAS data were also collected on a frozen solution of a 20 mM sample in CH_2Cl_2. XAS data for $[Mn^{III}(O_2)(Me_2EBC)]^+$ were collected on beamline X3B at the National Synchrotron Light Source (NSLS) at Brookhaven National Lab (storage ring conditions, 2.8 GeV, 100-300 mA) using previously reported parameters.[42] Contamination of higher harmonic radiation was minimized using a harmonic rejection mirror, manganese foil

spectra were simultaneously recorded for internal energy calibration, and the first inflection point of the K-edge energy was assigned to 6539.0 eV. Spectra were measured with 5 eV steps below the edge (6359-6529 eV) 0.3 eV steps in the edge region (6529-6564 eV), and steps corresponding to 0.05 $Å^{-1}$ above the edge in the EXAFS region. XAS data for a frozen sample of the orange solution were collected at beamline 2-2 at Stanford Synchrotron Radiation Lightsource (SSRL) using similar data collection parameters.

EXAFS data reduction and averaging were performed using the program EXAFSPAK.[46] The pre-edge background intensity was removed by fitting a Gaussian function to the pre-edge background and then subtracting this function from the whole spectrum. The spectrum was also fit with a three-segment spline with fourth-order polynomial components to remove low-frequency background. EXAFS refinement was carried out on $k^3\chi(k)$ data, using phase and amplitude functions obtained from *FEFF*, version 6,[47] and structural models of $[Mn^{III}(O_2)(Me_2EBC)]^+$ and $[Mn^{III}(OH)(Cl)(Me_2EBC)]^+$ with DFT-optimized coordinates. For each fit, the parameters r (average distance between Mn and scattering atom) and σ^2 (Debye-Waller factor) were optimized, while n, the number of atoms in the shell, was kept fixed. n was varied by integer steps systematically. The goodness-of-fit (GOF) was evaluated by the parameter F, where $F = \Sigma\ (\chi_{calcd} - \chi_{expt})^2 / N$, and N is the number of data points. The threshold energy, E_0, in electronvolts ($k = 0$ point) was kept at a common, variable value for every shell of a given fit.

2.2.7. Density Functional Theory Calculations. All DFT computations were performed with the *ORCA* 3.0.1 software package.[48] Models of $[Mn^{III}(O_2)(Me_2EBC)]^+$ and $[Mn^{III}(OH)(Cl)(Me_2EBC)]^+$ were built using the X-ray coordinates of the $[Mn^{II}(Cl)_2(Me_2EBC)]$ complex[43] and replacing both of the chloride ions with a side-on peroxo moiety for $[Mn^{III}(O_2)(Me_2EBC)]^+$ and one of the chloride ions with a hydroxide ligand for

$[Mn^{III}(OH)(Cl)(Me_2EBC)]^+$. These structures were optimized using the Becke-Perdew (BP86) functional[49,50] and converged to the $S = 2$ spin state using the SVP (Ahlrichs split valance polarized)[51,52] basis sets with SV/J auxiliary basis sets for carbon and hydrogen atoms with the larger TZVP (Ahlrichs triple-ζ valence polarized) and the auxiliary TZV/J basis sets for manganese, nitrogen, oxygen, and chloride atoms. The resolution of identity (RI) approximation[53] was used for all geometry and frequency calculations. Optimized geometries were verified as points of minimum energy with frequency calculations to ensure no negative frequencies. Solvation effects were included with COSMO, as implemented in ORCA[54], with acetone (for consistency and comparison with previous study[41,42]) and dichloromethane. Cartesian coordinates for all DFT-optimized structures are included in Supporting Information (Tables A2.1 and A2.2). Electronic transition energies were calculated for $[Mn^{III}(O_2)(Me_2EBC)]^+$ using the TD-DFT method[55-57] within the Tamm-Dancoff approximation[58,59] using the B3LYP functional[60-62] with the SVP basis set on carbon and hydrogen atoms and the larger TZVP basis set on all other atoms. 40 excited states were calculated by including all one-electron transitions within ±3 Hartrees of the HOMO/LUMO energies. TD-DFT-calculated electronic absorption spectra were generated using the calculated transition energies and oscillator strengths, assuming that the electronic transitions are well-described by Gaussian functions with full-width-half-maxima ($\nu_{1/2}$) of 2000 cm^{-1}, and that the extinction coefficient (ε_{max}) is related to the oscillator strength (f) as follows: $f = (4.61 \times 10^{-9})(\varepsilon_{max} \cdot \nu_{1/2})$. The spin-orbit coupling term (D_{SOC}) for the zero-field splitting parameters was calculated using the coupled-perturbed method, as shown to be appropriate for use with hybrid functionals.[63] The spin-spin term (D_{ss}) was calculated with spin-density from unrestricted natural orbitals (UNO) to avoid known errors that occur when using spin-unrestricted Kohn-Sham functions to treat this term.[64,65] Molecular orbitals (MOs) and

electron density difference maps (EDDMs) were visualized with isosurface plots generated using the gOpenMol program[66,67] with isodensity values of 0.05 and 0.005 b^{-3}, respectively.

Mn K-edge XAS pre-edge data for $[Mn^{III}(O_2)(Me_2EBC)]^+$ and $[Mn^{III}(OH)(Cl)(Me_2EBC)]^+$ were calculated using the TD-DFT method with the B3LYP functional and the def2-TZVP(-f) basis set[68] on all atoms and no RI approximation. Scalar relativistic effects were accounted for at the ZORA level and a dense integration grid (ORCA Grid4) and tight SCF convergence criteria were utilized. Calculated spectra were shifted to higher energy by 32.6 eV, as was determined previously to account for systematic errors in the computational treatment.[69] Calculated areas (A) were obtained from the calculated intensity (I) from the correlation A = 6.01(I) + 1.79, as established in a previous study of monomeric Mn^{II} and Mn^{III} complexes.[69]

2.3 Results and Analysis

The electronic absorption spectrum of the colorless $[Mn^{II}(Cl)_2(Me_2EBC)]$ complex shows no distinct features at energies below 400 nm (Figure 2.1A, black trace). A blue species is formed upon reaction of $[Mn^{II}(Cl)_2(Me_2EBC)]$ with 10 equiv. of KO_2 and 18-crown-6 in CH_2Cl_2 at -60 °C and is stable indefinitely at this temperature. The use of 10 equiv. of KO_2 is necessary to maximize the formation of the blue intermediate (Figure A2.1 in the Supporting Information). The superoxide radical is known to decay upon reaction with CH_2Cl_2,[70] decreasing the amount of viable superoxide radical available for reaction with $[Mn^{II}(Cl)_2(Me_2EBC)]$ (Figure A2.2 in the Supporting Information). The blue intermediate displays electronic absorption features at 650 and 400 nm (ε = 530 and 185 M^{-1} cm^{-1}, respectively, Figure 2.1A, blue trace).[71] When warmed to 0 °C, the blue solution decays to give an orange solution within ~3 minutes (Figure 2.1B). This

orange solution is characterized by weak electronic absorption bands at 410 and 890 nm, which are unchanged even after weeks at room temperature.

When [$Mn^{II}(Cl)_2(Me_2EBC)$] is reacted with less than 10 equiv. of KO_2, the formation of the blue intermediate is still observed, but it forms in substantially lower yields and decays at -60 °C to give a pink solution. For example, when [$Mn^{II}(Cl)_2(Me_2EBC)$] is treated with 4 equiv. of KO_2 and 20 equiv. of 18-crown-6, the blue intermediate forms in 60% yield (relative to the amount formed with 10 equiv. of KO_2), and, at -60 °C, converts over the course of 40 minutes to the pink solution, which has absorption features at 540 and 930 nm (ε = 66 and 47 M^{-1} cm^{-1}, respectively; Figure 2.1C, black solid trace). Under these conditions, precipitation is observed with formation of a purple solid that could not be isolated. When the blue intermediate is formed using 2 equiv. of KO_2, no precipitation is observed. In this case, the pink solution decays within 60 minutes at -60 °C to an orange solution with electronic absorption signals identical to those of the room-temperature decay product (Figure 2.1D, red solid trace). This decay reaction occurs within seconds at 25 °C. Thus, the decay of the blue intermediate is dependent on the yield in which it is formed. When the blue intermediate is formed in high yield using 10 equiv. of KO_2, it is indefinitely stable at -60 ºC, but decays at higher temperatures to give an orange solution. In contrast, if the blue intermediate is formed in lower yields, it decays at -60 ºC to give a pink solution, which evolves to the orange solution. This observed chemistry is summarized in Scheme 2.3. The characterization of the blue intermediate and the components of the pink and orange solutions are explored in the following sections.

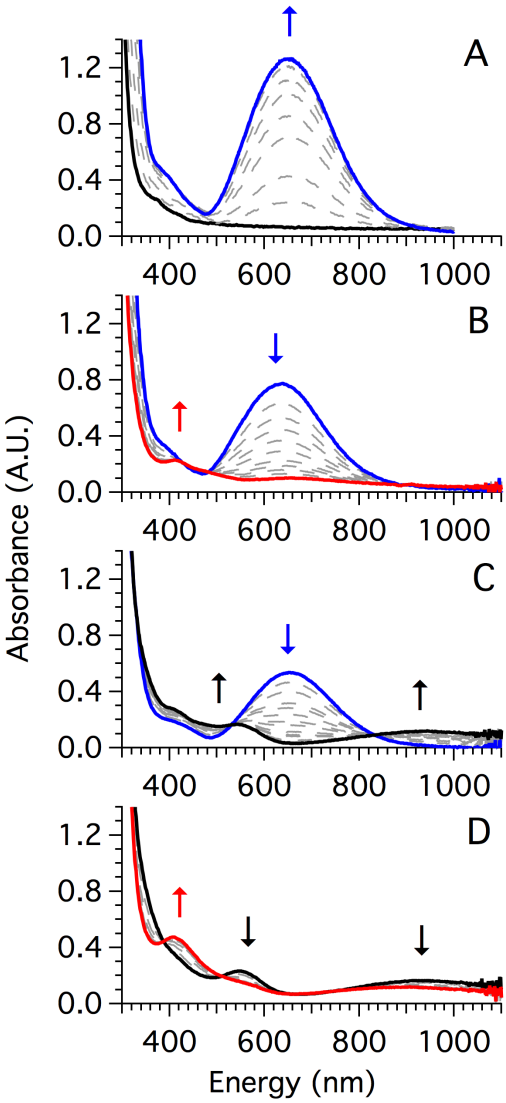

Figure 2.1. **A**) Formation of blue intermediate, $[Mn^{III}(O_2)(Me_2EBC)]^+$, (blue solid trace) from the reaction of 2 mM $[Mn^{II}(Cl)_2(Me_2EBC)]$ with 10 equiv. KO_2 and 18-crown-6 in CH_2Cl_2 at -60 °C. **B**) Decay of $[Mn^{III}(O_2)(Me_2EBC)]^+$ (formed with 10 equiv. KO_2 and 2 mM $[Mn^{II}(Cl)_2(Me_2EBC)]$) to the orange solution (red solid trace) in CH_2Cl_2 at 0 °C. **C**) Conversion of $[Mn^{III}(O_2)(Me_2EBC)]^+$ (formed with 4 equiv. KO_2 and 5 mM $[Mn^{II}(Cl)_2(Me_2EBC)]$) to the pink solution (black solid trace) in CH_2Cl_2 at -60 °C. **D**) Conversion of the pink solution to the orange solution in CH_2Cl_2 at -60 °C (formed with 4 equiv. KO_2 and 5 mM $[Mn^{II}(Cl)_2(Me_2EBC)]$).

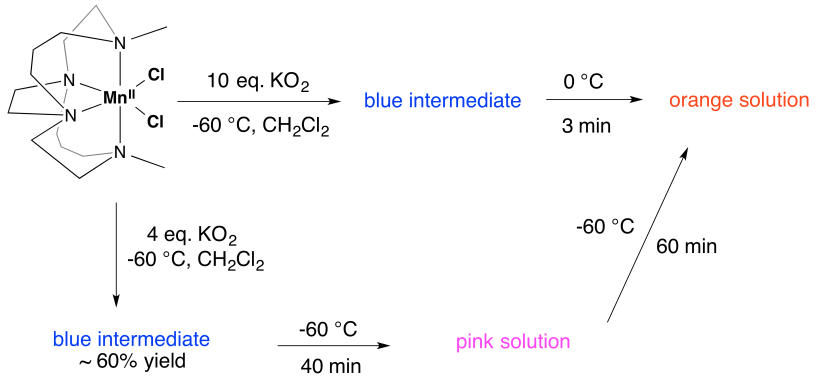

Scheme 2.3. Reactivity profile of $[Mn^{II}(Cl)_2(Me_2EBC)]$ with 10 and 4 equiv. KO_2. The rate of conversion of the blue intermediate to the pink solution, and the pink solution to the orange solution, depends on the equiv. of KO_2 used to form the blue intermediate. Faster decay rates are observed using fewer equiv. of KO_2. The 60% yield of the blue intermediate is relative to the amount formed when using 10 equiv. of KO_2.

2.3.1. Characterization of the Blue Intermediate by Electronic Absorption and EPR Spectroscopies.

The transition energies and extinction coefficients (ε) of the blue intermediate are similar to those observed for peroxomanganese(III) species. For example, Mn^{III}-peroxo adducts supported by the N4py, mL_5^2, and imL_5^2 ligands displayed λ_{max} values of 617, 585, and 542 nm, respectively, with corresponding ε values of 280, 335, and 484 $M^{-1}cm^{-1}$.[5,21,37,38] All attempts to characterize the blue intermediate by mass spectrometry, which has seen much use in characterization of Mn^{III}-peroxo adducts, proved unsuccessful. Because of the large excess of 18-crown-6 required for optimal formation, only 18-crown-6 was observed in ESI-MS experiments for the blue solution.

X-band parallel-mode EPR spectra of the blue intermediate at 5 K showed a 6-line signal at g_{eff} = 7.96, indicative of a mononuclear Mn^{III} species (Figure 2.2, black trace). The hyperfine splitting, A = 6.84 mT, is in excellent agreement with that observed for peroxomanganese(III) species (6-7 mT).[5] A plot of the product of signal intensity and temperature *versus* temperature of the g_{eff} = 7.96 signal from 5 - 30 K reveals an initial drop and a leveling at higher temperatures (Figure 2.2, inset). Such temperature-dependent behavior indicates that the m_s = ±2 doublet,

which gives rise to the g_{eff} = 7.96 EPR signal, is lowest in energy (D < 0 cm^{-1}).[72] To date, all Mn^{III}-peroxo species have D < 0 cm^{-1}.[5] The 5 K data were well simulated with S = 2, g = 1.98, A = 6.8 mT, D = -1.8 cm^{-1}, and E/D = 0.10(2) (Figure 2.2, red trace), with the goodness of fit largely dependent on the magnitude of E/D. The D value was refined to -2(1) cm^{-1} through fits of the variable-temperature EPR data (Figure 2.2, inset). The 5 K perpendicular-mode EPR spectrum of the blue intermediate shows an axial signal at g = 1.99 that is characteristic of the superoxide radical (Figure A2.3 in the Supporting Information, black trace). However, when the blue intermediate is formed using 10 eq. of KO_2, signals from the $[Mn^{II}(Cl)_2(Me_2EBC)]$ starting material are not observed, suggesting complete consumption of this species. In fact, the only EPR signals observed are from unreacted superoxide and the mononuclear Mn^{III} species. In contrast, when the blue intermediate is formed using less than 10 equiv. of KO_2, a perpendicular-mode signal is observed at g = 1.98 with A = 8.02 mT, which is associated with a mononuclear Mn^{II} species (Figure A2.3 in the Supporting Information, red trace).

As the formation of the blue intermediate in maximum yield required 10 equiv. of KO_2, we monitored the lifetime of the excess superoxide radical in solution prior to conducting reactivity studies. This was to determine if unreacted superoxide was influencing any further chemistry. The decay of the superoxide radical in CH_2Cl_2 in the absence of $[Mn^{II}(Cl)_2(Me_2EBC)]$ was monitored over 150 minutes by 5 K perpendicular-mode EPR experiments (Figure A2.2 in the Supporting Information). Aliquots of a solution with 10 equiv. of KO_2 and 10 equiv. of 18-crown-6 in CH_2Cl_2 at -60 °C were taken over time and frozen in EPR tubes. At 150 minutes, the EPR signal from the superoxide radical had decayed to < 25% of that of the original solution. Presumably, the presence of Mn^{II} would further facilitate superoxide radical decomposition by this time point. All further reactivity studies were performed after this time point.

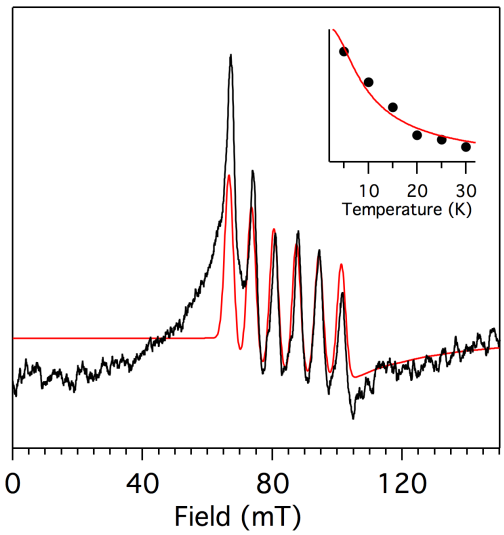

Figure 2.2. 5 K parallel-mode EPR spectrum of the blue intermediate (black trace) and simulation (red trace) with D = -1.8 cm^{-1} and E/D = 0.10(2). Inset: plot of signal intensity (at 84.4 mT) times temperature versus temperature (black dots) and fit (red trace) yielding D = -2(1) cm^{-1}.

2.3.2. Characterization of the Blue Intermediate by XAS. Given that EPR data for the blue intermediate revealed only a single Mn^{III} product when this species is generated using 10 equiv. of KO_2, we employed Mn K-edge XAS to further analyze this intermediate. Previously, $[Mn^{II}(Cl)_2(Me_2EBC)]$ $[Mn^{IV}(OH)_2(Me_2EBC)]^{2+}$, and $[Mn^{IV}(O)(OH)(Me_2EBC)]^{+}$ have been studied by XAS,[42] and the results of these studies provide an excellent benchmark for comparing with XAS data for the blue intermediate. Mn K-edge XAS data for the blue intermediate exhibit a rising edge at 6550.3 eV, which, as expected, is in between the edges reported for $[Mn^{II}(Cl)_2(Me_2EBC)]$ (6547.1 eV) and the Mn^{IV} complexes, $[Mn^{IV}(OH)_2(Me_2EBC)]^{2+}$ and $[Mn^{IV}(O)(OH)(Me_2EBC)]^{+}$ (6552.0, and 6551.8 eV, respectively,[42] see Figure 2.3). The edge energy of the blue intermediate reinforces the conclusion, based on EPR data, that the Mn in this solution is in the +3 oxidation state.

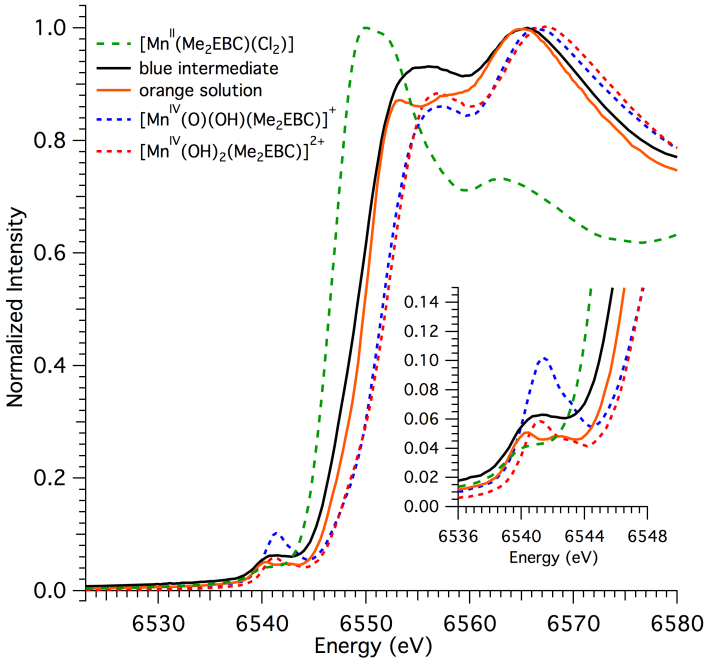

Figure 2.3. X-ray absorption near-edge structures of the blue intermediate (solid black trace), the orange solution (solid orange trace), $[Mn^{II}(Cl)_2(Me_2EBC)]$ (dashed green trace),[42] $[Mn^{IV}(OH)_2(Me_2EBC)]^{2+}$ (dashed red trace),[42] and $[Mn^{IV}(O)(OH)(Me_2EBC)]^{+}$(dashed blue trace).[42] Inset: Pre-edge region from 6536 to 6548 eV showing pre-edge features.

The Fourier transform of the extended X-ray absorption fine structure (EXAFS) of the blue intermediate is shown in Figure 2.4. The primary peak at R' = 1.7 Å^{-1} was fit with a shell of 1.8 O atoms at 1.85 Å, with additional contributions from a shell of 4 N atoms at 2.10 Å (Table 2.1, fit 4). A fit with a shell of 2.0 O atoms at 1.85 Å had a Debye-Waller factor that was too large for a shell at that distance. The fit with 1.8 O atoms would be consistent with 90% conversion to the Mn^{III}-peroxo species, $[Mn^{III}(O_2)(Me_2EBC)]^{+}$. In the Fourier-transform spectrum of the blue intermediate, two peaks are present at 2.03 and 2.35 Å, which have contributions from shells of N and C atoms from the Me_2EBC ligand. These peaks were acceptably fit with one shell of 4 N atoms at 2.10 Å (Figure 2.4, left). Fits of two shells of N atoms at 2.12 and 2.27 Å, corresponding to the $N_{equatorial}$ and N_{axial} lengths, respectively, better reproduce the Fourier-transform peaks at 2.03 and 2.35 Å^{-1} (Figure 2.4, right). However, these

fits resulted in a negative Debye-Waller factor for the shell of N atoms at 2.12 Å and a very large Debye-Waller factor for the shell of O atoms at 1.90 Å, which are physically unreasonable. We note that these fitting parameters were observed to be correlated, so these Debye-Waller factors could be of limited accuracy. In any case, the fit of the single N shell at 2.10 Å (fit 4) is an acceptable average of the four N distances calculated from DFT computations (2.28 Å, *vida infra*). Finally, a small peak at 3.3 Å was best fit with a shell of 4 C atoms at 2.92 Å and a shell of 6 C atoms at 3.44 Å. Overall, these fitting results are comparable to the recently reported EXAFS characterization of a peroxomanganese(III) species supported by the TMC ligand. In that case, the data were well-fit with a shell of 2 O atoms at 1.88 Å and a shell of 4 N atoms at 2.24 Å, as well as shells corresponding to scatterers from the TMC ligand.[73] Taken together, the edge energy and EXAFS fit provide excellent support for our assignment of the blue intermediate as the side-on peroxomanganese(III) species, $[Mn^{III}(O_2)(Me_2EBC)]^+$.

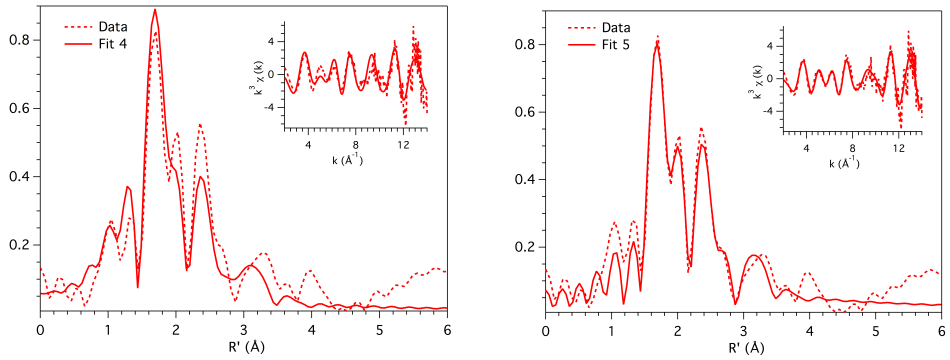

Figure 2.4. Experimental Fourier transform and k-weighted EXAFS (inset) for the blue intermediate, $[Mn^{III}(O_2)(Me_2EBC)]^+$, (- -) and overlay of fit 4 (—) (left) and fit 5 (—) (right).

Table 2.1. EXAFS Fitting Results for the Blue Intermediate, $[Mn^{III}(O_2)(Me_2EBC)]^+$

fit	Mn-N			Mn-O			Mn-C(1)			Mn-C(2)			Mn-N(2)			f-factor
	n	r(Å)	σ^2 (Å^2)^a	n	r(Å)	σ^2 (Å^2)^a	n	r(Å)	σ^2 (Å^2)^a	n	r(Å)	σ^2 (Å^2)^a	n	r(Å)	σ^2 (Å^2)^a	
1	6	2.32	43.0													0.945
2	4	2.10	2.9	1.8	1.85	4.2										0.745
3	4	2.10	3.3	1.8	1.85	4.3	4	2.94	6.3							0.706
4	***4***	***2.10***	***3.1***	***1.8***	***1.85***	***4.2***	***4***	***2.92***	***6.5***	***6***	***3.44***	***6.6***				***0.661***
5	2	2.12	-1.5	1.8	1.90	12.7	4	2.96	4.5	6	3.49	7.6	2	2.27	2.8	0.531

Fourier transform range is 2-14 Å (resolution 0.1317 Å). ^{a}Debye-waller factor × 10^3.

A full examination of the pre-edge region offers useful insight into the electronic structure of the peroxomanganese(III) complex. The pre-edge feature of $[Mn^{III}(O_2)(Me_2EBC)]^+$ occurs at 6540.8 eV, which lies between the pre-edge peak energies of the Mn^{II} and Mn^{IV} complexes supported by the Me_2EBC ligand[42] (Table 2.2, Figure A2.4). Analysis of the area of the pre-edge feature supplies information about the geometric environment of the Mn^{III} center. As the environment about the Mn center becomes less centrosymmetric and the amount of 4*p* character in the 3*d* manifold increases, μ_{el}-forbidden $1s \rightarrow 3d$ transitions are able to gain intensity by mixing with μ_{el}-allowed $1s \rightarrow 4p$ transitions. $[Mn^{III}(O_2)(Me_2EBC)]^+$ exhibits a pre-edge area of 9.5 (10^{-2} eV), which is intermediate between the previously studied Me_2EBC complexes. Specifically, the least centrosymmetric $[Mn^{IV}(O)(OH)(Me_2EBC)]^+$ complex displays a larger area of 14.2 10^{-2} eV and the more centrosymmetric $[Mn^{IV}(OH)_2(Me_2EBC)]^{2+}$ and $[Mn^{II}(Cl)_2(Me_2EBC)]$ complexes display smaller areas (6.9 and 3.9 10^{-2} eV , respectively) (Table 2.2). A detailed analysis of the specific transitions involved in the pre-edge of $[Mn^{III}(O_2)(Me_2EBC)]^+$, as well as the basis of the large pre-edge intensity, is discussed in the following section.

Table 2.2. Experimental Pre-edge Energies (eV), Heights, and Areas, and Calculated Pre-edge Energies, Intensities, Areas, and % 4*p* Character in Acceptor MOs in Me_2EBC-supported Complexes

	experimental			calculated				
complex	pre-edge energy	height	area	pre-edge energy	intensity	area	Mn 4p (%)	ref
$[Mn^{II}(Cl)_2(Me_2EBC)]$	6540.4	0.041	3.9	6540.2	0.12	2.5	0.7	[42]
blue intermediate ($[Mn^{III}(O_2)(Me_2EBC)]^+$)	6540.8	0.051	9.5	6541.0	0.72	6.1	6.3	[a]
orange solution ($[Mn^{III}(OH)(Cl)(Me_2EBC)]^+$)	6540.1	0.030	6.1	6540.2	0.49	4.7	1.2	[a]
	6542.3	0.022		6541.6				
$[Mn^{IV}(OH)_2(Me_2EBC)]^{2+}$	6541.0	0.066	6.9	6541.7	0.66	5.8	1.5	[42]
	6543.2	0.052		6542.5				
$[Mn^{IV}(O)(OH)(Me_2EBC)]^+$	6541.2	0.103	14.2	6541.9	2.63	17.6	6.9	[42]
	6543.3	0.072		6542.6				

[a]This work.

2.3.3. DFT Computations and Electronic Structure of $[Mn^{III}(O_2)(Me_2EBC)]^+$. DFT calculations were used to describe the electronic structure of $[Mn^{III}(O_2)(Me_2EBC)]^+$, as well as to provide a basis of comparison for X-ray absorption analysis. Coupled-perturbed (CP) DFT calculations were utilized to calculate the *D*-tensor orientation for $[Mn^{III}(O_2)(Me_2EBC)]^+$. The *z*-axis lies along the elongated N_{axial}-Mn-N_{axial} axis, and the *y*-axis bisects the O—O bond (Figure A2.5 in the Supporting Information, top left). The calculated Mn—O bond lengths (1.868 Å) are in excellent agreement with the EXAFS-determined distance of 1.85 Å and with those observed in other peroxomanganese(III) adducts.[5] The O—O bond of 1.450 Å is typical of a side-on bound peroxo. Calculated Mn—N bond lengths show two shorter Mn—$N_{equatorial}$ bonds of 2.132 and 2.133 Å, nearly identical to the Mn—$N_{equatorial}$ distance in the EXAFS data (2.10 Å). DFT calculated Mn—N_{axial} bonds of 2.427 and 2.432 Å are longer than the EXAFS-determined average (2.10 Å). These calculated distances also lie outside the range of Mn-N distances observed for other Mn^{III}-peroxo species (2.2 - 2.37 Å).[5,74] The agreement improves marginally

for optimizations performed using the meta-GGA TPSS functional[75] with D3 corrections[76,77] (Mn—N_{axial} of 2.393 Å). We note that it has been previously observed that DFT calculations are quite robust at reproducing short metal-ligand distances, but tend to show more error for longer M-L bonds.[78] Calculated ZFS parameters from the CP-DFT method were D = -1.75 cm^{-1} and E/D = 0.030. Although the value of E/D is underestimated relative to the experimental value of 0.10(2), the sign and magnitude of D is in good agreement with the experimental value (D = -2(1) cm^{-1}).

DFT calculations also provide a bonding description of the frontier MOs in $[Mn^{III}(O_2)(Me_2EBC)]^+$. With the D-tensor orientation described above, both the α-spin and β-spin Mn $3d_{xy}$ based orbitals (93α and 93β) are unoccupied and participate in σ-antibonding interaction with the peroxo ligand (Figure A2.5 in the Supporting Information, top right). As observed in other Mn^{III}-peroxo adducts,[5] there is a characteristically high amount of covalency between the Mn 3d orbitals and the peroxo moiety with 41% Mn 3d character and 47% O_2 character in 93α. With the high-spin d^4 electronic configuration of the peroxomanganese(III) species, the four remaining Mn 3d α-spin orbitals are all occupied, while the corresponding β-spin orbitals are unoccupied. Mn^{III}-O_2 π-antibonding character is present in both the Mn $3d_{yz}$ (88α and 91β) and the Mn $3d_{x^2-y^2}$ orbitals (87α and 89β). The Mn $3d_{z^2}$ MO primarily displays σ-interactions with the axial nitrogen atoms along the elongated z-axis of the D-tensor, with 33% Mn 3d character and 40% N 2p.

The TD-DFT calculated absorption spectrum of $[Mn^{III}(O_2)(Me_2EBC)]^+$ exhibits excellent agreement with the features observed experimentally (Figure 2.5), although the absorption intensities are not well reproduced. In the experimental absorption spectrum, the dominant feature is a peak at 650 nm. TD-DFT calculations reproduce this peak as a single transition at 620 nm that corresponds to a one-electron $d_{z^2} \rightarrow d_{xy}$ excitation (Figure 2.5 and Table A2.3 in the

Supporting Information), which is expected to be the lowest energy *d-d* transition given the *D*-tensor orientation. In the experimental spectrum, there is a broad shoulder from 370 to 470 nm (Figure 2.5, top). TD-DFT calculations predict a series of LMCT O_2 π^* ⟶ Mn 3*d* transitions in this region. The next two *d-d* transitions are observed at slightly higher energy, with the d_{yz} ⟶ d_{xy} transition at 370 nm and the $d_{x^2-y^2}$ ⟶ d_{xy} transition at 330 nm. Above this energy, high-intensity charge transfer transitions are predicted. Overall, the TD-DFT calculations reinforce the assignment of the blue intermediate as $[Mn^{III}(O_2)(Me_2EBC)]^+$.

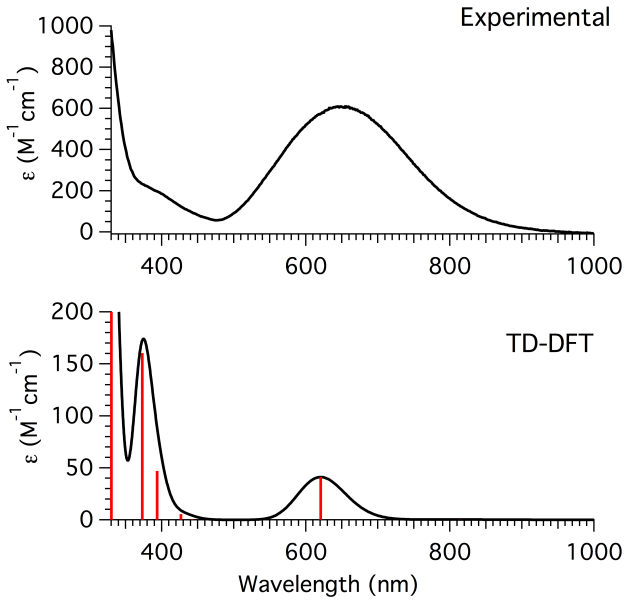

Figure 2.5. Experimental (top) and TD-DFT-calculated (bottom) absorption spectra of $[Mn^{III}(O_2)(Me_2EBC)]^+$. Units are given as molar extinction coefficients, ε ($M^{-1}cm^{-1}$), based on the initial concentration of $[Mn^{II}(Cl)_2(Me_2EBC)]$, to compare to TD-DFT calculated values.

TD-DFT calculations were also carried out to investigate the basis for the intense XAS pre-edge feature of $[Mn^{III}(O_2)(Me_2EBC)]^+$. The calculated pre-edge energy of 6541.0 eV is in excellent agreement with the experimentally determined energy of 6540.8 eV (Table 2.2; this comparison employed a standard shift in calculated pre-edge energies, as defined by DeBeer and co-workers[69]). The calculated pre-edge area for $[Mn^{III}(O_2)(Me_2EBC)]^+$ is 6.1 10^{-2} eV, which is

smaller than the experimental area (9.5 10^{-2} eV) but in excellent agreement with the trend observed in the series of Me_2EBC complexes (Table 2.2).[42] From the TD-DFT calculations, the pre-edge feature of $[Mn^{III}(O_2)(Me_2EBC)]^+$ arises from an envelope containing 6 transitions from the core Mn 1*s* orbital to the unoccupied Mn 3*d* frontier MOs (Figure A2.6 in the Supporting Information). Overall, the acceptor orbitals contain 6.3% Mn 4*p* orbital character, which is significantly higher than that observed for $[Mn^{IV}(OH)_2(Me_2EBC)]^{2+}$ (1.5% 4*p* character), but near that of $[Mn^{IV}(O)(OH)(Me_2EBC)]^+$ (6.9%). In the pre-edge envelope of $[Mn^{III}(O_2)(Me_2EBC)]^+$, the greatest contribution (4.5%) to the 4*p* character is the α-spin Mn $3d_{xy}$ (93α) MO. Indeed, excitation to this MO dominates the calculated pre-edge feature (Figure A2.6 in Supporting Information). Consequently, the high degree of covalency of the Mn^{III}-peroxo moiety in the Mn $3d_{xy}$ orbital accounts for the relatively high pre-edge intensity of $[Mn^{III}(O_2)(Me_2EBC)]^+$. The other pre-edge transitions are to the five β-spin Mn 3*d* orbitals (89β - 93β) (Figure 2.6), which contain a smaller amount of Mn 4*p* character. These excitations can be separated into lower- and higher-energy 1s-to-t_{2g} and 1s-to-e_g sets of transitions (using O_h symmetry labels), which gives rise to lower intensity shoulders flanking the intense 1s-to-$3d_{xy}$ (93α) transition (Figure A2.6 in the Supporting Information). These individual transitions are not resolved in the experimental pre-edge spectrum (Figure 2.3). On the basis of this analysis, the pre-edge intensity of a Mn^{III}-peroxo moiety should be reflective of Mn-O_2 covalency, and could be used as a means of comparing bonding for structurally similar complexes. Moreover, the addition of an electron to this highly covalent frontier MO, should weaken both Mn—O and O—O interactions, implicating this orbital as important for modulating the reactivity of peroxomanganese(III) species.

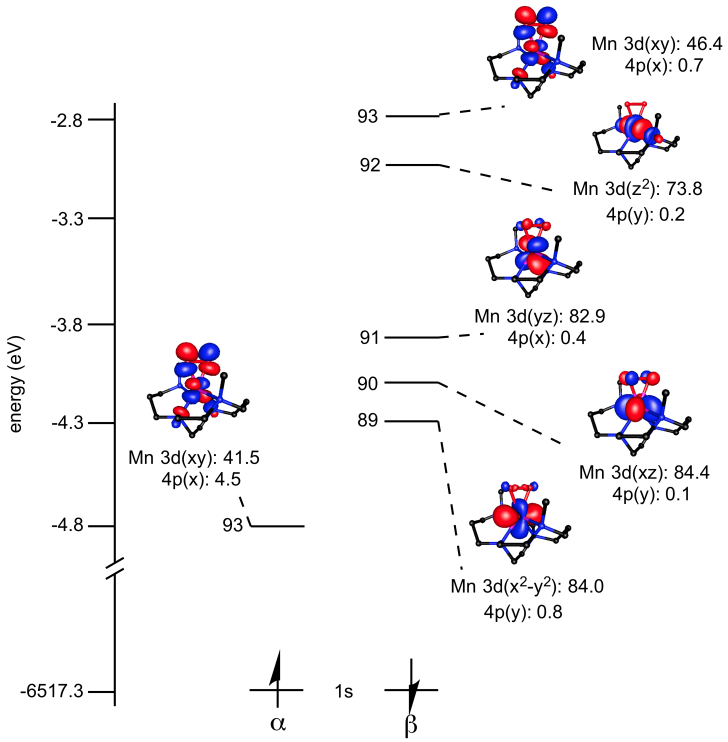

Figure 2.6. MO diagram of $[Mn^{III}(O_2)(Me_2EBC)]^+$ with energies for spin-unrestricted Kohn-Sham orbitals. Surface contour plots for Kohn-Sham Mn 3*d* based orbitals are shown with Mn 3*d* and 4*p* contributions listed.

2.3.4. Characterization of the Components of the Orange Solution. An orange solution forms from both the room-temperature decay product of $[Mn^{III}(O_2)(Me_2EBC)]^+$ as well as from the decay of the pink solution at -60 °C (Figure 2.1 and Scheme 2.3). The electronic absorption spectrum of this orange solution is unchanged for several weeks at room temperature, suggesting that this is the thermodynamic product of the $[Mn^{III}(O_2)(Me_2EBC)]^+$ decay reaction. After excess 18-crown-6 is removed from this orange solution by filtration and crystallization, a mass spectrum revealed a major ion peak of m/z = 361.2, corresponding to $[Mn^{III}(OH)(Cl)(Me_2EBC)]^+$ (Figure A2.7 in the Supporting Information). 5 K parallel-mode EPR data collected for the orange solution also indicate a mononuclear Mn^{III} species, showing a characteristic six-line feature with g_{eff} = 8.33 and A = 4.73 mT (Figure 2.7), which can be simulated using S = 2, g = 2.1 A = 5.0 mT, $|D|$ = +2.1(5) cm^{-1}, E/D = 0.06(2). Both the g-value and hyperfine splitting are quite distinct from those observed for $[Mn^{III}(O_2)(Me_2EBC)]^+$ (g_{eff} =

7.96 and A = 6.84 mT). The temperature dependent behavior of the g = 8.33 signal from 5 to 40 K (Figure 2.7, inset) is represented as the signal intensity times temperature *versus* temperature and shows an initial rise and then leveling at higher temperatures. This behavior indicates that the $m_s = \pm 2$ doublet is above the $m_s = 0$ sublevel, supporting $D > 0$ cm^{-1}.[72] The EPR spectrum of the orange solution also shows a very weak set of six signals centered at ~130 mT (g_{eff} = 5.3). These signals likely arise from a separate mononuclear Mn^{III} species with different ground-state properties.[79]

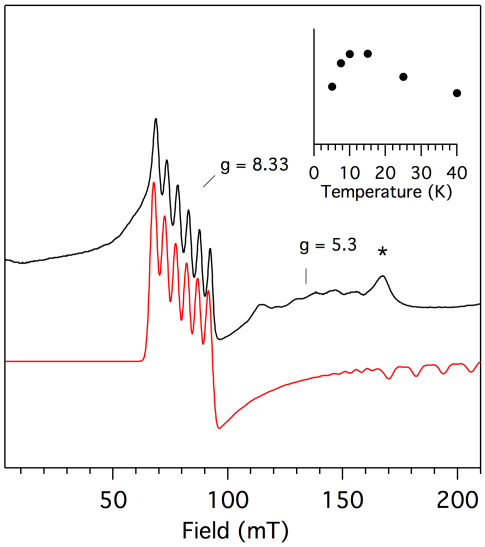

Figure 2.7. 5 K parallel-mode EPR spectrum of the orange solution in CH_2Cl_2. The small feature near 160 mT (indicated with an asterisk) is due to dissolved O_2, as has been previously observed.[37]

CP-DFT calculations for [Mn^{III}(OH)(Cl)(Me$_2$EBC)]$^+$ predict D = +2.10 cm^{-1} and E/D = 0.064, which are in excellent agreement with the experimental values ($|D|$ = +2.1(5) cm^{-1} and E/D = 0.06(2)). Here, the z-axis of the CP-DFT calculated D-tensor lies along the compressed (H)O—Mn—N$_{Me2EBC}$ axis, which accounts for the positive sign of D (with few exceptions,[80] an axial compression is associated with a positive D value for pseudo-octahedral Mn^{III} complexes[81]). The calculated Mn—O(H) distance of 1.835 Å is within the expected range for a Mn^{III}-hydroxide.[82-86] Under the calculated D-tensor orientation, the lowest energy α-spin and β-

spin orbitals belong to the closely spaced t_{2g} set that includes the Mn $3d_{xy}$ (86α, 88α, and 95β), Mn $3d_{yz}$ (89α, 90α, and 94β), and Mn $3d_{xz}$ (94α and 94β) MOs. (Because of high covalency with the chloride ligand, the frontier orbitals are heavily mixed, with the Mn 3*d* orbital occupancy distributed over several MOs; see Appendix 2, Table A2.5.) At higher energy, the e_g set is composed of Mn $3d_{x^2-y^2}$ (97α and 98β) and Mn $3d_{z^2}$ (98α and 97β) MOs. The e_g-based MOs exhibit a high degree of σ-antibonding character between the Mn^{III} center and the hydroxide and chloride ligands.

The TD-DFT-calculated electronic absorption spectrum of $[Mn^{III}(OH)(Cl)(Me_2EBC)]^+$ bears a reasonable resemblance to that observed for the orange solution (Figure 2.8). Experimentally, the orange solution shows features at 410 and 890 nm, with a small shoulder at 520 nm. TD-DFT calculations predict the lowest energy *d-d* transition of $[Mn^{III}(OH)(Cl)(Me_2EBC)]^+$ at 1100 nm, which arises from a one-electron excitation from the occupied α-spin Mn $3d_{x^2-y^2}$ (97α) MO to the unoccupied α-spin Mn $3d_{z^2}$ (98α) MO. The next *d-d* transition, from the Mn $3d_{xz}$-based MO (94α), is predicted at 600 nm. TD-DFT calculated transitions at 500 and 490 nm arise from LMCT transitions between Cl 3*p*-based MOs and the Mn $3d_{z^2}$ α-spin LUMO. The two remaining *d-d* transitions from Mn $3d_{yz}$ and $3d_{xy}$ are distributed over several states from 400 to 330 nm due to the large amount of covalency present in the Mn 3d manifold (Table A2.5). Thus, DFT-calculated properties of $[Mn^{III}(OH)(Cl)(Me_2EBC)]^+$ can account for the major features observed in both the EPR and electronic absorption spectra of the orange solution, suggesting that $[Mn^{III}(OH)(Cl)(Me_2EBC)]^+$ could be the predominant, but not sole, species in the orange solution.

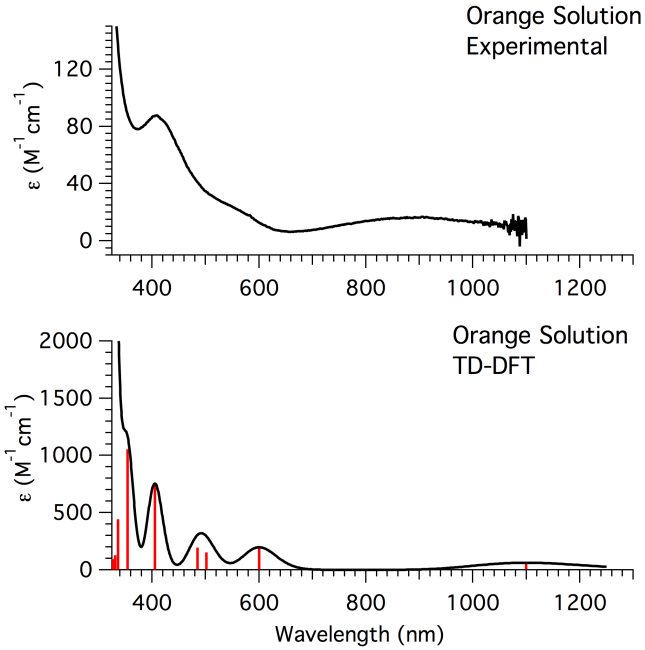

Figure 2.8. Experimental electronic absorption spectra of the orange solution (top) and TD-DFT-calculated absorption spectra of $[Mn^{III}(OH)(Cl)(Me_2EBC)]^+$ (bottom). Units are given as molar extinction coefficients, ε ($M^{-1}cm^{-1}$), based on the initial concentration of $[Mn^{II}(Cl)_2(Me_2EBC)]$, to compare to TD-DFT calculated values.

Further characterization of the orange solution was undertaken using Mn K-edge XAS. A frozen solution of orange crystals dissolved in acetonitrile yielded an edge energy of 6550.5 eV, nearly identical to that of $[Mn^{III}(O_2)(Me_2EBC)]^+$, and intermediate between the edges for Mn^{II} and Mn^{IV} Me_2EBC species (Table 2.2 and Figure 2.3), further supporting that the bulk of Mn in the orange solution is in the +3 oxidation state. The pre-edge feature of the orange solution shows two maxima at 6540.5 and 6542.3 eV, which are well fit with two bands (Figure A2.8 in the Supporting Information). The total area for this feature, 6.1 10^{-2} eV, is the smallest of the Mn^{III} and Mn^{IV} Me_2EBC-supported species (Table 2.2), although it is still larger than that of $[Mn^{II}(Cl)_2(Me_2EBC)]$. The TD-DFT-calculated pre-edge feature for a DFT-optimized model of $[Mn^{III}(OH)(Cl)(Me_2EBC)]^+$ shows excellent agreement with the experimental peak energies (Table 2.2 and Figure A2.9 in the Supporting Information), as well as the calculated total area. Further structural investigation of the orange solution was attempted through analysis of EXAFS

data. However, this analysis failed to yield high-quality fits with physically meaningful Debye-Waller factors. We attribute this to heterogeneity in the Mn^{III} centers present in the orange solution. This is supported by the EPR data of the orange solution, which reveal signals from two distinct mononuclear Mn^{III} centers (Figure 2.7). Our efforts to fit the EXAFS data of the orange solution are summarized in the Supporting Information (see Figure A2.11 and Table A2.6).

2.3.5. Characterization of the Components of the Pink Solution. When $[Mn^{III}(O_2)(Me_2EBC)]^+$ is formed in substoichiometric yields, this species evolves at low-temperature to a pink solution (Figure 2.1C and Scheme 2.3). We investigated the composition of this pink solution by EPR spectroscopy. The 5 K perpendicular-mode EPR data of the pink solution are primarily dominated by a signal at 347.4 mT (g = 1.98) with a hyperfine splitting of 8.02 mT, which is attributed to a mononuclear Mn^{II} compound (Figure 2.9, right). The appearance of this signal is quite distinct from that of the $[Mn^{II}(Cl)_2(Me_2EBC)]$ starting material in CH_2Cl_2, which shows broad resonances, lacking observed hyperfine splittings, spread over a field range of ~80–500 mT (Figure A2.12 in the Supporting Information). Hyperfine splittings for $[Mn^{II}(Cl)_2(Me_2EBC)]$ are only observed in a 1:10 butyronitrile/dichloromethane mixture (Figure A2.12 in the Supporting Information). The intense Mn^{II} feature of the pink solution at 347.4 mT was not observed in either sample of $[Mn^{II}(Cl)_2(Me_2EBC)]$. Given the distinct differences in the Mn^{II} signal observed for the pink solution and the $[Mn^{II}(Cl)_2(Me_2EBC)]$ starting material, we postulate that the pink solution contains a mononuclear Mn^{II} byproduct. Anxolabéhère-Mallart and coworkers observed an EPR signal very similar to that observed here upon addition of an excess of H_2O_2 in H_2O to $[Mn^{II}(mL_5^2)]^{2+}$. In that case, the EPR signal was attributed to a mononuclear Mn^{II} species with large ZFS and presumed to arise from $[Mn^{II}(H_2O)_6]^{2+}$.[37] Although that signal dominated the perpendicular-mode EPR spectrum, it was associated with only 8% of the Mn in the sample. Similarly, we propose that the 347.4 mT EPR

signal observed for the pink solution arises from a mononuclear Mn^{II} byproduct that represents a small fraction of Mn in the sample.

The perpendicular-mode EPR spectrum of the pink solution also shows a six-line signal at 131 mT (Figure 2.9, inset) with g_{eff} = 5.26 and a hyperfine splitting of 7.03 mT. This *g* value and hyperfine splitting are similar to those of mononuclear Mn^{IV} species,[44,87,88] and, importantly, are unique from the Mn^{II} feature observed in the pink solution as well as the Mn^{II} feature of the starting material. The shape of this signal is perturbed from that observed in other Mn^{IV} species[44,87,88] due to the presence of a broad feature at slightly lower field (~84 mT). This latter feature is attributed to $[Mn^{II}(Cl)_2(Me_2EBC)]$ starting material (Figure A2.12 in the Supporting Information). The observation of $[Mn^{II}(Cl)_2(Me_2EBC)]$ is not surprising, as only 60% of $[Mn^{II}(Cl)_2(Me_2EBC)]$ is converted to $[Mn^{III}(O_2)(Me_2EBC)]^+$ under the preparation conditions for this sample. In a less concentrated sample, this mononuclear Mn^{IV} signal at 131 mT (Figure 2.9, inset) was also observed with a spectral shape that is more similar to other Mn^{IV} species, although with less defined hyperfine splitting (Figure A2.13 in the Supporting Information).[89]

While the perpendicular-mode EPR spectrum of the pink solution reveals the presence of mononuclear Mn^{IV} and Mn^{II} species, the 5 K parallel-mode EPR spectrum shows a signal for a mononuclear Mn^{III} species (Figure 2.9, left). The *g* value and hyperfine splitting of this feature are identical to those of the Mn^{III} species observed in the parallel-mode EPR spectrum of the orange solution (g_{eff} = 8.32; and A = 4.73 mT), which was attributed to $[Mn^{III}(OH)(Cl)(Me_2EBC)]^+$. Therefore, the EPR data collectively indicate that the pink solution is a mixture of a mononuclear Mn^{IV}, Mn^{III}, and Mn^{II} species.

We attempted to determine if the mononuclear Mn^{III} and Mn^{IV} species observed in EPR samples of the pink solution are generated concomitantly from decay of $[Mn^{III}(O_2)(Me_2EBC)]^+$, or if the Mn^{III} species is formed by decay of the Mn^{IV} species. To do this, we collected EPR data

for samples prepared at different time points during the decay of $[Mn^{III}(O_2)(Me_2EBC)]^+$ to the pink solution. The perpendicular-mode spectra collected under these conditions were dominated by intense Mn^{II} signals that consistently obscured the weaker Mn^{IV} signal. Thus, we were not able to monitor the formation of the Mn^{IV} signal over time. However, in the parallel-mode spectra, we initially observed the g = 7.96 signal due to the $[Mn^{III}(O_2)(Me_2EBC)]^+$ complex (Supporting Information; Figure A2.15). After 15 minutes a new six-line signal was observed that overlapped with the signals of $[Mn^{III}(O_2)(Me_2EBC)]^+$. Over the course of 30 minutes, the $[Mn^{III}(O_2)(Me_2EBC)]^+$ was nearly diminished, while the second signal dominated. This second signal, which grew in with time, had g_{eff} = 8.33 and could be attributed to $[Mn^{III}(OH)(Cl)(Me_2EBC)]^+$. These observations suggest that the $[Mn^{III}(OH)(Cl)(Me_2EBC)]^+$ species resulted from the decay of the Mn^{III}-peroxo adduct.

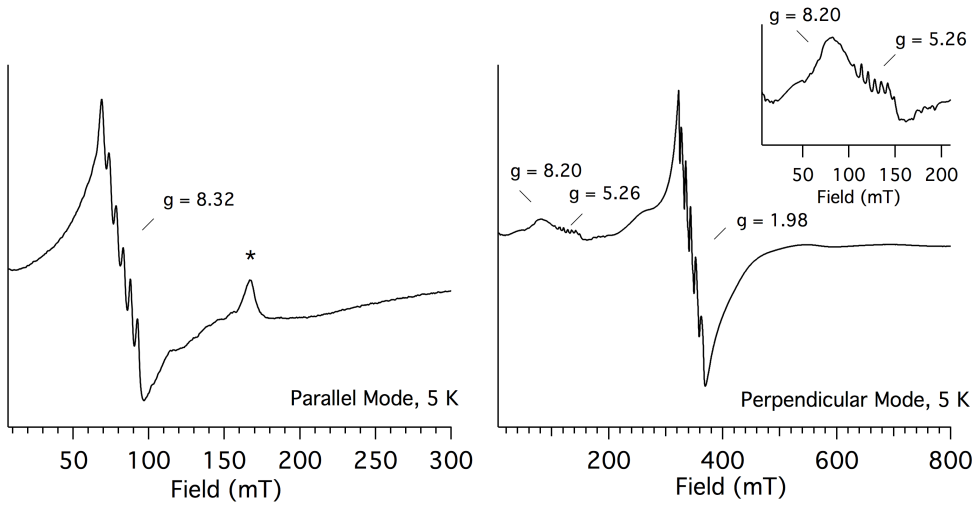

Figure 2.9. 5 K parallel-mode (left) and 5 K perpendicular-mode (right) EPR spectra of the pink solution with enlarged view of 0 – 200 mT in 5 K perpendicular mode (inset). The small feature near 160 mT (marked with an asterisk) is due to dissolved O_2, as has been previously observed.[37]

2.3.6. Comparison of the Electronic Absorption and EPR Properties of the Mn^{IV} Decay Product to Those of $[Mn^{IV}(O)(OH)(Me_2EBC)]^+$. Although EPR spectroscopy establishes the pink solution as a mixture of species, the electronic absorption spectrum of this

solution is highly reminiscent of that reported for the mononuclear Mn^{IV}-oxo complex, $[Mn^{IV}(O)(OH)(Me_2EBC)]^+$.[41] In an acetone/water mixture, $[Mn^{IV}(O)(OH)(Me_2EBC)]^+$ displayed bands at 870 and 530 nm (150 and 250 M^{-1} cm^{-1}, respectively) and was stable at room temperature.[41,43] In comparison, the pink solution, which is formed in CH_2Cl_2, has slightly lower band energies, 930 and 540 nm, and decays within 1 minute at room temperature. To determine if these band shifts and altered stability resulted from solvent differences, the $[Mn^{IV}(O)(OH)(Me_2EBC)]^+$ species was independently prepared[41,43] from $[Mn^{IV}(OH)_2(Me_2EBC)]^{2+}$ and NEt_3 in a 3:1 CH_2Cl_2/acetone mixture at -30 °C (we were unable to prepare the Mn^{IV}-oxo complex in pure CH_2Cl_2 due to the low solubility of $[Mn^{IV}(OH)_2(Me_2EBC)]^{2+}$ in CH_2Cl_2). In 3:1 CH_2Cl_2/acetone, $[Mn^{IV}(O)(OH)(Me_2EBC)]^+$ showed bands at 980 and 560 nm (Figure 2.10, black dashed trace) that were very similar, but not identical, to those of the pink solution. The independently prepared $[Mn^{IV}(O)(OH)(Me_2EBC)]^+$ complex in the CH_2Cl_2/acetone mixture also showed an EPR signal at g_{eff} = 5.20 with a hyperfine splitting of 7.01 mT (Figure A2.13 in the Supporting Information), consistent with previously reported EPR spectra of $[Mn^{IV}(O)(OH)(Me_2EBC)]^+$ in other solvents,[44,90] and nearly identical to those observed for the Mn^{IV} decay product present in the pink solution (g_{eff} = 5.26 and A = 7.03 mT). While both the electronic absorption and EPR properties of $[Mn^{IV}(O)(OH)(Me_2EBC)]^+$ in CH_2Cl_2/acetone are similar to those of the Mn^{IV} decay product, they are not identical. Therefore, the Mn^{IV} species generated from the decay of $[Mn^{III}(O_2)(Me_2EBC)]^+$ is *not* formulated as $[Mn^{IV}(O)(OH)(Me_2EBC)]^+$. However, given the spectral similarities between $[Mn^{IV}(O)(OH)(Me_2EBC)]^+$ and the Mn^{IV} decay product, we propose that the latter is a Mn^{IV}-oxo species, but with an anion other than hydroxide, such as a chloride, occupying the *cis* coordination site. To support this assignment, we performed TD-DFT calculations to predict an electronic absorption spectrum for the $[Mn^{IV}(O)(Cl))(Me_2EBC)]^+$

complex. The TD-DFT-calculated absorption spectrum (Figure A2.14 in the Supporting Information) shows good agreement between the experimental absorption spectrum of the pink solution, with bands at 1050 and 530 nm. Compared to the Mn^{IV}-oxohydroxo complex, the experimental absorption spectrum of the pink solution shows a slight red-shift of the lowest energy absorption band (Figure 2.10). The TD-DFT-calculated spectrum reproduces this trend well (Figure A2.14).

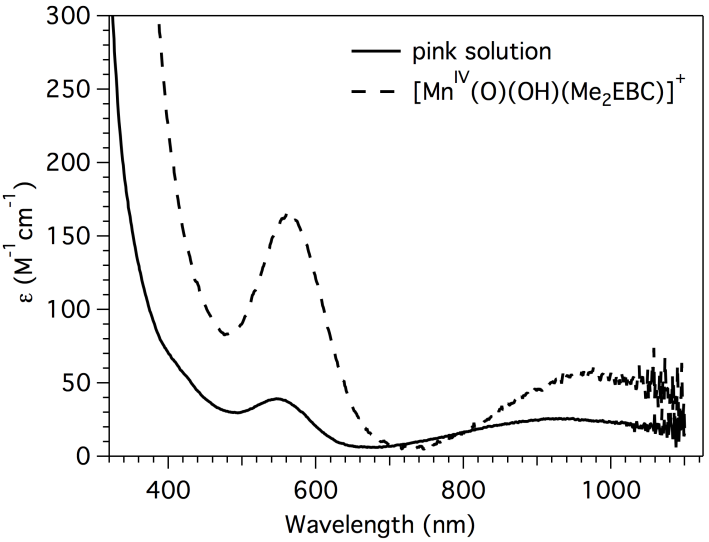

Figure 2.10. Electronic absorption spectrum of independently prepared $[Mn^{IV}(O)(OH)(Me_2EBC)]^+$ in a CH_2Cl_2/acetone mixture at -30 °C (black dashed trace) and the pink solution (black solid trace). Units are given as molar extinction coefficients, ε ($M^{-1}cm^{-1}$), based on the initial concentration of $[Mn^{II}(Cl)_2(Me_2EBC)]$, to compare to data for $[Mn^{IV}(O)(OH)(Me_2EBC)]^+$.

2.4 Discussion

Although there has been much recent success in generating peroxomanganese(III) species using a variety of reaction conditions and ligand platforms,[5] the ability to activate these adducts to generate high-valent, mononuclear intermediates has been challenging. There are a few reports of O—O bond activation of peroxomanganese(III) species to form oxo-bridged $Mn^{III}Mn^{IV}$ species.[37,87] While these processes offer insight into the formation of dimanganese(III,IV) cores

in Mn enzymes, such as Mn-RNR,[12] these dinuclear species with bridging oxo ligands are significantly less potent oxidants when compared with mononuclear Mn^{IV} centers with terminal oxo ligands. As Mn^{III}-peroxo adducts are often invoked as precursors to mononuclear Mn-oxo adducts,[91,92] it is important to identify systems where terminal Mn-oxo species can be formed by activation of Mn^{III}-peroxo units. This report of decay of a peroxomanganese(III) species to give, among other products, a mononuclear, high-valent Mn^{IV} species, offers unique insight into these processes.

The $[Mn^{III}(O_2)(Me_2EBC)]^+$ complex was prepared by reaction of $[Mn^{II}(Cl)_2(Me_2EBC)]$ with 10 equiv. of KO_2 and is stable indefinitely at -60 °C. The EPR signals for $[Mn^{III}(O_2)(Me_2EBC)]^+$ were similar to those observed for other Mn^{III}-peroxo adducts. With this preparation, an EPR signal for Mn^{II} was absent, suggesting full consumption of the $[Mn^{II}(Cl)_2(Me_2EBC)]$ starting material. When a solution of $[Mn^{III}(O_2)(Me_2EBC)]^+$ was warmed to 25 °C, it decayed to give an orange solution. This solution contains two mononuclear Mn^{III} products, one of which we have identified by ESI-MS as $[Mn^{III}(OH)(Cl)(Me_2EBC)]^+$ (Scheme 2.4). In addition, DFT-calculated ground- and excited-state properties of $[Mn^{III}(OH)(Cl)(Me_2EBC)]^+$ are consistent with the major EPR and electronic absorption features of the orange solution. On this basis we propose that $[Mn^{III}(OH)(Cl)(Me_2EBC)]^+$ is the major component of the orange solution and the predominant decay product of $[Mn^{III}(O_2)(Me_2EBC)]^+$. At room temperature, this decay process proceeds without the observation of any intermediates. The mechanism for this decay process is unclear.

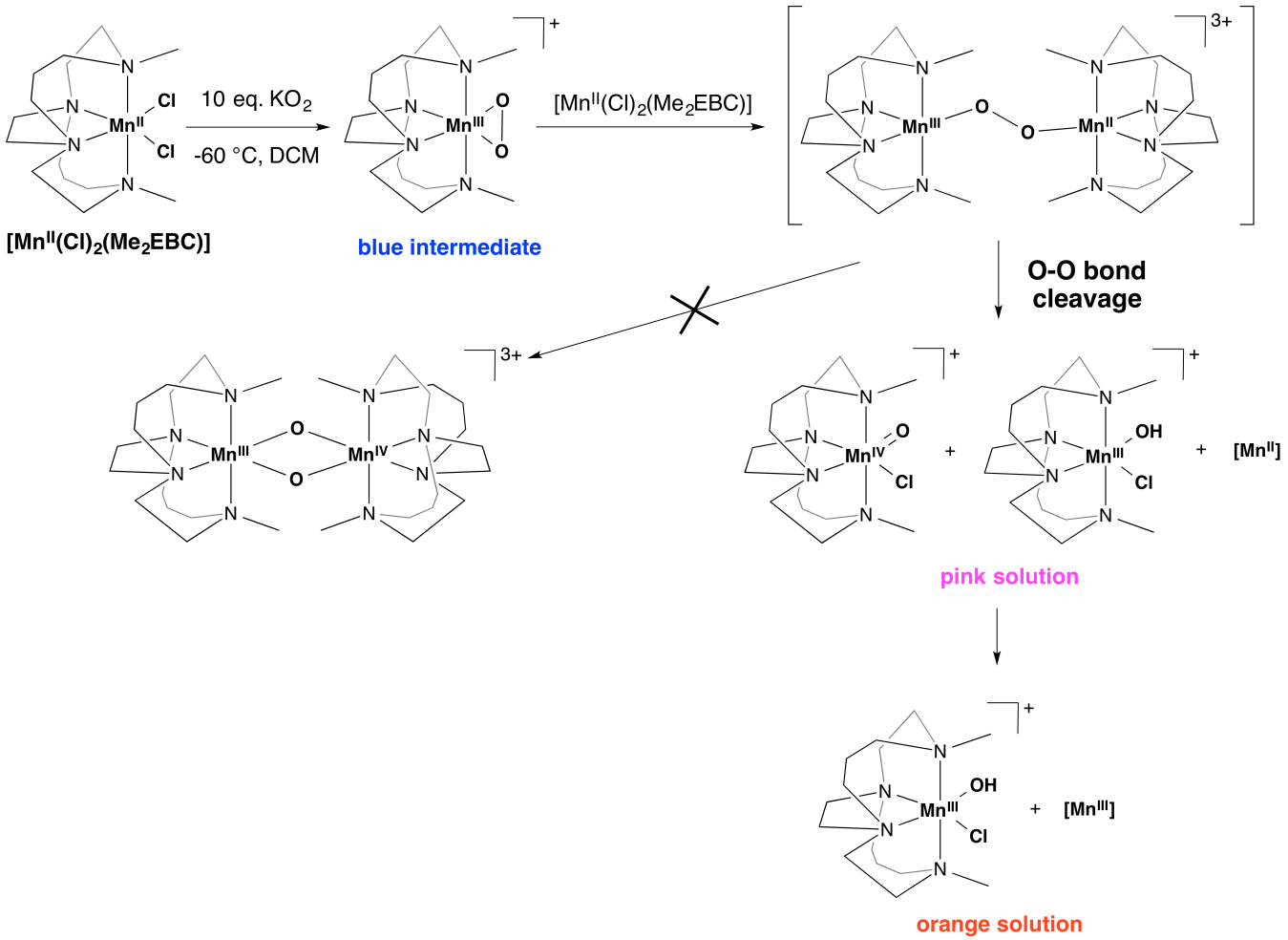

Scheme 2.4. Formation and proposed decay pathways of $[Mn^{III}(O_2)(Me_2EBC)]^+$ to give the Mn species identified in the pink and the orange solutions. The molecular formulations of the species labeled $[Mn^{II}]$ and $[Mn^{III}]$ are uncertain.

In contrast, when $[Mn^{III}(O_2)(Me_2EBC)]^+$ is formed in substoichiometric yield (60%), its decay is associated with the formation of a pink solution. EPR investigations reveal that this solution contains mononuclear Mn^{IV}, Mn^{III}, and Mn^{II} species. The Mn^{III} species has EPR signals identical to those of $[Mn^{III}(OH)(Cl)(Me_2EBC)]^+$, while the Mn^{IV} species has spectroscopic properties quite similar to those of $[Mn^{IV}(O)(OH)(Me_2EBC)]^+$. Accordingly, we formulated the Mn^{IV} species from this intermediate as $[Mn^{IV}(O)(Cl)(Me_2EBC)]^+$ (Scheme 2.4). We postulate that the decay of $[Mn^{III}(O_2)(Me_2EBC)]^+$, when formed in 60% yield, proceeds by attack of the peroxo ligand on the Mn^{II} center of unreacted $[Mn^{II}(Cl)_2(Me_2EBC)]$ starting material, leading to

formation of an unobserved μ-peroxodimanganese(II,III) intermediate (Scheme 2.4). This step is consistent with the known nucleophilicity of the Mn^{III}-peroxo moiety.[5] This peroxo-bridged species rapidly decays by one-electron oxidation of each Mn center, coupled to two-electron reduction of the bridging peroxo, to initiate cleavage of the O—O bond. A similar mode of reactivity was observed for the $[Mn^{III}(O_2)(N4py)]^+$ complex, which reacted with $[Mn^{II}(OTf)(N4py)]^+$ starting material to give the mixed-valence, dimeric product $[Mn^{III}Mn^{IV}(\mu\text{-}O)_2(N4py)_2]^{3+}$ (Scheme 2.1c).[38] In the present system, the steric bulk of the Me_2EBC ligand presumably prevents formation of a bis(μ-oxo) dimer.[93] Instead, we propose that O—O cleavage results in the formation of the mononuclear Mn^{IV} and Mn^{III} species detected by EPR spectroscopy, which we have formulated as $[Mn^{IV}(O)(Cl)(Me_2EBC)]^+$ and $[Mn^{III}(OH)(Cl)(Me_2EBC)]^+$ (Scheme 2.4). We note that the Mn—Mn distance in a μ-trans-1,2-peroxodimanganese(III,III) species reported by Coggins *et al.* was observed to be much longer (4.113 Å) than the corresponding μ-oxodimanganese(III,III) species (3.520 Å),[40] and is significantly longer than the Mn—Mn distance reported for the bis(μ-oxo)dimanganese(III,IV) species supported by the N4py ligand (2.6483(8) Å).[38] Thus, while a peroxo-bridged dimanganese intermediate might transiently form upon reaction of $[Mn^{III}(O_2)(Me_2EBC)]^+$ with $[Mn^{II}(Cl)_2(Me_2EBC)]$, we propose that the formation of a stable bis(μ-oxo)dimanganese product is not favored given the steric constraints of the the Me_2EBC ligand, resulting in the observation of mononuclear decay products.

To evaluate the proposal that the components of the pink solution result from reaction of $[Mn^{III}(O_2)(Me_2EBC)]^+$ with unreacted $[Mn^{II}(Cl)_2(Me_2EBC)]$, we prepared $[Mn^{III}(O_2)(Me_2EBC)]^+$ in high yields using 10 equiv. of KO_2. After waiting 150 minutes to allow for the decay of unreacted KO_2, we added one equiv. of $[Mn^{II}(Cl)_2(Me_2EBC)]$ to $[Mn^{III}(O_2)(Me_2EBC)]^+$ at -60 ºC. From this reaction, we observed the formation of the pink solution within 25 minutes (Figure

2.11). Thus, the formation of the pink solution is directly associated with a reaction with $[Mn^{III}(O_2)(Me_2EBC)]^+$ and $[Mn^{II}(Cl)_2(Me_2EBC)]$ (Scheme 2.4). In the absence of $[Mn^{II}(Cl)_2(Me_2EBC)]$, $[Mn^{III}(O_2)(Me_2EBC)]^+$ decays to a mononuclear Mn^{III} species, the orange solution, without the observation of any intermediates.

Although we have spectroscopic evidence for the formation of a Mn^{IV} species from the reaction of $[Mn^{III}(O_2)(Me_2EBC)]^+$ with $[Mn^{II}(Cl)_2(Me_2EBC)]$, this species is very unstable in CH_2Cl_2 and decays to give $[Mn^{III}(OH)(Cl)(Me_2EBC)]^+$ and a second Mn^{III} species, which are stable at room temperature for weeks. At present, the decay route for the Mn^{IV} product is unclear, but we note that $[Mn^{IV}(O)(OH)(Me_2EBC)]^+$, which is quite stable in a variety of solvents (MeCN, acetone, and water), also rapidly decays in CH_2Cl_2. Thus, the supposed advantage of the Me_2EBC platform in stabilizing high-valent Mn^{IV} species is neutralized in CH_2Cl_2. Unfortunately, we have been unable to prepare the Mn^{III}-peroxo complex in solvents other than CH_2Cl_2, including acetonitrile, butyronitrile, methanol, tetrahydrofuran, dimethylformamide, and dimethyl sulfoxide, and toluene, as well as mixtures of these solvents.

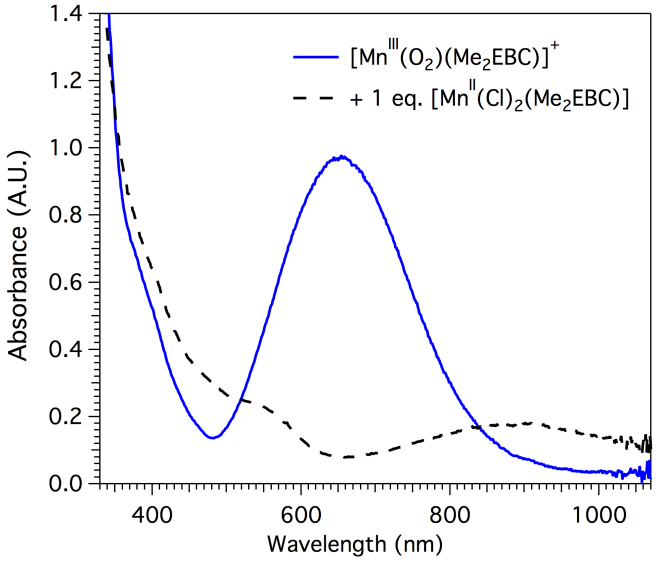

Figure 2.11. Addition of 1 equiv. of $[Mn^{II}(Cl)_2(Me_2EBC)]$ to $[Mn^{III}(O_2)(Me_2EBC)]^+$.

2.4.1. Comparison of the Electronic Structure and Bonding of Mn^{III}-peroxo and Mn^{III}-hydroxo Adducts. With our analysis of the XAS data of $[Mn^{III}(O_2)(Me_2EBC)]^+$ and $[Mn^{III}(OH)(Cl)(Me_2EBC)]^+$, we have now characterized Mn^{II}-, Mn^{III}-, and Mn^{IV}-Me_2EBC complexes with dichloro, oxohydroxo, dihydroxo, hydroxochloro, and peroxo ligands. This range of Mn-oxygen complexes supported by the same ligand system supplies new insight into changes in XAS pre-edge features with perturbations in Mn-ligand bonding. Recently, DeBeer and coworkers reported an X-ray emission study correlating the degree of O—O bond activation with a shift in the pre-edge peak energy, providing a useful spectroscopic benchmark.[94] Here, we have observed a marked difference in the XAS pre-edge spectra of $[Mn^{III}(O_2)(Me_2EBC)]^+$ and $[Mn^{III}(OH)(Cl)(Me_2EBC)]^+$. The pre-edge region of $[Mn^{III}(O_2)(Me_2EBC)]^+$ contains a single, broad peak, while $[Mn^{III}(OH)(Cl)(Me_2EBC)]^+$ shows two separate peaks (Supporting Information; Figures A2.4 and A2.8). On the basis of TD-DFT calculations, the pre-edge region of each complex is dominated by one transition to the unoccupied α-spin Mn 3*d* orbital, with a set of five weaker transitions to each of the β-spin Mn 3*d* e_g- and t_{2g}-derived orbitals also contributing to the pre-edge region. In the Mn^{III}-peroxo complex, the high covalency of the α-spin Mn $3d_{xy}$ orbital mixes in substantial Mn 4*p* character, presumably by a configuration interaction (CI) mechanism involving the Mn $3d_{xy}$, Mn $4p_x$, and peroxo π* orbitals. Covalency-induced metal 3*d*-4*p* mixing has been previously described in terms of a CI mechanism by DeBeer and Solomon.[95] Thus, we propose that the high Mn-peroxo covalency accounts for the significantly higher pre-edge intensity of $[Mn^{III}(O_2)(Me_2EBC)]^+$ relative to $[Mn^{III}(OH)(Cl)(Me_2EBC)]^+$ (Table 2.2). Additionally, this high covalency destabilizes the α-spin Mn $3d_{xy}$ MO, which is Mn-peroxo σ-antibonding. This causes the α-spin 1s-to-Mn $3d_{xy}$ excitation to occur at an energy intermediate between excitations to the β-spin Mn 3*d* e_g and t_{2g} orbitals (Figure A2.6 in Supporting Information). Because of the close proximity of these excitations,

they collectively contribute to a single pre-edge peak with a large width, as observed experimentally for $[Mn^{III}(O_2)(Me_2EBC)]^+$ (Figure 2.3). In contrast, for $[Mn^{III}(OH)(Cl)(Me_2EBC)]^+$, the TD-DFT calculations predict that excitation to the α-spin Mn 3*d* MO occurs at roughly the same energy as excitations to the β-spin Mn 3*d* t_{2g}-derived orbitals (Figure A2.9). At ~1.5 eV higher in energy, excitations to the β-spin Mn 3*d* e_g-derived orbitals are predicted. These two sets of transitions, well separated in energy, give rise to two distinct pre-edge peaks of comparable intensity, as observed experimentally for $[Mn^{III}(OH)(Cl)(Me_2EBC)]^+$ (Figure 2.3) and predicted by the TD-DFT calculations (Figure A2.9).

To date, the only other Mn^{III}-peroxo species that has been characterized by XAS is the $[Mn^{III}(O_2)(TMC)]^+$ complex of Nam and co-workers. This complex has a much lower edge energy (6547.1 eV) in comparison to that of $[Mn^{III}(O_2)(Me_2EBC)]^+$ (6550.3 eV).[73] In both cases, these edge energies were referenced to Mn foil (edge energy = 6439.0 eV). However, in both cases the Mn^{III}-peroxo adducts showed an edge shift to higher energy (2.4 and 3.2 eV, respectively) from their respective Mn^{II} complexes. Thus, the difference in edge energies between $[Mn^{III}(O_2)(TMC)]^+$ and $[Mn^{III}(O_2)(Me_2EBC)]^+$ likely arises from differences in the macrocyclic supporting ligands. Also of note are differences in pre-edge intensity between the Mn^{II} and Mn^{III}-peroxo complexes. Although $[Mn^{III}(O_2)(Me_2EBC)]^+$ shows a clear increase in pre-edge intensity compared with $[Mn^{II}Cl_2(Me_2EBC)]$, the pre-edge peak intensity of $[Mn^{III}(O_2)(TMC)]^+$ appears to be less than that of $[Mn^{II}(TMC)]^{2+}$.[73] This is presumably related to large distortions from centrosymmetry for the $[Mn^{II}(TMC)]^{2+}$ complex.

2.5 Conclusions

The generation of a high yield of a peroxomanganese(III) species supported by the macrocyclic ligand, Me_2EBC, allowed for a detailed spectroscopic and computational investigation into electronic structure and reactivity. $[Mn^{III}(O_2)(Me_2EBC)]^+$ displays unique reactivity and decays to mononuclear Mn^{IV} and Mn^{III} species. For the first time, Mn^{III}-peroxo and Mn^{III}-hydroxo species were evaluated by XAS and found to contain distinct markers in the pre-edge spectra that indicate differences in covalency between peroxo and non-peroxo-manganese(III) species. The activation of the Mn^{III}-peroxo species was observed to occur by reaction with a mononuclear Mn^{II} complex and is proposed to proceed through a transient dinuclear, peroxo-bridged $[Mn^{II}Mn^{III}(\mu\text{-}O_2)(Me_2EBC)_2]^{3+}$ intermediate that readily undergoes O—O bond cleavage. Thus, the Me_2EBC achieves a balancing act in terms of steric bulk; it is insufficiently bulky to prevent Mn^{III}-peroxo activation through the formation of a peroxo-bridged $Mn^{II}Mn^{III}$ intermediate, but it is sufficiently bulky to prevent the formation of a thermodynamically stable oxo-bridged $Mn^{III}Mn^{IV}$ product. However, although this work provides evidence for the formation of a mononuclear Mn^{IV} product from decay of a Mn^{III}-peroxo species, this is just one of several products of the decay reaction. The field of O—O bond activation of Mn^{III}-peroxo intermediates still lacks a system that is able to cleanly produce high-valent, mononuclear oxidants in the absence of low-valent side products. An understanding of the role of the ligand in both electronically activating the Mn^{III}-peroxo moiety, as well as utilizing steric control to modulate specific bond cleavage events, will be necessary to design systems that undergo activation more efficiently.

2.6 References

(1) Cotruvo, J. A. J.; Stubbe, J. *Metallomics* **2012**, *4*, 1020-1036.

(2) McEvoy, J. P.; Brudvig, G. W. *Chem. Rev.* **2006**, *106*, 4455-4483.
(3) Miller, A.-F. *Curr. Opin. Chem. Biol.* **2004**, *8*, 162-168.
(4) Wu, A. J.; Penner-Hahn, J. E.; Pecoraro, V. L. *Chem. Rev.* **2004**, *104*, 903-938.
(5) Leto, D. F.; Jackson, T. A. *J. Biol. Inorg. Chem.* **2014**, *19*, 1-15.
(6) Bull, C.; Niederhoffer, E. C.; Yoshida, T.; Fee, J. A. *J. Am. Chem. Soc.* **1991**, *113*, 4069-4076.
(7) Grove, L. E.; Brunold, T. C. *Comments Inorg. Chem* **2008**, *29*, 134-168.
(8) Hearn, A. S.; Stroupe, M. E.; Cabelli, D. E.; Lepock, J. R.; Tainer, J. A.; Nick, H. S.; Silverman, D. N. *Biochemistry* **2001**, *40*, 12051-12058.
(9) Hearn, A. S.; Tu, C. K.; Nick, H. S.; Silverman, D. N. *J. Biol. Chem.* **1999**, *274*, 24457-24460.
(10) Jackson, T. A.; Karapetian, A.; Miller, A.-F.; Brunold, T. C. *Biochemistry* **2005**, *44*, 1504-1520.
(11) Boal, A. K.; Cotruvo, J. A.; Stubbe, J.; Rosenzweig, A. C. *Science* **2010**, *329*, 1526-1530.
(12) Cotruvo, J. A. J.; Stich, T. A.; Britt, R. D.; Stubbe, J. *J. Am. Chem. Soc.* **2013**, *135*, 4027-4039.
(13) Borowski, T.; Bassan, A.; Richards, N. G. J.; Siegbahn, P. E. M. *J. Chem. Theory Comput.* **2005**, *1*, 686-693.
(14) Opaleye, O.; Rose, R.-S.; Whittaker, M. M.; Woo, E.-J.; Whittaker, J. W.; Pickersgill, R. W. *J. Biol. Chem.* **2006**, *281*, 6428-6433.
(15) Reinhardt, L. A.; Svedruzic, D.; Chang, C. H.; Cleland, W. W.; Richards, N. G. J. *J. Am. Chem. Soc.* **2003**, *125*, 1244-1252.
(16) Svedružic, D.; Jónsoon, S.; Toyota, C. G.; Reinhardt, L. A.; Ricagno, S.; Lindqvist, Y.; Richards, N. G. J. *Arch. Biochem. Biophys.* **2005**, *433*, 176-192.
(17) Tanner, A.; Bowater, L.; Fairhurst, S. A.; Bornemann, S. *J. Biol. Chem.* **2001**, *276*, 43627-43634.
(18) Annaraj, J.; Cho, J.; Lee, Y.-M.; Kim, S. Y.; Latifi, R.; de Visser, S. P.; Nam, W. *Angew. Chem. Int. Ed.* **2009**, *48*, 4150-4153.
(19) Cho, J.; Sarangi, R.; Nam, W. *Acc. Chem. Res.* **2012**, *45*, 1321-1330.
(20) Geiger, R. A.; Chattopadhyay, S.; Day, V. W.; Jackson, T. A. *J. Am. Chem. Soc.* **2010**, *132*, 2821-2831.
(21) Geiger, R. A.; Leto, D. F.; Chattopadhyay, S.; Dorlet, P.; Anxolabéhère-Mallart, E.; Jackson, T. A. *Inorg. Chem.* **2011**, *50*, 10190-10203.
(22) Groni, S.; Blain, G.; Guillot, R.; Policar, C.; Anxolabéhère-Mallart, E. *Inorg. Chem.* **2007**, *46*, 1951-1953.
(23) Kang, H.; Cho, J.; Cho, K.-B.; Nomura, T.; Ogura, T.; Nam, W. *Chem. Eur* **2013**, *19*, 14119-14125.
(24) Kitajima, N.; Komatsuzaki, H.; Hikichi, S.; Osawa, M.; Moro-oka, Y. *J. Am. Chem. Soc.* **1994**, *116*, 11596-11597.
(25) Seo, M. S.; Kim, J. Y.; Annaraj, J.; Kim, Y.; Lee, Y.-M.; Kim, S.-J.; Kim, J.; Nam, W. *Angew. Chem. Int. Ed.* **2007**, *46*, 377-380.

(26) Shook, R. L.; Gunderson, W. A.; Greaves, J.; Ziller, J. W.; Hendrich, M. P.; Borovik, A. S. *J. Am. Chem. Soc.* **2008**, *130*, 8888-8889.
(27) Shook, R. L.; Peterson, S. M.; Greaves, J.; Moore, C.; Rheingold, A. L.; Borovik, A. S. *J. Am. Chem. Soc.* **2011**, *133*, 5810-5817.
(28) Singh, U. P.; Sharma, A. K.; Hikichi, S.; Komatsuzaki, H.; Moro-oka, Y.; Akita, M. *Inorg. Chim. Acta* **2006**, *359*, 4407-4411.
(29) Pecoraro, V. L.; Hsieh, W.-Y. *Inorg. Chem.* **2008**, *2008*, 1765-1778.
(30) Mullins, C. S.; Pecoraro, V. L. *Coord. Chem. Rev.* **2008**, *252*, 416-443.
(31) Pawlak, P. L.; Panda, M.; Li, J.; Banerjee, A.; Averill, D. J.; Nikolovski, B.; Shay, B. J.; Brennessel, W. W.; Chavez, F. A. *Eur. J. Inorg. Chem.* **2015**, *2015*, 646-655.
(32) Company, A.; Lloret-Fillol, J.; Costas, M. In *Comprehensive Inorganic Chemistry II*; Elsevier B.V: 2013; Vol. 3, p 487-564.
(33) Sismore, M. F.; Selke, M.; Burstyn, J. N.; Valentine, J. S. *Inorg. Chem.* **1997**, *36*, 979-984.
(34) Ligand abbreviations: H_3bupa^{2-}: the dianion of Bis[(N′-tert-butylurealy)-N-ethyl]-(6-pivalamido-2-pyridylmethyl)amine; H_2bpaa^{-}: the anion of N-[Bis(6-pivalamido-2-pyridylmethyl)](N′-4 fluorophenylcarbamoylmethyl)amine; $L^7py_2^R$: $L^7py_2^H$ is 1,4-bis(2-pyridylmethyl)-1,4-diazepane, R with varying substituents; TMC: 14-TMC is 1,4,8,11-tetramethyl-1,4,8,11-tetraazacyclotetradecane and 13-TMC is 1,4,7,10-tetramethyl-1,4,7,10-tetraazacyclotridecane; mL52: N-methyl-N, N′, N′-tris(2-pyridylmethyl)ethane-1,2-diamine; N4py: N,N-bis(2-pyridylmethyl)-N-bis(2-pyridyl)methylamine; N_4O^{-}: anion of N-(2-hydroxybenzyl)-N,N'-bis[2-(N-methylimdazolyl)methyl]ethane-1,2-diamine); 6-Me-DPEN = N,N-bis(6-methyl-2-pyridylmethyl)ethane-1,2-diamine.
(35) Shook, R. L.; Borovik, A. S. *Inorg. Chem.* **2010**, *49*, 3646-3660.
(36) Geiger, R. A.; Chattopadhyay, S.; Day, V. W.; Jackson, T. A. *Dalton Trans.* **2011**, *40*, 1707-1715.
(37) Groni, S.; Dorlet, P.; Blain, G.; Bourcier, S.; Guillot, R.; Anxolabéhère-Mallart, E. *Inorg. Chem.* **2008**, *47*, 3166-3172.
(38) Leto, D. F.; Chattopadhyay, S.; Day, V. W.; Jackson, T. A. *Dalton Trans.* **2013**, *42*, 13014-13025.
(39) Ching, H. Y. V.; Anxolabéhère-Mallart, E.; Colmer, H. E.; Costentin, C.; Dorlet, P.; Jackson, T. A.; Policar, C.; Robert, M. *Chem. Sci.* **2014**, *5*, 2304-2310.
(40) Coggins, M. K.; Sun, X.; Kwak, Y.; Solomon, E. I.; Rybak-Akimova, E.; Kovacs, J. A. *J. Am. Chem. Soc.* **2013**, *135*, 5631-5640.
(41) Chattopadhyay, S.; Geiger, R. A.; Yin, G.; Busch, D. H.; Jackson, T. A. *Inorg. Chem.* **2010**, *49*, 7530-7535.
(42) Leto, D. F.; Jackson, T. A. *Inorg. Chem.* **2014**, *53*, 6179-6194.
(43) Yin, G.; Danby, A. M.; Kitko, D.; Carter, J. D.; Scheper, W. M.; Busch, D. H. *J. Am. Chem. Soc.* **2008**, *130*, 16245-16253.

(44) Yin, G.; McCormick, J. M.; Buchalova, M.; Danby, A. M.; Rodgers, K.; Day, V. W.; Smith, K.; Perkins, C. M.; Kitko, D.; Carter, J. D.; Scheper, W. M.; Busch, D. H. *Inorg. Chem.* **2006**, *45*, 8052-8061.
(45) Stoll, S.; Schweiger, A. *J. Magn. Reson.* **2006**, *178*, 42-55.
(46) George, G. N. In *EXAFSPAK* Stanford Synchrotron Radiation Laboratory; Stanford, CA, 1990.
(47) Rehr, J. J.; Mustre de Leon, J.; Zabinsky, S. I.; Albers, R. C. *J. Am. Chem. Soc.* **1991**, *113*, 5135-5140.
(48) Neese, F. *Wiley Interdiscip. Rev.* **2012**, *2*, 73-78.
(49) Becke, A. D. *J. Chem. Phys.* **1986**, *84*, 4524-4529.
(50) Perdew, J. P. *Phys. Rev. B* **1986**, *33*, 8822-8824.
(51) Schäfer, A.; Horn, H.; Ahlrichs, R. *J. Chem. Phys.* **1992**, *97*, 2571-2577.
(52) Schäfer, A.; Huber, C.; Ahlrichs, R. *J. Chem. Phys.* **1994**, *100*, 5829-5835.
(53) Neese, F. *J. Comput. Chem.* **2003**, *24*, 1740-1747.
(54) Sinnecker, S.; Rajendran, A.; Klamt, A.; Diedenhofen, M.; Neese, F. *J. Phys. Chem. A* **2006**, *110*, 2235-2245.
(55) Bauernschmitt, R.; Ahlrichs, R. *Chem. Phys. Lett.* **1996**, *256*, 454-464.
(56) Casida, E. M.; Jamorski, C.; Casida, K. C.; Salahub, D. R. *J. Chem. Phys.* **1998**, *108*, 4439-4449.
(57) Stratman, R. E.; Scuseria, G. E.; Frisch, M. J. *J. Chem. Phys.* **1998**, *109*, 8218-8224.
(58) Hirata, S.; Head-Gordon, M. *Chem. Phys. Lett.* **1999**, *302*, 375-382.
(59) Hirata, S.; Head-Gordon, M. *Chem. Phys. Lett.* **1999**, *314*, 291-299.
(60) Becke, A. D. *J. Chem. Phys.* **1993**, *98*, 1372-1377.
(61) Becke, A. D. *J. Chem. Phys.* **1993**, *98*, 5648-5652.
(62) Lee, C.; Yang, W.; Parr, R. G. *Phys. Rev. B* **1988**, *37*, 785-789.
(63) Neese, F. *J. Chem. Phys.* **2007**, *127*, 164112-164120.
(64) Sinnecker, S.; Neese, F. *J. Phys. Chem. A.* **2006**, *110*, 12267-12275.
(65) Riplinger, C.; Kao, J. P. Y.; Rosen, G. M.; Kathirvelu, V.; Eaton, G. R.; Eaton, S. S.; Kutateladze, A.; Neese, F. *J. Am. Chem. Soc.* **2009**, *131*, 10092-10106.
(66) Laaksonen, L. *J. Mol. Graphics* **1992**, *10*, 33-34.
(67) Bergman, D. L.; Laaksonen, L.; Laaksonen, A. *J. Mol. Graph. Model.* **1997**, *15*, 301-306.
(68) Weigend, F.; Ahlrichs, R. *Phys. Chem. Chem. Phys.* **2005**, *7*, 3297-3305.
(69) Roemelt, M.; Beckwith, M. A.; Duboc, C.; Collomb, M.-N.; Neese, F.; DeBeer, S. *Inorg. Chem.* **2011**, *51*, 680-687.
(70) Roberts, J. L. J.; Sawyer, D. T. *J. Am. Chem. Soc.* **1981**, *103*, 712-714.
(71) Molar extinction coefficients were calculated assuming 100% conversion of $[Mn^{II}(Cl)_2(Me_2EBC)]$ to $[Mn^{III}(O_2)(Me_2EBC)]^+$ under these conditions.
(72) Gupta, R., Taguchi, T., Borovik, A. S., Hendrich, M. P. *Inorg. Chem.* **2013**, *52*, 12568-12575.

(73) So, H.; Park, J.-H.; Cho, K.-B.; Lee, Y.-M.; Seo, M. S.; Cho, J.; Sarangi, R.; Nam, W. *J. Am. Chem. Soc.* **2014**, *136*, 12229−12232.
(74) Colmer, H. E.; Geiger, R. A.; Leto, D. F.; Wijeratne, G.; Day, V. W.; Jackson, T. A. *Dalton Trans.* **2014**, *43*, 17949-17963.
(75) Tao, J., Perdew, J. P., Staroverov, V. N., Scuseria, G. E. *Phys. Rev. Lett* **2003**, *91*, 146401.
(76) Grimme, S. A., J.; Ehrlich, S.; Krieg, H. *J. Chem. Phys.* **2010**, *132*, 154104.
(77) Grimme, S. E., S.; Goerigk, L. *J. Comput. Chem.* **2011**, *32*, 1456-1465.
(78) Neese, F. *J. Biol. Inorg. Chem.* **2006**, *11*, 702-711.
(79) As described by Hendrich and co-workers (see ref. 72), to determine the concentration of these Mn^{III} species from the EPR intensities, it is necessary to know the splitting of the $m_s = \pm 2$ doublet, which depends on *E/D* and *D*, and g_z,. Determining the last parameter requires multi-frequency EPR measurements, which have not been performed for this sample.
(80) Mossin, S., Weihe, H., Barra, A. L. *J. Am. Chem. Soc.* **2002**, *124*, 8764-8765.
(81) Krzystek, J. Y., G. J.; Park, J.-H.; Britt, R. D.; Meisel, M. W.; Brunel, L.-C.; Telser, J. *Inorg. Chem.* **2003**, *42*, 4610-4618.
(82) Wijeratne, G. B., Corzine, B., Day, V. W., Jackson, T. A. *Inorg. Chem.* **2014**, *53*, 7622-7634.
(83) Coggins, M. K., Brines, L. M., Kovacs, J. A. *Inorg. Chem.* **2013**, *52*, 12383-12393.
(84) Goldsmith, C. R., Cole, A. P., Stack, T. D. P. *J. Am. Chem. Soc.* **2005**, *2005*, 9904-9912.
(85) Shirin, Z.; Young, V. G., Jr.; Borovik, A. S. *Chem. Commun.* **1997**, 1967-1968.
(86) El Ghachtouli, S. L.-K., B.; Dorlet, P.; Guillot, R.; Anxolabehere-Mallart, E.; Costentin, C.; Aukauloo, A. *Energy Environ. Sci.* **2011**, *4*, 2041-2044.
(87) Leto, D. F.; Ingram, R.; Day, V. W.; Jackson, T. A. *Chem. Commun.* **2013**, *49*, 5378-5380.
(88) Parsell, T. H.; Behan, R. K.; Green, M. T.; Hendrich, M. P.; Borovik, A. S. *J. Am. Chem. Soc.* **2006**, *128*, 8728-8729.
(89) Although the Mn^{IV} and Mn^{II} centers should have different power saturation properties, attempts to better isolate the Mn^{IV} signal by saturating the Mn^{II} signal were unsuccessful; see Supporting Information, Figure A2.14.
(90) Dong, L.; Wang, Y.; Lv, Y.; Chen, Z.; Mei, F.; Xiong, H.; Yin, G. *Inorg. Chem.* **2013**, *52*, 5418-5427.
(91) Lyakin, O.; Ottenbacher, R.; Bryliakov, K.; Talsi, E. *Top. Catal.* **2013**, *56*, 939-949.
(92) Talsi, E.; Bryliakov, K. P. *Coord. Chem. Rev.* **2012**, *256*, 1418-1434.
(93) To the best of our knowledge, no oxo-bridged, dinuclear Mn complexes have been reported that feature the Me_2EBC ligand. This is likely due to the pendant N-methyl substituents, which crowd the Mn center. Figure A2.14 of Supporting

Information shows a space-filling model of the $[Mn^{III}(O_2)(Me_2EBC)]^+$ complex that demonstrates the steric impact of the N-methyl moieties.

(94) Rees, J. A.; Martin-Diaconescu, V.; Kovacs, J. A.; DeBeer, S. *Inorg. Chem.* **2015**, *54*, 6410-6422.

(95) DeBeer George, S. B., P.; Solomon, E.I. *J. Am. Chem. Soc.* **2005**, *127*, 667-674.

CHAPTER 3

Activation of a Mn^{III}-peroxo Intermediate by Brønsted Acid, Electrophilic Substrates, and Lewis Acids

3.1 Introduction

There are only a few reports of activation of Mn^{III}-peroxo species, and evidence for the formation of high-valent, mononuclear oxidants from Mn^{III}-peroxo complexes is severely lacking. There are only a few examples of activation to form dinuclear Mn species by activation with Mn^{II} or Mn^{III} centers,[1,2] the formation of a Mn^{III} species by the addition of electrophilic substrates,[3-5] the formation of a Mn^{III}-hydroperoxo species by acid addition,[6] and electrochemical reduction and cleavage of the O—O bond, or the Mn—O bond, in the presence of acid.[7] In all cases, activation of the Mn^{III}-peroxo species either does not form high-valent mononuclear species, or the formation of such species is fleeting and these products are unable to be captured and characterized. To date, all examples of Mn^{III}-peroxo activation require the reduction of the Mn^{III}-peroxo moiety with electrons supplied from a redox-active Mn center, a sacrificial reductant, or by electrochemical techniques.

The intrinsic reactivity of Mn^{III}-peroxo complexes is reflected in the electronic structure of the Mn^{III}-peroxo unit. In the common *D* tensor orientation, with the *z*-axis along the elongated N—Mn—N axis and the *y*-axis bisecting the O—O bond, the α-spin and β-spin Mn $3d_{xy}$ orbitals are the highest unoccupied frontier MOs (Figure 3.1). In this orientation, the Mn $3d_{xy}$ MO participates in a σ-antibonding interaction with the O_2 2p π* orbitals. This interaction involves a high degree of σ-covalency that is characteristic of Mn^{III}-peroxo complexes.[8,9] The four lower-energy Mn 3d-based MOs generally contain π-antibonding interactions in the Mn^{III}-peroxo unit with the α-spin orbitals occupied and the β-spin orbitals unoccupied. The activation of Mn^{III}-peroxo species requires the addition of an electron to the Mn $3d_{xy}$ orbital that will weaken both the O—O and the Mn—O bonds due to the strong covalency in the Mn^{III}-peroxo moiety. In order to break the O—O bond in a Mn^{III}-peroxo complex, an additional electron must be supplied. The control of subsequent bond cleavage events (i.e., Mn—O vs. O—O) is not fully understood,

although the supporting ligand system presumably plays a large role in directing the reactivity through electronics and sterics.

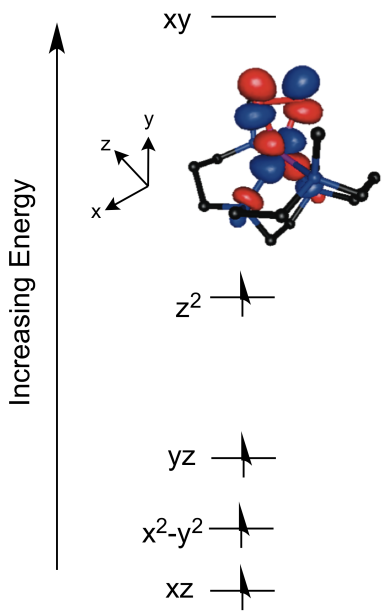

Figure 3.1. MO diagram of $[Mn^{III}(O_2)(Me_2EBC)]^+$ with d^4 configuration with the surface contour plot for the Kohn-Sham Mn 3d based orbital for the lowest unoccupied MO, Mn $3d_{xy}$.

In particular, the area of acid-assisted activation of Mn^{III}-peroxo intermediates is severely underexplored. One of the few examples of acid-assisted activation involves the protonation of the $[Mn^{III}(O_2)(TMC)]^+$ intermediate by the addition of 3 equiv. of $HClO_4$.[6] The formation of the Mn^{III}-hydroperoxo species occurs by protonation of the peroxo moiety, with the product retaining the O—O bond. While this species was a moderately active oxidant and able to perform OAT reactions, it was not able activate C—H bonds. Additionally, there was no conversion observed to a high-valent, Mn^{IV} oxidant by O—O bond cleavage of the Mn^{III}-hydroperoxo species. The only other example of acid-assisted activation of a Mn^{III}-peroxo complex is for the Mn^{III}-peroxo supported by the N_4O^- phenolato-containing ligand. The $[Mn^{III}(O_2)(N_4O)]$ complex was electrochemically generated by the reduction of dioxygen to superoxide at the electrode in

the presence of the $[Mn^{II}(N_4O)]$ species.[7] This Mn^{III}-peroxo species showed reactivity in the presence of acid; however, the activation products of this reaction were prone to degradation and did not allow for further trapping and characterization. Although a high-valent Mn^{IV} species is proposed to form from the activation of the $[Mn^{III}(O_2)(N_4O)]^+$ complex, this species was unfortunately not able to be characterized. In order to generate intermediates with greater stability to define the mechanism of activation of Mn^{III}-peroxo species, the more robust Me_2EBC ligand has been utilized. The Me_2EBC ligand provides an excellent platform to explore these reactions, as this ligand supports high-valent Mn^{IV} oxidants[10] and these species have been well characterized.[10-12] The use of substrates that allow for controlled addition of electrons and protons to the Mn^{III}-peroxo unit provide a means of determining the mechanism of activation. Reactivity studies of the $[Mn^{III}(O_2)(Me_2EBC)]^+$ complex with Brønsted acid, electrophilic substrates, and Lewis acids were performed, and the characterization and proposed mechanisms of the species formed from these reactions are outlined in this chapter.

3.2 Experimental Section

3.2.1. Materials. All chemicals and reagents used were ACS reagent grade or better and were purchased through commercial vendors and used without further purification.

3.2.2. Instrumentation. Electronic absorption experiments were performed on a Cary 50 Bio spectrophotometer (Varian) interfaced with a Unisoku cryostat (USP-203-A). EPR experiments were conducted on an X-band (9 GHz) Bruker EMXPlus spectrophotometer with a duel-mode cavity, an Oxford ESR900 continuous-flow liquid helium cryostat, and an Oxford ITC503 temperature system.

3.3.3. Reaction of $[Mn^{III}(O_2)(Me_2EBC)]^+$ with $HClO_4$. The $[Mn^{III}(O_2)(Me_2EBC)]^+$ complex was prepared as previously described[13] from the reaction of a 2 mM solution of

$[Mn^{II}(Cl)_2(Me_2EBC)]$ solution with 10 equiv KO_2 and 10 equiv 18-crown-6 in dichloromethane at -60 °C. After 150 minutes (previously determined time for excess superoxide to decay to < 25% of the original amount in the absence of Mn^{II}),[13] 10 equiv $HClO_4$ in dichloromethane was added by syringe to the $[Mn^{III}(O_2)(Me_2EBC)]^+$ solution at -60 °C. Upon addition of $HClO_4$, the solution immediately changed from blue to red with the appearance of a white precipitate. At room temperature, the solution was filtered by syringe and the resulting red solution was stable for 4 days at room temperature.

3.3.4. Reaction of the acid product of $[Mn^{III}(O_2)(Me_2EBC)]^+$ with base. The filtered red solution from the reaction of $[Mn^{III}(O_2)(Me_2EBC)]^+$ and $HClO_4$ was reacted with a solution of 2 equiv of $KOC(CH_3)_3$ in THF at 25 °C and followed by electronic absorption spectroscopy.

3.3.5. Reaction of the acid product of $[Mn^{III}(O_2)(Me_2EBC)]^+$ with DHA. A solution of 10 – 50 equiv DHA in dichloromethane at 25 °C was added to the filtered red solution from the reaction of $[Mn^{III}(O_2)(Me_2EBC)]^+$ and $HClO_4$.

3.3.6. Reaction of $[Mn^{III}(O_2)(Me_2EBC)]^+$ with Electrophilic Substrates. A 2 mM solution of $[Mn^{II}(Cl)_2(Me_2EBC)]$ was used to prepare the $[Mn^{III}(O_2)(Me_2EBC)]^+$ as previously described.[13] 150 minutes after maximum formation of the $[Mn^{III}(O_2)(Me_2EBC)]^+$ complex, a solution of 2 equiv of the substrate (1,2-diphenylhydrazine or 2,4,6-tri-*tert*-butylphenol) in dichloromethane was added via syringe at -60 °C.

3.3.7. Reaction of $[Mn^{III}(O_2)(Me_2EBC)]^+$ with Lewis Acids. A 2 mM solution of $[Mn^{II}(Cl)_2(Me_2EBC)]$ was used to prepare the $[Mn^{III}(O_2)(Me_2EBC)]^+$ as previously described.[13] 150 minutes after the maximum formation of the $[Mn^{III}(O_2)(Me_2EBC)]^+$ complex, a solution of 1 equiv of $Sc(OTf)_3$ in butyronitrile (the Lewis acid was insoluble in dichloromethane), or 1 equiv $Ca(OTf)_2$ in tetrahydrofuran was added via syringe at -60 °C.

3.3.8. EPR Experiments. Following the reaction of 2 mM $[Mn^{III}(O_2)(Me_2EBC)]^+$ with 10 equiv. $HClO_4$ in dichloromethane, 250 μL were transferred to a quartz EPR tube that was flash-frozen in liquid N_2. EPR spectra were acquired under non-saturating conditions, (20 dB) with frequencies of 9.4026 GHz (parallel-mode) and 9.6403 (perpendicular mode), 0.6 mT modulation amplitude, 100 kHz modulation frequency, and 163 ms time constant.

3.3.9. Mn K-edge X-ray absorption spectroscopy (XAS). An XAS sample of the acid product of $[Mn^{III}(O_2)(Me_2EBC)]^+$ was prepared by first forming the $[Mn^{III}(O_2)(Me_2EBC)]^+$ from the reaction of 20 mM $[Mn^{II}(Cl)_2(Me_2EBC)]$ with 10 equiv KO_2 and 10 equiv 18-crown-6 at -60 °C in dichloromethane. This $[Mn^{III}(O_2)(Me_2EBC)]^+$ was reacted with 10 equiv $HClO_4$ at -60 °C and filtered by syringe. Crystallization of this red solution at room temperature by ether diffusion with diethyl ether afforded red and white solid material that was separated with tweezers. The red solid was dissolved in acetonitrile to form a ~20 mM solution (based on the original $[Mn^{II}(Cl)_2(Me_2EBC)]$ concentration). 400 μL of this solution were frozen in an XAS sample cup. XAS data were collected at beamline 2-2 at Stanford Synchrotron Radiation Lightsource (SSRL) with previously reported conditions.[12] The contamination of higher harmonic radiation was minimized with a harmonic rejection mirror, manganese foil spectra were simultaneously recorded for internal energy calibration, and the first inflection point of the K-edge energy was assigned to 6539.0 eV. Spectra were measured with 5 eV steps below the edge (6359-6529 eV), 0.3 eV steps in the edge region (6529-6564 eV), and steps corresponding to 0.05 $Å^{-1}$ above the edge in the EXAFS region. EXAFS data reduction and averaging were performed using the program EXAFSPAK.[14] The pre-edge background intensity was removed by fitting a Gaussian function to the pre-edge background and then subtracting this function from the whole spectrum. The spectrum was fit with a three-segment spline with fourth-order polynomial components to remove low-frequency background.

3.3 Results and Analysis

3.3.1. Reactivity of $[Mn^{III}(O_2)(Me_2EBC)]^+$ with $HClO_4$. The previously characterized $[Mn^{III}(O_2)(Me_2EBC)]^+$ species[13] was prepared from a 2 mM solution of $[Mn^{II}(Cl)_2(Me_2EBC)]$ and 10 equiv KO_2 at -60 °C in dichloromethane. 150 minutes after the maximum formation of $[Mn^{III}(O_2)(Me_2EBC)]^+$, a solution of 10 equiv $HClO_4$ in dichloromethane was added. The addition of fewer equiv acid resulted in no reaction, presumably due to reaction of the acid with the large amount of 18-crown-6 that is able to bind H^+ ions in its cavity.[15] The $[Mn^{III}(O_2)(Me_2EBC)]^+$ species displays electronic absorption features at 650 and 400 nm (ε = 530 and 185 M^{-1} cm^{-1}, respectively, Figure 3.2, blue trace), and addition of the acid caused immediate decay of these features and appearance of a feature at 540 nm (ε = 340 M^{-1} cm^{-1}, Figure 3.2, black dashed trace). The resulting solution also contained a white precipitate that was filtered by syringe to give a red solution. This solution was used for further characterization and was stable at room temperature for 4 days.

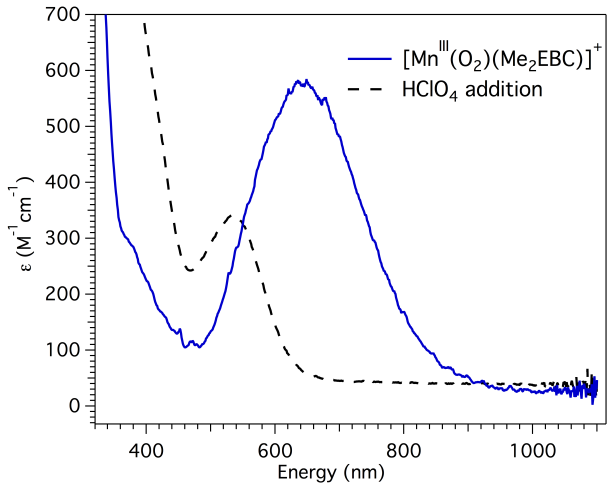

Figure 3.2. Formation of the acid product (black dashed trace) from the reaction of 10 equiv. $HClO_4$ with $[Mn^{III}(O_2)(Me_2EBC)]^+$ in dichloromethane at -60 °C.

To determine if the formation of the acid product was reversible upon change of pH, a basic solution of 2 equiv of $KOC(CH_3)_3$ was added to the acid solution at –60°C. The feature at 540 nm from the acid product immediately decayed to a product with a small shoulder at ~400 nm that unfortunately displayed no further reactivity (Figure 3.3). Thus, a reversible formation of the Mn^{III}-peroxo is not possible with this preparation.

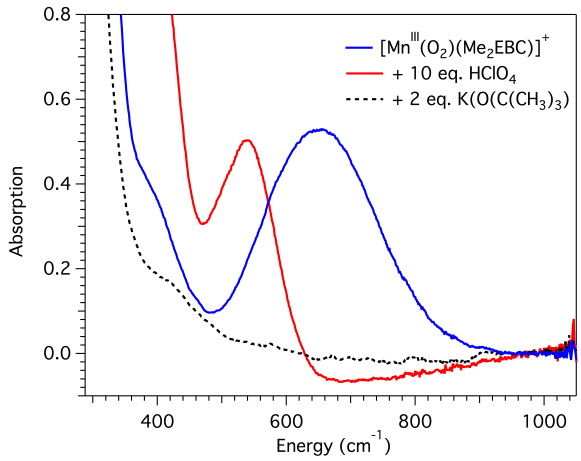

Figure 3.3. Electronic absorption spectrum of the addition of 2 equiv. of $KOC(CH_3)_3$ to the acid product at -60°C.

3.3.2. Spectroscopic Characterization of the Acid Product. X-band parallel-mode 5 K EPR spectra of a sample of the red solution following filtration display a 6-line spectrum indicative of a mononuclear Mn^{III} species at g_{eff} = 8.96 with a hyperfine splitting of 5.66 mT (Figure 3.3). These parameters are unique from those determined for other Mn^{III} species supported by the Me_2EBC ligand that were determined in a previous study.[13] The $[Mn^{III}(O_2)(Me_2EBC)]^+$ species contained an EPR signal at g_{eff} = 7.96 with a larger hyperfine splitting of 6.84 mT, which is similar to the parameters observed for other Mn^{III}-peroxo species.[8,9] The parallel-mode EPR spectra of the $[Mn^{III}(OH)(Cl)(Me_2EBC)]^+$ complex also displayed a signal shifted to lower-field, at g_{eff} = 8.33, with a hyperfine splitting of 4.73 mT. The

differences in the parameters of the red solution from these other Mn^{III} species indicate that the red solution is a new intermediate that contains a mononuclear Mn^{III} center. Variable-temperature EPR spectra were collected between 3.5 and 40 K. A plot of the EPR intensity at g_{eff} = 8.96 times temperature versus temperature shows a rapid initial decrease with a leveling at higher temperatures (Figure 3.3, inset). This behavior indicates $D < 0$ with the $m_s = \pm 2$ transition from the signal at g_{eff} = 8.33 at the lowest energy.[16] 5 K perpendicular-mode EPR spectra collected for the red solution show a small signal at g_{eff} = 2.0 with a hyperfine splitting of 9.5 mT which is typical of a mononuclear Mn^{II} species (Figure A3.1) which presumably forms as a decay product of the reaction with acid.

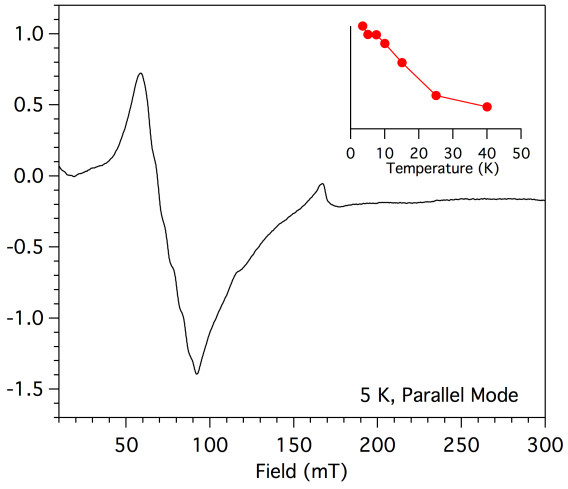

Figure 3.4. 5 K parallel-mode EPR spectrum of the acid product of $[Mn^{III}(O_2)(Me_2EBC)]^+$.

Table 3.1. Comparison of electronic absorption, EPR, and XAS spectroscopic properties of the acid product with $[Mn^{III}(O_2)(Me_2EBC)]^+$ and $[Mn^{III}(OH)(Cl)(Me_2EBC)]^+$.[13]

	λ_{max} (nm)	ε ($M^{-1}cm^{-1}$)	g_{eff}	D (cm^{-1})	E/D	pre-edge (eV)	Area	edge (eV)
$[Mn^{III}(O_2)(Me_2EBC)]^+$	650, 400	530, 185	7.96	-2(1)	0.10(2)	6540.8	9.5	6550.3
$[Mn^{III}(OH)(Cl)(Me_2EBC)]^+$	890, 410	20, 90	8.33	+2.1(5)	0.06(2)	6540.5	6.1	6550.5
Acid Product	540	340	8.96	[a]	[a]	6542.3 6540.3	4.9	6549.7

[a]Not determined

The red solution was also characterized with Mn K-edge XAS. Crystals of the red solution were dissolved in MeCN for an XAS sample. Several other species supported by the Me_2EBC ligand have previously been characterized by XAS, including Mn^{II}, Mn^{III}, and Mn^{IV} species, and these data provide a useful comparison to identify new intermediates. The edge energy of the red solution (6549.7 eV; Figure 3.4, red trace) is near the edge energies observed for the Mn^{III}-peroxo and Mn^{III}-hydroxo species (6550.3 and 6550.5 eV, respectively). The edge energy of the red solution is slightly lower than these Mn^{III} species, but this is not surprising as the average oxidation state of the bulk solution is likely lower due to the small amount of Mn^{II} decay product that was detected by EPR.

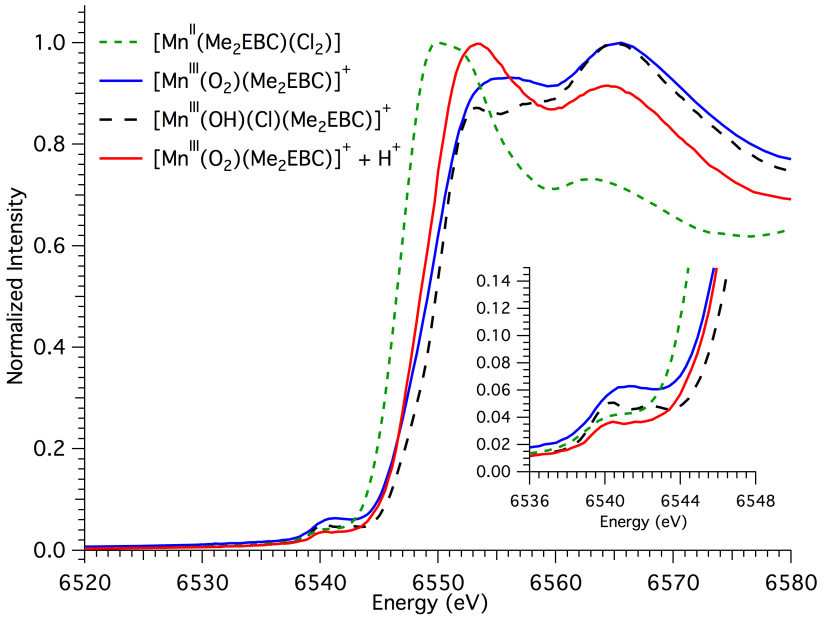

Figure 3.5. Mn K-edge X-ray absorption near-edge structures of the acid product (solid red trace), $[Mn^{III}(O_2)(Me_2EBC)]^+$ (solid blue trace),[13] $[Mn^{III}(OH)(Cl)(Me_2EBC)]^+$ (dashed black trace),[13] and $[Mn^{II}(Cl)_2(Me_2EBC)]$ (dashed green trace).[12] Inset: Pre-edge features in the pre-edge region from 6536 to 6548 eV.

The shape and energy of the pre-edge transitions also lend insight into the electronic environment about the Mn center, as these transition gain intensity with increasing 1s → 3d character that increases with a less centrosymmetric molecule. The pre-edge area of the red

solution (4.9 10^{-2} eV, Table 3.1) is smaller than the pre-edge area of the Mn^{III}-peroxo species (9.5 10^{-2} eV) where the large area was attributed to the high covalency in the Mn^{III}-peroxo Mn $3d_{xy}$ MO.[13] Structural information from the EXAFS region provides insight into the identity of the red solution, although a fit to these data could not be determined. The Fourier transform of the extended X-ray absorption fine structure (EXAFS) region contains a peak at 1.76 Å that is similar to that observed for the $[Mn^{III}(O_2)(Me_2EBC)]^+$ complex 1.70 Å (Figure 3.6, right). In that complex, this peak contained contributions from a shell of 4 N atoms from the ligand and 2 O atoms from the peroxo unit.[13] This peak is also lower than that observed for the $[Mn^{II}(Cl)_2(Me_2EBC)]$ species (2.01 Å, Figure 3.6, left),[12] which further supports the assignment of the main component of the red solution as a Mn^{III} species. The second feature in the Fourier transform of the red solution at 2.42 Å is comparable to the Fourier transform peak for the $[Mn^{III}(O_2)(Me_2EBC)]^+$ complex (2.35 Å) that had contributions from the N and C atoms of the Me_2EBC ligand.

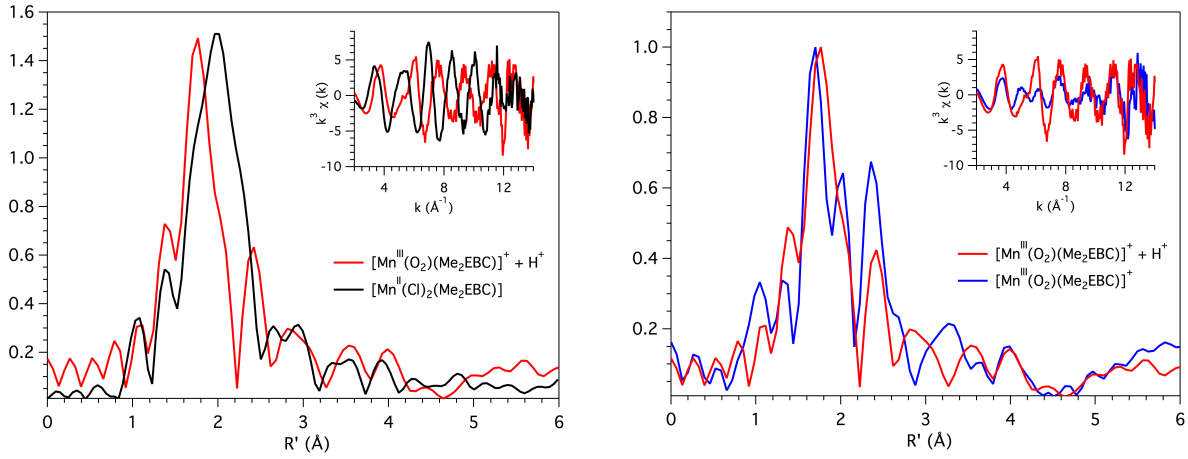

Figure 3.6. Experimental Fourier transform and k-weighted EXAFS (inset) comparing the acid product (left, red trace) and the $[Mn^{II}(Cl)_2(MeEBC)]$ complex[12] (left, black trace) and acid product (right, red trace) and the $[Mn^{III}(O_2)(MeEBC)]^+$ (right, blue trace).[13]

Further purification and characterization of the acid product was attempted with crystal growth from the filtered red solution. Crystallization of the filtered red solution at room temperature by vapor diffusion with diethyl ether produced a white crystalline material and a red solid. Unfortunately, the red solid was non-crystalline and not suitable for X-ray diffraction. Other methods of crystallization were attempted, including vapor diffusion with diethyl either at -40 °C and 0 °C and crystallization by evaporation at room temperature. All methods yielded non-crystalline red material. The products of these crystallizations were also investigated by ESI mass spectrometry. The crystalline white material was determined to be 18-crown-6 with *m/z* = 287.1 (18-crown-6 + Na^+). ESI-MS data for both the red solid and the filtered red solution only indicate *m/z* = 344.1, which corresponds to a $[Mn^{II}(Cl)(Me_2EBC)]^+$ species that could form as a decay product of the reaction with acid. Unfortunately, no ESI-MS experiments were able to provide conclusions about the identity of the Mn^{III} species produced from the reaction of $[Mn^{III}(O_2)(Me_2EBC)]^+$ and acid.

3.3.3. C—H Bond Activation with Acid Product of $[Mn^{III}(O_2)(Me_2EBC)]^+$. To investigate the reactivity of the acid product, reactivity by C—H bond activation of 9,10-dihydroanthracene was explored, as previously characterized Mn^{IV} species supported by the Me_2EBC ligand are known to react with this substrate.[10,17] Upon the addition of a large excess (50 equiv) DHA, the feature at 540 nm changed minimally over 800 minutes at 25 °C (Figure 3.7). Although this complex does not display any significant ability to activate C—H bonds, this is not unexpected with a Mn^{III} species. The addition of acid to the $[Mn^{III}(O_2)(Me_2EBC)]^+$ complex appears to form a stable Mn^{III} product, and there is no evidence for formation of a reactive, high-valent Mn^{IV} species that merited further investigation. As such, we pursued alternative methods of activation of the Mn^{III}-peroxo to target formation of high-valent species.

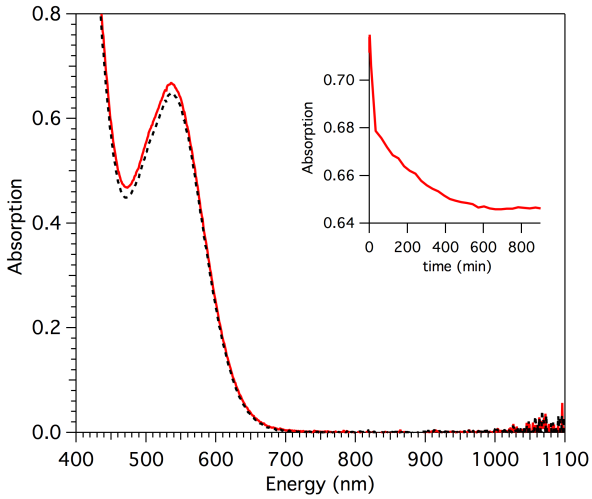

Figure 3.7. Electronic absorption spectrum of the acid product (red solid trace) and the addition of DHA (black dashed trace) after 800 minutes at 25 °C.

3.3.3. Reactivity of $[Mn^{III}(O_2)(Me_2EBC)]^+$ with Electrophilic Substrates. As the activation of $[Mn^{III}(O_2)(Me_2EBC)]^+$ to a high-valent Mn^{IV} species through Brønsted acid addition proved to be unsuccessful, electrophilic substrates were utilized in an attempt to cleanly activate the Mn^{III}-peroxo species to a high-valent intermediate. 1,2-diphenylhydrazine (DPH) was used as a hydrogen atom donor substrate, as it has been used successfully to supply electrons and protons to activate the Mn^{III}-peroxo complex supported by the H_3bupa^{2-} ligand.[3-5] 150 minutes after maximum formation of the $[Mn^{III}(O_2)(Me_2EBC)]^+$ complex in dichloromethane at -60 °C, a solution of 2 equiv of DPH in dichloromethane was added. The absorption feature at 650 from the Mn^{III}-peroxo species showed 38% decrease with the formation of a large band near 430 nm due to formation of the azobenzene product, which is the product of two hydrogen atom abstraction events from 1,2-diphenylhydrazine (Figure 3.8). An absorbance spectrum of this solution was collected in a cuvette with a path length of 0.5 cm (Figure A3.3) that gave an extinction coefficient of 429 $M^{-1}cm^{-1}$ for the peak at 430 nm from azobenzene (based on reported extinction coefficients for azobenzene[18]). This reaction afforded an estimated 55% conversion to azobenzene from DPH, which corresponds to the consumption of ~1 equiv DPH. Although the

$[Mn^{III}(O_2)(Me_2EBC)]^+$ complex reacted with this hydrogen atom donor, it required 2 equiv DPH to induce reactivity, instead of the stoichiometric quantity (0.5 equiv DPH). Presumably, another Mn species is produced in solution and is able to react with DPH to produce additional equiv of azobenzene (Scheme 3.1).

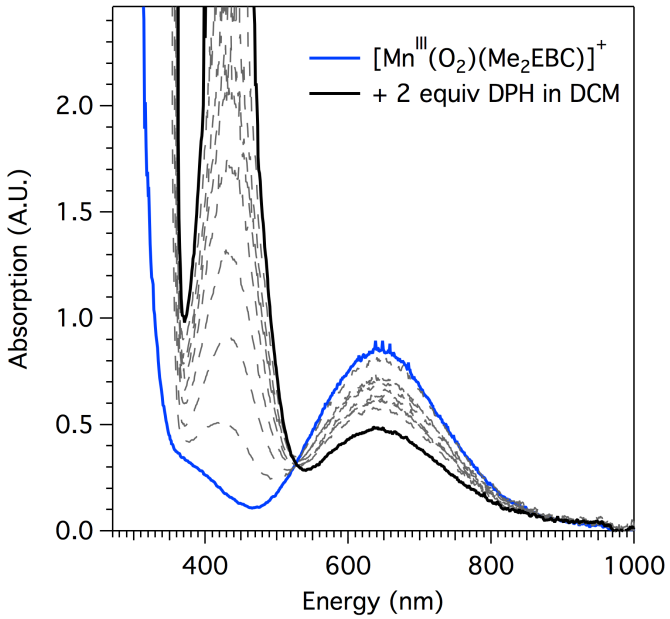

Figure 3.8. Electronic absorption spectrum of $[Mn^{III}(O_2)(Me_2EBC)]^+$ (solid blue line) and reaction with 2 equiv DPH (black solid line).

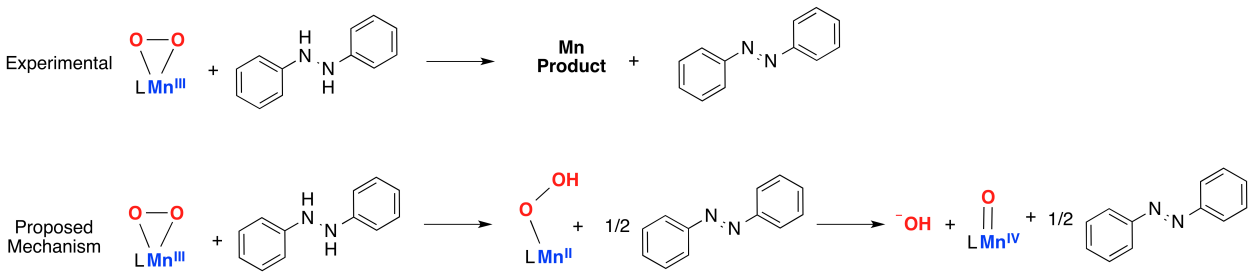

Scheme 3.1. Proposed reaction of $[Mn^{III}(O_2)(Me_2EBC)]^+$ with DPH.

Activation of the Mn^{III}-peroxo unit was attempted by reaction of $[Mn^{III}(O_2)(Me_2EBC)]^+$ with another potential hydrogen atom donor, 2,4,6-tri-*tert*-butylphenol (TTBP). This phenol

supplies a hydrogen atom to the Mn^{III}-peroxo unit and generates a phenoxyl radical species that was monitored by electronic absorption. Upon the addition of 1 equiv TTBP, the absorption peak at 650 nm decayed and new features were observed near 400 nm and 628 nm that are characteristic of the phenoxyl radical formed from the hydrogen atom abstraction event.[19] Based on an extinction coefficient of 400 $M^{-1}cm^{-1}$ of the peak at 628 nm,[19] approximately 1.4 mM phenoxyl radical is formed in solution. The features from the radical species then decayed in solution by a known reaction with O_2.[20] Overall, activation of $[Mn^{III}(O_2)(Me_2EBC)]^+$ by a hydrogen atom transfer from TTBP appears to provide a promising avenue for controlled reactivity. While the organic phenoxyl radical product has been detected, the Mn products formed require further investigation, although proposed mechanisms are given in Scheme 3.2.

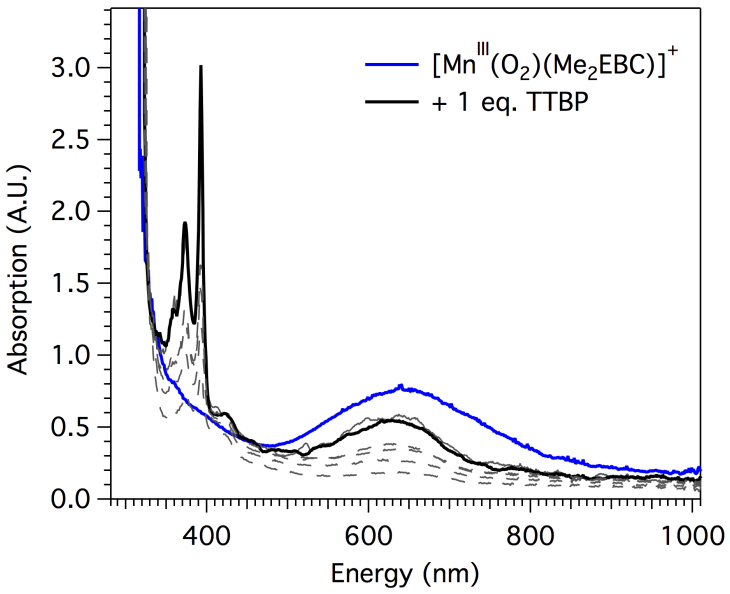

Figure 3.9. Electronic absorption spectrum of $[Mn^{III}(O_2)(Me_2EBC)]^+$ (solid blue line) and its reaction with 1 equiv TTBP (solid black line) and decay (dashed grey lines).

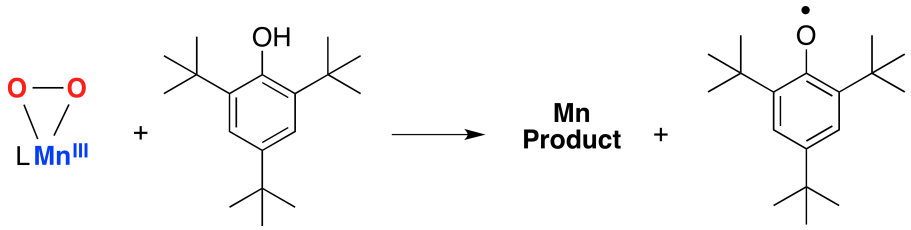

Scheme 3.2. Proposed reaction of $[Mn^{III}(O_2)(Me_2EBC)]^+$ with TTBP.

3.3.4. Reactivity of $[Mn^{III}(O_2)(Me_2EBC)]^+$ with Lewis Acids. Lewis acids have been shown to have an effect on the activation of Fe^{III}-peroxo species, potentially by modulating the large amount of electron density residing in the metal-peroxo unit (Figure 3.10).[21,22] A recent structural investigation of an intermediate formed from the reaction of an Fe^{III}-peroxo with Sc^{3+} showed that this adduct retains the η^2 coordination of peroxo unit, as well as an η^2 coordination of the Sc^{3+} species. This orientation may allow for control of the electron density in the Fe^{III}-peroxo unit.

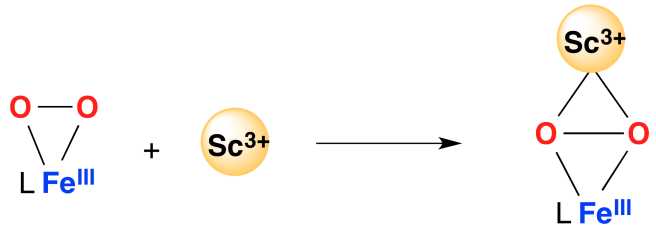

Figure 3.10. Binding of the Lewis acid to a Mn^{III}-peroxo species.[22]

The $[Mn^{III}(O_2)(Me_2EBC)]^+$ complex was prepared from 2 mM $[Mn^{II}(Cl)_2(Me_2EBC)]$, 10 equiv KO_2, and 10 equiv 18-crown-6 in dichloromethane at -60 °C; then, a solution of 1 equiv $Sc(OTf)_3$ in butyronitrile was added. Upon addition of the Sc^{3+} species, the peak at 650 nm from $[Mn^{III}(O_2)(Me_2EBC)]^+$ decayed and new peaks at 540 nm and a broad peak near 900 nm formed. Following the formation of this intermediate, the absorption spectra rose due to the formation of a precipitate. The resulting pink solution contained a purple precipitate, and both species quickly

decayed at room temperature to an orange solution. These absorption features as well as the formation of an insoluble purple precipitate are strikingly similar to the formation of an intermediate that contained a $[Mn^{IV}(O)(Cl)(Me_2EBC)]^+$ species from the reaction of $[Mn^{III}(O_2)(Me_2EBC)]^+$ with 1 equiv $[Mn^{II}(Cl)_2(Me_2EBC)]$ in dichloromethane at -60 °C.[13] In this case, the Sc^{3+} presumably forms an adduct with the Mn^{III}-peroxo species, as has been observed for Fe^{III}-peroxo species,[22] and is subsequently further activated to form a Mn^{IV}-oxo species. This process requires the addition of an electron, although the source of this reduction is unknown. Additionally, although the addition of a Lewis acid appears to be an alternative method of activation of the Mn^{III}-peroxo moiety to undergo O—O bond cleavage and the formation of a high-valent Mn^{IV}-oxo species, this reaction still is plagued by insolubility and solvent limitations that were encountered in the original study.

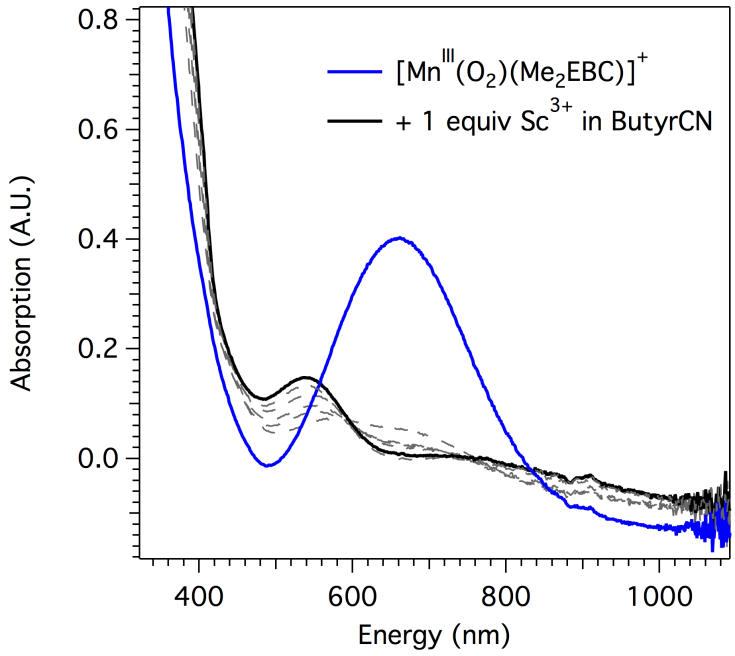

Figure 3.11. Electronic absorption spectrum of the addition of 1 equi. $Sc(OTf)_3$ in butyronitrile to $[Mn^{III}(O_2)(Me_2EBC)]^+$ in dichloromethane at -60 °C.

To compare to the reaction of $[Mn^{III}(O_2)(Me_2EBC)]^+$ with $Sc(OTf)_3$, reactivity with $Ca(OTf)_2$ was also investigated to determine the effect of the Lewis acidity on activation. When

a solution of 1 equiv $Ca(OTf)_2$ in tetrahydrofuran was added to the $[Mn^{III}(O_2)(Me_2EBC)]^+$ complex, the Mn^{III}-peroxo showed a much slower conversion to the pink intermediate that was similar to a previously characterized intermediate that contained a Mn^{IV}-oxo species.[13] Ca^{2+} appears to have more of a stabilizing effect than Sc^{3+} on the conversion reaction, suggesting that the Lewis acidity plays a large role in modulating the electron density and reactivity of the Mn^{III}-peroxo species. While this process of activation by Lewis acids is intriguing, the source of the electron in the reduction process is unknown, and limitations of solubility of the Mn^{IV}-oxo intermediate hinders further progress with the Me_2EBC ligand system.

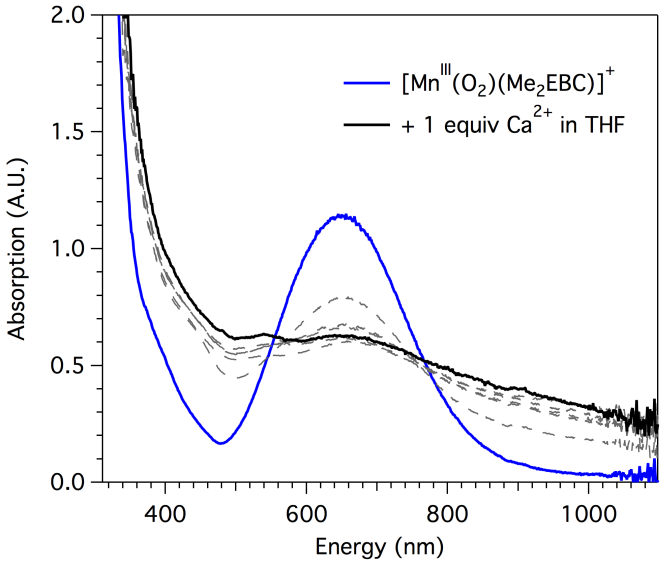

Figure 3.12. Electronic absorption spectrum of the addition of 1 equiv. $Ca(OTf)_2$ in tetrahydrofuran to $[Mn^{III}(O_2)(Me_2EBC)]^+$ in dichloromethane at -60 °C.

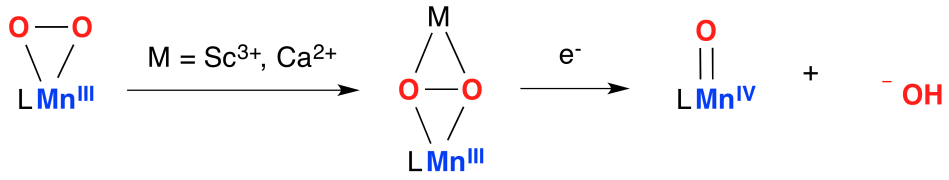

Scheme 3.3. Proposed reaction of $[Mn^{III}(O_2)(Me_2EBC)]^+$ with Lewis acids.

3.3.4. Future Experiments. The experiments outlined here highlight several promising pathways for activation of Mn^{III}-peroxo species. Activation via hydrogen atom transfer from electrophilic substrates provides an interesting avenue of activation that should be pursued further. The reactions with hydrogen atom donors, DPH and TTBP, were able to activate $[Mn^{III}(O_2)(Me_2EBC)]^+$ to produce the expected organic products, azobenzne and the phenoxyl radical, respectively. However, the Mn products of these reactions have not been characterized. To explore this chemistry, a full optimization of the reaction of $[Mn^{III}(O_2)(Me_2EBC)]^+$ with DPH and TTBP should first be performed, including optimization of the initial $[Mn^{II}(Cl)_2(Me_2EBC)]$ concentration, equiv Lewis acid, solvent for the Lewis acid, and reaction temperature. Iodometric titration experiments to determine the average oxidation state of the Mn species should be performed, as well as EPR spectroscopy to identify the oxidation states of all Mn components. Purification of the product solution by crystallization should be performed, and the purified species investigated by mass spectrometry, XRD, and XAS spectroscopy.

Reaction of Mn^{III}-peroxo species with Lewis acids has also demonstrated a potentially successful activation route. Preliminary evidence suggests possible formation of a high-valent Mn^{IV}-oxo species from the Mn^{III}-peroxo, although these reactions were complicated by the low temperature required for this reaction and poor solubility of the Mn^{IV}-oxo intermediate. While Mn^{IV} species supported by the Me_2EBC ligand are soluble in acetone, water, and other solvents,[10,11,17] these Mn^{IV} species have low solubility in dichloromethane.[13] Although these experiments with Lewis acids show a promising outlook for the reactivity of Mn^{III}-peroxo species, these complications limit progress for the Me_2EBC system. These reactions with Lewis acids should be conducted with a Mn^{III}-peroxo species supported by a ligand with cleaner formation of the Mn^{III}-peroxo species and better solubility of the Mn^{IV} product. An ideal candidate for further exploration of this chemistry would be a Mn^{III}-peroxo species that can be

formed from a less volatile oxidant, such as H_2O_2, can be formed in a range of solvents, and is stable at higher temperatures.

3.4 Discussion and Outlook

The activation of the $[Mn^{III}(O_2)(Me_2EBC)]^+$ species to a high-valent species by the addition of $HClO_4$ has proven challenging due to the large excess of 18-crown-6 required for the initial formation of the Mn^{III}-peroxo species. While activation by Lewis acid addition and hydrogen atom donation from electrophilic substrates has shown potential for activation, these reactions require further optimization and are limited by poor solubility of the Mn^{IV}-oxo intermediate and require low reaction temperatures. The reaction of $[Mn^{III}(O_2)(Me_2EBC)]^+$ with the hydrogen atom donor, TTBP, appeared to cleanly produce the expected organic product, although this system requires further investigation of the Mn products. Although the $[Mn^{III}(O_2)(Me_2EBC)]^+$ presents an attractive platform for O—O bond activation, practical aspects such as solubility have hindered further progress in this regard. The electronic absorption spectra of the addition of a Lewis acid to the Mn^{III}-peroxo species suggest that the O—O bond is cleaved and there is formation of a high-valent, mononuclear Mn^{IV}-oxo species. This Mn^{IV}-oxo species can alternatively be formed from the addition of $[Mn^{III}(O_2)(Me_2EBC)]^+$ and a Mn^{II} species.[13] Unfortunately, this species was plagued with the same problems of insolubility of the Mn^{IV} product and solvent limitations that were present in the previous preparation method. While further work with this ligand system is limited due to these problems, the activation of the $[Mn^{III}(O_2)(Me_2EBC)]^+$ species by various substrates, most successfully, by a hydrogen atom addition from TTBP, illustrates that these Mn^{III}-peroxo species can serve as precursors to powerful, high-valent, oxidants, and these pathways merit further exploration with other ligand and solvent systems.

3.5 References

(1) Groni, S.; Dorlet, P.; Blain, G.; Bourcier, S.; Guillot, R.; Anxolabéhère-Mallart, E. *Inorg. Chem.* **2008**, *47*, 3166-3172.
(2) Leto, D. F.; Chattopadhyay, S.; Day, V. W.; Jackson, T. A. *Dalton Trans.* **2013**, *42*, 13014-13025.
(3) Shook, R. L.; Borovik, A. S. *Inorg. Chem.* **2010**, *49*, 3646-3660.
(4) Shook, R. L.; Gunderson, W. A.; Greaves, J.; Ziller, J. W.; Hendrich, M. P.; Borovik, A. S. *J. Am. Chem. Soc.* **2008**, *130*, 8888-8889.
(5) Shook, R. L.; Peterson, S. M.; Greaves, J.; Moore, C.; Rheingold, A. L.; Borovik, A. S. *J. Am. Chem. Soc.* **2011**, *133*, 5810-5817.
(6) So, H.; Park, J.-H.; Cho, K.-B.; Lee, Y.-M.; Seo, M. S.; Cho, J.; Sarangi, R.; Nam, W. *J. Am. Chem. Soc.* **2014**, *136*, 12229−12232.
(7) Ching, H. Y. V.; Anxolabéhère-Mallart, E.; Colmer, H. E.; Costentin, C.; Dorlet, P.; Jackson, T. A.; Policar, C.; Robert, M. *Chem. Sci.* **2014**, *5*, 2304-2310.
(8) Colmer, H. E.; Geiger, R. A.; Leto, D. F.; Wijeratne, G.; Day, V. W.; Jackson, T. A. *Dalton Trans.* **2014**, *43*, 17949-17963.
(9) Leto, D. F.; Jackson, T. A. *J. Biol. Inorg. Chem.* **2014**, *19*, 1-15.
(10) Yin, G.; Danby, A. M.; Kitko, D.; Carter, J. D.; Scheper, W. M.; Busch, D. H. *J. Am. Chem. Soc.* **2008**, *130*, 16245-16253.
(11) Chattopadhyay, S.; Geiger, R. A.; Yin, G.; Busch, D. H.; Jackson, T. A. *Inorg. Chem.* **2010**, *49*, 7530-7535.
(12) Leto, D. F.; Jackson, T. A. *Inorg. Chem.* **2014**, *53*, 6179-6194.
(13) Colmer, H. E.; Howcroft, A. H.; Jackson, T. A. *Inorg. Chem.* **2016**, *55*, 2055-2069.
(14) George, G. N. In *EXAFSPAK* Stanford Synchrotron Radiation Laboratory; Stanford, CA, 1990.
(15) Steed, J. W.; Atwood, J. L. *Supramolecular Chemistry*; 2 ed.; Wiley, 2009.
(16) Gupta, R., Taguchi, T., Borovik, A. S., Hendrich, M. P. *Inorg. Chem.* **2013**, *52*, 12568-12575.
(17) Shi, S., Wang, Y., Xu, A., Wang, H., Zhu, D., Roy, S.B., Jackson, T.A., Busch, D.H., Yin, G. *Angew. Chem. Int. Ed.* **2011**, *50*, 7321-7324.
(18) Birnbaum, P. P. L., J. H.; Style, D. W. G. *Trans. Far. Soc.* **1953**, *49*, 735-744.
(19) Manner, V. W.; Markle, T. F.; Freudenthal, J. H.; Roth, J. P.; Mayer, J. M. *Chem. Commun.* **2008**, 256-258.
(20) Nath Das, T.; Dhanasekaran, T.; Alfassi, Z. B.; Neta, P. *J. Phys. Chem. A.* **1998**, *102*, 280-284.
(21) Lee, Y.-M.; Bang, S.; Kim, Y. M.; Cho, J.; Hong, S.; Nomura, T.; Ogura, T.; Troeppner, O.; Ivanović-Burmazović, I.; Sarangi, R.; Fukuzumi, S.; Nam, W. *Chem. Sci.* **2013**, *4*, 3917-3923.
(22) Li, F.; Van Heuvelen, K. M.; Meier, K. K.; Münck, E.; Que, L., Jr. *J. Am. Chem. Soc.* **2013**, *135*, 10198-10201.

CHAPTER 4

Geometric and Electronic Structure of a Peroxomanganese(III) Complex Supported by a Scorpionate Ligand

Reproduced from Colmer, H.E.; Geiger, R.A.; Leto, D.F.; Wijeratne, G.W.; Day, V.W.; Jackson, T.A., *Dalton Trans.*, **2014**, *43*, 17949-17963 with permission from the Royal Society of Chemistry. Crystal growth for X-ray crystallography and magnetic circular dichroism spectroscopy were carried out by Robert A. Geiger.

4.1 Introduction

Mononuclear peroxomanganese(III) species have been proposed to form in manganese containing enzymes, including manganese superoxide dismutase (MnSOD),[1-6] manganese-dependent homoprotocatechuate 2,3-dioxygenase (MndD),[7,8] and the oxalate-degrading enzymes oxalate oxidase[9,10] and oxalate decarboxylase.[11-13] These biological peroxomanganese(III) species are highly unstable and relatively little is known concerning their structural and electronic properties. In contrast, a variety of synthetic peroxomanganese(III) species have been generated and characterized, offering insights into the structural, electronic, and reactivity properties of this class of compound.[14-27] Members of this class of compound include side-on peroxomanganese(III) adducts (Mn^{III}-O_2) and end-on alkylperoxomanganese(III) adducts (Mn^{III}-OOR).[28,29] While there are several examples of Mn^{III}-O_2 complexes with anionic supporting ligands,[14,22,25,30] there are no detailed bonding descriptions of such complexes. As many enzymatic Mn^{III}-O_2 adducts are expected to feature anionic ligands, this represents a gap in knowledge. In addition, the electronic structures of crystallographically characterized Mn^{III}-O_2 adducts have not generally been explored in detail.[30]

A mononuclear Mn^{III}-O_2 complex supported by the monoanionic facially-coordinating trispyrazolyl Tp^{iPr2} ligand (Tp^{iPr2} = hydrotris(3,5-diisopropylpyrazol-1-yl)borate) and an ancillary, monodentate 3,5-isopropylpyrazole ($pz^{iPr2}H$) ligand was previously reported to be stable at room temperature for a few hours.[22] It was observed that the peroxo ligand in this [$Mn^{III}(O_2)(Tp^{iPr2})(pz^{iPr2}H)$] complex is bound to the Mn^{III} ion in a side-on (η^2) fashion, and the coordination sphere is completed by the four N-donors from the Tp^{iPr2} ligand and the monodentate $pz^{iPr2}H$ ligand. When this Mn^{III}-O_2 complex was cooled from 253 to 193 K, the $pz^{iPr2}H$ ligand formed a hydrogen bond with one O atom of the peroxo unit, and this changed the absorption spectrum.[22,27] Specifically, the absorption maxima shifted from 561 to 583 nm (17

820 to 17 150 cm^{-1}) causing the color of the complex to change from brown (at 253 K) to blue (at 193 K). In contrast, the frequency of the peroxo O-O vibration (ν_{O-O}), was not perturbed at all by this hydrogen bonding interaction. The absence of a shift in ν_{O-O} is surprising, but consistent with the statistically identical O-O bond lengths of the blue and brown isomers (1.43(1) and 1.428(7), respectively).[22] A slightly higher-energy ν_{O-O} frequency of 896 cm^{-1} was observed for the related complex [$Mn^{III}(O_2)$(Tp)(Me-Im)], which displays an intermolecular hydrogen-bond in the solid-state crystal structure (O-O of 1.42(1) Å).[22]

In a recent review,[23] we noted that Mn^{III}-O_2 adducts supported by the Tp^{iPr2} ligand[22,27] represent a unique geometry compared to other mononuclear Mn^{III}-O_2 adducts. Following a formalism proposed by Kitajima *et al.*,[22] if the peroxo unit is viewed as a monoligand, the τ parameter, as defined in Scheme 4.1, may be used to classify Mn^{III}-O_2 adducts along a spectrum of geometries from square pyramidal (τ = 0) to trigonal bipyramidal (τ = 1).[23 31] In contrast, crystallographically-characterized mononuclear Mn^{III}-O_2 adducts supported by tetramethylcylam (TMC) and its derivatives (Scheme 4.1) show τ parameters from 0 to 0.52, with the variation reflecting the size of the macrocyclic ring.[14,21,24] The Tp-supported Mn^{III}-O_2 adducts also appear distinct from other mononuclear Mn^{III}-O_2 species in terms of their electronic absorption properties, and this could be related to differences in geometric structure. While the blue and brown isomers of [$Mn^{III}(O_2)(Tp^{iPr2})(pz^{iPr2}H)$] show only very weak absorption features at ~560 - 580 nm, Mn^{III}-O_2 adducts supported by a variety of neutral N_4 ligands show moderately intense absorption bands from ~415 - 450 nm ($\varepsilon \approx$ 250 - 500 $M^{-1}cm^{-1}$), with lower-intensity features at ~590 - 620 nm.[23] However, a complication in this comparison is that, while the onset of more intense features at wavelengths lower than 450 nm are apparent in the published electronic absorption spectra of [$Mn^{III}(O_2)(Tp^{iPr2})(pz^{iPr2}H)$], no absorption maxima were reported.

On the basis of these considerations, we investigated whether a Mn^{III}-O_2 unit could be

supported by the related, but synthetically more accessible, Tp^{Ph2} ligand (Scheme 4.1) in order to more fully understand the spectroscopic properties of a Tp-supported Mn^{III}-O_2 adduct and determine the consequences of the pseudo-trigonal bipyramidal geometry. Herein, we describe the synthesis, structural, and spectroscopic characterization of $[Mn^{III}(O_2)(Tp^{Ph2})(THF)]$, which is formed by treatment of the corresponding Mn^{II} complex with excess KO_2. An X-ray diffraction (XRD) structure of $[Mn^{III}(O_2)(Tp^{Ph2})(THF)]$ reveals a mononuclear Mn^{III}-O_2 unit with the bulky phenyl groups shielding the peroxo ligand.

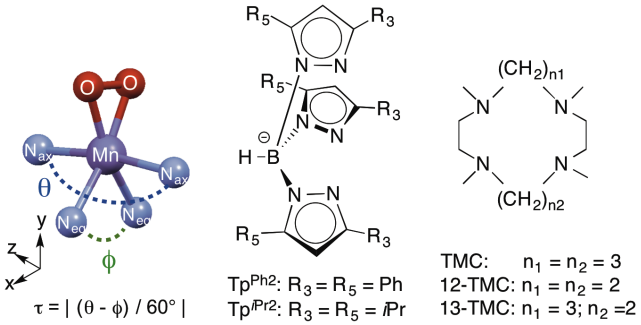

Scheme 4.1. Representative Mn^{III}-O_2 with calculation of τ (left), Tp type ligands (middle), and TMC type ligands (right).

Electronic absorption, electron paramagnetic resonance (EPR), magnetic circular dichroism (MCD) and variable-temperature, variable-field (VTVH) MCD spectroscopies are used to determine ground-state zero-field splitting parameters and electronic transition energies for this complex. The spin-allowed *d-d* transitions of $[Mn^{III}(O_2)(Tp^{Ph2})(THF)]$, which are highly sensitive to the coordination sphere of the Mn^{III} center, are found to be blue shifted in energy compared to those of other peroxomanganese(III) complexes. The electronic structure causing this perturbation was further investigated using density functional theory (DFT) and multi-reference *ab initio* computations. Previously, spectroscopic changes in some Mn^{III}-O_2 complexes have been attributed to variations in the Mn-O_{peroxo} bond lengths;[16,32] however, as the Mn-O_{peroxo} bond lengths of $[Mn^{III}(O_2)(Tp^{Ph2})(THF)]$ are within the range studied, they cannot account for the large spectroscopic perturbation observed. The combined spectroscopic and computational

analysis presented here reveals that, for this system, ligand perturbations perpendicular to the Mn^{III}-O_2 unit can account for spectral differences. This work thus expands upon our previous investigations aiming at defining structural origins of spectral variations in peroxomanganese(III) complexes.[16,18,23,32]

4.2 Experimental Section

4.2.1. Materials. All chemicals and solvents were obtained from commercial vendors at ACS reagent-grade or better and were used without further purification. Synthesis of the Mn^{II} complex was carried out under argon using a glovebox.

4.2.2. Instrumentation. ^{1}H NMR spectra were obtained on a Bruker DRX 400 MHz NMR spectrometer. Electronic absorption spectra were recorded on a Cary 50 Bio spectrophotometer (Varian) interfaced with a Unisoku cryostat (USP-203-A). ESI-mass spectrometry experiments were performed using an LCT Primers MicroMass electrospray-ionization time-of-flight instrument. EPR spectra were collected on Bruker EMXPlus instrument with a dual mode cavity. Magnetic circular dichroism (MCD) spectra were collected on a spectropolarimeter (Jasco J-815) interfaced with a magnetocryostat (Oxford Instruments SM-4000-8) capable of horizontal fields up to 8 T.

4.2.3. Preparation of $[Mn^{II}(Tp^{Ph2})(DMF)_3](OTf)$. Potassium tris(3,5 diphenylpyrazol)hydroborate (Tp^{Ph2}) was prepared as previously described by condensing 3 molar equivalents of 3,5-diphenylpyrazole with KBH_4.[33,34] $Mn(OTf)_2$ was prepared by a previously reported procedure by reacting equal molar amounts of $(CH_3)_3Si(OTf)$ and anhydrous $MnCl_2$.[24] The $[Mn^{II}(Tp^{Ph2})](OTF)$ complex was prepared by adding Tp^{Ph2} (1.0 g, 1.411 mmol) in 30 mL DMF to a stirred solution of $Mn(OTf)_2$ (0.497 g, 1.411 mmol) in 20 mL of DMF. The colorless solution was stirred for 4 hours. Precipitation of the crude product was obtained by

addition of diethyl ether. $[Mn^{II}(Tp^{Ph2})(DMF)_3](OTf)$ (1.39 g, 90%) M^+ [({$[Mn(Tp^{Ph2})]\}^+$) 724.2; requires M^+, 724.2].

4.2.4. In Situ Preparation of $[Mn^{III}(O_2)(Tp^{Ph2})(THF)]$ Complex. The yellow peroxomanganese(III) intermediate was formed by treating a THF solution of $[Mn^{II}(Tp^{Ph2})(DMF)_3](OTf)$ with a KO_2 slurry at ambient conditions. To optimize formation of the peroxomanganese(III) species, the slurry was prepared by stirring 25 equivalents of KO_2 in a 50:50 mixture of 2-Me-tetrahydrofuran:THF for 20 minutes. Treatment with smaller amounts of KO_2 resulted in lower yields of the Mn^{III}-O_2 species. 50 μL of the KO_2 slurry was added to the $[Mn^{II}(Tp^{Ph2})(DMF)_3](OTf)$ solution and stirred for 3 minutes, forming a brown precipitate. A second addition of 50 μL of the KO_2 slurry was added and the solution was stirred for 15 minutes. The brown precipitate was filtered from the solution, and a yellow solution was obtained. The peroxomanganese(III) intermediate was isolated by removing the solvent under vacuum and washing the solid residue with toluene to remove unreacted $[Mn^{II}(Tp^{Ph2})(DMF)_3](OTf)$.

4.2.5. X-ray Crystallography. Single needle crystals of $[Mn^{II}(Tp^{Ph2})(DMF)_3](OTf)$ were grown by layering heptane on a THF solution of the metal complex at ambient temperature. Single needle crystals of $[Mn^{III}(O_2)(Tp^{Ph2})(THF)]$ were grown by vapor diffusion of diethyl ether into a 50:50 mixture of 2-Me-tetrahydrofuran:THF at -20 ^oC. Diffracted intensities were measured for $[Mn^{II}(Tp^{Ph2})(DMF)_3](OTf)$ and $[Mn^{III}(O_2)(Tp^{Ph2})(THF)]$ using monochromated Cu-K_α radiation (λ = 1.54178) on a Bruker Single Crystal Diffraction System equipped with Helios high-brilliance multilayer X-ray optics, an APEX II CCD detector, and a Bruker MicroSTAR microfocus rotating anode X-ray source operated at 45 kV and 60 mA. Lattice constants were determined with the Bruker SAINT software package. The Bruker software package SHELXTL was used to solve the structure using "direct methods" techniques. All states

of weighted full-matrix least-squares refinement were conducted using F_o^2 data with the SHELXTL Version 6.10 software package.[35] Crystal data for $[Mn^{II}(Tp^{Ph2})(DMF)_3](OTf)$ and $[Mn^{III}(O_2)(Tp^{Ph2})(THF)]$ are supplied in Table 4.1, and full data collection and refinement parameters are summarized in the Electronic Supplementary Information (ESI) in Tables S1 and S2.

Table 4.1. Crystal data for $[Mn(Tp^{Ph2})(DMF)_3](OTf)$ ($C_{59}H_{63}BF_3MnN_9O_7S$) and $[Mn(O_2)(Tp^{Ph2})(THF)]$ ($C_{58}H_{62}BMnN_6O_5$).

formula	$C_{59}H_{63}BF_3MnN_9O_7S$	$C_{58}H_{62}BMnN_6O_5$
MW	1164.99	988.89
T, K	100(2)	100(2)
unit cell	monoclinic	monoclinic
a, Å	17.6441(10)	12.928(2)
b, Å	14.8052(8)	21.642(4)
c, Å	21.9441(11)	18.633(3)
a	90	90
b	93.243(4)	103.572(4)
g	90	90
V, Å^3	5723.2(5)	5067.5(15)
Z	4	4
d(calcd), g/cm^3	1.352	1.296
space group	P2(1)/n	P2(1)/n
R	0.0638	0.0514
R_w	0.1649	0.1474
GOF	0.928	1.077

$R = \Sigma \, ||F_o| - |F_c|| \, / \, \Sigma \, |F_o|$

$R_w = \{ \Sigma \, [w(F_o^2 - F_c^2)^2] \, / \, \Sigma \, [w(F_o^2)^2] \}^{1/2}$

4.2.6. EPR Experiments. A frozen sample of $[Mn^{II}(Tp^{Ph2})(DMF)_3](OTf)$ (250 μm) was prepared in THF at ambient temperature and flash-frozen in a quartz EPR tube in liquid N_2. Collection of EPR data in the same solvent as MCD experiments (75:25 mixture of 2-Me-tetrahydrofuran:THF, *vide infra*) was unsuccessful due to the propensity of this solvent system to partially melt during transfer of the EPR tubes from the liquid nitrogen storage dewar to the EPR cryostat, resulting in shattered EPR tubes. An EPR sample of $[Mn^{III}(O_2)(Tp^{Ph2})(THF)]$ was

prepared after filtering the brown precipitate from the yellow solution and confirming the characteristic spectrum of this complex by UV-visible spectroscopy. Frozen samples of [$Mn^{III}(O_2)(Tp^{Ph2})(THF)$] (250 μm), prepared using both the crude yellow residue and the purified residue obtained through a toluene wash, were prepared in THF at ambient temperature and flash-frozen in quartz EPR tubes in liquid N_2. All data were collected on an X-band (9 GHz) Bruker EMXPlus spectrophotometer with an Oxford ESR900 continuous-flow liquid helium cryostat and an Oxford ITC503 temperature system to regulate the temperature. To collect perpendicular and parallel-mode spectra, a Bruker ER4116DM dual-mode cavity was used. Spectra were collected under non-saturated conditions with 9.3918 GHz microwave frequency, 20 dB microwave power, 0.6 mT modulation amplitude, 100 kHz modulation frequency and 163 ms time constant. The Matlab-based EPR simulation software package *EasySpin,* developed by Stoll,[36] was used to simulate and fit all EPR spectra and to determine zero-field splitting parameters of the peroxomanganese(III) complex.

4.2.7. Magnetic Circular Dichroism Experiments. A frozen glass sample of [$Mn^{III}(O_2)(Tp^{Ph2})(THF)$] (15 mM) was prepared in 75:25 mixture of 2-Me-tetrahydrofuran:THF at ambient temperature, transferred to MCD cells, and flash-frozen in liquid N_2. The obtained MCD spectra were measured in mdeg (θ) and converted to Δε ($M^{-1}cm^{-1}$) using the standard conversion factor $\Delta\varepsilon = \theta/(32980 \cdot c \cdot d)$, where c is the concentration of the sample and d is the path length. MCD spectra were collected at 2, 4, 8, and 15 K for positive and negative field strengths of 1 to 7 T in 1 T increments. VTVH data were fit using the general method developed by Neese and Solomon.[37] Fits were performed for an $S = 2$ system with isotropic g-values of 2.00. Using a previously described protocol,[3] zero-field splitting (ZFS) parameters D and E/D were systematically varied while the transition moment products were optimized for a given set of

ZFS parameters. The goodness of fit was evaluated by the χ^2 factor; where χ^2 is the sum of the squares of the differences between experimental and fit data sets.

4.2.8. X-ray Absorption Spectroscopy. The $[Mn^{II}(Tp^{Ph2})(DMF)_3](OTf)$ XAS sample was prepared as a 4% (w/w) dispersion by grinding 8 mg of $[Mn^{II}(Tp^{Ph2})(DMF)_3](OTf)$ with 192 mg boron nitride into a powder with a mortar and pestle. Solution phase XAS samples of $[Mn^{III}(O_2)(Tp^{Ph2})(THF)]$ were prepared by several methods and then transferred to XAS sample holders and flash frozen in liquid N_2. Methods of solution preparation included: 15 mM $[Mn^{III}(O_2)(Tp^{Ph2})(THF)]$ in 50:50 2-Me-tetrahydrofuran:THF, 5 mM $[Mn^{III}(O_2)(Tp^{Ph2})(THF)]$ in THF, and 15 mM $[Mn^{III}(O_2)(Tp^{Ph2})(THF)]$ in THF with isolation by toluene wash. All attempts at XAS data collection for $[Mn^{III}(O_2)(Tp^{Ph2})(THF)]$ were thwarted by photoreduction or sample degradation. XAS spectra were recorded on beamline X3B at the National Synchrotron Light Source (NSLS), Brookhaven National Lab (storage ring conditions, 2.8 GeV, 100 - 300 mA). Mn K-edge X-ray absorption spectra over the energy range 6.4 – 7.4 keV (Si(111) monochrometer) were recorded on a powder sample maintained at 20 K with a helium Displex closed-cycle cryostat. XAS spectra were obtained as fluorescence excitation spectra using a solid-state 13-element germanium detector (Canberra). Contamination of higher harmonics radiation was minimized with a harmonic rejection mirror. Background fluorescence signal was reduced with a 3 μm chromium filter. A manganese foil spectrum was recorded concomitantly for internal energy calibration, and the first inflection point of the K-edge energy was assigned to 6539.0 eV. Spectra were measured with 5 eV steps below the edge (6359 – 6529 eV), 0.3 eV steps in the edge region (6529 – 6564 eV), and steps equivalent to 0.05 $Å^{-1}$ increments above the edge.

EXAFS data reduction and averaging were performed using the program EXAFSPAK.[38] The pre-edge background intensity was removed by fitting a Gaussian function to the pre-edge background and then subtracting this function from the whole spectrum. The spectrum was also

fit with a three-segment spline with fourth-order polynomial components to remove low-frequency background. EXAFS refinement was carried out on $k^3\chi(k)$ data, using phase and amplitude functions obtained from *FEFF*, version 6,[39] and a structural model of $[Mn^{II}(Tp^{Ph2})(DMF)_3](OTf)$ with XRD coordinates. For each fit, the parameters r (average distance between Mn and scattering atom) and σ^2 (Debye-Waller factor) were optimized, while n, the number of atoms in the shell, was kept fixed. n was varied by integer steps systematically. The goodness-of-fit (GOF) was evaluated by the parameter F, where $F = \Sigma\,(\chi_{calcd} - \chi_{expt})^2 / N$, and N is the number of data points. The threshold energy, E_0, in electronvolts (k = 0 point) was kept at a common, variable value for every shell of a given fit.

4.2.9. Density Functional Theory Calculations. The *ORCA* 3.0.1 software package was used for all DFT computations.[40] An initial model of $[Mn^{III}(O_2)(Tp^{Ph2})(THF)]$ was built using the X-ray coordinates obtained in this work. Models of the brown and blue isomers of $[Mn^{III}(O_2)(Tp^{iPr2})(pz^{iPr2}H)]$ were built using the X-ray coordinates of these complexes.[22] Geometry optimizations of these models were converged to the S = 2 spin state. These calculations employed the Becke-Perdew (BP86) functional[41,42] and the SVP (Ahlrichs split valence polarized)[43,44] basis sets with the SV/J auxiliary basis sets for all atoms except for manganese, nitrogen, and oxygen, where the larger TZVP (Ahlrichs triple-ζ valence polarized)[20] basis sets in conjunction with the TZV/J auxiliary basis sets were used. The resolution of identity (RI) approximation[45] was used for all calculations. Solvation effects associated with THF (dielectric constant ε = 7.25) for the Tp^{Ph2} complexes and toluene (dielectric constant ε = 2.40) for the Tp^{iPr2} complexes were incorporated using COSMO, as implemented in *ORCA*.[46] Cartesian coordinates for all DFT-optimized models are included in ESI (Tables S3-S8).

Electronic transition energies and intensities were computed for $[Mn^{III}(O_2)(Tp^{Ph2})(THF)]$ and the brown and blue isomers of $[Mn^{III}(O_2)(Tp^{iPr2})(pz^{iPr2}H)]$ using the TD-DFT method[47-49]

within the Tamm-Dancoff approximation.[50,51] These calculations employed the B3LYP functional,[52-54] and the SVP basis set for all atoms except for manganese, nitrogen, and oxygen, where the larger TZVP was used. For the $[Mn^{III}(O_2)(Tp^{Ph2})(THF)]$ calculation, 40 excited states were calculated by including all one-electron excitations within an energy window of ±3 Hartrees with respect to the HOMO/LUMO energies. Additionally, truncated versions of $[Mn^{III}(O_2)(Tp^{Ph2})(THF)]$ were also employed for TD-DFT calculations, however, the full molecule yielded the optimal results. For the larger $[Mn^{III}(O_2)(Tp^{iPr2})(pz^{iPr2}H)]$ complexes, 20 excited states were calculated using the full complex. Isosurface plots of molecular orbitals (MOs) and electron density difference maps (EDDMs) were generated using the gOpenMol program using isodensity values of 0.01 and 0.005 b^{-3}, respectively. Additional electronic transition calculations were performed for $[Mn^{III}(O_2)(Tp^{Ph2})(THF)]$ using the CASSCF calculations in conjunction with second-order-*N*-electron valence state perturbation theory (NEVPT2) method.[55] These calculations employed the RI approximation[45] and the TZVP basis set for manganese, nitrogen, and oxygen and SVP for all other atoms. The active space was selected to include CAS(4, 5), which includes all the 3*d* electrons of the Mn^{III} center, and was calculated with five quintet roots and ten triplet roots.

4.3 Results and Analysis

4.3.1. Structural properties of $[Mn^{II}(Tp^{Ph2})(DMF)_3](OTf)$. The Mn^{II} complex $[Mn^{II}(Tp^{Ph2})(DMF)_3](OTf)$ was generated by treatment of $Mn(OTf)_2$ with Tp^{Ph2} in dimethylformamide (DMF). Diffraction quality crystals were obtained by vapour diffusion of diethyl ether into the DMF solution of $[Mn^{II}(Tp^{Ph2})(DMF)_3](OTf)$. Figure 4.1 (left) displays an ORTEP diagram for $[Mn^{II}(Tp^{Ph2})(DMF)_3](OTf)$. Selected bond distances and angles are given in Table 4.2. The tridentate Tp^{Ph2} ligand is bound facially, creating three coordination sites

occupied by DMF ligands that complete the coordination sphere to give a six-coordinate Mn^{II} ion in a distorted octahedral geometry. The Mn-ligand bond lengths range from ~2.14 to 2.32 Å, typical of a high-spin Mn^{II} ion, and also consistent with reports of previously characterized Mn^{II} species supported by Tp-based ligands.[56-58] Specifically, the Mn-$N_{pyrazole}$ bond lengths of $[Mn^{II}(Tp^{Ph2})(DMF)_3](OTf)$ and other mononuclear Mn^{II} complexes fall within the range of 2.149(2) to 2.319(1) Å (Table 4.3). Figure 4.1 (right) displays a view along the three-fold axis of the space filling model for $[Mn^{II}(Tp^{Ph2})(DMF)_3](OTf)$ without the coordinated solvent molecules. This perspective highlights the open face of the metal ion that is shielded by the phenyl groups of the supporting ligand.

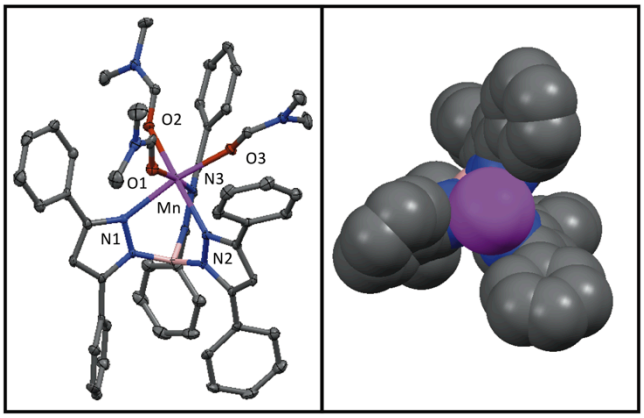

Figure 4.1. ORTEP diagram of $[Mn^{II}(Tp^{Ph2})(DMF)_3](OTf)$ (left) and space filling model (right). For the ORTEP diagram, hydrogen atoms and the counter anion have been removed for clarity. For the space filling model hydrogen atoms, coordinating solvents molecules, and the counter anion have been removed for clarity. The significant interatomic distances and angles are listed in Table 4.2.

Table 4.2. Selected bond lengths (Å) and angles (°) for $[Mn^{II}(Tp^{Ph2})(DMF)_3](OTf)$.

Mn-N(1)	2.286(1)	N(1)-Mn-O(3)	169.1(5)
Mn-N(2)	2.250(3)	N(2)-Mn-O(2)	172.0(2)
Mn-N(3)	2.319(1)	N(3)-Mn-O(1)	171.6(2)
Mn-O(1)	2.157(3)	N(1)-Mn-N(2)	83.3(4)
Mn-O(2)	2.141(6)	N(1)-Mn-N(3)	86.5(2)
Mn-O(3)	2.191(1)	N(2)-Mn-N(3)	86.7(9)

Table 4.3. Mn-$N_{pyrazole}$ bond lengths (Å) for $[Mn^{II}(Tp^{Ph2})(DMF)_3](OTf)$ and other $Mn^{II}(Tp)$ complexes.

	Mn-N(1)	Mn-N(2)	Mn-N(3)	Ref
$[Mn^{II}(Tp^{Ph2})(DMF)_3](OTf)$	2.286(1)	2.250(3)	2.319(1)	This work
$[Mn(Tp^{CO2Et,Me})(H_2O)_3]ClO_4$	2.254(4)	2.273(4)	2.307(4)	[56]
$[Mn(OAc)(Tp^{Ph,Me})(pz^{Ph,Me}H)]$	2.199(2)	2.282(2)	2.149(2)	[57]
$[Mn(Cl)(Tp^{iPr2})(pz^{iPr2}H)]$	2.151(2)	2.164(2)	2.243(2)	[57]

4.3.2. Conversion of $[Mn^{II}(Tp^{Ph2})(DMF)_3](OTf)$ to $[Mn^{III}(O_2)(Tp^{Ph2})(THF)]$. No intense features are observed in the electronic absorption spectra of tetrahydrofuran (THF) solutions of $[Mn^{II}(Tp^{Ph2})(DMF)_3](OTf)$ at energies below 33 000 cm^{-1} (Figure 4.2; dashed line). A weak feature is observed at ~28 000 cm^{-1} (ε = 20 $M^{-1}cm^{-1}$) that could arise from a Mn^{II}-to-ligand (Tp^{Ph2}) charge-transfer (CT) transition. While the intensity is very low for a CT feature, the intensity of this band is at least an order of magnitude larger than that expected for a spin-forbidden Mn^{II} ligand-field transition.[59] Treatment of $[Mn^{II}(Tp^{Ph2})(DMF)_3](OTf)$ with excess KO_2 at room temperature results in the formation of a yellow intermediate and a brown precipitate. After filtering the brown precipitate from the solution to obtain the yellow intermediate, new absorption features are present in the visible region. The absorption spectra of the yellow intermediate is characterized by a prominent band at 26 385 cm^{-1} and a weaker, broader band at 22 936 cm^{-1} (ε = 324 and 73 M^{-1} cm^{-1}, respectively).

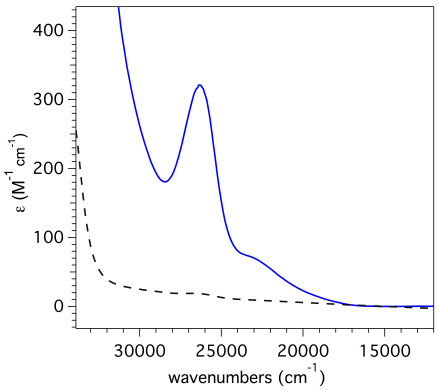

Figure 4.2. Electronic absorption spectra of $[Mn^{II}(Tp^{Ph2})(DMF)_3](OTf)$ (black dashed trace) and the yellow intermediate, $[Mn^{III}(O_2)(Tp^{Ph2})(THF)]$, (solid blue trace) at 298 K in THF.

For the previously reported [$Mn^{III}(O_2)(Tp^{iPr2})(pz^{iPr2}H)$] complex, a weak, broad band was observed at 17 800 cm^{-1} which shifted to 17 150 cm^{-1} when a pyrazole-peroxo hydrogen bond was formed.[22] More intense features were apparent at higher energy, but no band maxima were reported. The extinction coefficient for the ~17 000 cm^{-1} transition of [$Mn^{III}(O_2)(Tp^{iPr2})(pz^{iPr2}H)$] (~50 M^{-1} cm^{-1}) is similar to that of the lowest-energy band of the yellow intermediate. Thus, these data are supportive of the formulation of the yellow intermediate as a peroxomanganese(III) adduct. Unlike the low-energy absorption band of the [$Mn^{III}(O_2)(Tp^{iPr2})(pz^{iPr2}H)$] complex that red-shifts and increases in intensity upon cooling from 253 to 193 K,[14] the absorption bands of the yellow intermediate sharpen and show a slight blue-shift (~100 cm^{-1}) and increase in intensity (~17 % for the intense band at 26 320 cm^{-1}) when a 75:25 mixture of 2-Me-tetrahydrofuran:THF solution of the sample is cooled from 300 to 200 K (Figure A4.1).

4.3.3. X-ray Diffraction Structure of the yellow intermediate: [$Mn^{III}(O_2)(Tp^{Ph2})(THF)$]. Because of the high thermal stability of the yellow intermediate ($t_{1/2}$ = 4.5 days in THF), we were able to obtain single crystals suitable for XRD experiments. The XRD structure of the yellow needle crystals revealed a neutral mononuclear six-coordinate Mn^{III} complex with a side-on peroxo ligand and a coordinated THF molecule, [$Mn^{III}(O_2)(Tp^{Ph2})(THF)$] (Figure 4.3). Selected bond distances and angles are given the Table 4.4. The Mn^{III} ion is in a distorted octahedral geometry with an axial elongation along the (THF)O-Mn-N(1) axis (bond lengths of 2.313(7) Å and 2.375(2) Å, respectively). Here, the peroxo ligand and the N2 and N3 atoms of the Tp^{Ph} ligand define the equatorial plane. The other Mn-N bond distances are nearly identical, with Mn-N(2) and Mn-N(3) bond lengths of 2.09 Å. The peroxo ligand is nearly symmetrically bound to the Mn^{III} ion with Mn-O distances of 1.865(2) and 1.859(2). The O-O

bond length is 1.432(3) Å, which is typical of a peroxo ligand bound to a transition-metal ion and is in good agreement with other reported Mn^{III}-O_2 complexes (Table 4.2).[22,27,14,24,30] Considering the peroxo as a monoligand, a τ parameter of 1.2 is obtained, indicating that this complex is at the trigonal bipyramidal limit, similar to other Tp-supported Mn^{III}-O_2 adducts.[23] (The τ parameter of greater than 1, which would not be possible for authentic five-coordinate complexes, results from our specific definition of τ for Mn^{III}-O_2 adducts.[31]) Figure 4.3 (right) displays perpendicular views of the space filling model for $[Mn^{III}(O)_2(Tp^{Ph2})(THF)]$. The peroxo ligand is well shielded by the three phenyl groups of the Tp^{Ph2} ligand, which could account for the high thermal stability of this complex.

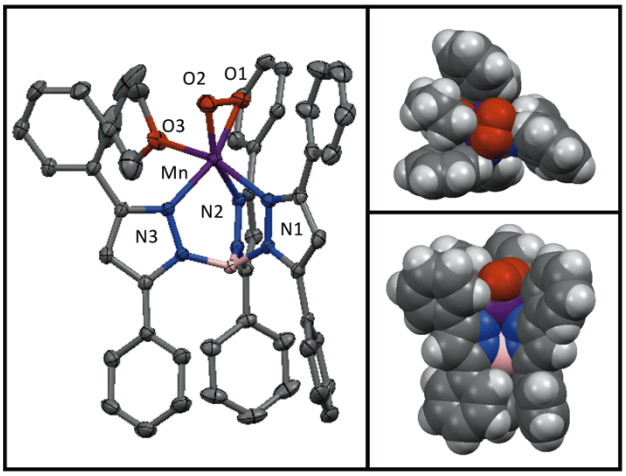

Figure 4.3. ORTEP diagram of $[Mn^{III}(O_2)(Tp^{Ph2})(THF)]$ (left) and space filling models (right). For the ORTEP diagram, hydrogen atoms have been removed for clarity. Select interatomic distances and angles are listed in Table 4.4.

Table 4.4. Selected bond lengths (Å) and angles (°) for $[Mn^{III}(O_2)(Tp^{Ph2})(THF)]$.

Mn-O(1)	1.865(2)	O(1)-O(2)	1.432(3)
Mn-O(2)	1.859(2)	N(2)-Mn-O(1)	109.1(2)
Mn-O(3)[a]	2.313(7)	N(3)-Mn-O(2)	111.9(9)
Mn-N(1)	2.375(2)	N(1)-Mn-O(3)[a]	163.1(2)
Mn-N(2)	2.095(2)	N(1)-Mn-N(3)	84.5(1)
Mn-N(3)	2.091(2)	N(1)-Mn-N(2)	84.6(9)

[a]O(3) refers to the O atom of the THF ligand.

4.4.4. EPR Experiments. X-band EPR spectra were collected for frozen solutions of $[Mn^{II}(Tp^{Ph2})(DMF)_3](OTf)$ and $[Mn^{III}(O_2)(Tp^{Ph2})(THF)]$ at 5 K in perpendicular and parallel mode. In perpendicular mode, a THF solution of $[Mn^{II}(Tp^{Ph2})(DMF)_3](OTf)$ exhibits a 6-line signal at g_1 = 2.03 with hyperfine splitting of 9.1 mT, indicative of mononuclear Mn^{II} (Figure 4.4, left; black trace). Additionally, a weaker feature at g_2 = 4.1 is present with hyperfine splitting of 7.9 mT. Upon the treatment of this solution with an excess of KO_2 and filtering to remove the brown precipitate, a 93% decrease in the intensity at g_1 is observed. (Figure 4.4, left; blue trace). No signals are observed in the parallel-mode spectrum of this crude solution. Isolation of $[Mn^{III}(O_2)(Tp^{Ph2})(THF)]$ by removing the solvent under vacuum and washing with toluene further decreased the intensity at g_1 by a total of 98% (Figure 4.4, left; red trace). A parallel mode spectrum of this purified sample of the yellow intermediate exhibits a characteristic Mn^{III} feature at g = 8.3 with hyperfine splitting of 5.06 mT (Figure 4.4, right). Variable-temperature parallel-mode spectra collected from 5 to 20 K revealed an inverse temperature dependence, indicating a negative sign of the axial zero-field splitting (ZFS) parameter D (Figure A4.2). The EPR data for $[Mn^{III}(O_2)(Tp^{Ph2})(THF)]$ were simulated with g = 1.98, S = 2, a hyperfine splitting of 5.1 mT and the ZFS parameters D = 2.0(5) cm^{-1} and E/D = 0.07(1). (Figure 4.4, right). The goodness of fit of the simulation was extremely sensitive to changes in the magnitude of E/D (varied in increments of 0.01 cm^{-1}) and less sensitive to the magnitude of D (varied in increments of 0.1 cm^{-1}). The sensitivity of these parameters arises because the value of E determines the splitting of the $m_s \pm 2$ levels that gives rise to the EPR signal, and a value of D that is greater than the microwave quantum value does not significantly

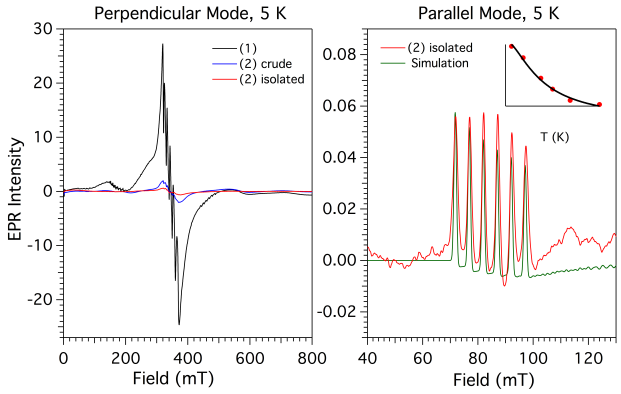

Figure 4.4. Left: 5 K perpendicular-mode EPR spectrum of the conversion of $[Mn^{II}(Tp^{Ph2})(DMF)_3](OTf)$ to $[Mn^{III}(O_2)(Tp^{Ph2})(THF)]$ and purification of $[Mn^{III}(O_2)(Tp^{Ph2})(THF)]$. Right: 5 K parallel-mode EPR spectrum of $[Mn^{III}(O_2)(Tp^{Ph2})(THF)]$ (red) and simulation (green) with D = -2.0(5), E/D = 0.07(1). Inset: signal intensity versus temperature of g = 8.3 signal. An EPR spectrum of $[Mn^{III}(O_2)(Tp^{Ph2})(THF)]$ showing a wider field is in Figure A4.3.

impact the EPR signal.

4.4.5. Further Spectroscopic Characterization of $[Mn^{III}(O_2)(Tp^{Ph2})(THF)]$. IR data collected for a KBr pellet of $[Mn^{III}(O_2)(Tp^{Ph2})(THF)]$ show a weak feature at 882 cm^{-1} (Figure A4.4) which is in the expected region for an O-O vibration of a mononuclear Mn^{III}-O_2 adduct (ν_{O-O} = 875 – 896 cm^{-1}).[23] Because solid samples of $[Mn^{III}(O_2)(Tp^{Ph2})(THF)]$ could only be successfully prepared using a large excess of KO_2, and we were unable to collect reliable IR data for solution samples of $[Mn^{III}(O_2)(Tp^{Ph2})(THF)]$, we did not attempt any isotopic labelling studies using $K^{18}O_2$. Although the peak at 882 cm^{-1} is not observed in the corresponding IR spectrum of $[Mn^{II}(Tp^{Ph2})(DMF)_3](OTf)$, (Figure A4.4), we cannot definitively assign the band at 882 cm^{-1} as the ν_{O-O} mode of $[Mn^{III}(O_2)(Tp^{Ph2})(THF)]$ in the absence of the isotopic labelling experiment.

To gain additional insights into the ground- and excited-state properties of $[Mn^{III}(O_2)(Tp^{Ph2})(THF)]$, we collected low- temperature MCD and VTVH MCD data. All MCD signals of $[Mn^{III}(O_2)(Tp^{Ph2})(THF)]$ observed from 15 000 to 32 000 cm^{-1} show *C*-term behavior (*i.e.*, their intensities show an inverse temperature dependence; see Figure A4.5). Figure 4.5

(bottom) shows the 2 K, 7 T MCD spectra of [$Mn^{III}(O_2)(Tp^{Ph2})$(THF)]. The corresponding 298 K electronic absorption spectrum is included for comparison (Figure 4.5, top). In the absorption spectrum, [$Mn^{III}(O_2)(Tp^{Ph2})$(THF)] shows low-intensity features from ~18 000 – 24 000 cm^{-1} with a slight maximum at 22 900 cm^{-1}. This fairly indistinct region of the absorption spectrum corresponds to a set of MCD features at 19 000 (-), 22 200 (+), 23 500 (-, shoulder), and 24 100 (-) cm^{-1}. The major absorption band at 26 320 cm^{-1} corresponds to an intense, positively-signed MCD band at roughly the same energy (26 200 cm^{-1}). An iterative Gaussian deconvolution of the absorption and MCD spectra reveals a total of nine electronic transitions from 16 500 to 31 000 cm^{-1} (Table A4.9). Tentative assignments can be made for these transitions on the basis of the different selection rules for electronic absorption and MCD spectroscopy, as well as previous spectral analysis of mononuclear Mn^{III}-O_2 adducts.[16] More detailed band assignments developed using TD-DFT computations are discussed later. Bands 2, 8, and 9, which are fairly prominent in the absorption spectrum but carry comparatively little MCD intensity are assigned as peroxo-to-manganese(III) CT transitions (Table 4.5).[60] Bands 4 and 6, which exhibit very narrow bandwidths in the MCD spectrum and carry essentially negligible absorption intensity, are assigned as spin-forbidden Mn^{III} *d-d* transitions (Table 4.5). The narrow widths of these transitions are indicative of small excited state distortions and suggest that these transitions are intra-configurational. Bands

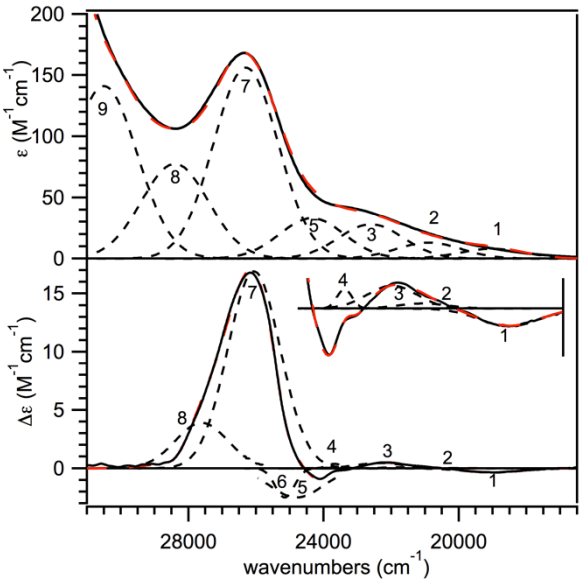

Figure 4.5. 298 K electronic absorption (top) and 2 K, 7 T MCD (bottom) spectra of [$Mn^{III}(O_2)(Tp^{Ph2})$(THF)]. Inset: An 15-fold enhancement of the 2 K, 7 T MCD spectra from 17 500 to 25 000 cm^{-1}. Individual Gaussian curves (black dotted lines) and their sums (red dashed lines) obtained from iterative fits of these data sets are displayed on their respective spectra. Only Gaussian bands 1 – 4 are shown in the inset. Conditions: Absorption data were collected for a 2.5 mM sample in THF. MCD data were collected for a 15 mM frozen glass sample in 75:25 solution of 2-Me-THF:THF.

1, 3, 5, and 7 exhibit high to moderate intensity and suggest that these transitions are intra-configurational. Bands 1, 3, 5, and 7 exhibit high to moderate intensity in the MCD spectrum and are assigned as the four ligand-field *d-d* transitions expected for an $S = 2$ Mn^{III} center (Table 4.5, Figure 4.6). Here, we note that the high energy of band 1 (19 000 cm^{-1}), which is the lowest-energy *d-d* transition, makes [$Mn^{III}(O_2)(Tp^{Ph2})$(THF)] unique compared to peroxomanganese(III) species supported by the tetradentate bis(pyridyl)- and bis(quinolinyl)-diazepane ligands, where

Table 4.5. MCD, electronic absorption, calculated TD-DFT, and NEVPT2 electronic transition energies (cm^{-1}) of $[Mn^{III}(O_2)(Tp^{Ph2})(THF)]$. Corresponding oscillator strengths are included in Table A4.14.

	Experimental		Calculated		
Band	Abs.	MCD	TD-DFT	NEVPT2	Assignment
1	19 000	19 000	20 500	25 700	d_z^2 - d_{xy} [c]
2	20 890	21 455	23 300	-	CT[d]
3	22 600	22 325	27 200	29 500	d_{yz} - d_{xy} [c]
4	- [a]	23 675	-	26 800[b]	SF[b]
5	24 350	24 800	28 800	31 600	$d_{x^2-y^2}$ - d_{xy} [c]
6	- [a]	25 150	-	30 500[b]	SF[b]
7	26 300	26 060	30 600	32 000	d_{xz} - d_{xy} [c]
8	28 400	27 609	29 500	-	CT[d]
9	28 350		29 800	-	CT[d, e]

[a]Band only apparent in low-temperature, 7 T MCD spectrum. [b]Mn^{III} spin-forbidden *d-d* transitions to triplet excited states [c]Assigned as a spin-allowed transition involving primarily the Mn 3*d* orbitals as indicated. [d]Assigned as peroxo-to-manganese(III) charge transfer transition. [e]Based on the low MCD intensity of band 9, this feature could arise from a Tp^{Ph2}-based charge-transfer transition.

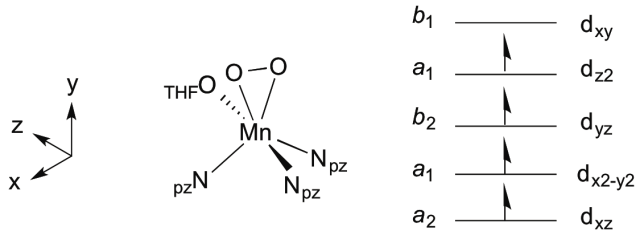

Figure 4.6. First coordination sphere of $[Mn^{III}(O_2)(Tp^{Ph2})(THF)]$ and *D*-tensor coordinate system from CP-DFT computations. The C_{2v} symmetry labels for the Mn 3*d* orbitals using the *D*-tensor coordinate system are provided.

the corresponding transition ranged from 13 650 – 16 630.[16,18,32] For that series of complexes, this variation was related to slight differences in one $Mn{-}O_{peroxo}$ distance (1.869 – 1.907 Å). Because the $Mn{-}O_{peroxo}$ distances of $[Mn^{III}(O_2)(Tp^{Ph2})(THF)]$ fall within this range (see Table 4.4), another structural perturbation must account for the high energy of band 1 in this case.

VTVH MCD spectroscopy[37,61] was used to probe both the ZFS parameters and transition polarizations of $[Mn^{III}(O_2)(Tp^{Ph2})(THF)]$. VTVH MCD curves obtained for

$[Mn^{III}(O_2)(Tp^{Ph2})(THF)]$ at 26 180 cm^{-1} are nested, indicating a moderate ZFS of the Mn^{III} ion (Figure 4.7) and were systematically fitted to obtain zero field splitting parameters. The best fits (χ^2 < 0.04) were obtained with D = -2.0 cm^{-1}, E/D = 0.05 and a predominant z- polarization (<1% x, <1% y-, and 98% z-polarization). These ZFS parameters are in excellent agreement with those obtained from the EPR data (D = -2.0(5) cm^{-1}; E/D = 0.07(1). In addition, these ZFS splitting parameters fall in the range of those reported for other peroxomanganese(III) adducts (D = -1.5 to -3.0 and E/D = 0.05 to 0.30).[16,19,20,25] Thus, the ZFS parameters of $[Mn^{III}(O_2)(Tp^{Ph2})(THF)]$ are not reflective of the unique τ parameter of this complex.

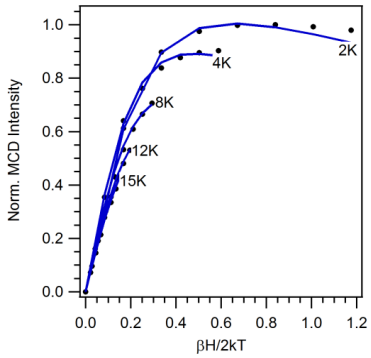

Figure 4.7. Experimental VTVH MCD data collected at 26 180 cm^{-1} for $[Mn^{III}(O_2)(Tp^{Ph2})(THF)]$ (···) and theoretical fit (—) using the following parameters: D = -2.00, E/D = 0.05, g_{iso} = 2.00, and 0.8% x, 0.8% y, and 98.4% z polarization.

4.4.6. X-ray Absorption Spectroscopy of $[Mn^{II}(Tp^{Ph2})(DMF)_3](OTf)$ and $[Mn^{III}(O_2)(Tp^{Ph2})(THF)]$. The Mn K-edge X-ray absorption data of $[Mn^{II}(Tp^{Ph2})(DMF)_3](OTf)$ shows a rising edge at 6547.5 eV, characteristic of a Mn^{II} species,[62,63] as well as a pre-edge feature at 6540.6 eV (Figure A4.6). The Fourier transform of the extended X-ray absorption fine structure (EXAFS) data of $[Mn^{II}(Tp^{Ph2})(DMF)_3](OTf)$ exhibits a primary peak at R' = 1.7 Å which was best fit with a shell of 3 O atoms at 2.16 Å and a shell of 3 N atoms at 2.28 Å (Figure 4.8, Table 4.6). Two smaller peaks are present in the Fourier transform at R' = 2.5 and 3.1 which were fit with a shell of 4 N atoms at 3.09 Å, a shell of 1 B atom at 3.33 Å, and a shell of 6 C

atoms at 3.49 Å. The fits of the EXAFS data show excellent agreement with the bond lengths determined through XRD, particularly with the EXAFS fits of the average Mn-N and Mn-O distances of 2.28 and 2.16 Å, respectively (Table A4.10).

Table 4.6. EXAFS Fitting Results for $[Mn^{II}(Tp^{Ph2})(DMF)_3](OTf)$.[a]

	Mn-O			Mn-N			Mn-N			Mn-B			Mn-C			
Fit[b]	*n*	*r*(Å)	σ^2 (Å^2)[c]	*n*	*r*(Å)	σ^2 (Å^2)[c]	*n*	*r*(Å)	σ^2 (Å^2)[c]	*n*	*r*(Å)	σ^2 (Å^2)[c]	*n*	*r*(Å)	σ^2 (Å^2)[c]	F-factor
1	6	2.18	7.41													0.612
2	3	2.14	3.29	3	2.26	2.58										0.598
3	3	2.14	3.53	3	2.26	2.84	5	3.10	3.14							0.552
10	3	2.16	3.88	3	2.27	3.53	3	3.08	0.60	1	3.30	6.05				0.535
15	***3***	***2.16***	***3.42***	***3***	***2.28***	***3.17***	***4***	***3.09***	***2.09***	***1***	***3.33***	***2.40***	***6***	***3.49***	***5.51***	***0.534***

[a]Fourier transform range is 2 – 14.5 Å (resolution 0.126 Å). [b]The fit numbers refer to all fits considered; see Table A4.11. [c]Debye-waller factors are scaled x 10^3.

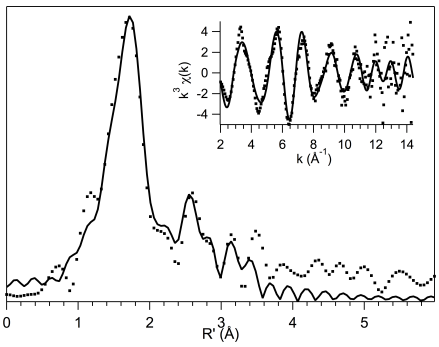

Figure 4.8. Fourier transform of Mn K-edge EXAFS data [$k^3\chi(k)$] and raw EXAFS spectra (insets), experimental data (···) and fits (−) for $[Mn^{II}(Tp^{Ph2})(DMF)_3](OTf)$.

We also attempted to collect Mn K-edge X-ray absorption data for $[Mn^{III}(O_2)(Tp^{Ph2})(THF)]$; however, all datasets showed signs of photoreduction or sample degradation which was evident by a shift in the edge energy and disappearance of the pre-edge feature (Figure A4.7). Several attempts were made to circumvent the sample instability, such as preparation with different solvents (50:50 mixture of 2-Me-tetrahydrofuran:THF, THF, and toluene) and by several methods of preparation, but sample degradation was observed in all cases when the sample was subjected to the X-ray beam.

4.4.7. Ligand Exchange Reactions of $[Mn^{III}(O_2)(Tp^{Ph2})(THF)]$. The observation of the solvent (THF) ligand in the X-ray structure of $[Mn^{III}(O_2)(Tp^{Ph2})(THF)]$ appeared to present an opportunity to perform ligand substitution reactions *cis* to the Mn^{III}-O_2 unit, under the assumption that the THF ligand might be labile. In a peroxomanganese(III) complex supported by the 13-TMC ligand (Scheme 4.1), substitution *trans* to the Mn^{III}-O_2 unit has been successful with anionic ligands.[14] Ligand substitution with a series of tetraalkylammonium salts (NR_4X; where X = N_3 and F) as well as pyridine-N-oxide was attempted by treating $[Mn^{III}(O_2)(Tp^{Ph2})(THF)]$ with an excess (100 equivalents) of NR_4X or pyridine-N-oxide at 25 ºC. In all cases, no change in the optical signatures of $[Mn^{III}(O_2)(Tp^{Ph2})(THF)]$ were observed, and ESI-MS experiments on aliquots of a solution of $[Mn^{III}(O_2)(Tp^{Ph2})(THF)]$ after addition of NR_4X provided no evidence for the formation of $[Mn^{III}(O_2)(Tp^{Ph2})(X)]^-$ complexes.

4.4.8. DFT Computations and Electronic Structure of $[Mn^{III}(O_2)(Tp^{Ph2})(THF)]$. DFT computations were performed to provide a detailed comparison of the electronic structure of $[Mn^{III}(O_2)(Tp^{Ph2})(THF)]$with that of other peroxomanganese(III) adducts. The DFT-geometry-optimized model of $[Mn^{III}(O_2)(Tp^{Ph2})(THF)]$ has metal-ligand bond lengths very similar to those observed crystallographically (Figure 4.9, top left panel). In particular, the Mn−O_{peroxo} distances are within 0.03 Å of their crystallographic values (calculated: 1.881 and 1.894 Å; XRD: 1.859(2) and 1.865(2) Å). The calculated Mn−N distances are all predicted to be slightly larger than their crystallographic counterparts but all are within 0.07 Å of the experimental values. The Mn−O(THF) bond length shows a difference of in 0.04 Å between experimental and computed values. Overall, all calculated metric parameters are in quite acceptable agreement with the XRD structure of $[Mn^{III}(O_2)(Tp^{Ph2})(THF)]$. Coupled-perturbed (CP) DFT calculations afforded the *D*-tensor orientation for $[Mn^{III}(O_2)(Tp^{Ph2})(THF)]$, (Figure 4.9, top left panel). The elongated N(1)–Mn–O(3) axis (see Figure 4.3 for atom numbering scheme) defines the *z*-axis of the *D*-

tensor, and the *y*-axis bisects the O–O bond vector. The CP-DFT calculated ZFS parameters were D = -1.37 cm^{-1} and E/D = 0.06. Although the CP-DFT method slightly underestimates the magnitude of D relative to the experimental value of -2.0 cm^{-1}, the relative magnitude agrees well with experimental value of D observed for other Mn^{III}-O_2 adducts[23] and is smaller than D values of other non-peroxo Mn^{III} species (-4 to -5 cm^{-1}).[64,65] E/D is in excellent agreement with experiment (0.05 - 0.08). The CP-DFT computations also reveal that the dominant contribution to D is through spin-orbit coupling (D_{SOC}), although the spin-spin coupling contribution is certainly non-negligible (D_{SS} = -0.32 cm^{-1}). Additionally, D_{SOC} was also calculated using the state-averaged CASSCF/NEVPT2 method. In this case D is overestimated (D_{SOC} = -2.91 cm^{-1}) and the system is predicted to be too rhombic (E/D = 0.28). The CASSCF/NEVPT2 method calculated a 29% contribution to D_{SOC} in the same sign (-) from components of the lowest-lying $^3T_1$ state (from parent O_h symmetry) at 18 400, 19 200, and 20 400 cm^{-1}. Similarly, 30% total contribution to D_{SOC} comes from the lowest-lying quintet states at 25 700 and 29 500 cm^{-1}. Additionally, a ^3A state at 30 500 cm^{-1} contributed 27% to D as well as 99% to E. Contributions from individual excited states are listed in Table A4.15.

Before discussing spectral assignments for [$Mn^{III}(O_2)(Tp^{Ph2})(THF)$], we describe the bonding in this complex, focusing on the frontier MOs. In the D-tensor orientation, both the spin-up and spin-down Mn^{III} $3d_{xy}$-based MOs (218α and 230β) are unoccupied and involved in Mn^{III}-O_2 σ-antibonding interactions (Figure 4.9, top right panel). The Mn^{III}-O_2 π-antibonding interaction is distributed over the Mn^{III} $3d_{x^2-y^2}$- (195α, 197α, 200α, 201α, and 219β) and $3d_{yz}$- (199α, and 225β) based MOs. For the $3d_{x^2-y^2}$- and $3d_{yz}$-based MOs, only the α-spin MOs are occupied. The strong σ-covalency of the Mn^{III}-O_2 unit is exemplified by the 34% Mn 3*d* and 52% O_2 *p* character in the α-spin Mn $3d_{xy}$ MO (218α), which is essentially identical to that calculated for other six-coordinate Mn^{III}-O_2 complexes using the same level of theory.[16] The Mn $3d_{z^2}$-based

MO of [$Mn^{III}(O_2)(Tp^{Ph2})$(THF)] largely reflects σ-interactions between the Mn–N(Tp) and Mn–O(THF) groups. The α-spin Mn $3d_z^2$ MO carries 21% Mn 3*d*, 23% N(Tp^{Ph2}) 2*p*, 2% O(THF) 2*p*, and 3% O_{peroxo} 2*p* character.

To develop detailed band assignments of the electronic transitions observed in the experimental absorption and MCD spectra (Figure 4.5, Table 4.5), electronic transition energies and intensities of [$Mn^{III}(O_2)(Tp^{Ph2})$(THF)] were calculated with the TD-DFT method. Overall, the TD-DFT calculated absorption spectrum for [$Mn^{III}(O_2)(Tp^{Ph2})$(THF)] shows good, qualitative agreement with the experimental absorption spectrum albeit with a consistent overestimation of transition energies. In the experimental absorption spectrum of [$Mn^{III}(O_2)(Tp^{Ph2})$(THF)], three absorption envelopes are observed (regions A, B, and C; see Figure 4.10). Region A, which extends from 18 000 to 25 000 cm^{-1} in the experimental absorption spectrum contains

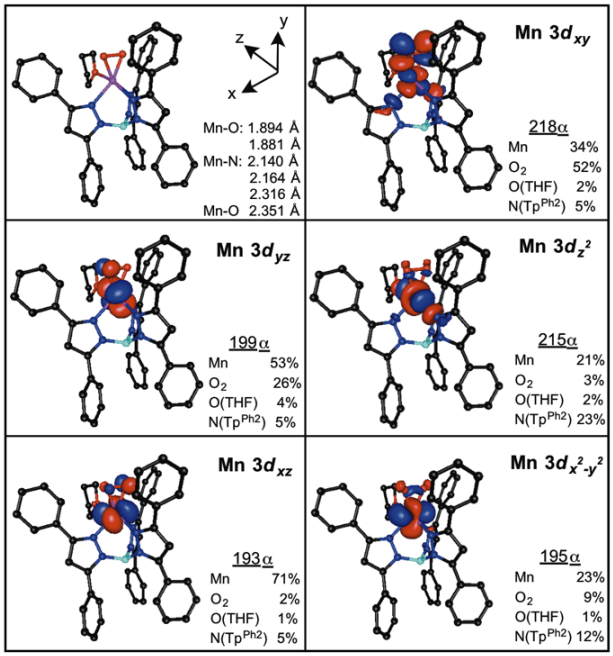

Figure 4.9. DFT-optimized structure of [$Mn^{III}(O_2)(Tp^{Ph2})$(THF)], with metal-ligand bond lengths and the *D*-tensor coordinate system from CP-DFT computations (top left panel), and surface contour plots of quasi-restricted Mn 3*d*-based orbitals (QROs). The sums of Mn 3*d* and ligand 2*p* contributions to the spin-up Kohn-Sham orbitals are listed next to the plots of the corresponding QROs.

contributions from bands 1 – 5. In the TD-DFT-calculated spectrum, region A contains contributions from the lowest-energy spin-allowed Mn^{III} *d-d* transition (state 2: $d_z^2 \rightarrow d_{xy}$; see Tables 5 and S12) at 20 500 cm^{-1} as well as a set of three peroxo-to-manganese(III) CT transitions from 23 000 to 25 500 cm^{-1} (states 3, 4, and 5). The calculated energy for the $d_z^2 \rightarrow d_{xy}$ transition is in excellent agreement with the experimental energy of band 1 (Table 4.5). Compared to other previously characterized peroxomanganese(III) species, the energy of the $d_z^2 \rightarrow d_{xy}$ transition is significantly shifted to higher energy. The peroxo-to-manganese(III) CT transitions in region A originate in the peroxo p* orbitals that are perpendicular, or out-of-plane, with respect to the Mn^{III}-O_2 unit (p_{op}*) and terminate in the spin-down Mn^{III} 3*d*-based MOs. However, these transitions are highly mixed, and this could account for the erroneously high TD-DFT-computed absorption intensity in this region. Nonetheless, these computations lend credence to the assignment of band 2 as a peroxo-to-manganese(III) CT transition.

Region B of the TD-DFT- computed absorption spectrum extends from 25 000 to 31 000 cm^{-1}. This region contains contributions from the three remaining spin-allowed Mn^{III} *d-d* transitions ($d_{yz} \rightarrow d_{xy}$, state 8; $d_{x^2-y^2} \rightarrow d_{xy}$, state 12; and $d_{xz} \rightarrow d_{xy}$, state 17), as well as additional peroxo-to-manganese(III) charge transfer transitions (Tables 5 and S12).[66] Compared to experiment, transitions in region B are calculated at too high an energy by ~5 000 cm^{-1}. Nonetheless, these calculations are generally supportive of the spectral assignments discussed previously. Additionally, state 17 is composed of the $d_{xz} \rightarrow d_{xy}$ transition, which corresponds to a

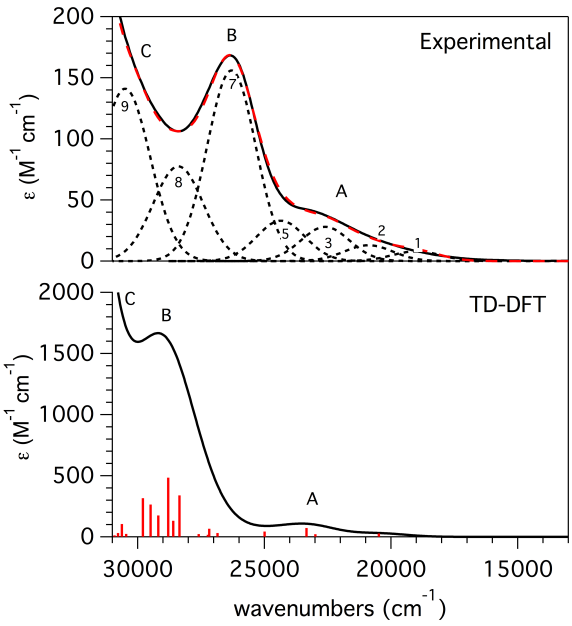

Figure 4.10. Experimental (top) and TD-DFT-calculated (bottom) absorption spectra of $[Mn^{III}(O_2)(Tp^{Ph2})(THF)]$.

z-polarized $^4B_1 \rightarrow {}^4A_2$ transition using the *D*-tensor coordinate system (Figure 4.6) and assuming idealized C_{2v} symmetry, with the *y*-axis as the pseudo-C_2 axis. This corroborates the assignment of band 7 as a $d_{xz} \rightarrow d_{xy}$ transition, as band 7 was characterized by VTVH MCD to be 98% *z*-polarized. Region C of the TD-DFT absorption spectrum is composed of peroxo-to-manganese(III) CT transitions with contributions from states 14 (29 500 cm^{-1}) and 15 (29 800 cm^{-1}). TD-DFT calculations incorrectly predict the ordering of these CT states with respect to the highest-energy *d-d* transition (state 17, 30 600 cm^{-1}), however, this is not unusual for TD-DFT calculations.

Additionally, the excited state energies of $[Mn^{III}(O_2)(Tp^{Ph2})(THF)]$ were calculated by the CASSCF/NEVPT2 method to exclude the possibility of TD-DFT-calculated charge-transfer states with erroneously high intensity and low energy (so-called "intruder states"), that can occur as artifacts. The CASSCF/NEVPT2 method also has the advantage that spin-forbidden excited

states can be treated. The *d-d* excited states from the CASSCF/NEVPT2 calculations agree well with the TD-DFT energies, confirming the presence of few intruder states in the latter spectrum. Importantly, two triplet excited states are predicted with energies (26 800 and 30 500 cm^{-1}) that interleave the quartet excited state energies (Table 4.5), supporting our assignment of bands 4 and 6 as spin-forbidden transitions. It should be noted that the TD-DFT method predicts a significant contribution to region B from state 10 in the TD-DFT calculations (Table A4.13); however, state 10 is predicted as a Ph(Tp^{2Ph}) $\rightharpoonup$ Mn intruder state. This transition is an anticipated artifact of the TD-DFT calculation and is not expected to contribute to the experimental absorption spectrum.

4.4.9. DFT Computations and Electronic Structure of the Blue and Brown Isomers of [$Mn^{III}(O_2)(Tp^{iPr2})(pz^{iPr2}H)$]. Due to the reasonable success in reproducing the spectroscopic properties of [$Mn^{III}(O_2)(Tp^{Ph2})$(THF)] with these computational methods, a similar approach was utilized for the isomers of [$Mn^{III}(O_2)(Tp^{iPr2})(pz^{iPr2}H)$] in an attempt to explain the thermochromic shift in the electronic absorption spectrum. The 22 nm (670 cm^{-1}) red shift in the electronic absorption spectrum upon cooling from 253 to 193 K was associated with the formation of a hydrogen bond between the pyrazole ligand and one O atom of the peroxo unit in the low-temperature isomer. TD-DFT calculations were performed on models of [$Mn^{III}(O_2)(Tp^{iPr2})(pz^{iPr2}H)$] built using the XRD coordinates of the isomers at 253 and 193 K (brown and blue isomers, respectively) in order to elucidate the nature of the changes in the absorption spectrum by determining the electronic structure. TD-DFT calculations were performed with both the unmodified XRD coordinates, as well as structures where the positions of the hydrogen atoms were optimized. Primarily, the optimization of the hydrogen atoms

resulted in a shorter hydrogen bond, with a 0.139 Å decrease between the H-donor atom and the

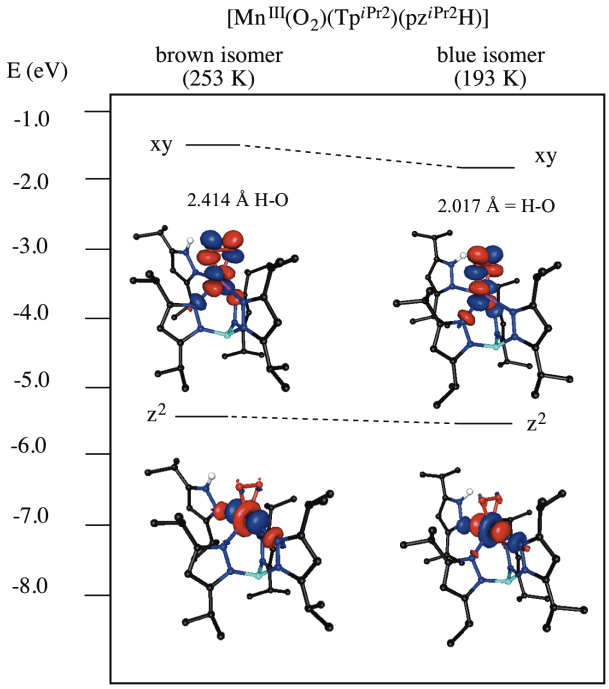

Figure 4.11. TD-DFT-calculated donor and acceptor orbitals for the lowest energy *d-d* transition in the brown and blue isomers of $[Mn^{III}(O_2)(Tp^{iPr2})(pz^{iPr2}H)]$. For clarity, all hydrogens except the hydrogen- bonding $H_{pyrazole}$ have been omitted.

Table 4.7. Selected Bond Lengths (Å) for $[Mn^{III}(O_2)(Tp^{iPr2})(pz^{iPr2}H)]$ for fully-optimized coordinates, unmodified XRD coordinates, and hydrogen-optimized coordinates.

Full Optimization	H-O[a]	N-H	O-O	Mn-O	Mn-O
blue	1.891	1.039	1.450	1.910	1.858
brown	1.890	1.039	1.450	1.858	1.910
XRD Coordinates[22]	H-O	N-H	O-O	Mn-O	Mn-O
blue	2.156	0.975	1.434	1.880	1.844
brown	2.464	0.977	1.429	1.850	1.851
Hydrogen Optimized	H-O	N-H	O-O	Mn-O	Mn-O
blue	2.017	1.033	1.434	1.880	1.844
brown	2.414	1.026	1.429	1.850	1.851

[a]H-O bond length listed is the shortest of the H-O bond lengths calculated.

O(peroxo) acceptor in the blue isomer and a corresponding decrease of 0.049 Å in the brown isomer (Table 4.7). TD-DFT calculations with both the hydrogen-optimized and XRD structures

reproduce the experimental absorption spectra well. TD-DFT calculations performed with the XRD coordinates predict a transition at 18 500 cm^{-1} for the brown isomer and a transition at 17 300 cm^{-1} for the blue isomer, in good agreement with the experimental values (17 820 and 17 150 cm^{-1}). The transition energies obtained through TD-DFT calculations with the hydrogen-optimized structures were at slightly higher energies of 18 900 and 17 500 cm^{-1} for the blue and brown isomers, respectively. Importantly, both the XRD and the hydrogen-optimized structures reproduce the red-shift that occurs as the complex is cooled from 253 to 193 K. With all TD-DFT calculations, this red-shifted transition involves a one- electron excitation between the α-spin Mn $3d_{z^2}$ MO (190α), which is highly mixed, and the unoccupied α-spin Mn $3d_{xy}$ MO 192α). The acceptor orbital exhibits strong σ-covalency of the Mn^{III}-O_2 unit, with 42 - 45% Mn 3*d* and 44 – 47% O_2 2*p* character (ESI, Tables S16 - S19), which is similar to other previously characterized Mn^{III}-O_2 complexes. The band shift in the experimental absorption spectrum of the blue isomer of [$Mn^{III}(O_2)(Tp^{iPr2})(pz^{iPr2}H)$] is due to the stabilization of the Mn $3d_{xy}$ acceptor MO, which carries significant peroxo ligand character, with the formation of the hydrogen bond (Figure 4.11). The hydrogen-optimized structure of the blue isomer exhibits the shortest hydrogen bond at 2.017 Å which is accompanied by the greatest stabilization of 0.2294 eV of the Mn $3d_{xy}$ acceptor MO (192 α) relative to the corresponding orbital of the brown isomer (Table 4.7, Figure 4.11). TD-DFT calculations with the unmodified XRD structures display a similar trend with the blue isomer showing a hydrogen bond of 2.156 Å and a stabilization of the acceptor MO in the blue isomer of 0.1679 eV relative to the brown isomer. Notably, when both the brown and blue isomers were fully optimized (*i.e.* the positions of all atoms were energy-minimized), the computations yielded isomeric structures with a hydrogen bond distances of 1.891 and 1.890 Å and equivalent Mn—O distances of 1.858 and 1.910 Å (Table 4.7).

4.4 Discussion

Although there have been a variety of synthetic peroxomanganese(III) species supported by anionic ligands,[14,22,25] there is still a lack of detailed bonding descriptions of such complexes. In particular, peroxomanganese(III) species supported by monoanionic and facially coordinating Tp ligands exhibit unusual electronic absorption spectra that have been unexplained by studies to date. In order to investigate the electronic structure of one of these species, a monomeric Mn^{III}-O_2 adduct supported by the Tp^{Ph2} ligand was synthesized and characterized by XRD, EPR, and MCD spectroscopies as well as TD-DFT and CASSCF/NEVPT2 computations. The high thermal stability of $[Mn^{III}(O_2)(Tp^{Ph2})(THF)]$, presumably due in part to the steric bulk of the phenyl groups of the Tp^{Ph2} ligand shielding the peroxo moiety, facilitated the determination of the crystal structure. The XRD structure of $[Mn^{III}(O_2)(Tp^{Ph2})(THF)]$ shows metric parameters in line with those collected for other peroxomanganese(III) species.[23] The Mn^{III} oxidation state was confirmed by EPR spectroscopy. Previously characterized peroxomanganese(III) species exhibit 6-line signals at ~80 mT with hyperfine splitting of 6-7 mT.[23] As $[Mn^{III}(O_2)(Tp^{Ph2})(THF)]$ displays a feature position of 84.6 mT and a hyperfine splitting of 5.1 mT. This hyperfine splitting is somewhat smaller than those of other non-peroxo manganese(III) species[67,68] and previously studied peroxomanganese(III) adducts[23], possibly suggesting a higher degree of covalency in the $[Mn^{III}(O_2)(Tp^{Ph2})(THF)]$ complex. Temperature dependence studies and simulation of the parallel-mode EPR feature yielded D = -2.0(5) cm^{-1} and E/D = 0.07(1), which are very similar to the ZFS parameters for other Mn^{III}-O_2 species which lie between -1.5 and -3.0 cm^{-1} for D and 0.05 to 0.30 for E/D.[23] In addition to supporting the assignment of this intermediate as a Mn^{III} species, the determination of these zero field splitting parameters for $[Mn^{III}(O_2)(Tp^{Ph2})(THF)]$ supply insight into the ground state properties of Mn^{III}-O_2 species.

To elucidate the origin of the blue-shift observed in the absorption spectrum of

$[Mn^{III}(O_2)(Tp^{Ph2})(THF)]$ compared to other members of the Mn^{III}-O_2 class of intermediates, we turned to MCD spectroscopy and TD-DFT calculations. Although we have previously attributed slight variations in the lowest-energy ligand-field transitions of Mn^{III}-O_2 adducts to differences in the the Mn—O_{peroxo} bond length,[16,18,32] this correlation fails here, as the Mn—O_{peroxo} distances of $[Mn^{III}(O_2)(Tp^{Ph2})(THF)]$ are within the range of Mn—O_{peroxo} bond lengths observed in the prior series. Instead, the high energy of band 1 in the MCD and electronic absorption spectra of $[Mn^{III}(O_2)(Tp^{Ph2})(THF)]$ (Figure 4.5) results from perturbations perpendicular to the Mn^{III}-O_2 unit. Specifically, elongation in the N(1)—Mn—O(3) bonding axis (Figure 4.9, top left panel), which is a result of weak σ-donation from the THF ligand, stabilizes the $3d_{z^2}$ MO and blue-shifts the $3d_{xy} \rightarrow 3d_{z^2}$ transition. This is reflected in the experimentally determined ligand-field excited state energies of $[Mn^{III}(O_2)(Tp^{Ph2})(THF)]$ compared to other Mn^{III}-O_2 species (Figure 4.12). The $3d_{xy}$ - $3d_{z^2}$ energy gap, $\Delta(3d_{xy} - 3d_{z^2})$, in $[Mn^{III}(O_2)(Tp^{Ph2})(THF)]$ is 4.5 eV, whereas $\Delta(3d_{xy} - 3d_{z^2})$ is 4.1 and 3.8 eV for the Mn^{III}-O_2 complexes $[Mn^{III}(O_2)(L^7py_2{}^H)]^+$ and $[Mn^{III}(O_2)(L^7py_2{}^{6\text{-}Me})]^+$, respectively ($L^7py_2{}^H$ and $L^7py_2{}^{Me}$ are neutral N_4 ligands).

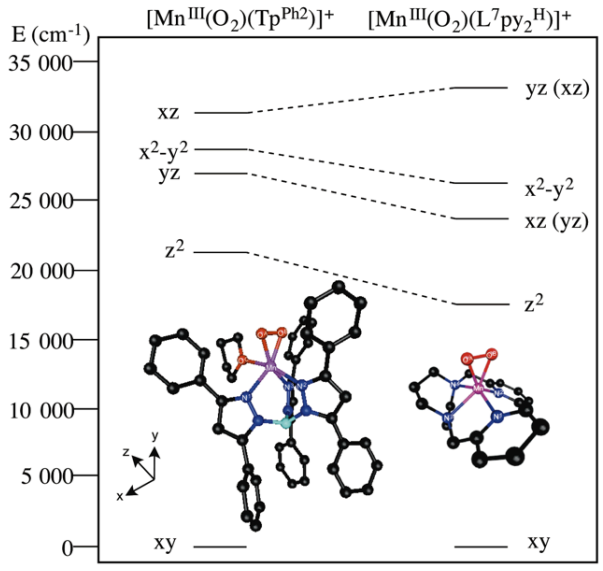

Figure 4.12. TD-DFT calculated *d-d* transitions in $[Mn^{III}(O_2)(Tp^{Ph2})(THF)]$ and $[Mn^{III}(O_2)(L^7py_2{}^H)]^+$. Following the hole formalism for these d^4 systems, the excited state is designated according to the *d* orbital hole. In *D*-tensor orientation of the $[Mn^{III}(O_2)(L^7py_2{}^H)]^+$

model, the *x* and *y* axes are swapped relative to [$Mn^{III}(O_2)(Tp^{Ph2})$(THF)]; the orbital labels corresponding to the coordinate system of [$Mn^{III}(O_2)(Tp^{Ph2})$(THF)] are shown in parentheses.

In our computational investigations of [$Mn^{III}(O_2)(Tp^{Ph2})$(THF)], two methods, TD-DFT and CASSCF/NEVPT2, were used to calculate electronic transitions energies. The more commonly used TD-DFT method is known to potentially introduce intruder states that do not contribute to the experimental spectrum. In general, the CASSCF/NEVPT2 method is accepted as a more reliable method for treating the excited states of transition metal complexes. In this present case, both methods overestimated the electronic transition energies compared to the experimentally observed bands, with the TD-DFT-calculated energies being closer to the experimental values. However, below 32 000 cm^{-1}, the absorption spectra of [$Mn^{III}(O_2)(Tp^{Ph2})$(THF)] calculated by both methods are comparable in their replication of the experimental spectrum with the exception of one intruder state in the TD-DFT calculation, which had a negligible effect on the primary features of the computed absorption spectrum. Here, TD-DFT calculations were sufficient to predict the electronic absorption spectrum, particularly the *d-d* transitions, and the use of the more input-rigorous CASSCF/NEVPT2 method may not be necessary in other similar cases. TD-DFT calculations were extended to investigate the brown and blue isomers of [$Mn^{III}(O_2)(Tp^{iPr2})(pz^{iPr2}H)$]. As previously reported, when the [$Mn^{III}(O_2)(Tp^{iPr2})(pz^{iPr2}H)$] species is cooled from 253 to 193 K, a hydrogen bond between the pyrazole ligand and one O atom of the peroxo unit is formed, and the absorption spectrum exhibits a 670 cm^{-1} red-shift. TD-DFT calculations permit the assignment of the red-shifted electronic transition to a Mn $d_{z^2} \rightarrow d_{xy}$ one-electron excitation. The Mn $3d_{xy}$ acceptor MO of both isomers contains a significant amount of peroxo ligand character. The hydrogen bonding interaction with the peroxo moiety, and the concomitant Mn-O bond elongation, stabilizes this MO in the blue isomer by 0.2294 eV relative to the brown isomer (Figure 4.11).

The stabilization of the Mn-O_2 σ-antibonding $3d_{xy}$ MO through a hydrogen-bonding

interaction is of potential relevance to two recent reports describing activation of Mn^{III}-O_2 adducts through chemical and electrochemical reduction. Using a Mn^{III}-O_2 adduct supported by a trianionic tripodal ligand with a hydrogen-bonding cavity around the peroxo, Borovik and co-workers showed that the two-electron reduction of a Mn^{III}-O_2 adduct using diphenylhydrazine led to O-O bond cleavage and the eventual formation of a hybrid oxo-/hydroxo-manganese(III) adduct.[69,26] A dihydroxomanganese(III) species was postulated as an intermediate in this process. These elementary steps feature in the catalytic reduction of O_2 to H_2O by the corresponding Mn^{II} complex. In a separate study, Anxolabéhère-Mallart, Policar, and Robert reported that the two-electron electrochemical reduction of a Mn^{III}-O_2 adduct supported by a phenolate-containing N_4O^- ligand (the protonated, phenol form of the ligand is *N*-)2-hydroxybenzyl)-*N*,*N*'-bis[2-(*N*-methylimidazolyl)methyl]ethane-1,2-diamine) causes O-O bond cleavage when the reduction is carried out in the presence of water.[70] Detailed electrochemical studies revealed that this process is kinetically controlled by the initial electron transfer that is also associated with a large reorganization energy. In both systems, hydrogen bonding to the peroxo ligand, either intramolecular with the supporting ligand or intermolecular with added water, is possible. On the basis of our computational work described here, hydrogen-bonding to the peroxo of a Mn^{III}-O_2 unit stabilizes the Mn $3d_{xy}$ orbital (Figure 4.11), which is the spin-α LUMO, potentially facilitating reduction of the Mn^{III}-O_2 unit. Because this MO contains a significant percentage of peroxo π* character, the addition of an electron to this MO would weaken the O-O bond, priming it for cleavage.

4.5 Conclusions

The conversion of $[Mn^{II}(Tp^{Ph2})(DMF)_3](OTf)$ to $[Mn^{III}(O_2)(Tp^{Ph2})(THF)]$ by KO_2 yielded a peroxomanganese(III) species exhibiting high thermal stability with unique spectral features in

both the electronic absorption and MCD spectra. The nature of these spectral deviations from previously characterized peroxomanganese(III) species arises from an axial elongation along the molecular z-axis, reducing the metal-ligand covalency, stabilizing the σ-antibonding Mn d_z^2 MO, and affording higher energy *d-d* transitions. Comparably, in the peroxomanganese(III) species supported by the Tp^{iPr2} ligand, a hydrogen bonding interaction stabilizes the acceptor MO, causing the thermochromic shift observed as the complex is cooled from 293 to 193 K. These perturbations in the electronic transitions of these peroxomanganese(III) species represent an example of a deviation in symmetry and metal-ligand bonding in Mn^{III}-(O_2) intermediates and could be applied in the identification of similar changes in the first coordination sphere of short-lived intermediates in enzymatic and model systems.

4.6 References

(1) Grove, L. E.; Brunold, T. C. *Comments on Inorganic Chemistry* **2008**, *29*, 134.
(2) Miller, A.-F. *Curr. Opin. Chem. Biol.* **2004**, *8*, 162.
(3) Jackson, T. A.; Karapetian, A.; Miller, A.-F.; Brunold, T. C. *Biochemistry* **2005**, *44*, 1504.
(4) Bull, C.; Niederhoffer, E. C.; Yoshida, T.; Fee, J. A. *Journal of the American Chemical Society* **1991**, *113*, 4069.
(5) Hearn, A. S.; Stroupe, M. E.; Cabelli, D. E.; Lepock, J. R.; Tainer, J. A.; Nick, H. S.; Silverman, D. N. *Biochemistry* **2001**, *40*, 12051.
(6) Hearn, A. S.; Tu, C. K.; Nick, H. S.; Silverman, D. N. *Journal of Biological Chemistry* **1999**, *274*, 24457.
(7) Gunderson, W. A.; Zatsman, A. I.; Emerson, J. P.; Farquhar, E. R.; Que, L.; Lipscomb, J. D.; Hendrich, M. P. *J. Am. Chem. Soc.* **2008**, *130*, 14465.
(8) Vetting, M. W.; Wackett, L. P.; Que, L., Jr.; Lipscomb, J. D.; Ohlendorf, D. H. *Journal of Bacteriology* **2004**, *186*, 1945.
(9) Opaleye, O.; Rose, R.-S.; Whittaker, M. M.; Woo, E.-J.; Whittaker, J. W.; Pickersgill, R. W. *Journal of Biological Chemistry* **2006**, *281*, 6428.
(10) Borowski, T.; Bassan, A.; Richards, N. G. J.; Siegbahn, P. E. M. *Journal of Chemical Theory and Computation* **2005**, *1*, 686.
(11) Reinhardt, L. A.; Svedruzic, D.; Chang, C. H.; Cleland, W. W.; Richards, N. G. J. *Journal of the American Chemical Society* **2003**, *125*, 1244.
(12) Svedružic, D.; Jónsoon, S.; Toyota, C. G.; Reinhardt, L. A.; Ricagno, S.; Lindqvist, Y.; Richards, N. G. J. *Archives of Biochemistry and Biophysics* **2005**, *433*, 176.

(13) Tanner, A.; Bowater, L.; Fairhurst, S. A.; Bornemann, S. *Journal of Biological Chemistry* **2001**, *276*, 43627.
(14) Annaraj, J.; Cho, J.; Lee, Y.-M.; Kim, S. Y.; Latifi, R.; de Visser, S. P.; Nam, W. *Angew. Chem. Int. Ed.* **2009**, *48*, 4150.
(15) Cho, J.; Sarangi, R.; Nam, W. *Acc. Chem. Res.* **2012**, *45*, 1321.
(16) Geiger, R. A.; Chattopadhyay, S.; Day, V. W.; Jackson, T. A. *Journal of the American Chemical Society* **2010**, *132*, 2821.
(17) Geiger, R. A.; Chattopadhyay, S.; Day, V. W.; Jackson, T. A. *Dalton Trans.* **2011**, *40*.
(18) Geiger, R. A.; Leto, D. F.; Chattopadhyay, S.; Dorlet, P.; Anxolabéhère-Mallart, E.; Jackson, T. A. *Inorganic Chemistry* **2011**, *50*, 10190.
(19) Groni, S.; Blain, G.; Guillot, R.; Policar, C.; Anxolabéhère-Mallart, E. *Inorganic Chemistry* **2007**, *46*, 1951.
(20) Groni, S.; Dorlet, P.; Blain, G.; Bourcier, S.; Guillot, R.; Anxolabéhère-Mallart, E. *Inorganic Chemistry* **2008**, *47*, 3166.
(21) Kang, H.; Cho, J.; Cho, K.-B.; Nomura, T.; Ogura, T.; Nam, W. *Chem. Eur* **2013**, *19*.
(22) Kitajima, N.; Komatsuzaki, H.; Hikichi, S.; Osawa, M.; Moro-oka, Y. *J. Am. Chem. Soc.* **1994**, *116*, 11596.
(23) Leto, D. F.; Jackson, T. A. *J. Biol. Inorg. Chem.* **2014**, *19*, 1.
(24) Seo, M. S.; Kim, J. Y.; Annaraj, J.; Kim, Y.; Lee, Y.-M.; Kim, S.-J.; Kim, J.; Nam, W. *Angewandte Chemie International Edition* **2007**, *46*, 377.
(25) Shook, R. L.; Gunderson, W. A.; Greaves, J.; Ziller, J. W.; Hendrich, M. P.; Borovik, A. S. *Journal of the American Chemical Society* **2008**, *130*, 8888.
(26) Shook, R. L.; Peterson, S. M.; Greaves, J.; Moore, C.; Rheingold, A. L.; Borovik, A. S. *J. Am. Chem. Soc.* **2011**, *133*, 5810.
(27) Singh, U. P.; Sharma, A. K.; Hikichi, S.; Komatsuzaki, H.; Moro-oka, Y.; Akita, M. *Inorganica Chimica Acta* **2006**, *359*, 4407.
(28) M.K., C.; Kovacs, J. A. *J. Am. Chem. Soc.* **2011**, *133*, 12470.
(29) Coggins, M. K.; V., M.-D.; S., D.; J.A., K. *J. Am. Chem. Soc.* **2013**, *135*.
(30) VanAtta, R. B.; Strouse, C. E.; Hanson, L. K.; Valentine, J. S. *Journal of the American Chemical Society* **1987**, *109*, 1425.
(31) For Mn^{III}-O_2 adducts, the τ parameter is used exclusively to compare angles between axial donors perpendicular to the Mn^{III}-O_2 unit with angles between equatorial donors parallel to the Mn^{III}-O_2 unit (Scheme 4.1). This differs somewhat from the conventional τ parameter used for authentic five-coordinate complexes. Most notably, τ values of greater than 1 are possible under the Mn^{III}-O_2 formalism.
(32) Geiger, R. A.; Wijeratne, G.; Day, V. W.; Jackson, T. A. *Eur. J. Inorg. Chem.* **2012**, 1598.
(33) Pecoraro, V. L.; Baldwin, M. J.; Gelasco, A. *Chem. Rev.* **1994**, *94*, 807.
(34) Vaska, L. *Acc. Chem. Res.* **1975**, *9*, 175.
(35) Sheldrick, G. M. Bruker-AXS 5465 E. Cheryl Parkway, Madison, WI 53711-5373 USA, 2000.
(36) Stoll, S.; Schweiger, A. *J. Magn. Reson.* **2006**, *178*, 42.
(37) Neese, F.; Solomon, E. I. *Inorganic Chemistry* **1999**, *38*, 1847.
(38) George, G. N. In *EXAFSPAK* Stanford Synchrotron Radiation Laboratory; Stanford, CA, 1990.
(39) Rehr, J. J.; Mustre de Leon, J.; Zabinsky, S. I.; Albers, R. C. *Journal of the American Chemical Society* **1991**, *113*, 5135.

(40) Neese, F., The ORCA program system, *Wiley Interdiscip. Rev.: Comput. Mol. Sci.* 2012, p 73.
(41) Becke, A. D. *J. Chem. Phys.* **1986**, *84*, 4524.
(42) Perdew, J. P. *Phys. Rev. B* **1986**, *33*, 8822.
(43) Schäfer, A.; Horn, H.; Ahlrichs, R. *J. Chem. Phys.* **1992**, *97*, 2571.
(44) Schäfer, A.; Huber, C.; Ahlrichs, R. *J. Chem. Phys.* **1994**, *100*, 5829.
(45) Neese, F. *Journal of Computational Chemistry* **2003**, *24*, 1740.
(46) Sinnecker, S.; Rajendran, A.; Klamt, A.; Diedenhofen, M.; Neese, F. *Journal of Physical Chemistry A* **2006**, *110*, 2235.
(47) Bauernschmitt, R.; Ahlrichs, R. *Chem. Phys. Lett.* **1996**, *256*, 454.
(48) Casida, E. M.; Jamorski, C.; Casida, K. C.; Salahub, D. R. *J. Chem. Phys.* **1998**, *108*, 4439.
(49) Stratman, R. E.; Scuseria, G. E.; Frisch, M. J. *J. Chem. Phys.* **1998**, *109*, 8218.
(50) Hirata, S.; Head-Gordon, M. *Chem. Phys. Lett.* **1999**, *302*, 375.
(51) Hirata, S.; Head-Gordon, M. *Chem. Phys. Lett.* **1999**, *314*, 291.
(52) Becke, A. D. *J. Chem. Phys.* **1993**, *98*, 1372.
(53) Becke, A. D. *J. Chem. Phys.* **1993**, *98*, 5648.
(54) Lee, C.; Yang, W.; Parr, R. G. *Phys. Rev. B* **1988**, *37*, 785.
(55) Angeli, C.; Cimiraglia, R.; Evangelisti, S.; Leininger, T.; Malrieu, J. P. *J. Chem. Phys.* **2001**, *114*, 10252.
(56) Hammes, B. S.; Carrano, M. W.; Carrano, C. J. *J. Chem. Soc., Dalton Trans.* **2001**, 1448.
(57) Singh, U. P.; Sharma, A. K.; Tyaji, P.; Upreti, S.; Singh, R. K. *Polyhedron* **2006**, *25*, 3628.
(58) Schultz, D. A.; Vostrikova, K. E.; Bodnar, S. H.; Koo, H.-J.; Whangbo, M.-H.; Kirk, M. L.; Depperman, E. C.; Kampf, J. W. *J. Am. Chem. Soc.* **2003**, *125*, 1607.
(59) Lever, A. B. P. *Inorganic Electronic Spectroscopy*; 2nd ed.; Elsevier: Amsterdam; New York, 1984.
(60) Band 9 has exceptionally low MCD intensity and could also be assigned as a Tp^{Ph2} to Manganese(III) CT transition.
(61) Oganesyan, V. S.; George, S. J.; Cheesman, M. R.; Thomson, A. J. *J. Chem. Phys.* **1999**, *110*, 762.
(62) Leto, D. F.; Chattopadhyay, S.; Day, V. W.; Jackson, T. A. *Dalton Trans.* **2013**, *42*, 13014.
(63) Leto, D. F.; Jackson, T. A. *Inorg. Chem.* **2014**, *53*, 6179.
(64) Neese, F. *J. Am. Chem. Soc.* **2006**, *128*, 10213.
(65) Krzystek, J.; Ozarowski, A.; Telser, J. *Coordination Chemistry Reviews* **2006**, *250*, 2308.
(66) These transitions are all highly mixed, and the natures of the excited states were identified through visualization of electron density difference maps (EDDMs.
(67) Krivokapic, I.; Noble, C.; Klitgaard, S.; Tregenna-Piggott, P.; Weihe, H.; Barra, A.-L. *Angew. Chem. Int. Ed.* **2005**, *44*, 3613.
(68) Krzystek, J.; Yeagle, G. J.; Park, J.-H.; Britt, R. D.; Meisel, M. W.; Brunel, L.-C.; Joshua, T. *Inorg. Chem.* **2003**, *42*, 4610.
(69) The metric parameters in the crystal structure of this complex indicate that a proton is nearly equally shared between the supporting ligand and a coordinated oxygen atom.
(70) Ching, H. Y. V.; Anxolabéhère-Mallart, E.; Colmer, H. E.; Costentin, C.; Dorlet, P.; Jackson, T. A.; Policar, C.; Robert, M. *Chemical Science* **2014**, *5*.

CHAPTER 5

Mechanisms of O—O Bond Cleavage in Mn^{III}-peroxo Intermediates by Electrochemical Methods

Portions of this chapter were reproduced from Ching, H.Y.V., Anxolabéhère-Mallart, E., Colmer, H.E., Costentin, C., Dorlet, P., Jackson, T.A., Policar, C., Robert, M. *Chem. Sci.*, **2014**, *5*, 2304-2310 with permission from the Royal Society of Chemistry. Electrochemical experiments were carried out by H.Y. Vincent Ching and Elodie Anxolabéhère-Mallart**.**

5.1 Introduction

O—O bond activation remains a critical step in the catalytic cycles of many enzymes such as the cytochrome P450 enzymes,[1,2] but the specific structural and electronic parameters promoting this reaction are not well defined. Specifically, the precursor step to the formation of the active oxidant Fe^{IV}-oxo species, Compound I, contains the delivery of an electron and a proton to a superoxo species, forming an Fe^{III}-hydroperoxo intermediate. With the delivery of another proton, the O—O bond is cleaved and the active oxidant, the Fe^{IV}-oxo species, is formed.[1] This O—O bond cleavage to generate the high-valent oxidant species is also observed in other enzyme systems, such as methane monooxygenase,[3] and there are examples of non-heme Fe^{III}-peroxo model complexes that decay by O—O bond cleavage.[4-8] In contrast, little is known about the O—O bond cleavage of Mn^{III}-peroxo species in Mn-containing enzymes or model complexes. In principle, the O—O bond in a Mn^{III}-peroxo complex can be broken with the delivery of two electrons.[9] However, Mn^{III}-peroxo species supported by model systems have yet to replicate the controlled delivery of electrons and protons to achieve O—O bond cleavage as the cytochrome P450 enzymes are able to do, although there have been recent advances in this regard. Strategies to control the reactivity of the Mn^{III}-peroxo species include reaction with redox-active Mn^{II} and Mn^{III} species,[10-12] the addition of protons using a Brønsted acid,[13,14] and the addition of protons and electrons through hydrogen atom addition by electrophilic substrates.[13,15,16] While there are now many reports of the formation and characterization of Mn^{III}-peroxo species,[9] there is little known about the thermodynamic parameters that control the activation of the O—O bond to generate high-valent oxidants.

To date, there is only one report of acid-assisted activation of a Mn^{III}-peroxo intermediate to a high-valent Mn^{IV} species. A Mn^{III}-peroxo species supported by a pentadentate, N_4O^-, phenolato-containing ligand was generated electrochemically by the reaction of the $[Mn^{II}(N_4O)]^+$

complex and superoxide that was generated by the reduction of molecular oxygen to superoxide at an electrode in DMF (Scheme 5.1).[13] The consumption of superoxide is evident in the CV spectra that show a loss of reversibility of the O_2/O_2^- reduction wave with titration of $[Mn^{II}(N_4O)]^+$ (Figure 5.1). Subsequent reduction of this $[Mn^{III}(O_2)(N_4O)]$ species in the presence of a weak acid resulted in the formation of high-valent products of O—O bond cleavage (Scheme 5.2). Although these products could not be isolated, this study provides unique insight into the reductive activation of Mn^{III}-peroxo species, as the electron transfer process to the Mn^{III}-peroxo, and any associated reorganizational energy, can be followed by electrochemical methods.

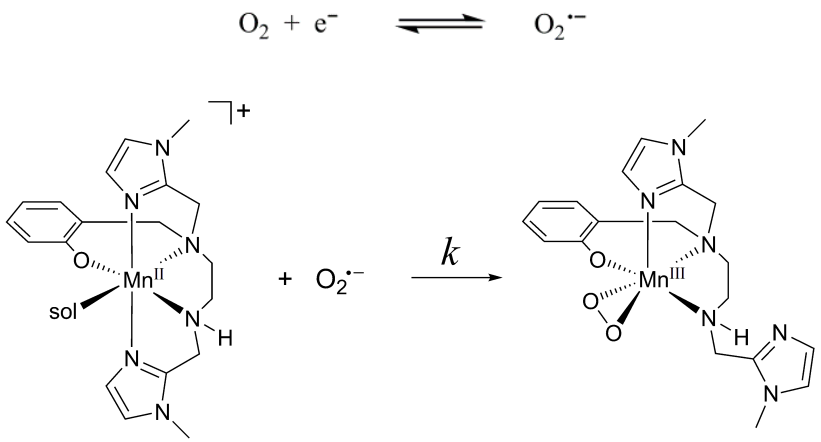

Scheme 5.1. Electrochemical reduction of O_2 to superoxide and reaction of $[Mn^{II}(N_4O)]^+$ with superoxide to form $[Mn^{III}(O_2)(N_4O)]$.

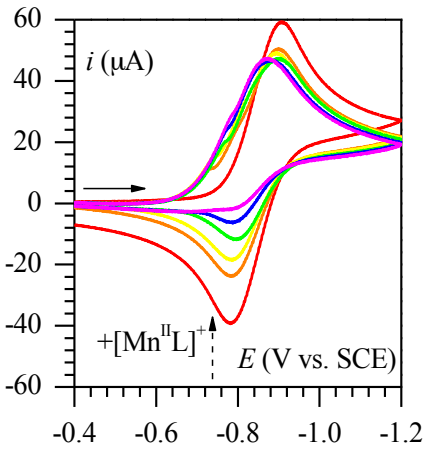

Figure 5.1. Cyclic voltammetry of O_2 (1.0 mM, air saturated) in DMF + 0.1 M Bu_4NPF_6 with increasing concentration of $[Mn^{II}(N_4O)]^+$: 0 (red), 0.4 (orange), 0.6 (yellow), 0.8 (green), 1.0 (blue), and 1.2 (magenta) mM at 0.2 V/s at a glassy carbon disk electrode at 293 K.

The generation of the Mn^{III}-peroxo species by reaction of $[Mn^{II}(N_4O)]^+$ and superoxide formed from the electrochemical reduction of O_2 provides a unique method of controlling the electron flow to the Mn center. This method provides a rare example of formation of the Mn^{III}-peroxo species from molecular oxygen as well as supply control over subsequent reduction events to generate activated products from the Mn^{III}-peroxo species. This study comprises the only example of reactivity of a Mn^{III}-peroxo intermediate controlled by the strength of the acid added to the reaction. When $[Mn^{III}(O_2)(N_4O)]^+$ was electrochemically generated in the presence of a strong acid ($HClO_4$), the behavior of the CV spectra are consistent with Mn—O cleavage and formation of H_2O_2.

In contrast, in the presence of a weak acid (H_2O), rather than Mn—O bond cleavage, O—O bond cleavage occurs upon reduction of $[Mn^{III}(O_2)(N_4O)]$. In the presence of H_2O, $[Mn^{III}(O_2)(N_4O)]$ is reduced at -1.65 V vs SCE in a two-electron reduction event (Figure 5.2, left). To provide experimental insight into the mechanism of activation of the Mn^{III}-peroxo species, analysis of the CV wave at variable scan rates was performed. The shift in potential with respect to the scan rate allowed for calculation of the transfer coefficient, α, of 0.35 that yielded a large reorganizational energy of 2.25 eV (Figure 5.2, right), suggestive of an O—O bond

cleavage process concerted with the electron transfer process.[13] Cleavage of the O—O bond by the first one-electron reduction yields generates a transient Mn^{IV}-dioxo species that readily undergoes protonation of the oxo ligands and reduction of the Mn center to form a Mn^{III}-dihydroxo species (Scheme 5.2). These events were independent of the concentration of H_2O, indicating that the rate limiting step is not protonation. Instead, modeling of the variable scan rate data shows that this process is kinetically controlled by the first electron transfer. The proposed reaction chemistry is summarized in Scheme 5.2.

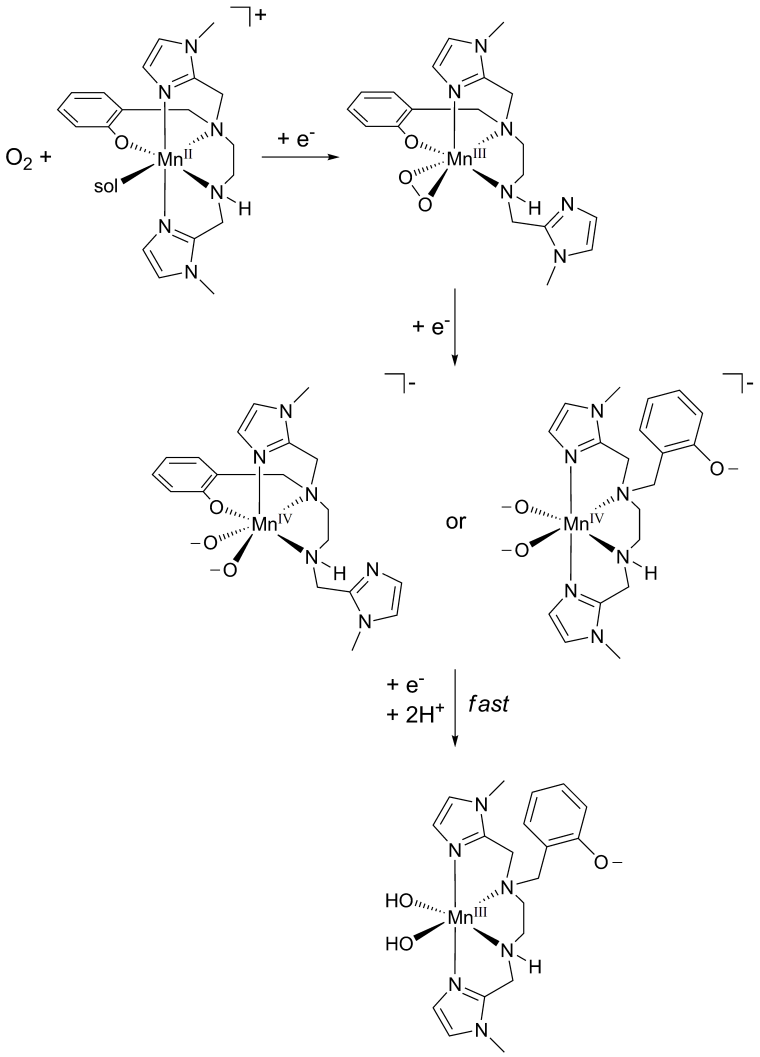

Scheme 5.2. Electrochemical reduction of O_2 in the presence of weak acid and $[Mn^{II}(N_4O)]^+$.

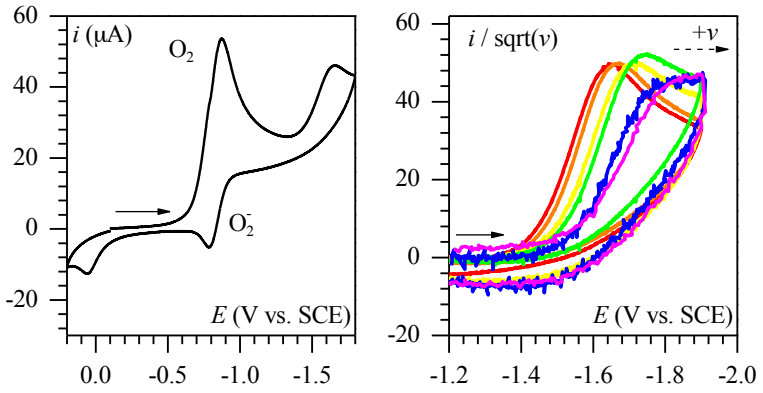

Figure 5.2. Cyclic voltammetry of O_2 (1.0 mM, saturated air) in DMF + 0.1 M Bu_4NPF_6 with $[Mn^{II}L]^+$ (1.2 mM) at 0.2 V/s at a glassy carbon disk electrode at 293 K (left) and at variable scan rates of 0.1 (red), 0.2 (orange), 0.5 (yellow), 1 (green), 2 (blue), and 5 (magenta) V/s.

The acid-assisted reductive activation of $[Mn^{III}(O_2)(N_4O)]$ illustrates the versatility of Mn^{III}-peroxo activation, exhibiting either Mn—O bond cleavage and H_2O_2 formation in the presence of strong acid or O—O bond cleavage and the formation of high-valent intermediates in presence of weak acid. However, the products of these reactions were unstable and could not be identified experimentally. Additionally, the Mn^{III}-peroxo species could not be independently prepared and therefore is not well defined.

To determine the most favorable binding mode of the ligand and the lowest-energy structure of the Mn^{III}-peroxo species, DFT calculations were employed. The reduction and O—O bond cleavage processes for the $[Mn^{III}(O_2)(N_4O)]$ complex were investigated by DFT calculations. Additionally, the effect of ligand structure on the reductive activation processes was evaluated by performing DFT calculations of the reduction and O—O bond cleavage events for Mn^{III}-peroxo species supported by the Me_2EBC and TMC ligands (Figure 5.3). The Me_2EBC and TMC ligands provide a good basis of comparison for the $[Mn^{III}(O_2)(N_4O)]$ complex, as both of ligands support Mn^{III}-peroxo species with well-defined binding modes and have been well-characterized.[10,17,18] Activation of these Mn^{III}-peroxo species was explored by calculations of

stepwise reduction and O—O bond cleavage processes as well as a process with concerted reduction and O—O bond cleavage.

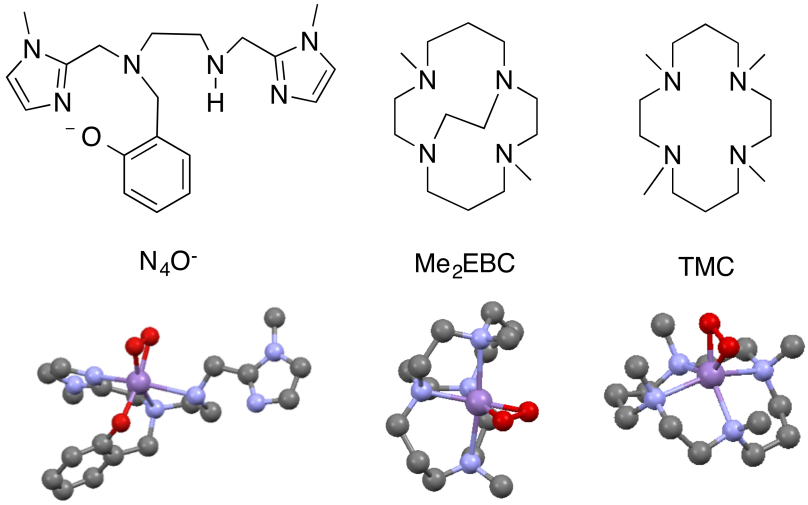

Figure 5.3. N_4O^-, Me_2EBC, and TMC ligands (top) and corresponding DFT-calculated Mn^{III}-peroxo species (bottom).

5.2 Experimental Section

5.2.1. Density Functional Theory Calculations. DFT computations were performed using the *ORCA* 3.0.1. software package.[19] A model of of $[Mn^{III}(O_2)(N_4O)]$ was built from the X-ray coordinates of $[Mn^{II}(N_4O)]$.[20] The $[Mn^{III}(O_2)(Me_2EBC)]^+$ complex was discussed in Chapter 2. A model of $[Mn^{III}(O_2)(TMC)]^+$ was built from X-ray coordinates of the published structure.[18] All structures were optimized with the Becke-Perdew (BP) functional[21,22] with the SVP (Ahlrichs split valance polarized) basis sets[23-25] and the auxiliary SV/J on C and H atoms. The larger TZVP (Ahlrichs triple-ζ valence polarized) basis set and the auxiliary TZV/J basis sets were used on Mn, N, and O atoms. The resolution of identity (RI) approximation[26] was used for all calculations and solvation effects were implemented with dimethylformamide with the COSMO model.[27] Models of $[Mn^{III}(O_2)(N_4O)]$, $[Mn^{III}(O_2)(Me_2EBC)]^+$, and $[Mn^{III}(O_2)(TMC)]^+$ were converged to the $S = 2$ spin state. Frequency calculations of the optimized structures were performed using the same parameters to confirm that no negative frequencies occurred,

indicating minimum energy structures. Single point energies of all complexes were calculated with the B3LYP functional[28-30] and the TZVPP basis set. These parameters were shown to provide good agreement with experimental data in a study comparing various density functionals.[13]

5.2.2. DFT O—O Bond and Reduction Potential Calculations. To locate products of the O—O bond cleavage reaction, surface scans varying the length of the O—O bond were performed using the same level of theory as the geometry optimization calculations. Optimization, frequency, and single point energy calculations were performed for the minimum energy species. Transition states were located using the ScanTS tool in ORCA. Further refinement of the transition state structures was achieved using a saddle point finder followed by frequency and single point energy calculations. Models for one-electron reduced complexes were generated by adding an electron to an optimized structure and performing new optimization, frequency, and single point energy calculations of the reduced complex. Reduction potentials (vs SCE) were calculated by the difference in energies of the pair of complexes in the reduction process. The DFT-calculated reorganizational energy of the reduction of $[Mn^{III}(O_2)(N_4O)]$ was calculated from the difference in energy of the one-electron reduced species optimized at the reactant geometry ($[Mn^{III}(O_2)(N_4O)]^-$) and the one-electron reduced species optimized at the product geometry ($[Mn^{IV}(O)_2(N_4O)]^-$).[31] All O—O bond cleavage and reduction calculations were performed for two spin states of each complex (triplet and quintet states for each Mn^{III} and Mn^{V} species and quartet and sextet states for each Mn^{II} and Mn^{IV} species). Cartesian coordinates for all DFT-optimized structures are given in Appendix 5, Tables A5.1 - A5.7 (N_4O^-), Tables A5.8 - A5.14 (Me_2EBC), and Tables A 5.15 – A5.21 (TMC).

5.3 Results and Analysis

For the three Mn^{III}-peroxo complexes supported by the N_4O^-, Me_2EBC, and TMC ligands (Figure 5.3), three mechanisms of reductive activation were considered. First, a stepwise reaction with reduction from the Mn^{III}-peroxo to Mn^{II}-peroxo and subsequent O—O bond cleavage was considered (Figure 5.4, pathway A). Second, calculations were performed for a stepwise pathway with O—O bond cleavage of the Mn^{III}-peroxo species to form a Mn^{V}-dioxo with subsequent reduction (Figure 5.4, pathway B). Finally, we investigated a concerted pathway with O—O bond cleavage coupled with the reduction process (Figure 5.4, pathway C).

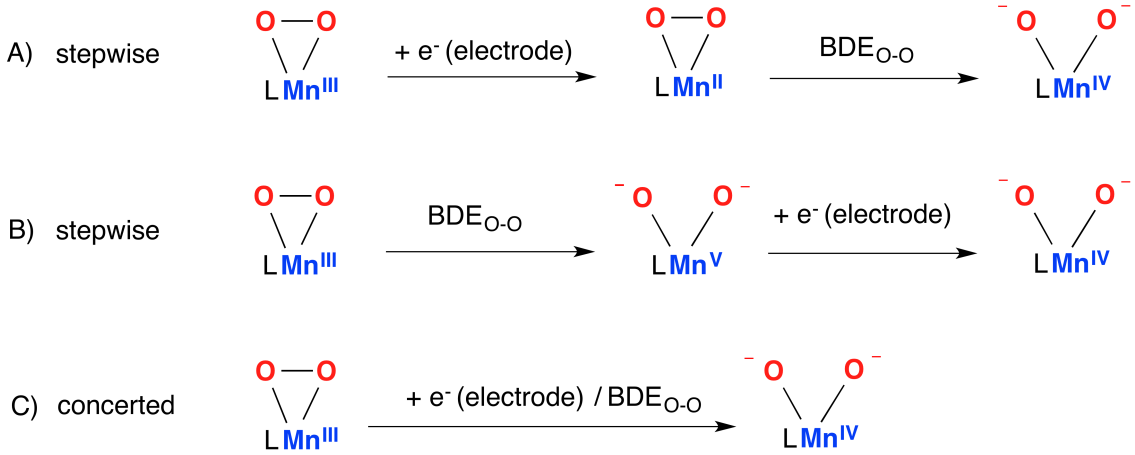

Figure 5.4. Calculated activation pathways of $LMn^{III}(O_2)$ (L = N4O⁻, Me_2EBC, TMC). A) stepwise reduction and O—O bond cleavage, B) stepwise O—O bond cleavage and reduction, C) concerted reduction and O—O bond cleavage

5.3.1. Reactivity Pathways of $[Mn^{III}(O_2)(N_4O)]$. Upon formation of the $[Mn^{III}(O_2)(N_4O)]$ complex, one arm of the ligand dissociates to accommodate binding of the side-on peroxo ligand, as has been observed with other Mn^{III}-peroxo species supported by flexible, pentadendate ligands.[12] Various models of this complex were previously investigated, and dissociation of the N6 methylimidazole arm (Figure 5.3) provided the most favorable species (i.e. lowest energy DFT structure) and good agreement between calculated and experimental spectroscopic properties.[13] The first pathway of reactivity (Figure 5.4, pathway A) explored for

the activation of the $[Mn^{III}(O_2)(N_4O)]$ complex is a stepwise process with an initial reduction of the Mn^{III}-peroxo to a Mn^{II}-peroxo species followed by O—O bond cleavage. This complex is formally described as a Mn^{II}-peroxo, although a Mn^{III}-superoxo description could also be appropriate. Reduction at the electrode of the quintet $[Mn^{III}(O_2)(N_4O)]$ complex can lead to quartet and sextet $[Mn^{II}(O_2)(N_4O)]^-$ complexes. Calculated reduction potentials for conversion of the Mn^{III}-peroxo complex to either Mn^{II}-peroxo species are too low compared to the experimental reduction potential (calculated values of -3.10 and -1.96 V for quartet and sextet products, respectively, versus the experimental value of -1.65 V vs SCE; see Figure 5.5). Thus, a reduction of $[Mn^{III}(O_2)(N_4O)]$ to a Mn^{II}-peroxo, without structural rearrangement, is more uphill thermodynamically than the observed electrochemical process.

The thermodynamic parameters of the subsequent O—O bond cleavage event were examined by setting the lowest energy sextet $[Mn^{II}(O_2)(N_4O)]^-$ complex as the relative zero of energy. With this complex as a reference, the quartet $[Mn^{II}(O_2)(N_4O)]^-$ complex is 26.0 kcal/mol higher in energy (Figure 5.5). From the sextet or quartet Mn^{II}-peroxo intermediate, the O—O bond cleavage is an extremely downhill process, with the resulting quartet Mn^{IV}-dioxo complex stabilized by 28.6 kcal/mol and the sextet Mn^{IV}-dioxo stabilized by 9.9 kcal mol (Figure 5.5, right). Calculations for the transition state of this process were attempted, however, a transition state for the formation of the more thermodynamically stable quartet product could not be located. For the sextet process, a barrier of 7.7 kcal/mol was calculated. Due to the high energy of the Mn^{II}-peroxo intermediate, as well as the large potential required for the initial reduction process, it was determined that this stepwise pathway of electron-transfer followed by O—O cleavage is unlikely to proceed.

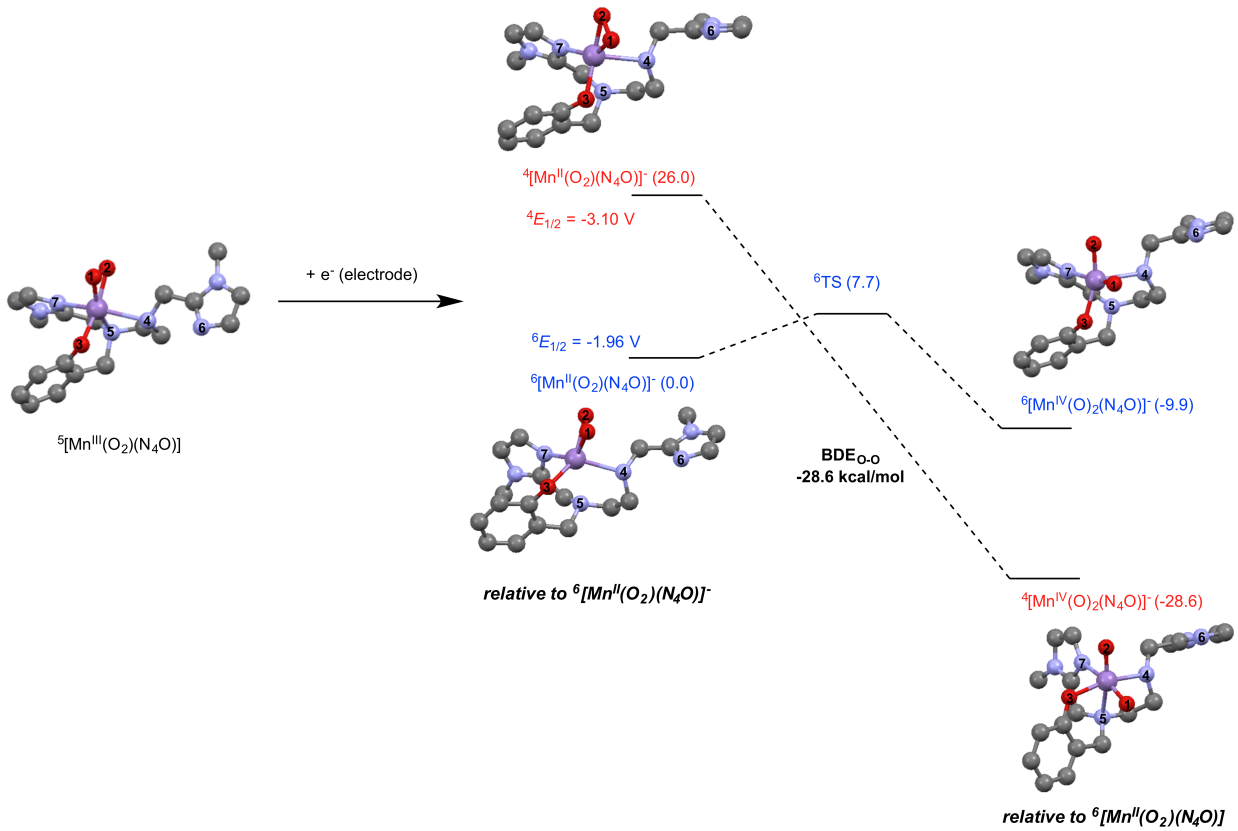

Figure 5.5. Stepwise reduction of $[Mn^{III}(O_2)(N_4O)]$ followed by O—O bond cleavage (pathway A).

A second stepwise mechanism (Figure 5.4, pathway B) involves initial O—O bond cleavage of the Mn^{III}-peroxo to form a Mn^{V}-dioxo species and a following reduction process to form the Mn^{IV}-dioxo product. We note that spontaneous O—O bond cleavage processes have been observed for Fe^{III}-peroxo intermediates.[7,8] The thermodynamic product of the O—O bond cleavage process of a Mn^{III}-peroxo, triplet $[Mn^{V}(O)_2(N_4O)]$, is destabilized by 7.9 kcal/mol relative to the quintet $[Mn^{III}(O_2)(N_4O)]$ complex, with the quintet $[Mn^{V}(O)_2(N_4O)]$ is at higher energy (12.0 kcal/mol) (Figure 5.6, left). In this O—O bond cleavage process, there is also a high activation energy (35.2 kcal/mol) for the conversion of Mn^{III}-peroxo to the triplet Mn^{V}-dioxo species. A barrier to the higher energy quintet species could not be located. This O—O bond cleavage of a Mn^{III}-peroxo in the absence of added protons or electrons is quite unfavorable.

Following the O—O bond cleavage, we next explored reduction of the Mn^{V}-dioxo species by one electron to form the quartet $[Mn^{IV}(O)_2(N_4O)]^-$ complex ($^{3\text{-to-}4}E_{1/2}$ = -0.39 V) or the sextet $[Mn^{IV}(O)_2(N_4O)]^-$ complex ($^{5\text{-to-}6}E_{1/2}$ = -1.13 V). Although these calculated reduction potentials are within the range experimentally observed, the large barrier of the initial O—O bond cleavage renders this stepwise pathway an improbable mechanism of reactivity.

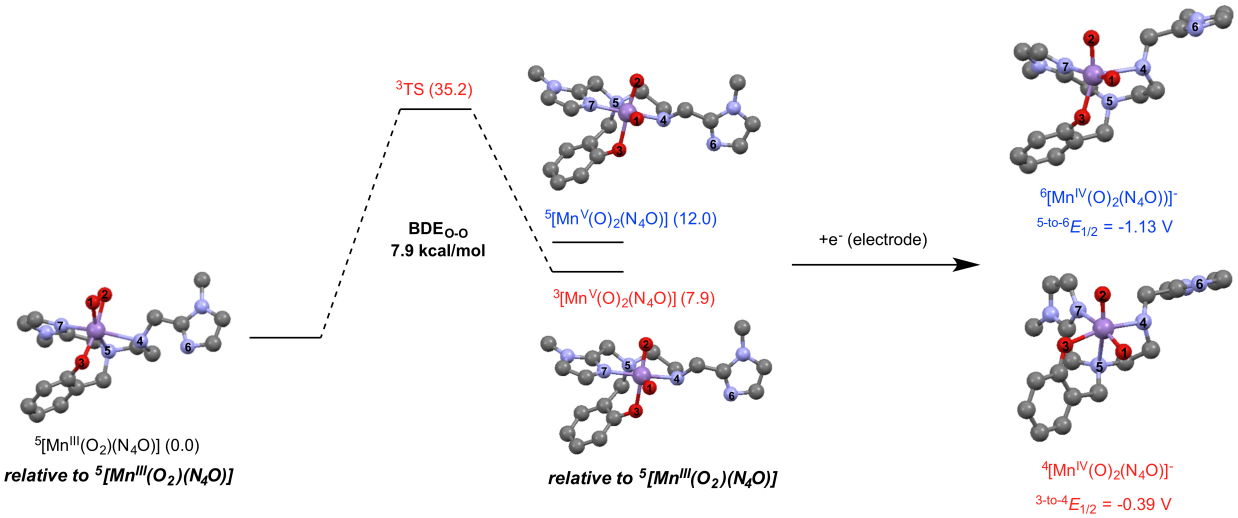

Figure 5.6. Stepwise O—O bond cleavage of $[Mn^{III}(O_2)(N_4O)]$ followed by reduction (pathway B).

The third pathway (C) considered involves a process where the electron transfer is concerted with O—O bond cleavage. Here, the calculated reduction potentials for both the sextet and quartet $[Mn^{IV}(O)_2(N_4O)]$ species are in reasonable agreement with the experimental reduction potential (-1.46 and -0.67 V, respectively, Figure 5.7), with the quartet $[Mn^{IV}(O)_2(N_4O)]$ species as the most stable product. The calculated reorganizational energy of 2.71 eV is in reasonable agreement with the experimental reorganizational energy of 2.25 eV, and these large reorganizational energies are compatible with a concerted mechanism of O—O bond cleavage with the reduction event. Together, these experimental details and the computational results indicate that the reduction and O—O bond cleavage processes occur in a

concerted fashion, with stepwise processes involving large activation energies and/or high-energy intermediates.

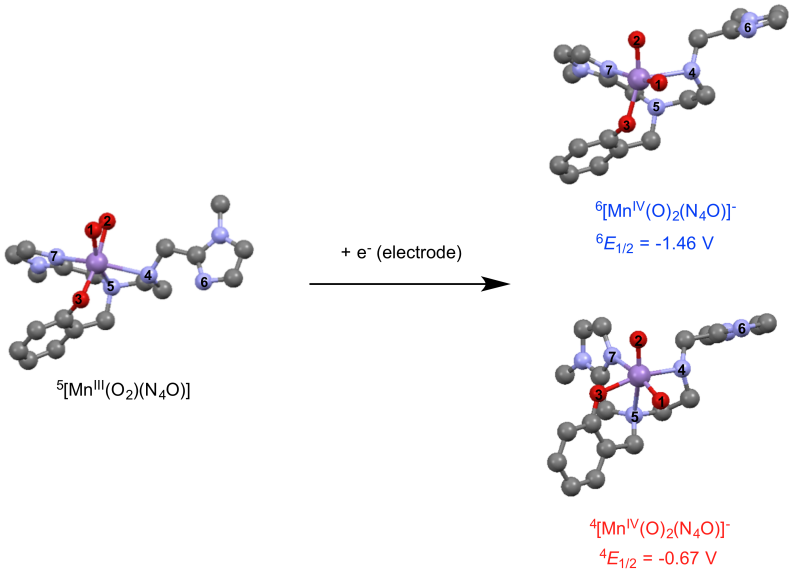

Figure 5.7. Concerted O—O bond cleavage and reduction of $[Mn^{III}(O_2)(N_4O)]$ (pathway C).

5.3.2. Reactivity Pathways of $[Mn^{III}(O_2)(Me_2EBC)]^+$. To compare the calculated and experimental parameters of reactivity for the $[Mn^{III}(O_2)(N_4O)]$ complex, similar calculations were performed with the $[Mn^{III}(O_2)(Me_2EBC)]^+$ complex, as this well-characterized Mn^{III}-peroxo species has been shown to undergo activation to a high-valent Mn^{IV} species,[10] and this ligand is known to support stable high-valent Mn^{IV} species.[32,33] For this system, the stepwise pathway (pathway A) with reduction of the Mn^{III}-peroxo complex to the sextet or quartet Mn^{II}-peroxo species occurs with reduction potentials of -1.63 and -2.47 V, respectively (Figure 5.8, left). This reduction results in the generation of the high-energy Mn^{II} intermediate that was also calculated with the Mn^{III}-peroxo species supported by the N_4O^- ligand. In this case, the reduction process is more favorable (less negative $E_{1/2}$ values), presumably because $[Mn^{III}(O_2)(Me_2EBC)]^+$ is cationic while $[Mn^{III}(O_2)(N_4O)]$ is neutral. By setting the sextet Mn^{II}-peroxo at the relative zero of energy, the quartet Mn^{II}-peroxo lies 19.3 kcal/mol above the sextet complex. This species readily

undergoes O—O bond cleavage with a downhill reaction to the quartet Mn^{IV}-dioxo product (-26.9 kcal/mol) and the sextet Mn^{IV}-dioxo (-16.3 kcal/mol). Neither the quartet or sextet transition states for this reaction were located, potentially due to the large stabilization of the product complexes. Similar to the Mn^{III}-peroxo complex supported by N_4O^-, the formation of the high-energy Mn^{II} intermediate indicates that this process is unlikely to proceed by electron-transfer followed by O—O cleavage. However, the calculated reduction potential for sextet $[Mn^{III}(O_2)(Me_2EBC)]^+$ (-1.63 V) is slightly less than that calculated potential for the reduction of sextet $[Mn^{III}(O_2)(N_4O)]$ (-1.96 V), indicating that the Me_2EBC ligand may provide a better platform for Mn^{III}-peroxo reduction and activation.

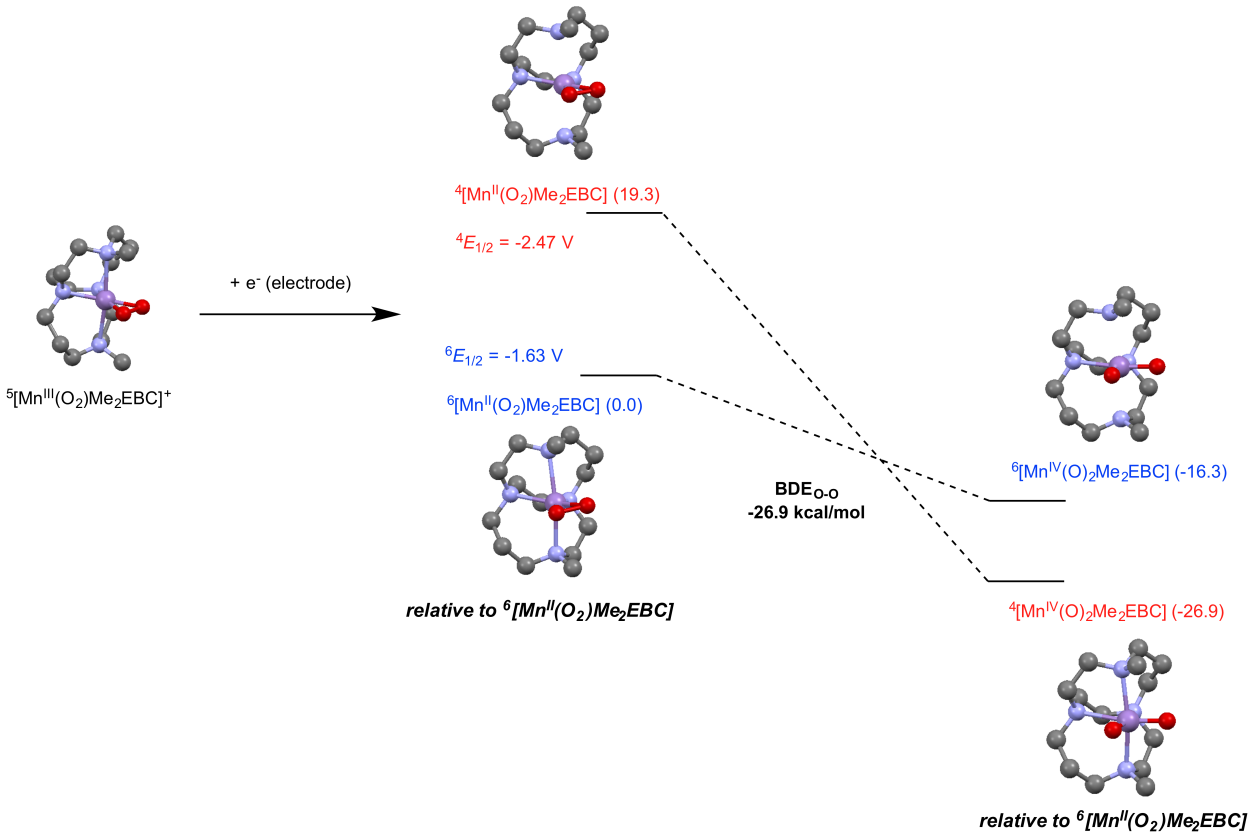

Figure 5.8. Stepwise reduction of $[Mn^{III}(O_2)(Me_2EBC)]^+$ followed by O—O bond cleavage (pathway A).

The alternative stepwise mechanism (Figure 5.4, pathway B) of an initial O—O bond cleavage followed by a reduction process also suggests that the Me_2EBC ligand contains

advantages for O—O bond activation. A lower $BDE_{O—O}$ of 2.3 kcal/mol for the initial O—O bond cleavage event was calculated for the reaction of quintet $[Mn^{III}(O_2)(Me_2EBC)]^+$ to triplet $[Mn^{V}(O)_2(Me_2EBC)]^+$. However, a large barrier (33.8 kcal/mol) is present in this reaction (Figure 5.9, left), similar to the O—O bond cleavage of the Mn^{III}-peroxo species supported by N_4O^- (Figure 5.6). The transition state structure contains a compressed N_{axial}-Mn-N_{axial} axis that contributes to the high energy of this species. The subsequent reduction of $[Mn^{V}(O)_2(Me_2EBC)]^+$ by one electron to form the Mn^{IV}-dioxo species requires a small potential of -0.77 or -0.42 V to the sextet and quartet species. These values are more positive than those calculated for the $[Mn^{III}(O_2)(N_4O)]$ complex. While these calculated parameters indicate slight advantages of the Me_2EBC platform over N_4O^-, both of these stepwise mechanisms for the activation of $[Mn^{III}(O_2)(Me_2EBC)]^+$ are impeded by a high-energy Mn^{II}-peroxo intermediate in the first scenario and a thermodynamically inaccessible barrier for O—O bond cleavage in the second case.

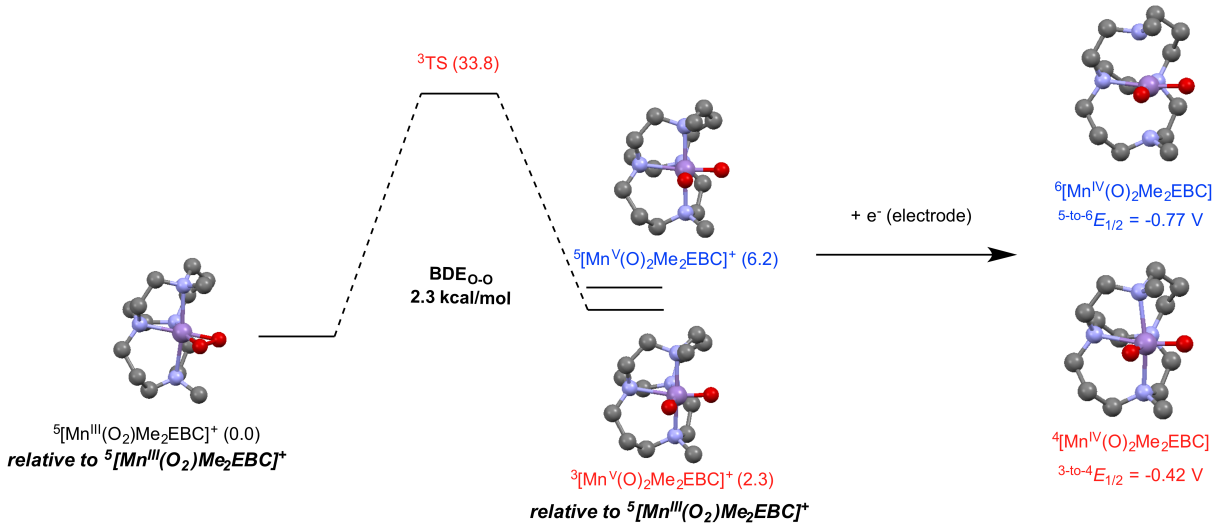

Figure 5.9. Stepwise O—O Bond cleavage of $[Mn^{III}(O_2)(Me_2EBC)]^+$ followed by reduction (pathway B).

The activation of $[Mn^{III}(O_2)(Me_2EBC)]^+$ by a concerted process of reduction and O—O bond cleavage (pathway C) offers the most likely reaction pathway. Similar to the calculated

processes for the $[Mn^{III}(O_2)(N_4O)]$ complex, the reduction potential for this process (-0.92 and -0.30 V for sextet and quartet species, respectively, Figure 5.10) is less than the required potential that was necessary to reduce $[Mn^{III}(O_2)(N_4O)]$, and is likely within the range needed to reduce $[Mn^{III}(O_2)(Me_2EBC)]^+$. Additionally, both of these reduction potentials are significantly less than those calculated for the N_4O^- supported species, supporting the hypothesis that the Me_2EBC ligand is able to better stabilize O—O bond cleavage and reduction.

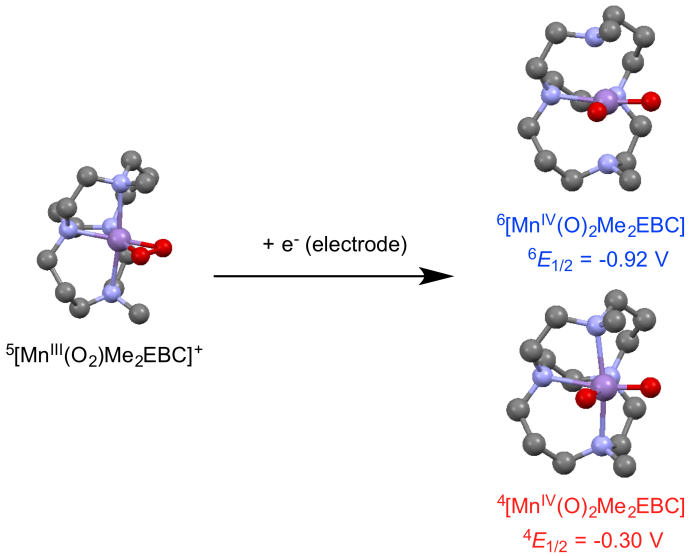

Figure 5.10. Concerted O—O bond cleavage and reduction of $[Mn^{III}(O_2)(Me_2EBC)]^+$ (pathway C).

5.3.3. Reactivity Pathways of $[Mn^{III}(O_2)(TMC)]^+$. The TMC ligand and its ring-contracted derivatives have been widely used to support Mn^{III}-peroxo species[14,17,18,34] and could potentially provide a favorable framework for the reduction of the Mn^{III}-peroxo moiety. The macrocyclic framework of the ligand offers a contrast to the flexible N_4O^- ligand and provides a structural comparison to the rigid Me_2EBC ligand. The first reactivity pathway (Figure 5.4, pathway A) considered involves initial reduction of the Mn^{III}-peroxo species to the Mn^{II}-peroxo followed by O—O bond cleavage to the Mn^{IV}-dioxo. The initial reduction step to the sextet Mn^{II}-peroxo species requires a potential of -1.44 V and a larger potential of -2.56 V to the quartet

species (Figure 5.11, left; Table 5.2). These values are comparable to those observed for $[Mn^{III}(O_2)(Me_2EBC)]^+$. The subsequent O—O bond cleavage to generate the Mn^{IV}-dioxo species lacks the large driving force that was calculated for the complexes supported by the N_4O^- and Me_2EBC ligands. Although the Mn^{II}-peroxo species is a high-energy intermediate, the Mn^{IV}-dioxo species is only stabilized by -8.3 kcal/mol for the quartet $[Mn^{IV}(O)_2(TMC)]^+$ complex and by -3.3 kcal/mol for the sextet $[Mn^{IV}(O)_2(TMC)]^+$ complex (Figure 5.11, right), which is less than the driving force calculated for the Mn^{III}-peroxo species supported by the N_4O^- and Me_2EBC ligands (Table 5.1).

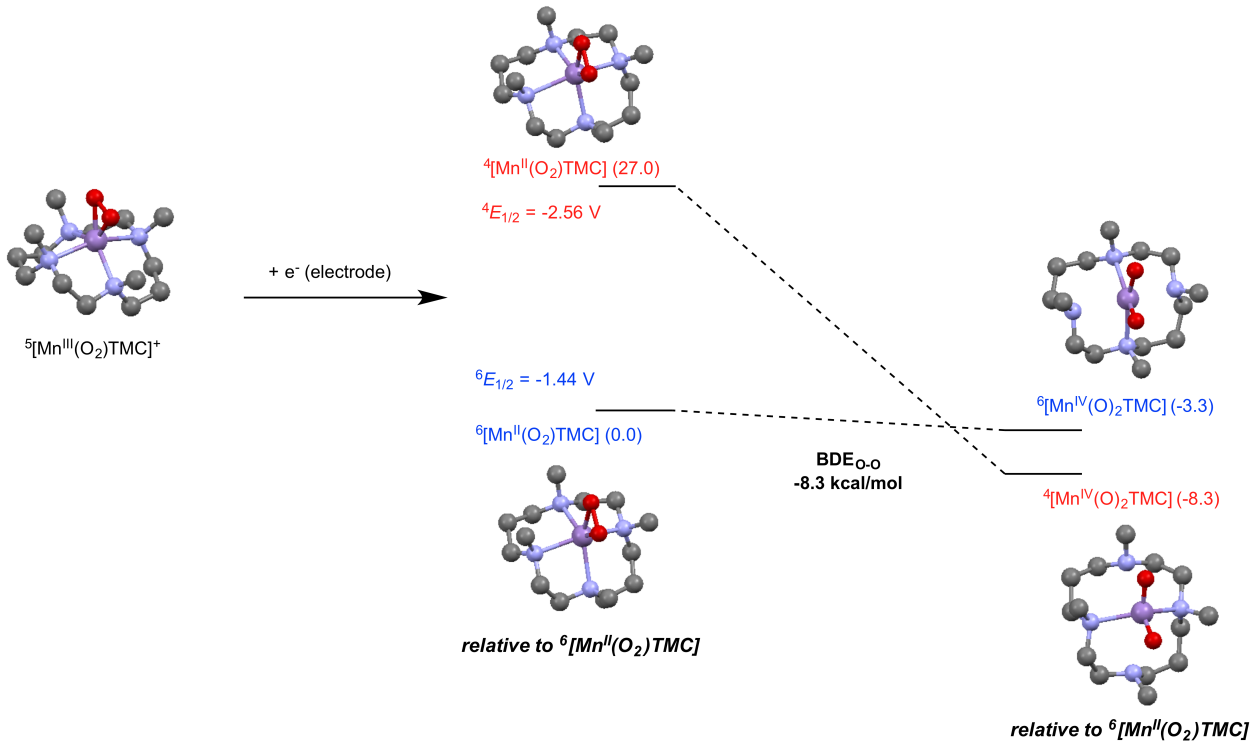

Figure 5.11. Stepwise reduction of $[Mn^{III}(O_2)(TMC)]^+$ followed by O—O bond cleavage.

The stepwise reaction (pathway B) of O—O bond cleavage followed by reduction also displayed significant differences from those for the Me_2EBC and N_4O^- supported complexes. In the O—O bond cleavage process of $[Mn^{III}(O_2)(TMC)]^+$ to generate the triplet or quintet $[Mn^{V}(O)_2(TMC)]^+$ species, a large $BDE_{O—O}$ of 27.0 kcal/mol was calculated that was greater

than that observed for the other Mn^{III}-peroxo species investigated in this study (Figure 5.12, left and Table 5.1). A transition state could not be located for either surface of this O—O bond cleavage process. The follow-up reduction of this unstable Mn^{V}-dioxo species to the Mn^{IV}-dioxo requires relatively low potentials of -0.12 and 0.17 V for the sextet and quartet Mn^{IV}-dioxo species, respectively (Figure 5.12, right). Although these subsequent reduction steps are feasible reactions, the initial O—O bond cleavage is thermodynamically uphill and this stepwise process is unfavorable.

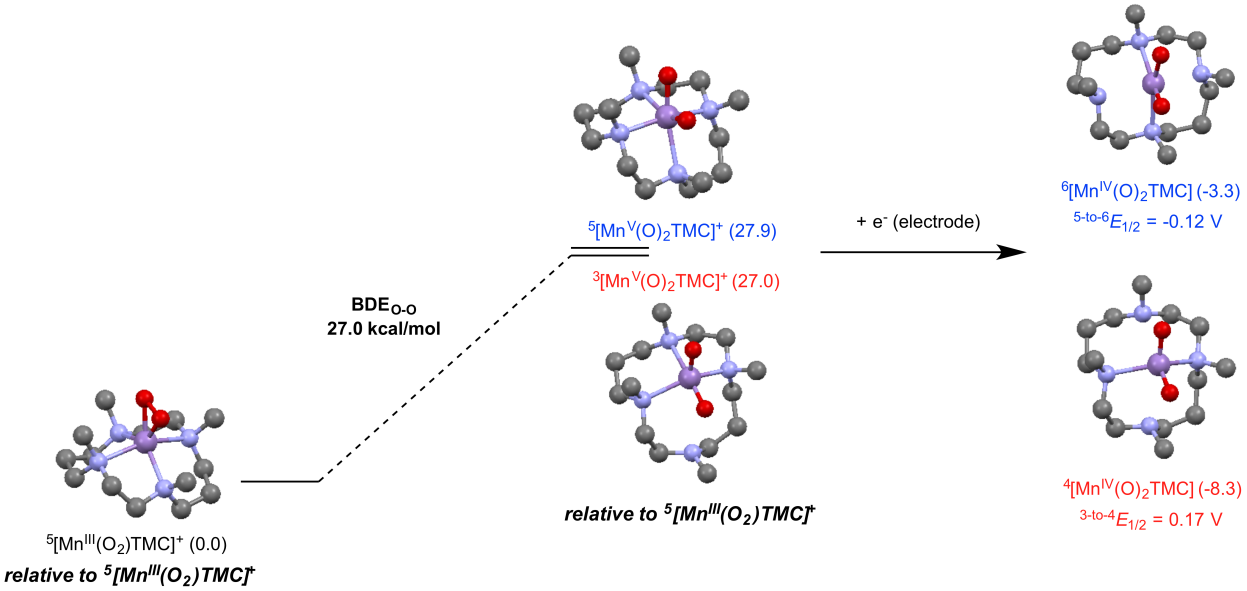

Figure 5.12. Stepwise O—O Bond cleavage of $[Mn^{III}(O_2)(TMC)]^+$ followed by reduction.

The final mechanism (pathway C) considered for the activation of $[Mn^{III}(O_2)(TMC)]^+$ is a concerted pathway with O—O bond cleavage coupled with reduction. The calculated potential for the reduction of quartet $[Mn^{III}(O_2)(TMC)]^+$ to the sextet $[Mn^{IV}(O)_2(TMC)]$ species occurs at -1.26 V and at -1.01 V for the quartet $[Mn^{IV}(O)_2(TMC)]$ species (Figure 5.13, Table 5.2). These relatively low reduction potentials (compared to the experimental reduction potential required to reduce $[Mn^{III}(O_2)(N_4O)]$) indicate that this concerted reduction and O—O bond cleavage

pathway is the most favorable pathway of Mn^{III}-peroxo activation. However, these potentials are larger than those calculated for the concerted reduction and O—O bond cleavage of $[Mn^{III}(O_2)(N_4O)]$ or $[Mn^{III}(O_2)(Me_2EBC)]^+$. As such, although O—O bond cleavage and reduction may occur with the $[Mn^{III}(O_2)(TMC)]^+$, this process is less favorable than with Mn^{III}-peroxo species supported by the N_4O^- or Me_2EBC ligands.

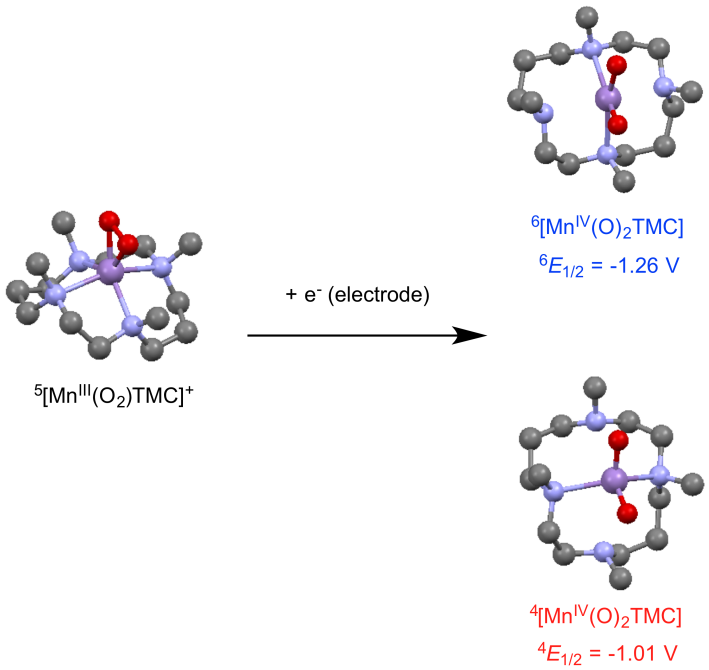

Figure 5.13. Concerted O—O bond cleavage and reduction of $[Mn^{III}(O_2)(TMC)]^+$.

5.4 Discussion

Several Mn^{III}-peroxo species supported by different ligand structures, including a flexible N_4O^-, a cross-clamped Me_2EBC, and a macrocyclic TMC ligand, were computationally investigated to define the most favorable mechanism of reduction and O—O bond cleavage of a Mn^{III}-peroxo complex and to compare ligand effects on O—O bond activation. Experimentally, the $[Mn^{III}(O_2)(N_4O)]$ complex was activated in the presence of weak acid by electrochemical reduction and O—O bond cleavage to produce a high-valent Mn^{IV}-dioxo intermediate (Scheme 5.2). Although this high-valent species was reduced and protonated to form the Mn^{III}-dihydroxo final product, this is the first example of acid-driven reductive activation of a Mn^{III}-peroxo to a

high-valent Mn complex.[13] In order to define the mechanism of activation of this and other Mn^{III}-peroxo species, the thermodynamic parameters driving the reduction and bond cleavage events were explored as a function of ligand parameters. For all three of the Mn^{III}-peroxo species investigated, a reduction process concerted with O—O bond cleavage was determined to be the most favorable pathway.

The advantage of the concerted pathway is most pronounced for the Mn^{III}-peroxo complex supported by the N_4O^- ligand. Here, the stepwise reduction process followed by O—O bond cleavage (pathway A) is unlikely to proceed as it required a large reduction potential (-1.96 V vs SCE, Table 5.2) to reduce the $[Mn^{III}(O_2)(N_4O)]$ complex to the sextet $[Mn^{II}(O_2)(N_4O)]^-$ intermediate, which is beyond the experimental reduction potential[13] for $[Mn^{III}(O_2)(N_4O)]$ (-1.65 V vs SCE). Pathway B is also unfavorable as the barrier for O—O bond cleavage is thermodynamically inaccessible (35.2 kcal/mol). The calculated concerted reduction and O—O bond cleavage process (pathway C) that generates the quartet $[Mn^{IV}(O)_2(N_4O)]$ complex requires a small reduction potential (-0.67 V vs SCE). The calculated energies and reduction potentials of these three pathways, in combination with the large experimental reorganizational energy of $[Mn^{III}(O_2)(N_4O)]$, indicate that the reduction process is concerted with the O—O bond cleavage in the Mn^{III}-peroxo moiety.

Table 5.1. Calculated thermodynamic parameters for O—O bond cleavage (kcal/mol) for $[Mn^{III}(O_2)(N_4O)]$, $[Mn^{III}(O_2)(Me_2EBC)]^+$, and $[Mn^{III}(O_2)(TMC)]^+$ for pathway A and B.

	BDE_{O-O} (kcal/mol)		**$\Delta G^{\neq}$**
	(A)	(B)	(B)
	$Mn^{II}(O_2) \rightarrow Mn^{IV}(O)_2$	$Mn^{III}(O_2) \rightarrow Mn^{V}(O)_2$	$Mn^{III}(O_2) \rightarrow Mn^{V}(O)_2$
$[Mn^{III}(O_2)(N_4O)]$	-28.6	7.9	35.2
$[Mn^{III}(O_2)(Me_2EBC)]^+$	-26.9	2.3	33.8
$[Mn^{III}(O_2)(TMC)]^+$	-8.3	27.0	not found

Table 5.2. Calculated reduction potentials (V vs SCE) for concerted and stepwise pathways of reduction of $[Mn^{III}(O_2)(N_4O)]$, $[Mn^{III}(O_2)(Me_2EBC)]^+$, and $[Mn^{III}(O_2)(TMC)]^+$ for pathways A, B, and C.

	(A) Reduction $Mn^{III}(O_2)$ → $Mn^{II}(O_2)$		(B) Reduction $Mn^{V}(O_2)$ → $Mn^{IV}(O)_2$		C) Concerted Reduction / O-O Cleavage	
	$^4E_{1/2}$	$^6E_{1/2}$	$^{3\text{-to-}4}E_{1/2}$	$^{5\text{-to-}6}E_{1/2}$	$^4E_{1/2}$	$^6E_{1/2}$
$[Mn^{III}(O_2)(N_4O)]$	-3.10	-1.96	-0.39	-1.13	**-0.67**	-1.46
$[Mn^{III}(O_2)(Me_2EBC)]^+$	-2.47	-1.63	-0.42	-0.77	**-0.30**	-0.92
$[Mn^{III}(O_2)(TMC)]^+$	-2.56	-1.44	0.17	-0.12	**-1.01**	-1.26

For the $[Mn^{III}(O_2)(Me_2EBC)]^+$ complex, the concerted reduction and bond cleavage process is the most favorable pathway of activation. This complex requires the smallest reduction potential for this reaction (-0.30 V vs SCE, Table 5.2), compared to the concerted pathways for all three Mn^{III}-peroxo species. While the stepwise reduction and bond cleavage pathway (pathway A), is more favorable than that of $[Mn^{III}(O_2)(N_4O)]$, this pathway is unlikely to take precedence over the much smaller reduction potential required for the concerted pathway. Pathway B is also unlikely to occur as there is a large barrier for O—O bond cleavage (33.8 kcal/mol), although the $BDE_{O—O}$ for $[Mn^{III}(O_2)(Me_2EBC)]^+$ (2.8 kcal/mol) is smaller than that of $[Mn^{III}(O_2)(N_4O)]$ (7.9 kcal/mol). In general, while the concerted pathway is the most favorable pathway of activation for $[Mn^{III}(O_2)(Me_2EBC)]^+$, each pathway shows increased favorability over the activation of $[Mn^{III}(O_2)(N_4O)]$. This increased stability is presumably due to the moderate amount of steric bulk and rigidity of this cross-clamped cyclam ligand. In a separate study, the Me_2EBC ligand directed the reactivity of the Mn^{III}-peroxo species to monomeric products by preventing the formation of oxo-bridged dimanganese products due to the bulk of the ligand.[10] Additionally, the Me_2EBC ligand has been shown to provide a stabilizing effect to high-valent Mn^{IV}-oxo species that are often prone to degradation pathways.[32,33] The framework of the Me_2EBC ligand, while somewhat rigid, still allows for differences in axial elongation and compression that can occur with conversion to different intermediates.[33,35]

The calculated activation pathways for $[Mn^{III}(O_2)(TMC)]^+$ contain several anomalies compared to the other Mn^{III}-peroxo species, although, the concerted pathway is still predicted to be the most favorable overall. The reduction potential in Pathway C to reduce $[Mn^{III}(O_2)(TMC)]^+$ to the $[Mn^{IV}(O)_2(TMC)]$ complex (-1.01 V vs SCE) is more favorable than the stepwise Pathway A to reduce $[Mn^{III}(O_2)(TMC)]^+$ to $[Mn^{II}(O_2)(TMC)]^+$ (-1.44 V vs SCE), however, this complex shows the least difference between the potentials of these pathways. Additionally, the second step in Pathway A, O—O bond cleavage, is significantly less thermodynamically downhill (-8.8 kcal/mol) than the $[Mn^{III}(O_2)(N_4O)]$ and $[Mn^{III}(O_2)(Me_2EBC)]^+$ species (-28.6 and -26.9 kcal/mol, respectively; Table 5.1). Pathway B also displays decreased favorability with a strong O—O bond (27.0 kcal/mol), which is over threefold the strength of the O—O bond of $[Mn^{III}(O_2)(N_4O)]$ (7.8 kcal/mol). This could account for the high thermal stability of $[Mn^{III}(O_2)(TMC)]^+$ observed experimentally.[17,18] Overall, the favorability of each pathway of activation for $[Mn^{III}(O_2)(TMC)]^+$ is significantly diminished. Indeed, in a study of $[Mn^{III}(O_2)(TMC)]^+$ with activation by acid addition, the O—O bond in this complex is retained, and, instead, a Mn—O bond is broken to form an end-on Mn^{III}-hydroperoxo species.[14] This loss of reactivity of the O—O bond is likely due, in part, to the equatorial binding mode of the macrocyclic TMC structure. This ligand is used for its ability to retain its structure and is known to support η^1 substituents well, such as the Mn^{III}-hydroperoxo[14] and Fe^{IV}-oxo species.[36-39] While the TMC ligand has been widely used to support side-on peroxo species,[14,17,18,34] these calculations indicate that there is limited reactivity of the O—O bond to produce a more sterically crowded *cis*-Mn^{IV}-dioxo species. In particular, the calculated reactivity parameters of the $[Mn^{III}(O_2)(N_4O)]$ and the $[Mn^{III}(O_2)(TMC)]^+$ species illustrates the importance of obtaining the appropriate balance of ligand rigidity to achieve successful O—O bond activation.

5.5 Conclusions

The thermodynamic parameters and reduction potentials calculated for three pathways for the $[Mn^{III}(O_2)(N_4O)]$, $[Mn^{III}(O_2)(Me_2EBC)]^+$, and $[Mn^{III}(O_2)(TMC)]^+$ complexes indicate that there is an energetic advantage to a reduction process that is concerted with the O—O bond cleavage event. Stepwise calculation of reduction followed by O—O bond cleavage required reduction potentials beyond experimental parameters, and stepwise calculation of O—O bond cleavage followed by reduction contained high reaction barriers for the bond cleavage process. The only process that predicted experimentally feasible results was the concerted reduction and bond cleavage pathway. Additionally, differences in these pathways between the three complexes with varying ligand properties indicate that a moderate amount of steric bulk and rigidity is optimal for the activation of the Mn^{III}-peroxo species.

5.6 References

(1) *Cytochrome P450: Structure, Mechanism, and Biochemistry*; Plenum: New York, 1995.

(2) McLain, J. L.; Lee, J.; Groves, J. T. In *Biomimetic Oxidations Catalyzed by Transition Metal Complexes*; Meunier, B., Ed.; Imperial College Press: London, 2000, p 91-169.

(3) Tinberg, C. E.; Lippard, S. J. *Biochemistry* **2009**, *48*, 12145-12158.

(4) Li, F.; Meier, K. K.; Cranswick, M. A.; Chakrabarti, M.; Van Heuvelen, K. M.; Münck, E.; Que, L., Jr. *J. Am. Chem. Soc.* **2011**, *133*, 7256-7259.

(5) Li, F.; Van Heuvelen, K. M.; Meier, K. K.; Münck, E.; Que, L., Jr. *J. Am. Chem. Soc.* **2013**, *135*, 10198-10201.

(6) Solomon, E. I.; Decker, A.; Lehnert, N. *Proc. Natl. Acad. Sci.* **2003**, *100*, 3589-3594.

(7) Oloo, W. N.; Que, L., Jr. *Acc. Chem. Res.* **2015**, *48*, 2612-2621.

(8) Nam, W. *Acc. Chem. Res.* **2015**, *48*, 2415-2423.

(9) Leto, D. F.; Jackson, T. A. *J. Biol. Inorg. Chem.* **2014**, *19*, 1-15.

(10) Colmer, H. E.; Howcroft, A. H.; Jackson, T. A. *Inorg. Chem.* **2016**, *55*, 2055-2069.

(11) Groni, S.; Dorlet, P.; Blain, G.; Bourcier, S.; Guillot, R.; Anxolabéhère-Mallart, E. *Inorg. Chem.* **2008**, *47*, 3166-3172.

(12) Leto, D. F.; Chattopadhyay, S.; Day, V. W.; Jackson, T. A. *Dalton Trans.* **2013**, *42*, 13014-13025.

(13) Ching, H. Y. V.; Anxolabéhère-Mallart, E.; Colmer, H. E.; Costentin, C.; Dorlet, P.; Jackson, T. A.; Policar, C.; Robert, M. *Chem. Sci.* **2014**, *5*, 2304-2310.
(14) So, H.; Park, J.-H.; Cho, K.-B.; Lee, Y.-M.; Seo, M. S.; Cho, J.; Sarangi, R.; Nam, W. *J. Am. Chem. Soc.* **2014**, *136*, 12229−12232.
(15) Shook, R. L.; Gunderson, W. A.; Greaves, J.; Ziller, J. W.; Hendrich, M. P.; Borovik, A. S. *J. Am. Chem. Soc.* **2008**, *130*, 8888-8889.
(16) Shook, R. L.; Peterson, S. M.; Greaves, J.; Moore, C.; Rheingold, A. L.; Borovik, A. S. *J. Am. Chem. Soc.* **2011**, *133*, 5810-5817.
(17) Annaraj, J.; Cho, J.; Lee, Y.-M.; Kim, S. Y.; Latifi, R.; de Visser, S. P.; Nam, W. *Angew. Chem. Int. Ed.* **2009**, *48*, 4150-4153.
(18) Seo, M. S.; Kim, J. Y.; Annaraj, J.; Kim, Y.; Lee, Y.-M.; Kim, S.-J.; Kim, J.; Nam, W. *Angew. Chem. Int. Ed.* **2007**, *46*, 377-380.
(19) Neese, F. *Wiley Interdiscip. Rev.* **2012**, *2*, 73-78.
(20) Cisnetti, F.; Lefèvre, A.-S.; Guillot, R.; Lambert, F.; Blain, G.; Anxolabéhère-Mallart, E.; Policar, C. *Eur. J. Inorg. Chem.* **2007**, *2007*, 4472-4480.
(21) Becke, A. D. *J. Chem. Phys.* **1986**, *84*, 4524-4529.
(22) Perdew, J. P. *Phys. Rev. B* **1986**, *33*, 8822-8824.
(23) Bull, C.; Niederhoffer, E. C.; Yoshida, T.; Fee, J. A. *J. Am. Chem. Soc.* **1991**, *113*, 4069-4076.
(24) Schäfer, A.; Horn, H.; Ahlrichs, R. *J. Chem. Phys.* **1992**, *97*, 2571-2577.
(25) Schäfer, A.; Huber, C.; Ahlrichs, R. *J. Chem. Phys.* **1994**, *100*, 5829-5835.
(26) Neese, F. *J. Comput. Chem.* **2003**, *24*, 1740-1747.
(27) Sinnecker, S.; Rajendran, A.; Klamt, A.; Diedenhofen, M.; Neese, F. *J. Phys. Chem. A.* **2006**, *110*, 2235-2245.
(28) Becke, A. D. *J. Chem. Phys.* **1993**, *98*, 1372-1377.
(29) Becke, A. D. *J. Chem. Phys.* **1993**, *98*, 5648-5652.
(30) Lee, C.; Yang, W.; Parr, R. G. *Phys. Rev. B* **1988**, *37*, 785-789.
(31) Rosso, K. M.; Smith, D. M. A.; Dupuis, M. *J. Chem. Phys.* **2003**, *118*, 6455-6466.
(32) Chattopadhyay, S.; Geiger, R. A.; Yin, G.; Busch, D. H.; Jackson, T. A. *Inorg. Chem.* **2010**, *49*, 7530-7535.
(33) Yin, G.; Danby, A. M.; Kitko, D.; Carter, J. D.; Scheper, W. M.; Busch, D. H. *J. Am. Chem. Soc.* **2008**, *130*, 16245-16253.
(34) Kang, H.; Cho, J.; Cho, K.-B.; Nomura, T.; Ogura, T.; Nam, W. *Chem. Eur* **2013**, *19*, 14119-14125.
(35) Leto, D. F.; Jackson, T. A. *Inorg. Chem.* **2014**, *53*, 6179-6194.
(36) Jackson, T. A.; Rohde, J.-U.; Seo, M. S.; Sastri, C. V.; DeHont, R.; Ohta, T.; Stubna, A.; Kitagawa, T.; Münck, E.; Nam, W.; Que, L., Jr. *J. Am. Chem. Soc.* **2008**, *130*, 12394-12407.
(37) Kim, S. O.; Sastri, C. V.; Seo, M. S.; Kim, J.; Nam, W. *J. Am. Chem. Soc.* **2005**, *127*, 4178-4179.
(38) Lee, Y.-M.; Hong, S.; Morimoto, Y.; Shin, W.; Fukuzumi, S.; Nam, W. *J. Am. Chem. Soc.* **2010**, *132*, 10668-10670.
(39) Sastri, C. V.; Lee, J.; Oh, K.; Lee, Y. J.; Lee, J.; Jackson, T. A.; Ray, K.; Hirao, H.; Shin, W.; Halfen, J. A.; Kim, J.; Que, L., Jr.,; Shaik, S.; Nam, W. *Proc. Natl. Acad. Sci.* **2007**, *104*, 19181-19186.

CHAPTER 6

Spectroscopic and Computational Investigation of Low-Spin Mn(III) Bis(scorpionate) Complexes

Reproduced from: Colmer, H.E.; Margarit, C.G.; Smith, J.M.; Jackson, T.A.; Telser, J.T., *Eur. J. Inorg. Chem.*, **2016**, DOI: 10.1002/ejic.201501250, with permission from John Wiley & Sons, Inc.

6.1 Introduction

Manganese complexes supported by "scorpionate" ligands, specifically derivatives of the hydridotris(pyrazolyl)borate anion (Tp^-), have been used to model intermediates formed in Mn-dependent enzymes.[1] These applications have featured Tp^- ligands containing pyrazole groups modified with bulky isopropyl or phenyl substituents in the 3- and 5-positions. Such studies have also featured Mn^{II} and Mn^{III} ions in the expected high-spin states (S = 5/2 and S = 2, respectively). In contrast, the homoleptic Mn^{III} complexes supported by the Tp^- and Tp^{*-} ligands (Figure 6.1; Tp^{*-} = hydridotris(3,5-dimethylpyrazolyl)borate) both possess an S = 1 spin state, which is extremely unusual for Mn^{III} centers.[2] Other than the hexacyanido complex, $[Mn^{III}(CN)_6]^{3-}$,[3] the "classic" example of coordination favoring low-spin ground states, there are very few examples of Mn^{III} coordination complexes with S = 1 ground states. These include an interesting class of complexes with a *cis*-N4O2 donor set (oximato-N, azo-N, and carboxylato-O), such as bis[((2-carboxylatophenyl)azo)benzaldoximato]manganate(III).[4] A related class of complexes is the tris(quinine oximates), with *mer*- and *fac*-O3N3 donor sets.[5] Other, perhaps more expected examples of low-spin Mn(III) are the porphyrin complexes $[Mn(TPP)(CN)_2]^-$,[6] and $[Mn(TPP)(Im)_2]^-$, where TPP = tetraphenylporphyrin dianion, Im = imidalozate anion,[7] and a saturated macrocyclic analog, $[Mn(cyclam)(CN)_2]^+$ (cyclam = 1,4,8,11-tetraazacyclotetradecane).[8]

Related to the above trispyrazolylborate complexes is the $[\{Ph(MeIm)_3B\}_2Mn^{III}]^+$ complex (Figure 6.1), where $PhB(MeIm)_3^-$ (phenyltris(3-methylimidazol-2-yl)borate) is a C_3-symmetric scorpionate-like, monoanionic *N*-heterocyclic carbene (NHC) donor,[9] which also displayed an S = 1 ground state.[10] Structurally, both the tris(pyrazolyl)borate- and related NHC-ligated complexes display distorted O_h geometries with D_{3d} symmetry (Figure 6.1).

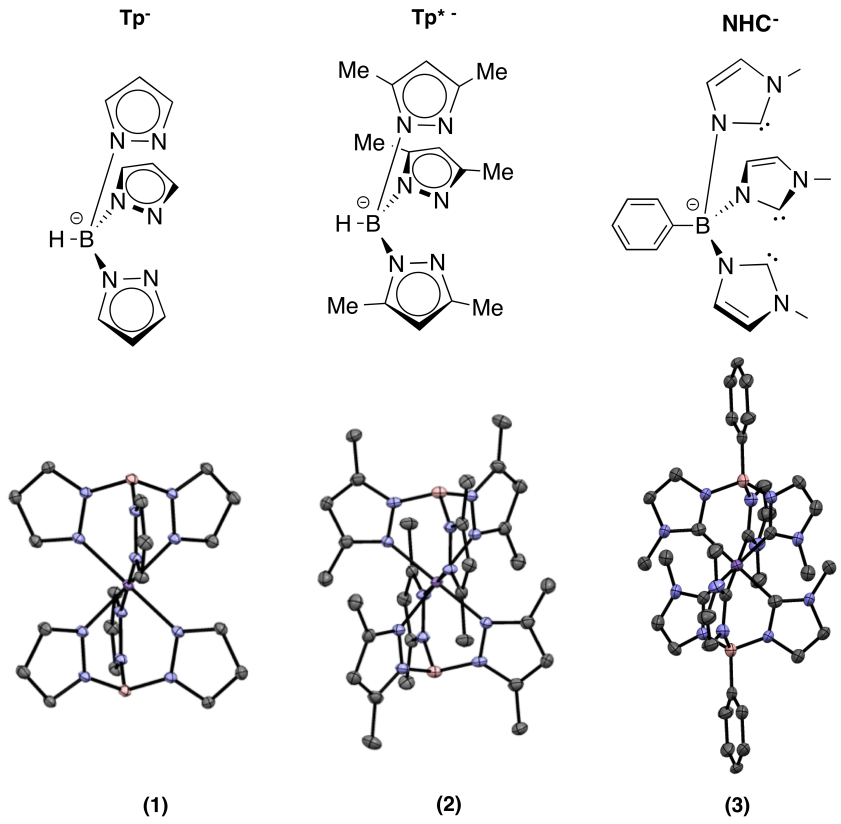

Figure 6.1. Tp^-, Tp^{*-}, and $PhB(MeIm)_3^-$ (NHC^-) ligands (top) and XRD structures[2,10] of **1**, **2**, and **3** (bottom).

As previously noted, the X-ray diffraction structures of the $[Tp_2Mn]^+$ (**1**) and $[Tp^*_2Mn]^+$ (**2**) complexes show little distortion from idealized O_h geometry,[11] with each complex having an inversion center and near perfect C_3 axes coincident with the B–Mn–B vector (Figure 6.1).[2] All N–Mn–$N_{adjacent}$ angles for **1** are within 2.6º of the idealized 90º expected for O_h geometry, and the Mn–N distances fall within the narrow range of 1.979 - 1.988 Å. Complex **2** has slightly longer Mn–N bond lengths (1.992 - 1.999 Å) and N–Mn–$N_{adjacent}$ angles even closer to 90º (89.75 - 90.49º).[2] The solid-state structure of $[\{Ph(MeIm)_3B\}_2Mn^{III}]^+$ (**3**) is similar to those of **1** and **2**, with Mn–C distances ranging from 2.014 - 2.037 Å, but with slightly smaller C–Mn–$C_{adjacent}$ angles of 85.82 - 87.32 Å.[10]

The modest structural changes between **1**, **2**, and **3** nonetheless give rise to differences in axial (D) and rhombic (E) ground-state zero-field splitting (zfs) parameters. The sign and

magnitude of the zfs parameters were determined through high-frequency and -field electron paramagnetic resonance (HFEPR) spectroscopy (**1** and **2**), dc magnetic susceptibility (**1**, **2**, and **3**) and frequency domain Fourier-transform THz-EPR spectroscopy (**1**).[10] Through the HFEPR experiments, the zero field splitting of **1** was characterized as D = +17.97(1), E = 0.42(2) cm^{-1}, and for **2** of D = +15.89(2), E = 0.04(1) cm^{-1}. The dc magnetic susceptibility measurements yielded comparable values, with D = +18.07 cm^{-1} for **1** and D = +14.60 cm^{-1} for **2**. The facile oxidation of **3** prevented collection of any rational HFEPR data; however, magnetometry measurements for **3** yielded a substantially larger magnitude of D than those of **1** and **2**, with an estimate of D = -49.9 cm^{-1}. It was suggested that the significantly larger value of D for **3** was potentially a sign of an orbitally-degenerate ground state (*i.e.*, ^3E), which could result from the much greater σ-donating properties of this ligand. We note for comparison that while zfs parameters were not determined for the previously-reported octahedral S = 1 $[Mn^{III}(CN)_6]^{3-}$ complex, this species displayed a room-temperature effective magnetic moment significantly above the expected spin-only value (μ_{eff} = 3.98 μ_B versus 2.83 μ_B, respectively), which was attributed to first-order spin-orbit coupling within a $^3T_{1g}$ ground state.[3b] For **1**, **2**, and **3**, density functional theory (DFT) and Hartree-Fock (HF) calculations employed to help understand the ground-state properties of these complexes were able to reproduce the trend in zfs parameters for **1** and **2**, but the D values were too low in magnitude by ~40% compared to experiment.[10] Moreover, the DFT approach failed completely when applied to **3**, as a D value comparable in magnitude to that of **1** and **2** was predicted (calculated D = +8.26 cm^{-1}), in clear disagreement with the experimental estimate.

While the ground-state magnetic properties of **1** and **2** are well-defined, the optical properties are underexplored. All that had been hitherto reported are the diffuse reflectance absorption spectra of **1** and **2** reveal major bands at 390 – 395 and 400 nm, respectively, with

shoulders at 460 – 465 and 475 nm.[2,10] The higher-energy features have been attributed to metal-to-ligand charge transfer (MLCT) transitions, while the shoulders are presumed to derive from the $^3T_{1g} \rightarrow {}^3E_g$ transition, using symmetry labels from the parent O_h group.[2] Given the rarity of $S = 1$ Mn^{III} centers, further exploration of the optical properties of these complexes is warranted. In addition, better insight into the molecular basis for the significantly enhanced zfs of **3** is also of interest. Overall, understanding how small perturbations in structurally similar complexes give rise to large changes in zfs is an important challenge for contemporary inorganic computational chemistry.[12]

In this work, the electronic structure of **1** and **2** were further explored using low-temperature magnetic circular dichroism (MCD) and variable-temperature, variable-field (VTVH) MCD spectroscopy coupled with *ab initio* complete active space self-consistent field (CASSCF) calculations with second-order *n*-electron valence state perturbation theory (NEVPT2) correction. (We note that corresponding MCD investigations of **3** were repeatedly thwarted by the facile oxidation of this complex, as well as the strong MCD signals of the Mn^{IV} decay product.) As described elsewhere,[13] analysis of MCD spectra of paramagnetic transition-metal complexes can yield ligand-field and charge-transfer transition energies, which can greatly complement analysis of electronic absorption spectra. Moreover, the VTVH behavior of a given MCD signal is reflective of both ground-state spin Hamiltonian parameters (*g*-values and, for $S >$ ½ systems, zfs parameters) and the transition moment product of the electronic transition under interrogation. Thus, a careful analysis can yield transition polarizations for randomly-oriented samples, which can be a great aid in developing spectral assignments. While this approach has been used with success in analyzing the electronic structure of a limited number of mononuclear Mn^{III} centers in Mn-dependent enzymes[14] and corresponding model complexes,[1e,13e,15] all of these previous examples contained $S = 2$ Mn^{III} centers. To the best of our knowledge, the MCD

method has not been applied to Mn^{III} centers with $S = 1$ ground states. Here we have analyzed the variable-temperature behavior of the MCD data of **1** and **2** to provide band assignments that permit a comparison of the electronic structures of these complexes. The results of the MCD analysis are also used to validate the electronic structure computations. The CASSCF/NEVPT2 calculations are able to better reproduce the zfs parameters of **1** and **2** than DFT methods. More significantly, the CASSCF/NEVPT2 calculations properly predict a large magnitude D value for **3**, which can be related to the increased σ-donor properties of the NHC ligands.

6.2 Experimental Section

6.2.1. Materials. Solid samples of **1** and **2** with SbF_6^- as the counteranion were either supplied by F. A. Schultz or prepared following the procedure his group reported.[2] A solid sample of **3** with $CF_3SO_3^-$ as the counteranion was prepared as previously described.[10] All other chemicals were obtained from commercials vendors and used without further purification.

6.2.2. Magnetic Circular Dichroism Experiments. Magnetic circular dichroism (MCD) spectra were collected on a spectropolarimeter (Jasco J-815) interfaced with a magnetocryostat (Oxford Instruments SM-4000-8) capable of horizontal fields up to 8 T. MCD spectra were collected at 2, 4, 8, and 15 K for positive and negative field strengths of 1 to 7 T in 1 T increments. All MCD samples were prepared as thin mull samples by preparing a thick paste using Fluorolube®. Unfortunately, although prepared in an argon-filled glovebox and immediately flash-frozen in liquid nitrogen upon removal from the box, we were unable to collect MCD spectra for **3** that were not contaminated with signals associated with the Mn^{IV} oxidation product, $[\{PhB(MeIm)_3\}_2Mn^{IV}]^{2+}$, which has been previously reported as the bis(triflate) salt,[23] prepared via oxidation of a Mn^{II} precursor, rather than from **3**. The MCD

properties of $[\{PhB(MeIm)_3\}_2Mn^{IV}]^{2+}$ are of interest in their own right and will be reported in a separate study.

6.2.3. Computational Methods. The ORCA 3.0.1 software package[24] was used for DFT and *ab initio* CASSCF/NEVPT2 calculations. Initial models of **1**, **2**, and **3** were obtained from X-ray crystal structures,[2,10] and used for subsequent calculations without modification. In the case of **1** and **3**, subsequent calculations were also performed using models where the positions of the hydrogen atoms were energy minimized using DFT methods, but all other atoms retained their crystallographic positions. Comparison of calculated zfs parameters for these two structures revealed only very minor changes (changes in D of less than 0.2 cm^{-1}) following the constrained optimization. Cartesian coordinates for all complexes examined are included in Supporting Information (Tables A6.1 – A6.5). DFT calculations[25] performed for **1**, **2**, and **3** used the B3LYP functional[26] and SVP (Ahlrichs split valance polarized)[27] basis set with the SV/J auxiliary basis set on carbon and hydrogen atoms with the larger TZVP (Ahlrichs triple-ζ valence polarized) on manganese, nitrogen, and boron atoms (for **1** and **2**) as well as the coordinating carbon atoms (for **3**). The resolution of identity (RIJCOSX)[28] approximation was used for all calculations. State-averaged CASSCF/NEVPT2 calculations[29] employed the RI approximation and the SVP basis set for carbon and hydrogen as well as the TZVP basis set for manganese, nitrogen, boron, and coordinating C (for **3**) atoms. For **1**, **2**, and **3**, the calculations were performed with five quintet roots, ten triplet roots, and ten singlet roots and the active space CAS(4,5). A representative ORCA input file for the CASSCF/NEVPT2 calculation of **1** is given in Appendix A6.

6.3 Results and Discussion

6.3.1. Ligand Field Theory Analysis of $S = 1$ Mn^{III} Centers. Before discussing the MCD spectra of **1** and **2**, we first summarize the previously described electronic structure

description of these complexes, as this provides an excellent framework for understanding the MCD data. Because of the trigonal symmetry of these complexes, the Mn^{III} 3*d* orbital splitting pattern is atypical for a six-coordinate complex. With the molecular *z*-axis along the B–Mn–B vector (*i.e.*, the trigonal axis), and thus not oriented along any metal-ligand bond axis, the Mn^{III} $3d_z^2$ orbital (a_{1g} symmetry, using D_{3d} labels) is lowest in energy and doubly-occupied (Figure 6.2). At higher energy are a set of e_g orbitals ($d_{x^2-y^2}$, d_{xy}), each of which contains one electron. At highest energy, and unoccupied, lie another e_g set (d_{xz}, d_{yz}). It is important to consider that, because of the D_{3d} symmetry there is mixing within and between the e_g sets, and the canonical labels (*i.e.*, $d_{x^2-y^2}$ and d_{xy}) are not meaningful.[16] Although there are alternative frameworks that take such mixing into account,[17] we will nonetheless use the conventional orbital labels for the sake of familiarity.

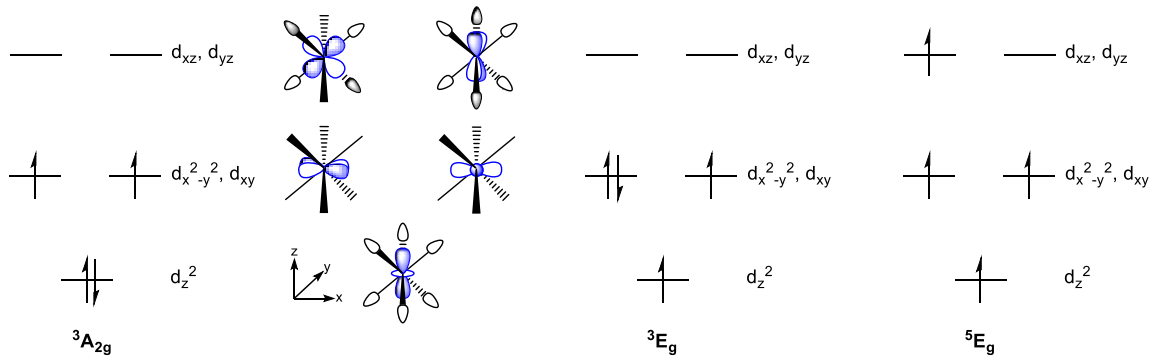

Figure 6.2. Left: Low-spin d^4 orbital splitting of **1**, **2**, and **3** in D_{3d} symmetry with ground state electron occupancy and schematic MO plots showing Mn^{III} 3*d* orbitals with appropriate symmetry-adapted linear combinations of ligand orbitals. Right: Electron occupancies for the two lowest excited states, ^3E_g and ^5E_g, are shown for comparison.

The ligand-field excited-states arising from this orbital splitting pattern are summarized in Figure 6.3, where the parent O_h states are included for comparison. The $^3T_{1g}$ ground state of O_h symmetry splits into $^3A_{2g}$ and ^3E_g components. The configurations for these states are shown in Figure 6.2 (right). On the basis of previous magnetic measurements, **1** and **2** have a $^3A_{2g}$

ground-state, estimated by LFT and AOM calculations to be ~4 000 cm^{-1} below the ^3E_g state.[10] The ground-state of **3** could not be determined from the previous work, although the splitting between the $^3A_{2g}$ and ^3E_g states is certainly smaller. The previous analysis also placed the ^5E_g excited state (i.e., the "conventional", high-spin state) of **1** and **2** at ~14 000 and ~12 000 cm^{-1}, respectively, above the $^3A_{2g}$ ground-state. At significantly higher energy, there are a cluster of triplet states (Figure 6.3), all of which should contribute to the optical properties of these complexes.

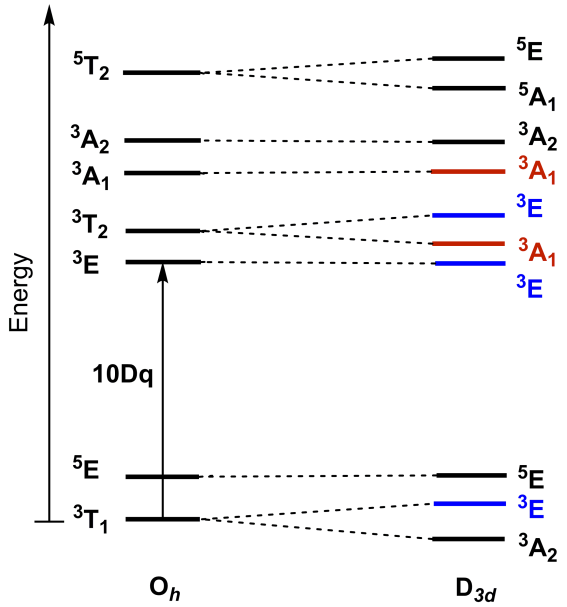

Figure 6.3. Ligand-field energy level diagram for S = 1 Mn^{III} (d^4) system in O_h and D_{3d} symmetries (g subscripts have been omitted for clarity in both cases). The ^3E (blue) and $^1A_1$ (red) excited states will give rise to x,y- and z-polarized transitions, respectively.

For **1** and **2**, electronic transition assignments are aided using transition polarizations. For example, $^3A_2 \rightarrow {}^3E$ excitations will be x,y-polarized, while $^3A_2 \rightarrow {}^3A_1$ transitions will be z-polarized. In principle, transition polarizations can be obtained from analysis of variable-temperature, variable-field MCD data, which are sensitive to both ground-state spin Hamiltonian parameters and transition polarizations.[13b,13c] In this analysis, the MCD signal intensity is monitored as a function of magnetic field strength at various fixed temperatures. Then the resulting MCD curves can be fitted using standard methods. This approach is often used to

determine zfs parameters and transition polarizations for paramagnetic metal complexes.[13a-c,13f] However, detailed analysis of VTVH MCD data using common fitting procedures is warranted only when VTVH MCD data collected at a specific wavelength contain contributions from a *single electronic excited state*. The large cluster of closely-space triplet states expected for **1** and **2** (Figure 6.3) renders this scenario unlikely. Accordingly, we deem it unwise to fit VTVH MCD data for **1** and **2** using standard methods.

However, because **1** and **2** contain triplet ground states with fairly sizeable zero-field splittings, the temperature-dependent behavior of the MCD signals can be used directly to determine transition polarizations. This situation is completely analogous to MCD studies of S = 1 $[Fe^{IV}=O]^{2+}$ complexes.[18] As described by Solomon and co-workers,[18c] for such systems, z-polarized transitions (i.e., with the external field along x/y) will show an inverse temperature dependence that is typical of paramagnetic centers, with signal intensity decreasing as temperature is increased. Under these conditions, the lowest-energy sublevel (M_S = -1) is MCD active (Figure 6.4, right). In contrast, x,y-polarized transitions (external field along z) will show a more complicated temperature dependence. For these transitions, MCD signal intensity will be small at lowest temperatures, because the MCD-inactive M_S = 0 sublevel will be predominantly populated under these conditions (Figure 6.4, left). MCD intensity for these x,y-polarized transitions will show an initial rise with increasing temperature, as the M_S = -1 and +1 sublevels are thermally populated, and then decrease in intensity at higher temperatures. We note that, unlike the "typical" VTVH MCD analysis, this analysis does not provide quantitative determination of zfs parameters. However, this is not a significant drawback in the present case, as accurate values for the D and E parameters of **1** and **2** have been determined by other methods.

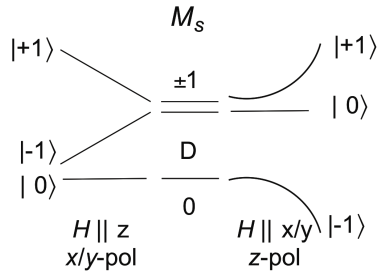

Figure 6.4. Magnetic-field-induced splitting of M_s sublevels for an S = 1 ground state with sizeable zfs (D). The left-hand side shows the response of an S = 1 ground state when the magnetic field is along the z-axis, which would correspond to an x,y-polarized transition. The right-hand side shows the response when the magnetic field is along the x/y-axis, which would correspond to a z-polarized transition. This analysis assumes a small rhombic splitting, which is appropriate for **1** and **2**.

6.3.2 Magnetic Circular Dichroism Studies of 1 and 2. MCD studies of **1** and **2** were performed to compare the ligand-field transition energies for these complexes, and provide electronic transition energies to use in validating electronic structure computations. MCD data for **2** are discussed first, as their interpretation is marginally more straightforward. MCD spectra collected for **2** at different magnetic field strengths and temperatures are shown in Figure 6.5 (left and right, respectively). From the variable-field MCD data (Figure 6.5, left), a minimum of six bands can be identified. Bands 1 and 2 contribute to a pseudo-A term (temperature-dependent, derivative-shaped feature), centered at 23 000 cm^{-1}, which dominates the MCD spectra. This MCD features roughly corresponds to the shoulder observed in the solid-state electronic absorption spectrum at 21 100 cm^{-1} that was tentatively assigned as the $^3T_{1g} \rightarrow {}^3E_g$ transition (using O_h symmetry labels).[2] The MCD intensity of the components of the pseudo-A term maximize (*i.e.*, show the most intense positive and negative features) at 15 K, indicating an x,y-polarized transition. Thus, the pseudo-A term can be attributed to the $^3A_2 \rightarrow {}^3E$ (^3E_g) excitation (Figure 6.3), supporting the assignment made for the electronic absorption spectrum of **2**. Indeed, an orbitally-degenerate (or near-degenerate) E excited state should exhibit strong in-state spin-orbit coupling, giving rise to an MCD pseudo-A term.[13a,13b,13d] Bands 3 and 4, which

are at slightly higher energy (23 730 and 25 270 cm^{-1}), are *z*-polarized, as the intensity for these bands are maximized at 2 K and decrease with increasing temperature (Figure 6.5, right). Bands 3 and 4 are therefore assigned as the $^3A_2 \rightarrow {}^3A_1$ ($^3T_{2g}$) and $^3A_2 \rightarrow {}^3A_1$ ($^3A_{1g}$) excitations, respectively.

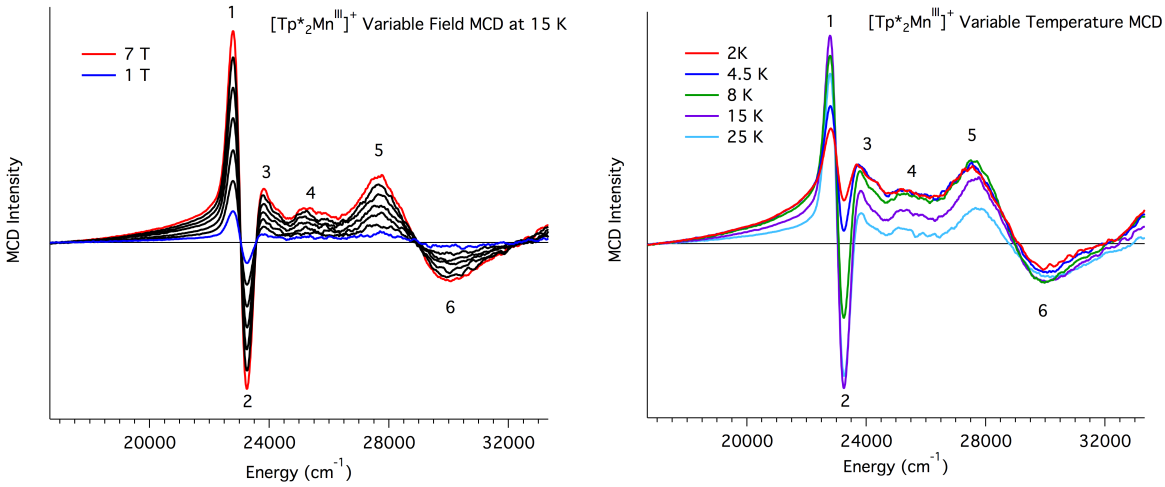

Figure 6.5. 15 K variable-field (left; field decreasing from 7 to 1 T in 1 T increments; the 7 T trace is in red and the 1 T trace is in blue) and 7 T variable-temperature (right) MCD spectra of a mull sample of **2**.

Bands 5 and 6 form another pseudo-A term centered at 28 800 cm^{-1} (Figure 6.5). Band 5 appears to show an inverse temperature dependence, consistent with a *z*-polarized transition, although there is no increase in MCD intensity from 8 to 2 K. Band 6 shows a minor increase in intensity with increasing temperature. Thus, band 6 could arise from an *x,y*-polarized transition that is overlapping with *z*-polarized transition(s). In any case, the development of precise band assignments for this spectral region is complicated by the large number of closely-spaced transitions with different MCD signs and temperature dependencies. As described in more detail below, CASSCF/NEVPT2 calculations for **2** predict four electronic transitions from 26 420 – 27 470 cm^{-1}.

Table 6.1. MCD Band Energies,[a] Polarizations, and Assignments for **2** and **1**

2				**1**			
band	energy	polarization	assignment	band	energy	polarization	assignment
1	22 790	*x,y*	$^3A_2 \rightarrow {}^3E\ (^3E_g)$	1	23 640	*x,y*	$^3A_2 \rightarrow {}^3E\ (^3E_g)$
2	23 250	*x,y*		2	24 500	*x,y*	
3	23 730	*z*	$^3A_2 \rightarrow {}^3A_1\ (^3T_{2g})$	3	25 050	*z*	$^3A_2 \rightarrow {}^3A_1\ (^3T_{2g})$
4	25 270	*z*	$^3A_2 \rightarrow {}^3A_1\ (^3A_{1g})$	4	26 000[b]	*x,y*	$^3A_2 \rightarrow {}^3E\ (^3T_{2g})$
5	27 530	*z*	[c]	5	25 950		$^3A_2 \rightarrow {}^3A_1\ (^3A_{1g})$
6	29 980	*x,y*	$^3A_2 \rightarrow {}^3E\ (^3T_{2g})$	6	28 870	*x,y*	$^3A_2 \rightarrow {}^3E\ (^3T_{2g})$
				7	32 000		*B*-term

[a] Because of the complex appearance and variable-temperature behavior of the MCD spectra of **1** and **2**, band energies are based on the observed maxima of the MCD features rather than being obtained through a Gaussian deconvolution. [b] The position of this band is poorly-defined. [c] The assignment for this band is uncertain.

At first glance, the MCD spectrum of **1** looks quite different from that of **2** (see Figures 5.5 and 5.6). Given the structural similarities of these complexes, as well as their similar electronic absorption properties, this is unexpected. However, a more detailed analysis of the temperature- and field-dependence of the MCD spectrum of **1** reveals that its excited-state energies are actually quite similar to those of **2** (Table 6.1). The major difference is a fairly uniform blue-shift in the transition energies of **1**, which would be consistent with its slightly stronger ligand field, as imposed by shorter Mn–N bond lengths. The difference in appearance of the MCD spectra of **1** and **2** arises because of subtle shifts in the energies of the strongly overlapping *x,y*- and *z*-polarized transitions. For example, band 1 in the MCD spectra of **1** shows an increase in MCD intensity with increasing temperature, with a maximum at 15 K. This behavior marks band 1 as an *x,y*-polarized transition arising from the $^3A_2 \rightarrow {}^3E\ (^3E_g)$ excitation. The energy of this excitation is blue-shifted, but by only ~900 cm^{-1}, compared to **2**. For **1**,

however, the negative component of this pseudo-*A* term (band 2, 24 500 cm^{-1}) is obscured by overlap with band 3, which is only slightly higher in energy (25 050 cm^{-1}) and shows an inverse temperature dependence characteristic of a *z*-polarized transition. Band 3 is thus assigned as the $^3A_2 \rightarrow {}^3A_1$ ($^3T_{2g}$) excitation, which is blue-shifted by 1 300 cm^{-1} compared to **2** (Table 6.1). At higher energies, the overlap of several transitions (bands 4 – 6) leads to complex temperature-dependent behavior (Figure 6.6, right), and unambiguous band assignments are not possible. However, as band 6 shows an increase in MCD intensity from 2 – 8 K, it arises from an *x,y*-polarized transition, and is assigned as the positively-signed component of the $^3A_2 \rightarrow {}^3E$ ($^3T_{2g}$) transition. We tentatively identify the negative-component of this transition to band 4, which occurs near 26 000 cm^{-1} (Figure 6.6). The temperature-dependence of the MCD signal between 25 500 and 28 000 cm^{-1} requires a negatively-signed MCD signal that maximizes intensity at a temperature other than 2 K (band 4) and a positively-signed MCD signal near 26 000 cm^{-1} with maximum intensity at 2 K (band 5). On the basis of these observations, we attribute band 5 to the $^3A_2 \rightarrow {}^3A_1$ ($^3A_{1g}$) transition. Lastly, band 7, which shows intensity changes as a function of field but not temperature, is tentatively attributed to an MCD *B*-term signal.[13d]

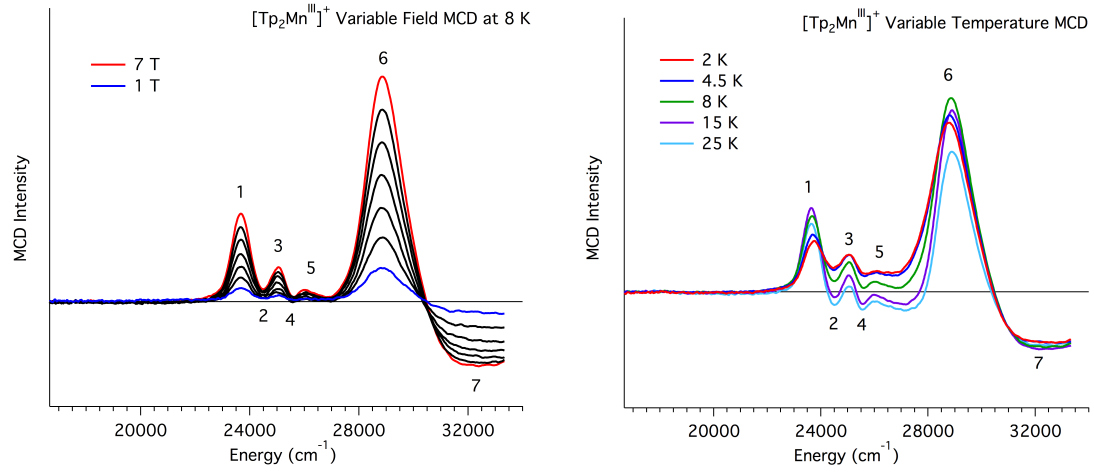

Figure 6.6. 8 K variable-field (left; field decreasing from 7 to 1 T in 1 T increments; the 7 T trace is in red and the 1 T trace is in blue) and 7 T variable-temperature (right) MCD spectra of a mull sample of **1**.

6.3.3. CASSCF/NEVPT2-calculated Electronic Structure.

6.3.3.1. Ligand-field Excited-state Energies for 1 and 2. In order to better understand the MCD properties of **1** and **2**, as well as identify structural and electronic factors contributing to the different zfs of **1**, **2**, and **3**,[10] we performed CASSCF/NEVPT2 calculations for these three complexes. This efficient *ab initio* method has been shown to be quite reliable at treating the ground- and excited-state properties of large transition metal complexes.[1e,12,19] First, we will compare the calculated ligand-field excited-state energies with the MCD data of **1** and **2**. Then we will discuss calculated zfs parameters for **1**, **2**, and **3** in light of previously published HFEPR and magnetic susceptibility measurements.

Ligand-field state energies from CASSCF/NEVPT2 calculations for **1** and **2** are provided in Table 6.2 and Figure 6.7. For both complexes, these calculations predict a $^3A_2$ ground state with a low-lying $^3E(^3T_{1g})$ state at 4 200 and 4 400 cm^{-1}, respectively (because of slight deviations from true D_{3d} symmetry in the models, all ^3E states are split slightly, as shown in Table 6.2; when referring to E states in the text, we will give the energy of the lowest component). This result is in excellent agreement with previous AOM and LFT calculations for these complexes.[10] The $^5E(^5E_g)$ excited state, which is the lowest-energy quintet state, is at similar energy (4 400 and 3 800 cm^{-1} for **1** and **2**, respectively). Thus, for **2**, $^5E(^5E_g)$ is the lowest-lying excited state. The next triplet excited states for **1** and **2**, $^3E(^3E_g)$, are at 24 250 and 23 140 cm^{-1}, respectively. These calculated energies are not only in excellent agreement with the experimental energies (23 640 and 22 790 cm^{-1}, respectively), the slight red-shift calculated for **2** nicely reproduces the observed trends from the MCD data, where the lowest-energy band of **2** (band 1) is 1 050 cm^{-1} less than the corresponding band of complex **1** (Table 6.2). For **1**, a cluster of four additional triplet excited states ($^3A_1$, ^3E, $^3A_1$, and $^3A_2$) are predicted within the narrow range of 25 180 and 27 880 cm^{-1} (Table 6.2), in good agreement with our assignments of bands 3 – 6, which appear

from 25 000 to 29 000 cm^{-1} in the MCD spectra of **1** (Figure 6.6). The corresponding calculated excited states for **2** are red-shifted relative to **1**, appearing from 24 350 to 27 280 cm^{-1} (Table 6.1), also in excellent agreement with the MCD data for **2** that show a cluster of at least three bands in this region (Figure 6.5). On the basis of these calculations, band 5 of **2** is tentatively attributed to a component of the $^3A_2 \rightarrow {}^3E(^3T_2)$ excited state. The MCD intensity of this transition should overlap considerably with the MCD intensities of the $^3A_2 \rightarrow {}^3A_1(^3T_2)$ and $^3A_2 \rightarrow {}^3A_1(^3A_1)$ transitions, which are all of similar energy (Table 6.2). This would account for the unusual temperature dependence of band 5. At slightly higher energy, $^5A_1$ and ^5E excited states are predicted for both complexes. It is possible that these states, as well as charge-transfer excited states, could also contribute to bands 6 and/ or 7 in the higher-energy region of the MCD spectra of **1** and **2**. Taken together, the CASSCF/NEVPT2 excited-state energies corroborate assignments that the visible electronic absorption and MCD features of **1** and **2** arise from a cluster of closely-spaced triplet excited states. These calculations also reproduce the slightly smaller ligand-field strength imposed by the Tp^{*-} ligands of **2**.

Table 6.2. CASSCF/NEVPT2-Calculated Electronic Transitions Energies (cm^{-1}) for **1**, **2**, and **3**, and MCD Band Energies for **1** and **2**.

Transition	CASSCF/NEVPT2			MCD[a]	
	1	**2**	**3**	**1**	**2**
$^3A_2 \rightarrow {}^3E\ (^3T_{1g})$	4 200 4 380	4 400 4 490	980 1 100		
$^3A_2 \rightarrow {}^5E\ (^5E_g)$	4 400 4 920	3 800 4 220	14 180 15 580		
$^3A_2 \rightarrow {}^3E\ (^3E_g)$	24 250 24 950	23 140 24 190	33 550 34 480	23 640 24 500	22 790 23 250
$^3A_2 \rightarrow {}^3A_1\ (^3T_{2g})$	25 180	24 350	34 520	25 050	23 730
$^3A_2 \rightarrow {}^3E\ (^3T_{2g})$	25 380 25 670	24 860 25 090	34 520 35 280	26 000 28 870	29 980
$^3A_2 \rightarrow {}^3A_1\ (^3A_{1g})$	27 020	26 420	35 500	25 950	25 270
$^3A_2 \rightarrow {}^3A_2\ (^3A_{2g})$	27 880	27 280	36 230		
$^3A_2 \rightarrow {}^5A_1\ (^5T_{2g})$	28 920	27 390	51 140		
$^3A_2 \rightarrow {}^5E\ (^5T_{2g})$	29 200 33 450	27 470 32 450	51 420 52 990		

[a] The MCD energies given here correspond to the observed band maxima in the 8 K, 7 T spectra. Because the MCD spectra reflect the overlap of a large number of electronic transitions with different signs and temperature-dependent intensities, the energies of the band maxima could very well be different than the energies of the electronic transitions.

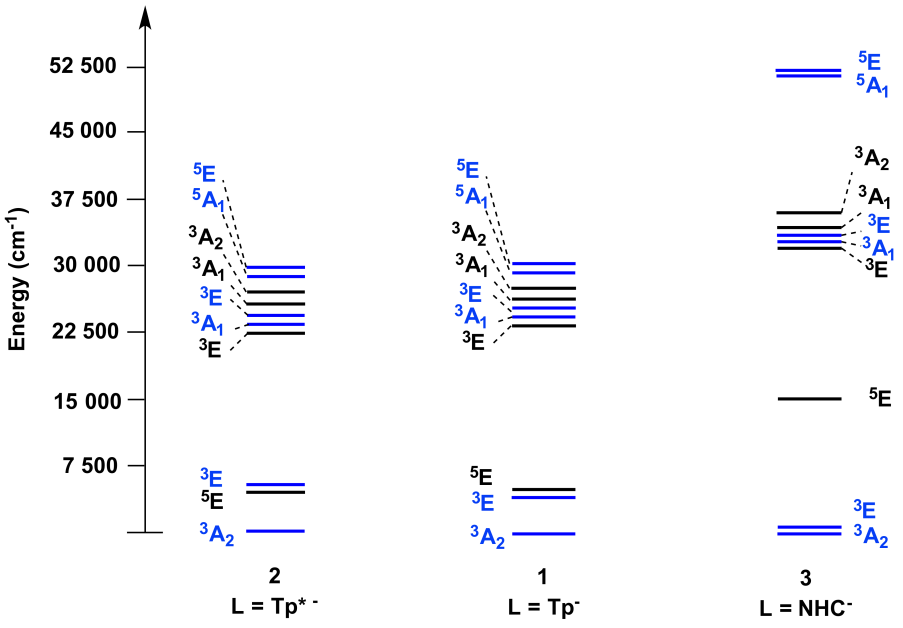

Figure 6.7. CASSCF/NEVPT2-calculated states for **2** (left), **1** (center), and **3** (right).

6.3.3.2. Ground-state zfs Parameters for 1, 2, and 3. The *ab initio* CASSCF/NEVPT2 calculations were also used to provide insight into the zfs parameters of the low-spin Mn^{III} complexes. The D values predicted for **1** and **2** (+16.30 and +14.33 cm^{-1}, respectively; Table 6.3), are each within 10% (< 2 cm^{-1} in absolute terms) of their experimental values (+17.97 and +15.89 cm^{-1}, respectively). This is significantly better agreement than that observed for the previously reported DFT-calculated zfs parameters,[10] which are included in Table 6.3 for comparison. It is important to note that the D value computed by the CASSCF/NEVPT2 method includes only the spin-orbit coupling contribution (D_{SOC}). The spin-spin coupling contribution (D_{SSC}) is omitted. However, the previously-reported CP-DFT computations gave D_{SSC} of 1.0 - 1.8 cm^{-1},[10] showing that this term is only a minor contributor to the overall D value. The CASSCF/NEVPT2-calculated E/D values are also in good agreement with their experimental counterparts (Table 6.3), but with **2** predicted to be slightly too rhombic. CASSCF/NEVPT2 calculations for **3** predict a D value of +37.11 cm^{-1}, which is more than twice as large as that of **1** or **2**. This is consistent with the experimental observation that **3** has a D value unusually large in magnitude.[10] However, the calculated D value for **3** is positive, which is in disagreement with the experimental estimate (D = -49.9 cm^{-1}). The E/D value calculated for **3** (0.042) is, however, in excellent agreement with the experimental value (0.040).

It must be noted, however, that the experimental situation regarding HFEPR and magnetometry for **3** was much inferior to that for **1** and **2**.[10] Both **1** and **2** have orbitally non-degenerate ground states, well separated in energy from excited states, so that an S = 1 spin Hamiltonian analysis of the HFEPR and magnetic data was appropriate and highly successful in fitting both types of measurement with essentially the same parameter set.[10] In contrast, as discussed below, **3** has an electronic ground state that is not suitable for a simple, spin Hamiltonian analysis. Moreover, complex **3** exhibited no HFEPR spectra and obtaining magnetic

data was complicated by the reactivity of the complex. The situation for **3** can be contrasted to that for another, reactive, early transition metal complex with an $S = 1$ ground state, namely *trans*-[$TiCl_2(py)_4$] (py = pyridine), which contains Ti^{II} ($3d^2$), and has a ^3E electronic ground state.[19j] This Ti^{II} complex did exhibit HFEPR spectra, which, together with the magnetic data, were analyzed using an $S = 1$ spin Hamiltonian to yield a large magnitude, but negative D value, with a small rhombic component, which component was the origin of the observed HFEPR signal. The observation of HFEPR for the Ti^{II} complex with its negative D value versus the lack of any HFEPR signal for **3** is consistent with its D value being large in magnitude, but positive in sign, as suggested here by computations.[20] On the other hand, although the determination of sign of zfs solely from magnetic susceptibility is in general problematic,[21] fitting of the experimental dc susceptibility data for **3** was unequivocal in support of a negative value for D (see Figure A6.1).

Table 6.3. Experimental, and Calculated Zero Field Splitting Parameters for **1**, **2**, and **3**[a]

	Experimental[b]			CP-DFT[b]			CASSF/NEVPT2		
	1	**2**	**3**	**1**	**2**	**3**	**1**	**2**	**3**
D	17.97	15.89	-49.90	10.78	9.42	8.26	16.30	14.33	37.11
E/D	0.023	0.003	0.040	0.004	0.001	0.045	0.020	0.014	0.042
E	0.42	0.04	2.00	0.042	0.016	0.371	0.324	0.200	1.56

[a] D and E values are in cm^{-1}. [b] Experimental and CP-DFT-computed ZFS parameters were taken from reference 10. These previously reported CP-DFT calculations revealed that D is dominated by the spin-orbit coupling component (D_{SOC}), which accounted for 90 - 95% of the overall magnitude. The spin-spin coupling component (D_{SSC}) contributes the remainder.

Regardless of the ambiguity in the sign of zfs in **3**, the CASSCF/NEVPT2 calculations also afford the opportunity to understand the basis for the different zfs parameters of **1**, **2**, and **3** in terms of contributions from ligand-field excited states, as shown in Figure 6.8 and Tables A6.6 – A6.8. For **1** and **2**, the components of the $^3T_{1g}$ parent state of O_h symmetry make contributions to D of ~2 cm^{-1} in magnitude, but these contributions are of opposite sign and effectively cancel. The dominant contributions to D come from singlet excited states; in particular the $^1A_1(^1T_{2g})$ and

$^1A_1(^1A_{1g})$ excited states both provide large positive contributions (Figure 6.8). For **1**, these excited states are at slightly lower energy and make larger contributions, accounting for the increase in magnitude of *D* for **1** as compared with **2**. For complex **3**, the $^1A(^1T_{2g})$ and $^1A_1(^1A_{1g})$ states still make large contributions to *D*, but the low-lying $^3E(^3T_{1g})$ state makes the dominant contribution. The $^3E(^3T_{1g})$ state of **3** is only ~1 000 cm^{-1} higher in energy than the $^3A_2$ ground state, which would lead to stronger mixing between these states. Thus, the large increase in *D* of **3** compared to **1** and **2** has its origin in a substantially smaller splitting between the $^3A_2$ ground state and lowest $^3E(^3T_{1g})$ excited state.

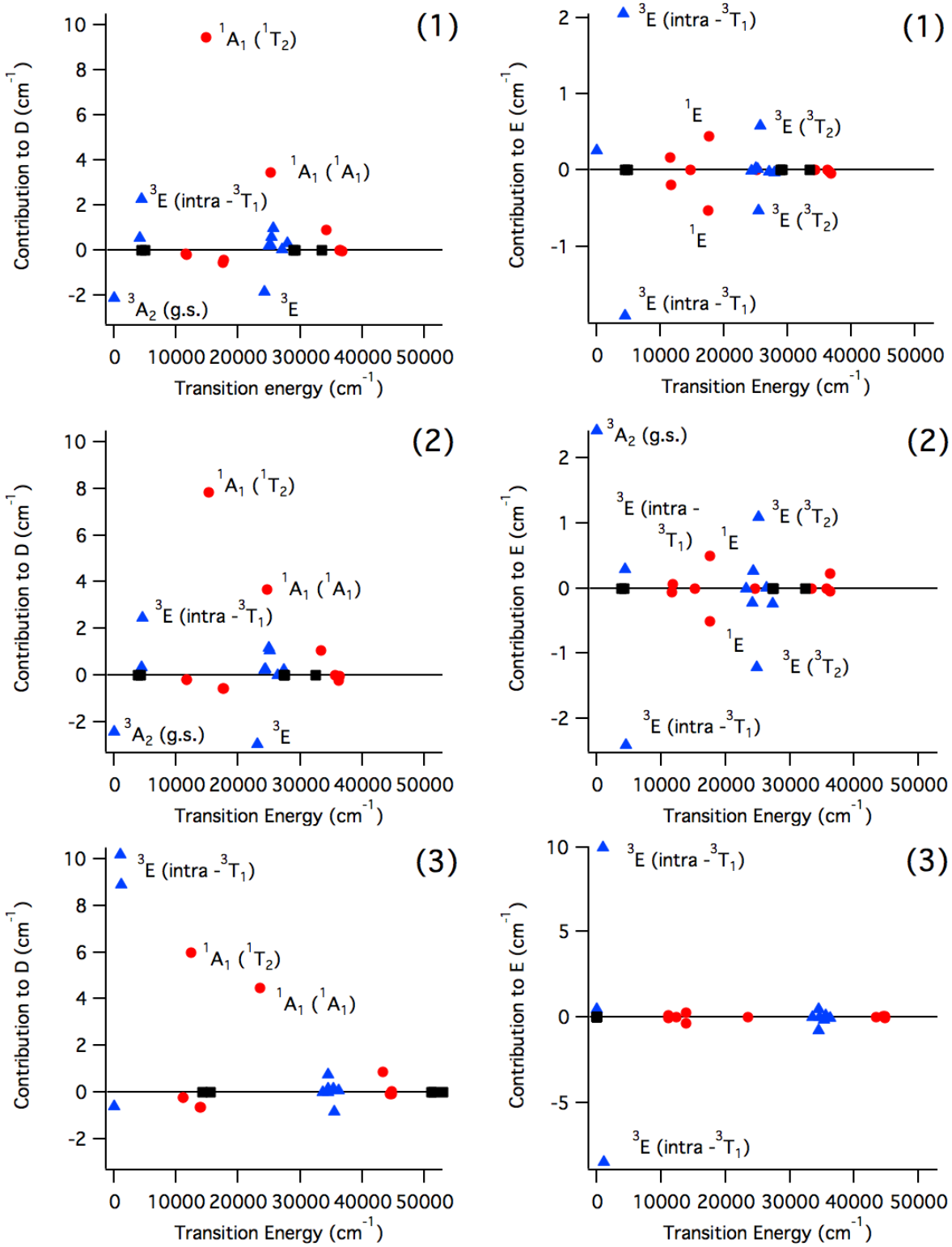

Figure 6.8. Contributions of excited state singlets (red circles), triplets (blue triangles), and quintets (black squares) to *D* (left) and *E* (right) for **1** (top), **2** (middle), and **3** (bottom).

For all three complexes, contributions to the rhombic zfs parameter *E* come predominantly from components of the parent $^3T_{1g}$ ground state, and, in the case of **1** and **2**, the $^1E(^1T_{1g})$, states also contribute (Figure 6.8, right). However, the different components of these E states make oppositely-signed contributions to *E*. Because these E excited states are nearly degenerate, their oppositely-signed contributions are roughly equal in magnitude, which accounts for the small *E* values observed for each complex. On the basis of these observations, the slightly larger rhombicity of **3** can be attributed to larger, albeit still quite small, distortions from true trigonal symmetry.

6.3.3.3. Electronic Structures Descriptions of 1, 2, and 3. As described above, changes in the ligand-field excited-state energies of **3**, compared to **1** and **2**, can account for large changes observed in zfs parameters. In this section we discuss the structural and electronic differences that account for these observations. On the basis of the CASSCF/NEVPT2 calculations, **1** and **2** contain $^3A_2$ ground states, arising from a $(d_z^2)^2(d_{xy},\ d_{x^2-y^2})^2(d_{xz},\ d_{yz})^0$ configuration (95% contribution to the CASSCF wavefunction). For each of these complexes, the higher-energy $(d_z^2)^1(d_{xy},\ d_{x^2-y^2})^3(d_{xz},\ d_{yz})^0$ configuration makes only a 1% contribution to the ground-state wavefunction. Figure 6.9 shows surface contour plots of the CASSCF frontier orbitals for **1**; corresponding plots for **2** and **3** are in Supporting Information (Figures A6.2 and A6.3). These orbital plots echo the bonding description anticipated from ligand-field theory (Figure 6.1); they also highlight the high degree of mixing between the $e(d_{xy},\ d_{x^2-y^2})$ and $e(d_{xz},\ d_{yz})$ sets.

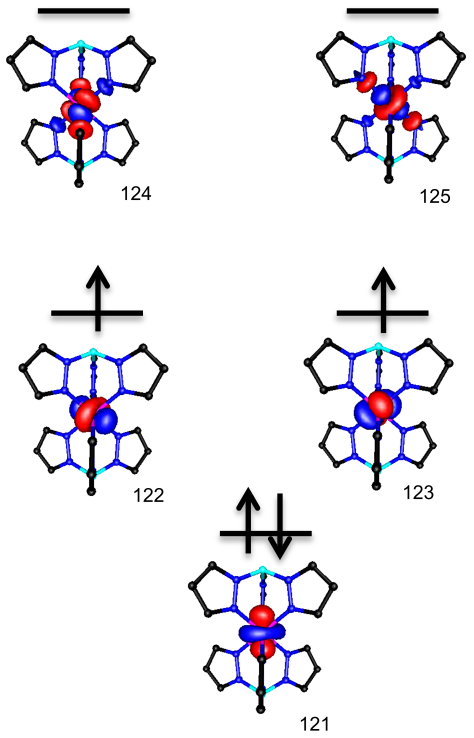

Figure 6.9. Surface contour plots of Mn^{III} 3d-based orbitals for **1** from the CASSCF calculation, with the orbital numbers reflecting the energy ordering. Corresponding orbitals for **2** and **3** are shown in Supporting Information (Figures A6.2 and A6.3, respectively).

Although the CASSCF/NEVPT2 calculations show that **3** retains a $^3A_2$ ground state, the lowest-lying ^3E excited state is now only ~1 000 cm^{-1} higher in energy. In addition, the ground-state CASSCF wavefunction for **3** contains modest multiconfigurational character, being composed of 87% $(d_z^2)^2(d_{xy}, d_{x^2-y^2})^2(d_{xz}, d_{yz})^0$ and 11% $(d_z^2)^1(d_{xy}, d_{x^2-y^2})^3(d_{xz}, d_{yz})^0$. Another marked difference for **3** is that the higher-energy triplet excited states are blue-shifted dramatically, as seen in Figure 6.7. In fact, after the $^3E(^3T_{2g})$ state, the lowest-energy triplet excited state is at 33 550 cm^{-1}. This result appears to be in conflict with the electronic absorption spectrum of **3**, which shows bands at ~550 and 400 nm (18 180 and 25 000 cm^{-1}). Accordingly, the high energy of the calculated excited states is very likely an artifact of the CASSCF/NEVPT2 calculations. A common drawback of the CASSCF method is that it leads to an overly ionic description of bonding. While the purpose of the NEVPT2 correction is to remedy this deficiency through the introduction of dynamic correlation, the extent to which this occurs can

vary from system to system.[19g] Unfortunately, our attempts to compensate through a larger CAS(8,7) active space met with failure due to lack of CASSCF convergence even when using modest level shifting.

The small splitting between the $^3A_2$ and ^3E states of **3** can be understood on the basis of the increased σ-donation of the NHC ligand. The strong σ-donating ability of this type of NHC ligand was previously identified for a set of four-coordinate Ni^{II} complexes through classical LFT.[22] To illustrate the difference in covalency among these three Mn^{III} complexes, we turned to ground-state DFT computations. As shown in Table 6.4, the Mn^{III} $3d_z^2$ MO of **3** is more covalent than those of **1** and **2**, containing three-fold greater ligand character. In addition, the $3d_z^2$ MO of **3** is mixed with the $3d_{yz}$ MO, causing its appearance to differ substantially compared to the corresponding MOs for **1** and **2** (Figure 6.10). This enables π-interactions between the $3d_z^2$ orbital of the Mn^{III} center and the NHC ligand, which further destabilizes this MO. The $3d_z^2$-$3d_{yz}$ mixing in **3** is presumably related to slightly larger distortions from true D_{3d} symmetry for this complex as compared to **1** and **2**.[10] In contrast, the ligand character in the Mn^{III} $3d_{x^2-y^2}$ and $3d_{xy}$ MOs of all complexes is equal (~50% when summed over both MOs). Consequently, the $3d_z^2$–($3d_{x^2-y^2}$, $3d_{xy}$) splitting is smaller for **3** than for **1** and **2** (2.7 eV versus 4 eV). This effect is illustrated in Figure 6.10 and is consistent with the results of the CASSCF/NEVPT2 computations. It could be envisioned that structural differences between **1**, **2**, and **3** facilitate greater σ-overlap between the NHC donors and the Mn $3d_z^2$ orbital by contracting the C–Mn···B angles and distorting the donor atoms away from the Mn center along the *z*-axis (the Mn···B vector),. However, the average C–Mn···B angles of **3** (52.5º) are only marginally smaller than the corresponding N–Mn···B angles of **1** and **2** (53.3º and 54.8º, respectively). Thus, any increase in σ-covalency of the Mn^{III} $3d_z^2$ MO is predominantly electronic in origin, and relates to the far greater σ-donating properties of the NHC ligand as compared to Tp^- and Tp^{*-}. At the same time,

the distortions from true trigonal symmetry for **3** appear to facilitate greater π-covalency in the $3d_z^2$ MO, which further decreases the $3d_z^2$–($3d_{x^2-y^2}$, $3d_{xy}$) splitting.

Table 6.4. DFT-calculated Percent Contributions and Orbital Energies (eV) to Selected Frontier MOs of **1**, **2**, and **3**.

	$3d_z^2$ [a]				$3d_{x^2-y^2}$ [a]				$3d_{xy}$ [a]			
	MO	energy	% Mn	% L[b]	MO	energy	% Mn	% L[b]	MO	energy	% Mn	% L[b]
1	121β	-9.5	93	4	122β	-5.6	70	26	123β	-5.6	70	26
2	169β	-8.8	93	3	170β	-4.8	71	24	171β	-4.8	72	23
3	185β	-7.1	75	11	186β	-4.4	55	30	187β	-4.0	72	18

[a] Mn^{III} $3d_{x^2-y^2}$ and $3d_{xy}$ orbitals are the highest-energy, singly-occupied molecular orbitals.
[b] Ligand orbitals are the sum of the pyrazolyl carbon and nitrogen atoms for **1** and **2** and the sum of the N–C–N moiety for **3**.

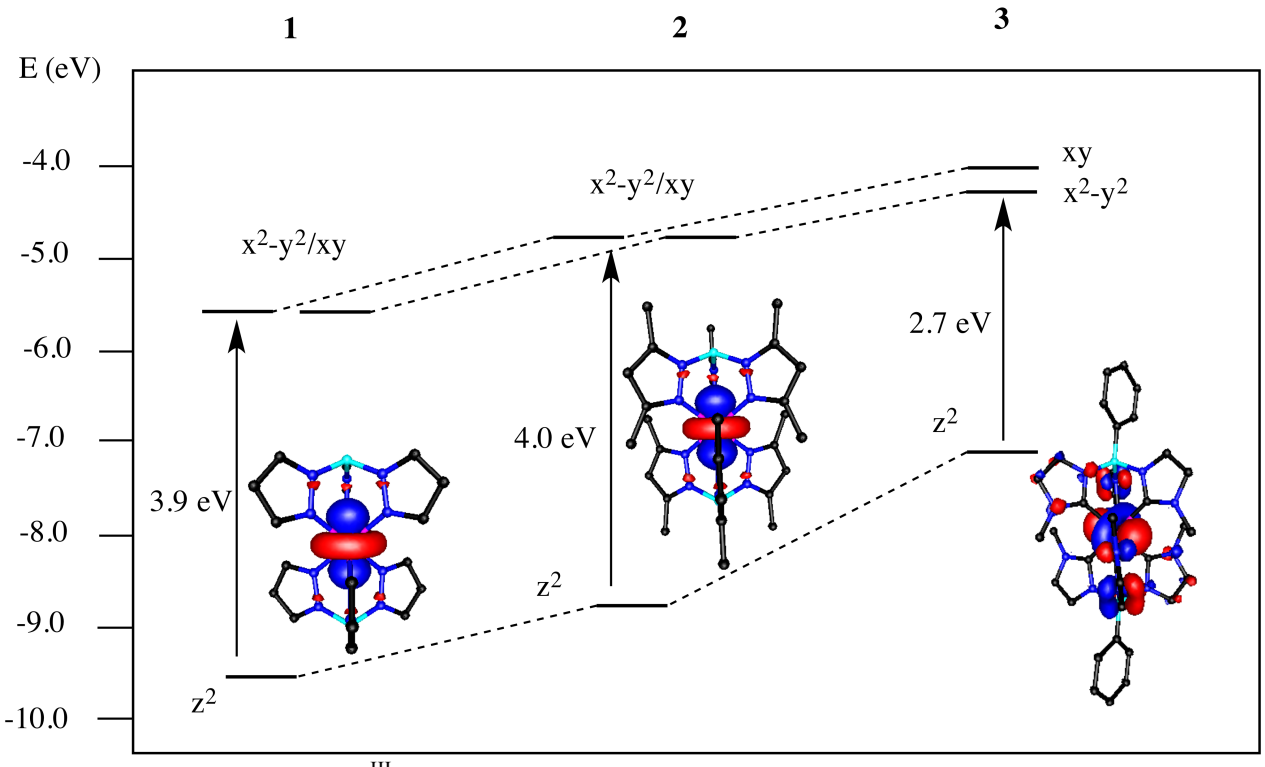

Figure 6.10. Energies of Mn^{III} frontier MOs of **1**, **2**, and **3**, highlighting the strong destabilization of the d_z^2 MO of **3**. Surface contour plots of the Mn^{III} d_z^2 MO of each complex are shown.

6.4 Conclusions

Six-coordinate Mn^{III} in the absence of very strong field ligands (e.g., cyanide) typically affords high-spin (S = 2) complexes, with some interesting exceptions.[4-5] The remarkable and versatile scorpionate ligand, both in its original, hydridotris(pyrazolyl)borate form, and in a newer aryltris(carbene)borate form, which contains the popular *N*-heterocyclic carbene (NHC) donor, leads to bis(scorpionate) complexes of Mn^{III} in the low spin (based on octahedral geometry conventions) state (S = 1). This phenomenon can be attributed qualitatively to the strong donor properties of the scorpionate ligand in combination with the rigorously trigonal symmetry of the bis(scorpionate) Mn^{III} complexes. However, a deeper understanding of this phenomenon had not been provided as the computational requirements for such an analysis are significant. Additionally, such an analysis requires knowledge of the electronic excited states of the complex, which had not been apparent from electronic absorption spectroscopy. MCD spectroscopy, however, provides such information quite effectively. This approach has been shown to be quite powerful in the treatment of high-spin Mn^{III} centers.[1e,13e,14a,14c-f,15a,15b] As demonstrated here, MCD spectroscopy is equally adept at treating low-spin Mn^{III} systems. This technique, particularly with the use of variable fields and temperatures (VTVH-MCD) allowed elucidation of the range of relevant electronic excited states for **1** and **2**. Unfortunately, the propensity of **3** to oxidize to its Mn^{IV} congener, which complex (in the characterized form, $[\{PhB(MeIm)_3\}_2Mn](CF_3SO_3)_2$), is itself of interest and exhibits very strong absorption bands, precluded MCD studies of **3**. This is unfortunate, as such studies would have not only provided electronic transition energies, but could also have helped determine the sign of D. At present, the D value of –49.90 cm^{-1} for **3** rests on fits of previously reported dc magnetic susceptibility measurements.[10] All attempts to refine this value, through HF-EPR or MCD measurements, have been hampered by the instability of **3** towards oxidation to the Mn^{IV} form. Nevertheless,

computational studies of **3** demonstrated a significant difference from **1** and **2**, namely that the lowest lying triplet excited state is much closer in energy in the tris(carbene)borate complex, a consequence of the strong σ-donor properties of the NHC ligand. This was previously postulated on the basis of a detailed ligand-field theory analysis of these complexes.[10] In general, the previous ligand-field theory analysis is fully consistent with the results of the CASSCF/NEVPT2 computations, illustrating the power of this traditional approach. The higher-energy Mn^{III} d_z^2 MO in **3**, as established by the computations described here, might be the basis for **3** being remarkably easy to oxidize, with the Mn^{IV} oxidation state stabilized by over 1 V in comparison to **1** and **2**.[23] In any case, this difference in electronic structure is indeed the basis for the much larger magnitude zfs in **3** versus **1** and **2**, which led to the previously observed dramatic differences in magnetic susceptibility and HFEPR spectroscopic behavior for the two types of complexes, and suggesting a role for supporting ligands in tuning zfs. Our combined VTVH-MCD ab initio computational methods have unraveled the electronic structure of a series of unusual bis(scorpionate) complexes of Mn^{III}, revealing the impact of the great tunability of the scorpionate ligand.

6.5 References

[1] a) N. Kitajima; H. Komatsuzaki; S. Hikichi; M. Osawa; Y. Moro-oka, *J. Am. Chem. Soc.* **1994,** *116*, 11596-11597; b) N. Kitajima; M. Osawa; M. Tanaka; Y. Morooka, *J. Am. Chem. Soc.* **1991,** *113*, 8952-8953; c) M. Osawa; K. Fujisawa; N. Kitajima; Y. Moro-oka, *Chem. Lett.* **1997,** *26*, 919-920; d) U. P. Singh; A. K. Sharma; S. Hikichi; H. Komatsuzaki; Y. Moro-oka; M. Akita, *Inorg. Chim. Acta* **2006,** *359*, 4407-4411; e) H. E. Colmer; R. A. Geiger; D. F. Leto; G. B. Wijeratne; V. W. Day; T. A. Jackson, *Dalton Trans.* **2014,** *43*, 17949-17963.

[2] F. Hossain; M. A. Rigsby; C. T. Duncan; P. L. Milligan; R. L. Lord; M. H. Baik; F. A. Schultz, *Inorg. Chem.* **2007,** *46*, 2596-2603.

[3] W. E. Buschmann; L. Liable-Sands; A. L. Rheingold; J. S. Miller, *Inorg. Chim. Acta* **1999,** *284*, 175-179.

[4] J. M. Smith, *Comments on Inorganic Chemistry* **2008,** *29*, 189-233.

[5] A. P. Forshaw; J. M. Smith; A. Ozarowski; J. Krzystek; D. Smirnov; S. A. Zvyagin; T. D. Harris; H. I. Karunadasa; J. M. Zadrozny; A. Schnegg; K. Holldack; T. A. Jackson; A. Alamiri; D. M. Barnes; J. Telser, *Inorg. Chem.* **2013,** *52*, 144-159.

[6] The X-ray structures of **1** and **2** were of the SBF_6^- salts, **1**(SBF6) and **2**(SBF6), which we have also examined here. The related X-ray structure of **3** was of the triflate salt, **3**(OTf).
[7] M. Atanasov; D. Aravena; E. Suturina; E. Bill; D. Maganas; F. Neese, *Coord. Chem. Rev.* **2015,** *289–290*, 177-214.
[8] a) M. L. Kirk; K. Peariso, *Curr. Opin. Chem. Biol.* **2003,** *7*, 220-227; b) F. Neese; E. I. Solomon, *Inorg. Chem.* **1999,** *38*, 1847-1865; c) V. S. Oganesyan; S. J. George; M. R. Cheesman; A. J. Thomson, *J. Chem. Phys.* **1999,** *110*, 762-777; d) S. B. Piepho; P. N. Schatz, *Group Theory in Spectroscopy with Applications to Magnetic Circular Dichroism*. Wiley: New York, 1983; p 634; e) A. Westphal; A. Klinkebiel; H.-M. Berends; H. Broda; P. Kurz; F. Tuczek, *Inorg. Chem.* **2013,** *52*, 2372-2387; f) F. Paulat; N. Lehnert, *Inorg. Chem.* **2008,** *47*, 4963-4976.
[9] a) J. Whittaker; M. Whittaker, *J. Am. Chem. Soc.* **1991,** *113*, 5528-5540; b) T. A. Jackson; T. C. Brunold, *Acc. Chem. Res.* **2004,** *37*, 461-470; c) T. A. Jackson; C. T. Gutman; J. Maliekal; A.-F. Miller; T. C. Brunold, *Inorg. Chem.* **2013,** *52*, 3356-3367; d) T. A. Jackson; A. Karapetian; A.-F. Miller; T. C. Brunold, *J. Am. Chem. Soc.* **2004,** *126*, 12477-12491; e) T. A. Jackson; J. Xie; E. Yikilmaz; A.-F. Miller; T. C. Brunold, *J. Am. Chem. Soc.* **2002,** *124*, 10833-10845; f) T. A. Jackson; E. Yikilmaz; A.-F. Miller; T. C. Brunold, *J. Am. Chem. Soc.* **2003,** *125*, 8348-8363.
[10] a) R. A. Geiger; G. Wijeratne; V. W. Day; T. A. Jackson, *Eur. J. Inorg. Chem.* **2012**, 1598-1608; b) R. A. Geiger; S. Chattopadhyay; V. W. Day; T. A. Jackson, *J. Am. Chem. Soc.* **2010,** *132*, 2821-2831; c) R. E. Linder; J. R. Rowlands, *Spectrosc. Lett.* **1971,** *4*, 227-36.
[11] A. P. Forshaw; R. P. Bontchev; J. M. Smith, *Inorg. Chem.* **2007,** *46*, 3792-3794.
[12] a) F. Neese, *ORCA - an ab initio, Density Functional and Semiempirical Program Package*, *Version 3.0*, Max Planck Institute for Chemical Energy Conversion, 2013; b) F. Neese, *Wiley Interdisciplinary Reviews: Computational Molecular Science* **2012,** *2*, 73-78.
[13] F. Neese, *J. Chem. Phys.* **2007,** *127*, 164112-164119.
[14] a) A. D. Becke, *J. Chem. Phys.* **1993,** *98*, 1372-1377; b) A. D. Becke, *J. Chem. Phys.* **1993,** *98*, 5648-5652; c) C. Lee; W. Yang; R. G. Parr, *Phys. Rev. B* **1988,** *37*, 785-789.
[15] a) A. Schäfer; H. Horn; R. Ahlrichs, *J. Chem. Phys.* **1992,** *97*, 2571-2577; b) A. Schäfer; C. Huber; R. Ahlrichs, *J. Chem. Phys.* **1994,** *100*, 5829-5835.
[16] F. Neese, *J. Comput. Chem.* **2003,** *24*, 1740-1747.
[17] C. Angeli; R. Cimiraglia; S. Evangelisti; T. Leininger; J.-P. Malrieu, *J. Chem. Phys.* **2001,** *114*, 10252-10264.
[18] This orbital mixing is more extensive than that observed for a system with D_{3h} symmetry, as in that case the d_{xy} and $d_{x^2-y^2}$ orbitals transform as e´, while the d_{xz} and d_{yz} orbitals transform as e´´.
[19] a) B. R. McGarvey, *J. Chem. Phys.* **1963,** *38*, 388-392; b) B. R. McGarvey; J. Telser, *Inorg. Chem.* **2012,** *51*, 6000-6010.
[20] a) A. Decker; J.-U. Rohde; E. J. Klinker; S. D. Wong; L. Que, Jr.; E. I. Solomon, *J. Am. Chem. Soc.* **2007,** *129*, 15983-15996; b) A. Decker; M. D. Clay; E. I. Solomon, *J. Inorg. Biochem.* **2006,** *100*, 697-706; c) A. Decker; J.-U. Rohde; L. Que, Jr.; E. I. Solomon, *J. Am. Chem. Soc.* **2004,** *126*, 5378-5379.
[21] a) C. Duboc; D. Ganyushin; K. Sivalingam; M.-N. Collomb; F. Neese, *J. Phys. Chem. A* **2010,** *114*, 10750-10758; b) J. M. Zadrozny; M. Atanasov; A. M. Bryan; C.-Y. Lin; B. D. Rekken; P. P. Power; F. Neese; J. R. Long, *Chem. Sci.* **2013,** *4*, 125-138; c) M. Atanasov; J. M. Zadrozny; J. R. Long; F. Neese, *Chem. Sci.* **2013,** *4*, 139-156; d) M. Atanasov; D. Ganyushin; D. A. Pantazis; K. Sivalingam; F. Neese, *Inorg. Chem.* **2011,** *50*, 7460-7477; e) D. Maganas; J. Krzystek; E. Ferentinos; A. M. Whyte; N. Robertson; V. Psycharis; A.

Terzis; F. Neese; P. Kyritsis, *Inorg. Chem.* **2012,** *51*, 7218-7231; f) M. Atanasov; P. Comba; S. Helmle; D. Müller; F. Neese, *Inorg. Chem.* **2012,** *51*, 12324-12335; g) D. Schweinfurth; M. G. Sommer; M. Atanasov; S. Demeshko; S. Hohloch; F. Meyer; F. Neese; B. Sarkar, *J. Am. Chem. Soc.* **2015,** *137*, 1993-2005; h) I. Schapiro; K. Sivalingam; F. Neese, *J. Chem. Theory Comput.* **2013,** *9*, 3567-3580; i) M. Atanasov; D. Ganyushin; K. Sivalingam; F. Neese, *Struct. Bonding (Berlin, Ger.)* **2012,** *143*, 149-220; j) G. B. Wijeratne; E. M. Zolnhofer; S. Fortier; L. N. Grant; P. J. Carroll; C.-H. Chen; K. Meyer; J. Krzystek; A. Ozarowski; T. A. Jackson; D. J. Mindiola; J. Telser, *Inorg. Chem.* **2015**.

[22] MCD investigations of **3** were complicated by the strong absorption bands of the Mn(IV) decomposition product. HFEPR of **3** did show some Mn(IV), but this Kramers (half-integer spin) signal is narrow and easily identified and would not interfere with signal from the non-Kramers (integer spin) complex **3**. Relaxation effects, which may be significant due to the close lying excited state, may also prevent observation of HFEPR, even in the case of a negative *D* value.

[23] a) O. Kahn, *Molecular Magnetism*. VHC Publishers, Inc.: New York, NY, 1993; b) J. Krzystek; A. T. Fiedler; J. J. Sokol; A. Ozarowski; S. A. Zvyagin; T. C. Brunold; J. R. Long; L.-C. Brunel; J. Telser, *Inorg. Chem.* 2004, *43*, 5645-5658.

[24] I. Nieto; R. P. Bontchev; A. Ozarowski; D. Smirnov; J. Krzystek; J. Telser; J. M. Smith, *Inorg. Chim. Acta* **2009,** *362*, 4449-4460.

CHAPTER 7

Oxidation Pathways of High-Valent Mn^{IV} Intermediates

7.1 Introduction

High-valent metal-oxo intermediates are featured in numerous enzymes critical for biological processes, such as cytochrome P450 enzymes,[1,2] where the Fe^{IV}-oxo porphyrin-cation-radical species is formed in the catalytic cycle and is responsible for oxidation of the substrate molecule. There have been many efforts to replicate the controlled reactivity and efficiency of these enzymes in high-valent Fe species supported by model ligand systems, with successful examples of substrate oxidation.[3-7] There are also examples of formation of high-valent Mn-oxo species and subsequent substrate oxidation,[8-13] although this chemistry is not as well understood. In particular, it is difficult to predict and reproduce the specificity of product distribution that enzymatic systems are able to efficiently achieve. It is of great interest to produce rationally designed ligand systems to target specific substrate oxidation reactions, although this work is ongoing.

The cross-clamped Me_2EBC ligand provides an excellent avenue to explore the factors that direct the product distribution in substrate oxidation reactions, as this ligand is able to support two stable high-valent Mn^{IV} species, a Mn^{IV}-oxohydroxo species and a Mn^{IV}-dihydroxo species (Figure 7.1), that are both capable of oxidizing 9,10-dihydroanthracene (DHA).[13-15] These high-valent species are well-characterized, both structurally[13] and spectroscopically.[16-18] $[Mn^{IV}(OH)_2(Me_2EBC)]^{2+}$ can be easily prepared from a reaction with $[Mn^{II}(Cl)_2(Me_2EBC)]$ and hydrogen peroxide and ammonium hexafluorophosphate, and $[Mn^{IV}(O)(OH)(Me_2EBC)]^{+}$ forms upon a change in pH to 8.8.[13,15] Additionally, experimental activation enthalpies ($\Delta H^{\ddagger}$ = 13.1 ± 0.7 and 12.1 ± 1.8 kcal/mol) and entropies ($\Delta S^{\ddagger}$ = -27.9± 2.0 and -24.5 ± 2.2 cal mol^{-1} K^{-1}) for $[Mn^{IV}(OH)_2(Me_2EBC)]^{2+}$ and $[Mn^{IV}(O)(OH)(Me_2EBC)]^{+}$, respectively, are known,[19] and these values provide a method of comparison and validation for calculated transition state energies. The experimental bond dissociation energies (BDE_{OH} = 83 and 84.3 kcal/mol, respectively) for

$[Mn^{IV}(OH)_2(Me_2EBC)]^{2+}$ and $[Mn^{IV}(O)(OH)(Me_2EBC)]^{+}$ have been determined[20] and experimental driving forces can be estimated from the difference in the experimental bond dissociation energies (BDE_{OH}) and the bond dissociation energy of DHA (BDE_{CH} = 78 kcal/mol). (Scheme 7.1).[20,21] These value are useful for comparison to the calculated driving forces.

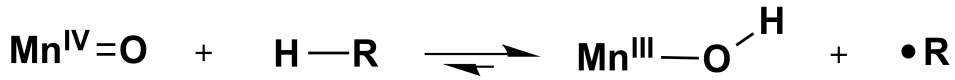

Scheme 7.1. Hydrogen atom abstraction by a Mn^{IV}-oxo for thermodynamic driving force calculation.

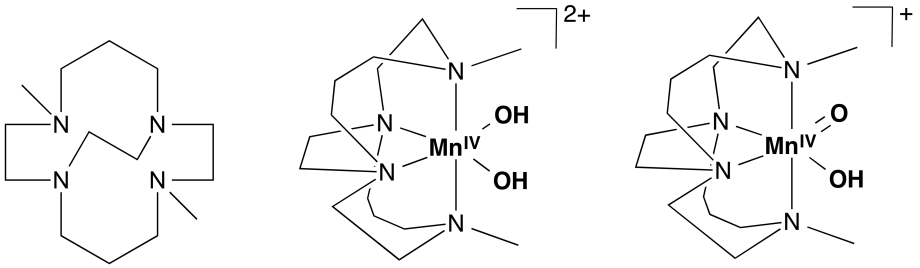

Figure 7.1. Me_2EBC ligand (left), Mn^{IV}-dihydroxo (middle) and Mn^{IV}-oxohydroxo (right) complexes supported by the Me_2EBC ligand.

Although the Mn^{IV}-dihydroxo and Mn^{IV}-oxohydroxo complexes differ by only one proton, they are able to direct product distribution in C—H bond oxidation of DHA, producing either anthracene or anthraquinone as the major product, respectively (Figure 7.2). The Mn^{IV}-oxohydroxo species also displays a 15-fold rate enhancement for the initial C—H bond cleavage step.[12,13,15] To generate the anthracene product, the Mn^{IV}-dihydroxo species undergoes a hydrogen atom transfer from DHA to the Mn^{IV} center, forming a monohydroanthracene radical and a Mn^{III}-aquahydroxo species. Presumably, a second hydrogen atom transfer yields the anthracene major product and the Mn^{II}-diaqua complex (Figure 7.2, top).

In contrast, the Mn^{IV}-oxohydroxo complex directs products to anthraquinone. This reaction is proposed to proceed through the same initial step of hydrogen atom transfer from DHA to the Mn^{IV} center. Here, this reaction yields the monohydroanthracene radical and a Mn^{III}-

dihydroxo species. To generate the hydroxylated anthraquinone species, the second step requires a rebound pathway with transfer of one hydroxide from the Mn center to form a Mn^{II}-hydroxide complex and monohydroxyanthracene, which is then over-oxidized to form anthraquinone (Figure 7.2, bottom). To define the characteristics of each complex that stabilize specific pathways of reactivity, DFT calculations were employed to calculated thermodynamic parameters for the reactivity of DHA with each Mn^{IV} species.

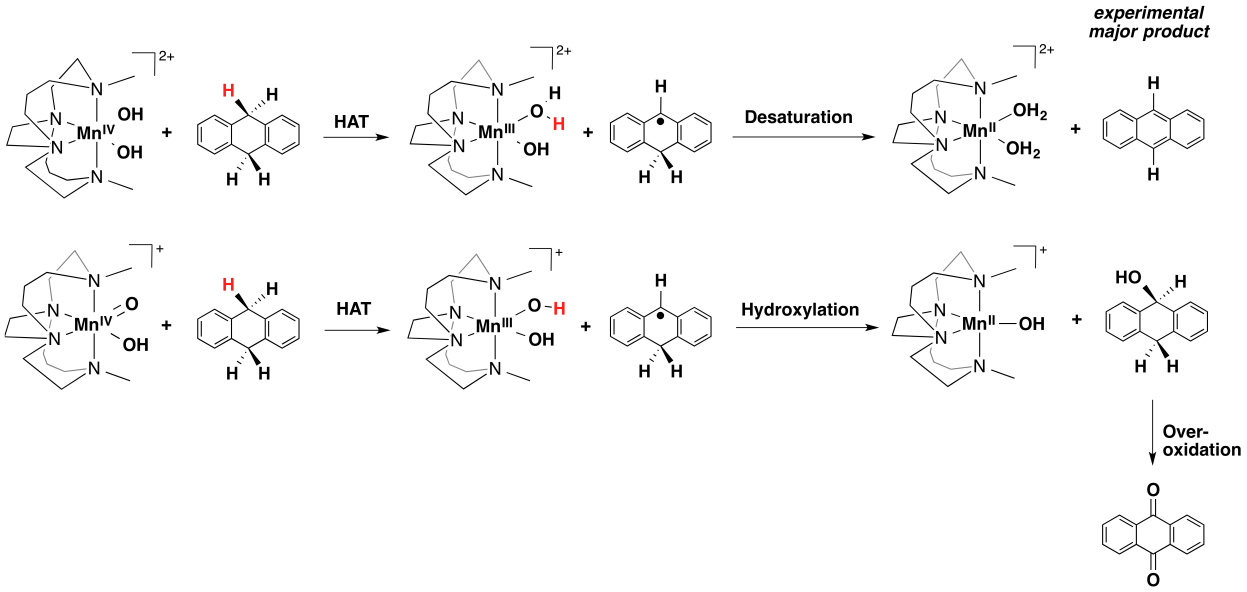

Figure 7.2. Experimentally observed major products for the reaction of DHA with $[Mn^{IV}(OH)_2(Me_2EBC)]^{2+}$ and $[Mn^{IV}(O)(OH)(Me_2EBC)]^{+}$ and proposed pathways for substrate oxidation.

7.2 Experimental Section

7.2.1. Computational Methods. All DFT calculations were performed using the *ORCA* 2.8.0 software package.[22] Models of $[Mn^{IV}(OH)_2(Me_2EBC)]^{2+}$ and $[Mn^{IV}(O)(OH)(Me_2EBC)]^{+}$ were built from the crystal structure of $[Mn^{IV}(OH)_2(Me_2EBC)]^{2+}$.[13] Geometry optimizations of all structures were performed using the hybrid B3LYP functional[23-25] with the Ahlrichs split valance polarized (SVP) and auxiliary SV/J basis sets[26,27] on carbon and hydrogen atoms with the larger Ahlrichs triple-ζ valence polarized (TZVP) and the auxiliary TZV/J basis sets on all other atoms. Solvation effects with dielectric constants associated with acetone were used with

the COSMO model[28] in *ORCA* and the resolution of identity approximation was used for all calculations.[29] Frequency calculations were performed for all optimized structures to obtain thermodynamic data and to ensure that no negative frequencies occurred for all non-transition state structures, or a single negative frequency to indicate a transition state structure. Single point energy calculations were performed using the B3LYP functional[23-25] and the TZVPP basis set on all atoms. Surface scans for hydrogen atom transfer reactions were performed by varying the distance between the hydrogen atom and the oxygen atom coordinated to the Mn center in 0.1 to 0.2 Å step size. Transition states were located after performing a general surface scan by using the ScanTS tool in ORCA, with refinement of the transition state structures with a saddle point finder followed by frequency and single point energy calculations. Cartesian coordinates for these calculations are listed in Appendix 7, Tables 7.1 – 7.20.

7.3 Results and Discussion

The initial hydrogen atom transfer from DHA to $[Mn^{IV}(O)(OH)(Me_2EBC)]^+$ or $[Mn^{IV}(OH)_2(Me_2EBC)]^{2+}$ begins with a reactant complex (RC) that contains the Mn^{IV} species and DHA (Figure 7.2, left). The RC species proceeds through a transition state (TS) to form the intermediate (I) that is composed of a Mn^{III} complex with a monohydroanthracene radical (Figure 7.2, middle). This intermediate species then undergoes one of several product-forming steps to produce either the hydroxylated product, monohydroanthracene, or the desaturated product, anthracene (Figure 7.2, right). Potential pathways for the hydrogen atom transfer reactions of DHA with $[Mn^{IV}(O)(OH)(Me_2EBC)]^+$ and $[Mn^{IV}(OH)_2(Me_2EBC)]^{2+}$ to form I are explored first, then we examine the several pathways by which I can evolve to products.

7.3.1. Hydrogen Atom Transfer of $[Mn^{IV}(O)(OH)(Me_2EBC)]^+$ with DHA. Hydrogen atom transfer for both quartet and sextet spin states of $[Mn^{IV}(O)(OH)(Me_2EBC)]^+$ were

considered, as the lowest-energy structure of the initial Mn^{IV} species is in the quartet state while the final Mn^{II} product is in the sextet state.[13,18] The hydrogen atom transfer between the Mn^{IV}-oxohydroxo moiety and DHA begins on a quartet surface, with three unpaired electrons populating the lowest-lying Mn 3d orbitals. A sextet surface is much higher in energy (Figure 7.3, right), as expected, with a radical formed on the ligand through elongation of the two of the Mn—N distances by 0.3 Å (Table 7.1). Metric parameters from a geometry-optimized model of the quartet $[Mn^{IV}(O)(OH)(Me_2EBC)]^+$ shows a Mn=O distance of 1.670 Å and a longer Mn—OH distance of 1.844 Å (Figure 7.3, Table 7.1). These calculated values are similar to the experimentally determined distances through Mn K-edge X-ray absorption spectroscopy of a 1.71 Å distance for the Mn^{IV}=O bond and a 1.84 Å distance for the Mn^{IV}-OH bond in $[Mn^{IV}(O)(OH)(Me_2EBC)]^+$.[17]

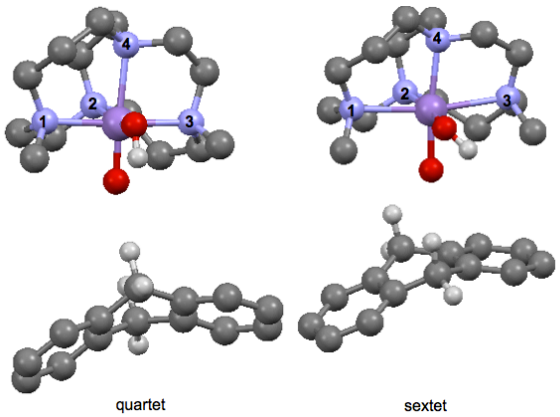

Figure 7.3. Geometry optimized model of ^{4}RC (left) and ^{6}RC (right) of DHA and $[Mn^{IV}(O)(OH)(Me_2EBC)]^+$.

The lowest-energy transition state for the reaction of $[Mn^{IV}(O)(OH)(Me_2EBC)]^+$ and DHA occurs on the quartet reaction surface at an O-H bond length of 1.487 Å and a free energy of 7.8 kcal/mol. (Figure 7.4). The corresponding sextet transition state occurs at a higher free energy of 18.9 kcal/mol relative to ^{4}RC and is slightly later in the reaction coordinate, with an O—H bond length of 1.564 Å. The activation enthalpy (12.8 kcal/mol) of the lower-lying quartet

transition state is in excellent agreement with the experimentally determined activation enthalpy of 12.1 ± 1.8 kcal/mol.[13] The calculated entropic contribution to this transition state is 5.1 kcal/mol (Table 7.1) compared to the experimental activation entropy of -7.3 kcal/mol (at 298 K). Unfortunately, these calculations poorly reproduce the entropic contribution. The spin density on the Mn center of 3.82 of ^{4}TS also reflects a late transition state with the Mn species in the transition state closest to a Mn^{III} center.

Table 7.1. Metric parameters complexes formed from $[Mn^{IV}(O)(OH)(Me_2EBC)]^+$ and DHA HAT and follow-up steps.

Reaction		Mn-O[a]	Mn-O[b]	Mn-N1	Mn-N2	Mn-N3	Mn-N4
HAT	^{4}RC	1.670	1.844	2.156	2.181	2.147	2.267
	^{4}TS	1.753	1.871	2.434	2.200	2.458	2.200
	^{4}I	1.856	1.862	2.463	2.182	2.456	2.181
	^{6}RC	1.861	1.860	2.434	2.145	2.458	2.155
	^{6}TS	1.879	1.860	2.458	2.174	2.467	2.166
	^{6}I	1.862	1.855	2.462	2.182	2.456	2.180
Desaturation	^{6}TS	2.030	1.965	2.452	2.297	2.461	2.307
	^{6}PC	2.482	2.033	2.423	2.319	2.398	2.292
Hydroxylation	^{6}TS	2.039	1.985	2.428	2.315	2.453	2.324
	^{6}PC	3.727	1.985	2.356	2.290	2.408	2.255

[a]From Mn^{IV}-oxo in $[Mn^{IV}(O)(OH)(Me_2EBC)]^+$. [b]From Mn^{IV}-hydroxo in $[Mn^{IV}(O)(OH)(Me_2EBC)]^+$.

Table 7.2. Thermodynamic parameters (kcal/mol) for HAT and follow-up reactions for $[Mn^{IV}(O)(OH)(Me_2EBC)]^+$ and $[Mn^{IV}(OH)_2(Me_2EBC)]^{2+}$.

		$[Mn^{IV}(O)(OH)(Me_2EBC)]^+$			$[Mn^{IV}(OH)_2(Me_2EBC)]^{2+}$		
Reaction	Complex	ΔH	ΔS*T[a]	ΔG	ΔH	ΔS*T[a]	ΔG
HAT	^{4}RC	0.0	0.0	0.0	0.0	0.0	0.0
	^{4}TS	12.8	5.1	7.8	15.8	1.9	13.9
	^{4}I	-17.6	2.9	-20.5	-3.0	1.8	-4.8
	^{6}RC	19.9	3.3	16.6	15.8	1.7	14.1
	^{6}TS	26.5	7.6	18.9	19.6	1.9	17.7
	^{6}I	-13.6	5.2	-18.8	-2.5	2.6	-5.0
Desaturation[b]	^{6}TS	8.6	2.6	6.0	6.6	-0.1	6.7
	^{6}PC	-24.9	-0.4	-24.6	-20.5	2.4	-22.9
Hydroxylation[b]	^{6}TS	11.0	2.7	8.3	14.2	2.5	11.7
	^{6}PC	-14.2	1.1	-15.3	-1.9	-0.6	-1.2
Electron Transfer[b]	^{6}PC	20.21	2.55	18.7	-11.8	0.9	-12.6

[a]At 25 °C. [b]Relative to ^{6}I.

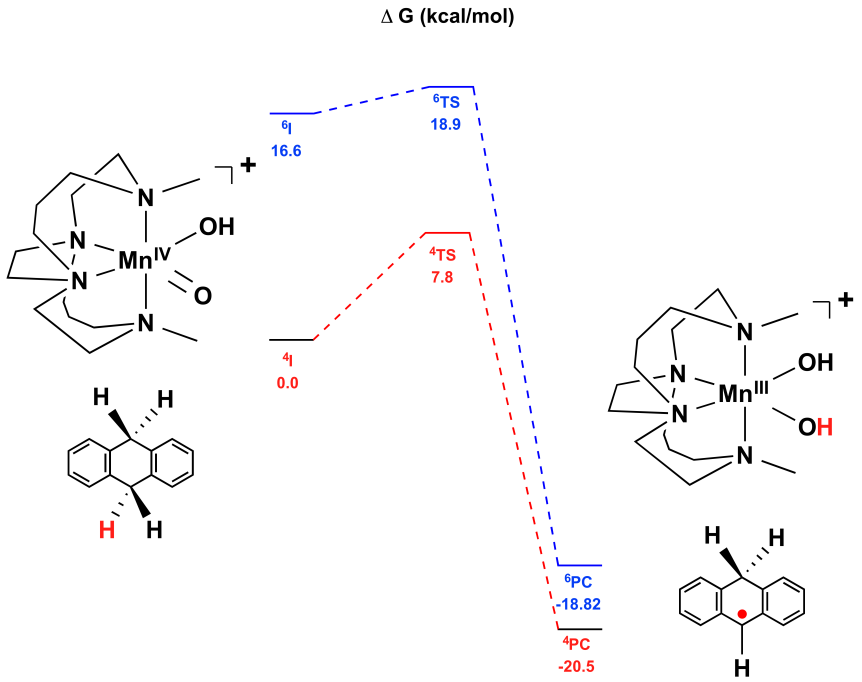

Figure 7.4. Quartet and sextet surfaces of the hydrogen atom transfer between DHA and $[Mn^{IV}(O)(OH)Me_2EBC]^+$.

In the ^{4}TS complex of the HAT from DHA to $[Mn^{IV}(O)(OH)Me_2EBC]^+$, the O—H—C angle of 174.54° in the is essentially linear, indicating approach of the hydrogen atom through the sterically accessible σ* pathway that involves the Mn^{IV} $3d_z^2$ MO (Figure 7.6). The nature of

the oxo character in the Mn^{IV}-oxohydroxo species is important for the modulation of the thermodynamic driving force.[30,31] The substrate can approach through a vertical pathway (σ*) and interact with the Mn d_z^2 MO of the Mn^{IV}-oxo moiety; alternatively, the substrate can approach through a pathway horizontal (π*) to the oxo motif and interact with MOs of π symmetry on the Mn^{IV}-oxo.[30-32] While HAT by Fe^{IV}-oxo species are known to proceed via both σ* as well as by pathways with π* symmetry,[30,32,33] Mn^{IV}-species are generally observed to undergo HAT by σ* pathways.[34] Additionally, in another Mn^{IV}-species supported by the Bn-TPEN ligand, it has been suggested that this species reacts through a more complicated spin manifold with excitation of one electron from a σ^*_{yz} MO to a σ^*_{xy} MO.[34] In the Me_2EBC ligand system, this excitation is not required for HAT, and the lowest-energy pathway is on the quartet surface.

In the $[Mn^{IV}(O)(OH)(Me_2EBC)]^+$ species, the RC contains the z axis along the Mn^{IV}-oxo bond, the y axis along the Mn^{IV}-hydroxide bond, and the x axis along the Mn—N_{axial} bond (Figure 7.6, left). In this orientation, the Mn $3d_z^2$ MO is σ-antibonding with the oxo moiety, and the $3d_{x^2-y^2}$ lies below and is σ-antibonding with the ligand. The d_{xz} and d_{yz} MOs are is π-antibonding, and the d_{xy} is nonbonding. In the reactant complex, there is little interaction of the Mn 3d orbitals with the substrate (Figure 7.6, left), and the Mn 3d orbital splitting pattern of $[Mn^{IV}(O)(OH)Me_2EBC]^+$ is in agreement with the previously determined electronic structure determined through MCD spectroscopy.[16]

In the transition state, there is a large degree of mixing in the Mn $3d_{x^2-y^2}$, d_z^2, and d_{yz} MOs that mix with the MHA species (Figure 7.6, middle). This mixing occurs to facilitate eventual transfer of the electron through reorganization of the electronic structure with a coordinate shift in the intermediate complex (Figure 7.6, right), with a new z′ axis along the Mn—N_{axial} bond and the x axis along the Mn-oxo bond. The shift to a new z′ axis allows transfer of the electron to the

new Mn $3d_{z^2}'$ MO. Although this pathway involves transfer to the Mn $3d_{z^2}'$ MO, it cannot be described as a true σ* pathway. Instead, this transfer is characterized by the high degree of mixing and reorganization. As the reaction proceeds through the transition state to the intermediate complex, the spin density is transferred from the MHA C 2p to an MO with mixed Mn 3d character (Figure 7.6, right), and the system can follow a spin crossing from the quartet to the sextet surface. It should be noted that these quartet and sextet spin states in this intermediate complex are nearly isoenergetic, differing by a spin flip, with the quartet exhibiting antiferromagnetic coupling between the high-spin (S=2) Mn^{III} species and the MHA radical, and the sextet state with ferromagnetic coupling.

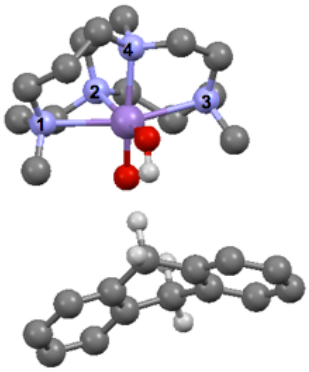

Figure 7.5. Geometry optimized model of ^{4}TS complex for HAT with $[Mn^{IV}(O)(OH)(Me_2EBC)]^+$ and DHA.

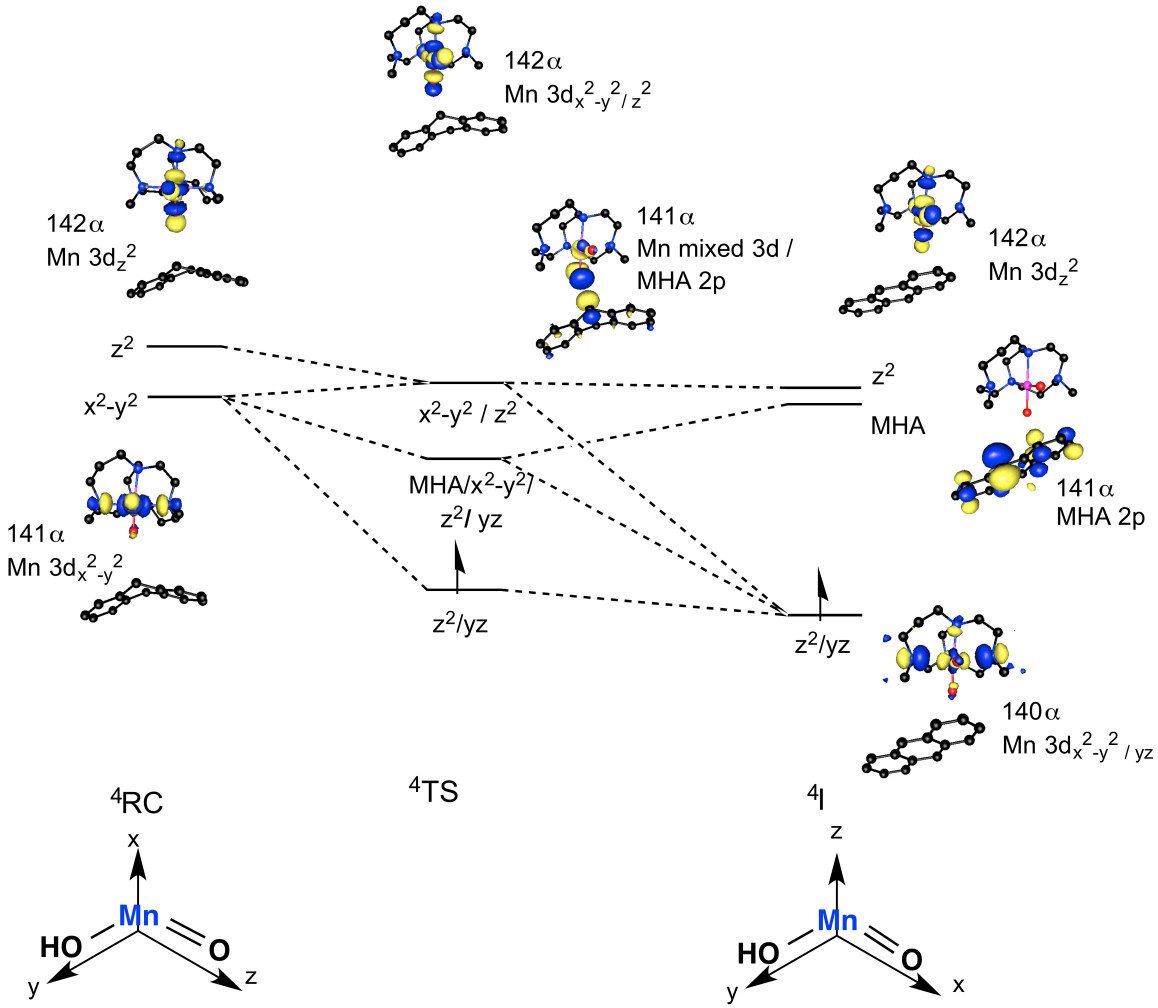

Figure 7.6. Orbital energies and surface contour plots for ^{4}RC, ^{4}TS, and ^{4}I of the HAT of DHA to $[Mn^{IV}(O)(OH)(Me_2EBC)]^+$ with coordinate systems specified for ^{4}RC and ^{4}I.

The intermediate complex on the quartet surface for HAT with DHA and $[Mn^{IV}(O)(OH)(Me_2EBC)]^+$ has a Mn^{III} center, two equivalent O—H bond lengths of 0.971 Å, and a monohydroanthracene radical approximately 5 Å away from the Mn^{III}-dihydroxo species (Figure 7.7). The Mn—N bond distances are elongated in this species, however, these calculated values are overestimated from expected values observed in other species supported by the Me_2EBC ligand.[13,15] The calculated spin density supports the Mn^{III} intermediate with a spin density of 3.97 on the Mn center. The unpaired electrons in the Mn 3d orbitals interact with the unpaired electron on the MHA radical, resulting in a quartet intermediate with antiferromagnetic

coupling. With a spin flip, this structure should be isoenergetic to the sextet intermediate with five unpaired electrons and ferromagnetic coupling on the Mn center. While some differences are observed between the enthalpic and entropic contributions for ^{4}I and ^{6}I (Table 7.2), this may be due to a shallow potential energy surface with weaker substrate-complex interaction for the $[Mn^{IV}(O)(OH)(Me_2EBC)]^+$ than is observed for the $[Mn^{IV}(OH)_2(Me_2EBC)]^{2+}$ species. The experimentally expected energy of this intermediate is 6.3 kcal/mol (Scheme 1),[20,21] which is derived from difference in the bond dissociation energies of the Mn^{IV}-oxohydroxo complex and the substrate, 84.3 and 78 kcal/mol, respectively.[13,20] The calculated free energy of this intermediate was -20.5 kcal/mol (enthalpic contribution of -17.6 kcal/mol and entropic contribution of 2.9 kcal/mol) and shows a large overprediction of the driving force that is commonly observed with the B3LYP functional.[35] The driving force for this reaction was also calculated with reactant and product species calculated separately and compared with the values for the RC and PC species. With this method, the driving force was only slightly less overpredicted, at -18.9 kcal/mol (-16.8 and 2.1 kcal/mol enthaplic and entropic contributions, respectively). Although this driving force does not represent the experimental value well, the calculated activation energy for this process was in good agreement. Better agreement of the driving force with the experimental results may be achieved by a study comparing more recently developed functionals for these calculations. Additionally, all experiments for the determination of the activation energies and bond dissociation energies were performed in a 4:1 acetone/water mixture.[19,20] These calculations were conducted with a solvation model for acetone, however, the presence of water may be important for accurate reproduction of these driving forces. We attempted to model these interactions by including several water molecules around the Mn structure, however, these calculations failed to converge to a stable complex that contained the Mn species, the substrate, and the water molecules. These calculations likely require a more

extensive network of water molecules, and it is possible that the water molecules may facilitate the hydrogen atom transfer. Unfortunately, these effects cannot be implemented in these calculations with the current methods used, and a more accurate driving force will likely require an approach combined with molecular dynamics to include these solvation effects.

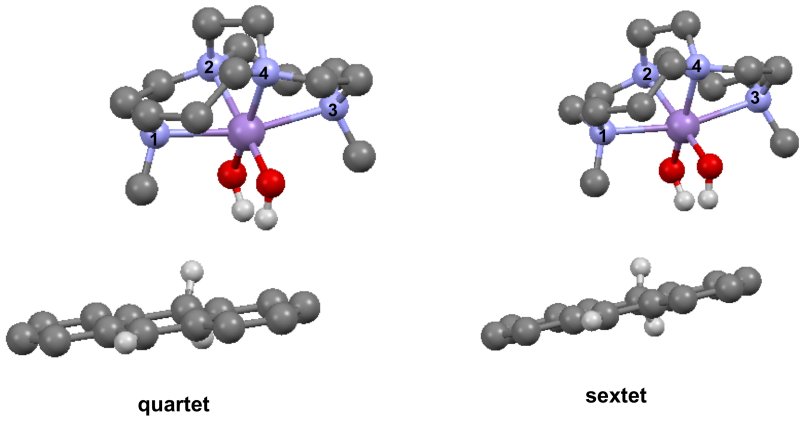

Figure 7.7. Geometry optimized model of ^{4}I and ^{6}I of $[Mn^{IV}(O)(OH)(Me_2EBC)]^+$ and DHA.

7.3.2. Hydrogen Atom Transfer of $[Mn^{IV}(OH)_2(Me_2EBC)]^{2+}$ with DHA. Metric parameters from a geometry-optimized model (Figure 7.8) of the reactant complex of $[Mn^{IV}(OH)_2(Me_2EBC)]^{2+}$ in the known S = 3/2 ground state[18] show two identical Mn—OH distances of 1.808 Å. These values show good agreement with the experimental distances determined through Mn K-edge X-ray absorption spectroscopy of 1.80 Å[17] and through an X-ray diffraction crystal structure of 1.81 Å.[15] In the reactant complex, the hydrogen atom from DHA lies 3.692 Å from the accepting oxygen site at an O—H—C angle of 97.06° and a Mn—O—H angle of 165.18°. The complex has a distorted octahedral geometry with an average Mn—N distance of 2.146 Å with an average deviation from this value of 0.006 Å (Table 7.3).

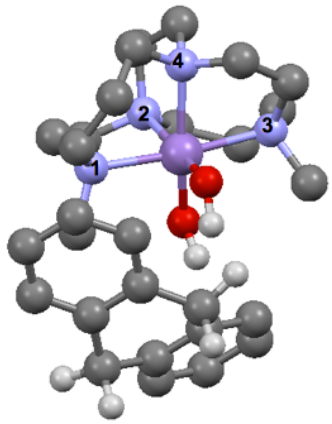

Figure 7.8. ^{4}RC structure of $[Mn^{IV}(OH)_2(Me_2EBC)]^{2+}$ and DHA.

Table 7.3. Metric parameters complexes formed from $[Mn^{IV}(OH)_2(Me_2EBC)]^{2+}$ and DHA HAT and follow-up steps.

Reaction	Complex	Mn-O[a]	Mn-O[b]	Mn-N1	Mn-N2	Mn-N3	Mn-N4
HAT	^{4}RC	1.808	1.808	2.148	2.145	2.157	2.135
	^{4}TS	2.036	1.825	2.210	2.272	2.207	2.137
	^{4}I	2.381	1.827	2.170	2.128	2.198	2.288
	^{6}RC	1.858	1.845	2.300	2.138	3.120	2.168
	^{6}TS	2.093	1.827	2.173	2.130	2.192	2.260
	^{6}I	2.382	1.827	2.172	2.128	2.200	2.287
Desaturation	^{6}TS	4.077	1.987	2.349	2.294	2.413	2.234
	^{6}PC	2.271	2.371	2.314	2.293	2.312	2.279
Hydroxylation	^{6}TS	4.074	2.124	2.386	2.249	2.310	2.254
	^{6}PC	2.343	2.588	2.297	2.242	2.276	2.289

[a]Mn—O bond that participates in initial HA. [b]Mn—O bond that participates in second HAT for desaturation reaction.

The transition state for the reaction of $[Mn^{IV}(OH)_2(Me_2EBC)]^{2+}$ and DHA occurs on the quartet reaction surface at an O—H distance of 1.423 Å with a free energy of 13.9 kcal/mol. The calculated $\Delta H^{\ddagger}$ is 15.8 kcal/mol and $\Delta S^{\ddagger}$ is 1.9 kcal/mol (Figure 7.9) in agreement with the experimentally determined activation enthalpy of 13.2 ± 0.7 kcal/mol and enthalpy of -8.3 kcal/mol (at 298 K).[13] Unfortunately, the calculated entropic contribution is a poor representation

of the experimental value, however, this is a small contribution, in this case. The hydroxide ligand that accepts the hydrogen atom has an elongated Mn—O distance of 2.036 Å while the second hydroxide ligand only slightly elongated at 1.825 Å (Figure 7.10). The Mn—N bonds show slight elongations (Table 7.3) and the spin density on the Mn center at this transition state is 3.99, suggesting a late transition state that is closest to the Mn^{III} intermediate complex.

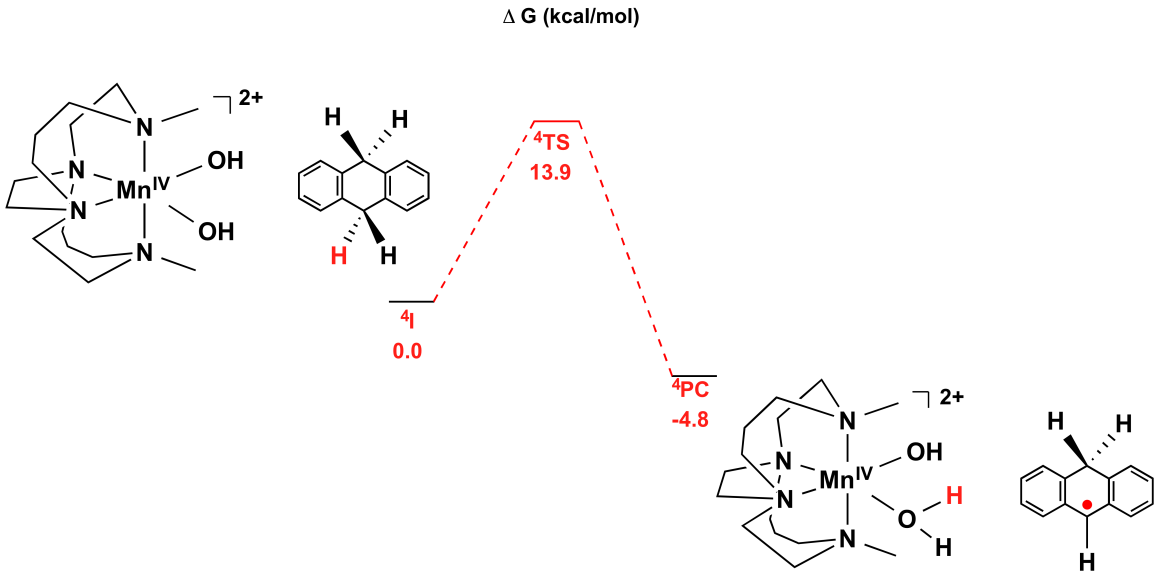

Figure 7.9. Quartet surface of the hydrogen atom transfer between DHA and $[Mn^{IV}(OH)_2Me_2EBC]^+$.

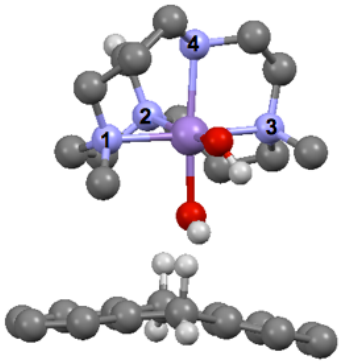

Figure 7.10. Geometry optimized model of HAT ^{4}TS of $[Mn^{IV}(OH)_2(Me_2EBC)]^{2+}$ and DHA.

At the transition state for HAT with DHA and $[Mn^{IV}(OH)_2(Me_2EBC)]^{2+}$, the Mn—O—H angle has tightened to 159.59°. The O—H—C angle of 170.12°, though four degrees smaller

than that of the transition state of the Mn^{IV}-oxohydroxo complex, is essentially linear and indicates a σ* pathway approach through the Mn $3d_z^2$ MO. Here, a C_2 axis of symmetry exists along the Mn-hydroxo axes. The z-axis lies along the Mn—N_{axial} bond, with the symmetric x and y axes along the Mn-hydroxo axes. The electronic structure of $[Mn^{IV}(OH)_2(Me_2EBC)]^{2+}$ contains the Mn $3d_{x^2-y^2}$ MO that is σ-antibonding with both hydroxide moieties and the Mn $3d_z^2$ MO is at lower energy. The Mn $3d_{xy}$ MO is nonbonding and the Mn $3d_{yz}$ and d_{xz} MOs are π-antibonding. In the transition state, the complicated mixing that was present in the Mn^{IV}-oxohydroxo species does not occur, and there are primarily contributions from the Mn $3d_{x^2-y^2}$ and $3d_z^2$ MOs. As the complex approaches the transition state, the C_2 symmetry is broken, and the Mn $3d_{x^2-y^2}$ and $3d_z^2$ MOs mix to generate two MOs with localized electron density along each Mn-hydroxo axis (Figure 7.11, middle). This allows transfer of the electron to the Mn $3d_z^2$ MO through a clear σ* pathway. As the reaction proceeds through the transition state to the intermediate complex, the spin density is transferred from the MHA C 2p to the Mn $3d_{x^2-y^2/xy}$ MO (Figure 7.11, right). The system can then follow a spin crossing from the quartet to the sextet surface, with ferromagnetic coupling of the four unpaired d electrons in the Mn^{III} center and the radical MHA electron.

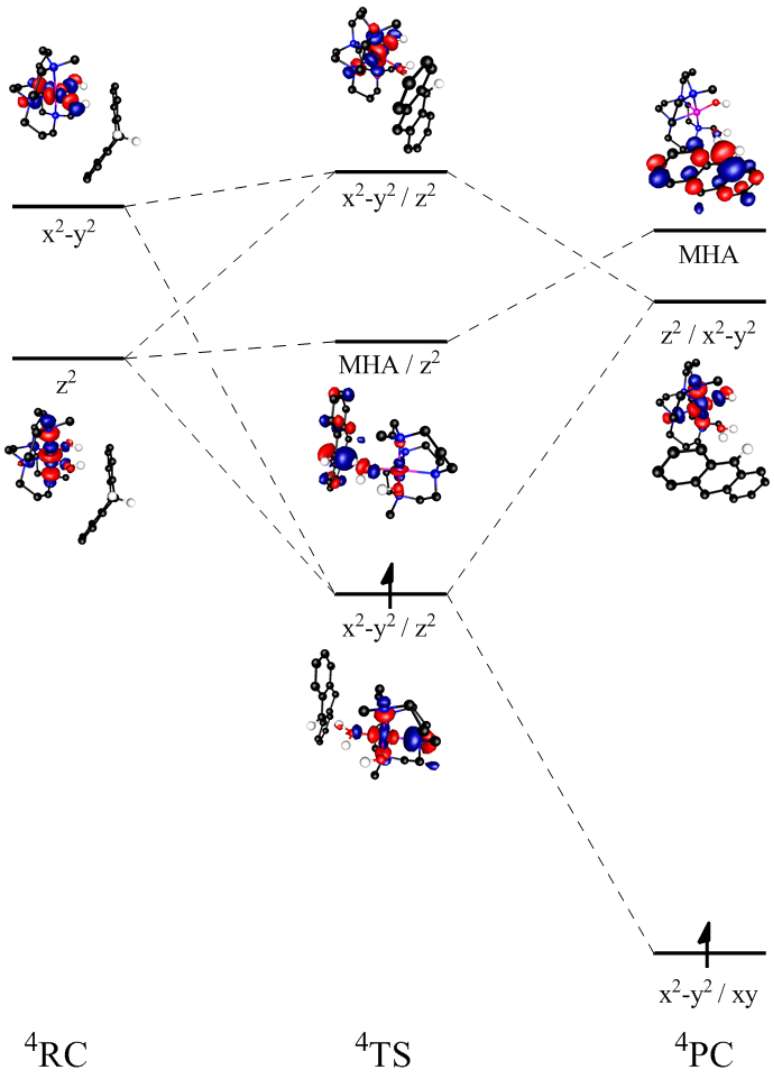

Figure 7.11. Relative orbital energies and surface contour plots for ^{4}RC, ^{4}TS, and ^{4}I of the HAT of DHA to $[Mn^{IV}(OH)_2(Me_2EBC)]^{2+}$.

The intermediate complex for the HAT of DHA and $[Mn^{IV}(OH)_2(Me_2EBC)]^{2+}$ on the quartet surface occurs at an O—H bond length of 0.981 Å and consists of a $[Mn^{III}(OH)(OH_2)(Me_2EBC)]^{2+}$ complex and the MHA radical. The aqua Mn—O distance is elongated at 2.381 Å and the hydroxide Mn—O is essentially unchanged from the transition state bond length at 1.827 Å. This intermediate structure contains an O—H—C angle of 174.71° and a tightened Mn—O—H angle of 149.23°. From the transition state, the Mn—N bonds show slight elongation (Table 7.3) and the Mulliken spin density on the Mn center is 4.08, supporting an S=3/2 center. Here, there is ferromagnetic coupling of the four unpaired *d* electrons and the

radical MHA electron. The experimental driving force of this reaction is ~ 5.0 kcal/mol, based on the bond dissociation energy of the $[Mn^{IV}(OH)_2(Me_2EBC)]^{2+}$ species and the substrate, 84 and 78 kcal/mol, respectively.[13] These calculations reproduce this driving force well with the free energies of the quartet intermediate (-4.8 kcal/mol with) and the sextet intermediate (-5.1 kcal/mol, Table 7.2). The driving force was also examined by separately calculating the reactants and product species, and this method provided a driving force of -5.4 kcal/mol with enthalpic and entropic contributions of -4.1 and 1.2 kcal/mol, respectively. While this method failed to provide an accurate calculation of the driving force for the $[Mn^{IV}(O)(OH)(Me_2EBC)]^{+}$ species, it is able to accurately reproduce both the experimental activation energy and driving force for the $[Mn^{IV}(OH)_2(Me_2EBC)]^{2+}$ reaction with DHA. In general, these HAT calculations for $[Mn^{IV}(O)(OH)(Me_2EBC)]^{+}$ and $[Mn^{IV}(OH)_2(Me_2EBC)]^{2+}$ indicate differences in the orbital mixing and electron transfer in the transition state, as well as possible differences in solvation that impact the value of the driving force.

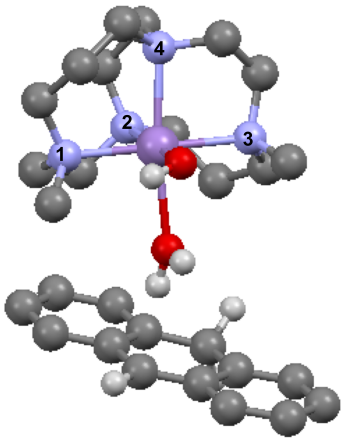

Figure 7.12. Geometry optimized model of HAT ^{4}I of $[Mn^{IV}(OH)_2(Me_2EBC)]^{2+}$ and DHA.

7.3.3. Product Formation Steps for $[Mn^{IV}(O)(OH)(Me_2EBC)]^{+}$. With the HAT reactions for both complexes complete, we now move on to the subsequent product formation reactions. The major organic product experimentally observed for $[Mn^{IV}(O)(OH)(Me_2EBC)]^{+}$ is

the hydroxylated substrate, monohydroanthracene, that undergoes over-oxidation to form the final anthraquinone product.[14] As the reaction proceeds past the Mn^{III}-dihydroxo intermediate formed from the HAT with $[Mn^{IV}(O)(OH)(Me_2EBC)]^+$ and DHA, several product formation pathways are possible. In order to determine the factors driving the selection of this pathway, mechanisms of a second HAT or an OH rebound step were explored, as these processes are known for other Mn-oxo species.[36] In addition, HAT reactivity by electron transfer and formation of a carbocation on the substrate followed by proton transfer has been observed in other Mn-oxo species,[36] and this pathway was also explored (Figure 7.13).

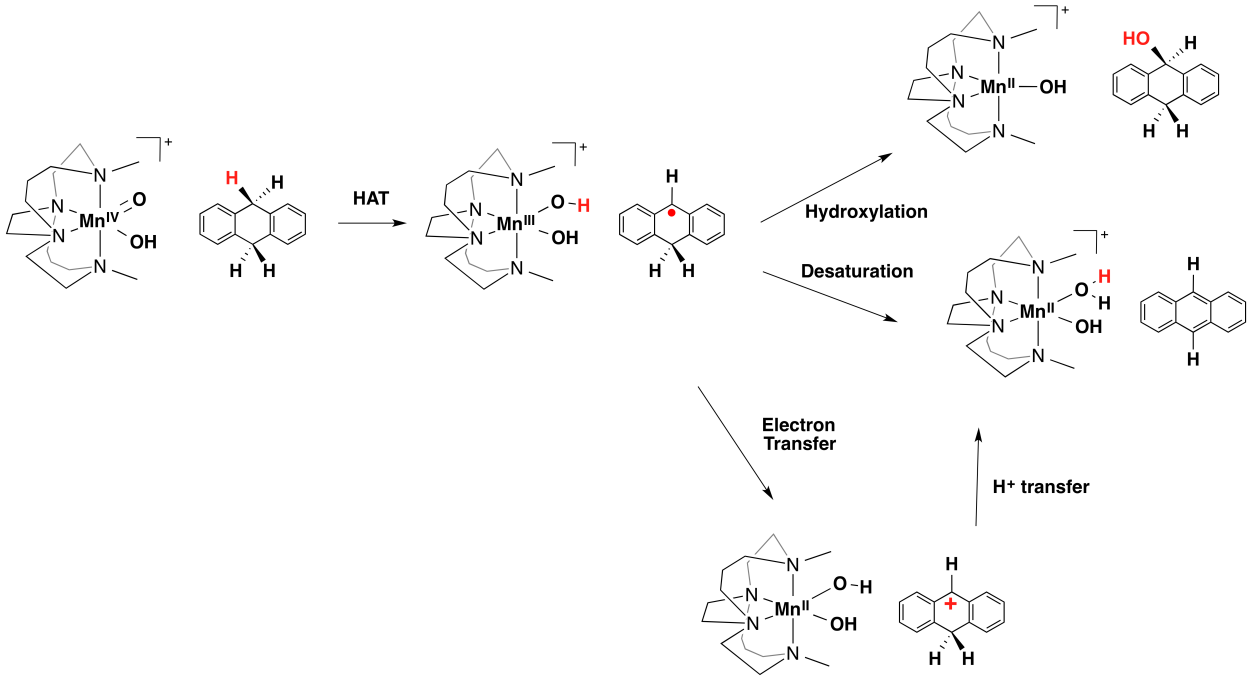

Figure 7.13. Pathways evaluated for Mn^{III}-dihydroxo intermediate formed from $[Mn^{IV}(O)(OH)(Me_2EBC)]^+$ and DHA.

The hydroxylation pathway through an OH rebound step results in transfer of a hydroxide moiety to the substrate, generating a $[Mn^{II}(OH)(Me_2EBC)]^+$ species and the hydroxylated substrate product, anthraquinone. This reaction had a calculated energy barrier of 8.3 kcal/mol (enthalpic and entropic contributions of 11.0 and 2.7 kcal/mol, respectively) and a driving force of -15.3 kcal/mol (enthalpic and entropic contributions of -14.2 and 1.1 kcal/mol, respectively;

see Figure 7.14, left and Table 7.2. In the desaturation pathway, a second hydrogen atom transfer occurs between a hydrogen atom from the MHA radical and the $[Mn^{III}(OH)_2(Me_2EBC)]^+$ intermediate species, yielding the $[Mn^{II}(OH)(OH_2)(Me_2EBC)]^+$ complex and the desaturated substrate products, anthracene (Figure 7.14, right). It should be noted that a substrate reorientation is necessary to orient the second hydrogen atom on the opposite side of the substrate toward the Mn complex, but this process should presumably occur at room temperature. For this desaturation reaction, a barrier of 6.0 kcal/mol was calculated (enthalpic and entropic contributions of 8.6 and 2.6 kcal/mol, respectively; see Figure 7.14, right and Table 7.2) with a driving force of -24.6 kcal/mol (enthalpic and entropic contributions of -14.2 and 1.1 kcal/mol, respectively). Unfortunately, these calculations predict a lower barrier and a larger driving force for the desaturation pathway, which is not the experimentally observed product.

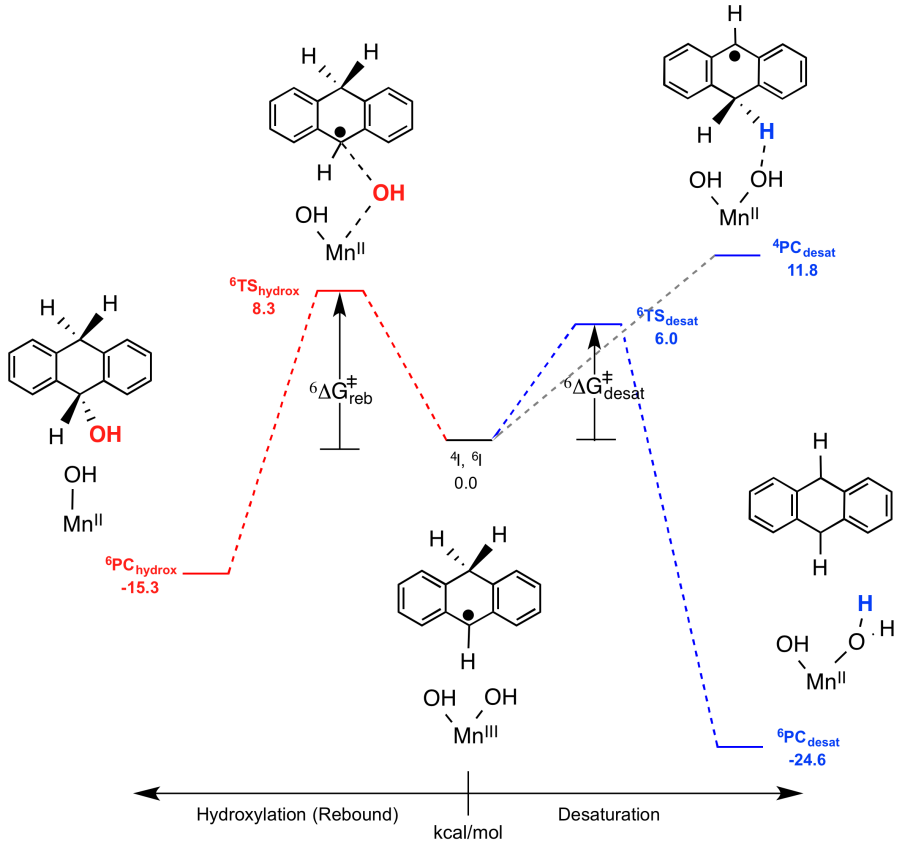

Figure 7.14. Energy profiles of hydroxylation and desaturation reactions of the Mn^{III}-dihydroxo intermediate formed from the HAT reaction of $[Mn^{IV}(O)(OH)(Me_2EBC)]^+$ and DHA.

Alternatively, desaturation can proceed by a sequential electron transfer and protron transfer process. This requires a one electron oxidation of substrate and reaction of $[Mn^{III}(OH)(OH)(Me_2EBC)]^+$ to form a $[Mn^{II}(OH)(OH)(Me_2EBC)]$ species with the formation of a carbocation on the substrate. These products then undergo a proton transfer from the substrate to the oxygen, yielding a $[Mn^{II}(OH)(OH_2)(Me_2EBC)]^+$ species and the desaturated substrate product, anthracene. For this complex, the carbocation pathway is uphill by 18.7 kcal/mol (enthalpic and entropic contributions of 20.21 and 2.55 kcal/mol, respectively; see Figure 7.15 and Table 7.2).

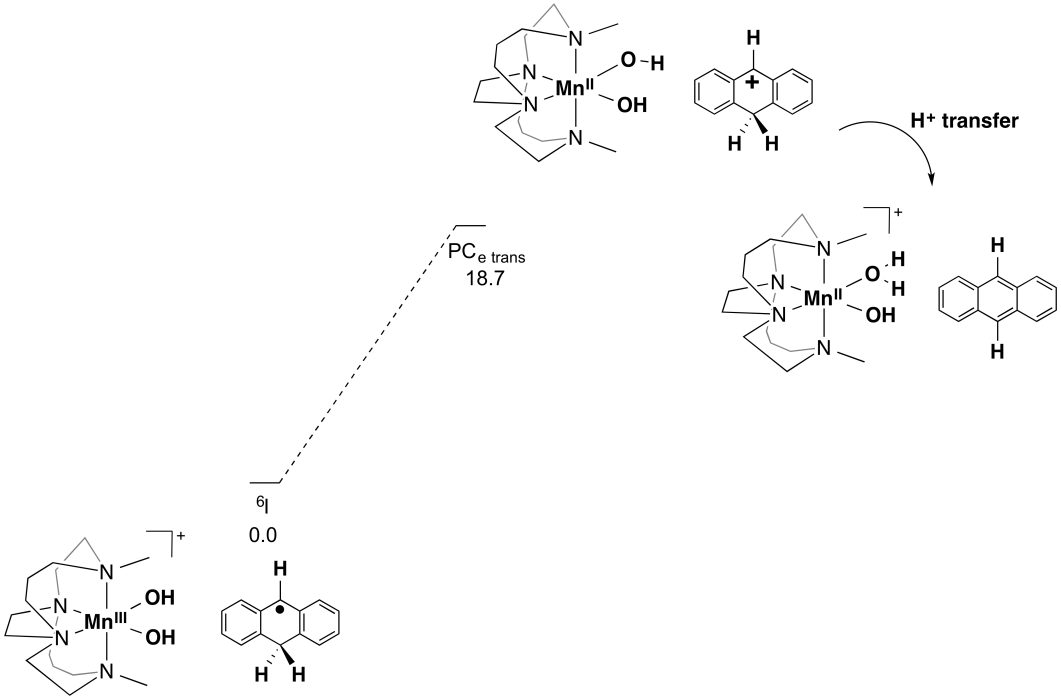

Figure 7.15. Electron transfer reaction for the Mn^{III}-dihydroxo intermediate.

7.3.4. Product Formation Steps for $[Mn^{IV}(OH)_2(Me_2EBC)]^{2+}$. The $[Mn^{IV}(OH)_2(Me_2EBC)]^{2+}$ complex has been experimentally observed to produce primarily the desaturated substrate, anthracene.[14] In order to determine the factors that drive this pathway selection, mechanisms of a second HAT, OH rebound, and electron transfer were all evaluated.

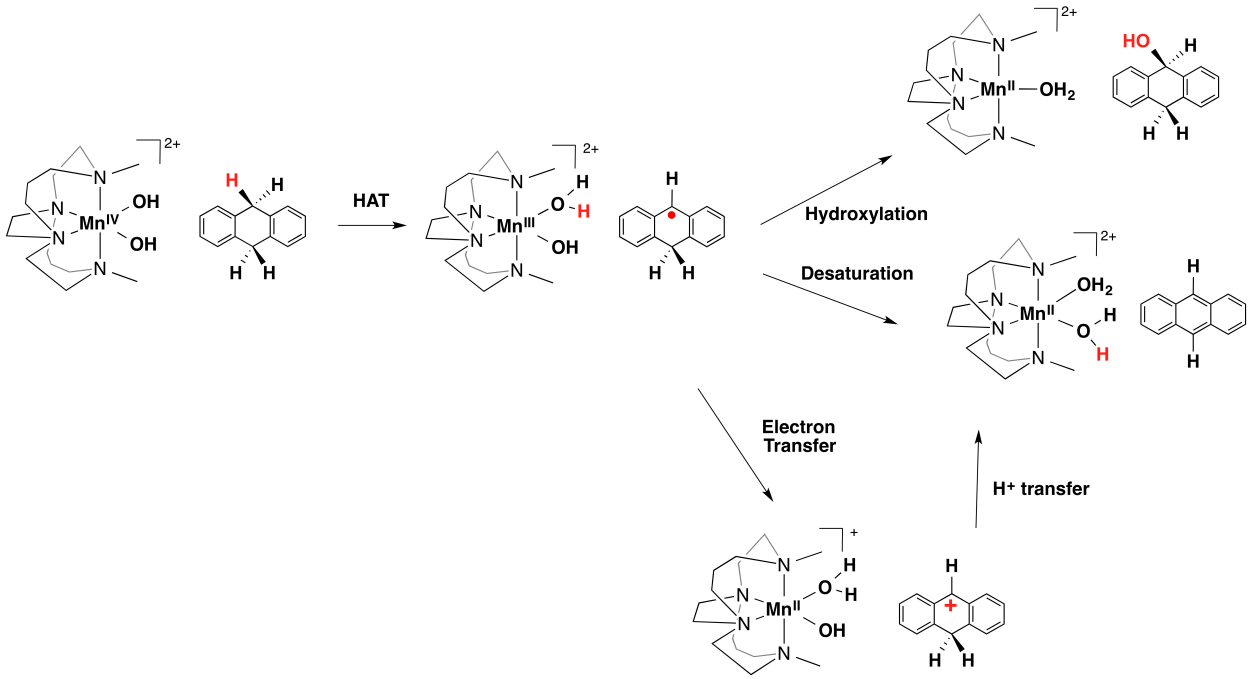

Figure 7.15. Pathways evaluated for Mn^{III}-dihydroxo intermediate formed from $[Mn^{IV}(OH)_2(Me_2EBC)]^{2+}$ and DHA.

For the desaturation pathway through a second hydrogen atom transfer, a hydrogen atom from the MHA radical is transferred to the $[Mn^{III}(OH)(OH_2)(Me_2EBC)]^{2+}$ species, yielding the diaqua complex, $[Mn^{II}(OH_2)_2(Me_2EBC)]^{2+}$ and the desaturated substrate products, anthracene. For this process, a barrier of 6.7 kcal/mol was calculated with enthalpic and entropic contributions of 6.6 and -0.1 kcal/mol, respectively (Figure 7.16, right and Table 7.2). The hydroxylation pathway through the OH rebound step results in transfer of a hydroxide group to the substrate to produce a $[Mn^{II}(OH_2)(Me_2EBC)]^{2+}$ species and the hydroxylated substrated product, anthraquinone. The calculated reaction barrier for this reaction was 11.7 kcal/mol with enthalpic and entropic contributions of 14.2 and 2.5 kcal/mol, respectively (Figure 7.16, left and Table 7.2). Experimentally, the observed product is the desaturation product, and these calculations reproduce this finding well. Similar to the HAT calculations for $[Mn^{IV}(O)(OH)(Me_2EBC)]^{+}$ and $[Mn^{IV}(OH)_2(Me_2EBC)]^{2+}$, this method reproduces the

experimental results for $[Mn^{IV}(OH)_2(Me_2EBC)]^{2+}$, but overestimates the driving force in both cases for $[Mn^{IV}(O)(OH)(Me_2EBC)]^{+}$.

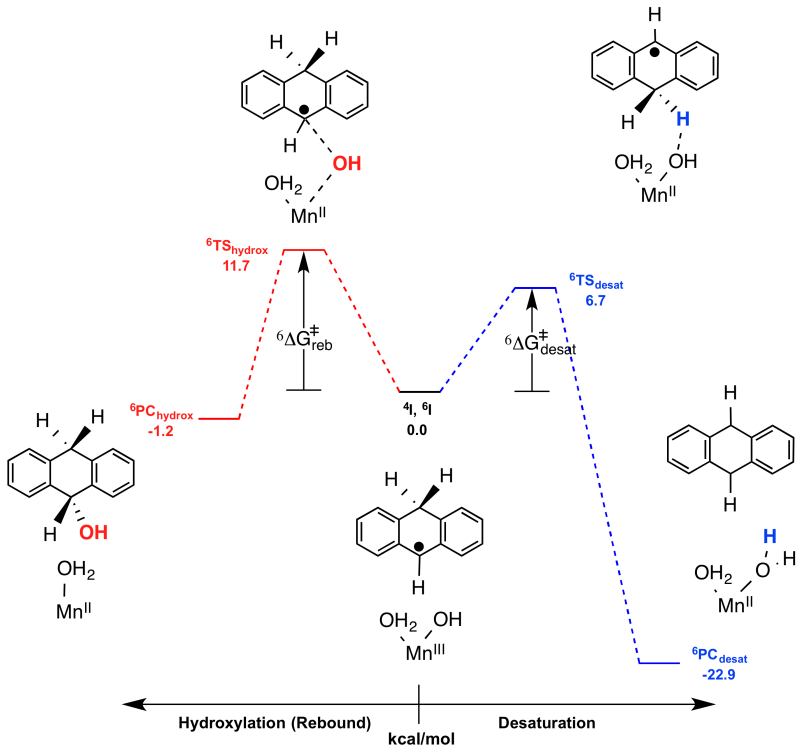

Figure 7.16. Energy profiles of hydroxylation and desaturation reactions of the Mn^{III}-aquahydroxo intermediate formed from the HAT reaction of $[Mn^{IV}(OH)_2(Me_2EBC)]^{+}$ and DHA.

The alternative electron transfer pathway requires a one electron oxidation of the substrate and reaction of $[Mn^{III}(OH)(OH_2)(Me_2EBC)]^{2+}$ to form a $[Mn^{II}(OH)(OH_2)(Me_2EBC)]^{+}$ species with the formation of a carbocation on the substrate. These products then undergo a proton transfer from the substrate to the oxygen, yielding a $[Mn^{II}(OH_2)_2(Me_2EBC)]^{2+}$ species and the desaturated substrate product, anthracene. This process may not require a large rearrangement, and this pathway is downhill by -12.63 kcal/mol (enthalpic and entropic contributions of -11.75 and 0.89 kcal/mol, respectively; see Figure 7.17 and Table 7.2). Overall, this pathway of electron transfer and is less favorable than desaturation by HAT.

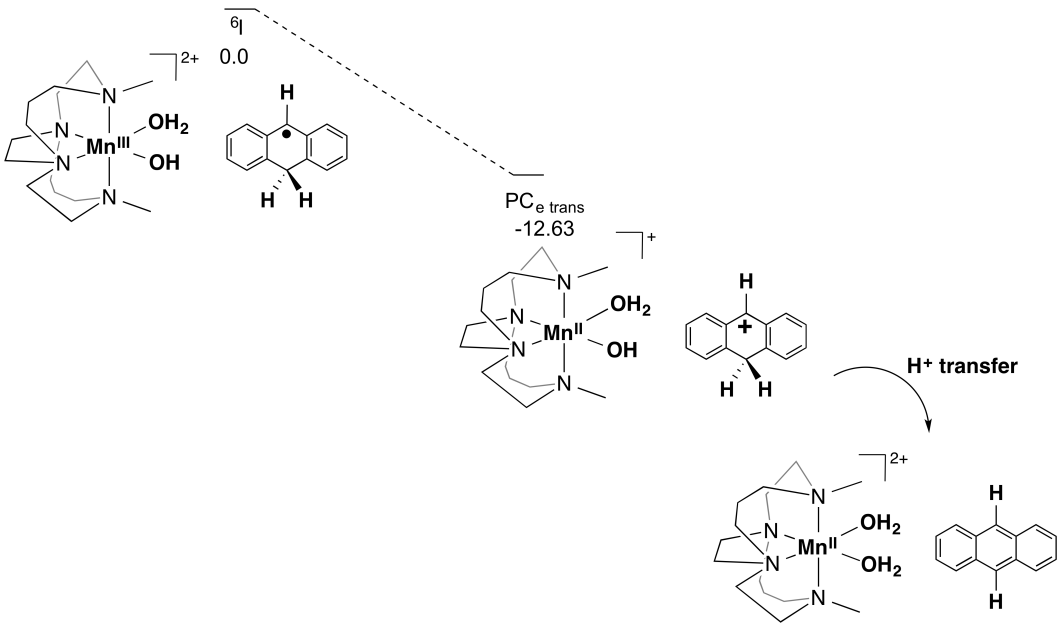

Figure 7.17. Electron transfer reaction of the Mn^{III}-aquahydroxo intermediate.

7.4 Conclusions and Outlook

While there has been much debate about the properties that control HAT reactions from driving force and bond strength,[37] spin state and spin density,[38-40] pathway of reactivity,[30,32,33] and other parameters, reactivity and product distributions of C—H bond activation reactions are not fully understood. In part, this is due to the vastly different nature of the complexes studied.[37] Due to these complexities, the $[Mn^{IV}(O)(OH)(Me_2EBC)]^+$ and $[Mn^{IV}(OH)_2(Me_2EBC)]^{2+}$ complexes provide an excellent opportunity to probe the HAT reaction, as well as the product formation steps, as these complexes only differ by the presence of an additional proton. In general, although DFT calculations overpredict the driving of the HAT with $[Mn^{IV}(O)(OH)(Me_2EBC)]^+$, the calculated activation energies for both complexes and the driving force for $[Mn^{IV}(OH)_2(Me_2EBC)]^{2+}$ are in reasonable agreement with experimental activation energies and bond dissociation energies. The product formation steps predict the correct desaturated product for $[Mn^{IV}(OH)_2(Me_2EBC)]^{2+}$; however, the desaturation product is overpredicted for $[Mn^{IV}(O)(OH)(Me_2EBC)]^+$, and the experimentally observed hydroxylation

products are higher in energy. In an attempt to account for this discrepancy, we performed the calculations of the HAT reactions of $[Mn^{IV}(OH)_2(Me_2EBC)]^{2+}$ and $[Mn^{IV}(O)(OH)(Me_2EBC)]^{+}$ with implementation of a dispersion force correction in *ORCA*.[41] Unfortunately, the inclusion of this effect only further stabilized the driving force of the HAT of $[Mn^{IV}(O)(OH)(Me_2EBC)]^{+}$ (Figure 7.18) and had little change on the driving force of the HAT reaction for $[Mn^{IV}(OH)_2(Me_2EBC)]^{2+}$ (Figure 7.19). Other modifications to these calculations should be attempted, such as the use of newer functionals that may provide a more accurate representation of the driving force for reactions involving $[Mn^{IV}(O)(OH)(Me_2EBC)]^{+}$. Additionally, while all experimental work was performed in a 4:1 acetone-water solvent mixture, these calculations could only be performed with a solvation model for acetone. A more sophisticated approach to model these solvation effects may be required to provide an accurate driving force for these reactions.

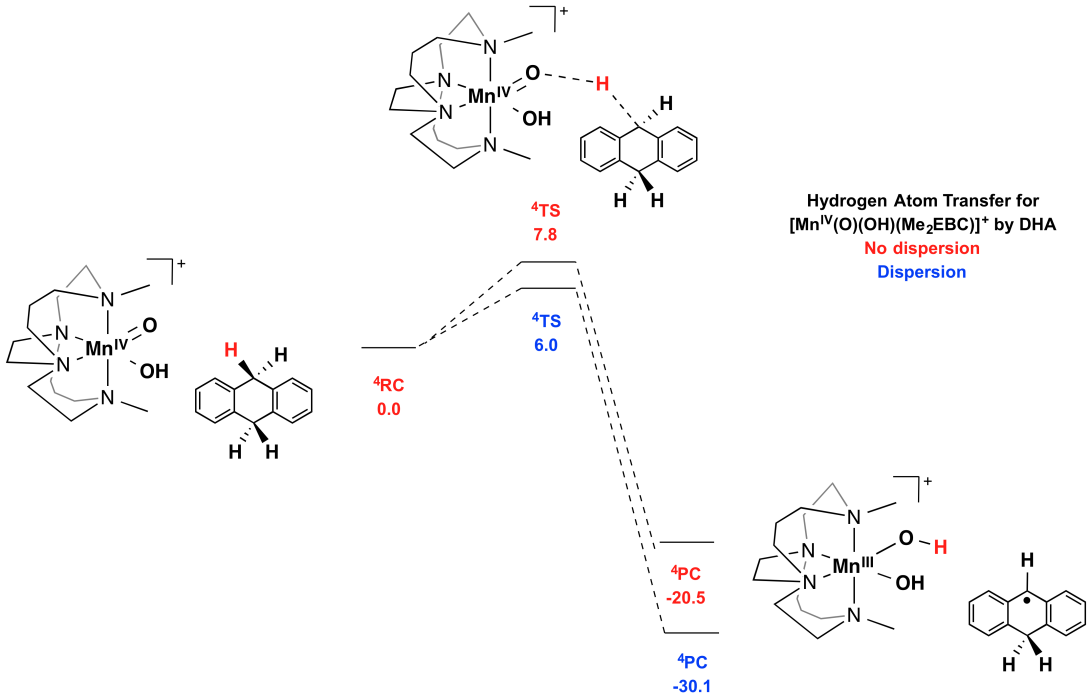

Figure 7.18. Quartet surfaces of the hydrogen atom transfer between DHA and $[Mn^{IV}(O)(OH)(Me_2EBC)]^{+}$ with (blue) and without (red) a dispersion correction.

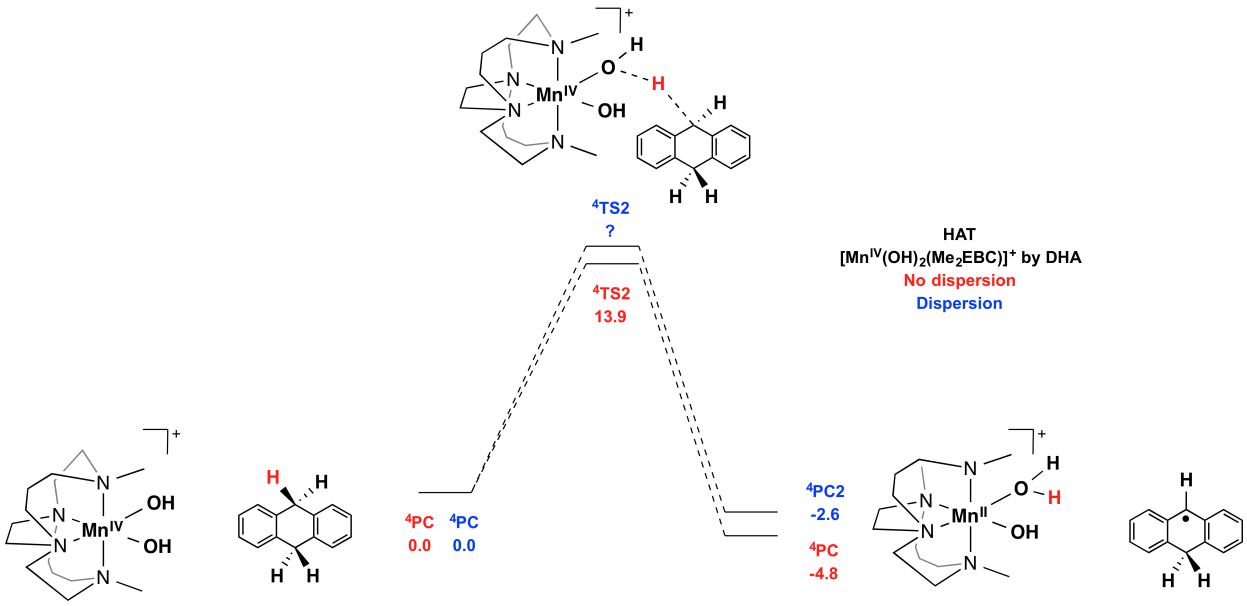

Figure 7.19. Quartet surfaces of the hydrogen atom transfer between DHA and $[Mn^{IV}(OH)_2(Me_2EBC)]^{2+}$ with (blue) and without (red) a dispersion correction.

For the $[Mn^{IV}(OH)_2(Me_2EBC)]^{2+}$ complex, the HAT pathway of approach of the H atom in the transition state proceeds through a σ^* pathway through the Mn d_z^2 MO. The inclusion of the proton in $[Mn^{IV}(OH)_2(Me_2EBC)]^{2+}$ did not direct the pathway of approach to a π^* pathway, but instead provided localization of electron density along each Mn-hydroxo axis in the transition state of the HAT reaction. In contrast, the approach of substrate with the $[Mn^{IV}(O)(OH)(Me_2EBC)]^{+}$ contains a high degree of mixing and a coordinate system reorganization in the intermediate complex. Additionally, the difference in product distribution for $[Mn^{IV}(OH)_2(Me_2EBC)]^{2+}$ and $[Mn^{IV}(O)(OH)(Me_2EBC)]^{+}$ was reflected in differences in the transition states for hydroxylation and desaturation for both species. While the transition state energies for desaturation for both complexes are similar (6.7 and 6.0 kcal/mol, respectively), a higher barrier was observed for $[Mn^{IV}(OH)_2(Me_2EBC)]^{2+}$ (11.7 and 8.3 kcal/mol, respectively). Finally, another product formation pathway of electron transfer has been proposed;[34,40] however, for both complexes, these calculations are less favorable than the desaturation or hydroxylation steps and can be ruled out for the reactivity of these complexes.

7.5 References

(1) *Cytochrome P450: Structure, Mechanism, and Biochemistry*; Plenum: New York, 1995.
(2) Meunier, B.; de Visser, S. P.; Shaik, S. *Chem. Rev.* **2004**, *104*, 3947-3980.
(3) Groves, J. T. *J. Inorg. Biochem.* **2006**, *100*, 434-447.
(4) Hohenberger, J.; Ray, K.; Meyer, K. *Nat. Comm.* **2012**, *3*, 1718.
(5) Nam, W. *Acc. Chem. Res.* **2015**, *48*, 2415-2423.
(6) Oloo, W. N.; Que, L., Jr. *Acc. Chem. Res.* **2015**, *48*, 2612-2621.
(7) Sastri, C. V.; Lee, J.; Oh, K.; Lee, Y. J.; Lee, J.; Jackson, T. A.; Ray, K.; Hirao, H.; Shin, W.; Halfen, J. A.; Kim, J.; Que, L., Jr.,; Shaik, S.; Nam, W. *Proc. Natl. Acad. Sci.* **2007**, *104*, 19181-19186.
(8) Chen, J.; Lee, Y.-M.; Davis, K. M.; Wu, X.; Seo, M. S.; Cho, K.-B.; Yoon, H.; Park, Y. J.; Fukuzumi, S.; Pushkar, Y. N.; Nam, W. *Journal of the American Chemical Society* **2013**, *135*, 6388-6391.
(9) Collins, T. J.; Gordon-Wylie, S. W. *Journal of the American Chemical Society* **1989**, *111*, 4511-4513.
(10) Garcia-Bosch, I.; Company, A.; Cady, C. W.; Styring, S.; Browne, W. R.; Ribas, X.; Costas, M. *Angewandte Chemie, International Edition in English* **2011**, *50*, 5648-5653.
(11) Leto, D. F.; Ingram, R.; Day, V. W.; Jackson, T. A. *Chemical Commun.* **2013**, *49*, 5378-5380.
(12) Parsell, T. H.; Behan, R. K.; Green, M. T.; Hendrich, M. P.; Borovik, A. S. *J. Am. Chem. Soc.* **2006**, *128*, 8728-8729.
(13) Yin, G.; Danby, A. M.; Kitko, D.; Carter, J. D.; Scheper, W. M.; Busch, D. H. *J. Am. Chem. Soc.* **2008**, *130*, 16245-16253.
(14) Shi, S., Wang, Y., Xu, A., Wang, H., Zhu, D., Roy, S.B., Jackson, T.A., Busch, D.H., Yin, G. *Angew. Chem. Int. Ed.* **2011**, *50*, 7321-7324.
(15) Yin, G.; McCormick, J. M.; Buchalova, M.; Danby, A. M.; Rodgers, K.; Day, V. W.; Smith, K.; Perkins, C. M.; Kitko, D.; Carter, J. D.; Scheper, W. M.; Busch, D. H. *Inorg. Chem.* **2006**, *45*, 8052-8061.
(16) Chattopadhyay, S.; Geiger, R. A.; Yin, G.; Busch, D. H.; Jackson, T. A. *Inorg. Chem.* **2010**, *49*, 7530-7535.
(17) Leto, D. F.; Jackson, T. A. *Inorg. Chem.* **2014**, *53*, 6179-6194.
(18) Leto, D. F.; Massie, A. A.; Colmer, H. E.; Jackson, T. A. *Inorg. Chem.* **2016**, *55*, 3272-3282.
(19) Wang, Y.; Shi, S.; Wang, H.; Zhu, D.; Yin, G. *Chem. Commun.* **2012**, *48*, 7832-7834.
(20) Yin, G.; Danby, A. M.; Kitko, D.; Carter, J. D.; Scheper, W. M.; Busch, D. H. *J. Am. Chem. Soc.* **2007**, *129*, 1512-1513.
(21) Mayer, J. M. *Acc. Chem. Res.* **1998**, *31*, 441-450.
(22) Neese, F., *ORCA - an ab initio, Density Functional and Semiempirical Program Package*, *Version 2.8*, University of Bonn, 2009.
(23) Becke, A. D. *J. Chem. Phys.* **1993**, *98*, 1372-1377.
(24) Becke, A. D. *J. Chem. Phys.* **1993**, *98*, 5648-5652.
(25) Lee, C.; Yang, W.; Parr, R. G. *Phys. Rev. B* **1988**, *37*, 785-789.
(26) Schäfer, A.; Horn, H.; Ahlrichs, R. *J. Chem. Phys.* **1992**, *97*, 2571-2577.
(27) Schäfer, A.; Huber, C.; Ahlrichs, R. *J. Chem. Phys.* **1994**, *100*, 5829-5835.

(28) Sinnecker, S.; Rajendran, A.; Klamt, A.; Diedenhofen, M.; Neese, F. *J. Phys. Chem. A*. **2006**, *110*, 2235-2245.
(29) Neese, F. *J. Comput. Chem.* **2003**, *24*, 1740-1747.
(30) Decker, A.; Rohde, J.-U.; Klinker, E. J.; Wong, S. D.; Que, L., Jr.,; Solomon, E. I. *J. Am. Chem. Soc.* **2007**, *129*, 15983-15996.
(31) Geng, C.; Ye, S.; Neese, F. *Angew. Chem. Int. Ed.* **2010**, *49*, 5717-5720.
(32) Solomon, E. I.; Decker, A.; Lehnert, N. *Proc. Natl. Acad. Sci.* **2003**, *100*, 3589-3594.
(33) England, J.; Prakash, J.; Cranswick, M. A.; Mandal, D.; Guo, Y.; Münck, E.; Shaik, S.; Que, L., Jr. *Inorg. Chem.* **2015**, *16*.
(34) Cho, K.-B.; Shaik, S.; Nam, W. *J. Phys. Chem. Lett.* **2012**, *3*, 2851-2856.
(35) Zhao, Y.; Truhlar, D. G. *Acc. Chem. Res.* **2008**, *41*, 157-167.
(36) Hull, J. F.; Balcells, D.; Sauer, E. L. O.; Raynaud, C.; Brudvig, G. W.; Crabtree, R. H.; Eisenstein, O. *J. Am. Chem. Soc.* **2010**, *132*, 7605-7616.
(37) Mayer, J. M. *Acc. Chem. Res.* **2011**, *44*, 36-46.
(38) Balcells, D.; Raynaud, C.; Crabtree, R. H.; Eisenstein, O. *Chem. Commun.* **2007**.
(39) Saouma, C. T.; Mayer, J. M. *Chem. Sci.* **2014**, *5*, 21-31.
(40) Shaik, S.; Hirao, H.; Kumar, D. *Acc. Chem. Res.* **2007**, *40*, 532-542.
(41) Grimme, S. E., S.; Goerigk, L. *J. Comput. Chem.* **2011**, *32*, 1456-1465.

CHAPTER 8

Summary

8.1 Summary

This work involves the formation and activation of several Mn^{III}-peroxo intermediates (Chapters 2-4), reductive activation of Mn^{III}-peroxo species by electrochemical methods (Chapter 5), characterization of a series of unusual low-spin Mn^{III} species supported by scorpionate ligands (Chapter 6), and substrate oxidation pathways of high-valent Mn^{IV} intermediates (Chapter 7). It is critical to understand the fundamental interactions that promote activation of metal(III)-peroxo species to high-valent intermediates, as this reactivity is observed in catalytic cycles of many metal-containing enzymes such as the cytochrome P450 enzymes[1,2] and invoked for many synthetic oxidant catalysts.[3-14] In addition, Mn^{III}-peroxo species are proposed to form in many enzymatic systems, such as Mn superoxide dismutase,[15-19] Mn ribonucleotide reductase,[20,21] Mn oxalate oxidase,[22,23] and Mn oxalate decarboxylase,[24-26] and a better understanding of structure-function relationships in these Mn^{III}-peroxo intermediates is necessary to elucidate the mechanisms of these enzymes.

While there are now many examples of model complexes containing Mn^{III}-peroxo species,[27] controlled activation of these Mn^{III}-peroxo intermediates has been a challenging task for many years, with only a few examples of activation of these species by reaction with a redox active Mn center,[28,29] acid-assisted activation,[30] and reaction with electrophilic substrates.[13,30-32] The wide range of supporting ligand structures used to form these intermediates further complicates the understanding of Mn^{III}-peroxo reactivity, and a detailed investigation of the role of the ligand in the activation of Mn^{III}-peroxo intermediates through model complexes is required. Prior to this work, the only examples of activation of Mn^{III}-peroxo species by a redox-active metal have resulted in the formation of a dinuclear product instead of a high-valent, mononuclear species.[28,29] These examples utilized flexible ligands with multiple possible binding modes, enabling dissociation of an arm of the ligand to accommodate the Mn^{III}-peroxo species

and subsequent formation of a bis(μ-oxo) dimangangese product. In contrast, we have explored the reactivity of a Mn^{III}-peroxo species with a more rigid ligand structure that cannot reorient through another binding mode, and this ligand rigidity potentially prevented the formation of the dinuclear products. Electrochemical activation of another Mn^{III}-peroxo species in the presence of acid has also been observed, and the supporting ligand for this reactivity was flexible and prone to degradation.[30] This method of electrochemical activation should be explored with Mn^{III}-peroxo species supported by more rigid ligands. Finally, Borovik and coworkers reported activation through electrophilic substrate addition that was performed with a Mn^{III}-peroxo complex supported by a tripodal ligand with a hydrogen bonding network around the peroxo unit.[13,31,32] This ligand scaffold provides stabilization for the Mn^{III}-peroxo motif; however, these effects may over-stabilize the Mn^{III}-peroxo intermediate, as conversion to a high-valent species was not achieved for this complex. Instead, the Mn^{III}-peroxo species was activated to form a hybrid Mn^{III}-O/OH species with a Mn—O bond length intermediate between those in a Mn^{III}-oxo and Mn^{III}-hydroxo complex with a similar ligand. The ligands used in these examples of Mn^{III}-peroxo activation contain many characteristic differences and further studies with additional supporting ligands are necessary. In general, the appropriate balance between stability and reactivity for activation of Mn^{III}-peroxo species to high-valent, mononuclear intermediates has not been achieved, and this work contributes to the determination of factors that promote this activation pathway.

We have shown successful activation of the $[Mn^{III}(O_2)(Me_2EBC)]^+$ complex supported by a rigid, cross-clamped cyclam ligand by reaction with redox-active Mn^{II} to generate high-valent, mononuclear products. Presumably, the reaction pathway to generate mononuclear products is driven by steric control from the ligand framework.[33] Prior to this study, such reactivity had been proposed, but the products of activation of Mn^{III}-peroxo species were either unable to be

characterized or the reactivity led to the formation of unreactive dinuclear species. This work provides the first example of the activation of a Mn^{III}-peroxo species to mononuclear products with characterization of these species. The rigidity and open *cis* coordination sites that the Me_2EBC ligand facilitates could be incorporated into the design of other ligands to target mononuclear product formation from the activation of Mn^{III}-peroxo species. Specifically, derivatives of the Me_2EBC ligand with varying electronic and steric motifs could be utilized to further define the structure-function relationships in Mn^{III}-peroxo activation. Additionally, X-ray absorption spectroscopy of the $[Mn^{III}(O_2)(Me_2EBC)]^+$ intermediate as well as one of the products of reactivity, $[Mn^{III}(OH)(Cl)(Me_2EBC)]^+$, provided a distinct marker in the pre-edge region for differences in covalency between the Mn^{III}-peroxo and Mn^{III}-hydroxo moieties. This could be used to distinguish such motifs in biological systems.

In addition to activation by a redox-active Mn^{II} species, additional reactivity studies of $[Mn^{III}(O_2)(Me_2EBC)]^+$ were performed through the addition of protons from Brønsted acids, the addition of hydrogen atoms from electrophilic substrates, and modulation of the electronic environment of the Mn^{III}-peroxo moiety through Lewis acid addition. There are a only a few recent reports of successful activation of Mn^{III}-peroxo species through the use of Brønsted acids[30,34] and electrophilic substrates,[31,32] and Lewis acids have recently been shown to assist in the activation of an Fe^{III}-peroxo to a high-valent Fe^{IV}-oxo intermediate.[9,35] The $[Mn^{III}(O_2)(Me_2EBC)]^+$ shows promising reactivity with electrophilic substrates and Lewis acids, although experimental complications suggest that a Mn^{III}-peroxo with a similar, but modified supporting ligand would be optimal for further activation studies. Specifically, this system was complicated by the large excess of superoxide necessary to maximally form the Mn^{III}-peroxo species. The coordinated chloride anions in the starting Mn^{II} complex presumably contribute to this issue. While replacement of the chloride ions with other anions was unsuccessful for the

$[Mn^{II}(Cl)_2(Me_2EBC)]$ complex, Mn^{III}-peroxo solubility and reactivity could be improved with substitution of the chloride anion or initial preparation of the Mn^{II} complex with more labile anions. Additionally, only dichloromethane could be used to form the Mn^{III}-peroxo, and the subsequently formed Mn^{IV} intermediate was insoluble, and/or quite unstable, in this solvent. This chemistry could be further improved if the Mn^{III}-peroxo species could be formed in other solvents, as dichloromethane is known to react with superoxide and also posed difficulties for Mn K-edge XAS data collection. These sparse examples of Mn^{III}-peroxo activation illustrate the difficulty of controlled activation of Mn^{III}-peroxo species; however, this work as well as other recent advances,[8,9,30,32,33,35,36] furthers the understanding of important parameters for successful activation.

An unusually stable Mn^{III}-peroxo intermediate supported by a scorpionate-type ligand, Tp^{Ph2}, was characterized through spectroscopic methods and computationally investigated. The high stability of this species arises from the bulky nature of the supporting ligand, and provides an example of a ligand with a large amount of steric bulk that hinders activation of the Mn^{III}-peroxo unit. The electronic absorption of the $[Mn^{III}(O_2)(Tp^{Ph2})(THF)]^+$ complex displayed an unusual blue-shift of the lowest-energy transition, and the nature of this shift was determined as a result of an axial elongation that stabilized the donor MO in this transition. Multireference *ab initio* calculations of the electronic structure of this species were compared with those for a Mn^{III}-peroxo complex supported by a derivative of the ligand, Tp^{iPr2}, and stabilizing effects from the ligands were determined. While the $[Mn^{III}(O_2)(Tp^{Ph2})(THF)]^+$ complex exhibited high stability, and consequently, low reactivity, this study provided insight into the influence of the ligand in providing an axial elongation and the resulting stabilizing effect in the electronic structure of this Mn^{III}-peroxo species.

An alternative method of activation of Mn^{III}-peroxo species was utilized through electrochemical formation and reduction. O—O bond cleavage was achieved when the Mn^{III}-peroxo species was electrochemically reduced in the presence of a weak acid, while Mn—O bond cleavage and H_2O_2 generation resulted in the presence of a strong acid. The mechanism of O—O bond cleavage was explored, and the electrochemical data establish a large experimental reorganizational energy that is consistent with a mechanism with concerted reduction and O—O bond cleavage. This unique method of activation by electrochemical methods allows for insight into the mechanism of activation, and is the only example of targeted Mn—O versus O—O bond activation. Mechanisms of O—O bond activation were computationally explored for Mn^{III}-peroxo species supported by a pentadentate, N_4O^- ligand, a cross-clamped Me_2EBC ligand, and a macrocyclic TMC ligand. For all cases, a concerted process of reduction and O—O bond cleavage was favored over stepwise processes, and the role of the ligand in promoting Mn^{III}-peroxo activation was evaluated. Upon reduction and O—O bond cleavage, the species supported by the N_4O^- ligand undergo further reorganization and degradation, presumably due to the flexible nature of this ligand. As such, this ligand is not ideal for further studies. The small reduction potential calculated for the Mn^{III}-peroxo species supported by the Me_2EBC ligand indicated that this ligand framework provides a good environment for concerted O—O bond cleavage and reduction. The favorability of this reaction presumably results from the stable supporting structure and moderate steric bulk of the Me_2EBC ligand, as well as the availability of two *cis* coordination sites to accommodate O—O bond cleavage in the Mn^{III}-peroxo moiety to a *cis*-Mn^{IV}-dioxo intermediate. In contrast, the calculated reduction potential for the Mn^{III}-peroxo supported by the TMC ligand was less favorable than that of the Mn^{III}-peroxo supported by the Me_2EBC ligand, as the TMC framework cannot as easily sustain the O—O bond cleavage and formation of a *cis*-Mn^{IV}-dioxo species. This Me_2EBC ligand, or derivatives of this ligand, is an

ideal candidate for these electrochemical experiments, although these studies will require preparation of the Mn^{II} species with a coordinating species more labile than the chloride anions to successfully perform these electrochemical experiments. Additionally, these computations could be expanded to other ligand systems that contain *cis* open coordination sites to compare to the Mn^{III}-peroxo species supported by the Me_2EBC ligand, and to identify other potentially useful ligand platforms for reductive O—O bond activation.

A series of Mn^{III} species in an unusual low-spin (S=1) configuration were characterized by magnetic circular dichroism spectroscopy and multireference *ab initio* calculations (CASSCF/NEVPT2). The potentially orbitally-degenerate ground state of these low-spin Mn^{III} complexes cannot be treated with DFT calculations, and there are few examples of other successful electronic structure methods for S=1 Mn^{III} species. Three complexes supported by scorpionate-type ligands, Tp and Tp^*, as well as a structurally related N-heterocyclic carbene complex, contain only small structural perturbations, but display large differences in the electronic transitions. The CASSCF/NEVPT2 calculations were able to reproduce the zero field splitting in these complexes and revealed that an increase in σ-donation properties from the ligand causes a shift in a low-lying triplet state. These calculations contributed to the understanding of the electronic structure of low-spin Mn^{III} species, which remain quite rare. These methods could be utilized to explore the electronic structures of other complexes with unusual spin states, as there have been few successful attempts to explore these and other similar complexes.

Oxidation of organic substrates by high-valent Mn species, both in synthetic catalyst systems as well as in enzymes, are critical reactions to understand and control. However, model systems lack the specificity and efficiency that is present in enzyme systems. A set of high-valent Mn^{IV} species that differ only by one proton, $[Mn^{IV}(O)(OH)(Me_2EBC)]^+$ and

$[Mn^{IV}(OH)_2(Me_2EBC)]^{2+}$, display a 15-fold difference in rate of reaction with DHA and are able to direct product distribution toward hydroxylation and desaturation, respectively. The fundamental parameters that modulate this reactivity were explored through DFT computations. While DFT overestimates the driving force in several reactions, stabilization of the desaturated product was correctly predicted for the reaction of DHA with $[Mn^{IV}(OH)_2(Me_2EBC)]^{2+}$, and alternative mechanisms of electron transfer was determined to be unfavorable. Additionally, while there are many studies describing HAT reactions with Mn^{IV}-oxo species,[4,5,37] reactivity with Mn^{IV}-hydroxo species is not as well understood.[38] This study could be expanded to include HAT of other Mn-hydroxo complexes as well as the product formation steps. The discrepancy between several of the calculated driving forces with the experimental bond dissociation energies could potentially be improved by exploring alternate functionals and additional methods of calculation. In particular, the inclusion of water in the solvent model for these calculations is likely critical for accurately reproducing the experimental thermodynamic parameters, as all experimental measurements were performed in a solvent mixture of water and acetone. Modeling of these solvent effects was attempted with inclusion of water molecules around the complex and substrate species; however, calculations with these components did not converge to a stable structure. Further investigation of these solvent effects and the role of water in facilitating the HAT reaction could be explored through a combined quantum mechanics and molecular dynamics approach.

8.2 References

(1) *Cytochrome P450: Structure, Mechanism, and Biochemistry*; Plenum: New York, 1995.
(2) Meunier, B.; de Visser, S. P.; Shaik, S. *Chem. Rev.* **2004**, *104*, 3947-3980.
(3) Chattopadhyay, S., et al. *Inorg. Chem.* **2010**, *49*, 7530-7535.

(4) Chen, J.; Lee, Y.-M.; Davis, K. M.; Wu, X.; Seo, M. S.; Cho, K.-B.; Yoon, H.; Park, Y. J.; Fukuzumi, S.; Pushkar, Y. N.; Nam, W. *Journal of the American Chemical Society* **2013**, *135*, 6388-6391.
(5) Cho, K.-B.; Shaik, S.; Nam, W. *J. Phys. Chem. Lett.* **2012**, *3*, 2851-2856.
(6) England, J.; Martinho, M.; Farquhar, E. R.; Frisch, J. R.; Bominaar, E. L.; Münck, E.; Que, L., Jr. *Angewandte Chemie, International Edition in English* **2009**, *48*, 3622-3626.
(7) England, J.; Prakash, J.; Cranswick, M. A.; Mandal, D.; Guo, Y.; Münck, E.; Shaik, S.; Que, L., Jr. *Inorg. Chem.* **2015**, *16*.
(8) Leto, D. F.; Ingram, R.; Day, V. W.; Jackson, T. A. *Chemical Commun.* **2013**, *49*, 5378-5380.
(9) Li, F.; Van Heuvelen, K. M.; Meier, K. K.; Münck, E.; Que, L., Jr. *J. Am. Chem. Soc.* **2013**, *135*, 10198-10201.
(10) Liu, W.; Groves, J. T. *J. Am. Chem. Soc.* **2010**, *132*, 12847–12849.
(11) Oloo, W. N.; Que, L., Jr. *Acc. Chem. Res.* **2015**, *48*, 2612-2621.
(12) Sastri, C. V.; Lee, J.; Oh, K.; Lee, Y. J.; Lee, J.; Jackson, T. A.; Ray, K.; Hirao, H.; Shin, W.; Halfen, J. A.; Kim, J.; Que, L., Jr.,; Shaik, S.; Nam, W. *Proc. Natl. Acad. Sci.* **2007**, *104*, 19181-19186.
(13) Shook, R. L.; Borovik, A. S. *Inorg. Chem.* **2010**, *49*, 3646-3660.
(14) Yin, G.; Danby, A. M.; Kitko, D.; Carter, J. D.; Scheper, W. M.; Busch, D. H. *J. Am. Chem. Soc.* **2008**, *130*, 16245-16253.
(15) Bull, C.; Niederhoffer, E. C.; Yoshida, T.; Fee, J. A. *J. Am. Chem. Soc.* **1991**, *113*, 4069-4076.
(16) Grove, L. E.; Brunold, T. C. *Comments Inorg. Chem* **2008**, *29*, 134-168.
(17) Hearn, A. S.; Stroupe, M. E.; Cabelli, D. E.; Lepock, J. R.; Tainer, J. A.; Nick, H. S.; Silverman, D. N. *Biochemistry* **2001**, *40*, 12051-12058.
(18) Jackson, T. A.; Karapetian, A.; Miller, A.-F.; Brunold, T. C. *Biochemistry* **2005**, *44*, 1504-1520.
(19) Miller, A.-F. *Curr. Opin. Chem. Biol.* **2004**, *8*, 162-168.
(20) Boal, A. K.; Cotruvo, J. A.; Stubbe, J.; Rosenzweig, A. C. *Science* **2010**, *329*, 1526-1530.
(21) Cotruvo, J. A. J.; Stich, T. A.; Britt, R. D.; Stubbe, J. *J. Am. Chem. Soc.* **2013**, *135*, 4027-4039.
(22) Borowski, T.; Bassan, A.; Richards, N. G. J.; Siegbahn, P. E. M. *J. Chem. Theory Comput.* **2005**, *1*, 686-693.
(23) Opaleye, O.; Rose, R.-S.; Whittaker, M. M.; Woo, E.-J.; Whittaker, J. W.; Pickersgill, R. W. *J. Biol. Chem.* **2006**, *281*, 6428-6433.
(24) Reinhardt, L. A.; Svedruzic, D.; Chang, C. H.; Cleland, W. W.; Richards, N. G. J. *J. Am. Chem. Soc.* **2003**, *125*, 1244-1252.
(25) Svedružic, D.; Jónsoon, S.; Toyota, C. G.; Reinhardt, L. A.; Ricagno, S.; Lindqvist, Y.; Richards, N. G. J. *Arch. Biochem. Biophys.* **2005**, *433*, 176-192.
(26) Tanner, A.; Bowater, L.; Fairhurst, S. A.; Bornemann, S. *J. Biol. Chem.* **2001**, *276*, 43627-43634.
(27) Leto, D. F.; Jackson, T. A. *J. Biol. Inorg. Chem.* **2014**, *19*, 1-15.
(28) Groni, S.; Dorlet, P.; Blain, G.; Bourcier, S.; Guillot, R.; Anxolabéhère-Mallart, E. *Inorg. Chem.* **2008**, *47*, 3166-3172.
(29) Leto, D. F.; Chattopadhyay, S.; Day, V. W.; Jackson, T. A. *Dalton Trans.* **2013**, *42*, 13014-13025.

(30) Ching, H. Y. V.; Anxolabéhère-Mallart, E.; Colmer, H. E.; Costentin, C.; Dorlet, P.; Jackson, T. A.; Policar, C.; Robert, M. *Chem. Sci.* **2014**, *5*, 2304-2310.
(31) Shook, R. L.; Gunderson, W. A.; Greaves, J.; Ziller, J. W.; Hendrich, M. P.; Borovik, A. S. *J. Am. Chem. Soc.* **2008**, *130*, 8888-8889.
(32) Shook, R. L.; Peterson, S. M.; Greaves, J.; Moore, C.; Rheingold, A. L.; Borovik, A. S. *J. Am. Chem. Soc.* **2011**, *133*, 5810-5817.
(33) Colmer, H. E.; Howcroft, A. H.; Jackson, T. A. *Inorg. Chem.* **2016**, *55*, 2055-2069.
(34) So, H.; Park, J.-H.; Cho, K.-B.; Lee, Y.-M.; Seo, M. S.; Cho, J.; Sarangi, R.; Nam, W. *J. Am. Chem. Soc.* **2014**, *136*, 12229−12232.
(35) Lee, Y.-M.; Bang, S.; Kim, Y. M.; Cho, J.; Hong, S.; Nomura, T.; Ogura, T.; Troeppner, O.; Ivanović-Burmazović, I.; Sarangi, R.; Fukuzumi, S.; Nam, W. *Chem. Sci.* **2013**, *4*, 3917-3923.
(36) Coggins, M. K.; Sun, X.; Kwak, Y.; Solomon, E. I.; Rybak-Akimova, E.; Kovacs, J. A. *J. Am. Chem. Soc.* **2013**, *135*, 5631-5640.
(37) Balcells, D.; Raynaud, C.; Crabtree, R. H.; Eisenstein, O. *Chem. Commun.* **2007**.
(38) Shi, S., Wang, Y., Xu, A., Wang, H., Zhu, D., Roy, S.B., Jackson, T.A., Busch, D.H., Yin, G. *Angew. Chem. Int. Ed.* **2011**, *50*, 7321-7324.

APPENDIX A2.

Table A2.1. Cartesian coordinates (Å) for DFT energy minimized $[Mn^{III}(O_2)(Me_2EBC)]^+$ model.

Atom	x	y	z
Mn	-1.999037959	0.085623654	0.875353632
O	-0.904006409	1.585928621	1.069979651
O	-1.902258405	1.478712704	2.116209922
N	-0.485774984	-1.355486156	2.109997903
N	-3.632430608	1.254933863	-0.496299429
N	-3.70933121	-1.167420939	1.095628379
N	-1.381447082	-1.273393832	-0.648554784
C	-1.241815835	-2.196660104	3.09047065
C	-2.650402729	-1.674567649	3.409337581
C	-3.719123433	-2.007276739	2.36017245
C	-4.87891205	-0.221747532	1.106390628
C	-4.95255159	0.656555284	-0.146732743
C	-3.279503847	1.136660034	-1.945729505
C	-1.81236483	0.763057394	-2.20198881
C	-1.48615361	-0.729558005	-2.062563422
C	0.250243558	-2.144605668	1.080930736
C	0.0563051	-1.580870086	-0.329584988
C	-2.272001278	-2.473041513	-0.457240338
C	-3.693820051	-2.035445998	-0.13507331
C	0.437204017	-0.445742844	2.83101598
C	-3.572845773	2.676036427	-0.078143364
H	-0.653525689	-2.280153131	4.030895113
H	-1.324103196	-3.227171197	2.688126165
H	-2.6266038	-0.584582783	3.625478548
H	-2.980271072	-2.159545922	4.352286091
H	-4.726484577	-1.913833983	2.813488633
H	-3.612264503	-3.069335353	2.061184773
H	-4.768892654	0.401177232	2.016533515
H	-5.828587043	-0.792913069	1.20747757
H	-5.71725543	1.443437637	0.029360311
H	-5.324303328	0.067874358	-1.006881758
H	-3.517290225	2.093939869	-2.460615242
H	-3.931630657	0.36956836	-2.411309391
H	-1.134086096	1.381680105	-1.575332389
H	-1.576955652	1.03272935	-3.253226165
H	-0.526349274	-0.946078621	-2.573038482
H	-2.259261927	-1.319442286	-2.594802975
H	-0.085181571	-3.198183717	1.123009257
H	1.340524131	-2.169683104	1.295488067
H	0.613642839	-0.630657955	-0.452195484
H	0.464200862	-2.303591432	-1.070879906

H	-1.874989683	-3.079933231	0.375109432
H	-2.255178154	-3.120123879	-1.359417931
H	-4.104675595	-1.458243515	-0.981251792
H	-4.354836961	-2.917542947	-0.00023559
H	-0.142857007	0.208189091	3.507567248
H	1.179828478	-1.028465116	3.423188874
H	0.965377751	0.202739465	2.109517609
H	-2.554141564	3.069045241	-0.250540488
H	-3.7847621	2.758766319	1.002693867
H	-4.308055295	3.285643303	-0.652255301

Table A2.2. Cartesian coordinates (Å) for DFT energy minimized $[Mn^{III}(OH)(Cl)(Me_2EBC)]^+$ model.

Atom	x	y	z
Mn	-0.29432316	0.608235256	0.009171428
O	-1.531116338	1.962442737	-0.046373229
Cl	1.521749012	2.336842158	0.157395836
H	-1.053758018	2.810644307	0.04771947
N	-0.386834605	0.509441653	2.266488688
N	-0.14653704	0.427660845	-2.218484706
N	0.860509873	-1.183174296	-0.138544878
N	-1.971445036	-0.961415946	0.179445821
C	0.940524608	0.183895144	2.914919812
C	2.01944741	-0.454502876	2.024405774
C	1.584752208	-1.602241499	1.121177965
C	1.833726653	-0.828548862	-1.22474214
C	1.120628658	-0.350018874	-2.501722256
C	-1.363129113	-0.247932246	-2.823158661
C	-2.677702889	0.064954788	-2.106223095
C	-3.027216132	-0.810269435	-0.889710234
C	-1.409479486	-0.542339791	2.582595212
C	-2.515626972	-0.637728454	1.533611134
C	-1.340990791	-2.320450782	0.16894709
C	-0.01618543	-2.323991045	-0.578417943
C	-0.865751235	1.816451286	2.803347839
C	-0.052449773	1.796083284	-2.807209746
H	1.353475106	1.132851552	3.304541596
H	0.736530771	-0.460180754	3.79732908
H	2.514840531	0.32981724	1.419398806
H	2.796685124	-0.851495046	2.709586181
H	2.466967549	-2.19912525	0.806345933
H	0.9185397	-2.294619743	1.670138984
H	2.484397007	-0.029652865	-0.823974093
H	2.471429579	-1.708989848	-1.45894811
H	1.825497828	0.288074734	-3.067472838
H	0.874267397	-1.200754721	-3.1658507
H	-1.422979486	0.071285056	-3.885868801
H	-1.192163684	-1.339686013	-2.846083467
H	-2.70327704	1.135203816	-1.825219356
H	-3.50042416	-0.088002198	-2.835421663
H	-3.932280938	-0.384987763	-0.413490965
H	-3.303965061	-1.828596011	-1.234989865
H	-0.888476069	-1.511220584	2.687204723
H	-1.867012978	-0.334492385	3.574333646

H	-3.048952273	0.328124002	1.448631188
H	-3.254096352	-1.404945053	1.859241945
H	-1.181703814	-2.650554549	1.211038279
H	-2.025160509	-3.066084673	-0.286612693
H	-0.183852408	-2.240694459	-1.663128615
H	0.520605976	-3.283281275	-0.420707858
H	-0.182804869	2.61890899	2.469775169
H	-0.887354156	1.781773575	3.914441566
H	-1.879309743	2.029998671	2.423032095
H	-0.990399442	2.344092706	-2.605030849
H	0.785742395	2.342579401	-2.34036128
H	0.100549615	1.724156097	-3.905778218

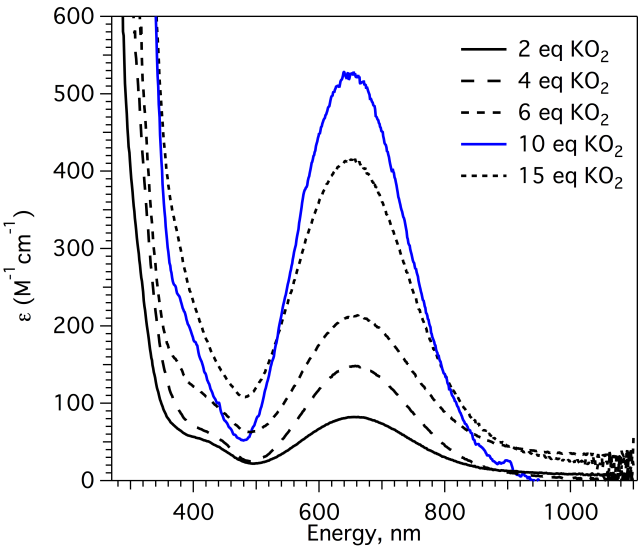

Figure A2.1. Optimization of formation of $[Mn^{III}(O_2)(Me_2EBC)]^+$ using different equivalents of KO_2 in CH_2Cl_2 at -60 °C.

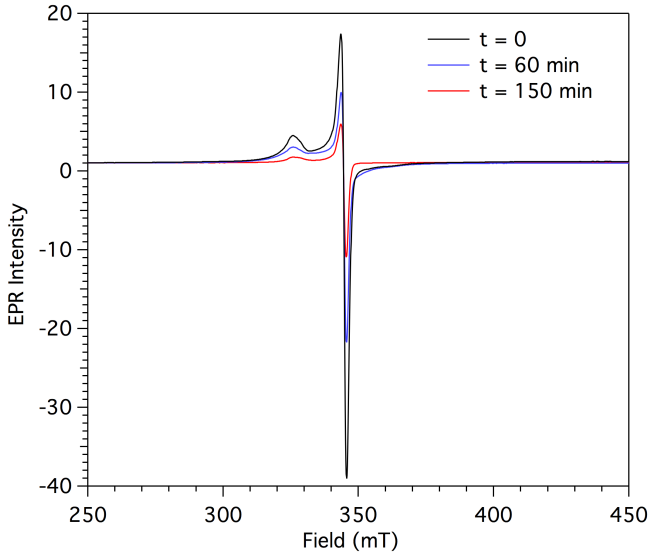

Figure A2.2. 5 K perpendicular-mode EPR spectrum of decay of KO_2 in CH_2Cl_2 at -60 °C in the absence of $[Mn^{II}(Cl)_2(Me_2EBC)]$.

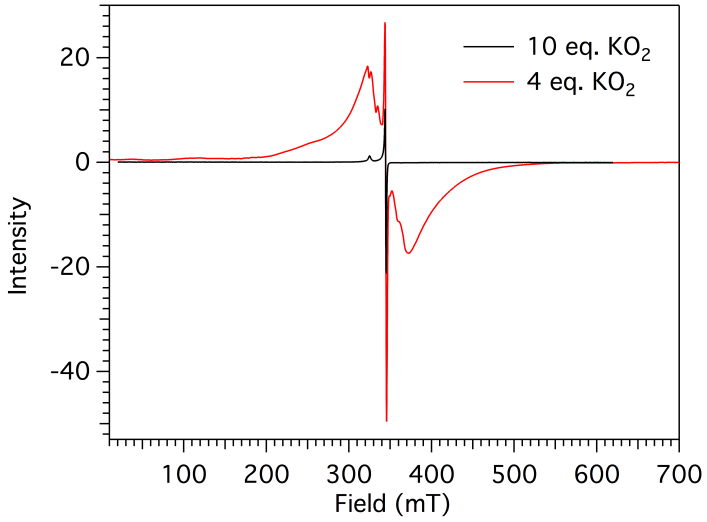

Figure A2.3. 5 K perpendicular-mode EPR spectrum of the blue intermediate $[Mn^{III}(O_2)(Me_2EBC)]^+$ formed with 10 equiv. of KO_2 (black trace) and 4 equiv. KO_2 (red trace) in CH_2Cl_2 at -60 °C upon formation of $[Mn^{III}(O_2)(Me_2EBC)]^+$.

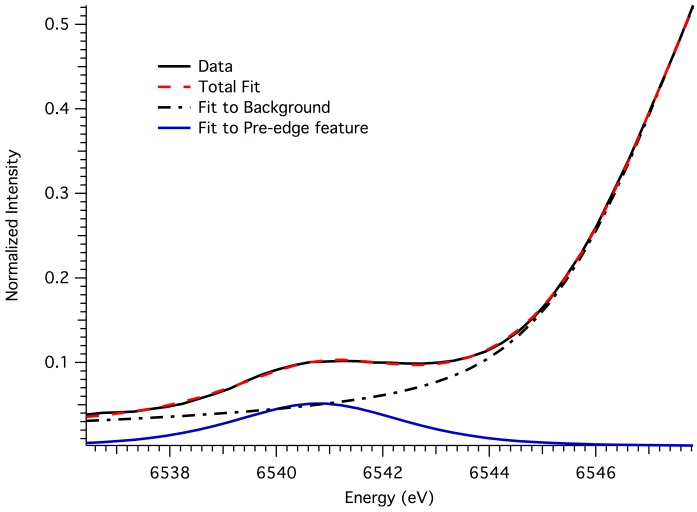

Figure A2.4. Mn K-edge pre-edge data (solid black trace) and fit (red dashed trace) for $[Mn^{III}(O_2)(Me_2EBC)]^+$. Broken black traces represent fits to the background and the solid blue trace represents the fits to the pre-edge peak.

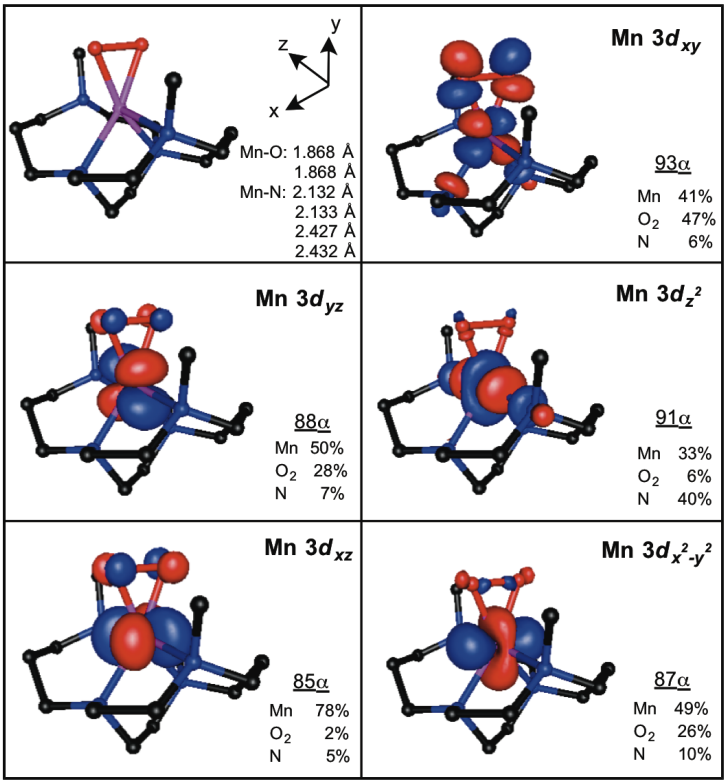

Figure A2.5. DFT-optimized structure of $[Mn^{IV}(O_2)(Me_2EBC)]^+$ with metal-ligand bond lengths and the *D*-tensor coordinate system from CP-DFT computations (top left panel) with *y*-axis bisecting the O—O bond vector and the *z*-axis along the elongated N_{axial}-Mn-N_{axial} axis. Surface contour plots of quasi-restricted Mn 3*d*-based orbitals (QROs). Total Mn 3*d* and ligand 2*p* contributions to the spin-up Kohn-Sham orbitals are listed next to each plot of the corresponding QRO.

Table A2.3. TD-DFT Calculated Energies, Percent Contributions from Dominant One-electron Excitations, and Oscillator Strengths for the Major Electronic Transitions of $[Mn^{III}(O_2)(Me_2EBC)]^+$.

region	state	energy (cm^{-1})	f_{osc}	transition[a]	%	donor MO	acceptor MO	comments	EDDM
A	2	16111.1	0.000379	91a → 93a	92.8	Mn d_{z^2}	Mn d_{xy}	d-d	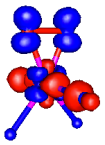
B	3	22642.9	0.000005	88b → 89b	98.9	O_2 π*	Mn $d_{x^2-y^2}$	LMCT	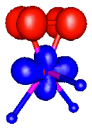
	4	23434.4	0.000050	88b → 90b	73.7	O_2 π*	Mn d_{xz}	LMCT	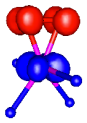
				90a → 93a	13.6	N π	Mn d_{xy}		
	5	25405.0	0.000433	88b → 91b	97.4	O_2 π*	Mn d_{yz}	LMCT	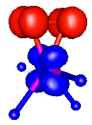
	6	26800.0	0.001478	88a → 93a	50.2	Mn d_{yz}	Mn d_{xy}	d-d	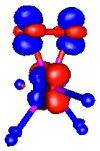
				90a → 93a	35.6	N π	Mn d_{xy}		
	7	30284.6	0.003280	87a → 93a	75.6	Mn $d_{x^2-y^2}$	Mn d_{xy}	d-d	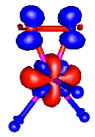
				84a → 93a	17.3	Mn d_{z^2}	Mn d_{xy}		
	8	31290.5	0.000052	88b → 93b	58.6	O_2 π*	Mn d_{xy}	LMCT	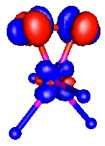
	9	32767.5	0.039624	89a → 93a	29.1	N π	Mn d_{xy}	LMCT	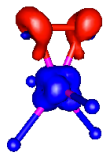
				86b → 93b	18.3	O_2 π*	Mn d_{xy}		
				88b → 90b	13.0	O_2 π*	Mn d_{xz}		
				88b → 92b	13.1	O_2 π*	Mn d_{z^2}		
				90a → 93a	10.4	N π	Mn d_{xy}		
	10	32963.2	0.005345	88b → 92b	85.7	O_2 π*	Mn d_{z^2}	LMCT	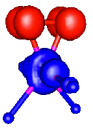
	11	34086.7	0.001024	85a → 93a	29.6	Mn d_{xz}	Mn d_{xy}	d-d	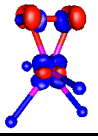
				86b → 90b	25.9	O_2 π*	Mn d_{xz}		

[a]Transitions over 10% are included.

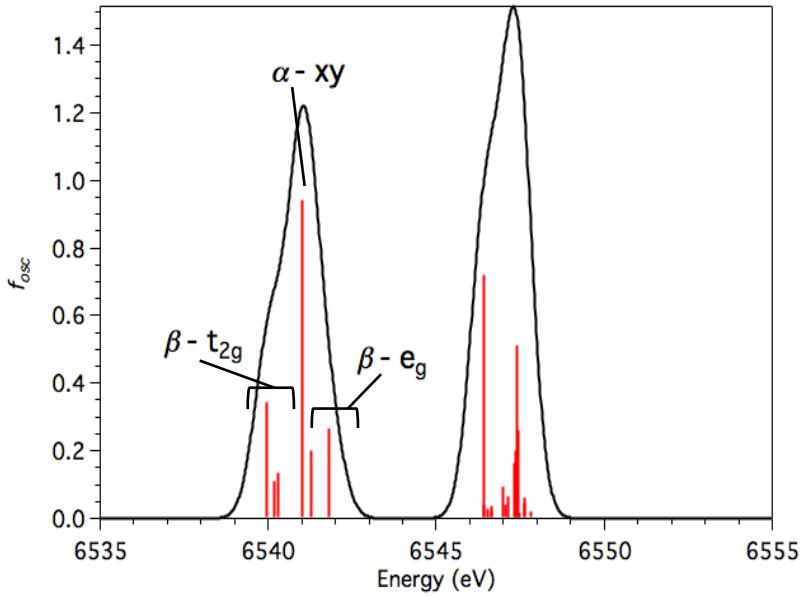

Figure A2.6. TD-DFT-calculated XANES spectrum for $[Mn^{III}(O_2)(Me_2EBC)]^+$. The higher energy feature at 6547 eV corresponds to metal-to-ligand charge-transfer transitions.

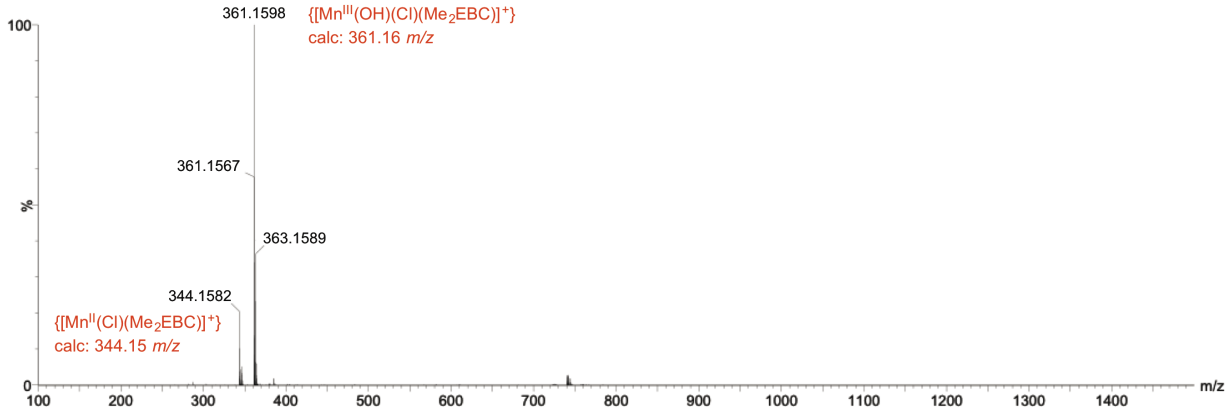

Figure A2.7. ESI Mass spectrum of purified orange solution, showing a dominant peak associated with $[Mn^{III}(OH)(Cl)(Me_2EBC)]^+$.

Table A2.4. TD-DFT Calculated Energies, Percent Contributions from Dominant One-electron Excitations, and Oscillator Strengths for the Major Electronic Transitions of $[Mn^{III}(OH)(Cl)(Me_2EBC)]^+$.

state	energy (cm^{-1})	f_{osc}	transition	%	donor MO	acceptor MO	comments	EDDM
1	9094.9	0.000576	97a → 98a	92.7	Mn $d_{x^2-y^2}$	Mn d_{z^2}	d-d	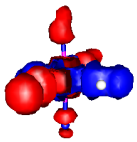
2	16660.1	0.001821	94a → 98a	79.3	Mn d_{xz}	Mn d_{z^2}	d-d	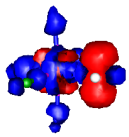
3	19934.2	0.001406	96a → 98a	80.9	Cl 2p	Mn d_{z^2}	LMCT	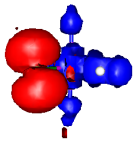
4	20612.4	0.001793	95a → 98a	82.7	Cl 2p	Mn d_{z^2}	LMCT	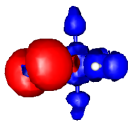
5	24677	0.006955	93a → 98a	33.5	Cl 2p	Mn d_{z^2}	d-d	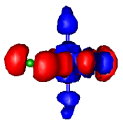
			90a → 98a	22.8	Mn d_{yz}	Mn d_{z^2}		
			89a → 98a	18.2	Mn d_{yz}	Mn d_{z^2}		
6	28229.1	0.009716	93a → 98a	31.5	Cl 2p	Mn d_{z^2}	d-d	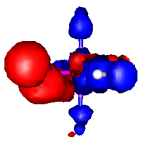
			90a → 98a	16.1	Mn d_{yz}	Mn d_{z^2}		
			88a → 98a	11.2	Mn d_{xy}	Mn d_{z^2}		
7	29747.1	0.004075	93a → 98a	20.0	Cl 2p	Mn d_{z^2}	d-d / LMCT	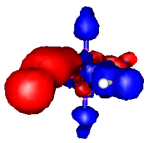
			88a → 98a	18.4	Mn d_{xy}	Mn d_{z^2}		
			86a → 98a	13.3	Mn d_{xy}	Mn d_{z^2}		
8	30217.3	0.001180	93b → 94b	91.1	Cl 2p	Mn d_{yz}	LMCT	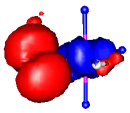
9	30624.8	0.000873	93b → 95b	65.4	Cl 2p	Mn d_{xy}	LMCT	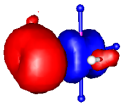
			92b → 94b	29.1	Cl 2p	Mn d_{yz}		
10	30985	0.004387	92b → 94b	48.9	Cl 2p	Mn d_{yz}	LMCT	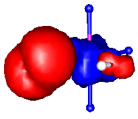
			93b → 95b	18.1	Cl 2p	Mn d_{xy}		
			92b → 95b	19.5	Cl 2p	Mn d_{xy}		

[a]Transitions over 10% are included.

Table A2.5. Energies (eV) and Compositions (%) of the O and Cl 2p-based MOs and the Mn 3d-based MOs Based on Spin-Unrestricted B3LYP DFT Computations for $[Mn^{III}(OH)(Cl)(Me_2EBC)]^+$ from energy minimized DFT structures.

orbital	occupancy	spin	energy (eV)	Mn 3d	O(H) 2p	Cl 2p	N 2p
86 (xy)	1.0	↑	-12.5897	24.4	0.3	0.7	8.0
87	1.0	↑	-12.5258	9.3	0.4	0.3	4.4
88 (xy)	1.0	↑	-12.4091	29.8	2.1	0.5	5.4
89 (yz)	1.0	↑	-12.3128	35.6	10.3	1.8	15.0
90 (yz)	1.0	↑	-11.9780	25.3	6.9	7.2	20.2
91	1.0	↑	-11.4066	1.2	32.3	12.0	22.3
92	1.0	↑	-11.1392	2.9	14.7	1.8	36.5
93	1.0	↑	-10.7026	3.6	7.3	31.4	29.2
94 (xz)	1.0	↑	-10.3394	15.0	55.7	1.1	15.1
95 (Cl 2p)	1.0	↑	-9.8576	2.0	1.9	90.2	0.9
96 (Cl 2p)	1.0	↑	-9.7716	2.4	1.6	88.5	0.9
97 (x^2-y^2)	1.0	↑	-9.0304	27.9	0.7	27.2	29.0
98 (z^2)	0.0	↑	-6.1437	52.1	17.7	4.2	15.0
92 (Cl 2p)	1.0	↓	-9.8776	1.8	1.9	90.5	0.4
93 (Cl 2p)	1.0	↓	-9.7885	1.4	2.6	87.6	1.0
94 (yz)	0.0	↓	-4.8925	90.4	1.1	1.4	0.8
95 (xy)	0.0	↓	-4.8527	91.2	1.0	1.9	1.1
96 (xz)	0.0	↓	-4.7951	86.6	7.5	0.4	0.9
97 (z^2)	0.0	↓	-3.8729	72.3	6.5	5.7	6.5
98 (x^2-y^2)	0.0	↓	-3.6932	78.6	1.4	1.5	10.0

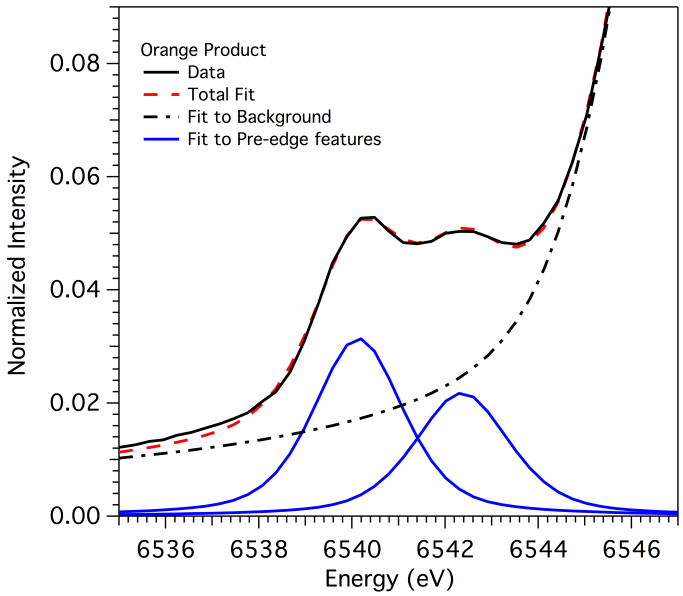

Figure A2.8. Mn K-edge pre-edge data (solid black trace) and fit (red dashed trace) for the orange solution. Broken black traces represent fits to the background and the solid blue trace represents the fits to the pre-edge peak.

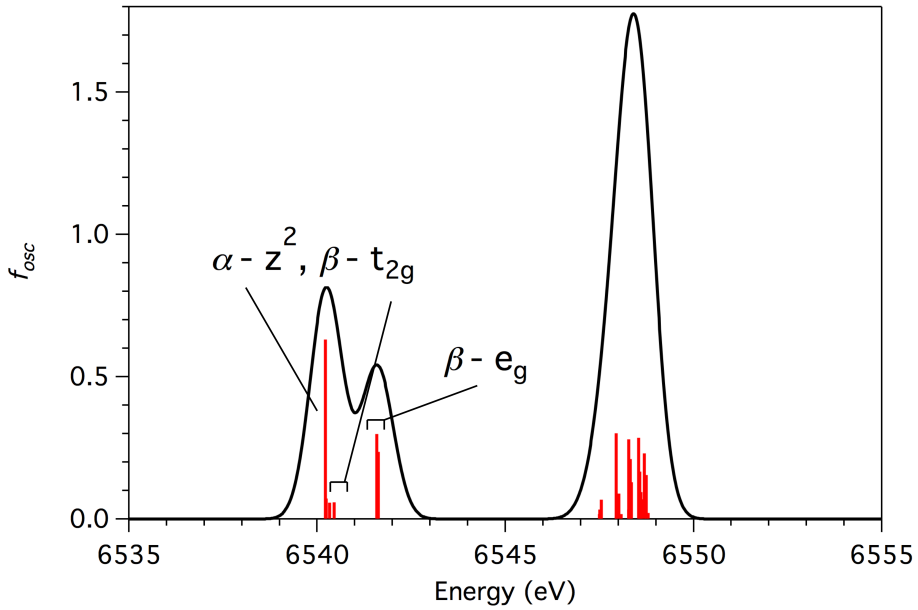

Figure A2.9. TD-DFT calculated XANES spectrum for $[Mn^{III}(OH)(Cl)(Me_2EBC)]^+$. The higher energy feature at 6548 eV corresponds to metal-to-ligand charge-transfer transitions.

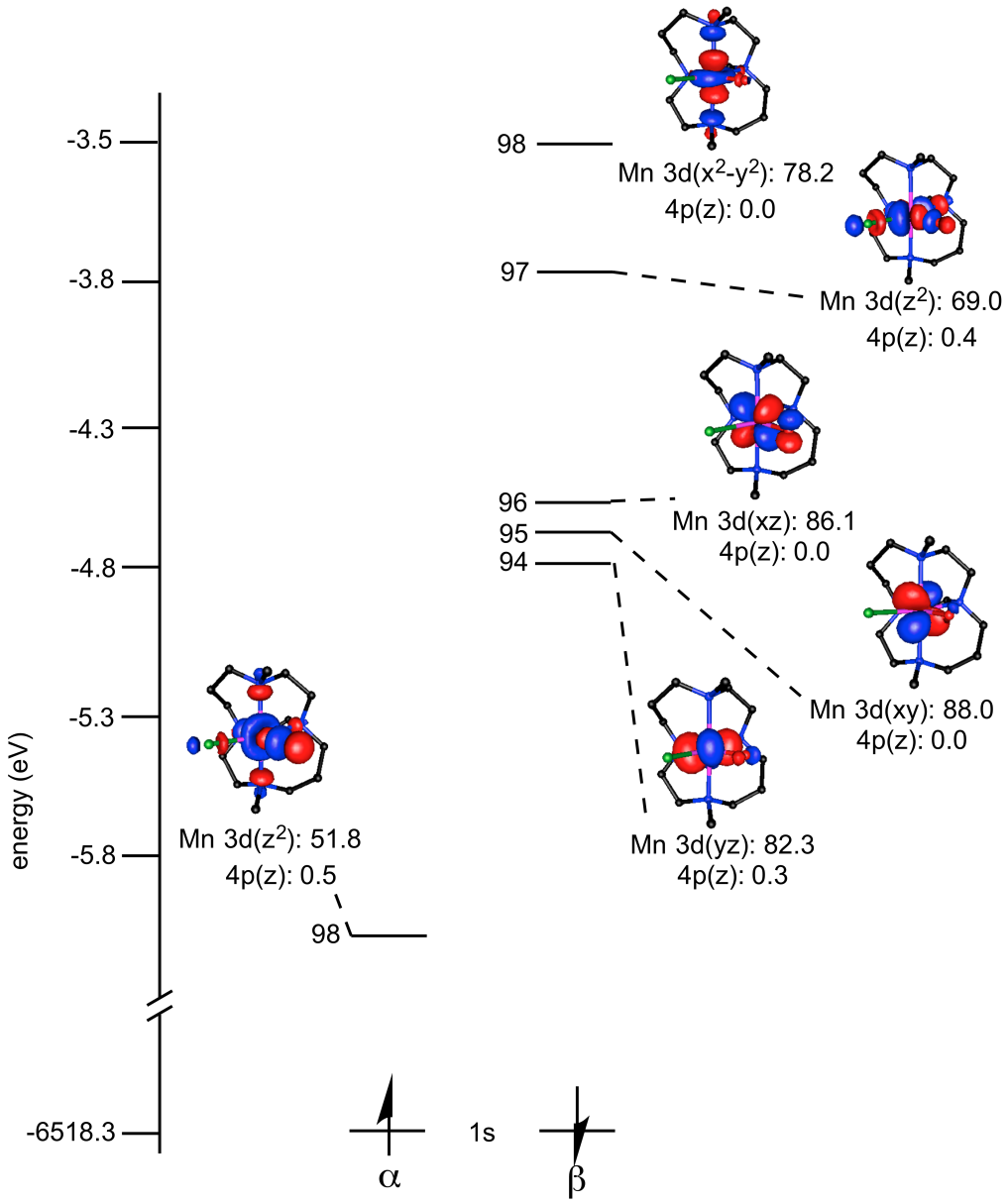

Figure A2.10. MO diagram of $[Mn^{III}(OH)(Cl)(Me_2EBC)]^+$ with energies for spin-unrestricted Kohn-Sham orbitals. Surface contour plots for Kohn-Sham Mn 3*d* based orbitals are shown with Mn 3*d* and 4*p* contributions listed.

EXAFS Analysis of the Orange Solution

Further structural investigation of the orange solution was sought from the analysis of EXAFS data. The Fourier transform of these data contains a primary peak in the Fourier transform (R' = 1.6 $Å^{-1}$) as well as peaks at peaks at 1.99 and 2.33 $Å^{-1}$ (Figure 8). Similar to fits of $[Mn^{III}(O_2)(Me_2EBC)]^+$, a large number of shells within coordination distance of the Mn atom were necessary to successfully model these peaks. Additionally, the distances and Debye-Waller factors describing the oxygen, nitrogen, and chlorine shells were observed to be correlated in these fits, resulting in several physically meaningless Debye-Waller factors (a negative Debye-Waller factor for the O atom shell and factors too large for N and/or C shells at the specified distances). However, a large number of fits determined that six shells were necessary to reasonably model the experimental data. The primary Fourier transform peak at 1.6 $Å^{-1}$ is fit with a shell of 1 O atom at 1.86 Å with contributions from shells of N atoms (1 N atom at 2.12 Å and a shell of 3 N atoms at 2.39 Å, fit 9). DFT computations predict a similar Mn—O(H) distance (1.835 Å). The distances of the two N shells are in agreement with DFT-calculated Mn—N bond lengths that show a short Mn—N bond *trans* to the hydroxide ligand (2.136 Å), an elongated bond *trans* to the chloride ligand (2.303 Å) and Mn-N_{axial} bond lengths of 2.261 and 2.240 Å. Similar to fits of $[Mn^{III}(O_2)(Me_2EBC)]^+$, two separate shells of N atoms were necessary to model both of the peaks at 1.99 and 2.33 $Å^{-1}$. The improvement of the fit by the addition of two shells of N atoms is demonstrated by the difference in the goodness of fit between fit 10 (two shells of N atoms) and fit 4 (one shell of N atoms). While this fit has a negative Debye-Waller factor for the O shell, all other fits resulted in unreasonably large factors for N or C shells at those distances. Importantly, the Fourier transform data of the orange solution differs from that of $[Mn^{III}(O_2)(Me_2EBC)]^+$ with a third peak present at 2.66 $Å^{-1}$, which was could only be fit with a shell of 1 Cl atom at 2.41 Å (Fit 9). Fits with physically reasonable bond lengths of Cl and N

atoms also required the combination of a shell of 1 Cl atom as well as a shell of 4 C atoms at 2.97 Å and a shell of 6 C atoms at 3.09 Å. DFT-computations of $[Mn^{III}(OH)(Cl)(Me_2EBC)]^+$ predict a Mn—Cl bond at 2.512 Å, which is slightly overestimated from the fit, but still acceptable. Distances of the two shells of C atoms are reasonable averages of DFT-calculated Mn—C distances within the macrocyclic ligand. All fits without the Cl shell and two C shells resulted in extremely large Debye-Waller factors for N and C shells (Table 3). The best fit without a negative Debye-Waller factor for the O shell still resulted in an unsatisfactory model of the data, and contained unreasonably large Debye-Waller factors for the N shell (fit 4).

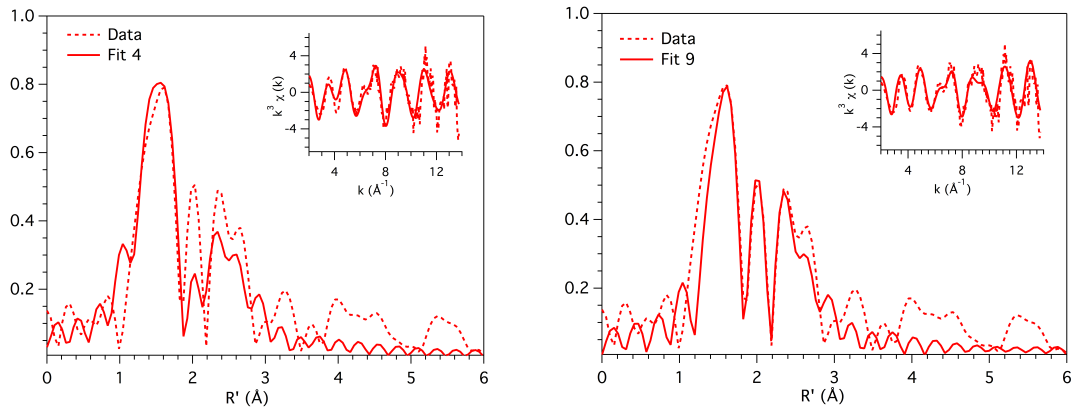

Figure A2.11. Experimental Fourier transform and *k*-weighted EXAFS (inset) for the organe solution (- -) and overlay of fit 4 (—) (left) and fit 9 (—) (right).

Table A2.6. EXAFS Fitting Results for the Orange Solution.

fit	Mn-N			Mn-O			Mn-N(2)			Mn-C(1)			Mn-C(2)			Mn-Cl			f - factor
	n	r(Å)	$\sigma^{2\,a}$	n	r(Å)	$\sigma^{2\,a}$	n	r(Å)	$\sigma^{2\,a}$	n	r(Å)	$\sigma^{2\,a}$	n	r(Å)	$\sigma^{2\,a}$	n	r(Å)	$\sigma^{2\,a}$	
1	6	2.02	3.3																0.726
2	4	2.18	17.9	2	1.85	1.6													0.679
3	4	2.21	40.0	1	1.86	-1.4				4	2.83	43.5	6	3.07	6.8	1	2.58	21.6	0.532
4	**4**	**2.16**	**19.3**	**2**	**1.85**	**1.6**				**4**	**2.92**	**12.0**	**6**	**3.06**	**6.0**				**0.572**
5	1	2.12	-1.9	2	1.87	3.0	3	2.29	7.9										0.613
6	1	2.12	2.5	1	1.87	-1.2	3	2.36	9.4							1	2.84	5.5	0.530
7	1	2.11	2.0	1	1.87	-1.1	3	2.34	9.2	4	3.08	8.0				1	2.82	9.6	0.507
8	1	2.12	1.6	2	1.87	-1.0	3	2.34	9.2	4	3.08	4.6							0.524
9	**1**	**2.12**	**3.6**	**1**	**1.86**	**-1.1**	**3**	**2.39**	**6.8**	**4**	**2.97**	**1.8**	**6**	**3.09**	**5.9**	**1**	**2.41**	**9.0**	**0.517**
10	1	2.12	1.7	1	1.86	-1.0	3	2.34	9.1	4	2.82	37.0	6	3.06	6.6				0.518

Fourier transform range is 2—13.8 Å (resolution 0.1317 Å). Debye-waller factors in $Å^2$ and are scaled × 10^3.

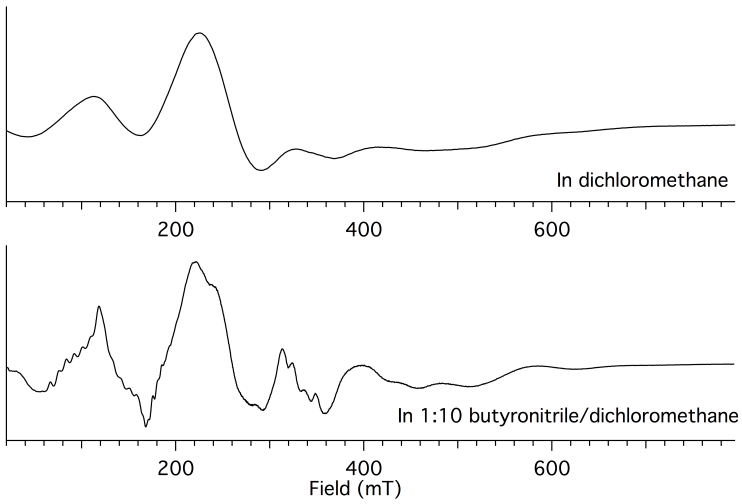

Figure A2.12. 5 K perpendicular-mode EPR spectrum of $[Mn^{II}(Cl)_2(Me_2EBC)]$ in dichloromethane (top) and 1:10 butyronitrile/dichloromethane (bottom).

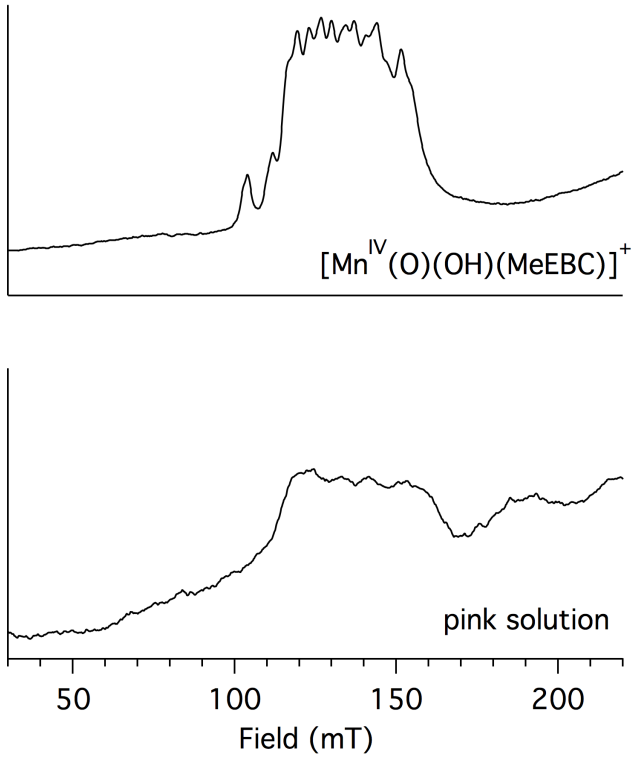

Figure A2.13. 5 K perpendicular-mode EPR spectrum of the pink solution in CH_2Cl_2 prepared from the decay of $[Mn^{III}(O_2)(Me_2EBC)]^+$ that was formed from a 2 mM $[Mn^{II}(Cl)_2(Me_2EBC)]$ with 2 equiv. KO_2 and 4 equiv. 18-crown-6 (bottom) and comparison to $[Mn^{IV}(O)(OH)(Me_2EBC)]^+$ (top) in a 3:1 CH_2Cl_2/acetone mixture.

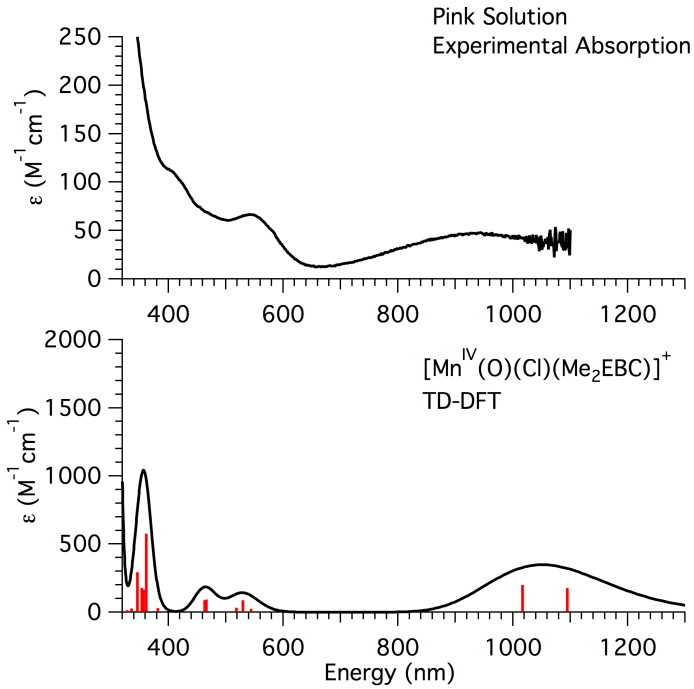

Figure A2.14. Experimental electronic absorption spectrum of the pink solution (top) and TD-DFT-calculated absorption spectrum of $[Mn^{IV}(O)(Cl)(Me_2EBC)]^+$ (bottom). Intensity in the experimental spectrum is represented extinction coefficients, ε ($M^{-1}cm^{-1}$), based on the starting $[Mn^{II}Cl_2(Me_2EBC)]$ concentration, to permit comparison to the TD-DFT calculated values.

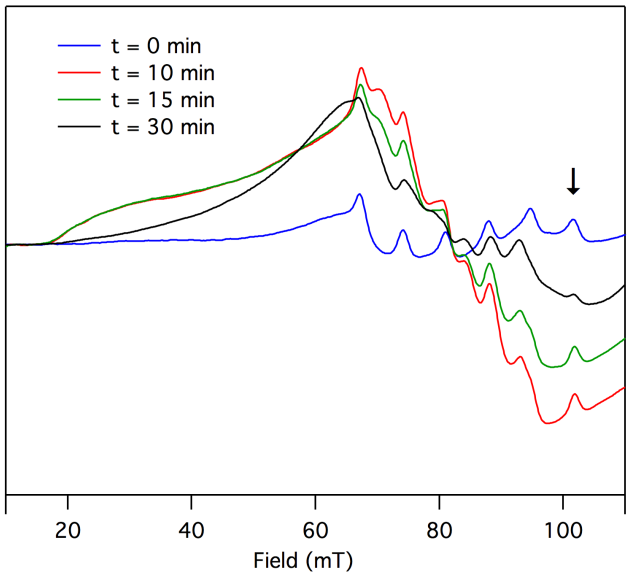

Figure A2.15. Parallel-mode X-band EPR spectra of the conversion of $[Mn^{III}(O_2)(Me_2EBC)]^+$ to the pink solution. $[Mn^{III}(O_2)(Me_2EBC)]^+$ is the sole species at t = 0 min (blue trace) at g_{eff} = 7.96 (an arrow marks the highest-field component of this six-line signal). Over 30 minutes, the signal associated with $[Mn^{III}(O_2)(Me_2EBC)]^+$ diminishes, as best evidenced by a loss in intensity of the highest-field component of this six-line signal. As this signal diminishes, a new set of six-line signals, characterized by g_{eff} = 8.33, appear. After 30 minutes, the g_{eff} = 7.96 is near fully diminished.

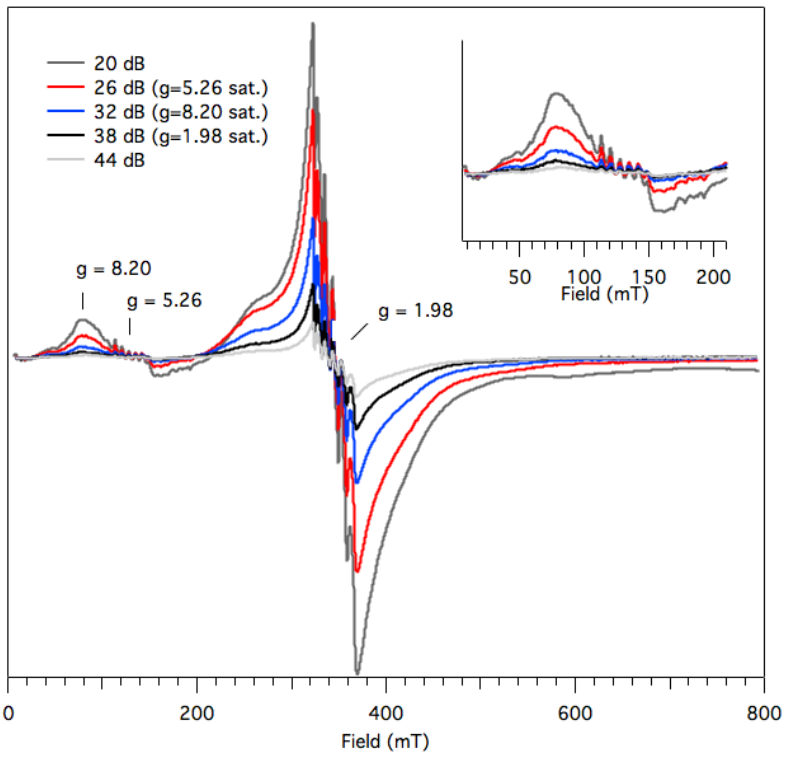

Figure A2.16. Perpendicular-mode X-band EPR spectra of the pink solution at different power levels.

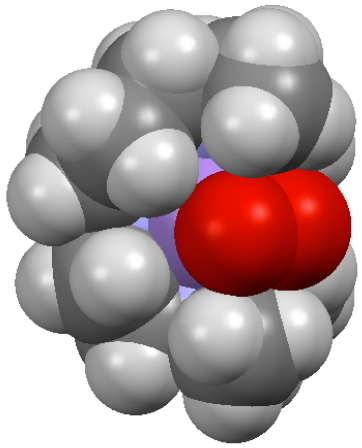

Figure A2.17. Space filling model of $[Mn^{III}(O_2)(Me_2EBC)]^+$.

APPENDIX A3.

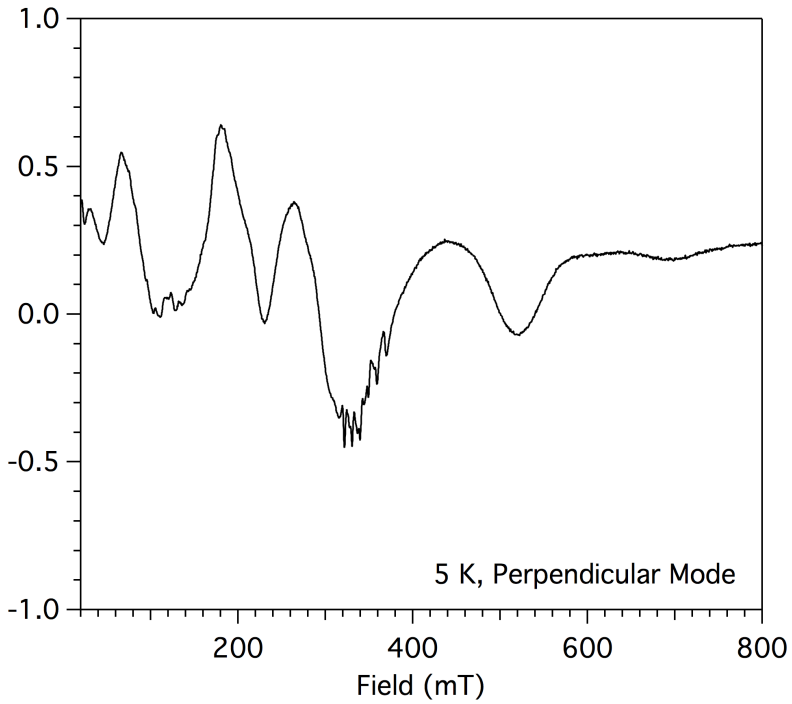

Figure A3.1. 5 K perpendicular-mode EPR spectrum of the acid product of $[Mn^{III}(O_2)(Me_2EBC)]^+$.

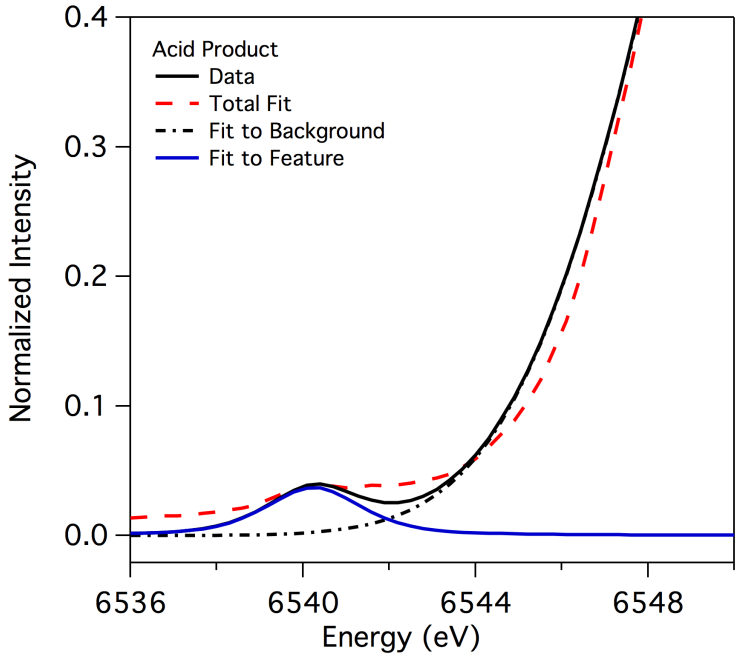

Figure A3.2. Mn K-edge pre-edge data (red dashed trace) and fit (black solid trace) for the acid product of $[Mn^{III}(O_2)(Me_2EBC)]^+$. Broken black traces represent fits to the background and the solid blue trace represents the fit to the pre-edge peak.

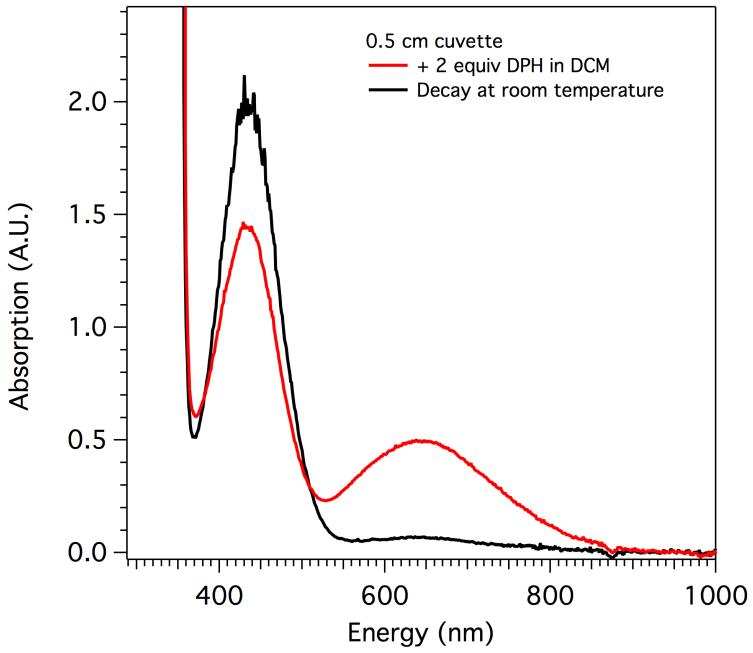

Figure A3.3. Electronic absorption spectra of the reaction of 2 mM $[Mn^{III}(O_2)(Me_2EBC)]^+$ in dichlormethane with 2 equiv DPH in dichloromethane at -60 °C in a 0.5 cm path length cuvette.

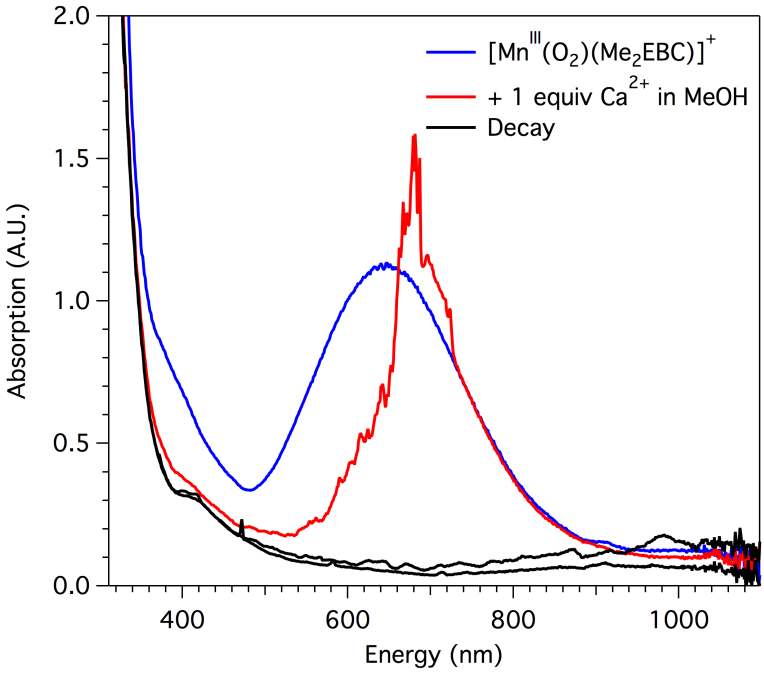

Figure A3.4. Electronic absorption spectra of the reaction of $[Mn^{III}(O_2)(Me_2EBC)]^+$ in dichlormethane with 1 equiv $Ca(OTf)_2$ in methanol at -60 °C.

APPENDIX A4.

Table A4.1. Crystal data and structure refinement for [Mn(Tp^{Ph2})$(DMF)_3$](OTf).

Empirical formula	$C_{59}H_{63}BF_3MnN_9O_7S$	
Formula weight	1164.99	
Temperature	100(2) K	
Wavelength	1.54178 Å	
Crystal system	Monoclinic	
Space group	P2(1)/n	
Unit cell dimensions	a = 17.6441(10) Å	a= 90°.
	b = 14.8052(8) Å	b= 93.243(4)°.
	c = 21.9441(11) Å	g = 90°.
Volume	5723.2(5) $Å^3$	
Z	4	
Density (calculated)	1.352 Mg/m^3	
Absorption coefficient	2.805 mm^{-1}	
F(000)	2436	
Crystal size	0.22 x 0.01 x 0.01 mm^3	
Theta range for data collection	10.74 to 66.71°.	
Index ranges	-20<=h<=20, -17<=k<=16, -24<=l<=25	
Reflections collected	19229	
Independent reflections	9144 [R(int) = 0.1286]	
Completeness to theta = 66.71°	90.2 %	
Absorption correction	Multi-scan	
Max. and min. transmission	1.000 and 0.793	
Refinement method	Full-matrix least-squares on F^2	
Data / restraints / parameters	9144 / 0 / 709	
Goodness-of-fit on F^2	0.928	
Final R indices [I>2sigma(I)]	R1 = 0.0638, wR2 = 0.1504	
R indices (all data)	R1 = 0.0984, wR2 = 0.1649	
Largest diff. peak and hole	1.402 and -0.894 $e.Å^{-3}$	

$R_1 = \Sigma \, ||F_o| - |F_c|| \, / \, \Sigma \, |F_o|$

$wR_2 = \{ \, \Sigma \, [w(F_o^2 - F_c^2)^2] \, / \, \Sigma \, [w(F_o^2)^2] \, \}^{1/2}$

Table A4.2. Crystal data and structure refinement for [$Mn(O_2)(Tp^{Ph2})(THF)$].

Empirical formula	$C_{58}H_{62}BMnN_6O_5$	
Formula weight	988.89	
Temperature	100(2) K	
Wavelength	1.54178 Å	
Crystal system	Monoclinic	
Space group	P2(1)/n	
Unit cell dimensions	a = 12.928(2) Å	a= 90°.
	b = 21.642(4) Å	b= 103.572(4)°.
	c = 18.633(3) Å	g = 90°.
Volume	5067.5(15) $Å^3$	
Z	4	
Density (calculated)	1.296 Mg/m^3	
Absorption coefficient	2.562 mm^{-1}	
F(000)	2088	
Crystal size	0.23 x 0.20 x 0.06 mm^3	
Theta range for data collection	3.18 to 66.52°.	
Index ranges	-15<=h<=15, -25<=k<=19, -21<=l<=21	
Reflections collected	45183	
Independent reflections	8594 [R(int) = 0.0482]	
Completeness to theta = 66.52°	96.2 %	
Absorption correction	Multi-scan	
Max. and min. transmission	1.000 and 0.810	
Refinement method	Full-matrix least-squares on F^2	
Data / restraints / parameters	8594 / 30 / 693	
Goodness-of-fit on F^2	1.077	
Final R indices [I>2sigma(I)]	R1 = 0.0514, wR2 = 0.1460	
R indices (all data)	R1 = 0.0528, wR2 = 0.1474	
Largest diff. peak and hole	0.944 and -0.535 $e.Å^{-3}$	

$R_1 = \Sigma \, ||F_o| - |F_c|| \, / \, \Sigma \, |F_o|$

$wR_2 = \{ \, \Sigma \, [w(F_o^2 - F_c^2)^2] \, / \, \Sigma \, [w(F_o^2)^2] \, \}^{1/2}$

Table A4.3. Cartesian coordinates (Å) for DFT energy minimized [$Mn^{III}(O_2)(Tp^{Ph2})(THF)$] model.

Atom	x	y	z
Mn	2.311278	5.168113	8.572887
O	3.759224	4.994203	7.408479
O	3.702012	3.944327	8.39639
O	3.642094	6.494182	10.025693
N	0.531187	4.095032	7.443028
N	1.29661	6.924038	8.086569
N	1.148728	4.746492	10.261434
N	-0.182102	5.072468	10.203946
N	-0.675955	4.675571	7.737045
N	0.002915	7.007179	8.533482
B	-0.777242	5.703335	8.899954
C	-1.695933	4.029288	7.074486
C	-1.115549	2.982868	6.349993
C	0.278409	3.060868	6.59728
C	-0.446171	8.298971	8.418836
C	0.597253	9.057491	7.86571
C	1.672346	8.164192	7.669132
C	-0.75983	4.883731	11.434879
C	0.246276	4.439276	12.307237
C	1.423074	4.346505	11.533707
C	-3.122816	4.41319	7.087925
C	-3.54652	5.755614	6.936598
C	-4.913374	6.0725	6.883498
C	-5.883315	5.057732	6.973848
C	-5.475734	3.718441	7.116625
C	-4.108853	3.39927	7.172456
C	1.30298	2.165797	6.016736
C	2.617277	2.598687	5.724944
C	3.542085	1.72037	5.134432
C	3.177311	0.397649	4.823422
C	1.871992	-0.04476	5.110218
C	0.945819	0.829963	5.700579
C	-1.782401	8.793367	8.814209
C	-2.36368	8.482828	10.065985
C	-3.606851	9.02433	10.429283
C	-4.289297	9.888691	9.554043
C	-3.71636	10.213329	8.310792
C	-2.473499	9.67219	7.944217
C	2.987638	8.483451	7.077143
C	3.620911	9.706662	7.406037
C	4.844505	10.061323	6.815830

C	5.45373	9.201693	5.882800
C	4.827141	7.989516	5.541610
C	3.603509	7.632058	6.130691
C	-2.188855	5.066142	11.768434
C	-2.529037	5.709462	12.984204
C	-3.871567	5.841674	13.374697
C	-4.898018	5.33189	12.558414
C	-4.571156	4.683966	11.353178
C	-3.22971	4.547236	10.961781
C	2.73614	3.843311	11.987691
C	3.221705	4.221099	13.263644
C	4.440482	3.716821	13.745588
C	5.192825	2.821935	12.961949
C	4.712988	2.431209	11.698561
C	3.493368	2.933361	11.214475
C	3.214411	7.534751	10.950286
C	4.458382	7.897943	11.769279
C	5.597298	7.621325	10.769254
C	5.096992	6.365083	10.052628
H	-1.633772	2.301757	5.664913
H	0.573997	10.127612	7.630868
H	0.117627	4.134897	13.352104
H	-2.798897	6.558025	6.835146
H	-5.222622	7.123673	6.760456
H	-6.956171	5.310218	6.927996
H	-6.227323	2.914172	7.187294
H	-3.795155	2.348989	7.294857
H	2.918763	3.630836	5.962713
H	4.561822	2.077277	4.912743
H	3.907777	-0.287954	4.361568
H	1.573301	-1.080472	4.877377
H	-0.067449	0.466800	5.937741
H	-1.830297	7.827967	10.772099
H	-4.042706	8.770735	11.409456
H	-5.266041	10.310907	9.842117
H	-4.242647	10.890437	7.617011
H	-2.034985	9.920592	6.963872
H	3.152575	10.380976	8.142642
H	5.326333	11.015049	7.088299
H	6.414766	9.479021	5.419004
H	5.291717	7.314972	4.803005
H	3.108311	6.694600	5.835317
H	-1.728767	6.118134	13.622552
H	-4.117554	6.347139	14.323221

H	-5.952724	5.435496	12.864199
H	-5.367271	4.272972	10.711187
H	-2.989236	4.012554	10.029806
H	2.638872	4.927288	13.878533
H	4.804938	4.026285	14.738921
H	6.149941	2.424872	13.338375
H	5.289454	1.720031	11.083498
H	3.111419	2.594062	10.240319
H	2.377791	7.134522	11.563455
H	2.839901	8.401869	10.357583
H	4.548801	7.229166	12.652852
H	4.433434	8.948472	12.128501
H	6.581008	7.462723	11.259597
H	5.697716	8.464468	10.05032
H	5.441171	6.266887	9.00275
H	5.355249	5.434518	10.608295
H	-1.937045	5.988601	9.095838

Table A4.4. Cartesian coordinates (Å) for DFT energy minimized [$Mn^{III}(O_2)(Tp^{Ph,Me})(THF)$] model.

Atom	x	y	z
Mn	0.000000	0.000000	0.000000
O	-1.854526	-0.208260	0.000000
O	-1.146840	-1.465504	0.000000
O	-0.005152	0.023431	-2.374784
N	0.554751	0.222984	2.288960
N	0.422438	2.040054	-0.095163
N	1.996603	-0.607940	-0.156403
N	2.941567	0.180790	0.448265
N	1.645044	1.035517	2.467048
N	1.679688	2.407126	0.310880
B	2.503175	1.458400	1.240795
H	1.965103	0.401315	-2.965131
H	0.811331	1.778758	-3.177974
H	1.094151	-0.767126	-4.910694
H	0.826253	0.924577	-5.468045
H	-1.346370	-0.758565	-5.322228
H	-1.507980	0.897011	-4.630129
H	-2.023934	-0.417048	-2.630224
H	-0.879026	-1.733182	-3.114965
C	1.952702	1.143215	3.805244
C	1.035736	0.348942	4.501687
C	0.171948	-0.203017	3.522113
C	1.934412	3.698883	-0.076457
C	0.790612	4.170579	-0.739223
C	-0.136448	3.106179	-0.731116
C	4.197678	-0.263296	0.117264
C	4.041581	-1.362002	-0.742549
C	2.650747	-1.560981	-0.875946
C	-0.976385	-1.094036	3.796608
C	-2.144382	-1.100905	2.999333
C	-3.225688	-1.936912	3.326875
C	-3.165543	-2.779826	4.451711
C	-2.007546	-2.782201	5.252257
C	-0.925333	-1.948628	4.927554
C	-1.507375	3.126127	-1.281144
C	-1.753936	3.779178	-2.513289
C	-3.055885	3.861944	-3.032318
C	-4.134627	3.297766	-2.326143
C	-3.901288	2.656452	-1.096238
C	-2.600070	2.571823	-0.574954
C	1.985969	-2.652351	-1.617856

C	2.486468	-3.035666	-2.886368
C	1.910216	-4.104372	-3.591907
C	0.826309	-4.811774	-3.039042
C	0.330039	-4.446494	-1.774390
C	0.904071	-3.377344	-1.066210
C	3.214759	4.419824	0.225905
C	3.086361	1.970499	4.335954
C	5.460792	0.367289	0.624043
C	0.933721	0.674864	-3.277404
C	0.565863	0.184153	-4.682396
C	-0.949525	-0.062209	-4.553541
C	-1.062399	-0.634444	-3.138688
H	3.492381	2.046726	1.615276
H	0.957352	0.250788	5.590734
H	0.649626	5.168311	-1.169924
H	4.840432	-1.993399	-1.147665
H	-2.207079	-0.447402	2.115160
H	-4.128744	-1.926589	2.693807
H	-4.016544	-3.435210	4.703125
H	-1.943596	-3.441719	6.133777
H	-0.016637	-1.972864	5.550875
H	-0.911633	4.216276	-3.075513
H	-3.228510	4.369022	-3.996197
H	-5.157363	3.361839	-2.732977
H	-4.742160	2.221369	-0.530538
H	-2.432990	2.092598	0.401633
H	3.331422	-2.480029	-3.326602
H	2.309877	-4.384938	-4.580270
H	0.372393	-5.651080	-3.591267
H	-0.510326	-5.003867	-1.327723
H	0.531657	-3.124044	-0.063106
H	3.369838	4.549662	1.319588
H	3.194452	5.427419	-0.239545
H	4.101007	3.875328	-0.167488
H	3.068625	1.962994	5.445390
H	3.021343	3.029507	4.001104
H	4.079329	1.584314	4.012533
H	5.570631	1.418656	0.277484
H	6.337323	-0.204244	0.255003
H	5.502460	0.379169	1.734679

Table A4.5. Cartesian coordinates (Å) for DFT energy minimized (for hydrogen atoms only) brown isomer of $[Mn^{III}(O_2)(Tp^{iPr2})(pz^{iPr2}H)]$ (253 K structure).

Atom	x	y	z
Mn	2.01447016	1.349043599	0.00327932
O	1.712240055	-0.326615503	0.730450237
O	2.367811342	0.559555395	1.639152294
N	2.569381402	3.340234155	0.001640721
N	2.792937349	3.972397518	-1.216212397
N	3.947886629	1.192752816	-1.177116358
N	4.117912651	2.102260045	-2.181296997
N	1.233897449	1.353811255	-1.909490532
N	1.672062199	2.330093985	-2.778835509
N	-0.159210252	2.109086546	0.699998912
N	-0.859296861	1.210045325	1.455327724
B	2.996300519	3.110552737	-2.462206373
C	3.787454413	3.454165474	2.993131239
C	1.86674869	4.974279105	3.237830859
C	2.455886111	3.869399126	2.418020921
C	2.616025286	4.266356113	0.959478637
C	2.860665187	5.504302762	0.396868278
C	2.970945886	5.293455297	-0.961904885
C	3.206054857	6.279747046	-2.063200645
C	1.874698219	6.828050971	-2.581475962
C	4.100847387	7.409017388	-1.59887337
C	6.003852607	-1.709410189	-0.494142106
C	6.088006664	0.098564147	1.193591245
C	5.315811129	-0.479740088	0.039542604
C	5.115977525	0.542211131	-1.042664969
C	6.040407695	1.030692222	-1.984553008
C	5.395657495	2.031762905	-2.688598938
C	5.925747057	2.985736292	-3.698944342
C	7.013596091	2.3730936	-4.546516414
C	6.423755122	4.212885809	-2.993617443
C	0.005324619	-1.705801692	-2.234321956
C	-2.048508986	-0.272497035	-1.992474278
C	-0.54458949	-0.370445183	-1.790810439
C	0.173855566	0.757666042	-2.468428894
C	-0.096685621	1.329517019	-3.714056819
C	0.862719409	2.324906221	-3.883583598
C	1.012792478	3.292288786	-5.011830047
C	2.034732059	2.779515382	-6.042506001
C	-0.333044931	3.544417767	-5.687733624
C	-1.450967226	4.155911148	-1.772148596

C	-1.002356082	5.525750777	0.237017502
C	-0.697443735	4.238458396	-0.443479224
C	-1.045907053	3.063013439	0.401085442
C	-2.295185976	2.757532126	0.959845089
C	-2.14972163	1.565167769	1.645280252
C	-3.097687502	0.748491441	2.40258236
C	-4.227705953	0.248965874	1.454545173
C	-3.723190819	1.539803196	3.527792252
H	-0.354361262	0.371998824	1.763691879
H	3.676292935	3.113065177	4.043772568
H	4.243273132	2.620107226	2.422992438
H	4.508410111	4.299281277	2.989795352
H	2.531783118	5.864013248	3.268240347
H	0.88062472	5.311221898	2.857078781
H	1.720589634	4.650506619	4.289054889
H	1.77573158	2.990844382	2.432308421
H	2.956159891	6.462479438	0.916085913
H	3.70437125	5.747437944	-2.898844762
H	1.334904717	7.375482022	-1.781174982
H	2.036146543	7.53277926	-3.42385506
H	1.208160533	6.017947568	-2.940294259
H	5.071812333	7.03982647	-1.21063067
H	4.314761818	8.111391529	-2.430743835
H	3.623063284	8.002044043	-0.79118299
H	6.109518663	-2.48261377	0.295768753
H	5.448301939	-2.168280216	-1.33787537
H	7.028599246	-1.480176919	-0.858130307
H	6.200823511	-0.644397389	2.011363574
H	7.109121353	0.411150477	0.885499576
H	5.582222854	0.986677743	1.62294455
H	4.303149229	-0.759236209	0.400778435
H	7.073389873	0.69534377	-2.126099346
H	5.086809832	3.278952675	-4.367033247
H	6.669122714	1.459838887	-5.073103477
H	7.368016027	3.092569673	-5.313302373
H	7.897092322	2.092119443	-3.935361836
H	7.278520559	3.965969435	-2.329104861
H	6.773051745	4.985932299	-3.711523812
H	5.645817098	4.677143115	-2.356449856
H	-0.488178326	-2.54014218	-1.692472192
H	-0.156837615	-1.872620312	-3.321042215
H	1.094385583	-1.780985407	-2.042690721
H	-2.449275581	0.696846903	-1.633958514
H	-2.327325608	-0.381171999	-3.062390422

H	-2.570412836	-1.082998676	-1.44260082
H	-0.33240542	-0.270904875	-0.705551579
H	-0.90404568	1.069261098	-4.403775521
H	1.389323155	4.251561273	-4.598116876
H	1.697531782	1.81699924	-6.479548044
H	2.161315683	3.506220351	-6.871859825
H	3.029009769	2.609204208	-5.583512946
H	-1.099558997	3.896796293	-4.969133068
H	-0.231788679	4.311622029	-6.482552527
H	-0.71988083	2.62432959	-6.172441027
H	-2.548237534	4.223727741	-1.611952554
H	-1.165037441	4.995726251	-2.440088451
H	-1.243499503	3.209296562	-2.305970988
H	-0.46299008	5.633502072	1.200144409
H	-0.719281511	6.392854455	-0.395755955
H	-2.087080987	5.630162473	0.456229108
H	0.386468577	4.181984348	-0.656693698
H	-3.210985307	3.354892561	0.887826743
H	-2.564875133	-0.134493521	2.817567651
H	-4.785319756	1.110287002	1.034505112
H	-3.821289915	-0.339514775	0.608619437
H	-4.948305457	-0.389209748	2.006268787
H	-2.96474	1.922830972	4.241348211
H	-4.281409147	2.415384522	3.136725249
H	-4.441569443	0.919544754	4.102939776
H	3.265055747	3.809138399	-3.404168309

Table A4.6. Cartesian coordinates (Å) for DFT energy minimized (for hydrogen atoms only) blue isomer of $[Mn^{III}(O_2)(Tp^{iPr2})(pz^{iPr2}H)]$ (193 K structure).

Atom	x	y	z
Mn	0.003281554	0.003672271	0.002376072
O	1.846980039	0.00327784	0.003695983
O	1.326432464	1.339191421	0.001040796
N	-1.861465091	0.941560535	0.033207174
N	-2.941409734	0.252532817	-0.421690018
N	-0.516025497	-0.335937192	-2.15315674
N	-1.777189772	-0.836061885	-2.392659211
N	-0.764292583	-1.873011845	0.216061439
N	-2.026184365	-2.141236763	-0.222154884
N	0.031948506	0.142757329	2.407450238
N	1.129695761	0.86378811	2.775800075
B	-2.72792984	-1.075433928	-1.185044751
C	-1.552656131	3.364767215	2.516288994
C	-1.450831401	4.475637592	0.344920437
C	-1.340691782	3.148854546	1.053758624
C	-2.291002951	2.106809597	0.52709932
C	-3.657793996	2.15685687	0.367572915
C	-4.071108359	0.99984759	-0.241485724
C	-5.424988969	0.558578284	-0.653382682
C	-6.493564245	1.038168042	0.303182221
C	-5.765639362	1.107149374	-2.015629346
C	1.601316085	1.603421689	-3.942945422
C	2.354509855	-0.687017262	-4.181994343
C	1.515911379	0.23224641	-3.421663028
C	0.0967369	-0.238429858	-3.337643447
C	-0.78205607	-0.661760185	-4.327230716
C	-1.963325382	-1.023426823	-3.72472465
C	-3.204788904	-1.602707879	-4.251644467
C	-3.616371695	-0.894257191	-5.529591549
C	-3.141252816	-3.013750163	-4.601566573
C	1.187479521	-4.007810111	2.562823058
C	2.038231612	-3.473436935	0.369414843
C	1.064095451	-3.067134033	1.396923213
C	-0.346459717	-2.998149685	0.842789784
C	-1.348205897	-3.929988991	0.80687533
C	-2.415360957	-3.383398917	0.15199075
C	-3.783207604	-3.918578148	-0.116767411
C	-4.781452644	-3.349648104	0.890060228
C	-3.75193933	-5.46478775	-0.036680421

C	-3.016885958	-0.200868297	3.377613894
C	-1.973161701	-1.816397704	4.749495316
C	-1.812414665	-0.97283549	3.550789108
C	-0.559279259	-0.187283303	3.58012752
C	0.226239409	0.346670885	4.624334921
C	1.293169021	1.006278189	4.083621882
C	2.411386533	1.777825793	4.615596095
C	2.227133901	3.233354269	4.529163254
C	2.711057955	1.440490994	6.025066535
H	1.673851264	1.247732559	1.986035665
H	-1.422664591	2.436769085	3.108142906
H	-0.839816475	4.115305949	2.918534564
H	-2.574568728	3.749432264	2.725248028
H	-2.449454039	4.93830458	0.497852058
H	-0.696544089	5.188388614	0.737547984
H	-1.289898216	4.38793117	-0.749557463
H	-0.318260302	2.745804484	0.893718635
H	-4.308688078	2.987149494	0.666224577
H	-5.437877128	-0.550011213	-0.691498007
H	-6.319924141	0.695909834	1.344496928
H	-6.549819979	2.146327104	0.323423302
H	-7.491617302	0.668870142	-0.009506611
H	-5.772956872	2.216911285	-2.002395674
H	-5.037481727	0.796916048	-2.793659769
H	-6.769924858	0.769169811	-2.347040904
H	1.001840883	2.321060138	-3.346074027
H	2.648946033	1.974990731	-3.939451473
H	1.241521298	1.673163594	-4.994171953
H	2.053702572	-0.74846944	-5.252213966
H	3.418197371	-0.365088135	-4.176512937
H	2.329030555	-1.723177557	-3.783666189
H	1.875011818	0.242501922	-2.368407865
H	-0.574736784	-0.69986727	-5.403757705
H	-4.000378795	-1.444860263	-3.494913941
H	-3.724282223	0.20321527	-5.400594096
H	-2.866475452	-1.05687865	-6.331780198
H	-4.584493419	-1.283877792	-5.906286201
H	-4.118528496	-3.384396478	-4.975683545
H	-2.393987637	-3.205812759	-5.401419694
H	-2.856090667	-3.669132207	-3.748948302
H	0.98665721	-5.058545975	2.26112186
H	2.216164606	-3.984621546	2.977133244
H	0.49014086	-3.76326832	3.391200995
H	2.026996345	-2.808661048	-0.519159864

H	3.074385906	-3.458038488	0.768991091
H	1.843898077	-4.506441423	0.006725637
H	1.307527909	-2.036927449	1.736890957
H	-1.302625373	-4.933553813	1.242809673
H	-4.091444475	-3.620051834	-1.140289929
H	-4.505598271	-3.644360744	1.923765902
H	-4.811850089	-2.242198892	0.856815963
H	-5.807433115	-3.724389031	0.692170337
H	-4.747587347	-5.887210003	-0.28174348
H	-3.012925408	-5.895984735	-0.740986501
H	-3.491524614	-5.804102017	0.986615673
H	-3.208039926	0.472545826	4.243518317
H	-3.006096449	0.443469685	2.476471192
H	-3.908209794	-0.857629089	3.28868026
H	-2.865564413	-2.470864608	4.666718453
H	-1.100576848	-2.476179265	4.942931423
H	-2.119033891	-1.202597694	5.665890234
H	-1.703851173	-1.646324323	2.670676072
H	0.021308796	0.237102947	5.696266931
H	3.30222586	1.506408385	3.99940545
H	1.374851379	3.571670446	5.157096959
H	3.129361386	3.774101411	4.883218184
H	2.02416239	3.590298321	3.497085984
H	2.897264726	0.357405455	6.182871877
H	3.607025414	1.984857007	6.386395748
H	1.872087028	1.725964463	6.695859394
H	-3.785877568	-1.512572101	-1.545398481

Table A4.7. Cartesian coordinates (Å) for DFT energy minimized (for hydrogen atoms only) brown isomer of $[Mn^{III}(O_2)(Tp^{iPr2})(pz^{iPr2}H)]$ (253 K structure).

Atom	x	y	z
Mn	1.841544249	1.622823228	-0.163209007
O	1.517299205	-0.05181286	0.695567336
O	2.220261861	0.917842393	1.513477577
N	2.418803064	3.607006142	-0.118279615
N	2.811588365	4.18741708	-1.300545407
N	3.845589071	1.285997299	-1.201209733
N	4.17127718	2.221227547	-2.151898905
N	1.146328873	1.707438728	-2.118406164
N	1.801346956	2.54417315	-2.992099894
N	-0.453133688	2.164718202	0.677798985
N	-0.821189834	1.132050295	1.477747968
B	3.103529459	3.280843024	-2.54072868
C	3.40730173	3.755162678	3.001226182
C	1.489391276	5.425727922	3.027383269
C	2.125018164	4.237980993	2.285818889
C	2.417904631	4.56425297	0.839602399
C	2.801885344	5.790230733	0.25465205
C	3.045185606	5.520809507	-1.101420163
C	3.422953886	6.47900693	-2.209209276
C	2.174672833	6.9231845	-3.004578282
C	4.197482457	7.693624194	-1.669424009
C	5.2529137	-2.006658557	-0.755697626
C	5.829116843	-0.395264984	1.130908309
C	4.897081997	-0.674039148	-0.066685186
C	4.912006212	0.475488819	-1.048242817
C	5.949273227	0.896831935	-1.917629027
C	5.450810011	2.011505687	-2.604152955
C	6.147074623	2.906828238	-3.604796088
C	7.117351434	2.114505079	-4.499440288
C	6.873547897	4.070978506	-2.893526591
C	-0.029703628	-1.34856496	-2.251028377
C	-2.128542846	-0.006084182	-2.772296103
C	-0.717426201	0.032815644	-2.161752568
C	0.146535079	1.097238555	-2.798186726
C	0.14783607	1.565218552	-4.129450392
C	1.209077466	2.477953171	-4.223902597
C	1.697109002	3.239758844	-5.4357979
C	2.765383441	2.430255837	-6.204779815

C	0.532483124	3.640266651	-6.359328901
C	-2.067632358	4.142699333	-1.452023849
C	-2.118968984	5.498501736	0.694740788
C	-1.439723801	4.338443037	-0.054643761
C	-1.469311495	3.0541103	0.746210682
C	-2.4877414	2.560341003	1.606424749
C	-2.035194489	1.31222328	2.061095643
C	-2.634583112	0.297879368	3.006861628
C	-4.025550662	-0.16680256	2.530407974
C	-2.683910916	0.83944621	4.45160654
H	-0.145080995	0.342961297	1.502401652
H	3.179890099	3.461682198	4.046884905
H	3.844646869	2.876232126	2.488054458
H	4.17354281	4.558271447	3.028131159
H	2.190092902	6.284728028	3.094173124
H	0.567107429	5.778362204	2.523523922
H	1.224055344	5.136225116	4.064386704
H	1.403647798	3.392984893	2.28299604
H	2.895998469	6.75825167	0.755535294
H	4.087635324	5.932497767	-2.911444787
H	1.470376335	7.479637512	-2.352021747
H	2.462641365	7.587144435	-3.845800867
H	1.630510456	6.05322151	-3.423308931
H	5.096916069	7.386092119	-1.099067204
H	4.525855477	8.343356722	-2.505799502
H	3.564611285	8.3124303	-0.999658523
H	5.185681675	-2.848177902	-0.035151365
H	4.566060522	-2.223473722	-1.598883922
H	6.288528481	-1.993455077	-1.157446231
H	5.776453521	-1.22308175	1.868615551
H	6.88683564	-0.298087166	0.805317467
H	5.542487755	0.541127881	1.649584537
H	3.858456191	-0.745684959	0.317114468
H	6.939779438	0.444952146	-2.035769167
H	5.365275535	3.350220291	-4.257135693
H	6.604477211	1.282170029	-5.022106136
H	7.568179649	2.778053211	-5.26557106
H	7.949619625	1.680986263	-3.906775694
H	7.677037153	3.686168205	-2.23167278
H	7.3360413	4.757787597	-3.632798728
H	6.176484243	4.66041411	-2.264554801
H	-0.638417145	-2.120197666	-1.735468351
H	0.095201413	-1.660954555	-3.309096771
H	0.971475397	-1.330201864	-1.776625518

H	-2.632308509	0.978894076	-2.70413991
H	-2.099101593	-0.3024415	-3.842070419
H	-2.757731427	-0.750134028	-2.242906323
H	-0.809399143	0.297336554	-1.087506668
H	-0.539652098	1.277002783	-4.930258736
H	2.180030375	4.17035071	-5.070436129
H	2.335297094	1.48674167	-6.60019657
H	3.158336571	3.015278331	-7.061947939
H	3.618530666	2.162342631	-5.55011695
H	-0.236140127	4.227494265	-5.817830636
H	0.905033536	4.25527499	-7.203713069
H	0.03538302	2.748686509	-6.795054888
H	-3.138249394	3.859440479	-1.368552359
H	-2.009524558	5.080373638	-2.043618644
H	-1.544854134	3.347748633	-2.019883294
H	-1.678764446	5.652267177	1.700851772
H	-2.015552409	6.445240748	0.12595938
H	-3.205481084	5.31152974	0.828120866
H	-0.367572729	4.593682903	-0.199587579
H	-3.431670866	3.049164319	1.870353366
H	-1.958368508	-0.585584031	2.999713874
H	-4.745546853	0.677966896	2.519487144
H	-3.983331757	-0.588764764	1.506267855
H	-4.431175059	-0.945974299	3.208266591
H	-1.676959845	1.137778315	4.806061054
H	-3.344881396	1.728587327	4.519558035
H	-3.079048152	0.068447875	5.145142235
H	3.505247264	3.965043589	-3.443683831

Table A4.8. Cartesian coordinates (Å) for DFT energy minimized (for hydrogen atoms only) blue isomer of $[Mn^{III}(O_2)(Tp^{iPr2})(pz^{iPr2}H)]$ (193 K structure).

Atom	x	y	z
Mn	-0.143372466	0.009476672	0.09138829
O	1.706896913	-0.144021844	0.019318459
O	1.308922384	1.249699234	0.073251099
N	-2.007420749	0.919261156	0.150692529
N	-3.066550209	0.247068582	-0.414283184
N	-0.644228416	-0.205138617	-2.125270207
N	-1.861327267	-0.780887533	-2.393729509
N	-0.90512222	-1.904881998	0.249909592
N	-2.152205259	-2.146080069	-0.27455667
N	0.071423721	0.251332125	2.576980067
N	1.187791979	0.991341553	2.79418746
B	-2.815458843	-1.077874653	-1.203849824
C	-2.234183199	3.950310133	2.332716817
C	-0.975629283	4.054246186	0.120825321
C	-1.545870888	3.134686476	1.224844449
C	-2.469881989	2.100121146	0.62541067
C	-3.856638813	2.180212658	0.376872469
C	-4.206231117	0.993863378	-0.285223256
C	-5.555850774	0.572582729	-0.82225487
C	-6.699403168	1.026069567	0.103704497
C	-5.764803916	1.091301606	-2.262593478
C	1.438787853	1.723622858	-4.391274078
C	2.436011719	-0.508732232	-3.677426094
C	1.375595084	0.569742544	-3.371217116
C	-0.008860766	-0.033524927	-3.301988384
C	-0.83309734	-0.507868816	-4.352888696
C	-2.003519799	-0.980214923	-3.744956257
C	-3.199925109	-1.656032307	-4.377347755
C	-3.532789644	-1.051657707	-5.753676619
C	-2.981349648	-3.182688953	-4.479576319
C	0.951502741	-4.124308839	2.636529614
C	1.937902843	-3.525637186	0.36871249
C	0.906235871	-3.142073229	1.454153984
C	-0.477225237	-3.038465804	0.85476914
C	-1.479880875	-4.024192941	0.729843954
C	-2.528299182	-3.430663068	0.009368346
C	-3.876263284	-4.008619788	-0.360549115

C	-4.960654998	-3.571421527	0.649851318
C	-3.821409896	-5.540821754	-0.487208961
C	-2.899932317	0.00483887	3.982160126
C	-1.599705832	-1.777946001	5.239648955
C	-1.647673218	-0.89925148	3.977280204
C	-0.381877585	-0.086464447	3.805816604
C	0.473748946	0.455826717	4.803033797
C	1.479590737	1.148716462	4.111948863
C	2.671416328	1.948325936	4.584388108
C	2.232287184	3.259018422	5.271962664
C	3.585657491	1.110191665	5.500279008
H	1.642297895	1.350763682	1.931412503
H	-2.634722043	3.296277974	3.133003578
H	-1.515756354	4.656932597	2.795697512
H	-3.075229071	4.553225411	1.930073276
H	-1.785969077	4.627950357	-0.375891207
H	-0.256627198	4.781116931	0.55267445
H	-0.443623962	3.467233881	-0.653771718
H	-0.696682853	2.579980708	1.67521757
H	-4.528748247	3.000246669	0.647262771
H	-5.565921908	-0.536660571	-0.859579729
H	-6.563213601	0.647912476	1.136790204
H	-6.767659544	2.13271873	0.152758274
H	-7.672530247	0.652218633	-0.274921897
H	-5.769144986	2.200800164	-2.285035942
H	-4.957178045	0.74538577	-2.938120406
H	-6.733047626	0.735042294	-2.671126294
H	0.69493431	2.512562775	-4.158803521
H	2.445304829	2.19103994	-4.388494136
H	1.24109614	1.365823849	-5.424176116
H	2.265556474	-0.971398676	-4.672918417
H	3.454473221	-0.06724732	-3.677681986
H	2.415029547	-1.313714893	-2.916296078
H	1.589124841	0.981534947	-2.363099017
H	-0.608067946	-0.50553306	-5.424571869
H	-4.071481059	-1.487029809	-3.710301795
H	-3.699013953	0.042543413	-5.689571611
H	-2.713186176	-1.227520054	-6.481146386
H	-4.449777948	-1.516494573	-6.170324485
H	-3.881203069	-3.683391745	-4.893891127
H	-2.122930054	-3.412437323	-5.144344338
H	-2.764620463	-3.62864589	-3.4880798
H	0.7363651	-5.163579847	2.309632518
H	1.960025357	-4.12652275	3.097460542

H	0.216913837	-3.85666273	3.422441432
H	1.929410727	-2.795962	-0.464632738
H	2.961523647	-3.543346885	0.796531975
H	1.721210704	-4.531914929	-0.047573786
H	1.170355908	-2.127817054	1.82310785
H	-1.44819936	-5.048506397	1.112671182
H	-4.156468191	-3.592511168	-1.351499587
H	-4.731930461	-3.959484316	1.664036056
H	-5.028043313	-2.467375544	0.718832698
H	-5.95565304	-3.959644463	0.348934758
H	-4.801070695	-5.93387129	-0.826585447
H	-3.050170179	-5.864500343	-1.214694864
H	-3.59319603	-6.020198348	0.487507954
H	-2.875649786	0.710221637	4.839585283
H	-2.970027167	0.598243982	3.049223954
H	-3.823404531	-0.604932993	4.070024165
H	-2.497353059	-2.426853918	5.298091824
H	-0.702779028	-2.42984462	5.253961722
H	-1.580896907	-1.159301256	6.161701865
H	-1.718044546	-1.564759008	3.089647958
H	0.378550771	0.353144636	5.889178733
H	3.253681842	2.221233327	3.676522427
H	1.638067565	3.049162139	6.185593365
H	3.116488202	3.858907736	5.571652833
H	1.608543577	3.879858774	4.59804484
H	3.929861321	0.186437158	4.993602279
H	4.480142711	1.694276112	5.799784133
H	3.053114595	0.811555136	6.427278862
H	-3.86385969	-1.505101017	-1.607867231

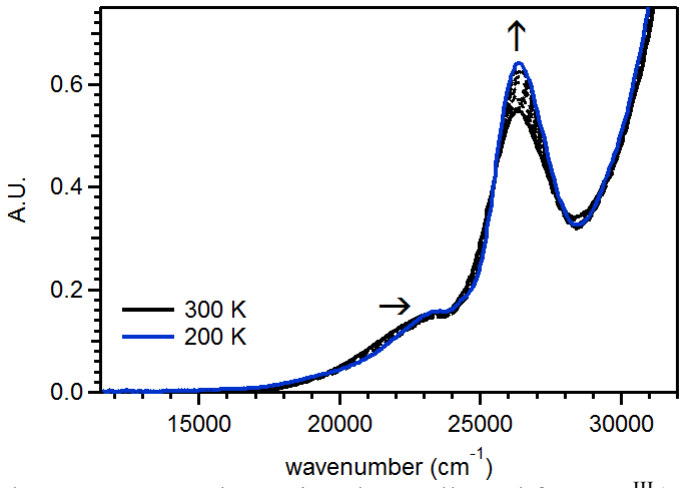

Figure A4.1. Variable-temperature absorption data collected for [$Mn^{III}(O_2)(Tp^{Ph2})$(THF)] in THF Data were collected from 300 – 200 K in 10 K increments.

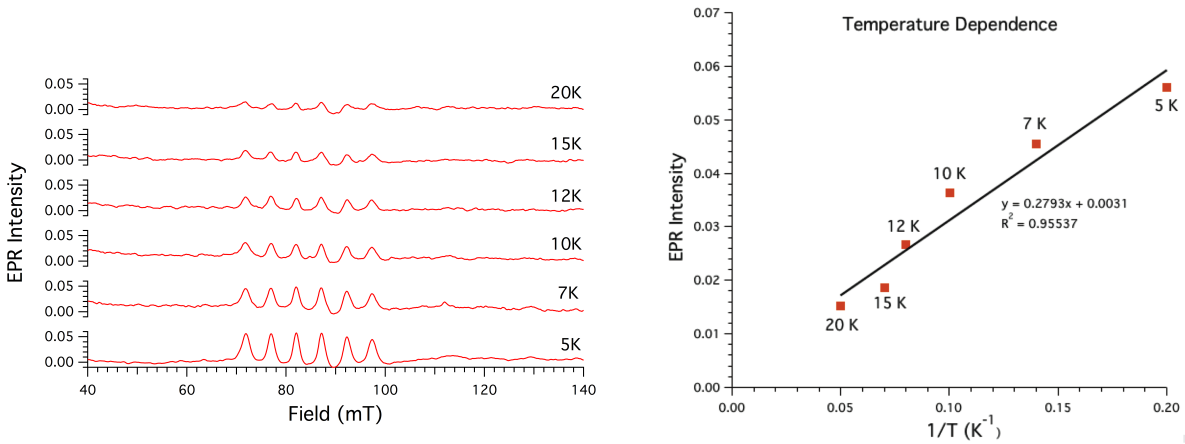

Figure A4.2. Variable-temperature parallel-mode EPR spectra collected for [$Mn^{III}(O_2)(Tp^{Ph2})$].

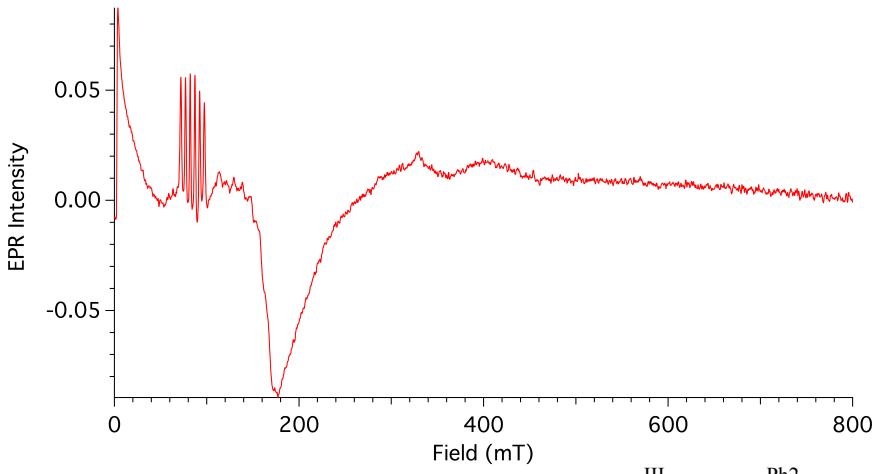

Figure A4.3. Full spectrum, parallel-mode X-band EPR of [$Mn^{III}(O_2)(Tp^{Ph2})$]. The large negative feature from 100 to 250 mT is due to O_2 dissolved in THF solution.

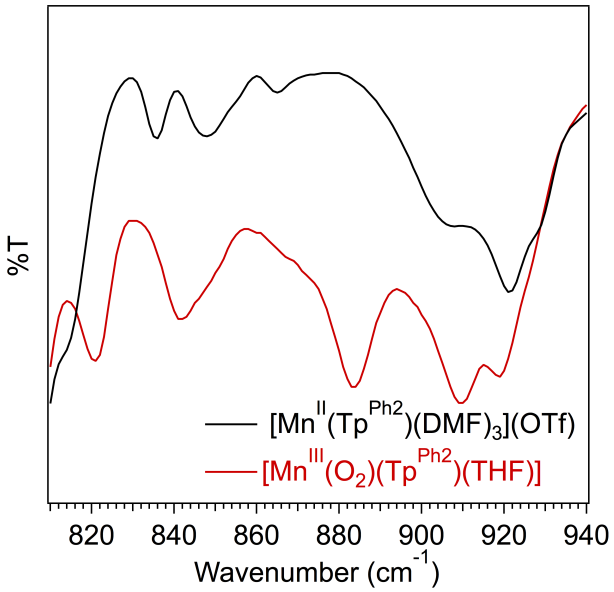

Figure A4.4. IR spectrum of $[Mn^{II}(Tp^{Ph2})(DMF)_3](OTf)$ (black) and $[Mn^{III}(O_2)(Tp^{Ph2})]$ (red) with a weak feature at 882 cm^{-1}.

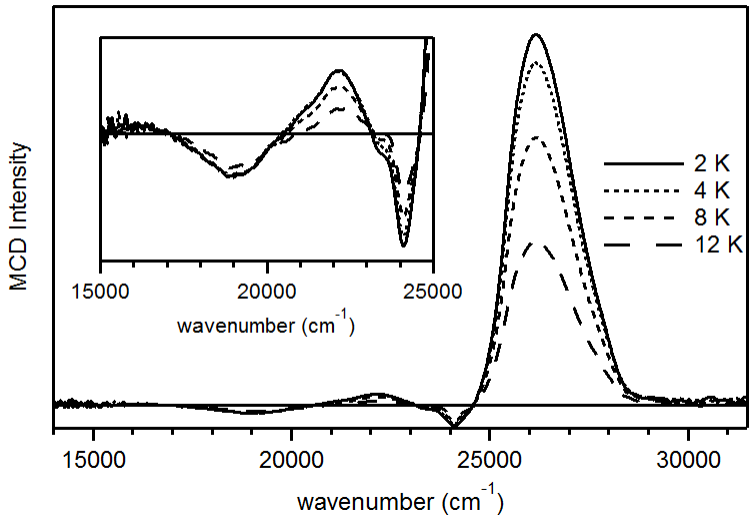

Figure A4.5. Variable-temperature 7 T MCD data collected for $[Mn^{III}(O_2)(Tp^{Ph2})(THF)]$ in THF. Inset: expanded view of low-intensity MCD features from 15 000 – 25 000 cm^{-1}. Data were collected at the temperatures indicated in the figure.

Table A4.9. Electronic transition energies (cm^{-1}), oscillator strengths (f_{exp}), and bandwidths (fwhm; cm^{-1}) from Gaussian deconvolutions of 298 K absorption and 2 K, 7 T MCD data of $[Mn^{III}(O_2)(Tp^{Ph2})(THF)]^{\cdot}$

band	energy	$f_{exp} \times 10^3$	fwhm
1	Abs: 19 000	0.083	Abs: 2248
	MCD: 19 000		MCD: 1998
2	Abs: 20 890	0.135	Abs: 2248
	MCD: 21 455		MCD: 1665
3	Abs: 22 600	0.290	Abs: 2248
	MCD: 22 325		MCD: 1665
4	Abs: NA		Abs: NA
	MCD: 23 675		MCD: 500
5	Abs: 24 350	0.342	Abs: 2248
	MCD: 24 800		MCD: 1832
6	Abs: NA		Abs: NA
	MCD: 25 150		MCD: 666
7	Abs: 26 300	167.64	Abs: 2331
	MCD: 26 060		MCD: 1832
8	Abs: 28 400	83.28	Abs: 2331
	MCD: 27 609		MCD: 1832
9	Abs: NA		Abs: NA
	MCD: 28 350		MCD: 999

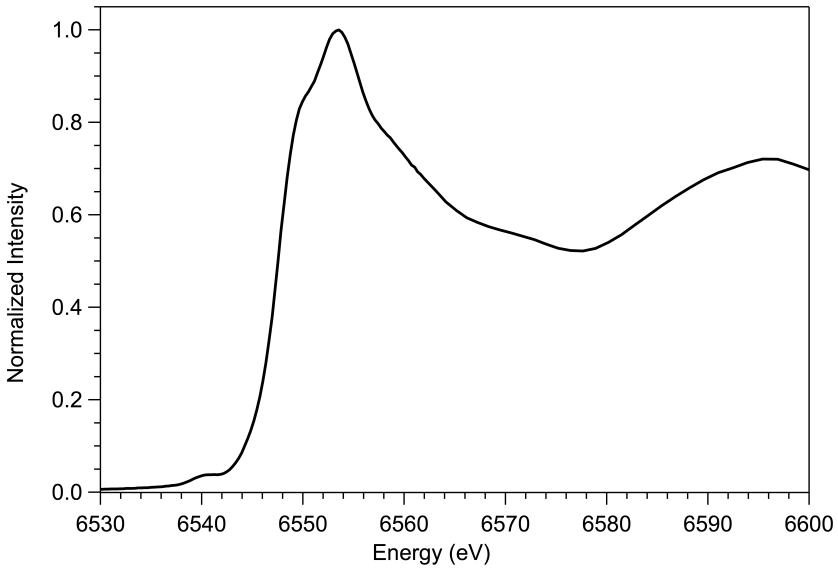

Figure A4.6. Mn K-edge X-ray Absorption data of $[Mn^{II}(Tp^{Ph2})(DMF)_3](OTf)$ with an edge at 6547.5 eV and a pre-edge feature at 6540.6 eV.

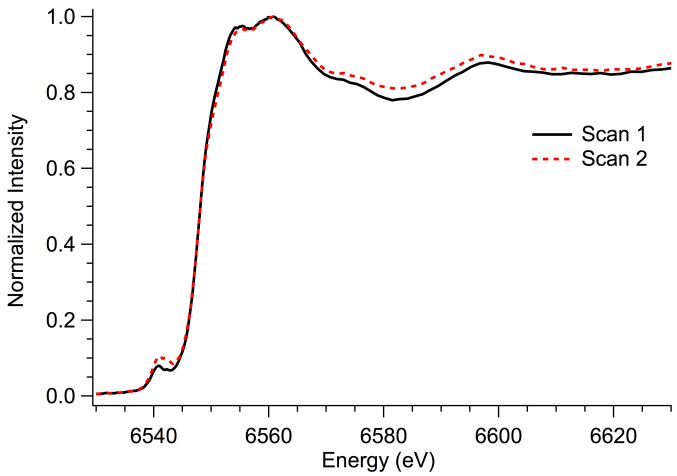

Figure A4.7. Mn K-edge X-ray Absorption data of $[Mn^{III}(O_2)(Tp^{Ph2})(THF)]$ with change in pre-edge feature from scan 1 to scan 2.

Table A4.10. Comparison of Mn-Ligand Bond Lengths from X-ray Diffraction (XRD) and EXAFS fits for $[Mn^{II}(Tp^{Ph2})(DMF)_3](OTf)$.

	XRD (Å)	EXAFS (Å)
Mn-N(1)	2.286(1)	2.28
Mn-N(2)	2.250(3)	2.28
Mn-N(3)	2.319(1)	2.28
Mn-O(1)	2.157(3)	2.14
Mn-O(2)	2.141(6)	2.14
Mn-O(3)	2.191(1)	2.14

Table A4.11. All EXAFS Fitting Results for $[Mn^{II}(Tp^{Ph2})(DMF)_3](OTf)$.

fit	Mn-O			Mn-N			Mn-N/C			Mn-B			Mn-C			F-factor
	n	r(Å)	σ^2	n	r(Å)	σ^2	n	r(Å)	σ^2	n	r(Å)	σ^2	n	r(Å)	σ^2	
1	6	2.18	7.41													0.612
2	3	2.14	3.29	3	2.26	2.58										0.598
3	3	2.14	3.53	3	2.26	2.84	5	3.10	3.14							0.552
4	3	2.14	3.44	3	2.26	2.87	6	3.10	4.72							0.558
5	3	2.14	3.44	3	2.27	2.26	5	3.18	8.15	1	3.11	-4.40				0.520
6	3	2.17	7.16	3	2.23	5.20	5	3.19	8.63	1	3.08	-3.80				0.526
7	3	2.14	3.86	3	2.26	2.78	5	3.09					6	3.18	-2.90	0.536
8	3	2.14	3.68	3	2.26	2.69	5	3.09	2.95				6	3.70	15.78	0.549
9	3	2.16	3.75	3	2.27	3.68	5	3.08	3.32	1	3.33	4.54				0.551
10	3	2.16	3.88	3	2.27	3.53	3	3.08	0.60	1	3.30	6.05				0.535
11	3	2.15	3.48	3	2.28	3.09	3	3.08	1.15	1	3.33	7.59	1	3.53	-1.70	0.528
12	3	2.16	3.62	3	2.28	3.59	3	3.08	0.67	1	3.31	5.03	6	3.54	22.79	0.532
13	3	2.15	3.39	3	2.28	2.98	3	3.09	0.61	1	3.31	3.69	6	3.50	7.43	0.531
14	3	2.16	3.31	3	2.28	3.17	6	3.10	5.11	1	3.35	1.61	6	3.51	2.66	0.540
15	*3*	*2.16*	*3.42*	*3*	*2.28*	*3.17*	*4*	*3.09*	*2.09*	*1*	*3.33*	*2.40*	*6*	*3.49*	*5.51*	*0.534*

Table A4.12. Energies (eV) and Compositions (%) of the O 2p-based MOs and the Mn 3d-based MOs Based on Spin-Unrestricted B3LYP DFT Computations for $[Mn^{III}(O_2)(Tp^{Ph2})(THF)]$.

orbital	occup	spin	energy	Mn 3d	O_2 2p	N 2p	O_{THF} 2p
193 (Mn xz)	1.0	↑	-8.662	71.2	2.0	5.4	1.0
195 (Mn xy/x^2-y^2)	1.0	↑	-7.942	23.3	8.6	11.9	0.5
197 (Mn x^2-y^2/ Tp^{Ph2})	1.0	↑	-7.630	12.8	3.4	17.5	0.2
199 (Mn yz/O_2 π_{op}*)	1.0	↑	-7.512	53.4	26.1	4.6	4.3
200 (Mn x^2-y^2/ Tp^{Ph2})	1.0	↑	-7.403	12.2	4.3	14.3	0.0
201 (Mn $xy/x^2-y^2/O_2$ π_{op}*)	1.0	↑	-7.265	21.8	16.7	9.0	12.0
213 (Tp^{Ph2})	1.0	↑	-6.297	2.1	0.9	24.9	0.2
214 (Mn z^2/Tp^{Ph2})	1.0	↑	-6.149	18.5	3.7	17.8	1.5
215 (Mn z^2/Tp^{Ph2})	1.0	↑	-6.059	21.4	3.0	22.5	1.6
216 (Tp^{Ph2})	1.0	↑	-5.803	0.4	0.2	22.2	0.0
217 (O_2 π_{op}*)	1.0	↑	-5.018	4.0	92.9	0.0	0.0
218 (Mn xy/O_2 π_{op}*)	0.0	↑	-1.582	34.0	52.1	4.7	0.0
213 (O_2 π^*)	1.0	↓	-5.141	5.4	88.8	0.7	0.2
214 (Mn yz/xy)	0.0	↓	-1.295	17.7	0.8	20.5	0.0
215 (Mn xz)	0.0	↓	-1.236	19.0	2.0	18.8	0.2
218 (Tp^{Ph2})	0.0	↓	-0.654	1.5	0.0	10.0	0.0
219 (Mn x^2-y^2/xy)	0.0	↓	-0.614	51.9	2.7	2.7	0.0
221 (Mn xz/Tp^{Ph2})	0.0	↓	-0.406	24.0	2.0	19.0	0.1
224 (Mn yz)	0.0	↓	-0.239	24.0	0.7	2.6	0.0
225 (Mn z^2)	0.0	↓	-0.180	48.6	1.7	2.5	0.0

Table A4.13. TD-DFT Calculated Energies, Percent Contributions from Dominant One-electron Excitations, and Oscillator Strengths for the Major Electronic Transitions of [$Mn^{III}(O_2)(Tp^{Ph2})$].

region	state	energy (cm^{-1})	f_{osc}	transition	%	donor MO	acceptor MO	comments	EDDM
A	1	10 000	0.000011	217α→218α	96	O_2 π*	O_2 π* / Mn d_{xy}	O_2 →Mn CT	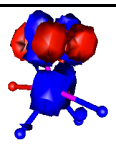
	2	20 500	0.000326	215α→218α	41	Mn d_{z^2}	O_2 π* / Mn d_{xy}	Mn d→d	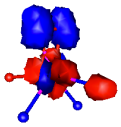
				214α→218α	32	Mn d_{z^2}	O_2 π* / Mn d_{xy}		
	3	23 000	0.000251	213β→214β	58	O_2 π*	Mn d_{xy} / d_{yz}	O_2 →Mn CT	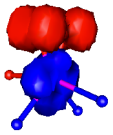
	4	23 300	0.000841	213β→215β	58	O_2 π*	Mn d_{xz}	O_2 →Mn CT	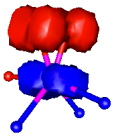
	5	25 500	0.000497	213β→219β	46	O_2 π*	Mn x^2-y^2/xy	O_2 →Mn CT	
B	8	27 200	0.000193	199α→218α	41	Mn d_{yz}	O_2 π* / Mn d_{xy}	Mn d→d	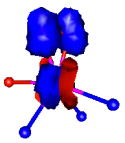
				201α→218α	11	Mn $d_{x^2-y^2}$/ d_{yz}	O_2 π* / Mn d_{xy}		
				195α→218α	3	Mn $d_{x^2-y^2}$/ d_{yz}	O_2 π* / Mn d_{xy}		
B	10	28 400	0.003914	216α→218α	61	Tp^{Ph2}	O_2 π* / Mn d_{xy}	Tp^{Ph2}→ Mn CT	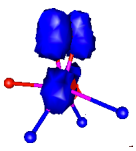
				195α→218α	5	Mn $d_{x^2-y^2}$/d_{yz}	O_2 π* / Mn d_{xy}	Mn d→d	
B	12	28 800	0.005577	215α→218α	8	Mn d_{z^2}	O_2 π* / Mn d_{xy}	Mn d→d	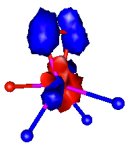
				200α→218α	8	Mn $d_{x^2-y^2}$	O_2 π* / Mn d_{xy}		
				199α→218α	8	Mn d_{yz}	O_2 π* / Mn d_{xy}		
				197α→218α	8	Mn $d_{x^2-y^2}$	O_2 π* / Mn d_{xy}		
				195α→218α	6	Mn $d_{x^2-y^2}$/ d_{yz}	O_2 π* / Mn d_{xy}		
C	14	29 500	0.003044	213β→221β	16	O_2 π_{op}*	Mn d_{xz}	O_2→ Mn CT	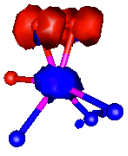
				213β→	16	O_2 π_{op}*	Mn d_{xz}	O_2→Mn	

				15β				CT	
				213β→218β	9	O_2 π_{op}*	Tp^{Ph2}		
				199α→218α	5	Mn d_{yz}	O_2 π*/Mn d_{xy}	Mn d→d	
C	15	29 800	0.003648	213β→224β	18	O_2 π_{op}*	Mn d_{yz}	O_2→ Mn CT	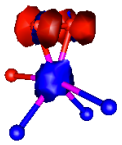
				213β→225β	17	O_2 π_{op}*	Mn d_{z^2}	O_2→Mn CT	
				213β→218β	8	O_2 π_{op}*	Tp^{Ph2}	O_2→Tp^{Ph2} CT	
B	17	30 600	0.001215	215α→218α	16	Mn d_{z^2}	O_2 π*/Mn d_{xy}	Mn d→d/ O_2	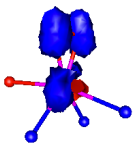
				214α→218α	8	Mn d_{z^2}	O_2 π*/Mn d_{xy}		
				193α→218α	6	Mn d_{xz}	O_2 π*/Mn d_{xy}		

[a]Electronic transition energies have been rounded to the nearest 100 cm^{-1}. Included in this table are all Mn d-d transitions, as well as charge-transfer (CT) transitions, with $f_{osc} > 0.003$. [b]Composition of molecular orbitals (MOs) involved in these electronic transitions are listed in Table S5. Spin-up and spin-down MOs are designated by ↑ and ↓, respectively. [c]Electron density difference maps (EDDMs) showing surface contour plots of loss (red) and gain (blue) of electron density for a given electronic transition. For clarity, only the Mn, N, and O atoms are shown in these plots.

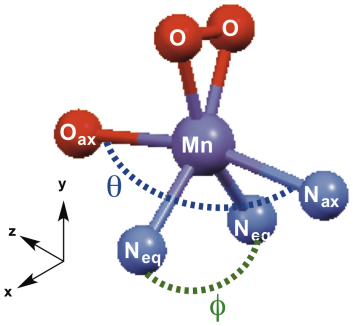

θ = 93.1(3)
ϕ = 163.0(9)

τ = | (θ - ϕ) / 60° |
τ = 1.17

Figure A4.8. Calculation of τ parameter for $[Mn^{III}(O_2)(Tp^{Ph2})]$. For clarity, only the primary coordination sphere of Mn, N, and O is shown.

Table A4.14. Band comparison of the experimental absorption and MCD transition energies, TD-DFT and NEVPT2 calculated transition energies in wavenumbers.

Band	Exp. Absorption		MCD	TD-DFT		CASSCF/NEVPT2		Assignment
	cm^{-1}	f_{exp} x 10^3	cm^{-1}	cm^{-1}	f_{osc} x 10^3	cm^{-1}	f_{osc} x 10^3	
1	19 000	0.083	19 000	20 500	0.326	25 700	0.164	d_z^2 - d_{xy}
2	20 890	0.135	21 455	23 300	0.841	-		CT
3	22 600	0.290	22 325	27 200	0.193	29 500	0.448	d_{yz} - d_{xy}
4	[b]	-	23 675	[c]	-	26 800[a]	0.000	SF[c]
5	24 350	34.20	24 800	28 800	5.577	31 600	0.198	$d_{x^2-y^2}$ - d_{xy}
6	[b]	-	25 150	[c]	-	30 500[a]	-	SF[c]
7	26 300	167.64	26 060	30 600	1.215	32 000	0.005	d_{xz} - d_{xy}
8	28 400	83.28	27 609	29 500	3.044	-	-	O_2-Mn CT
9	28 350		-	29 800	3.648	-	-	O_2-Mn CT

[a]Indicates spin-forbidden states calculated by NEVPT2 with negligible contribution to the absorption spectrum. [b]Band only apparent in low-temperature, 7 T MCD spectrum. [c]Mn^{III} spin-forbidden *d-d* transitions to triplet excited states.

Table A4.15. CASSCF/NEVPT2 calculated individual contributions to zero field splitting parameters. (D = -2.905 cm^{-1}, E/D = 0.275)

Multiplicity	Root	Energy (cm^{-1})	D (cm^{-1})	E
5	1	25688.2	-0.368	0.006
5	2	29493.3	-0.489	-0.005
5	3	32046.6	0.001	-0.037
5	4	31593.8	0.095	0.030
3	0	18355.4	-0.473	-0.035
3	1	19212.3	-0.337	0.017
3	2	20430.1	-0.014	0.002
3	3	22931.6	0.000	0.000
3	4	23652.4	-0.264	-0.006
3	5	23690.7	-0.011	0.005
3	6	25183.4	-0.113	0.037
3	7	24935.5	-0.145	-0.023
3	8	26826.9	-0.003	-0.002
3	9	30521.8	-0.784	-0.788

Table A4.16. Energies (eV) and Compositions (%) of the O 2p-based MOs and the Mn 3d-based MOs Based on Spin-Unrestricted B3LYP DFT Computations for [$Mn^{III}(O_2)(Ph^{iPr2})(pz^{iPr2}H)$] (193 K) from XRD coordinates.

orbital	occupancy	spin	energy (eV)	Mn 3d	O (2p)
186	1.0	↑	-6.4209	6.6	3.7
187	1.0	↑	-6.3665	12.1	4.6
188	1.0	↑	-6.1353	1.0	0.6
189	1.0	↑	-6.0422	0.7	0.3
190	1.0	↑	-5.4246	51.6	6.8
191	1.0	↑	-5.0085	5.8	65.2
192	0.0	↑	-1.0234	45.5	44.5
186	1.0	↓	-6.0434	0.2	0.4
187	1.0	↓	-5.1158	5.2	88.6
188	0.0	↓	-0.6623	56.8	3.4
189	0.0	↓	-0.6169	61.3	2.9
190	0.0	↓	-0.2795	75.1	3.1
191	0.0	↓	0.3637	0.7	0.6

Table A4.17. Energies (eV) and Compositions (%) of the O 2p-based MOs and the Mn 3d-based MOs Based on Spin-Unrestricted B3LYP DFT Computations for [$Mn^{III}(O_2)(Ph^{iPr2})(pz^{iPr2}H)$] (193 K) from hydrogen optimized DFT structures.

orbital	occupancy	spin	energy (eV)	Mn 3d	O (2p)
186	1.0	↑	-6.5581	3.9	3.1
187	1.0	↑	-6.5183	9.9	4.3
188	1.0	↑	-6.2916	1.0	0.5
189	1.0	↑	-6.1642	0.6	0.2
190	1.0	↑	-5.6258	49.4	6.8
191	1.0	↑	-5.2261	5.4	90.6
192	0.0	↑	-1.2706	43.3	46.5
186	1.0	↓	-6.1651	0.1	0.6
187	1.0	↓	-5.3378	4.5	88.2
188	0.0	↓	-0.8139	62.6	2.6
189	0.0	↓	-0.7628	61.0	4.2
190	0.0	↓	-0.4787	73.9	4.0
191	0.0	↓	0.2707	2.6	0.6

Table A4.18. Energies (eV) and Compositions (%) of the O 2p-based MOs and the Mn 3d-based MOs Based on Spin-Unrestricted B3LYP DFT Computations for [$Mn^{III}(O_2)(Ph^{iPr2})(pz^{iPr2}H)$] (253 K) from XRD coordinates.

orbital	occupancy	spin	energy (eV)	Mn 3d	O 2p
186	1.0	↑	-6.3618	13.4	5.1
187	1.0	↑	-6.2663	6.4	3.8
188	1.0	↑	-5.9808	1.0	0.3
189	1.0	↑	-5.9184	0.8	0.3
190	1.0	↑	-5.3902	51.3	6.5
191	1.0	↑	-4.8770	6.2	91.9
192	0.0	↑	-0.8555	45.0	44.4
186	1.0	↓	-5.9202	0.1	0.5
187	1.0	↓	-4.9824	5.9	89.0
188	0.0	↓	-0.5594	52.5	4.9
189	0.0	↓	-0.4820	61.5	3.4
190	0.0	↓	-0.1782	70.6	4.1
191	0.0	↓	0.4323	1.9	0.5
192	0.0	↓	0.6041	38.2	0.7

Table A4.19. Energies (eV) and Compositions (%) of the O 2p-based MOs and the Mn 3d-based MOs Based on Spin-Unrestricted B3LYP DFT Computations for [$Mn^{III}(O_2)(Ph^{iPr2})(pz^{iPr2}H)$] (253 K) from hydrogen optimized DFT structures.

orbital	occupancy	spin	energy (eV)	Mn 3d	O 2p
186	1.0	↑	-6.5267	11.8	5.0
187	1.0	↑	-6.4220	5.7	3.7
188	1.0	↑	-6.1397	1.4	0.6
189	1.0	↑	-6.1062	0.5	0.2
190	1.0	↑	-5.5686	50.0	6.5
191	1.0	↑	-4.9866	5.4	92.1
192	0.0	↑	-1.0412	42.4	46.6
187	1.0	↓	-5.0910	5.5	89.4
188	0.0	↓	-0.6845	51.8	4.2
189	0.0	↓	-0.6208	59.9	3.3
190	0.0	↓	-0.3412	70.0	3.8
191	0.0	↓	0.2922	2.2	0.6

Table A4.20. TD-DFT Calculated Energies, Percent Contributions from Dominant One-electron Excitations, and Oscillator Strengths for the Major Electronic Transitions of $[Mn^{III}(O_2)(Ph^{iPr2})(pz^{iPr2}H)]$ (193 K) from XRD coordinates.

band	state	energy (cm^{-1})	f_{osc}	transition	%	donor MO	acceptor MO	comments
i	1	14969.5	0.000049	191α → 192α	98	O_2	Mn d / O_2	LMCT
ii	2	17339.6	0.000664	190α→192α	96%	Mn d	Mn d / O_2	d → d
iii	3	24912.4	0.000093	187β → 188β	31	O_2	Mn d / O_2	LMCT
				187β → 189β	52	O_2	Mn d / O_2	LMCT
				187β → 190β	12	O_2	Mn d / O_2	LMCT
	4	25450.6	0.000505	187β → 188β	50	O_2	Mn d / O_2	LMCT
				187β → 189β	26	O_2	Mn d / O_2	LMCT

Table A4.21. TD-DFT Calculated Energies, Percent Contributions from Dominant One-electron Excitations, and Oscillator Strengths for the Major Electronic Transitions of $[Mn^{III}(O_2)(Ph^{iPr2})(pz^{iPr2}H)]$ (193 K) from hydrogen optimized DFT structures.

band	state	energy (cm^{-1})	f_{osc}	transition	%	donor MO	acceptor MO	comments
i	1	14583.9	0.000053	191α → 192α	98	O_2	Mn d / O_2	LMCT
ii	2	17466.1	0.000808	190α →192α	95	Mn d	Mn d / O_2	d → d
iii	3	25165.9	0.000022	187β →188β	58	O_2	Mn d	LMCT
				187β → 189β	26	O_2	Mn d	LMCT
				187β → 190β	11	O_2	Mn d	LMCT
	4	25939.3	0.000191	187β → 188β	23	O_2	Mn d	LMCT
				187β → 189β	50	O_2	Mn d	LMCT

Table A4.22. TD-DFT Calculated Energies, Percent Contributions from Dominant One-electron Excitations, and Oscillator Strengths for the Major Electronic Transitions of $[Mn^{III}(O_2)(Ph^{iPr2})(pz^{iPr2}H)]$ (253 K) from XRD coordinates.

band	state	energy (cm^{-1})	f_{osc}	transition	%	donor MO	acceptor MO	comments
i	1	15091.5	0.000032	191α → 192α	98	O_2	Mn d / O_2	LMCT
ii	2	18475.4	0.000670	190α →192α	95	Mn d	Mn d / O_2	d → d
iii	3	24717.0	0.000170	187β → 188β	26	O_2	Mn d / O_2	LMCT
				187β → 189β	54	O_2	Mn d / O_2	LMCT
				187β → 190β	1	O_2	Mn d / O_2	LMCT
	4	25274.5	0.000989	187β → 188β	53	O_2	Mn d / O_2	LMCT
				187β → 189β	25	O_2	Mn d / O_2	LMCT

Table A4.23. TD-DFT Calculated Energies, Percent Contributions from Dominant One-electron Excitations, and Oscillator Strengths for the Major Electronic Transitions of $[Mn^{III}(O_2)(Ph^{iPr2})(pz^{iPr2}H)]$ (253 K) from hydrogen optimized DFT structures.

band	state	energy (cm^{-1})	f_{osc}	transition	%	donor MO	acceptor MO	comments
i	1	14321.4	0.000023	191α → 192α	98	O_2	Mn d / O_2	LMCT
ii	2	18891.6	0.000724	190α → 192α	95	Mn d	Mn d / O_2	d → d
iii	3	24355.1	0.000061	187β → 188β	30	O_2	Mn d	LMCT
				187β → 189β	47	O_2	Mn d	LMCT
				187β → 190β	18	O_2	Mn d	LMCT
	4	25119.5	0.000522	187β → 188β	47	O_2	Mn d	LMCT
				187β → 189β	30	O_2	Mn d	LMCT

APPENDIX A5.

Table A5.1. Cartesian coordinates (Å) for DFT energy minimized $^{5}[Mn^{III}(O_2)(N_4O)]$ model.

Atom	x	y	z
Mn	1.764411	-0.671317	-0.187826
N	0.607411	1.395666	-0.622996
N	-0.355217	-1.329931	-0.405551
N	0.334352	4.252639	-1.267002
N	1.845646	-2.869712	0.395443
O	2.133407	-0.073118	1.562174
O	3.271217	0.092336	0.663741
O	2.183591	-1.008908	-2.05232
C	-0.848776	1.118449	-0.706503
C	-1.212702	-0.17999	0.020526
C	0.499923	3.814335	-0.016072
C	-0.047301	5.578132	-1.151707
N	0.238977	4.808778	0.899477
C	-0.107317	5.943813	0.181697
C	0.336817	4.710365	2.356281
C	0.973899	2.432685	0.36094
C	1.764051	-2.142115	-2.642239
C	0.618248	-3.378531	0.513225
C	2.724505	-3.922054	0.553651
N	0.666559	-4.722585	0.752992
C	2.007828	-5.082247	0.783639
C	-0.607121	-2.51706	0.460791
C	-0.473376	-5.618676	0.955336
C	0.40354	-2.573758	-2.520157
C	2.65858	-2.927105	-3.415287
C	-0.002214	-3.770068	-3.142247
C	0.896241	-4.546266	-3.896528
C	2.227389	-4.109953	-4.035553
C	-0.600641	-1.662771	-1.855965
H	0.92693	1.723245	-1.544307
H	-1.140302	1.066826	-1.772584
H	-1.451264	1.94384	-0.269275
H	-1.060976	-0.057417	1.111858
H	-2.290006	-0.410352	-0.143762
H	-0.26106	6.195173	-2.033414
H	-0.364263	6.880822	0.685818
H	-0.031116	5.651325	2.80082
H	1.386884	4.551482	2.670607
H	-0.285772	3.874934	2.730823
H	2.080621	2.414954	0.459761
H	0.585591	2.134917	1.354217

H	3.809221	-3.785343	0.48839
H	2.314145	-6.117887	0.959376
H	-0.841702	-2.147268	1.481467
H	-1.498458	-3.084752	0.113348
H	-0.10003	-6.654983	1.021454
H	-1.174139	-5.546375	0.101669
H	-1.007174	-5.367053	1.892038
H	3.701068	-2.585205	-3.513743
H	-1.054358	-4.087867	-3.047564
H	0.55802	-5.477343	-4.376598
H	2.942476	-4.701901	-4.629922
H	-0.591403	-0.69674	-2.396814
H	-1.625024	-2.086684	-1.951366

Table A5.2. Cartesian coordinates (Å) for DFT energy minimized $^{4}[Mn^{II}(O_2)(N_4O)]^{-}$ model.

Atom	x	y	z
Mn	0.593755	0.07304	-0.821821
N	-0.702157	2.081157	-0.612484
N	-2.295489	-0.379888	-0.661125
N	-0.289	5.145741	0.021498
N	0.171049	-1.552846	0.245376
O	2.0034	0.869158	0.151042
O	2.07057	1.284748	-1.274586
O	0.040868	-0.464947	-2.671541
C	-2.076671	2.042362	-1.141016
C	-2.904397	0.936195	-0.46792
C	-0.897775	4.197032	0.74351
C	-0.925534	6.330591	0.338345
N	-1.906266	4.738765	1.514247
C	-1.927322	6.102235	1.266349
C	-2.781814	4.036817	2.454295
C	-0.535975	2.733838	0.705021
C	-0.389192	-1.726712	-2.783959
C	-1.047496	-2.075356	0.555446
C	1.108285	-2.502616	0.661227
N	-0.894917	-3.309262	1.171076
C	0.461046	-3.581497	1.227461
C	-2.312658	-1.283047	0.491003
C	-1.969148	-4.184514	1.615814
C	-1.73059	-2.096092	-2.409417
C	0.449451	-2.745791	-3.325066
C	-2.164259	-3.423517	-2.592358

C	-1.322958	-4.415021	-3.129921
C	-0.005914	-4.06154	-3.495878
C	-2.675086	-1.018465	-1.932045
H	-0.082228	2.567341	-1.27539
H	-1.999746	1.836353	-2.22719
H	-2.608733	3.019093	-1.031767
H	-2.966046	1.130299	0.623128
H	-3.95593	0.986984	-0.848725
H	-0.627533	7.285186	-0.113665
H	-2.641721	6.762712	1.767854
H	-3.504895	4.759853	2.870016
H	-2.197529	3.598702	3.286603
H	-3.346036	3.234549	1.940943
H	0.533407	2.598608	0.969619
H	-1.119934	2.173146	1.460966
H	2.182229	-2.343258	0.518631
H	0.837736	-4.517329	1.652506
H	-2.396465	-0.636684	1.39974
H	-3.204586	-1.961125	0.507239
H	-1.528044	-5.104468	2.039482
H	-2.625514	-4.464307	0.765541
H	-2.587943	-3.697172	2.397222
H	1.475514	-2.463523	-3.614626
H	-3.201265	-3.68098	-2.311679
H	-1.687078	-5.446321	-3.261851
H	0.670878	-4.821485	-3.92261
H	-2.695914	-0.207921	-2.691531
H	-3.714787	-1.436322	-1.866174

Table A5.3. Cartesian coordinates (Å) for DFT energy minimized $^{6}[Mn^{II}(O_2)(N_4O)]^{-}$ model.

Atom	x	y	z
Mn	0.232291	0.334129	-0.592416
N	-1.177606	2.184132	-0.642775
N	-2.257882	-0.520319	-0.685031
N	-1.330124	5.110343	-0.594479
N	0.076346	-1.523375	0.645783
O	1.609662	1.323335	0.608626
O	1.756709	1.692863	-0.880004
O	0.387188	-0.736307	-2.423229
C	-2.565853	1.929118	-1.075543
C	-3.112832	0.653516	-0.421178
C	-1.328683	4.387954	0.529569

C	-1.585049	6.414772	-0.201859
N	-1.570351	5.180698	1.629624
C	-1.733783	6.481127	1.171638
C	-1.626756	4.741325	3.023015
C	-1.025494	2.915136	0.627699
C	-0.137277	-1.929324	-2.63747
C	-1.06852	-2.216549	0.618214
C	1.063248	-2.415433	1.025782
N	-0.855635	-3.51897	0.98361
C	0.501339	-3.658885	1.243565
C	-2.400729	-1.584926	0.325944
C	-1.856536	-4.583964	1.043148
C	-1.547325	-2.180966	-2.456933
C	0.668249	-3.029313	-3.075534
C	-2.072649	-3.462319	-2.716608
C	-1.260205	-4.527977	-3.147669
C	0.119508	-4.294275	-3.324643
C	-2.45384	-1.038697	-2.068072
H	-0.677073	2.723939	-1.361413
H	-2.558523	1.825345	-2.178536
H	-3.248991	2.777407	-0.840722
H	-3.149966	0.79957	0.677687
H	-4.166935	0.490775	-0.758665
H	-1.648486	7.232985	-0.930272
H	-1.939304	7.30692	1.860209
H	-1.851468	5.612315	3.662959
H	-0.657001	4.307656	3.336364
H	-2.423314	3.983825	3.16146
H	0.033187	2.728987	0.951796
H	-1.669866	2.439547	1.396995
H	2.109728	-2.104049	1.11773
H	0.924953	-4.62046	1.549633
H	-2.783166	-1.122171	1.26076
H	-3.148778	-2.35759	0.031358
H	-1.360079	-5.51836	1.357709
H	-2.308734	-4.736984	0.043471
H	-2.650009	-4.337495	1.774678
H	1.746645	-2.84804	-3.218291
H	-3.158018	-3.622645	-2.589119
H	-1.695672	-5.519545	-3.347026
H	0.776322	-5.113292	-3.664572
H	-2.269935	-0.183749	-2.75165
H	-3.52129	-1.349241	-2.198456

Table A5.4. Cartesian coordinates (Å) for DFT energy minimized $^{4}[Mn^{IV}(O)_2(N_4O)]^{-}$ model.

Atom	x	y	z
Mn	1.473699	-0.681331	0.712153
N	0.51137	1.094083	0.015301
N	-0.663726	-1.454141	-0.160467
N	0.632355	3.672269	-1.477366
N	1.708918	-2.738039	0.645137
O	0.718733	-0.665818	2.241257
O	3.057762	-0.091888	0.82728
O	1.826325	-0.720865	-1.661999
C	-0.980699	1.007486	-0.026812
C	-1.502529	-0.378243	0.403485
C	0.713964	3.581415	-0.146541
C	0.361524	5.00218	-1.746697
N	0.502952	4.806014	0.449096
C	0.283418	5.723263	-0.568022
C	0.550919	5.111915	1.879313
C	1.050492	2.326619	0.615467
C	1.550333	-1.806156	-2.344588
C	0.570372	-3.429808	0.505326
C	2.746323	-3.643028	0.597465
N	0.84276	-4.763866	0.39268
C	2.222971	-4.913544	0.445796
C	-0.773286	-2.754909	0.532138
C	-0.127033	-5.834064	0.162174
C	0.217865	-2.365872	-2.348766
C	2.535925	-2.494145	-3.127966
C	-0.070566	-3.529094	-3.084715
C	0.918563	-4.186359	-3.842851
C	2.223656	-3.650275	-3.857016
C	-0.85383	-1.590387	-1.631339
H	0.88088	0.980183	-0.946238
H	-1.333381	1.277939	-1.04352
H	-1.409213	1.764102	0.660695
H	-1.405468	-0.461173	1.501924
H	-2.577088	-0.474412	0.112636
H	0.233979	5.367913	-2.773416
H	0.089987	6.778715	-0.351923
H	0.196143	6.146017	2.032728
H	1.584879	5.025288	2.267437
H	-0.107582	4.424636	2.444083
H	2.152146	2.178116	0.67409

H	0.689385	2.387997	1.661779
H	3.78956	-3.321795	0.675298
H	2.691104	-5.899334	0.368523
H	-1.037136	-2.546285	1.589163
H	-1.567486	-3.406764	0.101014
H	0.386566	-6.805621	0.266662
H	-0.548658	-5.75622	-0.859755
H	-0.944934	-5.782199	0.904767
H	3.558204	-2.080634	-3.139895
H	-1.104271	-3.919628	-3.077499
H	0.675072	-5.095221	-4.415345
H	3.012331	-4.148287	-4.447532
H	-0.867105	-0.557306	-2.036756
H	-1.8576	-2.038065	-1.833586

Table A5.5. Cartesian coordinates (Å) for DFT energy minimized $^{6}[Mn^{IV}(O)_2(N_4O)]^{-}$ model.

Atom	x	y	z
Mn	0.788781	0.265177	-1.139085
N	-0.719565	2.128002	-0.640738
N	-2.254422	-0.373827	-0.847771
N	-0.368987	5.158958	0.214044
N	0.300508	-1.325629	0.172592
O	2.012807	0.895038	0.027465
O	1.584979	1.518863	-2.170851
O	0.194651	-0.799876	-2.748545
C	-2.073813	2.084403	-1.196782
C	-2.887766	0.9222	-0.603802
C	-0.962139	4.142667	0.852427
C	-1.039277	6.300398	0.611098
N	-1.99387	4.600063	1.647724
C	-2.047006	5.977717	1.503835
C	-2.864524	3.807912	2.517801
C	-0.566518	2.69366	0.709853
C	-0.387041	-1.991142	-2.813962
C	-0.868608	-1.883269	0.518428
C	1.297484	-2.123978	0.711758
N	-0.64882	-3.009879	1.26622
C	0.723056	-3.174842	1.395024
C	-2.242943	-1.317682	0.258737
C	-1.674422	-3.881167	1.839244
C	-1.78681	-2.163564	-2.535737
C	0.353047	-3.145195	-3.213066

C	-2.374454	-3.436611	-2.669647
C	-1.629535	-4.561638	-3.069919
C	-0.256215	-4.401778	-3.340602
C	-2.614762	-0.961237	-2.148883
H	-0.052623	2.583017	-1.285342
H	-1.974494	1.945407	-2.292456
H	-2.641557	3.036094	-1.045155
H	-2.981598	1.063189	0.492561
H	-3.930209	0.96595	-1.009909
H	-0.759457	7.293808	0.237822
H	-2.784884	6.580165	2.043044
H	-3.595365	4.483529	2.995209
H	-2.277833	3.302433	3.309157
H	-3.42047	3.049635	1.933181
H	0.507839	2.563377	0.958189
H	-1.133852	2.075495	1.434419
H	2.354392	-1.87778	0.569996
H	1.148011	-4.016554	1.949881
H	-2.57747	-0.79592	1.182673
H	-2.965254	-2.158233	0.114948
H	-1.176118	-4.716223	2.361452
H	-2.320867	-4.293832	1.040412
H	-2.300081	-3.326527	2.565186
H	1.426996	-3.017	-3.425729
H	-3.45332	-3.543288	-2.459971
H	-2.113042	-5.546081	-3.169335
H	0.348502	-5.269535	-3.654325
H	-2.467593	-0.162781	-2.907346
H	-3.70183	-1.239588	-2.168563

Table A5.6. Cartesian coordinates (Å) for DFT energy minimized $^{3}[Mn^{V}(O)_2(N_4O)]$ model.

Atom	**x**	**y**	**z**
Mn	1.585988	-0.614238	0.050051
N	0.749721	1.235788	-0.453231
N	-0.566933	-1.35918	-0.417881
N	0.884497	4.090084	-1.228078
N	1.785349	-2.599351	0.34854
O	0.965899	-0.431657	1.589841
O	3.163852	-0.130852	0.135717
O	1.715605	-0.891535	-1.967103
C	-0.733497	1.094804	-0.681404
C	-1.330188	-0.147525	-0.009252

C	0.770868	3.676335	0.037136
C	0.517968	5.423244	-1.218674
N	0.343989	4.693453	0.860514
C	0.186773	5.818336	0.066485
C	0.131983	4.629993	2.307927
C	1.119615	2.295514	0.519955
C	1.44836	-2.053574	-2.566126
C	0.622956	-3.251464	0.503164
C	2.803266	-3.520411	0.450049
N	0.864805	-4.575679	0.711963
C	2.241178	-4.761662	0.682038
C	-0.691282	-2.525474	0.497826
C	-0.142212	-5.62018	0.910562
C	0.129505	-2.599334	-2.49924
C	2.437647	-2.763342	-3.299737
C	-0.166976	-3.816577	-3.136126
C	0.820465	-4.508916	-3.863343
C	2.11888	-3.968589	-3.946013
C	-0.908031	-1.748129	-1.822592
H	1.18362	1.475746	-1.357388
H	-0.895822	1.060046	-1.774418
H	-1.260853	1.999686	-0.316592
H	-1.25479	-0.063068	1.089477
H	-2.406209	-0.227865	-0.285756
H	0.510524	6.025951	-2.135321
H	-0.14476	6.77194	0.489131
H	-0.309156	5.584824	2.642331
H	1.090463	4.471319	2.839337
H	-0.567098	3.810229	2.561805
H	2.213709	2.202757	0.684619
H	0.634099	2.059139	1.485247
H	3.854221	-3.234303	0.350744
H	2.684842	-5.751533	0.821724
H	-0.895197	-2.141488	1.517636
H	-1.531874	-3.194252	0.211049
H	0.375761	-6.582451	1.062374
H	-0.793321	-5.699025	0.018696
H	-0.758982	-5.398014	1.801693
H	3.454353	-2.343174	-3.353383
H	-1.192735	-4.218971	-3.07706
H	0.577773	-5.459155	-4.363621
H	2.899002	-4.500448	-4.51527
H	-1.002237	-0.803992	-2.394425
H	-1.905538	-2.242406	-1.831337

Table A5.7. Cartesian coordinates (Å) for DFT energy minimized $^{5}[Mn^{V}(O)_2(N_4O)]$ model.

Atom	x	y	z
Mn	1.419276	-0.680204	0.104558
N	0.589951	1.178435	-0.382751
N	-0.580747	-1.394326	-0.350229
N	0.667578	3.937806	-1.334029
N	1.691953	-2.6547	0.410351
O	1.029144	-0.401042	1.806959
O	2.998046	-0.088585	0.569823
O	1.895107	-0.867462	-1.839462
C	-0.905971	1.055892	-0.519469
C	-1.42562	-0.245728	0.097622
C	0.692384	3.631713	-0.033953
C	0.381997	5.290194	-1.393023
N	0.432452	4.734835	0.74584
C	0.239456	5.804068	-0.115579
C	0.406541	4.79347	2.208212
C	1.02385	2.273418	0.519686
C	1.590816	-1.980246	-2.512889
C	0.546404	-3.342316	0.508748
C	2.730013	-3.551557	0.528931
N	0.811271	-4.664255	0.69612
C	2.193181	-4.812038	0.713859
C	-0.768262	-2.626517	0.47434
C	-0.174254	-5.73341	0.869642
C	0.25794	-2.506429	-2.486908
C	2.567738	-2.661227	-3.290242
C	-0.049052	-3.67989	-3.200201
C	0.930203	-4.347607	-3.958446
C	2.236973	-3.822745	-4.00452
C	-0.810118	-1.688369	-1.810251
H	0.974434	1.383348	-1.3186
H	-1.159861	1.119174	-1.59372
H	-1.406437	1.915307	-0.031024
H	-1.346427	-0.199752	1.199752
H	-2.493701	-0.395028	-0.176886
H	0.291464	5.819071	-2.349923
H	0.01731	6.80693	0.262268
H	0.045537	5.789944	2.516346
H	1.419389	4.632228	2.626291
H	-0.281367	4.026733	2.613225
H	2.119015	2.150461	0.655872
H	0.566907	2.102979	1.512835
H	3.775737	-3.237072	0.468985

H	2.657779	-5.793159	0.847094
H	-1.044135	-2.311643	1.502061
H	-1.591931	-3.262893	0.085592
H	0.348603	-6.704092	0.82627
H	-0.923828	-5.694061	0.057014
H	-0.683616	-5.637967	1.847812
H	3.590493	-2.253056	-3.315315
H	-1.082543	-4.065514	-3.175785
H	0.674602	-5.263907	-4.512513
H	3.012358	-4.331816	-4.600366
H	-0.862646	-0.704409	-2.315723
H	-1.805548	-2.171603	-1.920043

Table A5.8. Cartesian coordinates (Å) for DFT energy minimized $^{5}[Mn^{III}(O_2)(Me_2EBC)]^{+}$ model.

Atom	**x**	**y**	**z**
Mn	-1.999037959	0.085623654	0.875353632
O	-0.904006409	1.585928621	1.069979651
O	-1.902258405	1.478712704	2.116209922
N	-0.485774984	-1.355486156	2.109997903
N	-3.632430608	1.254933863	-0.496299429
N	-3.70933121	-1.167420939	1.095628379
N	-1.381447082	-1.273393832	-0.648554784
C	-1.241815835	-2.196660104	3.09047065
C	-2.650402729	-1.674567649	3.409337581
C	-3.719123433	-2.007276739	2.36017245
C	-4.87891205	-0.221747532	1.106390628
C	-4.95255159	0.656555284	-0.146732743
C	-3.279503847	1.136660034	-1.945729505
C	-1.81236483	0.763057394	-2.20198881
C	-1.48615361	-0.729558005	-2.062563422
C	0.250243558	-2.144605668	1.080930736
C	0.0563051	-1.580870086	-0.329584988
C	-2.272001278	-2.473041513	-0.457240338
C	-3.693820051	-2.035445998	-0.13507331
C	0.437204017	-0.445742844	2.83101598
C	-3.572845773	2.676036427	-0.078143364
H	-0.653525689	-2.280153131	4.030895113
H	-1.324103196	-3.227171197	2.688126165
H	-2.6266038	-0.584582783	3.625478548
H	-2.980271072	-2.159545922	4.352286091

H	-4.726484577	-1.913833983	2.813488633
H	-3.612264503	-3.069335353	2.061184773
H	-4.768892654	0.401177232	2.016533515
H	-5.828587043	-0.792913069	1.20747757
H	-5.71725543	1.443437637	0.029360311
H	-5.324303328	0.067874358	-1.006881758
H	-3.517290225	2.093939869	-2.460615242
H	-3.931630657	0.36956836	-2.411309391
H	-1.134086096	1.381680105	-1.575332389
H	-1.576955652	1.03272935	-3.253226165
H	-0.526349274	-0.946078621	-2.573038482
H	-2.259261927	-1.319442286	-2.594802975
H	-0.085181571	-3.198183717	1.123009257
H	1.340524131	-2.169683104	1.295488067
H	0.613642839	-0.630657955	-0.452195484
H	0.464200862	-2.303591432	-1.070879906
H	-1.874989683	-3.079933231	0.375109432
H	-2.255178154	-3.120123879	-1.359417931
H	-4.104675595	-1.458243515	-0.981251792
H	-4.354836961	-2.917542947	-0.00023559
H	-0.142857007	0.208189091	3.507567248
H	1.179828478	-1.028465116	3.423188874
H	0.965377751	0.202739465	2.109517609
H	-2.554141564	3.069045241	-0.250540488
H	-3.7847621	2.758766319	1.002693867
H	-4.308055295	3.285643303	-0.652255301

Table A5.9. Cartesian coordinates (Å) for DFT energy minimized $^{4}[Mn^{II}(O_2)(Me_2EBC)]$ model.

Atom	x	y	z
Mn	-1.977005	0.140731	0.901194
O	-0.847163	1.683954	1.108661
O	-1.871794	1.578997	2.177753
N	-0.437275	-1.407341	2.143042
N	-3.689592	1.284491	-0.541216
N	-3.688968	-1.162109	1.067584
N	-1.403437	-1.278931	-0.621361
C	-1.223562	-2.209095	3.112316
C	-2.631772	-1.650057	3.388649
C	-3.691967	-1.994686	2.331423
C	-4.862478	-0.233927	1.079261
C	-4.970726	0.64464	-0.178036
C	-3.292258	1.160721	-1.964684

C	-1.817051	0.767845	-2.167429
C	-1.511949	-0.731492	-2.028578
C	0.25049	-2.177573	1.086589
C	0.02806	-1.592431	-0.317617
C	-2.278055	-2.488684	-0.462141
C	-3.699363	-2.050738	-0.142236
C	0.466852	-0.474258	2.831368
C	-3.613133	2.680206	-0.085621
H	-0.664445	-2.290057	4.074807
H	-1.318046	-3.247419	2.728012
H	-2.577558	-0.549128	3.53177
H	-2.985064	-2.087971	4.348271
H	-4.7025	-1.920318	2.78802
H	-3.571816	-3.059493	2.040873
H	-4.742113	0.40127	1.979056
H	-5.816702	-0.805479	1.191465
H	-5.769567	1.400499	0.004582
H	-5.329279	0.038871	-1.033923
H	-3.494993	2.12035	-2.497706
H	-3.937798	0.399995	-2.453743
H	-1.173805	1.354268	-1.476132
H	-1.530673	1.054728	-3.203365
H	-0.56246	-0.96048	-2.558553
H	-2.298806	-1.306235	-2.56098
H	-0.099038	-3.228603	1.119021
H	1.350355	-2.225957	1.263232
H	0.580234	-0.637787	-0.424317
H	0.442691	-2.310848	-1.067099
H	-1.890179	-3.097531	0.373998
H	-2.258348	-3.138811	-1.367109
H	-4.103793	-1.479902	-0.997097
H	-4.364337	-2.934452	-0.004369
H	-0.12931	0.196208	3.479488
H	1.230403	-1.016688	3.443662
H	0.966984	0.173974	2.088826
H	-2.58049	3.052036	-0.228164
H	-3.813401	2.727354	1.000424
H	-4.332999	3.334343	-0.638871

Table A5.10. Cartesian coordinates (Å) for DFT energy minimized $^{6}[Mn^{II}(O_2)(Me_2EBC)]$ model.

Atom	x	y	z
Mn	-1.929352	0.256522	0.9586
O	-0.81096	1.912396	1.137975
O	-1.762703	1.706938	2.339921
N	-0.469485	-1.342778	2.095985
N	-3.639786	1.259374	-0.476253
N	-3.76096	-1.236846	1.058876
N	-1.396176	-1.358333	-0.68901
C	-1.244946	-2.139043	3.093732
C	-2.672722	-1.628739	3.361203
C	-3.731548	-2.042383	2.322011
C	-4.896667	-0.278062	1.071702
C	-4.948618	0.625626	-0.168101
C	-3.237644	1.166574	-1.911377
C	-1.779534	0.732216	-2.147449
C	-1.516721	-0.783289	-2.067615
C	0.228356	-2.162794	1.071381
C	0.026004	-1.633479	-0.355107
C	-2.28819	-2.52582	-0.482783
C	-3.718612	-2.087875	-0.155632
C	0.47014	-0.427026	2.7781
C	-3.604085	2.664024	-0.015853
H	-0.682106	-2.167687	4.054712
H	-1.302752	-3.19169	2.744575
H	-2.661048	-0.523181	3.490056
H	-2.996423	-2.051724	4.336951
H	-4.739619	-2.001502	2.791004
H	-3.56953	-3.107823	2.053373
H	-4.776981	0.343444	1.983833
H	-5.876873	-0.808054	1.163101
H	-5.737415	1.392986	0.000117
H	-5.285644	0.043182	-1.047897
H	-3.410211	2.151005	-2.403892
H	-3.910489	0.448247	-2.42566
H	-1.103584	1.284067	-1.456419
H	-1.501446	1.052787	-3.17491
H	-0.588693	-1.022498	-2.632525
H	-2.335239	-1.314815	-2.597968
H	-0.127319	-3.209375	1.14131
H	1.323254	-2.207247	1.268465
H	0.572551	-0.675273	-0.480446

H	0.478931	-2.364188	-1.069905
H	-1.898438	-3.127541	0.357905
H	-2.297135	-3.200046	-1.370999
H	-4.119089	-1.511255	-1.008781
H	-4.370993	-2.986473	-0.052827
H	-0.109493	0.278149	3.404092
H	1.209737	-0.991734	3.396212
H	0.996359	0.188655	2.025251
H	-2.570103	3.046392	-0.113551
H	-3.846837	2.704199	1.062293
H	-4.31816	3.298788	-0.594778

Table A5.11. Cartesian coordinates (Å) for DFT energy minimized $^{4}[Mn^{IV}(O)_2(Me_2EBC)]$ model.

Atom	x	y	z
Mn	-1.912401	0.302688	0.981506
O	-0.591892	1.195514	0.403683
O	-2.554628	1.037536	2.368651
N	-0.569634	-1.187111	2.091602
N	-3.474325	1.259365	-0.390242
N	-3.718624	-1.238962	1.084025
N	-1.421777	-1.316532	-0.696616
C	-1.279505	-2.113137	3.051812
C	-2.724256	-1.744702	3.397104
C	-3.735533	-2.111092	2.305563
C	-4.831079	-0.262288	1.14583
C	-4.834491	0.731949	-0.021758
C	-3.216085	1.115776	-1.871728
C	-1.802915	0.680771	-2.266095
C	-1.553059	-0.822943	-2.107997
C	0.238368	-1.959948	1.085152
C	0.006715	-1.535437	-0.368969
C	-2.281379	-2.504611	-0.466463
C	-3.708136	-2.059776	-0.152828
C	0.305155	-0.267782	2.864103
C	-3.352161	2.692018	-0.016507
H	-0.676064	-2.17341	3.98439
H	-1.267891	-3.133374	2.616416
H	-2.794128	-0.661243	3.626435
H	-3.000233	-2.31746	4.308737
H	-4.764654	-2.105578	2.729548
H	-3.549013	-3.157378	1.983102
H	-4.68811	0.286851	2.095817

H	-5.822798	-0.777174	1.170421
H	-5.509406	1.571448	0.24705
H	-5.281274	0.263272	-0.919843
H	-3.462136	2.084262	-2.361132
H	-3.939941	0.379129	-2.276328
H	-1.053215	1.250348	-1.678791
H	-1.669328	0.925821	-3.341856
H	-0.637242	-1.111922	-2.670422
H	-2.387885	-1.375615	-2.588977
H	0.008843	-3.035992	1.207444
H	1.322327	-1.856814	1.303505
H	0.50337	-0.563716	-0.553079
H	0.463304	-2.307781	-1.035577
H	-1.884427	-3.0783	0.391491
H	-2.269193	-3.197698	-1.339385
H	-4.092485	-1.4529	-0.993508
H	-4.38476	-2.941558	-0.067594
H	-0.323771	0.312991	3.564648
H	1.075826	-0.840191	3.430405
H	0.778228	0.442442	2.161695
H	-2.331686	3.03691	-0.267873
H	-3.48376	2.78345	1.077091
H	-4.10586	3.306885	-0.560656

Table A5.12. Cartesian coordinates (Å) for DFT energy minimized $^{6}[Mn^{IV}(O)_2(Me_2EBC)]$ model.

Atom	x	y	z
Mn	-1.946074	0.219067	0.938633
O	-0.64072	1.416134	0.636016
O	-2.312199	1.269057	2.351587
N	-0.460497	-1.416102	2.140127
N	-3.675786	1.266328	-0.554409
N	-3.690267	-1.117773	1.117054
N	-1.364791	-1.228272	-0.621076
C	-1.232822	-2.28355	3.065893
C	-2.618515	-1.718105	3.416998
C	-3.71612	-1.967656	2.372663
C	-4.859772	-0.179381	1.123984
C	-4.971215	0.675463	-0.148062
C	-3.333918	1.104023	-1.990669
C	-1.853922	0.7643	-2.230004
C	-1.478005	-0.712578	-2.042601

C	0.286421	-2.135952	1.083641
C	0.071121	-1.5296	-0.311662
C	-2.246375	-2.421865	-0.41697
C	-3.668973	-1.980304	-0.107468
C	0.401679	-0.484918	2.887659
C	-3.558674	2.675292	-0.141594
H	-0.649427	-2.451131	4.002674
H	-1.354439	-3.285314	2.601484
H	-2.539201	-0.628539	3.625455
H	-2.961403	-2.210237	4.352775
H	-4.705911	-1.822209	2.853271
H	-3.684799	-3.033347	2.061982
H	-4.718112	0.471127	2.009505
H	-5.811562	-0.745709	1.255776
H	-5.7381	1.461621	0.037963
H	-5.370599	0.066821	-0.98349
H	-3.599144	2.032943	-2.549931
H	-3.967282	0.299606	-2.421653
H	-1.21182	1.400101	-1.581599
H	-1.61166	1.015896	-3.2852
H	-0.505337	-0.89951	-2.543389
H	-2.218763	-1.345465	-2.57546
H	-0.015646	-3.20209	1.087654
H	1.381592	-2.138244	1.287145
H	0.605631	-0.562679	-0.393932
H	0.494099	-2.227907	-1.071564
H	-1.858038	-3.012545	0.430548
H	-2.228025	-3.091513	-1.305572
H	-4.062092	-1.400595	-0.960328
H	-4.336497	-2.862719	0.011324
H	-0.222714	0.113114	3.577942
H	1.185178	-1.032363	3.468102
H	0.869266	0.225595	2.181331
H	-2.534214	3.032695	-0.357787
H	-3.698725	2.747125	0.952742
H	-4.301831	3.31886	-0.674516

Table A5.13. Cartesian coordinates (Å) for DFT energy minimized $^{3}[Mn^{V}(O)_2(Me_2EBC)]^{+}$ model.

Atom	**x**	**y**	**z**
Mn	-1.965942	0.180889	0.938618
O	-0.715267	1.096781	0.369854

O	-2.536338	0.908135	2.30773
N	-0.673472	-1.039491	2.10818
N	-3.425104	1.20218	-0.255593
N	-3.625772	-1.300145	0.995399
N	-1.423383	-1.29489	-0.732333
C	-1.321666	-1.58291	3.367384
C	-2.849109	-1.777295	3.379817
C	-3.513341	-2.303044	2.112166
C	-4.794255	-0.39794	1.207341
C	-4.805494	0.774888	0.210925
C	-3.283413	0.981151	-1.750135
C	-1.853884	0.789239	-2.245052
C	-1.279907	-0.627254	-2.084991
C	-0.181278	-2.164149	1.236618
C	-0.089631	-1.751724	-0.22386
C	-2.378673	-2.445499	-0.788744
C	-3.755158	-2.029377	-0.297529
C	0.499574	-0.212655	2.531157
C	-3.234099	2.661356	0.012806
H	-1.073085	-0.876253	4.179575
H	-0.804526	-2.537234	3.60411
H	-3.338722	-0.833478	3.683443
H	-3.062015	-2.50994	4.185622
H	-4.539654	-2.661298	2.347208
H	-2.963289	-3.180226	1.721601
H	-4.722358	-0.016224	2.239799
H	-5.741202	-0.975004	1.11322
H	-5.299362	1.635339	0.69846
H	-5.41091	0.534821	-0.684326
H	-3.745762	1.858251	-2.250724
H	-3.897902	0.107897	-2.036016
H	-1.184946	1.536608	-1.779515
H	-1.854597	0.996977	-3.335752
H	-0.201031	-0.594175	-2.332416
H	-1.753803	-1.294066	-2.833837
H	-0.865721	-3.022079	1.361499
H	0.81233	-2.505685	1.597073
H	0.611671	-0.90544	-0.342172
H	0.29204	-2.604279	-0.829
H	-1.992357	-3.267201	-0.159657
H	-2.444814	-2.850895	-1.818675
H	-4.246275	-1.369801	-1.032318
H	-4.416121	-2.915031	-0.180194
H	0.134673	0.685767	3.059499

H	1.148226	-0.811683	3.205235
H	1.072028	0.104211	1.643431
H	-2.240204	2.96959	-0.356666
H	-3.281712	2.835403	1.101737
H	-4.023986	3.243884	-0.507007

Table A5.14. Cartesian coordinates (Å) for DFT energy minimized $^{5}[Mn^{V}(O)_2(Me_2EBC)]^{+}$ model.

Atom	x	y	z
Mn	-2.000003	0.08678	0.886449
O	-0.768938	1.285154	0.568972
O	-2.355473	1.071139	2.288536
N	-0.66249	-1.094869	2.084857
N	-3.460593	1.17028	-0.286522
N	-3.6456	-1.294562	1.029767
N	-1.411618	-1.271544	-0.729089
C	-1.307638	-1.657586	3.339913
C	-2.839595	-1.701426	3.390468
C	-3.550442	-2.271983	2.167678
C	-4.803277	-0.370736	1.225011
C	-4.842043	0.712623	0.141569
C	-3.269148	0.984384	-1.777596
C	-1.811376	0.818031	-2.201724
C	-1.27123	-0.6106	-2.087496
C	-0.149674	-2.199	1.20229
C	-0.070233	-1.748932	-0.247333
C	-2.379777	-2.429738	-0.770923
C	-3.758374	-2.03125	-0.270143
C	0.499024	-0.257557	2.515882
C	-3.309492	2.627425	0.012982
H	-0.965904	-1.032836	4.185104
H	-0.884554	-2.671723	3.500935
H	-3.232117	-0.687699	3.608197
H	-3.105033	-2.329366	4.265972
H	-4.580647	-2.596151	2.430634
H	-3.023252	-3.173443	1.7992
H	-4.685672	0.087712	2.223467
H	-5.759282	-0.94044	1.217227
H	-5.411678	1.577212	0.530534
H	-5.386919	0.361355	-0.755053
H	-3.723131	1.862599	-2.282988
H	-3.855179	0.104264	-2.102773

H	-1.167545	1.522685	-1.637694
H	-1.730749	1.098539	-3.272533
H	-0.196411	-0.607358	-2.353892
H	-1.780022	-1.256964	-2.831098
H	-0.818957	-3.071336	1.310069
H	0.850927	-2.531123	1.551741
H	0.634005	-0.901928	-0.350648
H	0.300848	-2.582462	-0.883484
H	-1.980742	-3.246874	-0.144681
H	-2.448246	-2.835841	-1.799992
H	-4.261337	-1.380933	-1.004843
H	-4.404398	-2.927649	-0.15302
H	0.119583	0.632483	3.046356
H	1.152415	-0.85721	3.184976
H	1.071914	0.074912	1.634464
H	-2.312168	2.964494	-0.318555
H	-3.387351	2.779201	1.102836
H	-4.099409	3.196846	-0.521005

Table A5.15. Cartesian coordinates (Å) for DFT energy minimized $^{5}[Mn^{III}(O_2)(TMC)]$ model.

Atom	x	y	z
Mn	-2.000003	0.08678	0.886449
O	-0.768938	1.285154	0.568972
O	-2.355473	1.071139	2.288536
N	-0.66249	-1.094869	2.084857
N	-3.460593	1.17028	-0.286522
N	-3.6456	-1.294562	1.029767
N	-1.411618	-1.271544	-0.729089
C	-1.307638	-1.657586	3.339913
C	-2.839595	-1.701426	3.390468
C	-3.550442	-2.271983	2.167678
C	-4.803277	-0.370736	1.225011
C	-4.842043	0.712623	0.141569
C	-3.269148	0.984384	-1.777596
C	-1.811376	0.818031	-2.201724
C	-1.27123	-0.6106	-2.087496
C	-0.149674	-2.199	1.20229
C	-0.070233	-1.748932	-0.247333
C	-2.379777	-2.429738	-0.770923
C	-3.758374	-2.03125	-0.270143
C	0.499024	-0.257557	2.515882
C	-3.309492	2.627425	0.012982
H	-0.965904	-1.032836	4.185104
H	-0.884554	-2.671723	3.500935
H	-3.232117	-0.687699	3.608197
H	-3.105033	-2.329366	4.265972
H	-4.580647	-2.596151	2.430634
H	-3.023252	-3.173443	1.7992
H	-4.685672	0.087712	2.223467
H	-5.759282	-0.94044	1.217227
H	-5.411678	1.577212	0.530534
H	-5.386919	0.361355	-0.755053
H	-3.723131	1.862599	-2.282988
H	-3.855179	0.104264	-2.102773
H	-1.167545	1.522685	-1.637694
H	-1.730749	1.098539	-3.272533
H	-0.196411	-0.607358	-2.353892
H	-1.780022	-1.256964	-2.831098
H	-0.818957	-3.071336	1.310069
H	0.850927	-2.531123	1.551741
H	0.634005	-0.901928	-0.350648
H	0.300848	-2.582462	-0.883484
H	-1.980742	-3.246874	-0.144681

H	-2.448246	-2.835841	-1.799992
H	-4.261337	-1.380933	-1.004843
H	-4.404398	-2.927649	-0.15302
H	0.119583	0.632483	3.046356
H	1.152415	-0.85721	3.184976
H	1.071914	0.074912	1.634464
H	-2.312168	2.964494	-0.318555
H	-3.387351	2.779201	1.102836
H	-4.099409	3.196846	-0.521005

Table A5.16. Cartesian coordinates (Å) for DFT energy minimized $^{4}[Mn^{II}(O_2)(TMC)]$ model.

Atom	x	y	z
Mn	4.807378	12.868326	6.990112
O	4.353877	11.093923	6.403773
N	5.768018	13.985653	8.70104
N	6.979845	13.409367	5.975161
C	7.047404	14.550037	8.185203
H	7.730081	14.797825	9.034028
H	6.805833	15.506413	7.680108
C	7.76023	13.613828	7.21343
H	8.778493	14.022313	6.992777
H	7.909191	12.621543	7.681982
C	7.102708	14.585387	5.082811
H	8.090418	14.557029	4.555048
H	7.113892	15.495355	5.715941
C	5.978215	14.740305	4.057169
H	5.913422	13.848733	3.399876
H	6.269413	15.573665	3.383174
C	4.603815	15.099698	4.632709
H	4.723555	15.892463	5.400811
H	3.974809	15.528331	3.811034
C	6.08293	12.955838	9.727626
H	6.576767	13.416739	10.616939
H	6.749134	12.189259	9.295471
H	5.161522	12.439659	10.048261
C	7.41451	12.17915	5.290978
H	8.502334	12.206564	5.032123
H	6.840183	12.044935	4.354375
H	7.201285	11.315738	5.951336
O	5.261811	11.093718	7.575362
N	3.846449	13.985654	5.279255
N	2.634686	13.409226	8.005217

C	2.567065	14.549955	5.795167
H	1.884325	14.797733	4.94639
H	2.808573	15.506332	6.300294
C	1.854306	13.61365	6.766929
H	0.836009	14.022043	6.987578
H	1.705418	12.621361	6.298354
C	2.511843	14.585375	8.897419
H	1.524099	14.557121	9.42512
H	2.500729	15.495263	8.264178
C	3.636269	14.740402	9.923108
H	3.701002	13.8489	10.580499
H	3.345029	15.573836	10.596992
C	5.010694	15.099715	9.347604
H	4.890959	15.892508	8.57952
H	5.639703	15.52834	10.169276
C	3.531407	12.956008	4.252568
H	3.037701	13.417075	3.363279
H	2.864915	12.189632	4.684612
H	4.452701	12.439628	3.931941
C	2.199854	12.179214	8.689661
H	1.112101	12.206939	8.948773
H	2.774364	12.044953	9.626148
H	2.412539	11.315563	8.029466

Table A5.17. Cartesian coordinates (Å) for DFT energy minimized $^{6}[Mn^{II}(O_2)(TMC)]$ model.

Atom	x	y	z
Mn	4.807344	12.907056	6.990109
O	4.371373	11.020007	6.354853
N	5.867819	13.992303	8.864503
N	6.895408	13.437817	6.059915
C	7.124625	14.546989	8.299123
H	7.867651	14.75644	9.10652
H	6.881316	15.524631	7.836634
C	7.756189	13.623104	7.259641
H	8.758338	14.021454	6.97001
H	7.922798	12.620695	7.699486
C	6.998548	14.626019	5.17006
H	8.022515	14.650986	4.720925
H	6.911641	15.532224	5.803595
C	5.956617	14.720058	4.049877
H	5.96152	13.804234	3.423936
H	6.299285	15.529908	3.372032

C	4.530439	15.084338	4.479492
H	4.577635	15.921004	5.20821
H	3.970214	15.468037	3.590308
C	6.180231	12.935565	9.850087
H	6.757968	13.348387	10.712721
H	6.761819	12.131314	9.364891
H	5.24933	12.474475	10.224758
C	7.314931	12.208634	5.349124
H	8.392357	12.253214	5.059782
H	6.708246	12.072926	4.435498
H	7.121734	11.346424	6.017364
O	5.243931	11.018939	7.622634
N	3.746613	13.992201	5.11576
N	2.719194	13.437627	7.920547
C	2.48983	14.546758	5.681271
H	1.74665	14.756126	4.87398
H	2.733059	15.524428	6.143733
C	1.858407	13.622779	6.720782
H	0.8562	14.020986	7.010408
H	1.691971	12.620334	6.280953
C	2.616089	14.626034	8.810163
H	1.592058	14.651204	9.259134
H	2.703194	15.532098	8.176462
C	3.657854	14.720221	9.930483
H	3.652818	13.804555	10.55666
H	3.315147	15.53025	10.608092
C	5.084069	15.08438	9.500943
H	5.036949	15.921179	8.772374
H	5.644298	15.467937	10.390195
C	3.434118	12.935644	4.130016
H	2.856383	13.348648	3.267463
H	2.852487	12.131356	4.615096
H	4.36496	12.474497	3.755279
C	2.299427	12.208768	8.63173
H	1.222175	12.253938	8.921634
H	2.906492	12.072872	9.54508
H	2.491547	11.346217	7.963679

Table A5.18. Cartesian coordinates (Å) for DFT energy minimized $^{4}[Mn^{IV}(O)_2(TMC)]$ model.

Atom	x	y	z
Mn	4.806104	12.355318	6.989255
O	4.202446	11.392077	5.771255

N	6.024795	14.046075	9.088843
N	6.731925	13.263212	6.173497
C	7.246367	14.446243	8.382871
H	8.106959	14.58717	9.085274
H	7.07956	15.437143	7.917209
C	7.674503	13.41616	7.333443
H	8.680323	13.69944	6.941635
H	7.759516	12.418697	7.804958
C	6.752671	14.562153	5.413765
H	7.816944	14.732432	5.122397
H	6.491417	15.366109	6.127231
C	5.878169	14.74299	4.167822
H	5.921346	13.854444	3.505509
H	6.354226	15.559142	3.584138
C	4.425512	15.160784	4.42871
H	4.413845	15.952271	5.207972
H	4.002852	15.625901	3.499029
C	6.346762	13.136151	10.19129
H	6.945968	13.658531	10.981044
H	6.91123	12.267284	9.810248
H	5.42406	12.736386	10.64982
C	7.256544	12.173983	5.308912
H	8.269386	12.430119	4.918951
H	6.565397	11.996635	4.466407
H	7.319948	11.24366	5.903492
O	5.40924	11.392998	8.208118
N	3.590195	14.047404	4.892123
N	2.88199	13.264619	7.806403
C	2.368551	14.448616	5.597577
H	1.508501	14.590321	4.894726
H	2.535963	15.439342	6.063393
C	1.939249	13.418793	6.646749
H	0.933834	13.703135	7.038805
H	1.853014	12.421533	6.175016
C	2.863205	14.563676	8.566105
H	1.799061	14.735826	8.856831
H	3.126285	15.36714	7.852764
C	3.737193	14.743028	9.812665
H	3.692956	13.854087	10.474373
H	3.261482	15.559178	10.396638
C	5.190389	15.159739	9.552899
H	5.203156	15.952002	8.774431
H	5.612882	15.623684	10.483273
C	3.267433	13.138678	3.788802

H	2.66924	13.662513	2.999277
H	2.701689	12.270285	4.169
H	4.189781	12.73804	3.330348
C	2.356396	12.176034	8.671188
H	1.34412	12.4335	9.061726
H	3.047817	11.997682	9.513245
H	2.291411	11.245854	8.076553

Table A5.19. Cartesian coordinates (Å) for DFT energy minimized $^{6}[Mn^{IV}(O)_2(TMC)]$ model.

Atom	x	y	z
Mn	4.807417	12.650944	6.989868
O	4.129042	11.255921	6.09632
N	5.795594	13.97248	8.720373
N	6.977829	13.354588	5.985467
C	7.068181	14.523695	8.170311
H	7.755637	14.806221	9.001989
H	6.824908	15.462923	7.634761
C	7.76649	13.55229	7.22362
H	8.794059	13.927407	6.995183
H	7.876792	12.563484	7.709307
C	7.12324	14.53332	5.095107
H	8.093235	14.463571	4.543088
H	7.195388	15.439074	5.72954
C	5.979494	14.750009	4.10515
H	5.876428	13.88745	3.416101
H	6.274506	15.602701	3.458112
C	4.631276	15.113791	4.73824
H	4.79593	15.817324	5.58202
H	4.015093	15.660842	3.983749
C	6.137692	13.068427	9.849173
H	6.603654	13.650087	10.679795
H	6.834799	12.288005	9.500383
H	5.238099	12.549267	10.219262
C	7.401903	12.123931	5.290614
H	8.485059	12.157476	5.01773
H	6.811105	11.993847	4.364117
H	7.200557	11.259432	5.951516
O	5.487134	11.256348	7.883147
N	3.818693	13.97236	5.259855
N	2.6368	13.354484	7.994914
C	2.546093	14.523468	5.810001
H	1.858479	14.805854	4.978406

H	2.789267	15.462748	6.345488
C	1.848047	13.551933	6.756782
H	0.82038	13.926786	6.985223
H	1.737961	12.563068	6.271144
C	2.491321	14.533405	8.885033
H	1.521212	14.463808	9.436877
H	2.419328	15.439036	8.250416
C	3.63485	14.750274	9.875191
H	3.737698	13.887915	10.564523
H	3.339724	15.603167	10.521917
C	4.983227	15.113873	9.242374
H	4.818829	15.817783	8.398857
H	5.599435	15.66053	9.997149
C	3.476516	13.068811	4.130662
H	3.012569	13.651183	3.299421
H	2.777212	12.289945	4.478451
H	4.375586	12.54787	3.761826
C	2.212791	12.124026	8.690134
H	1.129711	12.157715	8.963306
H	2.803806	11.994084	9.616513
H	2.413738	11.259242	8.029496

Table A5.20. Cartesian coordinates (Å) for DFT energy minimized $^{3}[Mn^{V}(O)_2(TMC)]^{+}$ model.

Atom	x	y	z
Mn	4.563483	12.699332	6.785008
O	4.075911	11.358106	5.961241
N	6.240136	14.172901	9.319024
N	6.651278	13.317425	6.143615
C	7.266204	14.533771	8.353052
H	8.224042	14.760079	8.879766
H	6.964559	15.476195	7.856637
C	7.584029	13.435528	7.321599
H	8.60342	13.624518	6.916597
H	7.600892	12.452864	7.826892
C	6.854876	14.543882	5.296767
H	7.900772	14.507064	4.915359
H	6.792273	15.423512	5.965126
C	5.897929	14.770542	4.132329
H	5.906247	13.922567	3.418548
H	6.307891	15.630156	3.563291

C	4.476014	15.140033	4.546377
H	4.511713	15.884251	5.369179
H	3.944377	15.624888	3.695434
C	6.670965	13.308732	10.403216
H	7.251727	13.883565	11.16641
H	7.307416	12.491799	10.015669
H	5.796284	12.848471	10.899959
C	7.08289	12.112808	5.370792
H	8.148031	12.215064	5.065877
H	6.456211	11.994572	4.469442
H	6.966404	11.212021	6.000129
O	5.173637	12.19549	8.224459
N	3.664805	13.980546	5.018106
N	2.76875	13.201564	7.671284
C	2.358847	14.464819	5.555053
H	1.626671	14.624498	4.733309
H	2.517339	15.453211	6.025908
C	1.796814	13.467835	6.552128
H	0.840626	13.841604	6.97711
H	1.598836	12.493706	6.067588
C	2.880218	14.455947	8.515786
H	1.833724	14.680045	8.817676
H	3.186204	15.281379	7.844134
C	3.760248	14.481269	9.777949
H	3.822794	13.484798	10.256222
H	3.20846	15.116526	10.499744
C	5.172237	15.106745	9.647228
H	5.157543	15.90858	8.881448
H	5.410875	15.605477	10.618221
C	3.390881	13.072749	3.867063
H	2.954402	13.656495	3.026149
H	2.689573	12.280199	4.175287
H	4.317552	12.57935	3.528472
C	2.246646	12.068458	8.489273
H	1.258975	12.343255	8.915918
H	2.959781	11.836191	9.297121
H	2.141398	11.182835	7.838037

Table A5.21. Cartesian coordinates (Å) for DFT energy minimized $^{5}[Mn^{V}(O)_2(TMC)]^{+}$ model.

Atom	x	y	z
Mn	4.808519	12.915182	6.988671
O	4.264582	11.548699	6.050612

N	5.823468	14.040193	8.769075
N	6.7495	13.263907	6.087905
C	7.155348	14.450563	8.240165
H	7.882123	14.588719	9.070815
H	7.045868	15.438847	7.755128
C	7.675479	13.40598	7.26516
H	8.691451	13.680286	6.907147
H	7.738063	12.415165	7.750788
C	6.950133	14.50258	5.241224
H	7.954965	14.400801	4.776213
H	7.007949	15.365888	5.928132
C	5.925929	14.844511	4.16762
H	5.858924	14.058438	3.39024
H	6.329892	15.73549	3.644117
C	4.546056	15.218363	4.704476
H	4.643857	15.945083	5.538155
H	3.951829	15.715711	3.903318
C	6.067898	13.103031	9.9068
H	6.49706	13.672372	10.761291
H	6.773928	12.314544	9.600795
H	5.138007	12.606017	10.224935
C	7.14084	12.054564	5.310025
H	8.207805	12.127596	5.008489
H	6.510474	11.969829	4.408022
H	6.978817	11.163528	5.940759
O	5.369427	11.564259	7.924967
N	3.788963	14.039705	5.209681
N	2.866957	13.26324	7.892087
C	2.457937	14.450077	5.740431
H	1.72963	14.588243	4.911084
H	2.56785	15.438386	6.225289
C	1.938925	13.405568	6.716455
H	0.924198	13.681898	7.076723
H	1.870625	12.414804	6.231042
C	2.665438	14.502655	8.73832
H	1.660058	14.400538	9.201975
H	2.608536	15.365597	8.05099
C	3.688139	14.844901	9.812986
H	3.75518	14.058236	10.58973
H	3.283469	15.735557	10.33643
C	5.067804	15.218892	9.276281
H	4.970162	15.946858	8.443653
H	5.663083	15.714368	10.077773
C	3.541813	13.105733	4.069859

H	3.112609	13.677287	3.216833
H	2.833496	12.318591	4.374574
H	4.470094	12.607178	3.749547
C	2.477374	12.055643	8.673102
H	1.41326	12.133328	8.983581
H	3.113449	11.969524	9.570963
H	2.626572	11.16127	8.043574

APPENDIX A6.

Table A6.1. Cartesian Coordinates (Å) for $[Tp_2Mn^{III}]^+$ from the X-ray Structure of the SBF_6^- Salt Reported by Hossain *et al*.[1]

Atoms	x	y	z
Mn	0.000000	0.000000	0.000000
N	-1.298219	0.452619	-2.569391
N	-1.487075	0.485932	-1.218590
N	1.143867	0.897179	-2.526571
N	1.188861	1.061986	-1.172819
N	0.308645	-1.434115	-2.518745
N	0.334862	-1.577608	-1.163206
C	-2.429008	0.833196	-3.185626
C	-3.387430	1.115970	-2.227326
C	-2.750860	0.886838	-1.012508
C	2.073309	1.679886	-3.103288
C	2.731803	2.388021	-2.108180
C	2.145538	1.964263	-0.916021
C	0.528288	-2.620249	-3.104311
C	0.703306	-3.575485	-2.110506
C	0.572518	-2.873553	-0.913764
B	0.064445	-0.031922	-3.120703
N	1.298220	-0.452620	2.569390
N	1.487075	-0.485932	1.218590
N	-1.143866	-0.897179	2.526569
N	-1.188861	-1.061987	1.172818
N	-0.308645	1.434115	2.518744
N	-0.334862	1.577608	1.163204
C	2.429009	-0.833196	3.185625
C	3.387430	-1.115969	2.227326
C	2.750861	-0.886838	1.012506
C	-2.073309	-1.679886	3.103288
C	-2.731801	-2.388020	2.108179
C	-2.145539	-1.964262	0.916019
C	-0.528287	2.620251	3.104311
C	-0.703307	3.575487	2.110506
C	-0.572518	2.873554	0.913763
B	-0.064445	0.031922	3.120703
H	-2.551040	0.897883	-4.125240
H	-4.282022	1.403216	-2.368105
H	-3.153194	0.998047	-0.159065
H	2.248892	1.737765	-4.034930
H	3.429980	3.023130	-2.215235
H	2.388645	2.270294	-0.050576
H	0.559177	-2.780418	-4.040355
H	0.874305	-4.503156	-2.222366

H	0.641239	-3.257460	-0.047593
H	0.084465	-0.044429	-4.165260
H	2.551040	-0.897883	4.125239
H	4.282022	-1.403215	2.368104
H	3.153195	-0.998045	0.159063
H	-2.248893	-1.737765	4.034929
H	-3.429979	-3.023128	2.215235
H	-2.388645	-2.270295	0.050575
H	-0.559177	2.780418	4.040354
H	-0.874305	4.503156	2.222365
H	-0.641239	3.257460	0.047593
H	-0.084465	0.044429	4.165258

Table A6.2. Cartesian Coordinates (Å) for $[Tp^*_2Mn^{III}]^+$ from the X-ray Structure of the SbF_6^- Salt Reported by Hossain *et al*.[1]

Atoms	x	y	z
Mn	0.000000	0.000000	0.000000
N	-1.098004	-0.893044	2.532806
N	-1.274967	-1.000465	1.168473
N	-0.198271	1.428788	2.517449
N	-0.226788	1.619531	1.150284
N	1.365892	-0.511863	2.502175
N	1.513566	-0.617326	1.137742
B	0.029096	0.012214	3.065784
C	-2.027191	-1.633589	3.168392
C	-2.826661	-2.232282	2.206811
C	-2.334554	-1.814636	0.970455
C	-2.119446	-1.741695	4.656709
C	-2.874608	-2.193665	-0.383519
C	-0.403406	2.601878	3.143578
C	-0.567608	3.577712	2.177649
C	-0.451863	2.934993	0.943293
C	-0.440100	2.745104	4.633479
C	-0.577517	3.576779	-0.402162
C	2.495378	-0.894691	3.115766
C	3.406720	-1.271558	2.131791
C	2.765204	-1.083022	0.917892
C	2.658680	-0.856809	4.599334
C	3.343005	-1.352935	-0.441303
N	1.098004	0.893044	-2.532806
N	1.274967	1.000465	-1.168473
N	0.198271	-1.428788	-2.517449
N	0.226788	-1.619531	-1.150284
N	-1.365892	0.511863	-2.502175
N	-1.513566	0.617326	-1.137742
B	-0.029096	-0.012214	-3.065784
C	2.027191	1.633589	-3.168392
C	2.826661	2.232282	-2.206811
C	2.334554	1.814636	-0.970455
C	2.119446	1.741695	-4.656709
C	2.874608	2.193665	0.383519
C	0.403406	-2.601878	-3.143578
C	0.567608	-3.577712	-2.177649
C	0.451863	-2.934993	-0.943293
C	0.440100	-2.745104	-4.633479
C	0.577517	-3.576779	0.402162
C	-2.495378	0.894691	-3.115766

C	-3.406720	1.271558	-2.131791
C	-2.765204	1.083022	-0.917892
C	-2.658680	0.856809	-4.599334
C	-3.343005	1.352935	0.441303
H	0.032792	-0.045995	4.132663
H	-3.547938	-2.799290	2.356581
H	-1.258756	-1.969578	5.015564
H	-2.753390	-2.423086	4.890747
H	-2.405579	-0.900253	5.022223
H	-2.216229	-2.002027	-1.056087
H	-3.670723	-1.689004	-0.563686
H	-3.081103	-3.131425	-0.395422
H	-0.724938	4.482404	2.321196
H	-1.136096	2.188118	4.991215
H	-0.613351	3.660395	4.863474
H	0.404455	2.476302	5.001153
H	0.139294	3.281227	-0.967320
H	-0.535881	4.531792	-0.306480
H	-1.417727	3.330827	-0.796643
H	4.271993	-1.586036	2.262626
H	1.939632	-1.340061	5.012726
H	2.646073	0.054705	4.898712
H	3.496007	-1.261862	4.839086
H	2.657768	-1.252655	-1.106222
H	3.687943	-2.248184	-0.471211
H	4.053171	-0.730055	-0.616075
H	-0.032792	0.045995	-4.132663
H	3.547938	2.799290	-2.356581
H	1.258756	1.969578	-5.015564
H	2.753390	2.423086	-4.890747
H	2.405579	0.900253	-5.022223
H	2.216229	2.002027	1.056087
H	3.670723	1.689004	0.563686
H	3.081103	3.131425	0.395422
H	0.724938	-4.482404	-2.321196
H	1.136096	-2.188118	-4.991215
H	0.613351	-3.660395	-4.863474
H	-0.404455	-2.476302	-5.001153
H	-0.139294	-3.281227	0.967320
H	0.535881	-4.531792	0.306480
H	1.417727	-3.330827	0.796643
H	-4.271993	1.586036	-2.262626
H	-1.939632	1.340061	-5.012726
H	-2.646073	-0.054705	-4.898712

H	-3.496007	1.261862	-4.839086
H	-2.657768	1.252655	1.106222
H	-3.687943	2.248184	0.471211
H	-4.053171	0.730055	0.616075

Table A6.3. Cartesian Coordinates (Å) for $[\{Ph(MeIm)_3B\}_2Mn^{III}]^+$ from the X-ray Structure of the Triflate Salt, Reported by Forshaw *et al*.[2]

Atoms	x	y	z
Mn	0.000000	0.000000	0.000000
N	-0.532690	2.883865	-0.072978
N	-0.294955	2.369279	2.008292
N	-2.604145	-0.374379	-1.661786
N	-1.676532	1.568284	-1.887537
N	0.730903	2.022576	-2.065961
N	2.304474	0.528614	-2.015452
B	-0.604986	2.686611	-1.633335
N	0.532690	-2.883864	0.072979
N	0.294954	-2.369279	-2.008292
N	2.604145	0.374379	1.661786
N	1.676531	-1.568284	1.887537
N	-0.730904	-2.022576	2.065961
N	-2.304474	-0.528614	2.015452
B	0.604986	-2.686611	1.633335
C	-2.275626	4.565297	-2.382336
C	-0.952042	4.132256	-2.306027
C	-1.568938	0.384580	-1.202837
C	1.162482	0.889791	-1.421580
C	-0.556364	3.741358	1.967743
C	-0.284273	1.845446	0.764600
C	-0.303611	6.266066	-3.238937
C	0.036906	5.018770	-2.697966
C	-3.323439	0.299024	-2.628240
C	-2.612647	5.816712	-2.908834
C	3.163118	-0.620110	-1.709868
C	-2.726114	1.499563	-2.770577
C	-0.701981	4.046081	0.664002
C	1.590517	2.326260	-3.096355
C	2.592225	1.417025	-3.075976
C	-0.085294	1.651812	3.260174
C	-2.978358	-1.721828	-1.207352
C	-1.582747	6.669166	-3.348623
C	2.275626	-4.565298	2.382335
C	0.952043	-4.132256	2.306028
C	1.568939	-0.384581	1.202838
C	-1.162482	-0.889792	1.421579
C	0.556363	-3.741358	-1.967744
C	0.284273	-1.845446	-0.764600
C	0.303612	-6.266066	3.238937
C	-0.036906	-5.018769	2.697966

C	3.323440	-0.299025	2.628239
C	2.612648	-5.816712	2.908833
C	-3.163118	0.620110	1.709868
C	2.726114	-1.499564	2.770577
C	0.701980	-4.046081	-0.664002
C	-1.590517	-2.326260	3.096354
C	-2.592224	-1.417026	3.075975
C	0.085294	-1.651811	-3.260175
C	2.978358	1.721828	1.207352
C	1.582747	-6.669166	3.348622
H	-2.967216	3.995276	-2.070114
H	-0.619456	4.335904	2.707246
H	0.389051	6.844366	-3.537972
H	0.952007	4.779201	-2.599046
H	-4.085555	-0.019473	-3.097408
H	-3.521577	6.086790	-2.969356
H	2.795750	-1.107364	-0.942514
H	3.201405	-1.215685	-2.486758
H	4.064850	-0.305422	-1.494330
H	-2.987433	2.181595	-3.377605
H	-0.888111	4.907360	0.309820
H	1.496531	3.044074	-3.711116
H	3.341015	1.384151	-3.660246
H	0.065911	0.702056	3.071051
H	-0.877156	1.748144	3.829414
H	0.696105	2.020586	3.722904
H	-3.771827	-2.023656	-1.695125
H	-2.237542	-2.341562	-1.372775
H	-3.175199	-1.699560	-0.246722
H	-1.787999	7.520035	-3.719930
H	2.967216	-3.995276	2.070114
H	0.619456	-4.335903	-2.707245
H	-0.389051	-6.844366	3.537973
H	-0.952008	-4.779202	2.599046
H	4.085555	0.019473	3.097409
H	3.521577	-6.086790	2.969355
H	-2.795749	1.107364	0.942514
H	-3.201405	1.215686	2.486757
H	-4.064851	0.305423	1.494330
H	2.987433	-2.181594	3.377605
H	0.888110	-4.907359	-0.309820
H	-1.496532	-3.044074	3.711116
H	-3.341016	-1.384151	3.660246
H	-0.065911	-0.702055	-3.071051

H	0.877156	-1.748144	-3.829414
H	-0.696105	-2.020586	-3.722904
H	3.771827	2.023657	1.695126
H	2.237542	2.341563	1.372775
H	3.175199	1.699560	0.246722
H	1.787999	-7.520036	3.719929

Table A6.4. Cartesian Coordinates (Å) for $[Tp_2Mn^{III}]^+$ from the X-ray Structure of the SbF_6^- Salt Reported by Hossain *et al*.,[1] with Positions of Hydrogen Atoms Optimized by DFT Computations.

Atoms	x	y	z
Mn	-0.000001	-0.000001	0.000001
N	-1.297938	0.452303	-2.569588
N	-1.486977	0.485672	-1.218814
N	1.144086	0.897174	-2.526472
N	1.188880	1.062066	-1.172723
N	0.309157	-1.434225	-2.518619
N	0.335213	-1.577635	-1.163069
C	-2.428694	0.832702	-3.185995
C	-3.387278	1.115411	-2.227838
C	-2.750840	0.886430	-1.012923
C	2.073505	1.679965	-3.103112
C	2.731779	2.388241	-2.107958
C	2.145410	1.964479	-0.915852
C	0.529027	-2.620365	-3.104087
C	0.704035	-3.575521	-2.110203
C	0.573000	-2.873535	-0.913519
B	0.064860	-0.032098	-3.120692
N	1.297936	-0.452307	2.569589
N	1.486974	-0.485674	1.218816
N	-1.144088	-0.897176	2.526471
N	-1.188883	-1.062069	1.172724
N	-0.309160	1.434222	2.518620
N	-0.335216	1.577633	1.163068
C	2.428692	-0.832704	3.185995
C	3.387275	-1.115412	2.227840
C	2.750838	-0.886432	1.012922
C	-2.073508	-1.679967	3.103113
C	-2.731779	-2.388242	2.107959
C	-2.145413	-1.964480	0.915851
C	-0.529029	2.620365	3.104088
C	-0.704039	3.575521	2.110204
C	-0.573003	2.873534	0.913520
B	-0.064863	0.032096	3.120693
H	-2.475335	0.868511	-4.279803
H	-4.415923	1.451446	-2.391196
H	-3.134507	0.991051	0.007504
H	2.190530	1.690857	-4.192009
H	3.542174	3.113457	-2.231919
H	2.367844	2.256955	0.115468
H	0.547263	-2.705903	-4.195760

H	0.901852	-4.644229	-2.239182
H	0.638775	-3.233912	0.118418
H	0.088428	-0.046077	-4.323586
H	2.475289	-0.868599	4.279798
H	4.415905	-1.451494	2.391190
H	3.134558	-0.990923	-0.007494
H	-2.190572	-1.690783	4.192005
H	-3.542209	-3.113421	2.231910
H	-2.367800	-2.257021	-0.115464
H	-0.547179	2.705909	4.195761
H	-0.901786	4.644247	2.239167
H	-0.638835	3.233891	-0.118425
H	-0.088424	0.046080	4.323585

Table A6.5. Cartesian Coordinates (Å) for $[\{Ph(MeIm)_3B\}_2Mn^{III}]^+$ from the X-ray Structure of the Triflate Salt, Reported by Forshaw *et al*.,[2] with Positions of Hydrogen Atoms Optimized by DFT Computations.

Atoms	x	y	z
M	-0.000065	-0.000032	-0.000023
N	-0.527295	2.884866	-0.071802
N	-0.285071	2.369955	2.008869
N	-2.609320	-0.369420	-1.654897
N	-1.678502	1.571407	-1.883238
N	0.729338	2.020969	-2.068054
N	2.300107	0.523930	-2.021594
B	-0.604099	2.687649	-1.631949
N	0.527164	-2.884930	0.071757
N	0.284939	-2.370020	-2.008916
N	2.609189	0.369355	1.654850
N	1.678371	-1.571471	1.883192
N	-0.729470	-2.021033	2.068008
N	-2.300238	-0.523994	2.021548
B	0.603969	-2.687714	1.631902
C	-2.273028	4.569555	-2.376670
C	-0.950098	4.133926	-2.303826
C	-1.571419	0.387540	-1.198739
C	1.160398	0.887384	-1.424734
C	-0.543897	3.742541	1.968912
C	-0.278701	1.846019	0.765191
C	-0.299955	6.266399	-3.238600
C	0.039546	5.018474	-2.698441
C	-3.329844	0.305327	-2.619496
C	-2.608987	5.821592	-2.902366
C	3.157303	-0.626454	-1.718197
C	-2.730546	1.504683	-2.763497
C	-0.692361	4.047461	0.665538
C	1.586821	2.322899	-3.100738
C	2.586796	1.411704	-3.082939
C	-0.073509	1.652163	3.260245
C	-2.984970	-1.716102	-1.199378
C	-1.578584	6.671997	-3.344936
C	2.272898	-4.569620	2.376622
C	0.949969	-4.133991	2.303781
C	1.571290	-0.387606	1.198694
C	-1.160529	-0.887449	1.424686
C	0.543766	-3.742605	-1.968959
C	0.278571	-1.846083	-0.765238
C	0.299825	-6.266463	3.238554

C	-0.039676	-5.018538	2.698394
C	3.329715	-0.305392	2.619448
C	2.608857	-5.821657	2.902319
C	-3.157434	0.626389	1.718150
C	2.730416	-1.504749	2.763451
C	0.692229	-4.047526	-0.665584
C	-1.586951	-2.322963	3.100690
C	-2.586925	-1.411769	3.082892
C	0.073379	-1.652226	-3.260293
C	2.984840	1.716038	1.199332
C	1.578453	-6.672062	3.344889
H	-3.087912	3.930307	-2.002912
H	-0.594603	4.357596	2.872730
H	0.514949	6.939236	-3.558094
H	1.105480	4.772238	-2.588371
H	-4.200326	-0.130942	-3.119638
H	-3.661995	6.141661	-2.953995
H	2.890426	-1.016921	-0.722497
H	3.016840	-1.427112	-2.470526
H	4.216726	-0.308838	-1.730214
H	-2.977196	2.315123	-3.455032
H	-0.894361	5.013322	0.192627
H	1.429617	3.155604	-3.790278
H	3.471183	1.292232	-3.716997
H	0.417286	0.688673	3.049667
H	-1.036890	1.456688	3.772548
H	0.565576	2.255955	3.931728
H	-3.555203	-2.218952	-2.001368
H	-2.080796	-2.302019	-0.967762
H	-3.617777	-1.664602	-0.291606
H	-1.826597	7.658337	-3.770401
H	3.087805	-3.930370	2.002931
H	0.594426	-4.357735	-2.872730
H	-0.515095	-6.939326	3.557957
H	-1.105611	-4.772283	2.588424
H	4.200513	0.130638	3.119189
H	3.661864	-6.141725	2.953946
H	-2.909099	1.001328	0.711710
H	-2.998024	1.437908	2.454919
H	-4.217622	0.314004	1.756763
H	2.977588	-2.315492	3.454419
H	0.894110	-5.013397	-0.192636
H	-1.429764	-3.155722	3.790164
H	-3.471289	-1.292331	3.716976

H	-0.428667	-0.694247	-3.051239
H	1.037505	-1.445610	-3.766734
H	-0.555143	-2.261718	-3.936467
H	3.644528	2.174635	1.957615
H	2.086585	2.341842	1.070723
H	3.527845	1.672123	0.235414
H	1.826444	-7.658460	3.770232

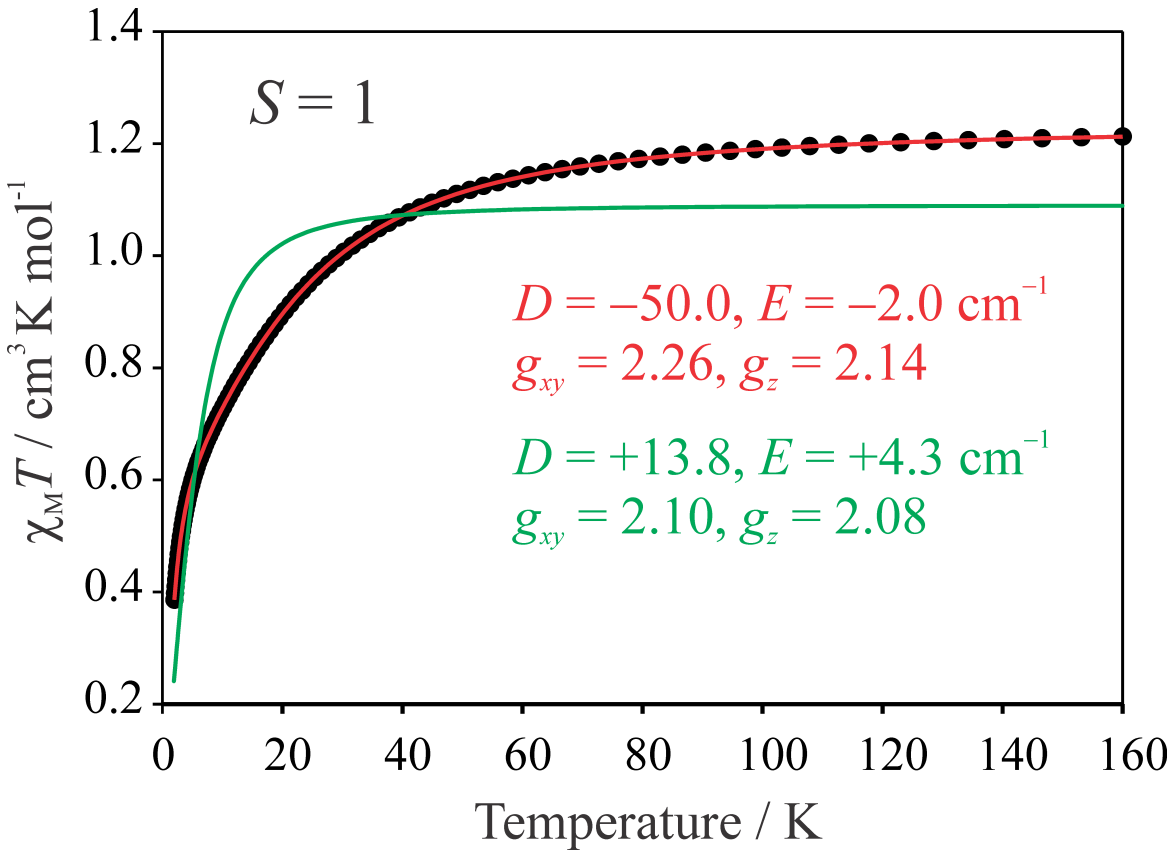

Figure A6.2. Fit of magnetic susceptibility data for **3** (field of 1000 Oe) demonstrating success of data fitting using $S = 1$ spin Hamiltonian with negative values of zfs (red trace and text) and failure of fit using positive values of zfs (green trace and text).

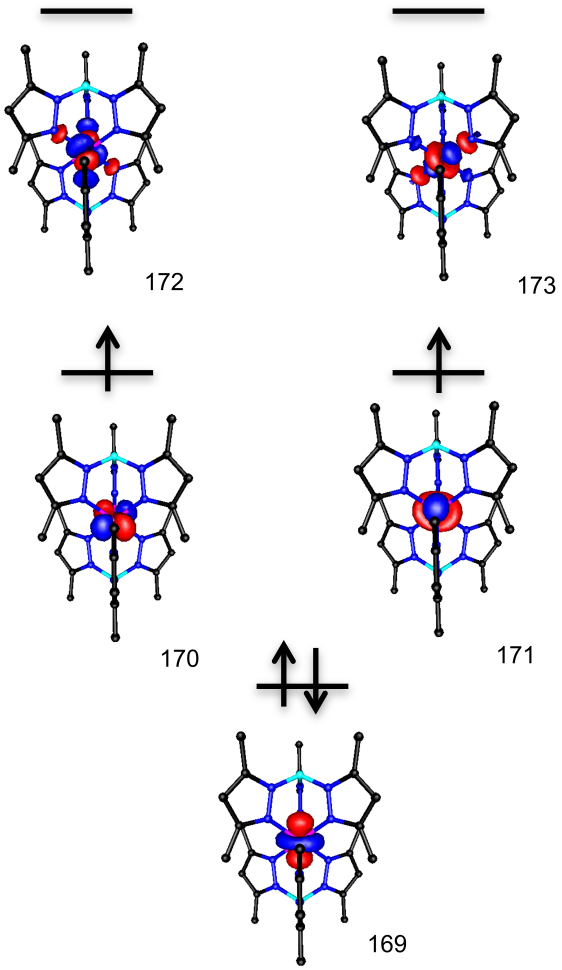

Figure A6.2. Surface contour plots of CASSCF-Calculated Mn^{III}-based orbitals of **2**. The numbers correspond to the CASSCF orbital ordering.

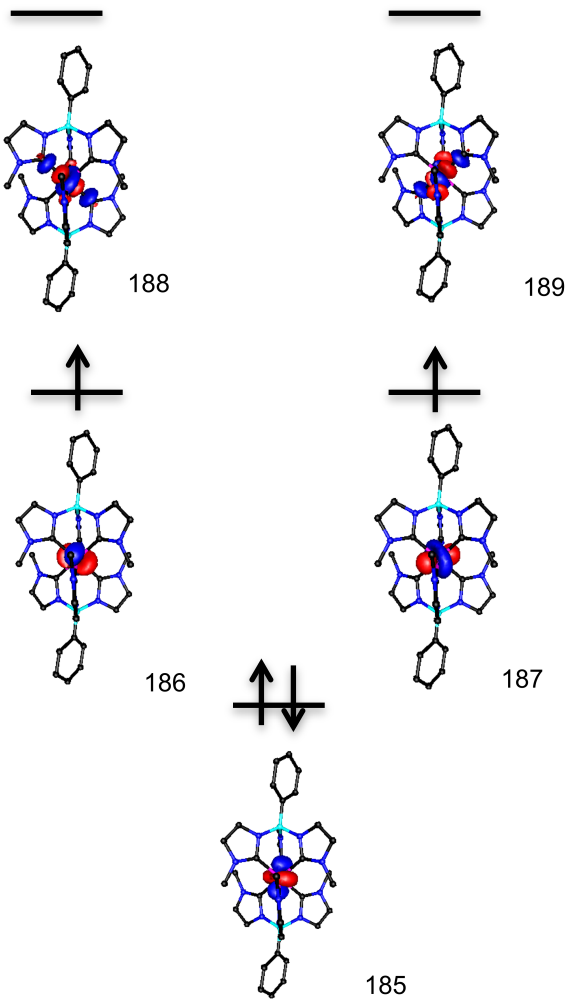

Figure A6.3. Surface contour plots of CASSCF-Calculated Mn^{III}-based orbitals of **3**. The numbers correspond to the CASSCF orbital ordering.

Table A6.6. CASSCF/NEVPT2-Calculated Energy Levels and Contributions to Zero Field Splitting from Ligand-Field States of $[Tp_2Mn^{III}]^+$.

State	Parent State[a]	Energy (cm^{-1})	D	% contribution to D	% contribution to D by parent state	E	% contribution to E	% contribution to E by parent state
$^3A_2$		0.0	-2.127	-13.05%	-13.05%	0.258	79.58%	79.58%
^3E	$^3T_1$	4199.3	0.533	3.27%	17.15%	2.059	635.11%	46.27%
		4381.3	2.262	13.88%		-1.909	-588.84%	
^5E	^5E	4440.0	0.000	-0.00%	0.00%	0.000	0.00%	0.00%
		4921.6	-0.000	0.00%		0.000	0.00%	
^1E	$^1T_2$	11532.1	-0.166	-1.02%	55.65%	0.164	50.59%	-8.02%
		11620.9	-0.200	-1.23%		-0.197	-60.77%	
$^1A_1$		14768.4	9.438	57.90%		0.007	2.16%	
^1E	^1E	17454.8	-0.557	-3.42%	-6.21%	-0.524	-161.63%	-23.44%
		17679.7	-0.455	-2.79%		0.448	138.19%	
^3E	^3E	24247.4	-1.861	-11.42%	-10.33%	-0.001	-0.31%	8.02%
		24946.4	0.177	1.09%		0.027	8.33%	
$^1A_1$	$^1A_1$	25153.6	3.447	21.14%	21.14%	0.000	0.00%	0.00%
$^3A_1$		25184.2	0.202	1.24%		0.016	4.94%	
^3E	$^3T_2$	25381.6	0.575	3.53%	10.61%	-0.530	-163.48%	21.28%
		25670.0	0.953	5.85%		0.583	179.83%	
$^3A_1$	$^3A_1$	27023.3	0.030	0.18%	0.18%	-0.016	-4.94%	-4.94%
$^3A_2$	$^3A_2$	27879.6	0.315	1.93%	1.93%	-0.028	-8.64%	8.64%
$^5A_1$		28921.2	0.000	0.00%		0.000	0.00%	
^5E	$^5T_2$	29195.8	0.000	0.00%	0.00%	0.000	0.00%	0.00%
		33476.7	0.000	0.01%		0.000	0.00%	
$^1A_1$	$^1A_1$	34206.5	0.891	5.47%	5.47%	0.005	1.54%	1.54%
$^1A_2$		36261.2	-0.005	-0.03%		0.003	0.93%	
^1E	$^1T_1$	36481.1	-0.024	-0.15%	-0.59%	-0.019	-5.86%	-18.20%
		36735.1	-0.067	-0.41%		-0.043	-13.26%	

[a] Parent state from O_h point group.

Table A6.7. CASSCF/NEVPT2-Calculated Energy Levels and Contributions to Zero Field Splitting from Ligand-Field States of $[Tp^*_2Mn^{III}]^+$ (**2**).

State	Parent State[a]	Energy (cm^{-1})	*D*	% contribution to *D*	% contribution by parent state to *D*	*E*	% contribution to *E*	% contribution to *E* by parent state
$^3A_2$	$^3T_1$	0.0	-2.443	-17.0%	-17.0%	2.422	1209.6%	1209.6%
^5E	^5E	3795.5	0.000	0.0%	0.0%	0.000	0.0%	0.0%
		4216.2	0.000	0.0%		0.000	0.0%	
^3E	$^3T_1$	4404.1	0.325	2.3%	19.3%	0.298	148.8%	-1053.7%
		4489.9	2.443	17.0%		-2.410	-1202.6%	
^1E		11729.8	-0.201	-1.4%		-0.007	-33.5%	
	$^1T_2$	11748.1	-0.212	-1.5%	51.9%	0.066	33.0%	-0.5%
$^1A_1$		15290.5	7.856	54.8%		0.000	0.0%	
^1E	^1E	17565.8	-0.559	-3.9%	-7.8%	-0.500	-251.7%	-3.0%
		17640.2	-0.563	-3.9%		0.498	248.7%	
^3E	^3E	23135.9	-2.977	-20.8%	19.3%	-0.004	-2.0%	-115.4%
		24186.1	0.214	1.5%		-0.230	-113.4%	
$^1A_1$	$^1A_1$	24633.5	3.687	25.7%	25.7%	0.000	0.0%	0.0%
$^3A_1$		24349.5	0.259	1.8%	1.8%	0.271	135.3%	135.3%
^3E	$^3T_2$	24861.9	1.187	8.3%	17.6%	-1.210	-606.3%	-73.9%
		25094.3	1.074	7.5%		1.091	544.8%	
$^3A_1$	$^3A_1$	26421.5	0.011	0.1%	0.1%	0.005	2.5%	2.5%
$^3A_2$	$^3A_2$	27280.1	0.231	1.6%	1.6%	-0.230	-116.4%	-116.4%
$^5A_1$		27386.9	0.000	0.0%		0.000	0.0%	
^5E	$^5T_2$	27474.3	0.000	0.0%	0.0%	0.000	0.0%	0.0%
		32451.4	0.000	0.0%		0.000	0.0%	
$^1A_1$	$^1A_1$	33307.9	1.045	7.3%	7.3%	0.000	0.0%	0.0%
$^1A_2$		35637.2	-0.004	0.0%		0.002	-1.0%	
^1E	$^1T_1$	36194.9	-0.219	-1.5%	-1.9%	0.221	110.4%	84.4%
		36269.0	-0.050	-0.3%		-0.050	-25.0%	

[a] Parent state from O_h point group.

Table A6.8. NEVPT2-Calculated Energy Levels and Contributions to Zero Field Splitting from Ligand-Field States of $[\{Ph(MeIm)_3B\}_2Mn^{III}]^+$ (**3**).

State	Parent State[a]	Energy (cm^{-1})	*D*	% contribution to *D*	% contribution to *D* by parent state	*E*	% contribution to *E*	% contribution to *E* by parent state
$^3A_2$		0.0	-0.606	-1.57%	-1.57%	0.496	29.23%	29.23%
^3E	$^3T_1$	981.4	10.213	26.43%	70.18%	9.939	585.68%	114.03%
		1098.5	8.924	23.09%		-8.474	-499.35%	
^1E	$^1T_2$	11065.1	-0.227	-0.59%	19.33%	-0.056	-3.30%	3.71%
		11142.3	-0.231	-0.60%		0.126	7.42%	
$^1A_1$		12401.9	5.989	15.49%		-0.005	-0.29%	
^1E	^1E	13876.2	-0.649	-1.68%	-4.47%	-0.347	-20.45%	-4.95%
		13912.6	-0.630	-1.63%		0.259	15.26%	
^5E	^5E	14176.4	0.000	0.00%	-4.16%	0.000	0.00%	0.79%
		15578.1	0.000	0.00%		0.000	0.00%	
$^1A_1$	$^1A_1$	23446.2	4.486	11.61%	15.68%	0.000	0.00%	0.00%
^3E	^3E	33551.4	0.011	0.03%	0.52%	-0.009	-0.53%	25.85%
		34477.7	0.138	0.36%		0.469	27.64%	
$^3A_1$	$^3T_2$	34522.5	0.737	1.91%	3.14%	-0.755	-44.49%	-49.23%
^3E		34526.7	-0.003	-0.01%		0.003	0.18%	
		35286.0	0.164	0.42%		-0.123	-7.25%	
$^3A_1$	$^3A_1$	35499.1	-0.828	-2.14%	-2.89%	0.131	7.72%	7.42%
$^3A_2$	$^3A_2$	36227.6	0.067	0.17%	0.23%	-0.064	-3.77%	-3.60%
$^1A_1$	$^1A_1$	43354.8	0.850	2.20%	2.97%	0.000	0.00%	0.00%
$^1A_2$	$^1T_1$	44504.6	-0.073	-0.19%	-0.52%	0.058	3.42%	6.07%
^1E		44687.7	-0.099	-0.26%		0.082	4.83%	
		44715.5	0.023	0.06%		-0.032	-1.89%	
$^5A_1$	$^5T_2$	51137.0	0.000	0.00%	0.00%	0.000	0.00%	0.00%
^5E		51417.4	0.000	0.00%		0.000	0.00%	
		52985.0	0.000	0.00%		0.000	0.00%	

[a] Parent state from O_h point group.

ORCA Input File for [Tp_2Mn^{III}] (1).

```
# MnIII(Tp)2 low-spin NEVPT2 calculation
! ROHF SVP SV/C RIJCOSX MORead RI-NEVPT2

%pal nprocs 12
      end

%MOInp "2a_MnIII_Tp2_TDDFT.qro"

%output
  Print [P_ReducedOrbPopMO_L]1
  end

%MaxCore 4000

%casscf nel 4
      norb 5
      nroots 5,10,10
      mult 5,3,1
      shiftup 0.1
      shiftdn 0.1
      nev_ristep -1
      trafostep ri
      nev_tpre 1e-10
      rel
      UV true
      DoSOC true
      gtensor true
      PrintLevel 3
      NInitStates 3
      TPrint 0.01
      end
      end

* xyz 1 3
 Mn     0.000000     0.000000     0.000000 newgto"TZVP"end
 N     -1.298219     0.452619    -2.569391  newgto"TZVP"end
 N     -1.487075     0.485932    -1.218590  newgto"TZVP"end
 N      1.143867     0.897179    -2.526571  newgto"TZVP"end
 N      1.188861     1.061986    -1.172819  newgto"TZVP"end
 N      0.308645    -1.434115    -2.518745  newgto"TZVP"end
 N      0.334862    -1.577608    -1.163206  newgto"TZVP"end
 C     -2.429008     0.833196    -3.185626
 C     -3.387430     1.115970    -2.227326
 C     -2.750860     0.886838    -1.012508
 C      2.073309     1.679886    -3.103288
 C      2.731803     2.388021    -2.108180
```

```
C     2.145538    1.964263   -0.916021
C     0.528288   -2.620249   -3.104311
C     0.703306   -3.575485   -2.110506
C     0.572518   -2.873553   -0.913764
B     0.064445   -0.031922   -3.120703  newgto"TZVP"end
N     1.298220   -0.452620    2.569390  newgto"TZVP"end
N     1.487075   -0.485932    1.218590  newgto"TZVP"end
N    -1.143866   -0.897179    2.526569  newgto"TZVP"end
N    -1.188861   -1.061987    1.172818  newgto"TZVP"end
N    -0.308645    1.434115    2.518744  newgto"TZVP"end
N    -0.334862    1.577608    1.163204  newgto"TZVP"end
C     2.429009   -0.833196    3.185625
C     3.387430   -1.115969    2.227326
C     2.750861   -0.886838    1.012506
C    -2.073309   -1.679886    3.103288
C    -2.731801   -2.388020    2.108179
C    -2.145539   -1.964262    0.916019
C    -0.528287    2.620251    3.104311
C    -0.703307    3.575487    2.110506
C    -0.572518    2.873554    0.913763
B    -0.064445    0.031922    3.120703  newgto"TZVP"end
H    -2.551040    0.897883   -4.125240
H    -4.282022    1.403216   -2.368105
H    -3.153194    0.998047   -0.159065
H     2.248892    1.737765   -4.034930
H     3.429980    3.023130   -2.215235
H     2.388645    2.270294   -0.050576
H     0.559177   -2.780418   -4.040355
H     0.874305   -4.503156   -2.222366
H     0.641239   -3.257460   -0.047593
H     0.084465   -0.044429   -4.165260
H     2.551040   -0.897883    4.125239
H     4.282022   -1.403215    2.368104
H     3.153195   -0.998045    0.159063
H    -2.248893   -1.737765    4.034929
H    -3.429979   -3.023128    2.215235
H    -2.388645   -2.270295    0.050575
H    -0.559177    2.780418    4.040354
H    -0.874305    4.503156    2.222365
H    -0.641239    3.257460    0.047593
H    -0.084465    0.044429    4.165258
*
```

References.

1. F. Hossain; M. A. Rigsby; C. T. Duncan; P. L. Milligan; R. L. Lord; M.-H. Baik; F. A. Schultz, *Inorg. Chem.* **2007,** *46*, 2596-2603.
2. A. P. Forshaw; J. M. Smith; A. Ozarowski; J. Krzystek; D. Smirnov; S. A. Zvyagin; T. D. Harris; H. I. Karunadasa; J. M. Zadrozny; A. Schnegg; K. Holldack; T. A. Jackson; A. Alamiri; D. M. Barnes; J. Telser, *Inorg. Chem.* **2013,** *52*, 144-159.

APPENDIX A7.

Table A7.1. Cartesian coordinates (Å) for DFT energy minimized model of ^{4}RC for HAT with $[Mn^{IV}(O)(OH)(Me_2EBC)]^+$ and DHA.

Atom	x	y	z
Mn	-0.235618	0.237312	0.507541
O	1.122341	1.139300	0.145629
O	-0.450653	0.812232	2.246526
H	2.511621	2.772833	0.966339
H	0.240928	1.476201	2.398635
N	0.991828	-1.440494	1.080216
N	-1.521610	1.783875	-0.244259
N	-2.168220	-0.926471	0.726574
N	-0.242895	-0.869523	-1.371541
C	0.240996	-2.554677	1.774636
C	-0.905153	-2.095678	2.668132
C	-2.231428	-1.798624	1.955239
C	-3.141854	0.201288	0.828417
C	-2.914555	1.226859	-0.271937
C	-1.118268	2.299673	-1.609352
C	-0.255784	1.398705	-2.501104
C	-0.640136	-0.071268	-2.576026
C	1.669682	-1.953770	-0.170664
C	1.182109	-1.283813	-1.462909
C	-1.133200	-2.061027	-1.255691
C	-2.419814	-1.710745	-0.526012
C	2.029042	-0.932166	2.023369
C	-1.498142	2.951342	0.683173
H	0.976655	-3.120488	2.369142
H	-0.138330	-3.251463	1.018022
H	-0.592955	-1.229519	3.263972
H	-1.114433	-2.913958	3.376770
H	-2.904539	-1.317490	2.678413
H	-2.706851	-2.749546	1.669105
H	-3.001873	0.664857	1.812716
H	-4.181425	-0.168935	0.771264
H	-3.644487	2.046404	-0.170163
H	-3.089371	0.785031	-1.259108
H	-0.551724	3.224132	-1.444503
H	-2.046835	2.583470	-2.131714
H	0.794530	1.489365	-2.195347
H	-0.330924	1.811970	-3.519973
H	-0.174618	-0.538933	-3.460289
H	-1.725684	-0.176257	-2.709430
H	1.532864	-3.042844	-0.214365
H	2.750004	-1.779782	-0.088227
H	1.766303	-0.377822	-1.652966
H	1.319959	-1.977268	-2.311319
H	-0.598345	-2.853002	-0.725993

H	-1.361952	-2.463132	-2.257018
H	-3.065520	-1.125212	-1.189461
H	-2.976608	-2.632743	-0.298977
H	1.550709	-0.615021	2.957055
H	2.755359	-1.733246	2.238994
H	2.528427	-0.071151	1.566205
H	-0.461933	3.287959	0.808210
H	-1.905497	2.668265	1.658076
H	-2.102178	3.768187	0.253401
C	3.182871	3.628763	1.192664
C	3.957444	3.848221	-1.535676
C	4.595114	3.233612	0.814143
C	4.978661	3.338958	-0.538695
C	2.696908	4.826394	0.403014
C	3.080510	4.935542	-0.949037
C	5.520201	2.761150	1.756121
C	6.276123	2.970005	-0.921185
C	1.876303	5.813474	0.967237
C	2.640344	6.029876	-1.706293
C	6.811392	2.386332	1.366338
C	7.191013	2.490449	0.023402
C	1.432388	6.898583	0.202957
C	1.816120	7.007769	-1.137943
H	3.105171	3.815754	2.274864
H	4.447552	4.194854	-2.458092
H	3.307384	3.000082	-1.832395
H	5.227332	2.688555	2.808068
H	6.574109	3.061692	-1.970219
H	1.585018	5.733466	2.019303
H	2.948182	6.119832	-2.752930
H	7.522545	2.020811	2.112393
H	8.200209	2.206616	-0.287927
H	0.794522	7.661855	0.657308
H	1.480516	7.857457	-1.739122

Table A7.2. Cartesian coordinates (Å) for DFT energy minimized model of ^{6}RC for HAT with $[Mn^{IV}(O)(OH)(Me_2EBC)]^{+}$ and DHA.

Atom	**x**	**y**	**z**
Mn	-0.485284	0.201903	0.988259
O	0.901604	1.411003	1.266515
O	-0.771255	0.400336	2.815068
H	2.729844	3.046366	0.981238
H	-0.786678	1.319265	3.129122
N	0.967596	-1.731443	1.266139
N	-2.133520	1.905641	0.336945
N	-2.218689	-0.986521	0.513077

N	0.097983	-0.209452	-1.034415
C	0.206585	-2.966603	1.614950
C	-1.184564	-2.697238	2.194888
C	-2.266875	-2.356529	1.166807
C	-3.384447	-0.171694	0.989415
C	-3.453911	1.220904	0.360306
C	-1.799293	2.517084	-0.982947
C	-0.342388	2.333516	-1.413944
C	-0.002346	0.960449	-1.997192
C	1.735757	-1.845725	-0.001525
C	1.529708	-0.648893	-0.934572
C	-0.791438	-1.336606	-1.477998
C	-2.206737	-1.114861	-0.982151
C	1.855173	-1.353637	2.387594
C	-2.053631	2.933698	1.395245
H	0.795221	-3.566528	2.331034
H	0.102836	-3.588187	0.712822
H	-1.138328	-1.935024	2.986906
H	-1.523441	-3.627795	2.680189
H	-3.252073	-2.453175	1.645408
H	-2.240997	-3.107989	0.364386
H	-3.282383	-0.098896	2.080671
H	-4.325504	-0.706658	0.772384
H	-4.196222	1.809456	0.924683
H	-3.845015	1.154994	-0.663139
H	-2.039875	3.594424	-0.954767
H	-2.453137	2.080528	-1.752350
H	0.344170	2.597844	-0.592890
H	-0.145452	3.058079	-2.221472
H	0.957378	1.025760	-2.530321
H	-0.753967	0.702277	-2.757841
H	1.453125	-2.774789	-0.513617
H	2.816518	-1.934111	0.198150
H	2.095006	0.220731	-0.572815
H	1.906691	-0.911324	-1.938010
H	-0.404471	-2.275716	-1.072501
H	-0.770574	-1.432617	-2.575351
H	-2.609917	-0.198435	-1.422676
H	-2.864943	-1.937529	-1.305167
H	1.257220	-1.204559	3.295581
H	2.606834	-2.143875	2.571604
H	2.361682	-0.408479	2.156933
H	-1.028598	3.324366	1.457699
H	-2.326387	2.499103	2.365913
H	-2.746607	3.769979	1.185949
C	3.435132	3.894424	0.861956
C	4.200368	3.240155	-1.825992
C	4.822110	3.339564	0.611434

C	5.199196	3.019170	-0.708012
C	2.942083	4.769479	-0.271381
C	3.316308	4.448294	-1.591411
C	5.731971	3.125747	1.657984
C	6.476980	2.494666	-0.953238
C	2.114024	5.878430	-0.041824
C	2.855814	5.241469	-2.652597
C	7.000736	2.592837	1.407612
C	7.375221	2.276460	0.096685
C	1.650793	6.659401	-1.105407
C	2.022993	6.340038	-2.416021
H	3.405540	4.444440	1.815342
H	4.714512	3.316834	-2.796472
H	3.554539	2.341182	-1.901736
H	5.441990	3.382276	2.681614
H	6.771724	2.255430	-1.979705
H	1.831567	6.134807	0.984028
H	3.156697	4.996419	-3.675995
H	7.698228	2.431029	2.234076
H	8.367726	1.866397	-0.109566
H	1.007127	7.521716	-0.910629
H	1.672505	6.949810	-3.253242

Table A7.3. Cartesian coordinates (Å) for DFT energy minimized model of ^{4}TS for HAT with $[Mn^{IV}(O)(OH)(Me_2EBC)]^+$ and DHA.

Atom	x	y	z
Mn	0.146596	-0.337173	-0.029103
O	1.791280	-0.875877	0.252945
O	0.479487	1.472367	-0.370726
H	2.988554	0.006328	0.251233
H	1.412106	1.697655	-0.231578
N	-0.308074	-0.114561	2.375776
N	0.064936	-0.905412	-2.394621
N	-1.972742	-0.029095	-0.530609
N	-0.614277	-2.339839	0.552599
C	-1.534280	0.684831	2.668233
C	-1.983071	1.594013	1.524850
C	-2.742122	0.901112	0.390414
C	-1.923236	0.568060	-1.902156
C	-1.192804	-0.308752	-2.923356
C	0.179651	-2.370432	-2.663011
C	0.755354	-3.184550	-1.502406
C	-0.229930	-3.479884	-0.369069
C	-0.365239	-1.494998	2.926591
C	-0.010065	-2.573980	1.899141
C	-2.101917	-2.208534	0.624750

C	-2.605783	-1.384807	-0.543478
C	0.886206	0.601413	2.866693
C	1.249670	-0.206989	-2.935239
H	-1.361503	1.292134	3.575162
H	-2.354974	-0.004078	2.918077
H	-1.135232	2.168733	1.127759
H	-2.693403	2.323539	1.950034
H	-3.205874	1.673632	-0.240053
H	-3.572770	0.324729	0.824733
H	-1.417329	1.535621	-1.795696
H	-2.948758	0.754199	-2.268224
H	-0.989005	0.309959	-3.813061
H	-1.851987	-1.115684	-3.269228
H	0.799351	-2.524290	-3.564301
H	-0.817418	-2.764223	-2.911472
H	1.672429	-2.716520	-1.113484
H	1.048636	-4.167972	-1.907120
H	0.183103	-4.284124	0.258110
H	-1.156411	-3.881440	-0.805817
H	-1.369631	-1.678207	3.331067
H	0.323829	-1.605273	3.780201
H	1.076557	-2.613029	1.744733
H	-0.337648	-3.553142	2.291050
H	-2.375404	-1.718188	1.563471
H	-2.581232	-3.201560	0.638477
H	-2.353899	-1.890222	-1.480911
H	-3.704672	-1.300301	-0.517531
H	0.948023	1.589352	2.389654
H	0.839207	0.739985	3.963384
H	1.789354	0.035689	2.609322
H	2.160127	-0.609567	-2.473367
H	1.190135	0.861515	-2.697031
H	1.315292	-0.337981	-4.031831
C	4.008690	0.622461	0.280819
C	5.534881	-1.691568	-0.422998
C	4.833966	-0.034579	1.340491
C	5.594310	-1.174345	0.998213
C	4.591337	0.546110	-1.093672
C	5.348231	-0.592719	-1.447419
C	4.863581	0.446898	2.660971
C	6.370454	-1.801474	1.981350
C	4.393723	1.567500	-2.039274
C	5.892231	-0.682090	-2.735429
C	5.636185	-0.189071	3.634978
C	6.392030	-1.317453	3.294080
C	4.935840	1.466579	-3.322259
C	5.686627	0.337068	-3.672029
H	3.711670	1.645156	0.557351

H	6.427149	-2.292741	-0.655697
H	4.674445	-2.386736	-0.500361
H	4.282526	1.336489	2.921442
H	6.968381	-2.678510	1.715583
H	3.813914	2.453111	-1.761741
H	6.486918	-1.559282	-3.007731
H	5.655873	0.198658	4.656899
H	7.004963	-1.817266	4.049032
H	4.778803	2.269117	-4.047872
H	6.119085	0.252435	-4.672587

Table A7.4. Cartesian coordinates (Å) for DFT energy minimized model of ^{6}TS for HAT with $[Mn^{IV}(O)(OH)(Me_2EBC)]^{+}$ and DHA.

Atom	x	y	z
Mn	0.011606	-0.011906	-0.033907
O	1.889987	-0.037767	-0.068312
O	0.180874	1.836230	-0.155753
H	3.066598	-1.055830	0.092628
H	1.109812	2.100006	-0.037902
N	-0.110474	-0.151501	2.426424
N	-0.337205	-0.229778	-2.457313
N	-2.152752	0.060256	-0.225228
N	-0.320961	-2.123849	0.314929
C	-1.377125	0.409960	2.978231
C	-2.092270	1.376939	2.033409
C	-2.905449	0.714661	0.919876
C	-2.385467	0.854012	-1.475212
C	-1.718075	0.255369	-2.716878
C	-0.096791	-1.615124	-2.949899
C	0.798850	-2.444079	-2.028842
C	0.106657	-3.053253	-0.807104
C	0.092351	-1.584312	2.763828
C	0.467085	-2.441978	1.550759
C	-1.796287	-2.252216	0.568023
C	-2.578098	-1.367858	-0.383102
C	1.033127	0.670865	2.871910
C	0.668810	0.686565	-3.032694
H	-1.163184	0.917330	3.936155
H	-2.057506	-0.420271	3.220400
H	-1.387642	2.111382	1.616408
H	-2.821932	1.944543	2.634867
H	-3.575374	1.467163	0.478824
H	-3.557347	-0.050116	1.367733
H	-1.995271	1.859889	-1.274034
H	-3.469990	0.939659	-1.663657
H	-1.723345	1.026635	-3.504362

H	-2.323111	-0.572850	-3.109271
H	0.349012	-1.572986	-3.960190
H	-1.063438	-2.127811	-3.068481
H	1.684721	-1.864010	-1.732434
H	1.174973	-3.301732	-2.610691
H	0.772888	-3.809362	-0.366377
H	-0.786636	-3.599758	-1.143578
H	-0.818999	-1.977468	3.233191
H	0.889444	-1.704004	3.516657
H	1.522544	-2.294733	1.293679
H	0.328866	-3.505070	1.814514
H	-2.008248	-1.954925	1.599270
H	-2.110280	-3.303632	0.471281
H	-2.396731	-1.685270	-1.413901
H	-3.660935	-1.472518	-0.206399
H	0.886636	1.710036	2.547179
H	1.125759	0.651553	3.974436
H	1.958940	0.299708	2.417546
H	1.675498	0.342157	-2.761685
H	0.530881	1.692871	-2.619957
H	0.580084	0.722747	-4.135158
C	4.162271	-1.488456	0.171803
C	4.027138	-4.413718	0.165390
C	4.314705	-2.247022	1.450312
C	4.255306	-3.657228	1.454556
C	4.465970	-2.247660	-1.077955
C	4.408492	-3.657661	-1.087836
C	4.512986	-1.563031	2.666181
C	4.396080	-4.345807	2.669436
C	4.796128	-1.562714	-2.263980
C	4.688831	-4.346691	-2.277797
C	4.643689	-2.256878	3.868149
C	4.583926	-3.657405	3.869920
C	5.063727	-2.256914	-3.442507
C	5.010130	-3.657667	-3.449606
H	4.708731	-0.532003	0.204731
H	4.554369	-5.380780	0.198279
H	2.953107	-4.683246	0.100175
H	4.574726	-0.470709	2.658483
H	4.361214	-5.439611	2.671447
H	4.845732	-0.469904	-2.250996
H	4.656601	-5.440563	-2.283414
H	4.800736	-1.710937	4.802074
H	4.692473	-4.211330	4.806200
H	5.320805	-1.711122	-4.354187
H	5.226012	-4.211531	-4.367217

Table A7.5. Cartesian coordinates (Å) for DFT energy minimized model of ^{4}I for HAT with $[Mn^{IV}(O)(OH)(Me_2EBC)]^+$ and DHA.

Atom	x	y	z
Mn	-0.448925	0.848005	0.016687
O	0.966487	1.754371	-0.770713
O	-0.605573	1.945218	1.513213
H	1.238596	2.583763	-0.346394
H	0.104427	2.597360	1.628660
N	1.052381	-0.833843	1.007725
N	-2.265088	2.021725	-1.147815
N	-2.223535	-0.271581	0.611618
N	-0.324620	-0.679889	-1.535832
C	0.412091	-1.628731	2.095081
C	-0.819384	-0.962306	2.710510
C	-2.104908	-1.085559	1.888308
C	-3.273023	0.780543	0.800336
C	-3.518769	1.634251	-0.447645
C	-2.299380	1.743305	-2.612511
C	-0.965558	1.258419	-3.180908
C	-0.653233	-0.222021	-2.946868
C	1.535646	-1.666997	-0.124290
C	1.103140	-1.131942	-1.491785
C	-1.263871	-1.765913	-1.106116
C	-2.539366	-1.165986	-0.548382
C	2.145103	-0.011835	1.565240
C	-1.944950	3.446284	-0.921614
H	1.156392	-1.830864	2.886559
H	0.122214	-2.611452	1.693601
H	-0.613470	0.089553	2.955593
H	-1.029650	-1.476340	3.663744
H	-2.957782	-0.811880	2.526586
H	-2.251675	-2.142553	1.620517
H	-2.928573	1.406623	1.633037
H	-4.225600	0.307250	1.097219
H	-4.086762	2.526646	-0.136561
H	-4.169419	1.096885	-1.150073
H	-2.623278	2.654038	-3.148352
H	-3.070413	0.984132	-2.812808
H	-0.137590	1.888280	-2.826145
H	-1.011367	1.378008	-4.276563
H	0.199001	-0.500680	-3.583491
H	-1.506864	-0.821349	-3.297891
H	1.179803	-2.697153	0.010501
H	2.636632	-1.731932	-0.123194
H	1.705471	-0.257331	-1.768762
H	1.265378	-1.920394	-2.247288
H	-0.779354	-2.374038	-0.336671

H	-1.484898	-2.441223	-1.948394
H	-3.040575	-0.583159	-1.326455
H	-3.243273	-1.958629	-0.245994
H	1.747938	0.645120	2.350921
H	2.935151	-0.650527	2.003794
H	2.576829	0.616522	0.777586
H	-0.983465	3.687795	-1.394740
H	-1.855609	3.639673	0.153733
H	-2.727468	4.098970	-1.352882
C	4.654007	2.960980	2.070161
C	4.428452	3.911600	-0.675997
C	5.686894	2.631014	1.141036
C	5.606128	3.083368	-0.209764
C	3.514493	3.739127	1.703681
C	3.376623	4.220067	0.366547
C	6.809812	1.852891	1.535333
C	6.630070	2.751158	-1.102784
C	2.499341	4.051477	2.649465
C	2.253043	4.983802	0.028054
C	7.814510	1.533643	0.630455
C	7.728800	1.983952	-0.697998
C	1.391869	4.813161	2.291680
C	1.263929	5.285824	0.973444
H	4.739736	2.605169	3.100388
H	4.801102	4.862248	-1.102006
H	3.945383	3.400310	-1.530002
H	6.871921	1.505433	2.570665
H	6.567801	3.100549	-2.138188
H	2.605363	3.684344	3.674128
H	2.150431	5.357062	-0.995605
H	8.670461	0.933918	0.951686
H	8.516260	1.736972	-1.414794
H	0.626671	5.049061	3.035798
H	0.399361	5.889524	0.686708

Table A7.6. Cartesian coordinates (Å) for DFT energy minimized model of ^{6}I for HAT with $[Mn^{IV}(O)(OH)(Me_2EBC)]^{+}$ and DHA.

Atom	x	y	z
Mn	-0.344320	0.437164	0.934929
O	1.185221	2.154859	1.309305
O	-1.087967	1.087192	2.480616
N	0.856823	-1.002549	2.028958
N	-1.734655	1.728166	-0.195956
N	-1.863694	-1.098192	0.262092
N	0.671824	-0.297550	-0.811970
C	3.760790	3.983344	0.759675

C	3.735094	4.119731	-2.150100
C	4.377308	2.927542	0.014810
C	4.347625	2.949628	-1.412747
C	3.080107	5.072034	0.126721
C	3.024313	5.147700	-1.297269
C	5.015876	1.837763	0.670643
C	4.929463	1.892734	-2.122023
C	2.443332	6.086102	0.893864
C	2.333759	6.206607	-1.896273
C	5.591007	0.801817	-0.056059
C	5.545262	0.823151	-1.460863
C	1.767899	7.131115	0.276547
C	1.707495	7.193321	-1.126267
H	0.875491	2.552320	2.142349
H	1.974987	2.668311	1.037366
H	-1.027348	0.568671	3.298373
H	3.843734	3.977367	1.850915
H	4.537858	4.631798	-2.716278
H	3.050615	3.748787	-2.934803
H	5.056407	1.830830	1.763930
H	4.909242	1.910059	-3.215966
H	2.493181	6.031590	1.985103
H	2.289961	6.265882	-2.988083
H	6.081276	-0.025112	0.464146
H	5.994801	0.011008	-2.037653
H	1.285244	7.903829	0.880707
H	1.175972	8.012389	-1.617431
C	0.035037	-1.974695	2.860025
C	-1.452306	-2.154246	2.521946
C	-1.845973	-2.361054	1.061989
C	-3.118911	-0.336692	0.468607
C	-3.088662	1.050269	-0.193132
C	-1.269221	1.976643	-1.610948
C	0.242198	2.090186	-1.756982
C	1.006783	0.765078	-1.844367
C	1.637186	-1.739230	0.973779
C	1.941375	-0.845180	-0.212963
C	-0.107628	-1.441549	-1.436753
C	-1.603574	-1.374175	-1.172878
C	1.828747	-0.328935	2.944058
C	-1.842275	3.049488	0.491536
H	0.097026	-1.635734	3.902347
H	0.555946	-2.944127	2.819961
H	-2.041928	-1.327188	2.944297
H	-1.770704	-3.047492	3.082326
H	-2.845519	-2.825297	1.008033
H	-1.155129	-3.064113	0.576121
H	-3.262488	-0.230740	1.550793

H	-3.984976	-0.895205	0.071049
H	-3.803856	1.688885	0.340342
H	-3.439777	0.991718	-1.231413
H	-1.750859	2.903282	-1.960049
H	-1.643134	1.174686	-2.256525
H	0.649847	2.733982	-0.966145
H	0.445676	2.615107	-2.703735
H	2.081492	0.977009	-1.764359
H	0.845939	0.321184	-2.836027
H	1.061989	-2.618899	0.667812
H	2.575583	-2.119723	1.406365
H	2.562517	0.008015	0.092489
H	2.504839	-1.406174	-0.975980
H	0.286883	-2.380041	-1.036847
H	0.086611	-1.463008	-2.517339
H	-2.070702	-0.594979	-1.780712
H	-2.071542	-2.322605	-1.485648
H	1.294355	0.323301	3.644902
H	2.385788	-1.093188	3.509143
H	2.535402	0.275284	2.366155
H	-0.877860	3.570137	0.449321
H	-2.119036	2.894947	1.539194
H	-2.602355	3.664985	-0.014931

Table A7.7. Cartesian coordinates (Å) for DFT energy minimized model of ^{4}RC for HAT with $[Mn^{IV}(OH)_2(Me_2EBC)]^{2+}$ and DHA.

Atom	x	y	z
Mn	-0.072477	0.369675	0.638463
O	1.664152	0.869299	0.705098
O	-0.777250	1.842010	1.415244
H	1.868593	1.774771	1.007291
H	-0.162237	2.547994	1.688616
N	0.155270	-0.667647	2.515993
N	-0.232363	1.216413	-1.329362
N	-2.077980	-0.316766	0.307666
N	0.415351	-1.573835	-0.099466
C	-1.156418	-1.169634	3.084894
C	-2.329176	-0.219931	2.907176
C	-2.985391	-0.193306	1.519087
C	-2.570206	0.620794	-0.763251
C	-1.548965	0.738861	-1.874487
C	0.911164	0.856507	-2.258607
C	1.680360	-0.443048	-1.994105
C	0.869616	-1.640408	-1.533710
C	1.115641	-1.821115	2.286955
C	1.513717	-2.001607	0.819582

C	-0.776133	-2.465912	0.072629
C	-2.059694	-1.724764	-0.247017
C	0.753021	0.268867	3.516547
C	-0.273820	2.708172	-1.250637
H	-0.982672	-1.351141	4.156582
H	-1.386332	-2.142924	2.642205
H	-2.041765	0.794098	3.209580
H	-3.111342	-0.542521	3.611782
H	-3.523818	0.756200	1.420998
H	-3.729945	-0.997371	1.439098
H	-2.742965	1.595631	-0.293068
H	-3.532927	0.260448	-1.159209
H	-1.904719	1.445736	-2.640490
H	-1.391866	-0.217336	-2.382944
H	1.629809	1.682720	-2.211637
H	0.485429	0.853687	-3.274367
H	2.500492	-0.253375	-1.290099
H	2.151985	-0.722726	-2.948459
H	1.465430	-2.560885	-1.638230
H	-0.020839	-1.772382	-2.161280
H	0.653196	-2.729753	2.691985
H	2.026154	-1.644226	2.871295
H	2.394099	-1.396702	0.582847
H	1.759599	-3.058198	0.627098
H	-0.786280	-2.852032	1.092940
H	-0.673901	-3.344115	-0.582776
H	-2.198171	-1.667931	-1.331762
H	-2.919656	-2.285802	0.142220
H	0.057681	1.090105	3.719834
H	0.942027	-0.283200	4.450223
H	1.698345	0.662659	3.131769
H	0.625086	3.077127	-0.746066
H	-1.162733	3.040314	-0.707499
H	-0.301496	3.110470	-2.275352
C	4.442208	3.684539	0.258688
C	2.758608	5.573648	-1.029042
C	4.227787	3.548179	-1.235481
C	3.391677	4.486026	-1.874830
C	3.173562	4.110945	0.968110
C	2.336581	5.052065	0.329350
C	4.827601	2.529110	-1.988571
C	3.171797	4.387004	-3.256015
C	2.812828	3.610046	2.228813
C	1.156689	5.468043	0.960286
C	4.609276	2.440272	-3.368289
C	3.779293	3.371156	-4.003199
C	1.630900	4.034634	2.856055
C	0.800026	4.964105	2.218432

H	5.215138	4.459141	0.436192
H	4.839493	2.753685	0.689072
H	3.502469	6.381450	-0.876286
H	1.910026	6.038025	-1.552565
H	5.471220	1.798428	-1.489777
H	2.518790	5.111305	-3.752077
H	3.470876	2.896874	2.734798
H	0.507126	6.193309	0.462162
H	5.083503	1.641511	-3.944930
H	3.599996	3.303928	-5.079673
H	1.368952	3.651954	3.846042
H	-0.120446	5.302659	2.700708

Table A7.8. Cartesian coordinates (Å) for DFT energy minimized model of ^{6}RC for HAT with $[Mn^{IV}(OH)_2(Me_2EBC)]^{2+}$ and DHA.

Atom	x	y	z
Mn	-0.494003	0.402020	0.895115
O	0.880129	1.611807	0.578540
O	-1.674400	1.621062	1.618289
N	0.457062	-0.610567	2.728798
N	-1.931364	0.979519	-1.813267
N	-2.146170	-0.969264	0.592878
N	0.618653	-1.133672	-0.092350
C	4.061595	3.190587	0.136966
C	3.199488	5.294454	-1.679756
C	4.625693	3.240606	-1.263466
C	4.204811	4.268849	-2.151609
C	3.638339	4.529313	0.696361
C	3.215812	5.556773	-0.190829
C	5.549294	2.272326	-1.712111
C	4.718329	4.303245	-3.464960
C	3.633709	4.769517	2.087222
C	2.799656	6.798120	0.334426
C	6.051435	2.313815	-3.020460
C	5.633730	3.334515	-3.901582
C	3.214829	6.005958	2.599591
C	2.795527	7.025465	1.718609
H	0.723212	2.509709	0.939133
H	3.155468	2.527529	0.122044
H	-1.315277	2.514653	1.803609
H	4.768004	2.683356	0.826282
H	3.311287	6.242077	-2.245968
H	2.177664	4.927044	-1.954156
H	5.883166	1.482463	-1.020102
H	4.398703	5.105671	-4.149059
H	3.973496	3.977236	2.773594

H	2.481075	7.596666	-0.354724
H	6.776451	1.556571	-3.356554
H	6.031552	3.375696	-4.927292
H	3.222004	6.182881	3.686175
H	2.473367	8.000584	2.115320
C	-0.548951	-1.431013	3.487716
C	-2.001442	-1.020152	3.231473
C	-2.627659	-1.545401	1.933393
C	-3.299210	-0.232545	-0.033225
C	-3.122090	0.194438	-1.506489
C	-0.934173	0.490329	-2.762957
C	0.526864	0.394146	-2.246697
C	0.967791	-0.906362	-1.559518
C	1.610110	-1.423979	2.217521
C	1.881828	-1.191117	0.726090
C	-0.199048	-2.385688	0.060454
C	-1.639750	-2.077758	-0.290108
C	0.929516	0.516565	3.575863
C	-1.954282	2.400441	-1.525730
H	-0.321942	-1.361888	4.573669
H	-0.413987	-2.496181	3.212478
H	-2.124706	0.077988	3.313812
H	-2.615593	-1.461996	4.044336
H	-3.720333	-1.373360	1.979439
H	-2.486136	-2.643416	1.880430
H	-3.489347	0.648970	0.607547
H	-4.203046	-0.878338	-0.017253
H	-4.017537	0.809409	-1.745448
H	-3.139838	-0.679658	-2.181770
H	-0.931401	1.209349	-3.613011
H	-1.276237	-0.484996	-3.158574
H	0.781844	1.271061	-1.618584
H	1.155812	0.468744	-3.156885
H	2.072081	-0.951101	-1.630169
H	0.594469	-1.778525	-2.132929
H	1.406403	-2.493324	2.413765
H	2.536700	-1.184932	2.778607
H	2.386831	-0.219597	0.570259
H	2.542896	-1.998512	0.343408
H	-0.128816	-2.737130	1.104225
H	0.205843	-3.197319	-0.579094
H	-1.695090	-1.754207	-1.343608
H	-2.282453	-2.977658	-0.200083
H	0.065143	1.135138	3.883314
H	1.442012	0.134541	4.486429
H	1.626073	1.148521	2.996135
H	-0.923418	2.794315	-1.453105
H	-2.499188	2.592335	-0.584048

H	-2.472083	2.932603	-2.359626

Table A7.9. Cartesian coordinates (Å) for DFT energy minimized model of ^{4}TS for HAT with $[Mn^{IV}(OH)_2(Me_2EBC)]^{2+}$ and DHA.

Atom	x	y	z
Mn	-0.003473	0.004533	0.056550
O	2.031378	-0.002432	0.134206
O	-0.089380	1.822793	-0.080193
N	-0.152438	0.055978	2.257775
N	0.085682	-0.254332	-2.136430
N	-2.244444	-0.176538	-0.270389
N	-0.253891	-2.082864	0.441357
C	4.585681	-0.748318	0.279339
C	4.863272	-3.620196	-0.210226
C	4.685765	-1.679057	1.421312
C	4.813795	-3.072283	1.195941
C	5.022741	-1.225323	-1.047232
C	5.165196	-2.613788	-1.293966
C	4.627321	-1.192557	2.747487
C	4.887335	-3.936948	2.297615
C	5.286572	-0.303861	-2.086583
C	5.578383	-3.040727	-2.563943
C	4.696548	-2.063615	3.829494
C	4.825941	-3.444546	3.603233
C	5.689540	-0.743735	-3.342659
C	5.836843	-2.120370	-3.582761
H	2.299370	0.924893	0.265382
H	3.362557	-0.503177	0.171572
H	0.678407	2.272599	-0.469112
H	4.925462	0.272375	0.513196
H	5.585006	-4.452011	-0.260805
H	3.885729	-4.093872	-0.436861
H	4.538924	-0.115582	2.917256
H	5.000725	-5.011319	2.126956
H	5.179151	0.766112	-1.887931
H	5.704180	-4.110163	-2.755790
H	4.659287	-1.675827	4.850368
H	4.887046	-4.134713	4.448555
H	5.898221	-0.022268	-4.136365
H	6.159913	-2.472946	-4.565694
C	-1.557702	0.375866	2.729384
C	-2.332677	1.342116	1.837014
C	-3.053087	0.726817	0.629281
C	-2.343839	0.254397	-1.696859
C	-1.334758	-0.473036	-2.574766
C	0.970312	-1.398203	-2.574296

C	1.296229	-2.483766	-1.540774
C	0.152954	-2.999986	-0.682382
C	0.300188	-1.295037	2.762374
C	0.620193	-2.288702	1.637770
C	-1.686451	-2.365971	0.792256
C	-2.634763	-1.614688	-0.124718
C	0.753135	1.118849	2.781205
C	0.593956	0.986930	-2.789273
H	-1.465648	0.796331	3.743317
H	-2.115813	-0.560757	2.840044
H	-1.683915	2.168120	1.519215
H	-3.123104	1.792752	2.458366
H	-3.447850	1.548351	0.015925
H	-3.923843	0.153156	0.981059
H	-2.166388	1.337103	-1.726556
H	-3.358617	0.067997	-2.089218
H	-1.450629	-0.135825	-3.617600
H	-1.529822	-1.550590	-2.581829
H	1.922972	-0.963717	-2.901365
H	0.505278	-1.848398	-3.465565
H	2.121176	-2.149578	-0.900345
H	1.686674	-3.341058	-2.110838
H	0.426051	-3.967311	-0.230887
H	-0.733295	-3.185625	-1.301563
H	-0.471149	-1.694820	3.432967
H	1.203013	-1.170825	3.374409
H	1.658001	-2.167825	1.308953
H	0.498447	-3.319709	2.008911
H	-1.857719	-2.085944	1.833406
H	-1.867869	-3.450440	0.730407
H	-2.647620	-2.086554	-1.113539
H	-3.661205	-1.699898	0.262119
H	0.426248	2.096671	2.409587
H	0.722708	1.117775	3.883046
H	1.779989	0.928524	2.450645
H	1.584799	1.237441	-2.389159
H	-0.096110	1.818504	-2.612421
H	0.679024	0.818549	-3.875137

Table A7.10. Cartesian coordinates (Å) for DFT energy minimized model of ^{6}TS for HAT with $[Mn^{IV}(OH)_2(Me_2EBC)]^{2+}$ and DHA.

Atom	x	y	z
Mn	0.023650	0.062691	0.061623
O	2.109154	0.231240	0.125368
O	-0.219677	1.811259	0.533586
N	-0.037513	-0.655542	2.111359
N	0.090063	0.614266	-2.058944

N	-2.194364	-0.174207	-0.303478
N	-0.039366	-2.029353	-0.332065
C	4.626390	-0.460812	0.439468
C	4.835789	-3.238751	-0.443928
C	4.596478	-1.532990	1.437702
C	4.697832	-2.896126	1.024081
C	5.138732	-0.748421	-0.903150
C	5.264109	-2.100215	-1.344638
C	4.454098	-1.238632	2.822243
C	4.653967	-3.913288	1.996903
C	5.515003	0.304666	-1.781652
C	5.770111	-2.357216	-2.632856
C	4.407186	-2.262456	3.773921
C	4.504452	-3.608120	3.360304
C	6.007576	0.030979	-3.061171
C	6.137637	-1.306753	-3.490400
H	2.304469	1.195546	0.115456
H	3.229465	-0.179499	0.245745
H	0.542071	2.303266	0.909023
H	4.861934	0.546792	0.832091
H	5.522910	-4.102680	-0.568505
H	3.853532	-3.628339	-0.811404
H	4.398843	-0.185307	3.140838
H	4.744889	-4.964810	1.680151
H	5.424922	1.347028	-1.435830
H	5.881468	-3.400732	-2.969128
H	4.305542	-2.018023	4.842365
H	4.474230	-4.418958	4.104151
H	6.300976	0.856783	-3.727327
H	6.531964	-1.529751	-4.493715
C	-1.449588	-0.663776	2.682032
C	-2.338618	0.484531	2.210130
C	-3.047494	0.282244	0.860698
C	-2.363492	0.728878	-1.487575
C	-1.321525	0.433527	-2.558802
C	1.059993	-0.209152	-2.883962
C	1.479929	-1.580960	-2.333575
C	0.392804	-2.450518	-1.716875
C	0.556138	-2.053623	2.111992
C	0.904566	-2.560114	0.704473
C	-1.432105	-2.545377	-0.087972
C	-2.467067	-1.602271	-0.680639
C	0.790085	0.244714	2.973628
C	0.460457	2.054872	-2.225559
H	-1.344636	-0.637988	3.786621
H	-1.920157	-1.633958	2.442602
H	-1.769929	1.433231	2.210634
H	-3.144994	0.604548	2.962686

H	-3.525717	1.238585	0.574379
H	-3.864996	-0.457095	0.981940
H	-2.265135	1.769253	-1.124515
H	-3.379976	0.618049	-1.925264
H	-1.487569	1.098441	-3.432308
H	-1.424722	-0.599335	-2.935765
H	1.976025	0.397660	-3.002972
H	0.616346	-0.317097	-3.895791
H	2.316862	-1.458272	-1.620630
H	1.900637	-2.144450	-3.190598
H	0.737249	-3.503835	-1.645462
H	-0.507247	-2.461381	-2.359425
H	-0.153333	-2.733447	2.619788
H	1.480448	-2.056628	2.720059
H	1.920969	-2.237136	0.417696
H	0.891059	-3.670953	0.689507
H	-1.581590	-2.659082	0.997279
H	-1.529846	-3.561449	-0.523415
H	-2.469009	-1.689465	-1.781632
H	-3.480779	-1.903993	-0.348783
H	0.320356	1.242851	3.022972
H	0.846125	-0.176311	3.998870
H	1.805417	0.334125	2.551401
H	1.455250	2.241092	-1.783011
H	-0.280399	2.697827	-1.722885
H	0.495776	2.297995	-3.308234

Table A7.11. Cartesian coordinates (Å) for DFT energy minimized model of ^{4}I for HAT with $[Mn^{IV}(OH)_2(Me_2EBC)]^{2+}$ and DHA.

Atom	x	y	z
Mn	-0.403029	0.486059	0.872748
O	1.080451	2.329553	1.132904
O	-1.233164	1.267415	2.300261
N	0.897685	-0.789763	2.050724
N	-1.638405	1.738420	-0.444888
N	-1.950333	-1.130823	0.399113
N	0.590372	-0.494246	-0.733216
C	3.911635	3.794176	0.755052
C	3.604516	4.245455	-2.106568
C	4.427899	2.818131	-0.155897
C	4.259184	2.994665	-1.562496
C	3.206772	4.958823	0.312662
C	3.011346	5.187710	-1.082561
C	5.106403	1.658849	0.313540
C	4.744500	2.013807	-2.434863
C	2.677453	5.894275	1.243737
C	2.290476	6.314266	-1.492312

C	5.587328	0.702864	-0.573095
C	5.401805	0.874431	-1.955865
C	1.969314	7.008395	0.812467
C	1.769183	7.220818	-0.562259
H	0.681732	2.846029	1.854612
H	1.964556	2.728077	0.982893
H	-0.906942	1.099612	3.198007
H	4.093662	3.662812	1.825831
H	4.357262	4.802426	-2.698427
H	2.832807	3.970311	-2.848556
H	5.253429	1.533496	1.390342
H	4.615450	2.148527	-3.513118
H	2.836694	5.721944	2.312006
H	2.138301	6.491595	-2.561452
H	6.111836	-0.178753	-0.195463
H	5.776037	0.124622	-2.657358
H	1.569034	7.718582	1.540682
H	1.210662	8.094678	-0.907388
C	0.178046	-2.058343	2.490301
C	-1.312995	-1.899552	2.784529
C	-2.255358	-2.015120	1.578653
C	-3.109565	-0.264733	0.038718
C	-2.713534	0.818419	-0.958031
C	-0.874958	2.357659	-1.593348
C	0.469681	1.725015	-1.970173
C	0.524985	0.207874	-2.064263
C	2.093473	-1.122497	1.177858
C	1.997971	-0.532050	-0.231362
C	0.048516	-1.886422	-0.890919
C	-1.467838	-1.904748	-0.784840
C	1.375415	-0.091094	3.282280
C	-2.300015	2.846377	0.307818
H	0.703097	-2.426225	3.384896
H	0.318764	-2.822157	1.718290
H	-1.507278	-0.974694	3.344580
H	-1.592751	-2.718601	3.466823
H	-3.277493	-1.797655	1.918326
H	-2.257179	-3.057903	1.227697
H	-3.486776	0.186092	0.966052
H	-3.927419	-0.863691	-0.398833
H	-3.603661	1.414167	-1.215578
H	-2.365251	0.372697	-1.895778
H	-0.682000	3.403571	-1.325158
H	-1.546465	2.372155	-2.466027
H	1.258519	2.086206	-1.296484
H	0.728078	2.121003	-2.964394
H	1.409180	-0.104983	-2.642554
H	-0.350586	-0.173519	-2.604190

H	2.207055	-2.213396	1.145447
H	3.004533	-0.733560	1.649743
H	2.380881	0.495843	-0.245309
H	2.624927	-1.119796	-0.921612
H	0.493759	-2.526085	-0.125107
H	0.374918	-2.293506	-1.860291
H	-1.909775	-1.485214	-1.694924
H	-1.813924	-2.947872	-0.734171
H	0.542146	0.055573	3.981235
H	2.130109	-0.713028	3.788080
H	1.811381	0.879089	3.020985
H	-1.542207	3.477406	0.784998
H	-2.951775	2.438393	1.085419
H	-2.895763	3.450994	-0.395016

Table A7.12. Cartesian coordinates (Å) for DFT energy minimized model of ^{6}I for HAT with $[Mn^{IV}(OH)_2(Me_2EBC)]^{2+}$ and DHA.

Atom	x	y	z
Mn	-0.406912	0.498021	0.873875
O	1.060144	2.355028	1.143399
O	-1.239768	1.262367	2.309444
N	0.907971	-0.778364	2.039243
N	-1.656620	1.750934	-0.433370
N	-1.942913	-1.126227	0.392762
N	0.589903	-0.463072	-0.741540
C	3.933931	3.789842	0.761021
C	3.622495	4.207167	-2.103863
C	4.445250	2.801087	-0.138651
C	4.268820	2.957911	-1.546823
C	3.215087	4.941000	0.306785
C	3.011314	5.149603	-1.090730
C	5.124206	1.647252	0.343279
C	4.744817	1.962674	-2.407860
C	2.676979	5.881470	1.227954
C	2.271993	6.259669	-1.511892
C	5.596996	0.677190	-0.532494
C	5.402098	0.828484	-1.916312
C	1.951438	6.979804	0.785164
C	1.741640	7.170819	-0.591220
H	0.663793	2.861554	1.873349
H	1.944371	2.753131	0.998567
H	-0.907911	1.092140	3.204696
H	4.120764	3.673213	1.832609
H	4.388664	4.765283	-2.677883
H	2.867658	3.933336	-2.862928
H	5.277399	1.537045	1.420862

H	4.609326	2.081965	-3.487137
H	2.842704	5.725246	2.297711
H	2.112895	6.420986	-2.582547
H	6.122022	-0.200057	-0.145542
H	5.769333	0.067233	-2.609127
H	1.544571	7.694064	1.505720
H	1.168771	8.031748	-0.945173
C	0.198667	-2.054989	2.471740
C	-1.292687	-1.908439	2.770843
C	-2.237941	-2.021320	1.566877
C	-3.110150	-0.266975	0.041319
C	-2.725815	0.826074	-0.949377
C	-0.900828	2.383384	-1.579527
C	0.448567	1.764347	-1.961993
C	0.515699	0.248368	-2.067258
C	2.103051	-1.095878	1.160106
C	1.999045	-0.494275	-0.243700
C	0.057830	-1.858068	-0.908020
C	-1.458035	-1.888301	-0.798066
C	1.384164	-0.084555	3.273952
C	-2.323816	2.848523	0.329266
H	0.728460	-2.425595	3.362433
H	0.342553	-2.812264	1.693850
H	-1.491525	-0.989005	3.338165
H	-1.565239	-2.734296	3.447825
H	-3.260402	-1.813214	1.911421
H	-2.233962	-3.061466	1.208202
H	-3.488217	0.174651	0.972723
H	-3.924360	-0.869728	-0.397775
H	-3.621647	1.416201	-1.200159
H	-2.376840	0.389463	-1.891119
H	-0.716111	3.429358	-1.305796
H	-1.573675	2.397120	-2.451206
H	1.234684	2.127155	-1.286023
H	0.703023	2.169449	-2.953560
H	1.400970	-0.053220	-2.649908
H	-0.358228	-0.135999	-2.607747
H	2.223795	-2.185674	1.117918
H	3.013177	-0.704843	1.632100
H	2.374028	0.536643	-0.250212
H	2.628623	-1.071212	-0.940631
H	0.509800	-2.499946	-0.148041
H	0.384715	-2.255670	-1.881156
H	-1.905480	-1.465525	-1.703935
H	-1.796295	-2.934287	-0.753962
H	0.551883	0.051550	3.976210
H	2.145026	-0.704001	3.773626
H	1.812412	0.890548	3.018054

H	-1.569055	3.481832	0.808306
H	-2.969779	2.430071	1.106137
H	-2.926532	3.453785	-0.367090

Table A7.13. Cartesian coordinates (Å) for DFT energy minimized model of ^{6}TS for desaturation from initial $[Mn^{IV}(O)(OH)(Me_2EBC)]^{+}$ and DHA complexes.

Atom	x	y	z
Mn	-0.012317	-0.003406	0.032264
O	2.015098	0.060995	0.117446
O	-0.198836	1.923001	-0.308662
H	2.251325	0.960297	-0.168063
H	0.512022	2.474875	0.050446
N	-0.271461	0.019154	2.479469
N	-0.234015	-0.594452	-2.337003
N	-2.255614	-0.420366	-0.230363
N	-0.103223	-2.233956	0.615254
C	-1.643162	0.422842	2.913202
C	-2.474262	1.131182	1.838502
C	-3.141084	0.207893	0.812213
C	-2.505319	0.210415	-1.555469
C	-1.663093	-0.374607	-2.695568
C	0.243739	-1.971326	-2.658652
C	1.186738	-2.575453	-1.615758
C	0.511418	-3.181646	-0.381050
C	0.126757	-1.326730	2.974349
C	0.678403	-2.251535	1.882336
C	-1.544781	-2.544292	0.828823
C	-2.411014	-1.899573	-0.245004
C	0.704453	1.047675	2.891903
C	0.638049	0.403313	-2.989512
H	-1.560977	1.075463	3.801213
H	-2.185970	-0.473937	3.248676
H	-1.873502	1.898148	1.326263
H	-3.295220	1.655872	2.356479
H	-3.929034	0.773776	0.290053
H	-3.658881	-0.601345	1.350800
H	-2.280339	1.278560	-1.431278
H	-3.572245	0.117716	-1.834697
H	-1.746890	0.311696	-3.554657
H	-2.097981	-1.325182	-3.033776
H	0.746025	-1.957747	-3.643422
H	-0.628114	-2.631850	-2.775758
H	1.952395	-1.843255	-1.321445
H	1.724610	-3.406052	-2.102418
H	1.251578	-3.798439	0.153345
H	-0.272833	-3.878989	-0.716609
H	-0.736622	-1.799512	3.460928
H	0.898095	-1.243308	3.758635

H	1.702820	-1.954693	1.621509
H	0.726186	-3.277972	2.294069
H	-1.852791	-2.168980	1.809951
H	-1.712764	-3.635354	0.847926
H	-2.116317	-2.284761	-1.226212
H	-3.466931	-2.188582	-0.100293
H	0.417625	2.019056	2.464944
H	0.740041	1.145234	3.994434
H	1.701524	0.786384	2.515991
H	1.678252	0.241872	-2.673621
H	0.339343	1.411921	-2.677773
H	0.585083	0.316712	-4.092172
C	4.755794	-3.505720	1.080948
C	4.588352	-0.725701	0.448199
C	4.880399	-3.111477	-0.273145
C	4.871819	-1.713842	-0.602068
C	4.682023	-2.573453	2.143788
C	4.670518	-1.168760	1.846829
C	5.055147	-4.072713	-1.314188
C	5.060716	-1.333215	-1.946371
C	4.661053	-2.998799	3.506535
C	4.664541	-0.249996	2.916292
C	5.232832	-3.667881	-2.622997
C	5.242156	-2.288028	-2.939847
C	4.650973	-2.073808	4.532297
C	4.660094	-0.689538	4.234890
H	4.766234	-4.572971	1.320399
H	5.039083	0.261926	0.264487
H	3.396960	-0.437073	0.293782
H	5.054658	-5.134798	-1.054862
H	5.063825	-0.270502	-2.203901
H	4.663315	-4.070128	3.724678
H	4.668023	0.821064	2.696288
H	5.372314	-4.408351	-3.414517
H	5.393966	-1.972291	-3.975294
H	4.642082	-2.405600	5.573391
H	4.664972	0.038679	5.050174

Table A7.14. Cartesian coordinates (Å) for DFT energy minimized model of ^{6}PC for desaturation from initial $[Mn^{IV}(O)(OH)(Me_2EBC)]^{+}$ and DHA complexes.

Atom	x	y	z
Mn	-0.124805	0.065763	0.720534
O	1.949761	1.286708	1.323615
O	0.915593	-0.929439	2.155452
H	1.983904	0.416625	1.813028

H	1.239337	-1.829043	2.005665
N	0.779763	-1.098590	-1.201874
N	-1.439194	1.345597	2.265103
N	-2.235405	-0.758571	0.378242
N	-0.808979	1.379729	-1.063828
C	0.043384	-2.384790	-1.430134
C	-0.878579	-2.838727	-0.290485
C	-2.240161	-2.135607	-0.210477
C	-2.733599	-0.782694	1.778403
C	-2.710335	0.586125	2.466625
C	-1.669780	2.753713	1.807616
C	-0.708394	3.245883	0.719908
C	-1.062935	2.818209	-0.709946
C	0.710909	-0.166306	-2.365479
C	0.356461	1.272629	-1.981432
C	-2.032191	0.724765	-1.605213
C	-2.942640	0.219301	-0.488943
C	2.191513	-1.381850	-0.862279
C	-0.636562	1.354454	3.510747
H	0.779524	-3.181356	-1.631445
H	-0.557922	-2.289757	-2.346652
H	-0.356856	-2.791056	0.680019
H	-1.088889	-3.907816	-0.462036
H	-2.934819	-2.761602	0.373644
H	-2.665014	-2.077436	-1.224292
H	-2.094896	-1.490927	2.328651
H	-3.768755	-1.172682	1.823571
H	-2.895286	0.422468	3.540889
H	-3.551962	1.195271	2.111435
H	-1.608745	3.425777	2.681458
H	-2.700741	2.840938	1.433557
H	0.330032	2.975117	0.968621
H	-0.746614	4.348714	0.728853
H	-0.507083	3.451982	-1.420177
H	-2.128038	3.033163	-0.888321
H	-0.017489	-0.551663	-3.090438
H	1.674693	-0.142312	-2.901690
H	1.207671	1.748212	-1.471010
H	0.179175	1.841753	-2.914289
H	-1.737503	-0.123420	-2.232875
H	-2.593532	1.412961	-2.261144
H	-3.271217	1.068277	0.119689
H	-3.856782	-0.221859	-0.923948
H	2.244307	-2.018190	0.030264
H	2.704469	-1.896467	-1.696032
H	2.721518	-0.445152	-0.645034
H	0.315648	1.870777	3.328766
H	-0.408327	0.324831	3.812295

H	-1.178861	1.873704	4.323207
C	3.633919	4.553234	-0.800021
C	5.125254	2.421628	0.279135
C	4.004003	4.595395	0.553876
C	4.772985	3.500423	1.109293
C	3.990725	3.479357	-1.632211
C	4.759075	2.383400	-1.078125
C	3.650037	5.690193	1.408691
C	5.152853	3.558753	2.490534
C	3.624341	3.430917	-3.017489
C	5.126437	1.297659	-1.939374
C	4.033913	5.706874	2.727129
C	4.795810	4.628574	3.274033
C	3.995324	2.370695	-3.808675
C	4.757308	1.291709	-3.262949
H	3.054935	5.381658	-1.219021
H	5.714152	1.598399	0.694903
H	2.855241	1.507551	1.046794
H	3.068410	6.515589	0.988450
H	5.735979	2.733326	2.908522
H	3.045195	4.259471	-3.434914
H	5.713480	0.474193	-1.522910
H	3.758499	6.548556	3.368218
H	5.094618	4.662580	4.325136
H	3.711583	2.347156	-4.864139
H	5.049019	0.459863	-3.909552

Table A7.15. Cartesian coordinates (Å) for DFT energy minimized model of ^{6}TS for hydroxylation from initial $[Mn^{IV}(O)(OH)(Me_2EBC)]^{+}$ and DHA complexes.

Atom	x	y	z
Mn	0.005111	0.003550	0.042115
O	2.044119	0.004376	0.033783
O	-0.035142	1.987262	0.110863
C	4.282558	-0.116432	0.056836
H	2.168541	0.958024	-0.103196
H	0.572669	2.405281	0.738837
N	-0.213655	-0.441084	2.444832
N	-0.292735	-0.066411	-2.366121
N	-2.281187	-0.235005	-0.231963
N	-0.250915	-2.302690	0.166717
C	-1.521202	0.029921	2.999948
C	-2.344798	0.930819	2.071404
C	-3.096956	0.206532	0.949428
C	-2.497007	0.682238	-1.382685
C	-1.716106	0.282230	-2.637916
C	0.127420	-1.364492	-2.974113

C	1.029994	-2.225108	-2.082985
C	0.305331	-3.050511	-1.014268
C	0.029711	-1.894517	2.647654
C	0.532376	-2.613563	1.392192
C	-1.704944	-2.571349	0.332691
C	-2.537971	-1.661244	-0.556140
C	0.895730	0.348796	3.013724
C	0.603564	1.017241	-2.816009
H	-1.333439	0.567363	3.945721
H	-2.127483	-0.848497	3.269674
H	-1.716007	1.730350	1.650230
H	-3.111569	1.418358	2.697811
H	-3.905615	0.859674	0.581783
H	-3.595705	-0.680633	1.370855
H	-2.181606	1.679365	-1.044107
H	-3.570307	0.740858	-1.648139
H	-1.782728	1.118082	-3.354613
H	-2.205604	-0.568115	-3.131903
H	0.642416	-1.163990	-3.931189
H	-0.771810	-1.942891	-3.233545
H	1.820056	-1.610910	-1.625910
H	1.538223	-2.953021	-2.738007
H	0.995778	-3.821002	-0.636031
H	-0.522927	-3.598098	-1.491653
H	-0.895101	-2.366055	3.005424
H	0.771014	-2.060788	3.448680
H	1.571671	-2.322284	1.179420
H	0.526833	-3.701455	1.597304
H	-1.987098	-2.399331	1.376431
H	-1.940279	-3.627930	0.112347
H	-2.279862	-1.849791	-1.602867
H	-3.608640	-1.911441	-0.447464
H	0.737467	1.415892	2.802652
H	0.961395	0.212679	4.110527
H	1.842145	0.045803	2.548118
H	1.642393	0.752092	-2.576122
H	0.359727	1.941146	-2.276512
H	0.516455	1.178063	-3.907849
C	4.905857	-0.074616	-2.771679
C	4.574937	-1.356189	-0.605120
C	4.912282	-1.358928	-1.984009
C	4.584239	1.143848	-0.567190
C	4.896513	1.190055	-1.952045
C	4.568888	-2.576497	0.112723
C	5.228441	-2.574116	-2.602384
C	4.573350	2.345838	0.184005
C	5.170699	2.428342	-2.544255
C	4.880331	-3.774942	-0.518975

C	5.210369	-3.773195	-1.884638
C	4.844726	3.566444	-0.423344
C	5.140928	3.608176	-1.795701
H	4.175376	-0.133644	1.134580
H	5.753553	-0.059620	-3.477188
H	4.007646	-0.073008	-3.422359
H	4.326380	-2.562216	1.178492
H	5.505389	-2.579756	-3.660594
H	4.350075	2.301737	1.253398
H	5.421081	2.468283	-3.608286
H	4.880590	-4.710818	0.045183
H	5.469870	-4.708298	-2.387866
H	4.833102	4.487258	0.164799
H	5.361896	4.562368	-2.281024

Table A7.16. Cartesian coordinates (Å) for DFT energy minimized model of ^{6}PC for hydroxylation from initial $[Mn^{IV}(O)(OH)(Me_2EBC)]^{+}$ and DHA complexes.

Atom	x	y	z
Mn	-0.553777	0.367522	0.741671
O	2.936407	1.673867	0.761883
O	0.618113	1.302954	2.042444
C	3.654801	2.874822	1.102063
H	2.071154	1.647705	1.271009
H	0.930425	0.811889	2.815977
N	0.521078	-1.779773	0.925832
N	-1.744235	2.332858	0.220008
N	-2.625277	-0.517210	0.327941
N	-0.297103	-0.263994	-1.408328
C	-0.509463	-2.786899	1.327079
C	-1.713924	-2.187336	2.070426
C	-2.886629	-1.712178	1.201746
C	-3.532141	0.618068	0.670606
C	-3.149588	1.916631	-0.040252
C	-1.107542	3.017880	-0.954958
C	0.029212	2.250539	-1.648516
C	-0.336547	0.920297	-2.322474
C	1.155158	-2.060159	-0.397552
C	1.054704	-0.883578	-1.380633
C	-1.364146	-1.246894	-1.729818
C	-2.707338	-0.841079	-1.128902
C	1.555086	-1.683912	1.979890
C	-1.699549	3.207003	1.415781
H	-0.031812	-3.556625	1.958234
H	-0.866888	-3.311016	0.430118
H	-1.382851	-1.380753	2.751787
H	-2.125158	-2.966260	2.733630

H	-3.731808	-1.474375	1.865494
H	-3.220889	-2.547535	0.566181
H	-3.483506	0.759296	1.761064
H	-4.581288	0.372835	0.422183
H	-3.854045	2.706210	0.277871
H	-3.289625	1.811966	-1.122528
H	-0.693566	3.976168	-0.608703
H	-1.886528	3.266880	-1.694874
H	0.876135	2.110846	-0.953257
H	0.416289	2.924911	-2.430347
H	0.339651	0.730389	-3.174124
H	-1.348663	0.991543	-2.746434
H	0.706031	-2.963515	-0.831169
H	2.222953	-2.294763	-0.266627
H	1.769763	-0.094802	-1.095313
H	1.346803	-1.239314	-2.386958
H	-1.072365	-2.226120	-1.340080
H	-1.472586	-1.371956	-2.822082
H	-3.085057	0.036985	-1.662769
H	-3.442593	-1.643744	-1.304151
H	1.087584	-1.439209	2.944429
H	2.092971	-2.643885	2.091760
H	2.275140	-0.893008	1.731741
H	-0.657240	3.420045	1.678302
H	-2.161923	2.694797	2.271717
H	-2.247633	4.150026	1.232805
C	4.557404	3.372729	-1.583294
C	5.111919	2.644936	0.763803
C	5.547052	2.859987	-0.558569
C	3.102197	4.071803	0.349906
C	3.521029	4.294188	-0.977112
C	6.017738	2.185132	1.729697
C	6.885402	2.600814	-0.889455
C	2.167337	4.934821	0.937944
C	2.980903	5.371047	-1.694479
C	7.350822	1.929186	1.392220
C	7.783775	2.134682	0.076770
C	1.632432	6.007540	0.215684
C	2.038103	6.222210	-1.106439
H	3.557418	3.053537	2.182113
H	5.082168	3.875199	-2.409884
H	4.039043	2.505262	-2.035235
H	5.673323	2.026507	2.755899
H	7.229670	2.774317	-1.913474
H	1.857890	4.764028	1.973464
H	3.311352	5.554654	-2.721672
H	8.050862	1.573942	2.153307
H	8.825150	1.941749	-0.195569

H	0.907392	6.677706	0.685456
H	1.631324	7.062267	-1.676186

Table A7.17. Cartesian coordinates (Å) for DFT energy minimized model of ^{6}TS for desaturation from initial $[Mn^{IV}(OH)_2(Me_2EBC)]^{2+}$ and DHA complexes.

Atom	x	y	z
Mn	-0.278449	0.480849	0.196140
O	0.641502	2.054609	0.987915
O	0.798765	2.073923	3.790567
N	1.287136	-1.055956	1.035444
N	-2.066120	1.783689	-0.768917
N	-2.017573	-0.920785	0.236886
N	0.133178	-0.724477	-1.711289
C	4.728991	4.518927	1.435424
C	2.986139	3.301001	-0.462149
C	5.156971	3.327959	0.807018
C	4.336195	2.737977	-0.210650
C	3.552161	5.211072	1.080924
C	2.714471	4.668210	0.053125
C	6.412789	2.740336	1.142041
C	4.819696	1.613795	-0.893850
C	3.203554	6.443188	1.710793
C	1.576016	5.381722	-0.335549
C	6.857093	1.619009	0.464368
C	6.064526	1.068511	-0.566601
C	2.065621	7.119828	1.317701
C	1.261684	6.592643	0.281126
H	0.905040	2.063564	2.807157
H	0.096611	2.845372	1.096690
H	0.971400	2.994250	4.039456
H	5.364712	4.946314	2.217648
H	2.648587	3.160023	-1.500428
H	2.234156	2.716413	0.164922
H	7.018158	3.196157	1.929159
H	4.226252	1.165945	-1.695850
H	3.849755	6.838104	2.499060
H	0.935734	4.990337	-1.129819
H	7.818459	1.163211	0.716552
H	6.431720	0.197487	-1.119738
H	1.784976	8.060257	1.796264
H	0.376029	7.143039	-0.044955
C	0.669314	-1.767547	2.204685
C	-0.840379	-1.556177	2.402792
C	-1.775126	-1.985836	1.259892
C	-3.143725	-0.033412	0.629803
C	-3.349181	1.147494	-0.335889

C	-1.846856	1.773344	-2.250766
C	-0.370311	1.616261	-2.659794
C	0.120974	0.181786	-2.908699
C	1.580218	-1.977992	-0.094403
C	1.490124	-1.287814	-1.454600
C	-0.880780	-1.821302	-1.805708
C	-2.205782	-1.482527	-1.128354
C	2.536523	-0.382998	1.451220
C	-1.998070	3.183312	-0.299295
H	1.172643	-1.416932	3.114699
H	0.886879	-2.845481	2.127782
H	-1.038853	-0.506046	2.694315
H	-1.114479	-2.143542	3.295635
H	-2.746064	-2.313506	1.670439
H	-1.349941	-2.860127	0.746208
H	-2.922181	0.348352	1.639972
H	-4.087868	-0.606700	0.700955
H	-3.979046	1.887899	0.179367
H	-3.923040	0.832891	-1.218406
H	-2.256561	2.706838	-2.674161
H	-2.432975	0.960878	-2.698320
H	0.281244	2.121630	-1.924053
H	-0.207705	2.159470	-3.604783
H	1.143757	0.236542	-3.308864
H	-0.492830	-0.279317	-3.697682
H	0.871898	-2.813689	-0.051078
H	2.583774	-2.426748	0.021008
H	2.207575	-0.457980	-1.501318
H	1.776251	-2.001413	-2.245327
H	-0.464143	-2.728280	-1.359972
H	-1.077020	-2.067303	-2.860703
H	-2.740960	-0.746554	-1.733899
H	-2.846829	-2.380949	-1.105093
H	2.329019	0.386315	2.199119
H	3.257930	-1.112261	1.862139
H	2.996293	0.111095	0.587520
H	-1.047734	3.631535	-0.624547
H	-2.065970	3.231254	0.797284
H	-2.819170	3.788357	-0.729548

Table A7.18. Cartesian coordinates (Å) for DFT energy minimized model of ^{6}PC for desaturation from initial $[Mn^{IV}(OH)_2(Me_2EBC)]^{2+}$ and DHA complexes.

Atom	x	y	z
Mn	-0.486092	0.653817	1.004804
O	0.576255	2.550956	1.659945
O	-1.609120	1.578195	2.876706

N	0.759207	-0.689883	2.418033
N	-1.871428	1.742013	-0.492161
N	-1.831212	-1.054178	0.320158
N	0.823685	-0.350475	-0.587618
C	4.602287	3.366238	0.097188
C	3.607665	4.297551	-2.370188
C	5.192409	2.911000	-1.093963
C	4.680236	3.389734	-2.361720
C	3.529822	4.273339	0.087274
C	3.018509	4.753441	-1.179989
C	6.291279	1.990172	-1.097925
C	5.291153	2.919373	-3.570364
C	2.916710	4.750293	1.295903
C	1.922313	5.678922	-1.176514
C	6.848135	1.563759	-2.279098
C	6.341139	2.033739	-3.530162
C	1.865214	5.640203	1.253648
C	1.360516	6.110771	0.000815
H	-1.585325	1.222658	3.783014
H	0.078520	2.872896	2.433304
H	-2.429514	2.102829	2.859135
H	4.993854	3.005875	1.053739
H	3.221535	4.663973	-3.326419
H	1.209716	3.262976	1.433504
H	6.681884	1.632017	-0.140813
H	4.903464	3.287031	-4.525029
H	3.316163	4.405889	2.254805
H	1.537557	6.039454	-2.135015
H	7.687457	0.863393	-2.268521
H	6.801385	1.680636	-4.456983
H	1.413461	6.002626	2.181224
H	0.526910	6.817446	-0.012392
C	-0.099464	-1.688598	3.158913
C	-1.571308	-1.816382	2.734345
C	-1.873057	-2.198799	1.283697
C	-3.137813	-0.354845	0.248926
C	-3.117947	0.908167	-0.628448
C	-1.146351	1.891381	-1.807861
C	0.386642	1.920853	-1.720177
C	1.092047	0.560198	-1.752708
C	1.748823	-1.369972	1.518115
C	2.047792	-0.610842	0.224413
C	0.169464	-1.620291	-1.025242
C	-1.349991	-1.510059	-1.011379
C	1.508665	0.137125	3.399706
C	-2.209941	3.098687	0.009564
H	-0.096464	-1.402884	4.220219
H	0.388204	-2.675367	3.109536

H	-2.130748	-0.906290	3.003760
H	-1.993388	-2.604415	3.378800
H	-2.866731	-2.675190	1.221087
H	-1.149904	-2.954224	0.947736
H	-3.419401	-0.088219	1.278812
H	-3.926508	-1.028093	-0.134942
H	-3.995959	1.509762	-0.352203
H	-3.255429	0.636996	-1.684021
H	-1.506372	2.814263	-2.292462
H	-1.447175	1.069938	-2.470130
H	0.714872	2.515423	-0.853606
H	0.757777	2.473084	-2.598487
H	2.178346	0.723852	-1.833083
H	0.794297	0.034268	-2.671968
H	1.372658	-2.372166	1.285972
H	2.699360	-1.525339	2.055332
H	2.508774	0.363294	0.451975
H	2.790989	-1.191080	-0.352699
H	0.477277	-2.430581	-0.356969
H	0.515684	-1.909514	-2.030564
H	-1.678584	-0.798947	-1.776016
H	-1.798002	-2.481648	-1.283175
H	0.814912	0.730538	4.010644
H	2.110472	-0.502870	4.068785
H	2.177917	0.828281	2.872792
H	-1.294860	3.689602	0.143028
H	-2.726038	3.036110	0.976620
H	-2.872508	3.625434	-0.698806

Table A7.19. Cartesian coordinates (Å) for DFT energy minimized model of ^{6}TS for hydroxylation from initial $[Mn^{IV}(OH)_2(Me_2EBC)]^{2+}$ and DHA complexes.

Atom	x	y	z
Mn	0.085411	0.672351	0.178287
O	1.397034	1.876558	1.336133
O	0.188825	2.232894	3.940007
N	1.447068	-1.268863	0.445734
N	-1.389002	2.370901	-0.347368
N	-1.820474	-0.350108	0.813506
N	-0.333984	-0.491562	-1.700443
C	2.888436	3.220698	1.373970
C	3.723056	3.163710	-1.384948
C	4.033653	2.404840	1.010898
C	4.442304	2.342847	-0.344587
C	2.510559	4.322017	0.512654
C	2.943815	4.330892	-0.837071
C	4.735941	1.680772	1.999574
C	5.516575	1.510605	-0.684810

C	1.813202	5.432609	1.041622
C	2.647396	5.445065	-1.631399
C	5.816118	0.878517	1.647012
C	6.195625	0.784432	0.298701
C	1.540347	6.536794	0.242643
C	1.954996	6.537057	-1.098782
H	0.519875	2.293714	3.018711
H	1.934846	1.214285	1.800944
H	-0.204648	3.101746	4.123003
H	2.710612	3.363427	2.440466
H	4.435092	3.509640	-2.150133
H	3.025479	2.501869	-1.938402
H	4.422212	1.758279	3.044463
H	5.841936	1.442500	-1.726342
H	1.499674	5.421677	2.088686
H	2.989101	5.472271	-2.669536
H	6.362402	0.322763	2.411897
H	7.038455	0.149640	0.013551
H	1.011985	7.397960	0.657366
H	1.748185	7.403582	-1.731751
C	0.723054	-2.184355	1.396316
C	-0.144387	-1.448829	2.427562
C	-1.605881	-1.211630	2.029192
C	-2.706404	0.812260	1.125918
C	-2.741664	1.827848	-0.012370
C	-1.282038	2.765620	-1.795103
C	-0.445694	1.843592	-2.691361
C	-0.868478	0.374888	-2.800672
C	1.629853	-1.864541	-0.920430
C	1.009762	-1.028725	-2.046835
C	-1.290869	-1.578795	-1.344989
C	-2.361233	-1.114643	-0.358921
C	2.775612	-0.964321	1.021048
C	-1.134514	3.550273	0.511854
H	1.467718	-2.813375	1.911638
H	0.094752	-2.872511	0.817737
H	0.332899	-0.499467	2.733778
H	-0.171064	-2.052525	3.348585
H	-2.122338	-0.739886	2.877248
H	-2.098063	-2.182179	1.863837
H	-2.322945	1.281957	2.044445
H	-3.735544	0.472365	1.340006
H	-3.420308	2.650635	0.269132
H	-3.169942	1.381390	-0.916306
H	-0.823892	3.763871	-1.838025
H	-2.295946	2.873665	-2.213425
H	0.622496	1.903889	-2.407704
H	-0.492786	2.283378	-3.700701

H	-0.536086	-0.042286	-3.766041
H	-1.965203	0.304780	-2.794570
H	1.223780	-2.884364	-0.924750
H	2.701710	-1.971375	-1.141902
H	1.657370	-0.168406	-2.282685
H	0.967385	-1.646540	-2.962403
H	-0.731279	-2.413129	-0.915410
H	-1.779975	-1.977801	-2.249896
H	-3.083510	-0.482856	-0.885721
H	-2.927525	-1.990749	-0.007328
H	2.668939	-0.558558	2.037487
H	3.388996	-1.878570	1.101688
H	3.304486	-0.236616	0.394101
H	-0.115252	3.914568	0.353525
H	-1.243882	3.272989	1.568867
H	-1.847440	4.362013	0.285483

Table A7.20. Cartesian coordinates (Å) for DFT energy minimized model of ^{6}PC for hydroxylation from initial $[Mn^{IV}(OH)_2(Me_2EBC)]^{2+}$ and DHA complexes.

Atom	x	y	z
Mn	-0.171170	0.658890	0.652579
O	1.744587	2.397814	0.691935
O	0.795228	0.796532	2.782028
N	1.208040	-1.040888	-0.044874
N	-1.657569	2.309156	1.148406
N	-2.021053	-0.677112	0.833631
N	-0.779124	0.501108	-1.499604
C	2.756661	3.463238	0.470129
C	4.641709	1.939661	-1.123990
C	4.063522	3.020385	1.086913
C	4.952188	2.230743	0.329175
C	2.885081	3.752889	-1.004413
C	3.802962	3.014893	-1.778630
C	4.367419	3.340646	2.419345
C	6.118135	1.746295	0.939785
C	2.145017	4.788114	-1.597405
C	3.948826	3.323533	-3.139149
C	5.538156	2.861363	3.014030
C	6.407906	2.052458	2.273508
C	2.300857	5.091735	-2.951932
C	3.206440	4.354156	-3.723329
H	0.345999	1.198932	3.547472
H	1.826365	2.149225	1.632143
H	1.391819	0.139637	3.184708
H	2.378960	4.359234	0.986657
H	5.575203	1.787648	-1.686447

H	4.105010	0.974271	-1.196508
H	3.680562	3.971062	2.993528
H	6.815607	1.135203	0.359268
H	1.452211	5.372596	-0.985270
H	4.669928	2.764750	-3.742774
H	5.777265	3.126839	4.047128
H	7.323049	1.668677	2.732388
H	1.727538	5.906167	-3.401820
H	3.355144	4.599887	-4.778427
C	0.618956	-2.374133	0.347731
C	-0.219946	-2.343337	1.630358
C	-1.707913	-2.012277	1.456653
C	-2.871403	0.165599	1.726943
C	-2.978679	1.605594	1.232857
C	-1.679839	3.369588	0.074523
C	-1.040243	3.020415	-1.280500
C	-1.462120	1.736015	-1.997769
C	1.320905	-0.893620	-1.539962
C	0.560201	0.312995	-2.115377
C	-1.653529	-0.691240	-1.665554
C	-2.653612	-0.815134	-0.518161
C	2.547225	-0.920274	0.582644
C	-1.377240	2.950035	2.460166
H	1.445377	-3.095006	0.458643
H	0.000429	-2.746349	-0.478094
H	0.240699	-1.681688	2.381463
H	-0.182868	-3.348207	2.081458
H	-2.191738	-2.057048	2.443181
H	-2.177139	-2.797877	0.845183
H	-2.426011	0.140321	2.732559
H	-3.888921	-0.255576	1.814179
H	-3.657535	2.161861	1.900617
H	-3.445079	1.633004	0.242420
H	-1.135488	4.239237	0.467116
H	-2.723783	3.696672	-0.067229
H	0.055427	3.041635	-1.186575
H	-1.287117	3.863242	-1.946580
H	-1.262475	1.833461	-3.079245
H	-2.546353	1.586425	-1.898247
H	0.980008	-1.823149	-2.013363
H	2.377729	-0.788476	-1.825009
H	1.132743	1.236230	-1.938811
H	0.480297	0.187782	-3.211009
H	-1.028681	-1.587178	-1.713230
H	-2.195395	-0.646904	-2.625925
H	-3.426425	-0.046622	-0.626986
H	-3.178093	-1.780031	-0.596924
H	2.476254	-1.121013	1.660687

H	3.250918	-1.652589	0.152065
H	2.943780	0.091421	0.438069
H	-0.365218	3.375769	2.465180
H	-1.469865	2.212379	3.269754
H	-2.099940	3.757640	2.666072